University of Rochester
Laboratory for Laser Energetics

DOE/SF/19460-275
January 1999

LLE 1998 Annual Report

October 1997 – September 1998

UR LLE

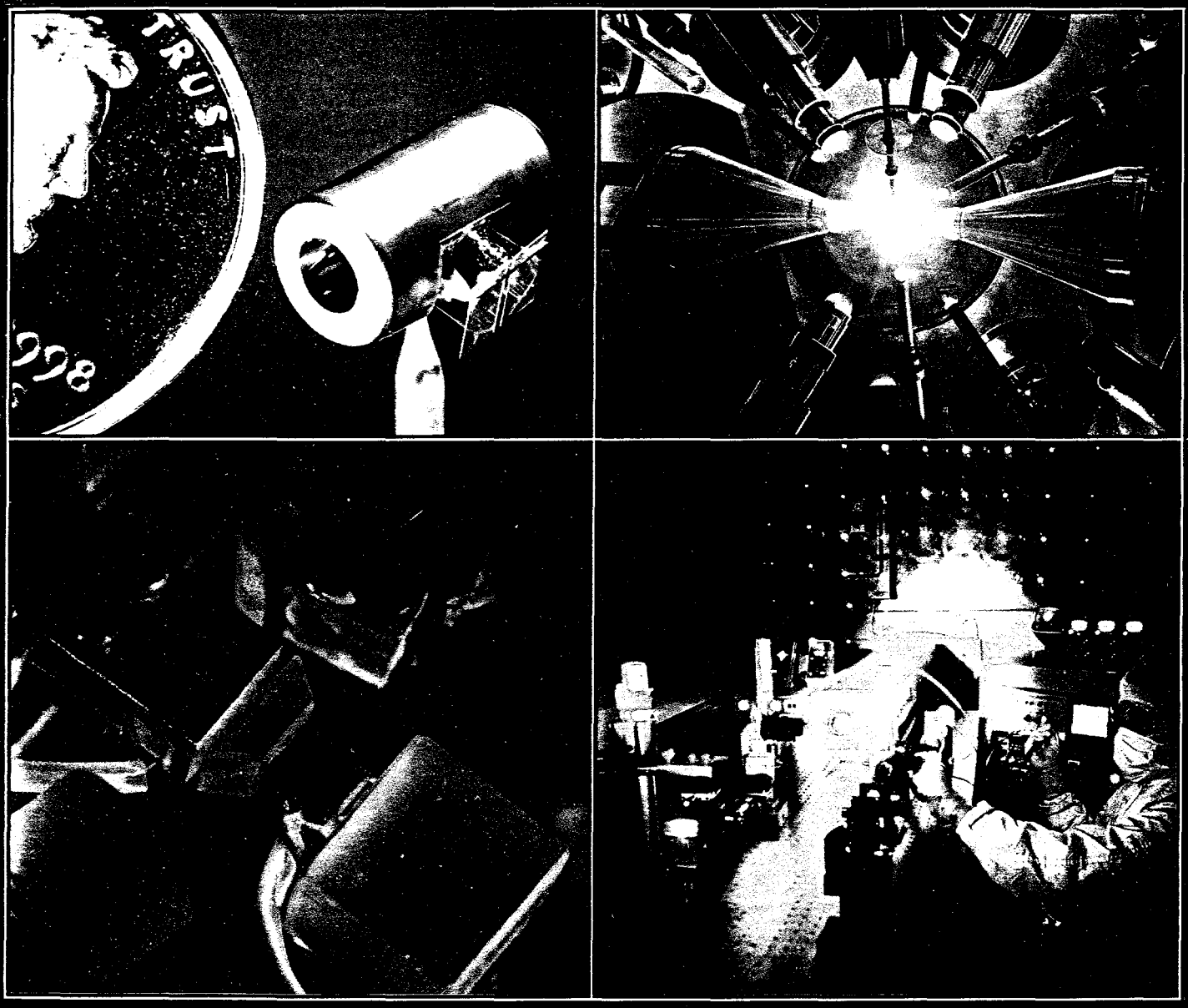

DISCLAIMER

University of Rochester
Laboratory for Laser Energetics

DOE/SF/19460-275
January 1999

LLE 1998 Annual Report

UR LLE

October 1997 – September 1998

Inertial Fusion Program and National Laser Users' Facility Program

Contents

Executive Summary

The fiscal year ending September 1998 (FY98) concluded the first year of the cooperative agreement (DE-FC03-92SF19460) five-year renewal with the U. S. Department of Energy (DOE). This report summarizes research at the Laboratory for Laser Energetics (LLE), the operation of the National Laser Users' Facility (NLUF), and programs involving the education of high school, undergraduate, and graduate students for FY98.

Progress in Laser Fusion

To evaluate the direct-drive approach to laser-driven inertial confinement fusion, we are planning to use the 30-kJ, 351-nm, 60-beam OMEGA laser to drive cryogenic solid DT-shell capsules that are hydrodynamically equivalent to the ignition/gain capsules planned for use on the National Ignition Facility. This year, in preparation for the cryogenic experiments, we conducted measurements of core and pusher conditions in surrogate capsule implosions (pp. 100–112). Measurements of the effects of imprint and unstable growth at the ablation surface have been carried out using the burnthrough technique, and target behavior during the deceleration phase has been investigated using Ti-doped shells surrounding an Ar-doped D_2 fill gas.

Other experiments have characterized an x-ray radiographic system for measuring mass modulations in planar laser-driven targets. Using the known sensitivity, resolution, and noise characteristics of this system, we have formulated a Wiener filter that reduces noise, compensates for detector resolution, and facilitates measurement of perturbations imprinted on targets by laser nonuniformity (pp. 242–250).

A soft x-ray microscope ($E < 3$ keV) with high spatial resolution (~3 μm) has been characterized and used for initial experiments on the OMEGA laser system (pp. 92–99). We report on details of the testing, calibration, and initial use of this microscope for studying the hydrodynamic stability of directly driven planar foils.

To increase the uniformity of drive on fusion targets, we have expanded the pulse-shape bandwidth of OMEGA's driver line from approximately 3 GHz to over 5 GHz by using a novel scheme that takes into account the transient carrier dynamics of the photoconductive switches used in the pulse-shaping subsystem (pp. 225–231). In complementary work to improve uniformity, we have performed calculations of near-field intensity modulations in high-intensity laser beams due to self- and cross-phase modulation between the orthogonally polarized laser beams emerging from KDP wedges placed into the OMEGA laser beamlines (pp. 232–241). Such wedges produce a reduction in the far-field speckle nonuniformity by polarization smoothing and are not expected to be a significant source of intensity modulation under expected operating conditions.

Based on previous extensive theoretical work, our theorists describe a simple procedure (pp. 20–31) to determine the Froude number Fr, the effective power index for thermal conduction ν, and the ablation-front thickness L_0 of laser-accelerated ablation fronts. These parameters are determined by fitting the density and pressure profiles obtained from one-dimensional numerical simulations with analytic isobaric profiles. These quantities are then used to calculate the growth rate of the ablative Rayleigh–Taylor instability using the theory developed by V. N. Goncharov *et al.*, Phys. Plasmas **3**, 4665 (1996).

The use of systematic perturbation methods to derive formulas for the Landau damping rates of electron-plasma and ion-acoustic waves produced formulas far more accurate than the standard formulas found in textbooks (pp. 113–119).

The simultaneous forward and backward stimulated Brillouin scattering (SBS) of crossed laser beams is described in detail beginning on p. 189. We have obtained new analytical solutions for the linearized equations governing the transient

phase of the instability and the nonlinear equations governing the steady state. These solutions show that backward SBS dominates the initial evolution of the instability, whereas forward SBS dominates the steady state.

Calculations of the damping of localized plasma waves have been made using a new physical approach that is linear in the wave field and avoids introducing complex particle velocities (pp. 200–211). The simplicity of this approach is obtained by invoking the time-reversal invariance of the Vlasov equation. This greatly simplifies the calculation of Landau damping of plasma waves in an infinite medium and "transit-time damping" of plasma waves localized in general geometries.

We have found a plausible explanation for observations of stimulated Raman scattering (SRS) that have been at odds with theoretical predictions (pp. 251–263). By calculating the collisionless damping rate of plasma waves confined within a small cylinder, we have found that plasma waves confined within small-radius filaments damp much more slowly than plane plasma waves in a homogeneous plasma. Predictions using these corrected rates, rather than rates obtained using the usual Landau theory for plane waves in homogeneous plasmas, provide a viable explanation of the anomalous SRS observations.

The indirect-drive approach to inertial confinement fusion involves laser beams that overlap as they enter the hohlraum. Because a power transfer between the beams adversely affects the implosion symmetry, it is important to understand the mechanisms that make such a power transfer possible. In a previous article [LLE Review **66**, 73 (1996)] we described a two-dimensional analysis of the power transfer between beams with top-hat intensity profiles in a homogeneous plasma. In the article beginning on p. 32, the calculations of the power transfer between crossed laser beams made possible by an ion-acoustic wave are extended to include three dimensions and arbitrary intensity profiles.

Diagnostics Development

A nuclear diagnostic for measuring the areal density of ICF targets is described in the article beginning on p. 15. This diagnostic is obtained by the addition of ^{3}He to the fuel and is based on the energy loss of the 14.7-MeV D-^{3}He proton in the target. This diagnostic will extend our ability to measure areal density to the high-density regime expected for cryogenic DD targets on OMEGA.

Development of the sweep deflection circuitry for the OMEGA multichannel streak camera, aided by a computer simulation model, is reported (pp. 6–14). Good agreement between the model predictions and measurements shows that using the model is an efficient means for conducting initial design, performance optimization, and correction of performance deficiencies for these cameras.

By placing a pinhole array in front of a flat-crystal x-ray spectrometer, we have developed a diagnostic technique with the ability to obtain simultaneously a large number of two-dimensional images over a wide range of photon energies at a high degree of spectral resolution. The article (pp. 182–188) presents images of Kα fluorescence pumped by core radiation, delineating the compressed, cold shell, and pumped by suprathermal electrons, showing that ~1% of the laser energy preheats the target.

Laser and Optical Technology

We have developed a new electrical waveform generator based on aperture-coupled striplines (pp. 1–5). The waveform generator is capable of producing shaped electrical waveforms with 50- to 100-ps structure over a 1- to 5-ns envelope at voltage levels suitable for OMEGA pulse-shaping applications. The design is a significant simplification over existing technology and offers many performance enhancements.

In an effort to identify an inexpensive shielding material to protect valuable laser optics from various forms of debris, we have screened perfluorinated polymer pellicles from various vendors. The optical-performance results of these tests (pp. 38–44) yielded the highest 351-nm-laser–damage thresholds ever recorded at LLE for 0.6-ns pulses.

Subsurface damage induced by microgrinding of glass is an important feature of the resulting surface that must be removed in any subsequent finishing operation. Analysis shows (pp. 45–49) how the depth of subsurface damage can be estimated from the measured surface roughness, how it can be correlated to the near-surface mechanical properties of the glass, and how ground-surface quality depends on the type of grinding process employed.

Polishing abrasives that have been bound in a solid matrix can offer several potential advantages over loose-abrasive processes for finishing optics. Research has established the various criteria for a successful bound-abrasive polisher, and we report results for six compositions used on a CNC generating machine to polish optical glass (pp. 50–58).

Our in-house development, scale-up, and manufacture of 60 continuous distributed phase plates with high laser-damage resistance (pp. 71–91) has been a great success. Inert ion beams were used to etch a continuously varying pattern into the surface of fused silica to form these devices.

High efficiency and good beam quality are potential advantages of the end-pumped solid-state lasers over the side-pumped ones. We describe the successful use of a transport fiber to end-pump a Nd:YLF laser, overcoming issues related to the astigmatic nature of the high-power, quasi-cw diode laser pumping source (pp. 120–124).

Using a single-beam *Z*-scan technique, we have determined values for the self-phase modulation coefficients in a KDP crystal at wavelengths of 1.053 μm, 0.527 μm, and 0.351 μm. The cross-phase modulation coefficients between 1.053 and 0.527 μm, measured by a two-color *Z*-scan, are also given (pp. 125–130).

A new model relates brittle material mechanical properties and grinding abrasive properties to the value of surface roughness that results from the cold working process (pp. 131–138). Surface roughness as measured by white-light interferometry can be used to establish an upper bound to the level of subsurface damage induced by grinding.

A series of experiments demonstrate a new scheme for converting the infrared light of OMEGA to the third harmonic in the ultraviolet over a bandwidth that is significantly wider than has been previously attainable (pp. 151–158). This innovative scheme, employing a second tripling crystal in addition to the doubler-tripler pair currently in use, was proposed by a scientist at Lawrence Livermore National Laboratory and adapted to the OMEGA system. Wider bandwidths on OMEGA will allow the use of broadband beam smoothing with faster smoothing times than have been employed until now.

We have made ultrahigh-dynamic-range measurements of high-contrast pulses using a second-order autocorrelator (pp. 159–170). This device is capable of measurements with dynamic ranges of up to $\sim 10^{12}$ at a time resolution of ~50 fs, the highest dynamic range yet achieved for measurements with this degree of time resolution.

During the year we developed a highly stable, diode-pumped Nd:YLF master oscillator for the OMEGA laser system (pp. 213–218). This new master oscillator produces either single-frequency *Q*-switched pulses or cw radiation for the OMEGA pulse-shaping system. The switchover between these two regimes requires no laser realignment. The new master oscillator is completely computer controlled and has been operating continuously in OMEGA for six months without operator intervention.

A negative-feedback–controlled regenerative amplifier has been part of the OMEGA laser system for the past two years. The negative feedback makes the energy output of the regenerative amplifier stable and insensitive to the variations in pulse energy. This amplifier's long-term output energy stability is the highest ever demonstrated for a millijoule-level laser system, either flashlamp pumped or diode pumped (pp. 219–224).

Advanced Technology

Despite angle dependence and polarization selectivity, the color of cholesteric liquid crystal (CLC) polysiloxane films can be quantified by standard colorimetry. A new fractured form of the film called "flakes" makes it possible to use the Center of Gravity Color Mixing Principle to predict the chromaticity of CLC color mixtures. Our results show how a complete color gamut can be produced by layering CLC films, mixing CLC's physicochemically, and mixing CLC flakes (pp. 59–70).

The optical and physical properties of polymer liquid crystal flakes, alone and embedded in carriers, have been explored (pp. 139–149). These materials have applications as color coating, polarizing paints, and inks.

Results from two ion-beam analysis techniques—Rutherford backscattering spectroscopy and nuclear resonance analysis—have been used to provide an accurate method for determining the complete elemental composition of capsules and target materials used at LLE (pp. 171–181). These new sources of information are more expansive than other analytical techniques in use, and the data are needed for interpreting the results of our experiments.

Laser Facility Report

We report on substantial improvements made to the OMEGA facility this year. The operations time has been extended to meet increased demand for shots, both by LLE scientists and by scientists from the Lawrence Livermore National Laboratory and the Los Alamos National Laboratory. Improvements in the laser system (including system modifications to increase the uniformity of drive on the target) and the experimental area are described in the article beginning on p. 266. The extended shift operations produced an increase in

the average number of shots/shot day from 5.2 to 9.8, with an increase in the average number of shots/week from 17 to 26. During the FY, 882 total target shots were taken.

National Laser Users' Facility (NLUF)

Beginning on p. 268, we summarize progress and experiments conducted by others as part of the National Laser Users' Facility. Since 1979, we have operated OMEGA for users under this program. During FY98, in addition to NLUF-supported programs, scientists from the National laboratories have conducted stockpile stewardship and indirect-drive laser experiments on OMEGA.

Fifteen proposals were submitted to NLUF for the next year (FY99). The table on p. 269 summarizes the principal investigators along with their affiliation and the proposed experimental programs that were approved by the Department of Energy Technical Evaluation Panel.

Education at LLE

As the only university major participant in the National ICF Program, education continues to be a most important mission for the Laboratory. Graduate students play a significant role in LLE's research activities and are participating in research using the world's most powerful ultraviolet laser for fusion research on OMEGA. Fourteen faculty from five departments collaborate with LLE's scientists and engineers. Presently 34 graduate students are pursuing Ph.D. degrees at the Laboratory. The research interests vary widely and include theoretical and experimental plasma physics, laser–matter interaction physics, high-energy-density physics, x-ray and atomic physics, nuclear fusion, ultrafast optoelectronics, high-power-laser development and applications, nonlinear optics, optical materials and optical fabrication technology, and target fabrication. Technological developments from ongoing Ph.D. research will continue to play an important role on OMEGA. One of our recent Ph.D. recipients, E. Korenic, was awarded the Glenn H. Brown prize from the International Liquid Crystal Society for one of the four best theses of liquid crystals in the world since 1994.

One hundred eighteen University of Rochester students have earned Ph.D. degrees at LLE since its founding. An additional 48 graduate students were funded by NLUF grants. The most recent University of Rochester Ph.D. graduates and their thesis titles are

V. Goncharov	*Self-Consistent Stability Analysis of Ablation Fronts in Inertial Confinement Fusion*
W. Grice	*Interference and Indistinguishability in Ultrafast Spontaneous Parametric Downconversion*
E. Turano	*Spatiotemporal Evolution of Stimulated Raman Scattering Driven by Short Laser Pulses*
B. Ucer	*Ultrafast Carrier Dynamics in Thin Porous Silicon Films*

Approximately 50 University of Rochester undergraduate students participated in work or research projects at LLE this past year. Student projects include operational maintenance of the OMEGA laser system, work in the materials and optical-thin-film coating laboratories, programming, image processing, and diagnostic development. This is a unique opportunity for these students, many of whom will go on to pursue a higher degree in the area in which they have participated at the Laboratory.

LLE continues to run a Summer High School Student Research Program (pp. 264–265) where this year eleven high school juniors spent eight weeks performing individual research projects. Each student is individually supervised by a staff scientist or an engineer. At the conclusion of the program, the students make final oral and written presentations on their work. The written reports are published as an LLE report.

In 1998, LLE presented its second Inspirational Science Teacher Award to Mr. David Crane of Greece Arcadia High School. Alumni of our Summer High School Research Program were asked to nominate teachers who had a major role in exciting their interest in science, mathematics, and/or technology. The award, which includes a $1000 cash prize, was presented at the High School Student Summer Research Symposium. Mr. Crane, a chemistry teacher, was nominated by Robert Dick, a participant in the 1991 program. (Mr. Dick is presently a Ph.D. candidate in Computer Science at Princeton University.) Mr. Dick writes that Mr. Crane's "academic competence, curiosity, and enthusiasm toward teaching allow him to motivate students who would otherwise fall through the cracks. Mr. Crane attracted students who wouldn't typically take difficult science courses."

Robert L. McCrory
Director

A High-Bandwidth Electrical-Waveform Generator Based on Aperture-Coupled Striplines for OMEGA Pulse-Shaping Applications

Pulsed-laser systems emit optical pulses having a temporal pulse shape characteristic of the particular type of laser design. Advances in technology have produced laser-pulse-shaping systems where the laser temporal profile can be specified in advance and controlled to a high degree of accuracy.[1–3] A pulse-shaping system has been in operation on OMEGA for several years. Temporally shaped optical pulses can be produced by applying shaped electrical waveforms to a dual-channel integrated-optics modulator.[1–3] These shaped electrical waveforms are sent to the optical modulator synchronized with the passage through the modulator of an optical pulse from a single-longitudinal-mode (SLM) laser.[4] The optical pulse exiting the modulator is then shaped in accordance with the voltage-dependent transfer function of the modulator. Hence, the electrical-waveform generator is an important component in any optical-pulse-shaping system incorporating optical modulators. This article discusses a greatly simplified pulse-shaping system based on an aperture-coupled-stripline (ACSL) electrical-waveform generator under development for OMEGA, and compares its many advantages over the existing OMEGA pulse-shaping system.

The Present OMEGA Pulse-Shaping System

The OMEGA pulse-shaping system uses an electrical-waveform generator based on an electrical reflection from a variable-impedance microstrip line (VIMSL).[3] Electrical-waveform generators based on stripline technology offer the highest temporal resolution over other systems due to their high-bandwidth capabilities, stripline-fabrication procedures, and achievable tolerances. The present OMEGA pulse-shaping system (outlined in Fig. 73.1) consists of many components. A cw mode-locked (CWML) laser is used to seed a regenerative amplifier (regen). The temporal width of the optical pulse injected into this regen is stretched in time with an intracavity etalon.[5] The output of the regenerative amplifier is amplified, and its leading edge is steepened with a stimulated Brillouin scattering (SBS) reflection from CCL_4.[6] This SBS pulse is amplified and sent to a fiber distribution system to illuminate photoconductive (PC) switches. Illumination of the PC switches activates the electrical-waveform generator, which produces the temporally shaped electrical waveforms that are sent to the optical modulator.[3,7] The subsequently shaped optical pulse from the modulator is sent to the OMEGA

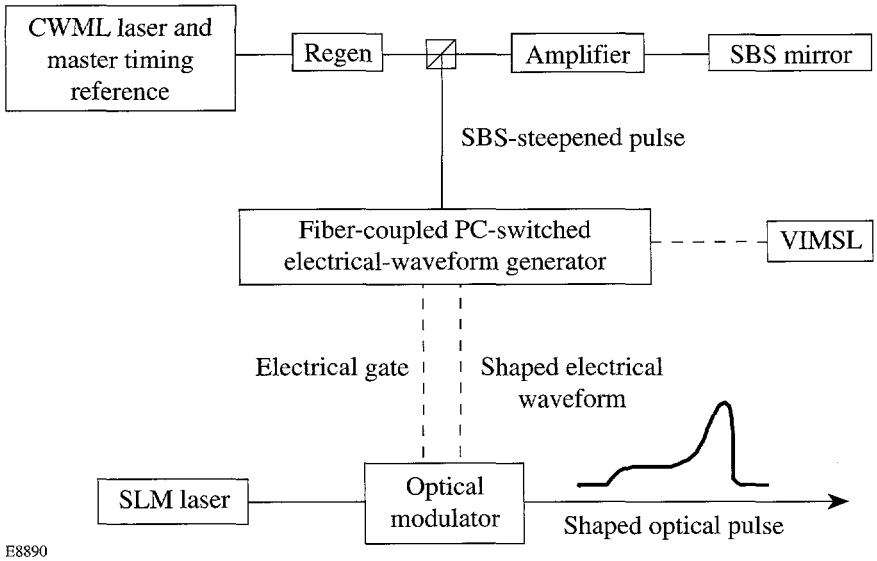

Figure 73.1
The OMEGA optical-pulse-shaping system. A cw mode-locked (CWML) laser seeds a regenerative amplifier (regen) whose output pulse is amplified and steepened by a stimulated Brillouin scattering (SBS) mirror. The SBS pulse activates a photoconductively (PC) switched electrical-waveform generator that drives the two channels of an optical modulator. The output from a single-longitudinal-mode (SLM) laser is temporally shaped by the optical modulator and injected into the OMEGA laser.

amplifiers with timing referenced with respect to the activation of the PC switches by the SBS pulse.

The VIMSL in OMEGA's electrical-waveform generator is a two-port electrical device.[3,7] A square electrical pulse is sent into one port of the device and propagates to the second terminated port. A shaped electrical waveform, generated by reflections along the length of the VIMSL, exits from the VIMSL through the input port and is sent to the optical modulator. This electrical-waveform generator has some anomalies that must be mitigated to achieve a high contrast (i.e., the ratio of the maximum pulse amplitude to the prepulse noise). The square electrical waveform sent to the VIMSL has a voltage stair step that is attributable to the finite "off" impedance and nonzero "on" impedance of the PC switches. The effects of this dc step are substantially minimized by applying a temporal delay to the shaped electrical waveform. In addition, there is a capacitively coupled voltage spike on the voltage waveform applied to the modulator that is attributable to the capacitance of the PC switch in the off state. To eliminate this prepulse and improve the contrast of the shaped optical pulses, a square electrical gate pulse is applied to the second channel of the modulator.

The ACSL Pulse-Shaping System

A pulse-shaping system with an electrical-waveform generator based on an ACSL has been developed. A layout of this ACSL pulse-shaping system is shown in Fig. 73.2. A square electrical waveform from a commercially available pulse generator is sent to an ACSL. The ACSL generates a shaped electrical waveform that is sent directly to the optical modulator for pulse shaping.

The design of the electrical-waveform generator is based on a four-layer, four-port ACSL and is modeled as a four-port electrical directional coupler. An exploded view of a practical device with four layers of material having dielectric constant ε_r is shown in Fig. 73.3. The important region of the ACSL for pulse shaping is the coupling region shown in cross section in Fig. 73.4. In operation, a square electrical waveform is launched into port 1 and propagates along electrode 1 to the terminated port 2 of the ACSL. As the square electrical waveform propagates along electrode 1 in the coupling region, the electrical signal is coupled through an aperture to electrode 2 in the backward direction and exits at port 4. By properly varying the width of the coupling aperture (s in Fig. 73.4) along the length of the ACSL, any desired temporally shaped electrical waveform can be generated at port 4 and sent to optical modulators for pulse shaping.

The ACSL system is characterized by an input and output impedance. The characteristic impedance Z_0 of the system is chosen to be 50 Ω to match the input impedance of the modulator channels. Ports 2 and 3 of the ACSL are terminated with this characteristic impedance to prevent reflections at these ports. The transition section of the ACSL is designed to accommodate the electrical connectors (stripline end launchers) required to transmit electrical signals from the standard coaxial electrical cables used as input and output to the ACSL to the coupling region of the ACSL (illustrated by the cross-sectional geometry in Fig 73.4). In the transition region (and in the coupling region when the aperture width is zero), the system can be thought of as two separate uncoupled and noninteracting ordinary striplines. To achieve a 50-Ω stripline in this section, the width of the electrode w is determined from well-known relations[8] involving the material parameters and the geometry of the ACSL.

To design and produce shaped voltage waveforms at port 4 of an ACSL, the electrical coupling coefficient from electrode 1 to electrode 2 (i.e., the ratio of the output-pulse voltage at port 4 to the input-pulse voltage at port 1) as a function of

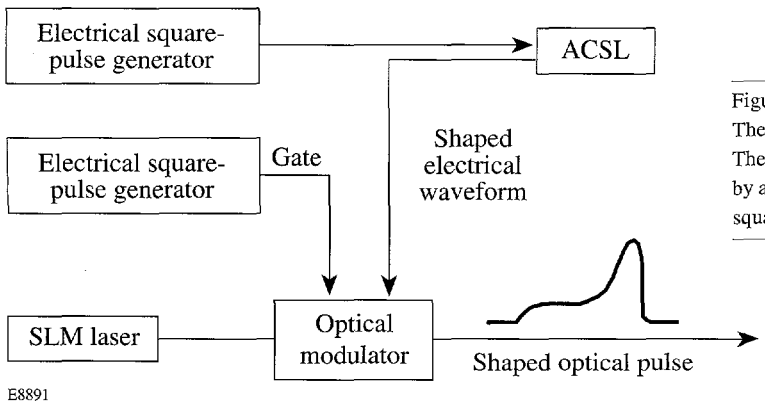

Figure 73.2
The aperture-coupled-stripline (ACSL) optical-pulse-shaping system. The output from an electrical square-pulse generator is temporally shaped by an ACSL and used to drive an optical modulator. A separate electrical square-pulse generator is used to gate the second channel of the modulator.

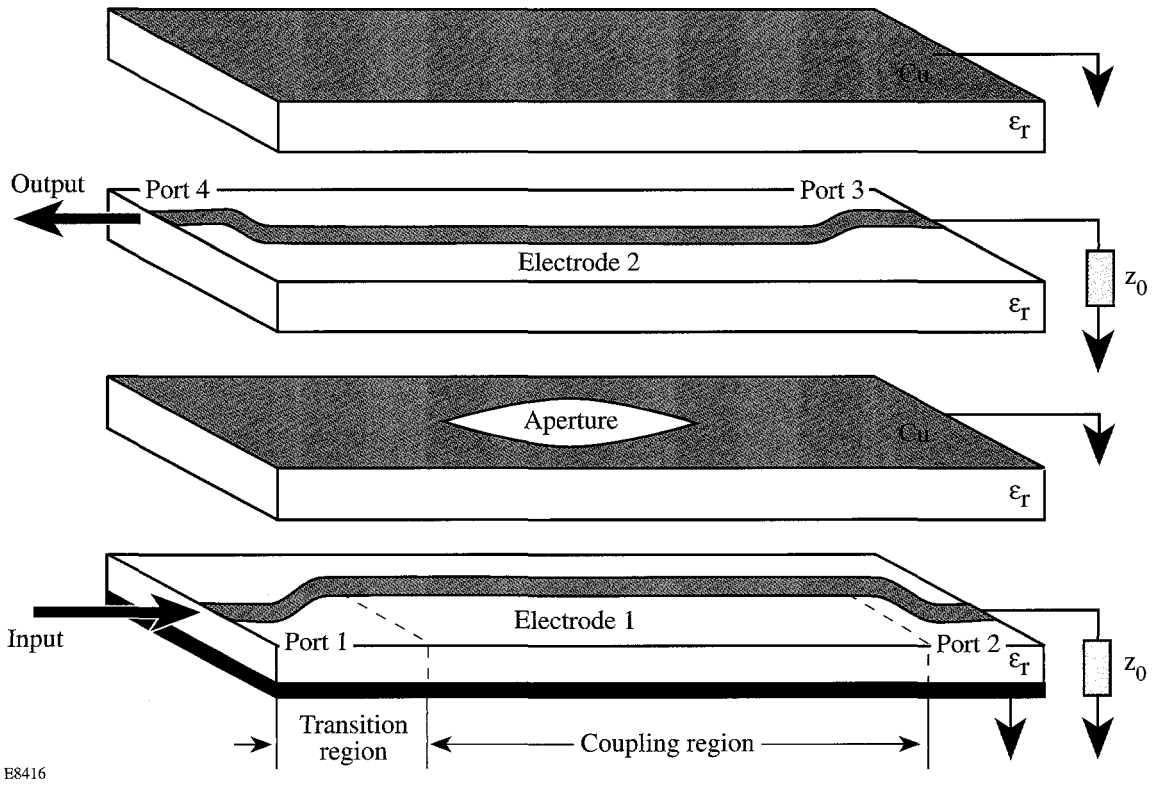

Figure 73.3
Exploded view of a practical four-layer, four-port ACSL. A square electrical waveform is launched into port 1 and propagates along electrode 1 to the terminated port 2. The electrical signal is coupled through an aperture to electrode 2 in the backward direction and a shaped electrical waveform exits at port 4.

aperture width s must be known. It is difficult to calculate this explicitly; however, simple experiments have been performed to measure this dependence. The data from these measurements are used in our model for designing ACSL devices.

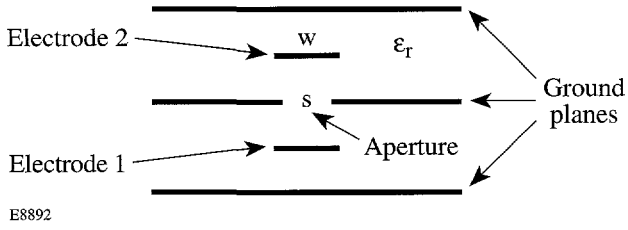

Figure 73.4
Cross-sectional view of an ACSL in the coupling region of Fig. 73.3. The electrode width w is chosen to provide a 50-Ω impedance structure. The amount of electrical coupling from electrode 1 to electrode 2 depends on the aperture width s.

Several ACSL devices have been fabricated and tested to determine the dependence of the electrical coupling coefficient on the aperture width s. A typical structure consists of four layers of RT/duroid®9 5880 microwave laminate material ($\varepsilon_r = 2.2$) sandwiched together as illustrated in Fig. 73.3. The two outer layers are 0.125 in. thick with 1 oz/ft^2 of copper on their outer surfaces. The stripline electrode width (w in Fig. 73.4) on the opposite side of these layers is 0.075 in. (experimentally verified to provide a 50-Ω impedance) and is machined with a precision programmable milling machine. (Note that electrode 2 in Fig. 73.3 is shown on an intermediate layer. This is for illustration purposes only. This electrode in our device is machined on the bottom of the layer above it, making the two outer layers completely identical.) The two center layers are 0.031 in. thick. One center layer has no copper on either surface and is used as a dielectric spacer. The other center layer has 1 oz/ft^2 of copper on one side only, with copper removed to form the appropriate coupling aperture. The

structure is easily disassembled to replace the aperture layer to produce different shaped electrical waveforms. Several other ACSL geometries with different layer thickness and electrode widths were tested, but as will be shown below, the above geometry produces a sufficiently high electrical coupling coefficient for our pulse-shaping application.

Three apertures having a width s that varies along the length of the line with the functional form of a simple Gaussian are used in the above structure to determine the dependence of the electrical coupling coefficient on the aperture width s. The maximum aperture widths of the three Gaussians are 5, 10, and 20 mm. Voltage measurements are made with a high-bandwidth (20-GHz)[10] sampling oscilloscope equipped with an electrical square-pulse generator for time domain reflectometer (TDR) measurements. The pulse from the TDR channel is sent into port 1 of the ACSL, and the output from port 4 is measured with a separate, high-bandwidth (20-GHz) channel of the oscilloscope. The time axis of the measured voltage waveforms is mapped to position along the ACSL using the electrical propagation velocity in the RT/duroid® material. From our measurements on the three Gaussian apertures, the electrical coupling coefficient versus aperture width is obtained and shown in Fig. 73.5. The data in Fig. 73.5 are used in our model to design ACSL devices that produce specific voltage waveforms for the optical-pulse-shaping system.

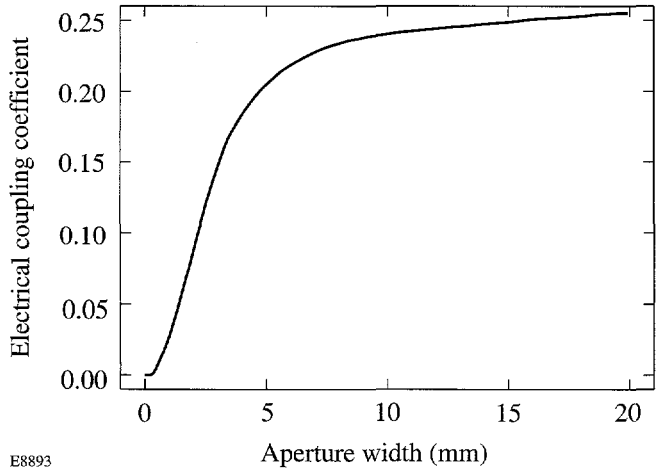

Figure 73.5
The electrical coupling coefficient, defined as the ratio of the output voltage at port 4 to the input voltage at port 1 in Fig. 73.3, plotted as a function of aperture width for an ACSL with the geometry discussed in the text.

The output voltage measured at port 4 of an ACSL with 5-mm-Gaussian aperture is plotted with a solid line in Fig. 73.6 (normalized to the voltage of the input square pulse applied to port 1) along with the prediction of our model plotted with a dashed line. For high coupling coefficients, depletion of the input square-pulse voltage as it propagates along electrode 1 cannot be neglected and is included in our model.

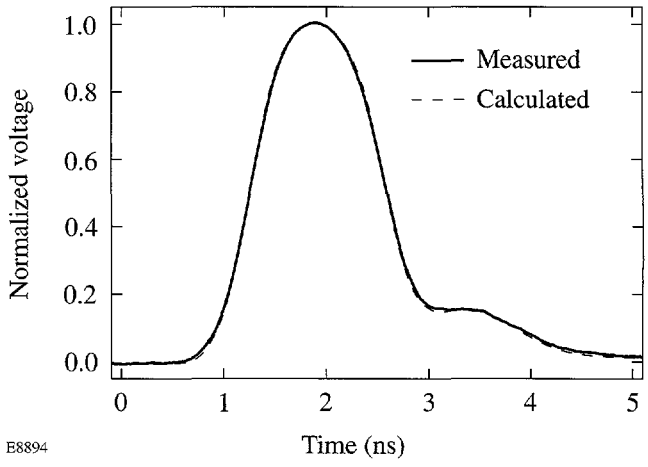

Figure 73.6
The measured output voltage waveform (solid line) from an ACSL having a Gaussian aperture along the length of the coupling region with a 5-mm maximum aperture width. The calculated output voltage from this structure (dashed line) is also shown.

Temporally shaped optical pulses have been produced using the pulse-shaping system shown in Fig. 73.2 with the ACSL geometry described above. A commercially available square-pulse generator[11] that provides a 35-V square pulse with 100-ps rise time is used as input to the ACSL. The half-wave voltage of the optical modulators used for pulse shaping is approximately 8 V. Hence, the coupling coefficients of 0.25 (shown in Fig. 73.5) obtainable with the ACSL structure described above are adequate for this application. To verify our ACSL model, the output voltage at port 4 of an ACSL designed to produce a specific optical pulse shape is sent to an optical modulator. The measured shaped optical pulse from the modulator is plotted with a solid line in Fig. 73.7; the optical pulse shape that is desired from this system is plotted with a dashed line. This figure illustrates the excellent performance and predictability of the ACSL pulse-shaping system.

Pulse-Shaping-Systems Comparison

By comparing the pulse-shaping systems shown in Figs. 73.1 and 73.2, it can be seen that the ACSL system eliminates the need for the CWML laser, the regen with SBS pulse steepener and amplifier, the fiber distribution system, and the PC switches. The key operational advantage of the ACSL pulse-shaping system that allows this simplification is

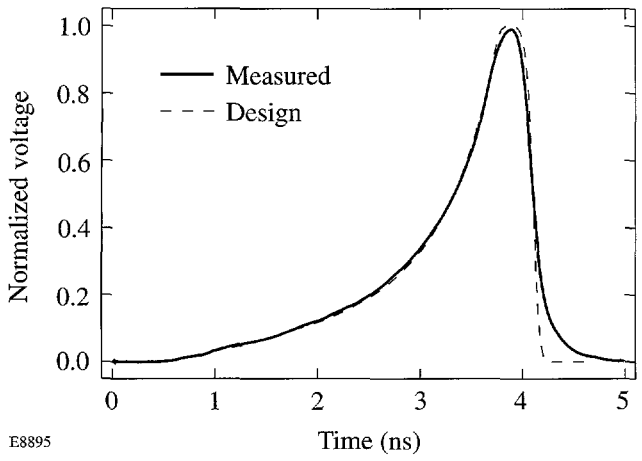

Figure 73.7
The measured temporally shaped optical pulse from an ACSL pulse-shaping system (solid line). The desired optical pulse shape (dashed line) from this system is also shown.

that the shaped electrical waveform from the ACSL exits from a different port than that used to input the square electrical pulse. Consequently, any suitable electrical square-pulse generator can be used to generate shaped electrical waveforms. In addition to this enormous simplification, there is no source of prepulse noise (capacitive voltage spike or dc offset voltage) since coupling cannot occur before application of the square electrical pulse to the ACSL. The system can also be accurately timed to the OMEGA master timing reference (38-MHz rf or 76-MHz CWML-laser optical pulses). The rms timing jitter between the 76-MHz CWML-laser optical pulses and the generation of the shaped electrical waveforms is measured to be less than 10 ps.

Conclusions

An optical-pulse-shaping system based on an ACSL has been designed and tested. This system produces temporally shaped optical pulses with high bandwidth suitable for OMEGA pulse-shaping applications. The design is a significant simplification over existing technology with improved performance capabilities.

ACKNOWLEDGMENT

This work was supported by the U.S. Department of Energy Office of Inertial Confinement Fusion under Cooperative Agreement No. DE-FC03-92SF19460, the University of Rochester, and the New York State Energy Research and Development Authority. The support of DOE does not constitute an endorsement by DOE of the views expressed in this article.

REFERENCES

1. R. B. Wilcox, U.S. Patent No. 4,667,161 (19 May 1987).
2. R. B. Wilcox *et al.*, in *Laser Coherence Control: Technology and Applications*, edited by H. T. Powell and T. J. Kessler (SPIE, Bellingham, WA, 1993), Vol. 1870, pp. 53–63.
3. A. Okishev, M. D. Skeldon, S. A. Letzring, W. R. Donaldson, A. Babushkin, and W. Seka, in *Superintense Laser Fields*, edited by A. A. Andreev and V. M. Gordienko (SPIE, Bellingham, WA, 1996), Vol. 2770, pp. 10–17.
4. A. V. Okishev and W. Seka, IEEE J. Sel. Top. Quantum Electron. **3**, 59 (1997).
5. M. D. Skeldon and S. T. Bui, J. Opt. Soc. Am. B **10**, 677 (1993).
6. M. D. Skeldon, A. Okishev, A. Babushkin, and W. Seka, in *First Annual International Conference on Solid State Lasers for Application to Inertial Confinement Fusion*, edited by M. André and H. T. Powell (SPIE, Bellingham, WA, 1995), Vol. 2633, pp. 422–429.
7. M. D. Skeldon, A. Okishev, S. A. Letzring, W. R. Donaldson, K. Green, W. Seka, and L. Fuller, in *Optically Activated Switching IV*, edited by W. R. Donaldson (SPIE, Bellingham, WA, 1994), Vol. 2343, pp. 94–98.
8. B. C. Wadell, *Transmission Line Design Handbook* (Artech House, Boston, 1991).
9. RT/duroid®, Rogers Corporation, Microwave Division, Chandler, AZ 85226.
10. 20-GHz sampling oscilloscope, Model No. HP54120B/54124A, Hewlett Packard, Santa Clara, CA 95052-8059.
11. Pulse generator, Model No. 4500E, Picosecond Pulse Labs, Boulder, CO 80306.

Sweep Deflection Circuit Development Using Computer-Aided Circuit Design for the OMEGA Multichannel Streak Camera

A streak camera is an electro-optic instrument capable of resolving high-speed, low-repetition-rate, pulsed laser phenomena. The basis of the instrument is a streak tube. The image of the light to be analyzed is focused onto a photocathode at the input end of the streak tube. The photocathode emits electrons in response to the intensity of the light. The electrons, focused into a beam, are accelerated and deflected to a luminescent screen at the other end of the tube. This electron beam, impinging upon the screen, produces an intensified image of the light being analyzed. This image is then optically coupled to a CCD (charge-coupled device) imager, which digitizes the information for storage. To study the temporal variation of pulsed light a streak mode of operation is utilized whereby the electron beam is swept across the phosphor at a predetermined rate to provide the dimension of time along the axis of the swept image. To sweep the electron beam a pair of electrostatic deflection plates are provided in the streak tube (see Fig. 73.8). The position of the beam is linearly related to the voltage potential on the deflection plates. A linear voltage ramp is applied to the deflection plates to produce a linear sweep with respect to time. The sweep deflection circuit described produces the voltage ramp needed for the temporal study of the beams within the OMEGA system.

The multichannel streak camera is being developed at LLE to measure multiple-beam power balance and timing following the 3ω frequency-conversion crystals on OMEGA. The camera design is built around a commercial streak tube.[1] The primary design goal is to be able to perform a temporal display of ten OMEGA beams simultaneously along with two fiducial timing beams. With six of these cameras all 60 OMEGA beams can be analyzed simultaneously. Other goals include remote automated operation, fiber-optic light interface to the photocathode, and a highly reliable modular design. The modular design is required to facilitate serviceability and minimize down time in the event of circuit failure. Circuit malfunctions can be quickly diagnosed to the module level and a functioning module can then be interchanged without significant recalibration of the instrument. The sweep module and streak camera frame are shown in Fig. 73.9.

Functionally the streak camera sweep module circuitry must synchronously output a bipolar, high-voltage ramp with a duration of 6 ns. The magnitude of the total end-to-end differential sweep voltage, as seen between the two deflection plates, is approximately 2000 V. This translates to a sweep of the electron beam across 40 mm of the streak tube display. Because errors in the linearity of the output ramp voltage translate directly to measurement errors in time resolution of the instrument, it is important to minimize deviations in the slope of the differential ramp voltage.

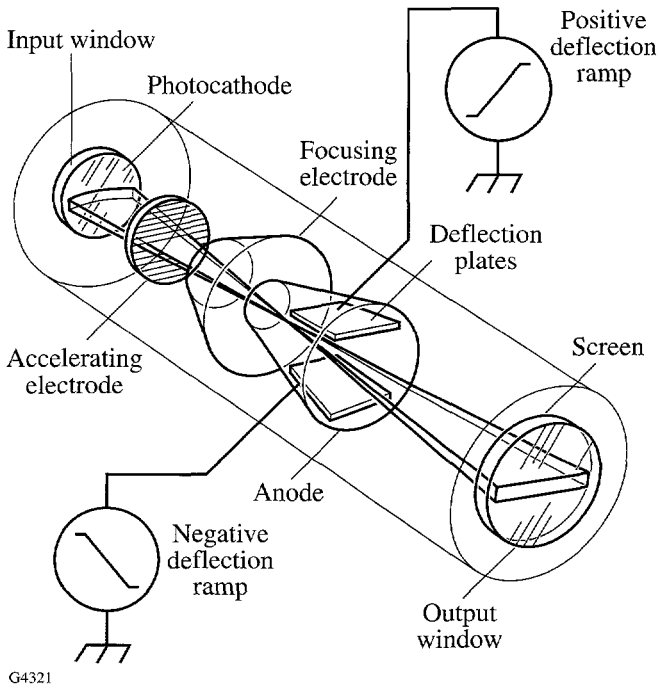

Figure 73.8
Streak tube schematic with deflection ramp sources.[1]

(a)

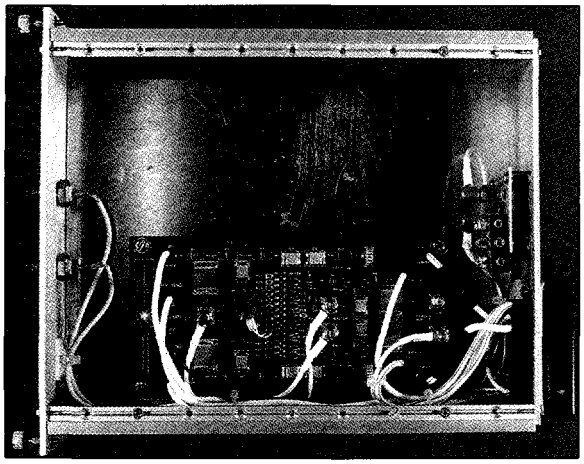

(b)

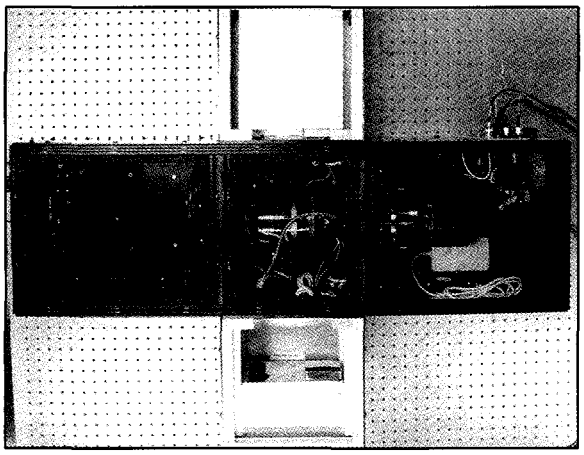

G4322

Figure 73.9
OMEGA multichannel streak camera: (a) sweep module and (b) streak camera frame.

The 6-ns sweep ramp is a high-bandwidth signal that requires care in design to account for nonideal component behavior. The particular problems encountered center around the stray reactive components, also known as parasitics, that are inherent in all electronic components. These parasitics are not usually a problem in low-frequency designs (<1 MHz) but become a significant contribution to performance, or lack thereof, in higher-frequency designs. The development of the streak camera sweep circuit accounts for the parasitics of the components to determine and correct for their effects. A circuit design accounting for all parasitics can become nearly impossible to solve in closed form resulting from the complexity of the component parasitic models. To aid in the design, a circuit simulator computer program is used to model the circuitry with parasitics.

The modular design approach used here, while it does provide serviceability, requires additional mechanical interface complexity within the system interconnect structure. The interface complexity results from added connectors and increased wiring length to accommodate packaging. These extra wire lengths and added connectors introduce additional parasitic elements into the circuit interface that degrade high-bandwidth performance and must be accounted for in any modeling.

The goal of the sweep module design is achieved through the use of computer-aided analysis of the circuit design. The computer model includes parasitics that contribute to nonideal behavior. The initial design is conducted using this model. From the initial design a first-pass circuit "breadboard" is built and tested. An increasing complexity of parasitic elements is included until the model output compares to the actual breadboard circuit performance. With the model output matching the actual circuit, a rapid investigation of ways to optimize performance can then be accomplished. Also, anomalies in the circuit operation and performance measurement system can be analyzed. Although the main emphasis for use of the computer circuit model is to understand and correct the effects of the parasitics, it is also a valuable tool for circuit design and circuit optimization. The following is a comparison of the modeled and measured results for the sweep circuit along with a discussion on using the model to understand and correct undesired circuit behavior.

Streak Sweep Circuit Fundamental Design

The basic circuit concept for the deflection voltage generator in the sweep module is a voltage step applied to an RLC (resistor, inductor, capacitor) series resonant circuit as illustrated in Fig. 73.10. The deflection circuit is bipolar, and each deflection plate is driven by an equivalent RLC circuit (see Fig. 73.8). The step is positive for one deflection circuit and negative for the other. This creates a voltage ramp that is twice the amplitude of that applied to one plate only. The C in the resonant circuit is formed by the capacitance of the deflection plate in the streak tube. The voltage across the capacitor (deflection plate) is given by the following exponentially decaying sinusoidal form and is illustrated in Fig. 73.11:[2]

$$V_c(t) = V_{\text{step}}\left\{1 - e^{-\alpha \cdot t}\left[\cos(A\ \alpha \cdot t) + \frac{\sin(A\ \alpha \cdot t)}{A}\right]\right\}, \quad (1)$$

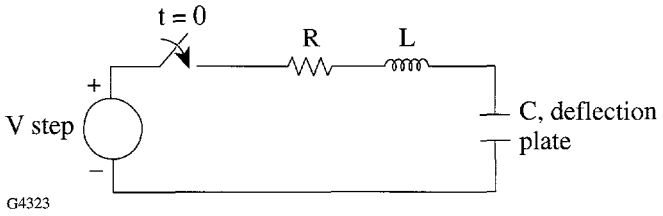

Figure 73.10
Basic RLC circuit with voltage step generator (R: resistor; L: inductor; C: capacitor).

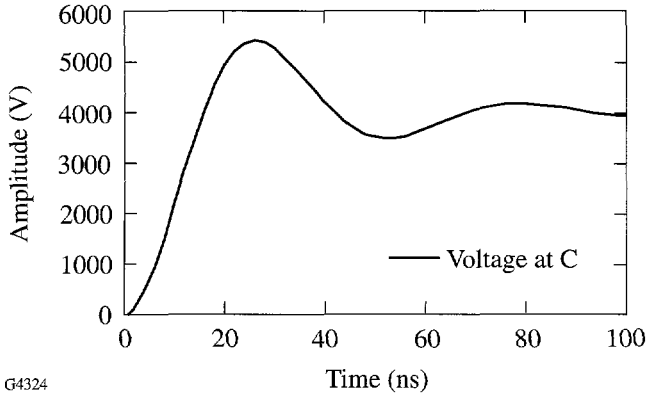

Figure 73.11
Exponentially decaying sinusoid produced by the step response of a series RLC circuit.

where

$$\alpha = \frac{R}{2L}, \quad A = \sqrt{4Q^2 - 1}, \quad Q = \frac{1}{R}\sqrt{\frac{L}{C}}.$$

Q represents the quality factor of the resonant circuit. The quality factor is the power stored by the resonant circuit divided by the power dissipated per cycle of the resonant frequency.

Ideally the sweep voltage should be a linear ramp. Although the voltage waveform produced by Eq. (1) is not linear, a section of the waveform in Fig. 73.11 between $t = 0$ and the voltage peak approximates a linear ramp. The linearity of this section is within a useable degree of accuracy for the streak camera sweep. The benefit in using the RLC resonator is that the sweep ramp can be adjusted by appropriate choice of R, L, and V_{step} without changing the circuit configuration. Another benefit is the low circuit complexity.

As an example of the achievable linearity, for a 4000-V step with a desired slope of 333 V/ns over a 2000-V range, the following values for R and L are used, given a 10-pF deflection plate capacitance: $R = 498\ \Omega$, $L = 6.3\ \mu$H. The waveform produced using these values has a slope of 306 V/ns at the start of the 2000-V sweep range (deflection plate voltage = 1340 V) and a slope of 310 V/ns at the end (deflection plate voltage = 3340 V). The center of the range has a slope of 333 V/ns as desired (deflection plate voltage = 2340 V). The slope deviates from an ideal linear slope by a maximum of 8.1% at the ends. This deviation translates into a maximum deflection-plate voltage error of 25 V, or a theoretical position error of 0.5 mm at the edges of the streak tube display used in the development. Choosing higher step voltages and higher circuit Q's will reduce this error.

To create the voltage step, a fast-switching, low-jitter, high-voltage circuit that can also accommodate high peak currents is necessary. Currently, the best device for this application is an avalanche transistor. An avalanche transistor is a bipolar junction transistor that can repetitively operate nondestructively in the current-mode second breakdown region.[3] When these transistors are off, they can hold off hundreds of volts with minimal conduction between the collector and emitter. When a small amount of carriers are injected into the base, the transistor goes from minimal conduction to current-mode second breakdown operation where the equivalent impedance between the collector and emitter drops to a few ohms. This action takes place in subnanosecond time frames. The transistor used for this project is the Zetex FMMT417.[4] This transistor is specifically designed for current-mode second breakdown operation. The FMMT417 transistor has a collector-to-emitter voltage self-breakdown of 320 V. Since each transistor can hold off >300 V, seven series-connected avalanche transistors are used for each of the two 2000-V step generators needed in the streak camera sweep circuit design. In a series-configured circuit only one of the transistors in the stack needs to be triggered to cause all of the remaining transistors to go into current-mode second breakdown. A schematic diagram of one sweep circuit of the bipolar sweep network is shown in Fig. 73.12.

Computer Modeling of the Sweep Circuit

The computer model for the sweep circuit is developed using Intusoft IsSpice4[5]—a commercially available version of the electronics-industry–accepted circuit analysis software called SPICE (Simulation Program Integrated Circuits Especially), which is based on Berkeley SPICE 3F.2.[6] This program accepts arbitrary circuit configurations and calculates

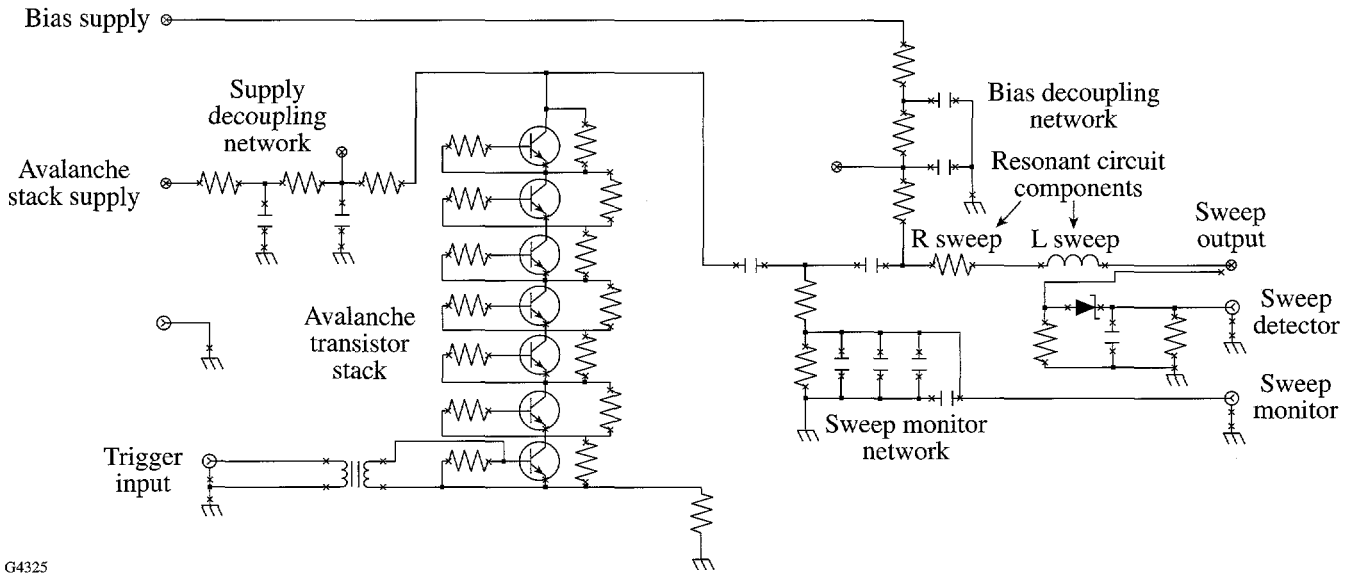

Figure 73.12
Schematic of the upper half of the multichannel streak camera sweep circuit.

currents and voltages throughout the circuit. A variety of analysis options are available in SPICE including dc, ac, and transient. For analyzing the streak sweep circuit, a transient, or time domain, analysis is performed. To simplify the model only half of the circuit is modeled, knowing that the other half provides identical results with inverted polarity. The sweep circuit is a bipolar, or balanced, configuration and can be divided into two equal parts along the line of symmetry. Each part can be analyzed independently without sacrificing accuracy. The model schematic is illustrated in Fig. 73.13.

A comparison of the schematics in Figs. 73.12 and 73.13 shows that there are significantly more components in the corresponding model network of Fig. 73.13. The components not shown in the actual circuit but shown in the model are the parasitic elements. These elements are determined through characterization of each component in the critical high-bandwidth signal path. Characterization is generally performed with calibrated test fixtures on a network analyzer. A network analyzer produces measurements of signal amplitude and phase in the frequency domain. The analyzer contains a swept calibrated signal source for excitation of the device under test and a tracking swept receiver for the measurements. One function of a network analyzer is to measure impedance of a component as a function of frequency. Care must be taken in these measurements to extract the actual component impedance from the characteristics of the test fixture. All components have parasitic lead inductance as well as capacitance to ground. Between the terminals of a component there exists parasitic capacitance. Component losses are encountered as series and parallel loss resistance. The designer must determine which of the parasitics to consider when constructing component models. Some parasitics may not affect the analysis significantly and may be omitted, but a safe rule to follow is to include any parasitics where the designer is uncertain of their effect. Once the overall circuit model is completed the parasitics can be varied to determine their effect on circuit performance.

In the model in Fig. 73.13 the avalanche stack is replaced by a pulsed voltage source, V1. This source simulates the waveform observed across the avalanche stack. The actual avalanche stack dc supply is simulated by a short circuit to ground at R12 since an ideal voltage source has 0-Ω impedance. L1 is added to simulate the combined inductance of the avalanche transistors and the interconnect wiring. R3 simulates the combined on-state resistance of the avalanche transistors in current-mode second breakdown. The network to the left of the avalanche stack simulator, including R1, R2, and R12, simulates the stack supply decoupling network with parasitics. Likewise, the network including R5, R6, and R11 forms the decoupling network with parasitics for the bias supply, V2. The *R* and *L* for the slope-forming resonant circuit are represented by R14 and L8, respectively. The right-hand connection to R10 is the output of the module. This point is followed by a high

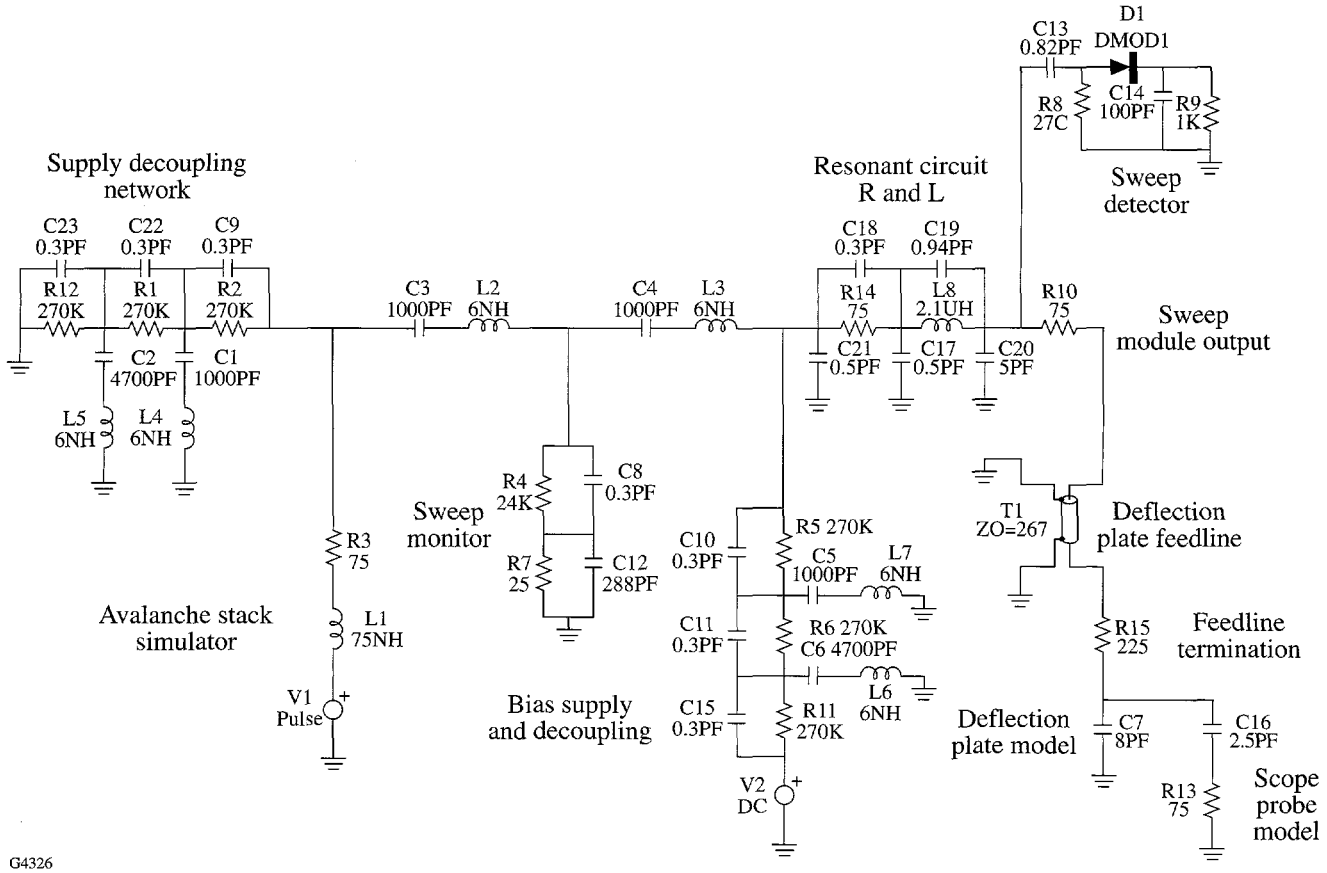

Figure 73.13
Schematic of the SPICE model for the multichannel streak camera sweep circuit.

impedance transmission line representing the feed wire to the deflection plate, C7. C16 and R13 represent a model of the oscilloscope probe used to monitor the performance of the sweep generator. The scope probe is modeled to determine its effective loading on the sweep waveform. The model also includes the sweep monitor network as well as the sweep detector network as seen in the original schematic of Fig. 73.12.

Model Results Versus Measured Results

Data from Figs. 73.14 and 73.15 illustrate a good correlation between the measured and model-predicted results for the sweep waveforms. The measured data is taken using a high-bandwidth oscilloscope connected to the deflection plates of the streak tube through 250-MHz-bandwidth, 100:1, high-impedance oscilloscope probes.[7,8] The plots in Fig. 73.14 are for one deflection plate voltage versus time. The other plate voltage is equivalent with opposite polarity. Figure 73.15 is the differential (slope) of the curves in Fig. 73.14. The desired theoretical slope is 167 V/ns for one deflection plate, or 333 V/ns for the differentially driven pair of plates to obtain a 6-ns sweep rate.

The curves presented are referenced in the time axis to the zero crossing of the deflection plate voltage. The illustrated curves extend past the active sweep time of 6 ns (active sweep time = −3 ns to +3 ns). Within the 6-ns time window the maximum voltage difference between the measured and modeled results is 29 V. The average slope within the window for the measured data is 167 V/ns and 168 V/ns for the SPICE data. The standard deviation of the measured slope from 167 V/ns is 14 V/ns and 10 V/ns for the SPICE model.

Utility of the SPICE Model

One of the fundamental uses of the SPICE model is to evaluate the performance of the sweep network with respect to the values of R and L, the sweep-rate–determining components. The initial values for these parts are determined by theoretical calculations base on Eq. (1) for the basic RLC

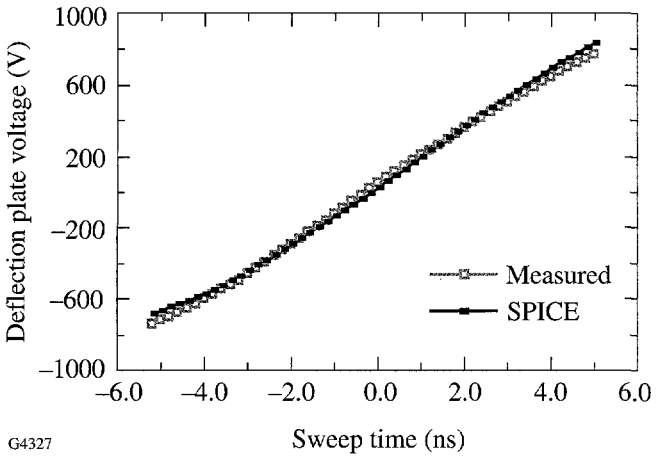

Figure 73.14
Measured sweep voltage and SPICE calculation.

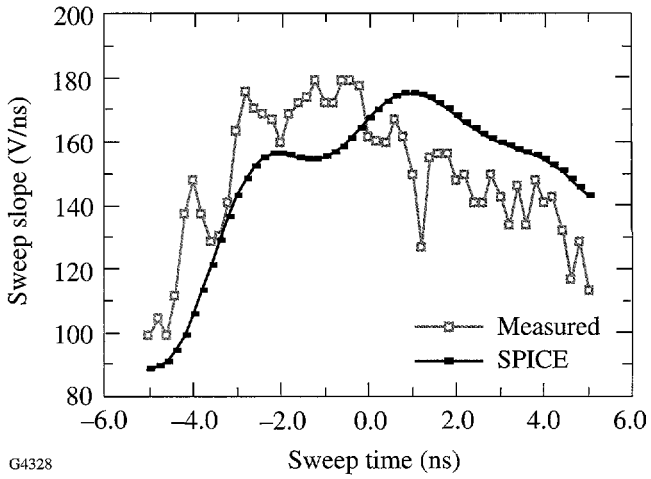

Figure 73.15
Measured sweep slope and SPICE calculation.

resonator circuit. The predicted performance of the actual circuit with the initial theoretical values can then be evaluated using the model. The values are then iteratively optimized within the model to account for the parasitics within the sweep module and streak camera. A set of values that meets the performance criteria is then determined prior to actually mounting the components in the hardware. This approach is used to develop the streak module with the results as presented in Figs. 73.14 and 73.15.

Another use for the model is to analyze and correct anomalies in the sweep waveform observed during the sweep module development. Three anomalies were found that affected the camera performance: (1) the effect of the oscilloscope probe loading on the sweep waveform; (2) a small, damped, high-frequency sinusoid superimposed on the sweep waveform; and (3) an inflection in the start of the sweep waveform.

The loading effects of the oscilloscope probes can only be evaluated experimentally by comparing the spacing of accurately timed fiducial light pulses on the streak camera output with and without the probes attached. During the streak camera development, short fiducial laser pulses with a precise period of 500 ps were applied to the photocathode of the streak tube. The pulse train from the fiducial laser appears as an intensity-modulated streak on the output screen. The distance between the peak intensity points on the output screen is directly related to the sweep rate ramp applied to the deflection plates. Comparing the distance between the peaks with and without the probes connected determines the effect of the probes on sweep rate. Using the SPICE model, a trivial effort is required to remove the simulated scope probes and calculate the change in the sweep speed. Figure 73.16 shows the change in the sweep speed as calculated by the SPICE model. The model-calculated sweep rate is 6.4 ns with the probes and 5.6 ns without. The measured sweep-rate change, using the fiducial method, is 6.6 ns with the probes and 5.6 ns with the probes removed. Good agreement is shown between the two methods. With this performance agreement the sweep-forming R and L values can be easily optimized in the model and applied to the actual circuit to compensate for oscilloscope probe loading. This is far less time consuming than optimization by iteratively changing the components in the actual sweep module and repeating the fiducial streak measurements. Also, knowing the magnitude of the probe-loading change allows actual oscilloscope-measured sweep voltage waveforms to be scaled to predict performance without the oscilloscope probe loading necessary to make the measurement.

During the initial tests of the streak camera a small sinusoidal modulation with a period of approximately 6 ns was observed superimposed on the oscilloscope display of the sweep ramp. This sinusoidal modulation was verified with streak measurements of the 500-ps-period fiducial optical timing pulse train in similar fashion to that used to determine effects of scope probe loading. Figure 73.17 shows the oscilloscope-measured sweep with the superimposed sinusoid. The model result verifies the oscilloscope measurements and is also plotted in Fig. 73.17. Figure 73.18 illustrates the verification plots from the fiducial measurements. This data agreement

proves that the problem is not just an artifact of the oscilloscope measurement. From the model it has been determined that the deflection-plate feed line is acting as a constant impedance transmission line terminated by the capacitive deflection plate. This reactively terminated transmission line forms a resonant circuit that has a center frequency close to that of the superimposed sinusoid. Network analyzer measurements of the feed line indicate that it has a characteristic impedance of 267 Ω with a delay of 1.5 ns. To remove the resonance problem the feed line is made lossy through the inclusion of distributed resistance. Theoretically, this decreases the Q of the resonant circuit formed by the feed line and reduces the sinusoidal current at resonance without significantly affecting the sweep ramp. Results from the model demonstrate that this approach is capable of removing the sinusoid. The plot in Fig. 73.19 is the result produced by the model with the feed line terminated to remove the resonance condition. It was later found that a lumped resistance equal to the characteristic impedance of the line could be connected in series at the deflection plate to produce the same result. This fix is supported by oscilloscope sweep waveform measurements as illustrated in Fig. 73.14.

The last problem observed relates to an inflection in the measured sweep waveforms near the start of the sweep ramp. This is again supported with the results of the model as illustrated in Fig. 73.20 near 3 ns. In this figure the time axis

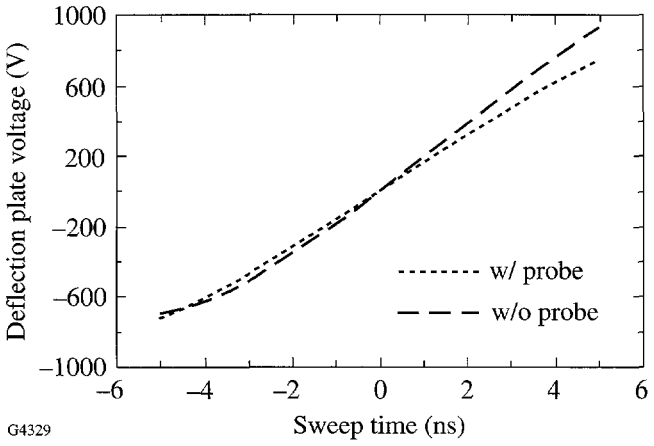

Figure 73.16
Calculated sweep-speed change with oscilloscope probe loading.

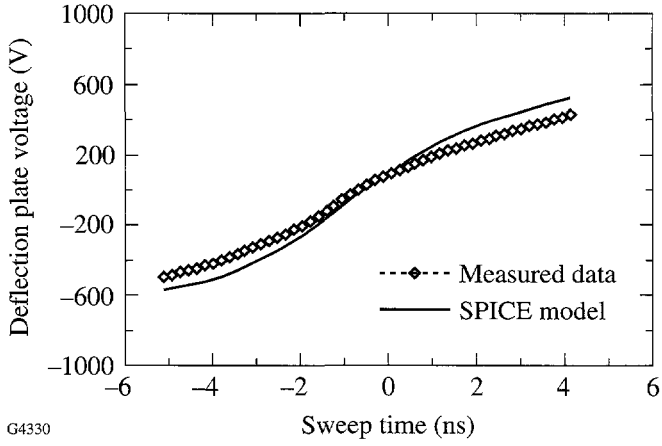

Figure 73.17
Measured sweep with superimposed sinusoid.

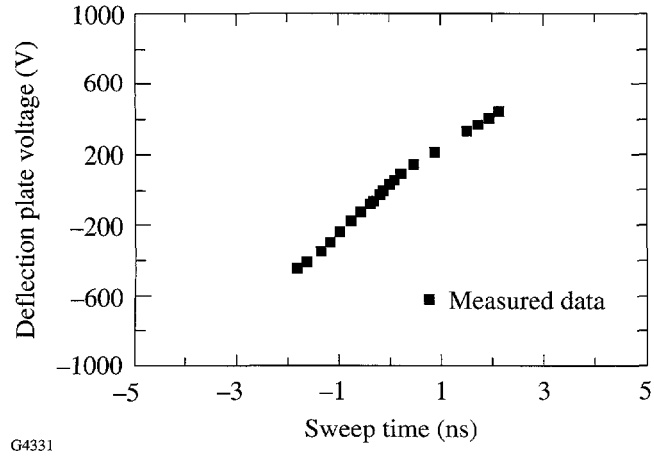

Figure 73.18
Measured sweep using optical fiducial marks.

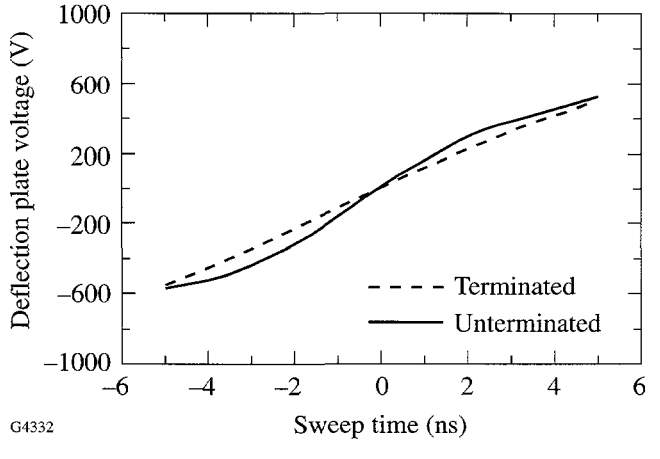

Figure 73.19
Calculated sweep with and without feed-line termination.

reference is at the start of the sweep waveform. Investigation of the inflection through its sensitivity to component value changes in the model led to the understanding of its cause. The inflection is caused by the resonance of the sweep-speed inductance (L8 in Fig. 73.13) with its parallel parasitic capacitance (C19). Using the model an investigation into the effect of the parasitic capacitance can be easily generated. It is found that a nonrealizable inductor is needed (an inductor with minimal parasitic C) to remove the inflection and that this problem cannot be eliminated. This analysis cannot be accomplished without the model since the model provides the freedom to change component characteristics outside the constraints imposed by realizable devices. Figure 73.21 shows the results of the model as the parasitic capacitance of the sweep inductor is varied. The point of this figure is that less inflection is produced by smaller parasitic capacitance.

Since the last problem is not resolvable using realizable components, the choice is made to alter the active sweep ramp range on the sweep waveform to avoid having the inflection within the active area of the sweep waveform. The operation range is altered by increasing the bias supply voltage, keeping all other circuit parameters fixed. In the waveform of Fig. 73.11, this is equivalent to setting the 2000-V active sweep ramp range to a section of the waveform closer to the peak voltage than directly in the middle between the waveform start and the peak. Care is taken to not move the range too close to the peak since linearity would be degraded at the end of the sweep ramp near the peak.

Conclusions

In this work we show that time-domain circuit modeling and simulation of the multichannel streak camera sweep circuit using SPICE is an accurate method of analysis. The accuracy is a direct result of the attention to the parasitics for the components and interconnections in the circuitry. The parasitics, while not a severe limitation in low-frequency analysis, are a great influence to the model results in wide-bandwidth and high-frequency analysis as encountered in the sweep circuit. Component parasitic elements are generally extracted from network analyzer terminal impedance measurements on individual components and circuit interconnects. The necessary complexity of the parasitic model utilized is determined by the calculated effect of the parasitic elements within the circuit application. A SPICE circuit model, when properly constructed using the parasitic component models, is a useful tool to analyze and optimize a design. The main benefit of the model is to present a theoretical evaluation of a circuit with parasitic elements where the complexity of obtaining a closed-form analysis is intractable. Optimization using the model analysis can help greatly in reducing the effects of parasitics. The theoretical computer analysis allows rapid circuit optimization iterations as compared to equivalent hardware implementation and measurement of the change. The model is extremely valuable in diagnosing anomalies in circuit performance. An accurate model can also provide useful performance-limit analysis through ideal, parasitic-free, component substitution.

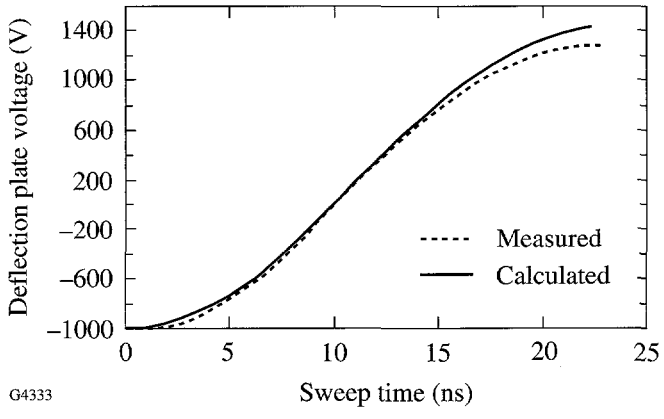

Figure 73.20
Sweep inflection.

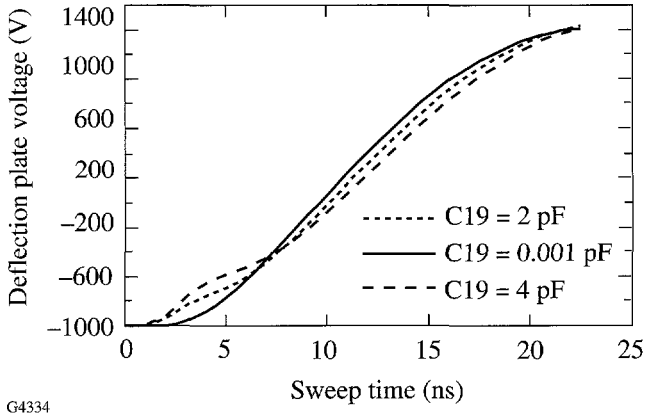

Figure 73.21
Calculated sweep with varying values of parasitic capacitance, C19, for the sweep-forming inductor, L8.

Utilizing the SPICE circuit model for the multichannel streak camera sweep module, an optimized design is developed that accommodates the component parasitics and parasitics introduced by the modular-design concept. Performance of the circuitry is optimized to remove, or accommodate, deflection-plate feedline effects, individual component parasitics, and oscilloscope probe loading. Sweep performance is optimized without the normal time-consuming change and test iterations necessary with a hardware-only approach.

ACKNOWLEDGMENT

This work was supported by the U.S. Department of Energy Office of Inertial Confinement Fusion under Cooperative Agreement No. DE-FC03-92SF19460, the University of Rochester, and the New York State Energy Research and Development Authority. The support of DOE does not constitute an endorsement by DOE of the views expressed in this article.

REFERENCES

1. P510PSU streak tube, Philips Photonics, Slatersville, RI 02876.
2. S. W. Thomas, R. L. Griffith, and W. R. McDonald, Opt. Eng. **25**, 465 (1986).
3. R. J. Baker, Rev. Sci. Instrum. **62**, 1031 (1991).
4. Zetex, Inc., Commack, NY 11725.
5. Intusoft, San Pedro, CA 90733-0710.
6. SPICE 3F.2, developed by the Department of Electrical Engineering and Computer Sciences, University of California, Berkeley, CA 94720.
7. Oscilloscope, Model No. 9360, LeCroy, Chestnut Ridge, NY 10977.
8. Oscilloscope probe, Model No. P5100, Tektronix, Inc., Wilsonville, OR 97070.

D-^{3}He Protons as a Diagnostic for Target ρR

Areal density (ρR) is an important parameter for measuring compression in ICF experiments. Several diagnostics employing nuclear particles have been considered to deduce this quantity in implosions. One diagnostic is the knock-on deuterons,[1] i.e., deuterons produced by the elastic scattering of fuel deuterons and primary neutrons from the DT reaction. The number of knock-ons contained in the high-energy peak (typically 16% of the total produced) of the emergent spectrum is proportional to the fuel areal density [$(\rho R)_f$] and the position of the peak provides a measure of the plastic areal density [$(\rho R)_{CH}$]. This diagnostic, however, is limited to $(\rho R)_{CH} \sim 100$ mg/cm^2 as higher compressions can considerably distort the emergent spectra, preventing a reliable interpretation of the signal.

For higher-density implosions, high-energy neutrons produced from the tertiary fusion reactions of the knock-on deuterons and tritons with the corresponding thermal fuel ions[2] have been considered as a diagnostic for fuel ρR. For instance, for "small" ρR (like those on OMEGA), the number of tertiary neutrons produced is proportional to $(\rho R)_f^2$, yielding a measure for the fuel areal density. However, since these neutrons are produced in tertiary reactions, their numbers are significantly lower relative to primary yields (typically by 5 to 6 orders of magnitude). This necessitates the development of new, sensitive neutron detectors.

An alternate technique for measuring high ρR is to use the primary protons from the D-^{3}He reaction, obtained by adding ^{3}He to the fuel. This diagnostic has the advantage that the charged-particle spectrometer for OMEGA,[3] currently being designed at MIT, can be used to detect the protons. In addition, these protons can serve as a diagnostic for cryogenic DD targets, which are being considered as initial cryogenic targets on OMEGA. DD targets do not have the drawbacks associated with the radioactivity of tritium and can be useful for standardizing laboratory techniques for cryogenics.

In what follows, we introduce the D-^{3}He proton diagnostic and set limits on the areal densities measurable through this method. We then examine the model dependence of this diagnostic by comparing results from a detailed time-dependent simulation and a simple model characterized by the conditions in the target around peak thermonuclear burn. This diagnostic is then discussed in the context of DT targets. Future areas of interest relating to this diagnostic will be discussed briefly.

The Diagnostic

The primary D-^{3}He protons are produced at an energy of 14.7 MeV from the reaction

$$D + {}^3He = \alpha + p(14.7\ \text{MeV}). \quad (1)$$

Protons lose energy as they traverse the target, and the energy loss of the emerging protons is proportional to ρR. Thus, unlike the knock-on diagnostic, which can provide a measure of the fuel and the tamper ρR individually, this diagnostic can be used to measure only the *total* ρR of the target. The interpretation of the signal can be complicated by the fact that this energy loss can be both temperature and density dependent.

Prior to its use on a cryogenic target, the D-^{3}He proton diagnostic can first be tested on current OMEGA gas targets. We demonstrate the diagnostic through a simple model for a typical gas target represented as a hot core (at 4 keV) surrounded by cold plastic (at 0.8 keV). The model serves to illustrate the limits of the diagnostic in terms of both ρR and temperatures in the target. We choose a fuel ρR of 30 mg/cm^2 corresponding to the typical fuel areal density during the time that the protons traverse the target in detailed 1-D simulations. The temperatures in the model are characteristic of the conditions during the peak thermonuclear burn. The emergent D-^{3}He proton spectrum, i.e., the normalized number of protons per unit energy interval, is shown in Fig. 73.22(a) for various values of plastic ρR. The figure shows the greater slowing down of the protons with increasing ρR of the plastic

To examine the reliability of this diagnostic in the context of its sensitivity to temperatures in the target, we vary the electron temperatures in the plastic [Fig. 73.22(b)]. For a lower plastic

temperature the spectra are influenced only for lower proton energies (which occur for larger values of ρR). This can be easily explained through the energy-loss formulae that contribute to the spectrum.[4] We first note that the energy loss of the protons is dominated by losses to electrons. In addition, the D-^{3}He protons have much higher velocities than the electrons in the target for a wide range of energies and temperatures. In this regime, the thermal motion of the electrons can be ignored altogether. (The energy-loss mechanism is then through the excitation of collective plasma oscillations in the plastic.) For OMEGA targets the cold plastic can have temperatures of 1 keV or less and thus will have only a small effect on the spectrum of the very energetic protons.

Detailed simulations through the 1-D code *LILAC*[5] of the same target indicate that the maximum ρR achieved in the target is about 70 mg/cm^2 for the fuel and 170 mg/cm^2 for the plastic [Fig. 73.23(a)]. The protons, however, provide a

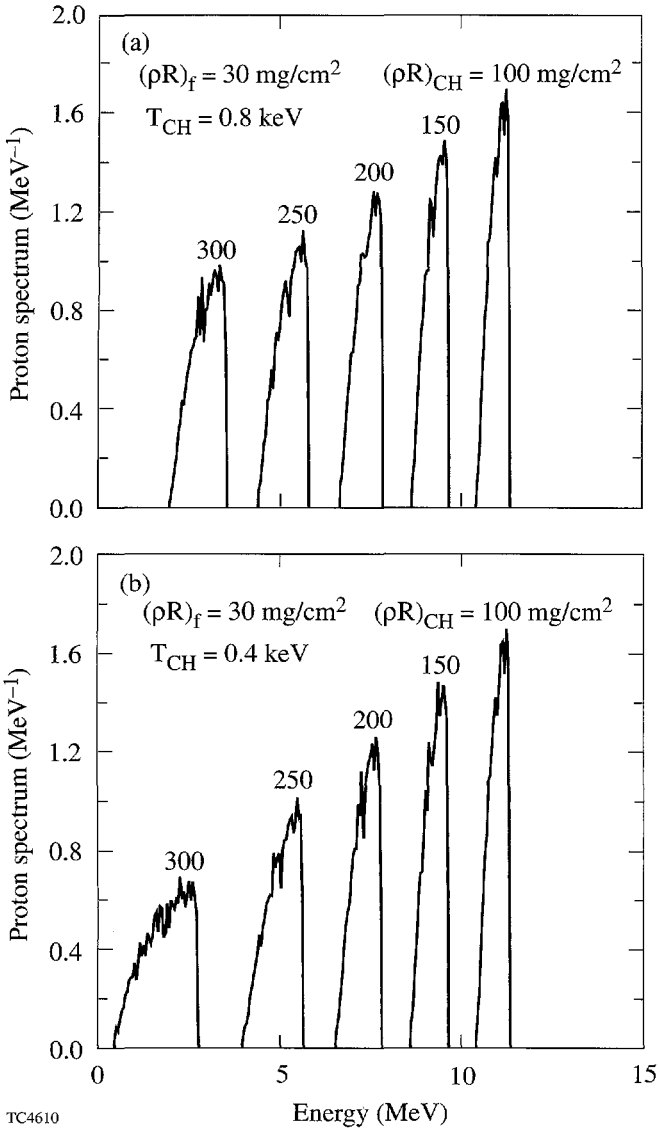

Figure 73.22
(a) Emergent D-^{3}He proton spectra (the normalized number of protons per unit energy interval) for the model (see text) with the choice of ρR as shown in the figure and with the plastic at a temperature of 0.8 keV. (b) Spectra of emergent protons with plastic at a temperature of 0.4 keV.

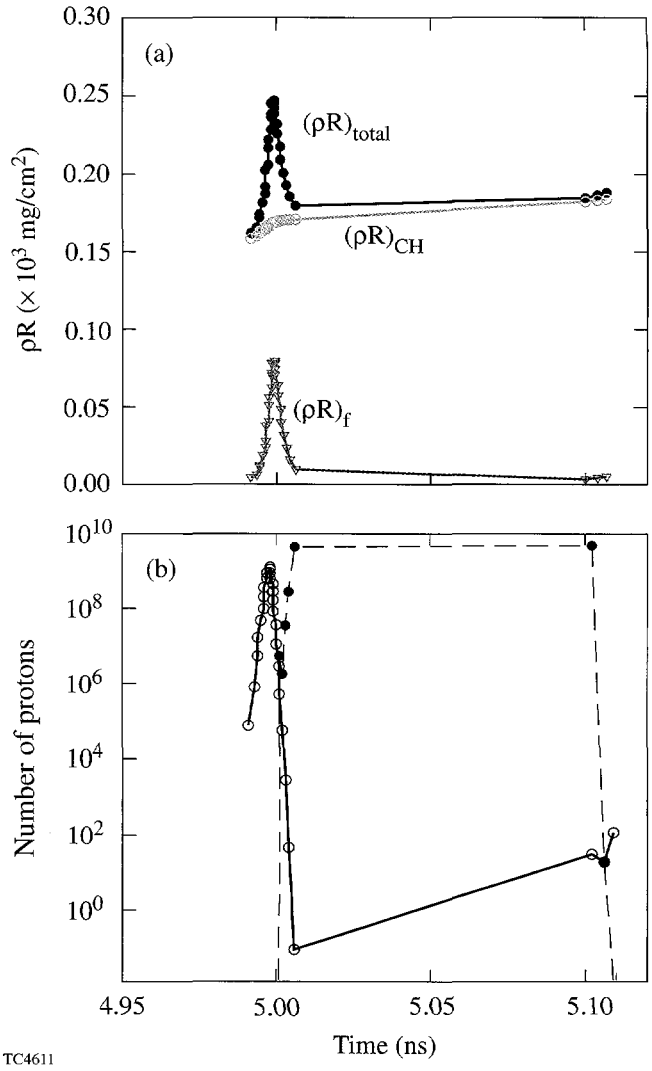

Figure 73.23
(a) Results from 1-D *LILAC* simulations for the ρR history of the target in Fig. 73.22(b); fuel ρR shown in triangles, plastic ρR shown in open circles, total target ρR shown in solid circles. (b) History of proton production in the target (open circles) and proton emission from the target (solid circles). The emergent protons measure an average total $\rho R \sim 200$ mg/cm^2.

measure of an average value of ρR, which is determined by the time that they traverse the target and can, in general, be less than the maximum value. Thus, by comparing the ρR history in Fig. 73.23(a), the history of proton production in the target [open circles in Fig. 73.23(b)], and the time history of protons exiting the target [solid circles in Fig. 73.23(b)], one can calculate the range of ρR measured through this diagnostic. The plastic ρR remains nearly constant at 170 mg/cm^2 during the time the protons traverse the target yielding this value as the average $(\rho R)_{CH}$. Furthermore, while a majority of the protons are produced near the peak value of $(\rho R)_f$ (70 mg/cm^2), they exit the target when the fuel ρR is lower (10 mg/cm^2), so that the protons sample a range of fuel ρR. Since the ρR of the plastic is so much larger than the average ρR of the fuel, the energy loss of the D-^{3}He proton should be characterized by $(\rho R)_{CH}$ in this example. The emergent proton spectrum from this simulation is shown in Fig. 73.24. One-dimensional time-dependent profiles obtained from *LILAC* were used as an input to the Monte Carlo particle-tracking code *IRIS*,[6] which calculated the spectrum emerging from the target. Since the detailed simulation indicates that the average $(\rho R)_{CH}$ measured by the protons is about 170 mg/cm^2, Fig. 73.24 must be compared with a model calculation (in Fig. 73.22) corresponding approximately to this value of the plastic fuel areal density. The comparison shows that the time-dependent evolution of the target has little influence on the position of the peak of the emergent proton spectrum. Both the model and the detailed simulation peak at approximately the same energy. This feature will simplify the interpretation of an experimental signal; the position of the peak depends only on the knowledge of the fuel and plastic ρR. The width of the emergent spectrum, on the other hand, can depend on the details of the spatial profile of proton production, density, and fuel temperature history of the target. Even so, the energies at the FWHM of the spectrum provide a reasonable measure of the range of ρR in the target when compared to the model in Fig. 73.22. Some energy loss also takes place in the hot-fuel region. The low-energy tail is due to protons produced in the innermost regions of the hot fuel slowing down in the fuel, followed by energy loss in the plastic. For a target with lower fuel ρR, the slowing down in the fuel will be less significant and the range of ρR can be inferred more reliably. For larger $(\rho R)_f$, this model dependence must be constrained through comparisons of detailed simulations with simple models approximating conditions during thermonuclear burn.

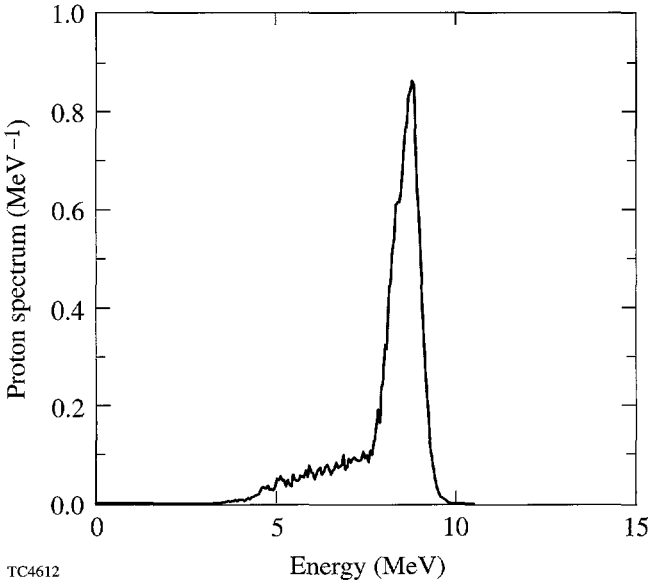

Figure 73.24
Cumulative spectrum of D-^{3}He protons escaping the target from a 1-D simulation.

The Diagnostic for DT Targets

The discussion thus far applies specifically to targets containing only deuterium and ^{3}He. The proton signal from these targets can be unambiguously identified as that due to the D-^{3}He proton. This signal is significantly larger than any other proton spectrum such as primary protons elastically scattered off fuel ions in the relevant energy region. We now discuss the diagnostic in the case where ^{3}He is added to the fuel that includes tritium in addition to deuterium.

Background related to the presence of tritium in the target is caused by the 14.1-MeV primary neutron from the DT reaction

$$\mathrm{D} + \mathrm{T} = \alpha + n(14.1\ \mathrm{MeV}). \tag{2}$$

One source of background arises from the elastic scattering of the 14.1-MeV primary DT neutrons off the protons in the plastic. The scattered protons have energies up to the maximum of 14.1 MeV.

Another important source of background arises when the 14.1-MeV neutron breaks up the deuteron in the reaction

$$\mathrm{D} + n = 2n + p, \tag{3}$$

where protons are produced with energies up to 11.8 MeV.

As seen in Fig. 73.22, the D-^{3}He proton spectrum can be significantly shifted downward due to energy losses in the

target for the range of ρR expected in high-density implosions on OMEGA. The interpretation of the diagnostic proton spectrum can then be complicated by protons from the background mentioned above in the relevant energy range. Figure 73.25 shows the emergent proton spectrum from the earlier simple model representation [corresponding to Fig. 73.22(a) with $(\rho R)_{CH}$ = 150 mg/cm^2] now being used for a gas target containing tritium in addition to deuterium and ^{3}He. The end point of the spectrum is at the maximum energy of the elastically scattered protons at 14.1 MeV. The proton background due to the deuteron breakup reaction is contained in Fig. 73.25 (and extends up to 4.5 MeV downshifted from the maximum of 11.8 MeV due to energy losses in the plastic). The D-^{3}He proton spectrum (whose range is shown as a dotted line) appears as an easily identifiable peak over the spectrum from the two sources of background mentioned above. A detailed simulation (not shown here) also shows the promise of this diagnostic for gas DT targets; the signal is somewhat broadened (with a width similar to Fig. 73.24) and is dominant over the background.

Several comments in the context of cryogenic targets are in order here. The background protons due to scattering in the plastic will be significantly reduced in this case because most of the plastic will have been ablated from the target before thermonuclear burn.

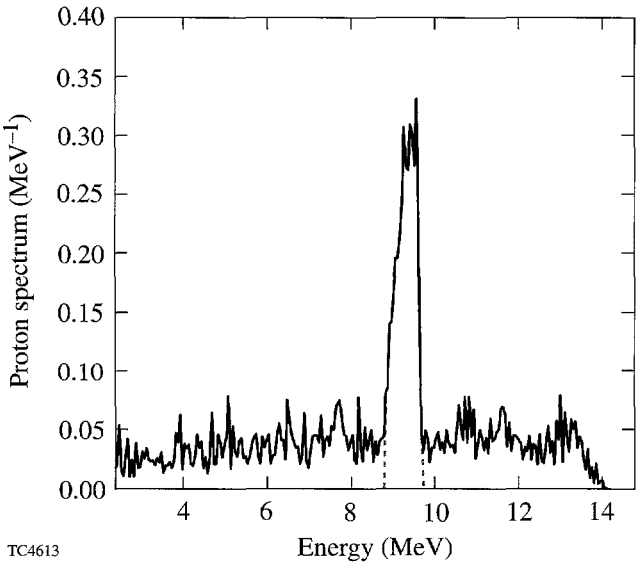

Figure 73.25
Spectrum of protons escaping a gas target containing DT and ^{3}He and modeled as described in the text. The peak is due to the D-^{3}He proton signal, and the background comprises protons from the deuteron breakup reaction and the elastic scattering of protons in the plastic. The dotted extension of the peak shows the range of the D-^{3}He proton signal.

In Fig. 73.26(a) we show the emergent proton spectrum from a 1-D simulation of an OMEGA cryogenic DT target. (The target comprises solid deuterium and tritium in a 1:1 ratio and encloses D-^{3}He gas. We ignore any confining plastic remnants that may exist during thermonuclear burn.) The D-^{3}He signal [shown as a dashed line in the region of its overlap with protons from the $(n,2n)$ reaction] extends from about 10 MeV to 14 MeV and is significantly broadened principally due to the time evolution of densities in the target. This dependence on the hydrodynamic evolution of the target can be constrained by comparing the emergent proton spectrum with that from a range of models similar to those used for the gas target in Fig. 73.22. However, the large $(n,2n)$ proton signal (about three orders of magnitude more protons are produced in the deuteron breakup reaction than in the D-^{3}He fusion) extends to about 11.8 MeV and makes the interpretation of the signal very dubious.

One possible method to lower this background is to include different proportions of deuterium and tritium in the solid fuel in order to reduce the yield of neutrons from the DT reaction and to reduce the numbers of protons from the $(n,2n)$ reaction. The proton spectrum from a target where the deuterium and tritium are in a ratio of 1:9 respectively is shown in Fig. 73.26(b). The number of background protons is significantly reduced, and the proton signal dominates in the region of overlap with the background. Thus, with some target optimization an unambiguous D-^{3}He proton signal can be obtained from cryogenic DT targets on OMEGA. In this context, tertiary neutrons mentioned earlier are a more attractive diagnostic for cryogenic DT targets because they have no background, place no constraints on the targets, and are applicable to higher densities.

Summary

In summary, the D-^{3}He proton spectrum is being considered as a means for inferring the total ρR of cryogenic DD targets. Using a gas target capable of achieving high areal densities, we have demonstrated that this diagnostic can be useful for up to $\rho R \sim 300$ mg/cm^2 for targets containing only D and ^{3}He. The reliability of this diagnostic is strengthened by its weak sensitivity to temperatures in the cold regions of the target for a wide range of ρR. For targets containing tritium, the interpretation of the signal is more difficult due to background arising from the 14.1-MeV primary DT neutron.

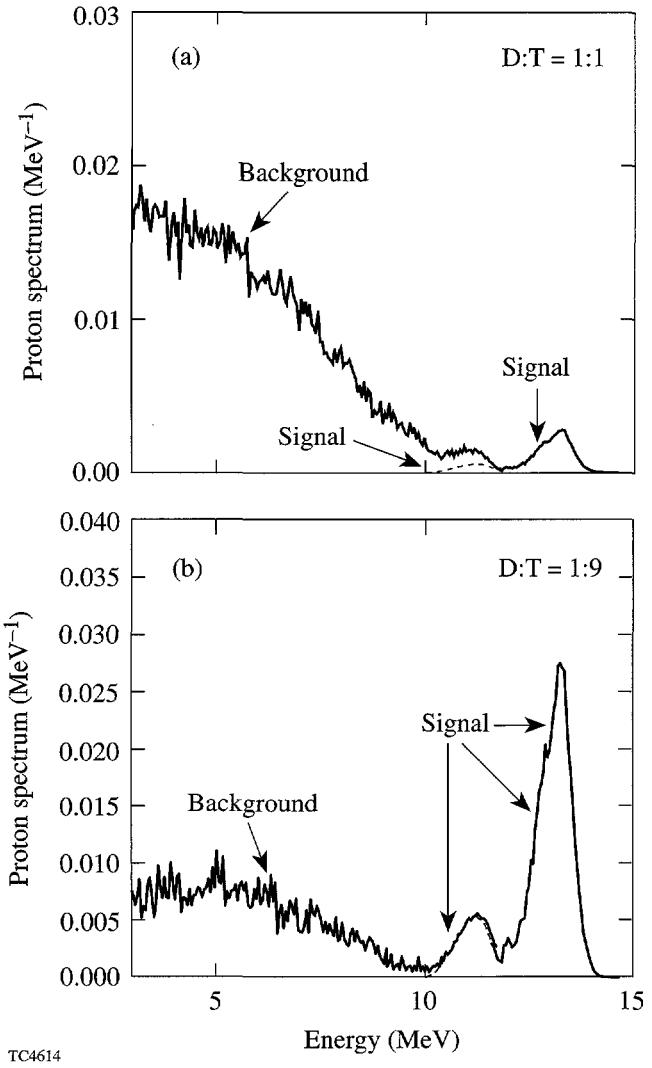

Figure 73.26
(a) Spectrum of emergent protons from an OMEGA cryogenic target with D:T = 1:1 in solid DT. D-^{3}He protons extend from about 10 MeV to 14 MeV. The dashed line is the extension of the signal in the region of its overlap with the background protons from the deuteron breakup reaction, which extends to 11.8 MeV. (b) Spectrum of protons from an OMEGA cryogenic target with D:T = 1:9.

Future Applications

This diagnostic could also serve as a method to measure gross asymmetries in the target that may arise due to energy imbalance in the beams, laser mispointing, etc. The D-^{3}He protons are produced isotropically, and any angular dependence of the proton yield or the spectrum is an indication of asymmetries in the target. Experimentally, track detectors placed strategically at various angles around the target could be used in conjunction with the charged-particle spectrometer to measure the various emergent proton spectra. Fuel areal densities could be inferred by comparing these spectra to calculations that include analytic angular variations in the target profiles. These measurements would track only gross variations in density (and temperature) constraining the calculations; inclusion of only "long"-wavelength perturbations to spherical symmetry should adequately model the emergent proton spectra. The Monte Carlo particle-tracking code *IRIS* is currently being modified with a view toward including such asymmetries in target profiles. Diagnostics for asymmetries in the target could then be developed.

ACKNOWLEDGMENT

This work was supported by the U.S. Department of Energy Office of Inertial Confinement Fusion under Cooperative Agreement No. DE-FC03-92SF19460, the University of Rochester, and the New York State Energy Research and Development Authority. The support of DOE does not constitute an endorsement by DOE of the views expressed in this article.

REFERENCES

1. S. Skupsky and S. Kacenjar, J. Appl. Phys. **52**, 2608 (1981).
2. D. R. Welch, H. Kislev, and G. H. Miley, Rev. Sci. Instrum. **59**, 610 (1988). See also Laboratory for Laser Energetics LLE Review **69**, 46, NTIS document No. DOE/SF/19460-152 (1996). Copies may be obtained from the National Technical Information Service, Springfield, VA 22161.
3. D. G. Hicks, C. K. Li, R. D. Petrasso, F. H. Seguin, B. E. Burke, J. P. Knauer, S. Cremer, R. L. Kremens, M. D. Cable, and T. W. Phillips, Rev. Sci. Instrum. **68**, 589 (1997).
4. J. D. Jackson, *Classical Electrodynamics*, 2nd ed. (Wiley, New York, 1975).
5. *LILAC*, E. B. Goldman, Laboratory for Laser Energetics Report No. 16, University of Rochester (1973).
6. *IRIS*, S. Cremer, University of Rochester Laboratory for Laser Energetics (unpublished).

Growth Rates of the Ablative Rayleigh–Taylor Instability in Inertial Confinement Fusion

In recent years, several authors[1–14] have studied the linear growth of the Rayleigh–Taylor (RT) instability in ablation fronts accelerated by laser irradiations. The determination of the instability growth rate is crucial to the success of inertial confinement fusion (ICF)[15,16] because an excessive distortion of the front could lead to a severe degradation of the capsule performance with respect to the final core conditions by seeding the deceleration-phase RT instability and preventing the onset of the ignition process.

For a successful implosion, ICF targets must be designed to keep the RT growth at an acceptable level. Because of the complexity of 2-D or 3-D codes and the mesh refinement needed to simulate hydro-instabilities, 2-D or 3-D simulations cannot be routinely used to study the capsule stability and mixing. The best approach to target design is to carry out a preliminary analysis by using 1-D simulations to study the main characteristics of the implosion and then processing the data with a mixing model to study the evolution of the instability and the induced rms deviations. Once the preliminary design is completed, the optimization can be carried out by using 2-D or 3-D codes. Since the mixing model predictions are based on the initial perturbation amplitude and linear growth rates, it is very important to generate an accurate and reliable growth-rate formula to be used in conjunction with the 1-D code output.

According to the linear classical theory,[17] the interface between a heavy fluid of constant density ρ_h and a light fluid of constant density ρ_l in a gravitational field g pointing toward the light fluid is unstable. A small perturbation would grow exponentially in time, $\sim e^{\gamma_{\rm cl} t}$, at a rate

$$\gamma_{\rm cl} = \sqrt{A_T^{\rm cl}\, kg}\,, \tag{1}$$

where $A_T^{\rm cl} = (\rho_h - \rho_l)/(\rho_h + \rho_l)$ is the Atwood number and k is the perturbation wave number.

If the density is smoothly varying between the two fluids and the minimum density-gradient scale length $L_m = \min\left|\rho/(d\rho/dx)\right|$ is finite, then a distinction must be made between those modes with wavelength larger and smaller than L_m. The long-wavelength modes ($kL_m << 1$) are not affected by the finite L_m and grow according to Eq. (1), while the short-wavelength modes ($kL_m >> 1$) are localized inside the smooth interface and grow at the rate[18]

$$\gamma = \sqrt{\frac{g}{L_m}}\,. \tag{2}$$

An asymptotic formula reproducing the results at short and long wavelengths can be easily generated by inspection of Eqs. (1) and (2) leading to

$$\gamma = \sqrt{\frac{A_T^{\rm cl} kg}{1 + A_T^{\rm cl} kL_m}}\,. \tag{3}$$

In laser-accelerated targets, the ablation process and the thermal transport add a great deal of complication to the evolution of the instability. The overdense target material (with density ρ_a) is ablated at a rate $\dot{m} = \rho_a V_a$, where V_a is the ablation velocity. The latter represents the penetration speed of the ablation front in the overdense target. The ablated material blowing off the target rapidly expands inside the ablation front and accelerates to large velocities relative to the overdense targets.

Several authors[1–14] have shown that the ablation process leads to a reduction of the instability growth rate. The so-called ablative stabilization was first discussed in Ref. 1 and thereafter extensively studied in Refs. 2–13. Because of the mathematical complexity of the problem, simplified analytic models such as the sharp boundary model have been used to describe the linear phase of the instability. However, such models are

heuristic in nature as they lack a proper closure, which is left to the physical intuition. For such reasons, different authors using different closure equations have produced different growth-rate formulas (see Refs. 1, 5, and 12). Numerical simulations have confirmed the stabilizing effect of ablation and indicated that, in some cases (as described later), the growth rate can be approximated by the following formula:

$$\gamma = 0.9\sqrt{kg} - 3.1\, kV_a . \tag{4}$$

Equation (4) was derived in Ref. 3 by fitting the numerical solution of the linearized conservation equations including ablation and electronic heat conduction. As stated in the **Growth Rates** section, Eq. (4) does not correctly reproduce the growth rates in the presence of a significant radiation energy transport leading to smooth density profiles. It is important to observe that Eq. (4) does not include the stabilizing effect of finite density-gradient scale length and it can only be applied to very sharp ablation fronts or modes with $kL_m << 1$.

Only very recently, the analytic stability theory of accelerated ablation fronts has been carried out in the limit of subsonic ablation flows[8–12] (i.e., fronts with ablation velocity less than the sound speed at the ablation front) by using complicated asymptotic matching techniques. Subsonic ablation fronts are characterized by two dimensionless parameters:[10] the Froude number $Fr = V_a^2/gL_0$ and the power index for thermal conduction $\nu\left(\kappa \sim T^{\nu}\right)$. Here, L_0 is the characteristic thickness of the ablation front, which is proportional to the minimum value of the density-gradient scale length[6] $L_m\left[L_0 = L_m \nu^{\nu}/(\nu+1)^{\nu+1}\right]$. The analytic theory developed in Refs. 8–11 shows that the instability growth rate is strongly dependent on the magnitude of the Froude number. For large Froude numbers,[9,10] the main stabilizing effects are ablation and blowoff convection, and the growth rate can be written in the following form:[9,12]

$$\gamma = \sqrt{A_T kg - A_T^2 k^2 V_a V_{\text{b.o.}}} - \left(1 + A_T\right) kV_a , \tag{5}$$

where

$$A_T \equiv \frac{1-\left(\rho_{\text{b.o.}}/\rho_a\right)}{1+\left(\rho_{\text{b.o.}}/\rho_a\right)}, \qquad V_{\text{b.o.}} = V_a \frac{\rho_a}{\rho_{\text{b.o.}}}, \tag{6a}$$

$$\frac{\rho_{\text{b.o.}}}{\rho_a} = \mu_0 \left(kL_0\right)^{1/\nu}, \qquad \mu_0 = \frac{(2/\nu)^{1/\nu}}{\Gamma\left(1+1/\nu\right)} + \frac{0.12}{\nu^2}, \tag{6b}$$

$\Gamma(x)$ is the gamma function and $V_{\text{b.o.}}$ is the velocity of the blowoff material at the distance $\sim\lambda$ from the ablation front. Observe that the cutoff wave number obtained by setting $\gamma = 0$ in Eq. (5) occurs at long wavelengths,[8]

$$k_c L_0 = \left[\frac{\mu_0(\nu)}{Fr}\right]^{\nu/(\nu-1)} \left\{1 + O\left[\left(kL_0\right)^{1/\nu}\right]\right\} << 1 , \tag{7}$$

and short-wavelength modes are stable. As shown in Refs. 9 and 10, Eq. (5) can be accurately fitted by Eq. (4) for $\nu = 2.5$ and $0.1 < Fr < 5$, thus suggesting that the latter can be applied to ablation fronts with large Froude numbers.

When the Froude number is less than unity ($Fr << 1$), the analytic stability theory becomes more complicated and can be carried out only in the limits of $\epsilon = kL_0 << 1$ and $\epsilon >> 1$. The analysis of Ref. 11 has shown that long-wavelength modes with wave numbers $\epsilon << 1$ have a growth rate $\gamma \simeq \sqrt{A_T kg} - \beta kV_a$, where $1 < \beta < 2$ is a function of ν, $\beta = \Gamma\left(1+2/\nu\right)/\Gamma^2\left(1+1/\nu\right)$. Short-wavelength modes ($kL_0 > 1$) are unstable, and the corresponding perturbations are mitigated by ablative convection, finite density gradient, and thermal smoothing. Their growth rate can be written as

$$\gamma = \sqrt{\alpha g/L_0 + c_0^2 k^4 L_0^2 V_a^2} - c_0 k^2 L_0 V_a$$

for $1 << kL_0 << Fr^{-1/3}$, and

$$\gamma = c_1 g/\left(V_a k^2 L_0^2\right) - c_2 kV_a$$

for the wave numbers near the cutoff ($k \approx k_c$). The parameters α and c_{0-2} have lengthy expressions described in Ref. 11, and a complete summary of the growth-rate formulas is given in Table 1 of Ref. 11. The cutoff wave number k_c of ablation fronts with small Froude numbers occurs at short wavelengths and scales as $k_c L_0 \sim Fr^{-1/3} >> 1$.

The growth-rate formulas obtained in Ref. 11 for small Froude numbers and short/long wavelengths can be combined with the formula (5) for large Froude numbers into a single expression that reproduces the analytic results in the appropriate limits ($Fr << 1$, $Fr >> 1$, $\epsilon << 1$, $\epsilon >> 1$). According to

Ref. 11, the asymptotic formula can be written in the following form:

$$\gamma = \sqrt{\hat{A}_T kg + \delta^2 k^4 L_0^2 V_a^2 + \left(\omega^2 - \frac{1}{\xi_l}\right) k^2 V_a^2} - \delta k^2 L_0 V_a - \hat{\beta} k V_a , \tag{8a}$$

where

$$\hat{A}_T = \frac{\xi_h - \xi_l}{\xi_h + \xi_l}, \qquad \xi_h = \left(1 + K_1 e^{-\frac{K_3}{\epsilon}}\right)^{-1}, \tag{8b}$$

$$\xi_l = \mu_0 \left(\frac{1}{\epsilon} + K_2\right)^{-\frac{1}{\nu}},$$

$$\hat{\beta} = \omega \frac{1 + T_1 \epsilon}{1 + T_2 \epsilon}, \quad T_1 = \frac{\beta_0 - \beta_1}{\beta_2 \beta_0}, \tag{8c}$$

$$T_2 = \frac{\beta_0 - \beta_1}{\beta_2 \beta_1},$$

$$\omega = \beta_0 \frac{1 + \left(1 + \hat{A}_T\right)/\beta_0 \sinh(Fr)}{1 + \sinh(Fr)}, \tag{8d}$$

$$\beta_0 = \frac{\Gamma\left(1 + \frac{2}{\nu + 0.1/\nu^4}\right)}{\Gamma^2\left(1 + \frac{1}{\nu + 0.1/\nu^4}\right)},$$

$$\beta_1 = \frac{1}{\xi_0 \sqrt{5}}, \qquad \beta_2 = B + \frac{\beta_0^2 + \beta_1^2}{2\delta\beta_1} - \frac{1 + K_1}{2\delta\beta_1}, \tag{8e}$$

$$\delta = \frac{1}{2\Upsilon}\left[K_1 A + \frac{1}{\nu K_2} \times \sqrt{\left(\frac{1}{\nu K_2} + K_1 A\right)^2 - 4K_1\beta_1\Upsilon - \frac{1 + K_1 \nu}{\nu^2 K_2^2}}\right], \tag{8f}$$

$$\Upsilon = \frac{25}{8}\frac{\xi_0^{2\nu+1}}{2\nu + 3}, \quad K_2 = \left[(1 + K_1)\mu_0\right]^{\nu}, \tag{8g}$$

$$K_1 = \frac{1}{\xi_0} - 1,$$

$$K_3 = \frac{1 + K_1}{K_1}\left(2\delta\Upsilon - \frac{1}{\nu K_2}\right), \qquad \mu_0 = \frac{(2/\nu)^{1/\nu}}{\Gamma\left(1 + \frac{1}{\nu}\right)} + \frac{0.12}{\nu^2}, \tag{8h}$$

$$\xi_0 = \frac{2\nu + 2}{2\nu + 3},$$

$$A = \frac{\sqrt{5}}{4}\frac{\xi_0^{\nu-1}}{(2\nu + 3)^2} \times \left[\sqrt{\frac{2}{5}\xi_0}\left(12\nu^2 + 25\nu + 18\right) + \frac{\nu + 2}{2\nu + 3}\left(8\nu^2 + 20\nu + 17\right)\right], \tag{8i}$$

$$B = \frac{\sqrt{5}}{4}\frac{\xi_0^{\nu-1}}{(2\nu + 3)^2} \times \left[\sqrt{\frac{2}{5}\xi_0}\left(8\nu^2 + 25\nu + 12\right) - \frac{8\nu^3 + 16\nu^2 + 7\nu + 4}{2\nu + 3}\right]. \tag{8j}$$

A detailed comparison of the growth rates obtained by using Eq. (8) and the numerical solutions of the conservation equations has demonstrated a remarkable agreement over a wide range of values for Fr, ν, and ϵ (see Ref. 11).

Despite its lengthy expression, the asymptotic formula can be easily computed once the Froude number Fr, the length L_0, the acceleration g, the ablation velocity V_a, and the power index for thermal conduction ν are known. The main difficulty in using Eq. (8) lies in the determination of the equilibrium parameters whose values are strongly dependent on the dominant energy transport mechanism. In this article, we describe a simple procedure to be used in conjunction with existing one-dimensional hydrodynamic codes to determine Fr, L_0, g, V_a,

and v. In addition, we apply this procedure to accelerated flat foils commonly used in ICF experiments and determine the unstable spectrum using Eq. (8). We also compare the analytic growth rates with the results of two-dimensional simulations obtained using the code *ORCHID*.[19] Numerical fits of Eq. (8) are also studied for different ablators, and simplified formulas are generated for a fast growth-rate estimate. It is the aim of this article to simplify the theoretical result of Betti *et al.* (Refs. 8–11) to make it useful to ICF target design.

Equilibrium Parameters

One-dimensional simulations are commonly used in ICF target design, and several 1-D codes describing laser-accelerated targets are available at universities and national laboratories. Among them, the most frequently used are the codes *LILAC*,[20] *HYADES*,[21] *LASNEX*,[22] etc. In this article, the authors have extensively used the code *LILAC*, a 1-D Lagrangian code including laser absorption, classical flux-limited thermal transport, and multigroup radiation diffusive transport. The equation-of-state package available in *LILAC* includes the ideal gas, Thomas–Fermi, and SESAME tables.

The analytic stability analyses are usually based on a single-temperature (or one-group) diffusive model for the heat transport, i.e., the heat flux is proportional to the temperature gradient, and the thermal conductivity follows a power law of the temperature, $\kappa = \kappa_a (T/T_a)^{\nu}$, where κ_a, T_a are the thermal conductivity and temperature calculated at the peak density, and ν is the power index. These simplifications make the problem solvable with analytic techniques.[8–12,14] If the radiated energy is negligible (low-Z materials, such as DT), the energy is transported mainly by electronic heat conduction. In this case, the power index $\nu = 2.5$ (as given by Spitzer[23]) and $L_0 = (\gamma_h - 1)/\gamma_h A \kappa_a/(\rho_a V_a)$, where γ_h is the ratio of the specific heats, $A = m_i/(1+Z)$ is the average particle mass, ρ_a is the maximum density, and V_a is the ablation velocity, respectively (see Ref. 8). However, if a significant amount of energy is present in the radiation field, then an accurate estimate of the energy transport requires the use of multigroup radiation transport models. In such models, the radiation energy spectrum is divided into several groups. Each group is described by a radiation temperature obeying an energy diffusion equation. Because of the complexity of such models, an analytic stability analysis would be intractable. For such reason, the analytic theories are based on a single-group model (one temperature). However, if the one-group diffusive transport model is used in the stability analysis, then one should at least make sure that such a model reproduces the one-dimensional hydrodynamic profiles obtained using the multigroup model. In other words, one should fit the multigroup hydro-profiles with the one-group profiles by properly selecting the value of ν and L_0. This is an essential requirement for the stability analysis, assuring that the linearization is performed about the right equilibrium. Of course, there is no guarantee that the two-dimensional effects are correctly included in the one-group model, even though the one-dimensional profiles are correctly reproduced. However, the RT is mainly a hydrodynamic instability, and one could hope that if the 1-D hydrodynamic profiles are correctly included, then the 2-D/3-D stability analysis would be independent of the heat transport model. This speculation could be verified *a posteriori* by comparing the analytic results with 2-D simulations including multigroup radiation transport.

In summary, the analytic analysis is based on the one-group subsonic diffusive transport model (or isobaric model). The parameters ν, Fr, and L_0 of such a model are determined by fitting the analytic hydro-profiles with those obtained from 1-D simulations including multigroup radiation transport. The results of the analytic stability theory are then compared with the full 2-D simulations including multigroup radiation transport.

As shown in Ref. 6, the density profile of subsonic ablation fronts, described by the one-temperature diffusive transport model, obeys the following first-order differential equation:

$$d\xi/dy = -\xi^{\nu+1}(1-\xi)/L_0, \tag{9}$$

where ξ is the density normalized to its peak value, $\xi = \rho/\rho_a$, and ν is the power index for thermal conduction. The equilibrium pressure is determined by the momentum-conservation equation $d(p+\rho U^2)/dy = \rho g$ and the mass conservation equation $[d(\rho U)/dy = 0]$, which can be rewritten in the following dimensionless form:

$$\frac{1}{\Pi_a}\frac{d\Pi}{dy} = \xi^2 \frac{d\xi}{dy} + \frac{\xi}{Fr\, L_0}, \qquad \xi U(y) = V_a, \tag{10}$$

where $\Pi = p/p_a$, $\Pi_a = V_a/\sqrt{p_a/\rho_a}$ is the normalized ablation velocity, and p_a is the pressure at the location of the peak density ρ_a. Observe that Eqs. (9) and (10) for the unknowns ξ and Π depend on the four parameters Π_a, Fr, L_0, and ν. Keeping in mind that our goal is to reproduce the hydro-profiles of the 1-D simulations, we determine these parameters by fitting the analytic hydro-profiles with the numerical ones. Let's define with $\xi_s = \rho/\rho_a$ and $\Pi_s = p/p_a$ the normalized simulated

density and pressure profiles. If the predictions of the one-group model were exact, then the simulated profiles would represent an exact solution of Eqs. (9) and (10); however, this is not the case, and replacing ξ with ξ_s in Eq. (9) leads to an error. For convenience, we take the logarithm of Eq. (9) and define the error as

$$\mathrm{er} = (\nu+1)\ln\xi_s - \ln L_0 - \ln\left(-\frac{d\xi_s}{dy}\frac{1}{1-\xi_s}\right). \quad (11)$$

Observe that er = 0 if $\xi_s = \xi$. In order to reproduce the simulated profiles over the entire ablation front, it is useful to minimize the integrated quadratic error (δ) defined as

$$\delta(\nu, L_0) \equiv \int_{\xi_{\min}}^{\xi_{\max}} \left[(\nu+1)\ln\xi_s - \ln L_0 - \ln\left(-\frac{d\xi_s}{dy}\frac{1}{1-\xi_s}\right)\right]^2 d\xi_s, \quad (12)$$

where $\xi_{\min}$, $\xi_{\max}$ are the minimum and the maximum values of the density of the fitting region defining the extension of the ablation front ($\xi_{\min} = 0.01$ and $\xi_{\max} = 0.99$ are two possible values). The minimization of δ is obtained by setting to zero the partial derivatives with respect to ν and L_0:

$$\frac{\partial\delta}{\partial L_0} = \frac{\partial\delta}{\partial\nu} = 0. \quad (13)$$

Substituting Eq. (12) into Eq. (13) leads to the following estimates of L_0 and ν:

$$\nu = \frac{c_1 a_1 - c_2 b_1}{a_1^2 - a_2 b_1} - 1, \qquad L_0 = \exp\left(\frac{+a_2 c_1 - a_1 c_2}{a_1^2 - a_2 b_1}\right), \quad (14)$$

where

$$a_1 = [\![\xi(\ln\xi - 1)]\!],$$
$$a_2 = [\![\xi(\ln\xi - 1)^2 + \xi]\!], \quad b_1 = [\![\xi]\!], \quad (15a)$$

$$c_1 = \int_{y(\xi_{\min})}^{y(\xi_{\max})} \ln\left[-\frac{d\xi_s}{dy}\frac{1}{1-\xi_s}\right]\frac{d\xi_s}{dy}dy, \quad (15b)$$

$$c_2 = \int_{y(\xi_{\min})}^{y(\xi_{\max})} \ln\xi_s \ln\left[-\frac{d\xi_s}{dy}\frac{1}{1-\xi_s}\right]\frac{d\xi_s}{dy}dy, \quad (15c)$$

and $[\![H(\xi)]\!] = H(\xi_{\max}) - H(\xi_{\min})$. In the same fashion, the Froude number and dimensionless ablation velocity Π_a can be determined by minimizing the integrated quadratic error η in the momentum conservation equation

$$\eta(Fr, \Pi_a) = \int_{y(\xi_{\min})}^{y(\xi_{\max})} \left(\frac{1}{\Pi_a^2}\frac{d\Pi_s}{dy} - \frac{1}{\xi_s^2}\frac{d\xi_s}{dy} - \frac{\xi_s}{FrL_0}\right)^2 dy, \quad (16)$$

where $\Pi_s = p_s/p_a$ is the simulated normalized pressure profile. After some straightforward algebra, the minimization with respect to Π_a and Fr yields

$$Fr = \frac{a_3 b_4 + b_3^2}{b_3 c_3 + a_3 c_4}\frac{1}{L_0}, \qquad \Pi_a^2 = \frac{a_3 b_4 + b_3^2}{c_3 b_4 - c_4 b_3}, \quad (17a)$$

where

$$a_3 = \int_{y(\xi_{\min})}^{y(\xi_{\max})} \left(\frac{d\Pi_s}{dy}\right)^2 dy,$$
$$b_3 = -\int_{y(\xi_{\min})}^{y(\xi_{\max})} \xi_s \frac{d\Pi_s}{dy} dy, \quad (17b)$$

$$b_4 = -\int_{y(\xi_{\min})}^{y(\xi_{\max})} \xi_s^2 dy, \quad c_3 = \int_{y(\xi_{\min})}^{y(\xi_{\max})} \frac{1}{\xi_s^2}\frac{d\Pi_s}{dy}\frac{d\xi_s}{dy}dy,$$
$$c_4 = \ln\frac{\xi_{\max}}{\xi_{\min}}. \quad (17c)$$

The integration limits $y(\xi_{\min})$, $y(\xi_{\max})$ represent the location of the points with density $\xi_{\min}$ and $\xi_{\max}$, respectively. Using the peak density ρ_a and the pressure at the location of the peak

density p_a, the acceleration and ablation velocity can be easily determined from Eqs. (14) and (17):

$$V_a = \Pi_a \sqrt{\frac{p_a}{\rho_a}}, \qquad g = \frac{V_a^2}{L_0}\frac{1}{Fr}. \tag{18}$$

This technique has been tested on the hydrodynamic profiles obtained using the code *LILAC*. We consider a planar CH foil of thickness $d = 18$ μm irradiated by a 0.35-μm-wavelength laser of 50-TW/cm^2 intensity with a 1-ns linear ramp. The pulse duration is 3 ns. The profiles obtained from the simulation are slowly varying in time. For the test, we consider the profiles at time $t = 2$ ns and substitute the simulated density and pressure into Eqs. (14), (17), and (18) and obtain $\nu = 0.7$, $L_0 = 0.24$ μm, $Fr = 0.032$, $g = 36$ μm/ns^2, and $V_a = 0.54$ μm/ns. Then, using these values, we solve Eqs. (9) and (10) to determine the analytic density and pressure profiles. Figure 73.27 shows the simulated and the analytic profiles for the CH target. The excellent agreement between the profiles shows the accuracy of the fitting procedure described above. In Fig. 73.28, the fitting parameters ν, L_0, and Fr are plotted as functions of time, and the dashed lines represent the corresponding average values. It is important to notice that the power index for thermal conduction to be used in the one-group model ($\nu = 0.7$) is well below the Spitzer[23] ($\nu = 2.5$) or the Zeldovich[24] value ($\nu \simeq 6.5$), thus showing the importance of the multigroup treatment of the radiation transport in plastic targets.

Lower-Z materials such as solid DT are a good test of the fitting procedure because they are expected to produce a very low level of radiation and to approximately follow the Spitzer model with $\nu \simeq 2.5$. We have considered a planar DT foil of thickness $d = 120$ μm irradiated by the pulse described above. Substituting the simulated profiles into Eqs. (9) and (10) yields $\nu = 2$, $L_0 = 0.03$ μm, and $Fr = 5$. This result indicates that radiation transport has a small effect in cryogenic DT targets.

Tables 73.I and 73.II show the time-averaged values of Fr, ν, L_0, and V_a for several plastic (CH) and DT targets of different thicknesses (Th) and laser intensities (I). It is important to observe that plastic targets have smooth density profiles (large density-gradient scale length), low ablation velocity, $\nu < 1$, and small Froude numbers while solid-DT targets have sharp profiles, large ablation velocity, $\nu \approx 2$, and large Froude numbers.

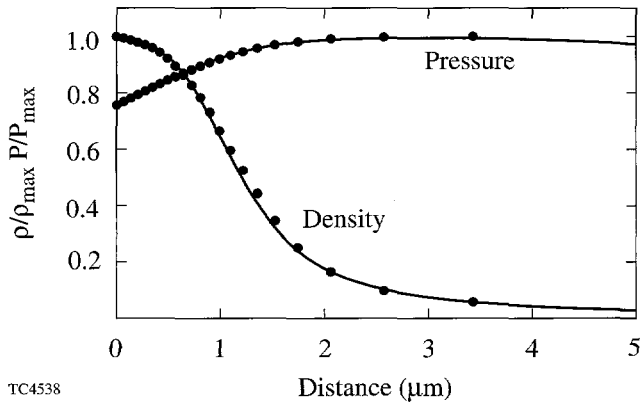

Figure 73.27
Normalized density and pressure profiles obtained by using isobaric model (solid lines) and 1-D numerical simulation (dots).

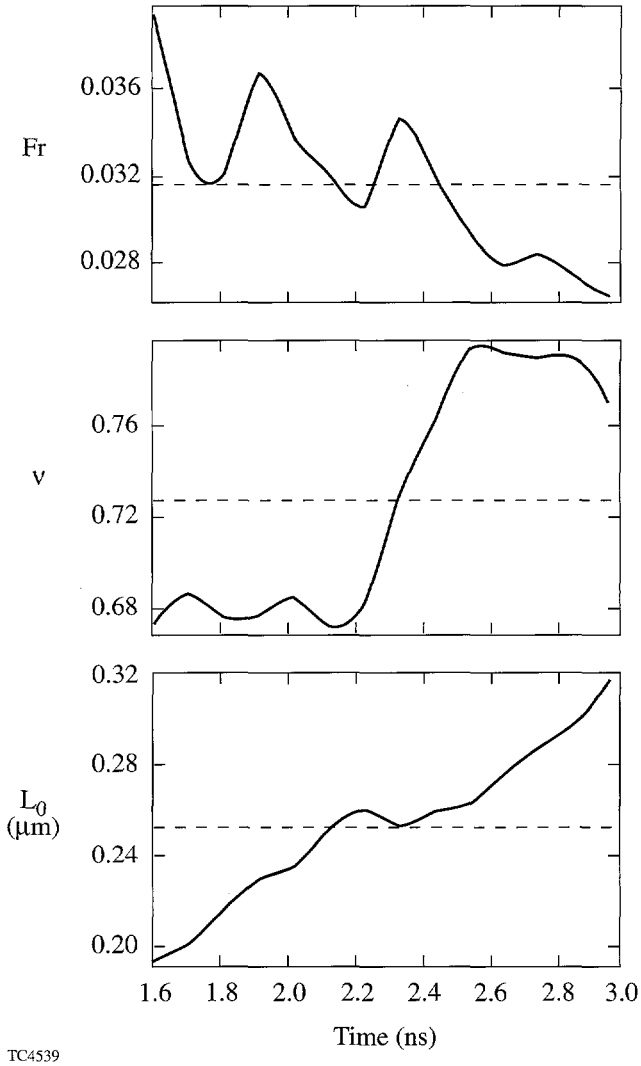

Figure 73.28
Temporal evolution (solid lines) and average values (dashed lines) of the Froude number Fr, power index for thermal conduction ν, and the characteristic thickness of ablation front L_0 for a CH target.

Growth Rates

1. Comparison with Numerical Results

Once the equilibrium parameters are calculated, Eq. (8) can be used to determine the growth rates. As discussed in the previous section, there is no guarantee that the analytic stability analysis using the one-temperature model would reproduce the results of the 2-D simulations using the multigroup radiation diffusion treatment even though the 1-D simulated and analytic hydrodynamic profiles are identical. It is necessary to validate the formula by comparing the analytic and the numerical growth rates.

As a first test of the analytic theory, we compare the analytic growth rates with Takabe's formula.[3] The latter has been derived by fitting the numerical solution of the exact, linearized, single-fluid conservation equations including Spitzer conductivity and a finite Mach number. This test is useful because it validates the assumption of subsonic flow and the simplification leading to the isobaric model.[5] Takabe's formula can be written in the following dimensionless form:[3]

$$\hat{\gamma} = \frac{\gamma}{\gamma_{\mathrm{cl}}} = \alpha_{\mathrm{T}} - \beta_{\mathrm{T}} X, \tag{19}$$

where $\gamma_{\mathrm{cl}} = \sqrt{kg}$ is the classical growth rate, $X = \sqrt{kV_a^2/g}$, $\alpha_{\mathrm{T}} \simeq 0.9$, and $\beta_{\mathrm{T}} \simeq 3.1$. Similarly, Eq. (8) can also be rewritten in dimensionless form:

$$\hat{\gamma} = \sqrt{\hat{A}_{\mathrm{T}} + \delta^2 \frac{X^6}{Fr^2} + \left(\omega^2 - \frac{1}{\xi_l}\right) X^2} - \delta \frac{X^3}{Fr} - \hat{\beta} X. \tag{20}$$

Table 73.I: CH targets.

Th (μm)	I (TW/cm^2)	$\langle Fr \rangle$	$\langle \nu \rangle$	$\langle L_0 \rangle$ (μm)	$\langle L_m \rangle$ (μm)	$\langle V_a \rangle$ (μm/ns)	$\langle g \rangle$ (μm/ns^2)	Growth Rate [fit of Eq. (8)]
10	50	0.03	0.8	0.2	0.7	0.8	95	$1.01\sqrt{\frac{kg}{1+kL_m}} - 1.8\,kV_a$
18	50	0.03	0.8	0.3	1.0	0.6	50	$1.01\sqrt{\frac{kg}{1+kL_m}} - 1.8\,kV_a$
20	100	0.04	0.9	0.3	1.1	0.9	76	$0.99\sqrt{\frac{kg}{1+kL_m}} - 1.7\,kV_a$
20	240*	0.05	0.9	0.2	0.7	1.3	130	$0.97\sqrt{\frac{kg}{1+kL_m}} - 1.6\,kV_a$
25	240*	0.05	0.9	0.2	0.7	1.2	123	$0.98\sqrt{\frac{kg}{1+kL_m}} - 1.6\,kV_a$

*Linear-rise laser pulse

Table 73.II: DT targets.

Th (μm)	I (TW/cm^2)	$\langle Fr \rangle$	$\langle \nu \rangle$	$\langle L_0 \rangle$ (μm)	$\langle L_m \rangle$ (μm)	$\langle V_a \rangle$ (μm/ns)	$\langle g \rangle$ (μm/ns^2)	Growth Rate [fit of Eq. (8)]
100	50	4.1	2.0	0.02	0.13	2.8	97	$0.94\sqrt{kg} - 2.6\,kV_a$
190	50	3.8	2.0	0.03	0.20	2.7	60	$0.94\sqrt{kg} - 2.6\,kV_a$
190	100	4.0	2.1	0.07	0.49	4.6	77	$0.94\sqrt{kg} - 2.6\,kV_a$

The growth rates calculated using Eq. (19) and Eq. (20) for ν = 2.5 and different Froude numbers are shown in Fig. 73.29. Observe that the two formulas approximately agree for Froude numbers between 0.1 and 5. This result is not surprising as Takabe's formula has been derived using Spitzer conductivity leading to sharp profiles (small L_0 and therefore relatively large Froude numbers). We conclude that the RT growth rate in low-Z materials with $Fr > 0.1$, such as solid DT, is well described by Takabe's formula over a wide range of Fr ($0.1 < Fr < 5$). For small Froude numbers or different values of ν, Takabe's formula doesn't provide an accurate estimate of the growth rate so Eq. (8) or its fitting formulas must be used.

When the ablation velocity is small or the density profile is smooth—as in the case of large radiation energy transport—we expect the Froude number to decrease. As shown in Fig. 73.29, Takabe's formula and Eq. (8) yield very different results for this case. In addition, radiative transport causes the deviation of the power index ν from the Spitzer value requiring a more general formula than Takabe's. For such targets, Eq. (8) can be compared only with the results of full 2-D simulations including a multigroup radiation-transport model. We consider the same 18-μm plastic target described in the previous section, and we simulate it with the code *ORCHID*. We then calculate the parameters ν, Fr, L_0, and V_a to be used in Eq. (8) by substituting *ORCHID* density and pressure profiles into Eqs. (14), (17), and (18) and find $Fr = 0.043$, $L_0 = 0.24$ μm, $V_a = 0.66$ μm/ns, $\nu = 0.96$, and $g = 43$ μm/ns^2. In Fig. 73.30, the growth rates obtained using *ORCHID* (dots) are compared with Eq. (8) (solid line), Takabe's (dot–dashed line), and modified Takabe's (dashed line) formulas. The latter is the Takabe's formula including the stabilizing effects of finite density-gradient scale length in a heuristic fashion,

$$\gamma_{\text{m.T.}} = \alpha_T \sqrt{\frac{kg}{1+kL_m}} - \beta_T k V_a , \qquad (21)$$

where L_m is the minimum density-gradient scale length, L_m = 0.93 μm. Observe that Takabe's and modified Takabe's formulas fail to reproduce the simulation results in the short-wavelength regime. Instead, the growth rates obtained with Eq. (8) are in excellent agreement with the simulated ones over the entire unstable spectrum.

Furthermore, we study different pulse shapes and different target materials. We consider a 20-μm-thick CH target irradiated by a square pulse with an intensity of 200 TW/cm^2 and 100-ps linear rise time. According to the *ORCHID* simulations, the hydrodynamic profiles reach a steady state after 1.3 ns. The growth rates of 30-μm and 15-μm wavelength perturbations are determined from the 2-D simulations yielding γ^{sim} (15 μm) = 4.9 ns^{-1} and γ^{sim} (30 μm) = 4.1 ns^{-1}. Using the *ORCHID* hydrodynamic profiles and Eqs. (14), (17), and (18), we estimate the relevant hydrodynamic parameters $\nu = 1.2$, L_0 = 0.22 μm, V_a = 2.0 μm/ns, Fr = 0.12, and g = 144 μm/ns^2. Substituting such parameters into the asymptotic formula [Eq. (8)] yields the theoretical growth rates γ^{th} (15 μm) = 4.9 ns^{-1} and γ^{th} (30 μm) = 4.06 ns^{-1}, reproducing the simulation results.

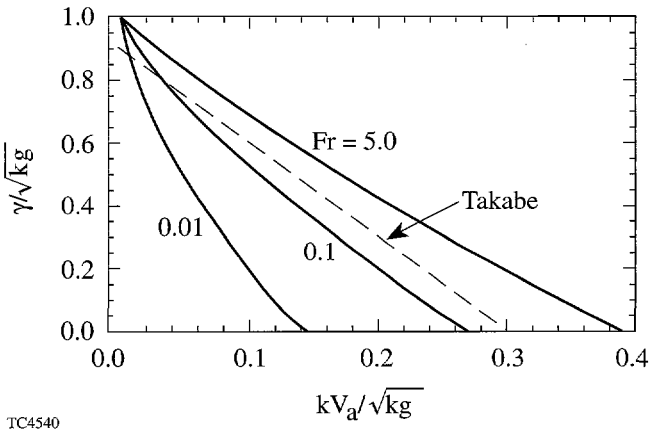

Figure 73.29
Normalized growth rate $\left(\gamma/\sqrt{kg}\right)$ versus normalized wave number $\left(\sqrt{kV_a^2/g}\right)$ calculated using the Takabe's formula (dashed line) and Eq. (8) (solid line) for different values of the Froude number and $\nu = 2.5$.

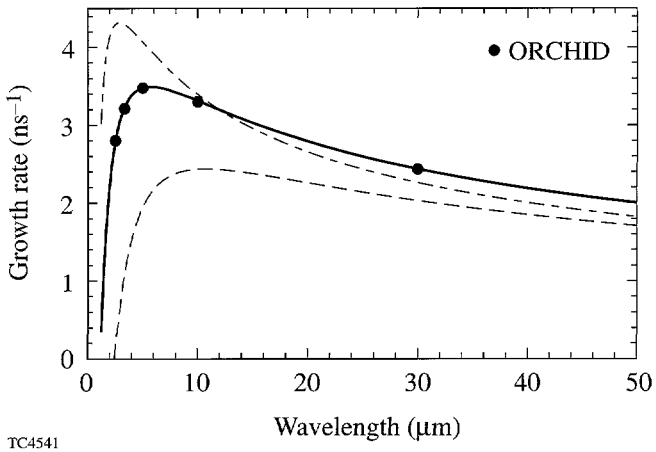

Figure 73.30
Unstable spectrum calculated using the analytic formula (8) (solid line) compared with the numerical results (dots) of 2-D hydrocode *ORCHID*, Takabe's formula (dot-dashed line) and modified Takabe's formula (dashed line).

Next, we simulate the evolution of 6-μm-wavelength surface perturbation on a 20-μm-thick beryllium foil irradiated by a square pulse with an intensity of 50 TW/cm^2 and 100-ps linear rise time. The steady state is reached after 1.5 ns and the *ORCHID* simulation yields the mode growth rate $\gamma^{\text{sim}} = 2.27\ \text{ns}^{-1}$. The simulated and analytic hydrodynamic profiles match for $\nu = 0.63$, $L_0 = 0.36\ \mu$m, $V_a = 0.73\ \mu$m/ns, $Fr = 0.06$, and $g = 25\ \mu\text{m/ns}^2$, thus yielding the theoretical growth rate $\gamma^{\text{th}} = 2.28\ \text{ns}^{-1}$ in good agreement with the numerical simulations.

These tests are a clear indication that Eq. (8) can be used to determine the RT growth rates for ablation fronts with large/small Froude numbers and short-/long-wavelength perturbations.

2. Fitting Formula for the Growth Rate

Although Eq. (8) provides an accurate estimate of the ablative RT growth rates, its expression is too complicated for practical applications. Without a doubt, a simplification of Eq. (8) would greatly help the target designers in the choice of the ablator material and the implementation of the RT mixing models. For this purpose, we simplify Eq. (8) using two well-known fitting formulas:

$$\gamma_1 = \alpha_1(Fr,\nu)\sqrt{kg} - \beta_1(Fr,\nu)kV_a, \tag{22}$$

$$\gamma_2 = \alpha_2(Fr,\nu)\sqrt{\frac{kg}{1+kL_m}} - \beta_2(Fr,\nu)kV_a, \tag{23}$$

where $L_m = L_0(\nu+1)^{\nu+1}/\nu^{\nu}$ is the minimum density-gradient scale length, and the α's and β's are functions of Fr and ν. It turns out that Eq. (22) is particularly accurate in fitting the large Froude number results, while Eq. (23) is suitable for low Froude numbers. This is not surprising as ablation fronts with small Froude numbers are unstable to modes with wavelengths smaller than the density-gradient scale length whose growth is strongly affected by the finite kL_m.

The calculation of the coefficients α_1, β_1 and α_2, β_2 is carried out using the standard fitting procedures of the Mathematica software package.[25] We define a range of interest for the mode wavelength from the cutoff λ_c to about 200 times the cutoff wavelength $\lambda_{\max} \approx 200\ \lambda_c$ (the parameters α and β have shown little sensitivity to the value of $\lambda_{\max}$). The α's and β's are determined by fitting the growth rate γ obtained using Eq. (8) with the formulas (22) and (23) over the wavelength range $\lambda_c < \lambda < \lambda_{\max}$. Figures 73.31 and 73.32 show the value of α, β for different Fr and ν. The solid section of the curves represents the region of optimum fit, i.e., the region where each formula fits the data at its best. According to the value of Fr and ν, one should use the formula corresponding to a solid curve.

As an example, we consider the plastic target used in the *ORCHID* simulations described in the previous section. The values $Fr = 0.043$ and $\nu = 0.96$ are obtained by processing the *ORCHID* hydro-profiles with the procedure described in the **Equilibrium Parameters** section. Using Fig. 73.32, we determine the optimum fit by using γ_2 with $\alpha_2 = 0.98$ and $\beta_2 = 1.64$. Figure 73.33 shows a plot of the unstable spectrum obtained using Eq. (8) (solid line) and the fitting formula γ_2 (dashed line). The excellent agreement between the two curves indicates that the fitting formula represents a good approximation of Eq. (8).

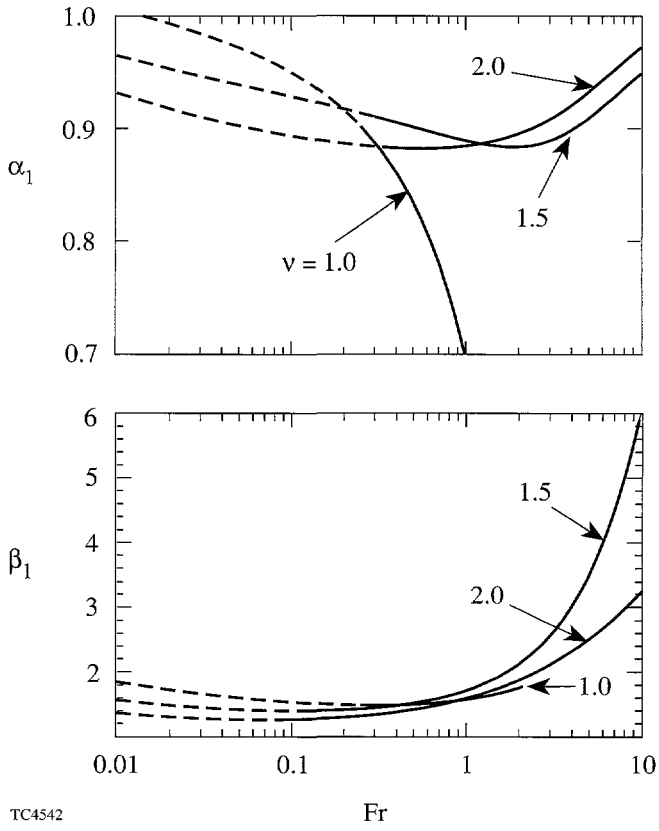

Figure 73.31
Plot of coefficients α_1, β_1 of the fitting formula (22) versus Froude number for different values of the power index ν. Solid line represents the regions of the best fit of the analytical formula (8) with Eq. (22).

We have determined the optimum fit for several plastic and solid-DT targets commonly used in direct-drive ICF experiments. Table 73.I shows the results of the fitting procedure described above for different laser pulses and plastic target thicknesses. It appears that over a wide range of thicknesses and laser powers, the growth rate of the RT instability for directly driven CH targets can be approximated by

$$\gamma_{CH} \approx 0.98\sqrt{\frac{kg}{1+kL_m}} - 1.7\ kV_a, \tag{24}$$

where $0.6 < L_m < 1\ \mu m$. The same formula has been derived for the aluminum-coated CH and beryllium targets. The corresponding time-averaged values of Fr, v, L_0, g, and V_a are shown in Tables 73.III and 73.IV, respectively. The growth rate for cryogenic DT targets is better represented by the fit γ_1, and Table 73.II shows the optimum fit for different flat targets driven by a 1-ns linear ramp followed by a flat-top pulse. These results indicate that the growth rate of solid-DT targets is well approximated by a Takabe-like formula

$$\gamma_{DT} \approx 0.94\sqrt{kg} - 2.7\ kV_a. \tag{25}$$

The RT growth rate for different ablator materials can be determined in the same fashion by using 1-D hydro-simulations to reproduce the density and pressure profiles; Eqs. (14), (17), and (18) to calculate the equilibrium parameters; and Figs. 73.31 and 73.32 to generate the growth-rate formulas.

It is very important that the 1-D hydrodynamic analytic profiles be carefully matched with the simulation results when determining the relevant equilibrium parameters. Even though the analytic theory yields satisfactory results for DT, CH, and Be targets, it might fail to reproduce the profiles of other materials. For instance, the hydrodynamic profiles of plastic targets with high-Z dopants are not well reproduced by the single temperature model, and Eq. (8) cannot be applied to determine the RT growth rate. The study of the RT instability in such targets is currently under investigation.

An interesting result of the analytic theory concerns those equilibria with $v \simeq 1$ and $Fr > 2$. Figure 73.31 shows that α_1 decreases dramatically with increasing Froude numbers. This result is not surprising as the same conclusion can be reached using the results of the self-consistent stability analysis of Ref. 9 reported in Eq. (5). The growth-rate formula (5) yields zero growth rate for equilibria with $v = 1$ and $Fr > 2$ when the

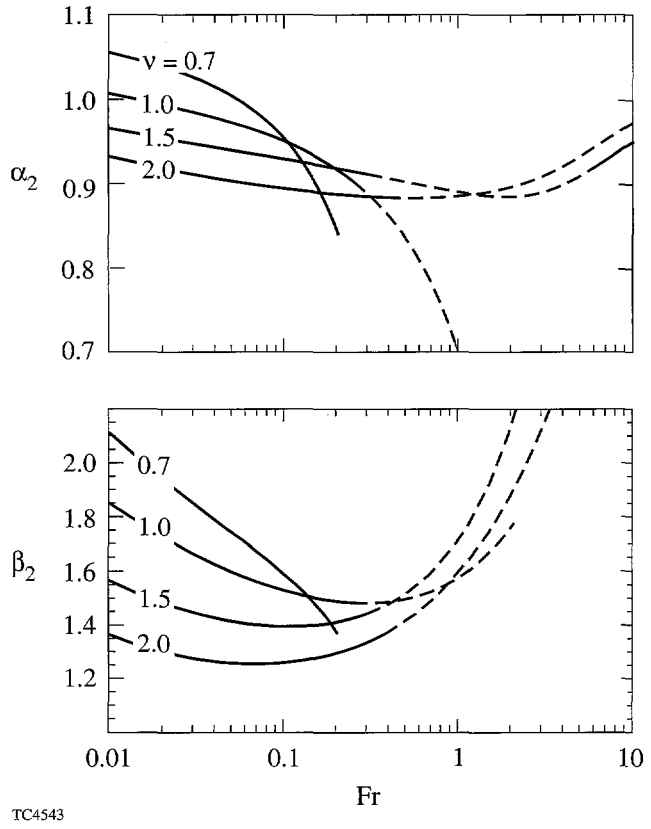

Figure 73.32
Plot of coefficients α_2, β_2 of the fitting formula (23) versus Froude number for different values of the power index v. Solid line represents the regions of the best fit of the analytical formula (8) with Eq. (23).

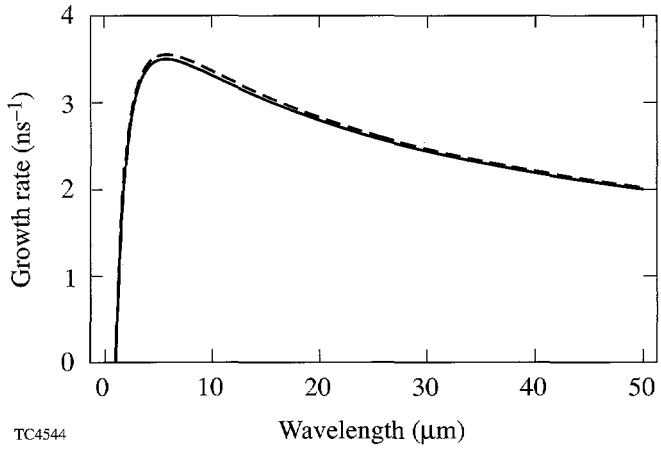

Figure 73.33
Unstable spectrum of the target described in the **Equilibrium Parameters** section calculated using the analytic formula (8) (solid line) and the fitting formula (23) (dashed line).

Table 73.III: Be targets.

Th (μm)	I (TW/cm^2)	$\langle Fr \rangle$	$\langle v \rangle$	$\langle L_0 \rangle$ (μm)	$\langle L_m \rangle$ (μm)	$\langle V_a \rangle$ (μm/ns)	$\langle g \rangle$ (μm/ns^2)	Growth Rate [fit of Eq. (8)]
16	50	0.05	0.7	0.2	0.6	0.6	40	$1.00\sqrt{\frac{kg}{1+kL_m}} - 1.7\,kV_a$
16	100	0.06	0.7	0.2	0.6	0.8	60	$0.99\sqrt{\frac{kg}{1+kL_m}} - 1.7\,kV_a$
32	100	0.06	0.6	0.4	1.2	0.8	28	$1.00\sqrt{\frac{kg}{1+kL_m}} - 1.7\,kV_a$
16	240*	0.10	0.8	0.1	0.4	1.1	28	$0.95\sqrt{\frac{kg}{1+kL_m}} - 1.7\,kV_a$

*Linear-rise laser pulse

Table 73.IV: CH targets with aluminum coating.

Th (μm)	I (TW/cm^2)	$\langle Fr \rangle$	$\langle v \rangle$	$\langle L_0 \rangle$ (μm)	$\langle L_m \rangle$ (μm)	$\langle V_a \rangle$ (μm/ns)	$\langle g \rangle$ (μm/ns^2)	Growth Rate [fit of Eq. (8)]
20+0.5	100	0.07	0.9	0.7	2.6	1.9	72	$0.97\sqrt{\frac{kg}{1+kL_m}} - 1.7\,kV_a$
20+1.0	100	0.08	0.7	1.6	5.0	2.8	63	$0.98\sqrt{\frac{kg}{1+kL_m}} - 1.7\,kV_a$

second term in the square root $-A_T^2 k^2 V_a V_{b.o.}$ (caused by overpressure of the blowoff region with respect to the overdense region) is larger than the instability-drive term $A_T kg$ for any wave number. This result has also been confirmed by solving the system (2)–(4) of Ref. 9 using an initial value code and is also in agreement with the numerical results of Kull (see Ref. 6). In addition, the numerical results seem to indicate that such a stabilization occurs for any $v \leq 1$. In conclusion, hydrodynamic profiles with $v \leq 1$ and $Fr > 2$ are RT stable for all wavelengths.

Conclusions

The growth rate of the ablative Rayleigh–Taylor instability is calculated using the analytic theory of Goncharov *et al.* (Ref. 11) and the output of one-dimensional simulations of laser-accelerated targets. The simulated density and pressure profiles are used to determine the equilibrium parameters Fr, V_a, g, v, and L_0 via a newly developed fitting procedure. Those parameters are then substituted into the self-consistent growth-rate formula of Goncharov *et al.* (Ref. 11). The accuracy of such a procedure has been tested by comparing the analytic growth rates for a plastic target with the ones obtained using two-dimensional simulations. This theory suggests that Takabe's formula represents a good approximation of the growth rates for only relatively large Froude numbers ($0.1 < Fr < 5$) and electronic heat conduction ($v \simeq 2.5$) but fails for small Froude numbers and radiative materials. The complicated asymptotic formula of Ref. 11, which is valid for arbitrary Froude numbers, has been simplified by using simple fits over a wide range of Froude numbers and power indices for thermal conduction. In addition, simple growth-rate formulas for solid DT, plastic (CH), and beryllium targets have been derived. Even though the analytic theory yields satisfactory results for DT, CH, and Be targets, it might not be adequate for other materials such as chlorinated plastic. The hydrodynamic profiles of plastic targets with high-Z dopants are not well reproduced by the single temperature model and Eq. (8) cannot be applied to determine the RT growth rate.

ACKNOWLEDGMENT

This work was supported by the U.S. Department of Energy Office of Inertial Confinement Fusion under Cooperative Agreement No. DE-FC03-92SF19460, the University of Rochester, and the New York State Energy Research and Development Authority. The support of DOE does not constitute an endorsement by DOE of the views expressed in this article.

REFERENCES

1. S. E. Bodner, Phys. Rev. Lett. **33**, 761 (1974).
2. K. O. Mikaelian, Phys. Rev. A **42**, 4944 (1990).
3. H. Takabe *et al.*, Phys. Fluids **28**, 3676 (1985).
4. C. P. Verdon, R. L. McCrory, R. L. Morse, G. R. Baker, D. I. Meiron, and S. A. Orszag, Phys. Fluids **25**, 1653 (1982).
5. H. J. Kull and S. I. Anisimov, Phys. Fluids **29**, 2067 (1986).
6. H. J. Kull, Phys. Fluids B **1**, 170 (1989).
7. J. D. Kilkenny, S. G. Glendinning, S. W. Haan, B. A. Hammel, J. D. Lindl, D. Munro, B. A. Remington, S. V. Weber, J. P. Knauer, and C. P. Verdon, Phys. Plasmas **1**, 1379 (1994).
8. R. Betti, V. N. Goncharov, R. L. McCrory, and C. P. Verdon, Phys. Plasmas **2**, 3844 (1995).
9. V. N. Goncharov, R. Betti, R. L. McCrory, P. Sorotokin, and C. P. Verdon, Phys. Plasmas **3**, 1402 (1996).
10. R. Betti, V. N. Goncharov, R. L. McCrory, P. Sorotokin, and C. P. Verdon, Phys. Plasmas **3**, 2122 (1996).
11. V. N. Goncharov, R. Betti, R. L. McCrory, and C. P. Verdon, Phys. Plasmas **3**, 4665 (1996).
12. A. R. Piriz, J. Sanz, and L. F. Ibanez, Phys. Plasmas **4**, 1117 (1997).
13. S. Atzeni, Nucl. Fusion **36**, 69 (1996).
14. J. Sanz, Phys. Rev. E **53**, 4026 (1996).
15. J. H. Nuckolls *et al.*, Nature **239**, 139 (1972).
16. J. D. Lindl, Phys. Plasmas **2**, 3933 (1995).
17. Lord Rayleigh, in *Scientific Papers* (Cambridge University Press, Cambridge, England, 1900), Vol. II, pp. 200–207; G. Taylor, Proc. R. Soc. London Ser. A **201**, 192 (1950).
18. A. B. Bud'ko and M. A. Liberman, Phys. Fluids B **4**, 3499 (1992).
19. R. L. McCrory and C. P. Verdon, in *Computer Applications in Plasma Science and Engineering*, edited by A. T. Drobot (Springer-Verlag, New York, 1991).
20. J. Delettrez and E. B. Goldman, Laboratory for Laser Energetics Report No. 36, University of Rochester (1976).
21. J. T. Larsen and S. M. Lane, J. Quant. Spectrosc. Radiat. Transf. **51**, 179 (1994).
22. G. B. Zimmerman and W. L. Kruer, Comments Plasma Phys. Control. Fusion **2**, 51 (1975).
23. L. Spitzer, Jr. and R. Härm, Phys. Rev. **89**, 977 (1953).
24. Ya. B. Zel'dovich and Yu. P. Raizer, in *Physics of Shock Waves and High-Temperature Hydrodynamic Phenomena*, edited by W. D. Hayes and R. F. Probstein (Academic Press, New York, 1966), Vol. I, p. 152.
25. S. Wolfram, *The Mathematica Book*, 3rd ed. (Wolfram Media/ Cambridge University Press, 1996).

Three-Dimensional Analysis of the Power Transfer Between Crossed Laser Beams

The indirect-drive approach to inertial confinement fusion[1] involves laser beams that overlap as they enter the hohlraum. Because a power transfer between the beams affects the implosion symmetry adversely, it is important to understand the mechanisms that make such a power transfer possible.

The power transfer between crossed laser beams made possible by an ion-acoustic (sound) wave (grating) has been studied theoretically[2–5] and experimentally.[6,7] Previously,[4] we made a two-dimensional analysis of the power transfer between beams with top-hat intensity profiles in a homogeneous plasma. In this article we extend our previous analysis to include three dimensions and arbitrary intensity profiles.

The interaction geometry is illustrated in Fig. 73.34. Notice that the beam axes intersect at the origin. It was shown in Ref. 4 that the steady-state interaction of the beams is governed by

$$\begin{aligned} \partial_x A_1 &= (i\alpha_1 - \beta_1)|A_2|^2 A_1, \\ \partial_y A_2 &= (i\alpha_2 + \beta_2)|A_1|^2 A_2, \end{aligned} \tag{1}$$

where the characteristic variables x and y measure distance in the propagation directions of beams 1 and 2, respectively. The beam amplitude $A_j = (u_j/c_s)(m_e/m_i)^{1/2}$ is the quiver velocity of electrons in the high-frequency electric field of beam j divided by a speed that is of the order of the electron thermal speed. The nonlinear coefficients

$$\alpha_j = \frac{\omega_e^2 \omega_s^2 (\omega_s^2 - \omega^2)}{2\omega_j v_j \left[(\omega_s^2 - \omega^2)^2 + 4\nu_s^2 \omega^2 \right]}, \tag{2}$$

$$\beta_j = \frac{\omega_e^2 \omega \nu_s \omega}{\omega_j v_j \left[(\omega_s^2 - \omega^2)^2 + 4\nu_s^2 \omega^2 \right]},$$

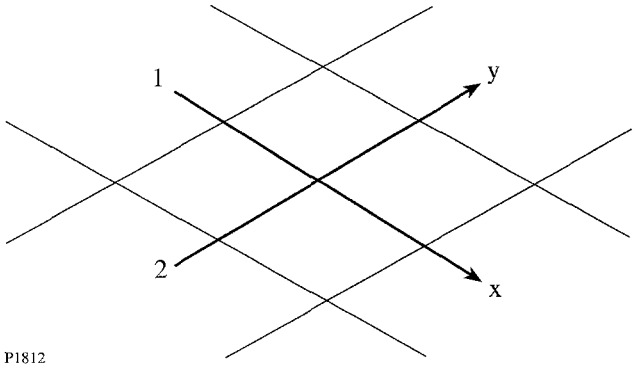

Figure 73.34
Geometry of the interaction of crossed laser beams. The characteristic coordinates x and y measure distance in the propagation directions of beams 1 and 2, respectively.

where ω_j is the frequency of beam j, v_j is the group speed of beam j, $\omega = \omega_1 - \omega_2$ is the difference between the beam frequencies, and $\omega_s = c_s|\mathbf{k}_1 - \mathbf{k}_2|$ and ν_s are the sound frequency and damping rate, respectively. Since $|\omega| << \omega_1$, the differences between ω_1 and ω_2, and v_1 and v_2, can be neglected in Eqs. (2). Henceforth, the subscripts on the nonlinear coefficients will be omitted. These coefficients characterize the way in which the grating responds to the low-frequency ponderomotive force. Apart from a factor of $|A_1|^2$, at resonance β is the spatial growth rate of stimulated Brillouin scattering (SBS) in the strong-damping limit.

It follows from Eqs. (1) that the beam intensities $I_j = |A_j|^2$ satisfy the equations

$$\partial_x I_1 = -2\beta I_2 I_1, \quad \partial_y I_2 = 2\beta I_1 I_2. \tag{3}$$

The boundary conditions are

$$I_1(-\infty, y, z) = J_1(y, z), \quad I_2(x, -\infty, z) = J_2(x, z), \tag{4}$$

where $J_1(y,z)$ and $J_2(x,z)$ are the upstream intensity profiles of the beams.

It follows from Eqs. (3) that the beam evolution in any characteristic plane, labeled by the associated value of z, is independent of the beam evolution in the neighboring planes. Consequently, the method used in Ref. 4 to analyze the two-dimensional interaction of the beam applies, with minor modifications, to the three-dimensional interaction considered herein. This method was used by several authors[8–10] to study the interaction of two pulses in one spatial dimension and time.

It is convenient to define

$$P_1(x,y,z)=\int_{-\infty}^{y} I_1(x,y',z)\,dy',$$
$$P_2(x,y,z)=\int_{-\infty}^{x} I_2(x',y,z)\,dx'. \tag{5}$$

Physically, $P_1(x,\infty,z)$ is the power per unit height in the slice of beam 1 that is a distance x from the center the interaction region, and $P_2(\infty,y,z)$ is the power per unit height in the slice of beam 2 that is a distance y from the center of the interaction region. By combining Eqs. (3) and (5), one can show that

$$\partial_x P_1 = J_2\left[1-\exp\left(2\beta P_1\right)\right]. \tag{6}$$

It follows from Eq. (6) that

$$2\beta P_1 = -\log\left\{1-\exp\left(-\xi\right)\left[1-\exp\left(-\eta\right)\right]\right\}, \tag{7}$$

where the distance variables

$$\xi = 2\beta\int_{-\infty}^{x} J_2(x',z)\,dx', \quad \eta = 2\beta\int_{-\infty}^{y} J_1(y',z)\,dy'. \tag{8}$$

It follows from Eq. (7), and the relations $I_1 = \partial_y P_1$ and $I_2 = J_2\exp(2\beta P_1)$, that

$$I_1 = \frac{J_1\exp\left(-\eta\right)}{\exp\left(\xi\right)-1+\exp\left(-\eta\right)},$$
$$I_2 = \frac{J_2\exp\left(\xi\right)}{\exp\left(\xi\right)-1+\exp\left(-\eta\right)}. \tag{9}$$

By combining Eqs. (3) and (5), one can also show that

$$2\beta P_2 = \log\left\{1+\exp\left(\eta\right)\left[\exp\left(\xi\right)-1\right]\right\}. \tag{10}$$

Equation (10) and the relations $I_2 = \partial_x P_2$ and $I_1 = J_1\exp(-2\beta P_2)$ are consistent with solutions (9).

It follows from Eqs. (7) and (10) that

$$P_2(x,y,z)-P_2(x,-\infty,z)=P_1(-\infty,y,z)-P_1(x,y,z), \tag{11}$$

which reflects the fact that the power gained by beam 2 must equal the power lost by beam 1. The power transfer for each slice, $T(z) = P_2(\infty,\infty,z) - P_2(\infty,-\infty,z)$, is given by

$$2\beta T = \log\left\{\exp\left(-w_2\right)+\exp\left(w_1\right)\left[1-\exp\left(-w_2\right)\right]\right\}, \tag{12}$$

where $w_1(z)=\eta(\infty,z)$ and $w_2(z)=\xi(\infty,z)$ are the normalized beam widths.

When $\alpha \neq 0$, the interaction of beams 1 and 2 causes their phases to be shifted by ϕ_1 and ϕ_2, respectively. By modifying the analysis of Ref. 4, one can show that the downstream phase shifts

$$\phi_1(y,z)=\alpha P_2(\infty,y,z), \quad \phi_2(x,z)=\alpha P_1(x,\infty,z). \tag{13}$$

According to the laws of geometric optics, the beams are deflected in the direction of increasing phase shift.

Equations (9), (12), and (13) are valid for arbitrary upstream intensity profiles. In the following examples we consider three different profiles: The first profile, $I(u,v)=\exp\left(-u^2-v^2\right)$, is Gaussian, as illustrated in Fig. 73.35(a). The second profile, $I(u,v)=\exp\left(-u^2-v^2\right)\cos^2(\pi u)\cos^2(\pi v)$, has hot spots with a central maximum, as illustrated in Fig. 73.35(b). The third profile, $I(u,v)=\exp\left(-u^2-v^2\right)\sin^2(\pi u)\sin^2(\pi v)$, has hot spots with a central minimum, as illustrated in Fig. 73.35(c). In Figs. 73.36–73.41 all intensities are normalized to I, the peak upstream intensity of a Gaussian beam; all distances are normalized to $1/2\beta I$, the SBS gain length; and all phase shifts are normalized to $\alpha/2\beta$.

In the first example the upstream intensity profiles $I_1(y,z)=\exp\left(-y^2-z^2\right)$ and $I_2(x,z)=0.5\exp\left(-x^2-z^2\right)$ are Gaussian. Contour plots of the downstream intensity profiles of beams 1 and 2 are displayed in Figs. 73.36(a) and 73.36(b), respectively. The downstream intensity of beam 2, which has a maximum of 1.2, is higher than the upstream intensity of beam 1. Both beams are distorted by the interaction. Beam 2 grows as it propagates in the positive y direction. Consequently, more power is siphoned from the $y > 0$ side of

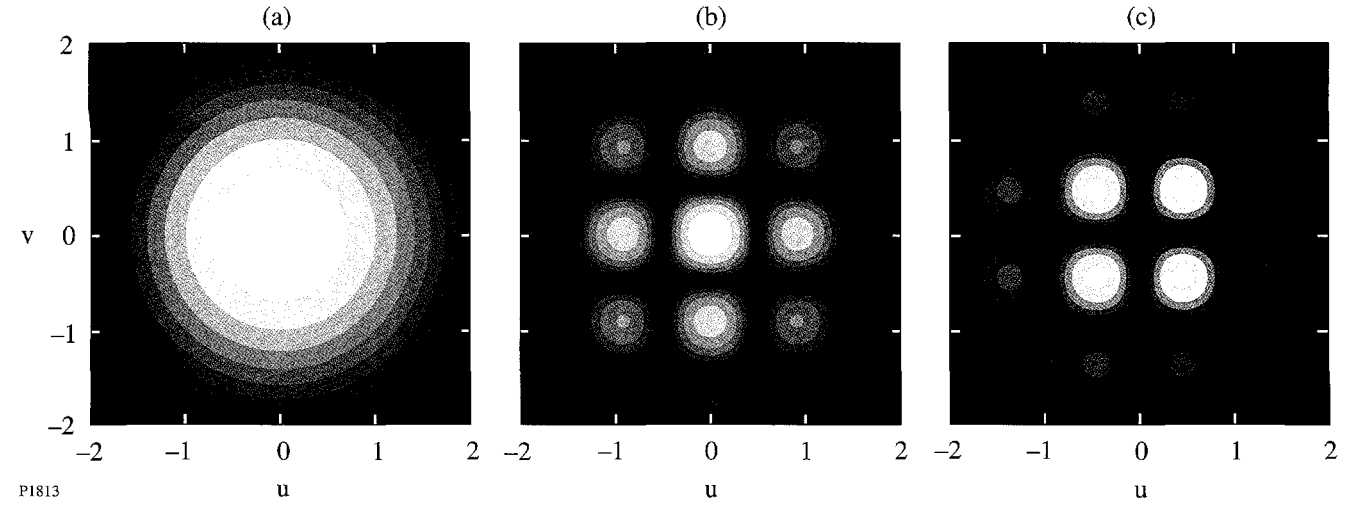

Figure 73.35
Logarithmic contour plots of the upstream intensity profiles used to generate Figs. 73.36–73.41. White represents high intensity; black represents low intensity. (a) Gaussian profile; (b) profile with hot spots and a central maximum; (c) profile with hot spots and a central minimum.

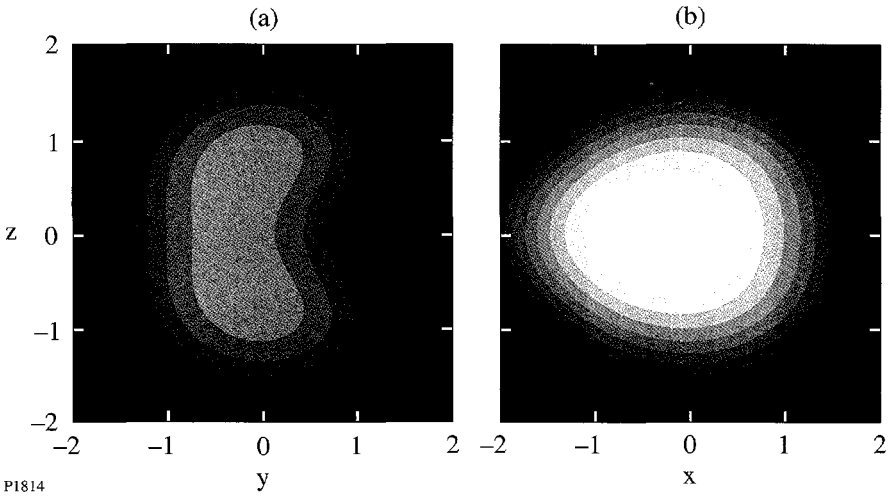

Figure 73.36
Logarithmic contour plots of the downstream intensity profiles of (a) beam 1 and (b) beam 2 corresponding to upstream intensity profiles that are Gaussian. White represents high intensity; black represents low intensity. Both beams are distorted by the interaction, and their centroids are shifted.

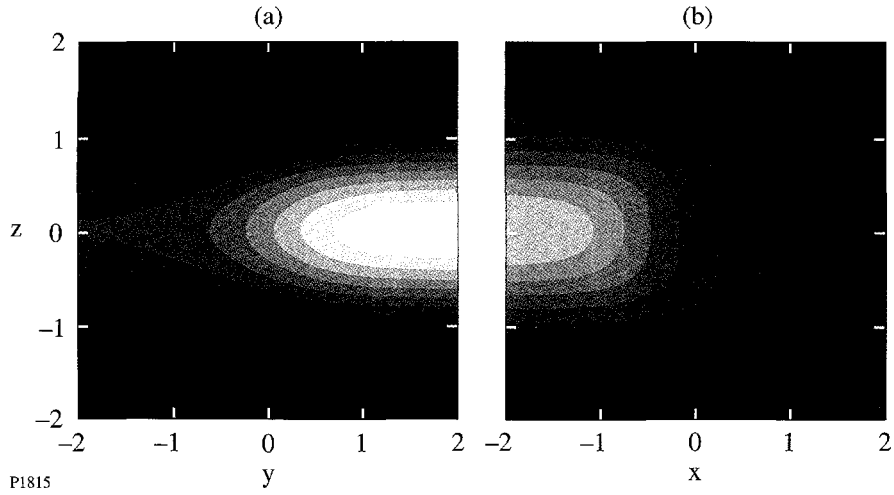

Figure 73.37
Linear contour plots of the downstream phase shifts of (a) beam 1 and (b) beam 2 corresponding to upstream intensity profiles that are Gaussian. White represents a large positive phase shift; gray represents a small positive phase shift; and black represents a phase shift of zero. Since the beams are deflected in the direction of increasing phase shift, beam 1 is deflected in the positive y direction and beam 2 is deflected in the negative x direction. The upper and lower parts of both beams are deflected toward the z axis.

beam 1 than from the $y < 0$ side, and the centroid of beam 1 is shifted in the negative y direction. The downstream intensity of beam 1 has off-axis maxima because the on-axis slice of beam 1 drives the interaction with the corresponding slice of beam 2 most strongly and is depleted most severely. Beam 1 is depleted as it propagates in the positive x direction. The centroid of beam 2 is shifted in the negative x direction because more power can be siphoned from the undepleted parts of beam 1 than from the depleted parts. Contour plots of the downstream phase shifts of beams 1 and 2 are displayed in Figs. 73.37(a) and 73.37(b), respectively. The maximal phase shift of beam 1 is 2.2. Since the beams are deflected in the direction of increasing phase shift, beam 1 is deflected in the positive y direction and beam 2 is deflected in the negative x direction ($\alpha > 0$). The upper and lower parts of both beams are deflected toward the z axis ($\alpha > 0$).

In the second example the upstream intensity profiles $I_1(y,z) = 4 \exp(-y^2 - z^2) \cos^2(\pi y) \cos^2(\pi z)$ and $I_2(x,z) = 2 \exp(-x^2 - z^2) \cos^2(\pi x) \cos^2(\pi z)$ produce intersecting filaments. The factors of 4 were included to make the beam powers in this example approximately equal to the beam powers in the first example. Contour plots of the downstream intensity profiles of beams 1 and 2 are displayed in Figs. 73.38(a) and 73.38(b), respectively. The maximal intensity of beam 2 is 4.6. According to Eqs. (9), the downstream intensities are the products of the upstream intensities and nonlinear transfer functions that depend on the (spatially integrated) power per unit height of each slice. Thus, the intensity profiles in this example evolve in a manner similar to those in the first example: The centroid of beam 1 is shifted in the negative y direction, and the centroid of beam 2 is shifted in the negative x direction. In this example, however, the

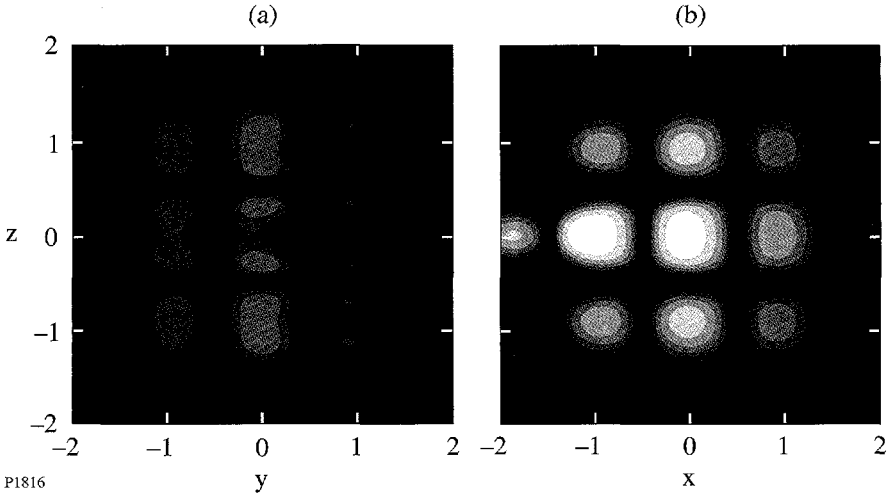

Figure 73.38
Logarithmic contour plots of the downstream intensity profiles of (a) beam 1 and (b) beam 2 corresponding to upstream intensity profiles that produce intersecting filaments. White represents high intensity; black represents low intensity. The beam distortions are more pronounced in this figure than in Fig. 73.36 because the hot-spot intensities are higher than the corresponding intensities of Gaussian beams.

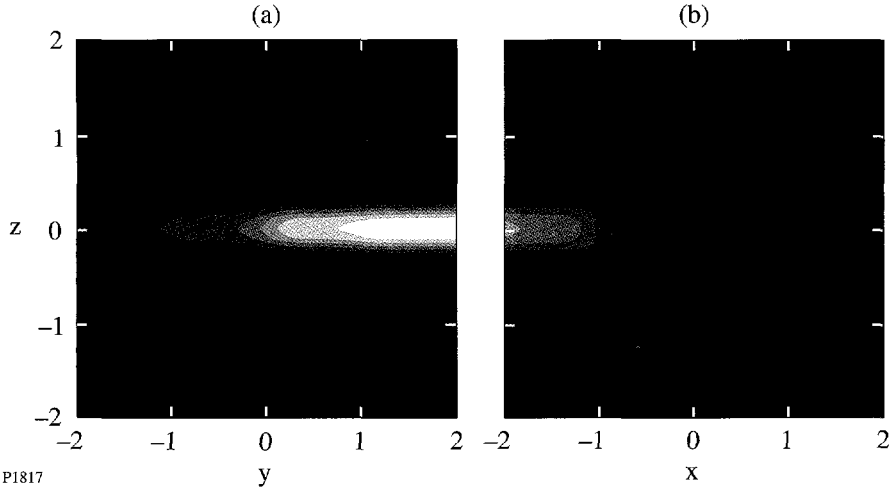

Figure 73.39
Linear contour plots of the downstream phase shifts of (a) beam 1 and (b) beam 2 corresponding to upstream intensity profiles that produce intersecting filaments. White represents a large positive phase shift; gray represents a small positive phase shift; and black represents a phase shift of zero. Beam 1 is deflected in the positive y direction, and beam 2 is defected in the negative x direction. The upper and lower parts of each row of hot spots are deflected toward the center of the row.

distortions are more pronounced because some slices contain twice the power per unit height of the corresponding slices in the first example. Contour plots of the downstream phase shifts of beams 1 and 2 are displayed in Figs. 73.39(a) and 73.39(b), respectively. The maximal phase shift of beam 1 is 5.1. Beam 1 is deflected in the positive y direction, and beam 2 is deflected in the negative x direction ($\alpha > 0$). The upper and lower parts of each row of hot spots are deflected toward the center of the row ($\alpha > 0$).

In the third example the upstream intensity profiles $I_1(y,z) = 4 \exp(-y^2 - z^2) \cos^2(\pi y) \cos^2(\pi z)$ and $I_2(y,x) = 2 \exp(-x^2 - z^2) \sin^2(\pi x) \sin^2(\pi z)$ produce nonintersecting filaments. Contour plots of the downstream intensity profiles of beams 1 and 2 are displayed in Figs. 73.40(a) and 73.40(b), respectively. The maximal intensity of beam 2 is 2.6. The distortions of the intensity profiles in this example are similar to those in the first and second examples. They are less pronounced, however, because the upstream intensity profiles

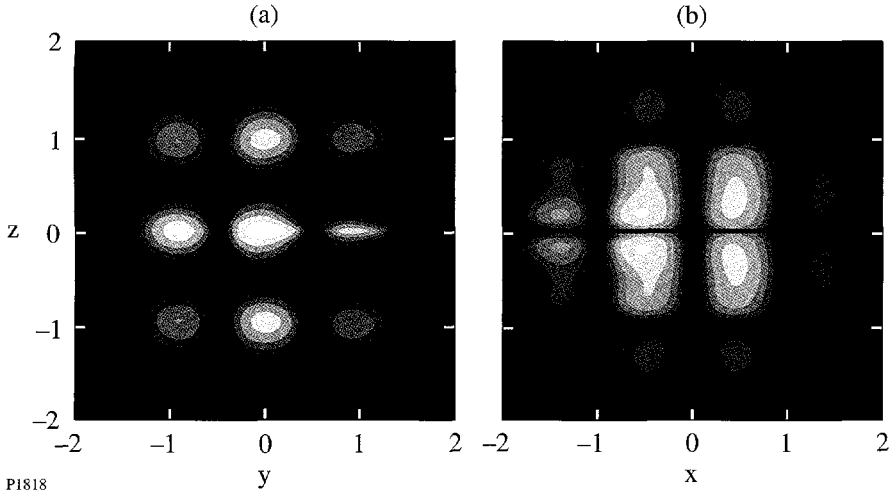

Figure 73.40
Logarithmic contour plots of the downstream intensity profiles of (a) beam 1 and (b) beam 2 corresponding to upstream intensity profiles that produce nonintersecting filaments. White represents high intensity; black represents low intensity. The beam distortions are less pronounced in this figure than in Fig. 73.36 because the beam filaments do not interact strongly.

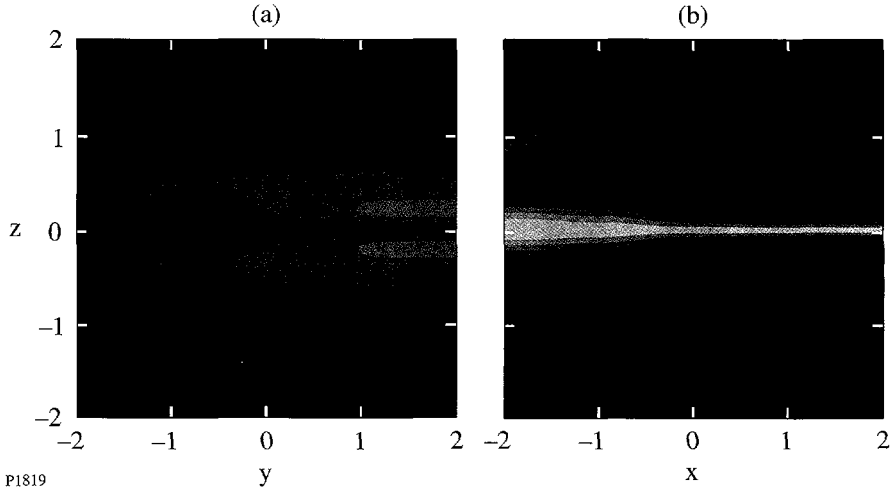

Figure 73.41
Linear contour plots of the downstream phase shifts of (a) beam 1 and (b) beam 2 corresponding to upstream intensity profiles that produce nonintersecting filaments. White represents a large positive phase shift; gray represents a small positive phase shift; and black represents a phase shift of zero. The beam deflections associated with this figure are less important than those associated with Fig. 73.39 because the regions of large phase shift are aligned with the regions of low intensity.

produce filaments that do not interact strongly. Contour plots of the downstream phase shifts of beams 1 and 2 are displayed in Figs. 73.41(a) and 73.41(b), respectively. The maximal phase shift of beam 1 is 2.1. According to Eqs. (13), each beam acquires a phase shift that reflects the intensity profile of the other beam. The regions of large phase shift, however, are aligned with the regions of low intensity, and beam deflections are less important in this example than in the first and second examples.

In summary, we made a three-dimensional analysis of the power transfer between crossed laser beams with arbitrary upstream intensity profiles. We derived simple formulas for the downstream intensity profiles [Eqs. (9)], the power transfer [Eq. (12)], and the downstream phase shifts that depend on the power transfer [Eqs. (13)]. The power transfer shifts the beam centroids, and the phase shifts alter the beam directions and focal lengths. For beams with hot spots in their upstream intensity profiles, the power transfer depends sensitively on whether the associated filaments intersect.

ACKNOWLEDGMENT

This work was supported by the National Science Foundation under Contract No. PHY-9415583, the United States Department of Energy (DOE) under Contract No. W-7405-ENG-36, the U.S. Department of Energy Office of Inertial Confinement Fusion under Cooperative Agreement No. DE-FC03-92SF19460, the University of Rochester, and the New York State Energy Research and Development Authority. The support of DOE does not constitute an endorsement by DOE of the views expressed in this article.

REFERENCES

1. J. D. Lindl, Phys. Plasmas **2**, 3933 (1995).
2. W. L. Kruer *et al.*, Phys. Plasmas **3**, 382 (1996).
3. V. V. Eliseev *et al.*, Phys. Plasmas **3**, 2215 (1996).
4. C. J. McKinstrie, J. S. Li, R. E. Giacone, and H. X. Vu, Phys. Plasmas **3**, 2686 (1996). Equations (3) and (4) of this paper were misstated. They should be $A_h = A_1 \exp[i(\mathbf{k}_1 \cdot \mathbf{r} - \omega_1 t)] + A_2 \exp[i(\mathbf{k}_2 \cdot \mathbf{r} - \omega_2 t)] + c.c.$ and $n_l = n \exp[i(\mathbf{k}_1 - \mathbf{k}_2) \cdot \mathbf{r}] + c.c.$, respectively. Equations (5) and (6) are correct.
5. C. J. McKinstrie, V. A. Smalyuk, R. E. Giacone, and H. X. Vu, Phys. Rev. E **55**, 2044 (1997).
6. R. K. Kirkwood *et al.*, Phys. Rev. Lett. **76**, 2065 (1996).
7. A. K. Lal, K. A. Marsh, C. E. Clayton, C. Joshi, C. J. McKinstrie, J. S. Li, and T. W. Johnston, Phys. Rev. Lett. **78**, 670 (1997).
8. M. Maier, W. Kaiser, and J. A. Giordmaine, Phys. Rev. **177**, 580 (1969).
9. B. I. Cohen, Phys. Fluids **17**, 496 (1974).
10. F. Y. F. Chu, Phys. Lett. **51A**, 129 (1975).

Characterization of Freestanding Polymer Films for Application in 351-nm, High-Peak-Power Laser Systems

A major roadblock to rapid progress in laser fusion is the enormous price of the necessary experimental facilities. Currently under planning or nearing construction are 40-cm-clear-aperture (per beam line), 200-or-more-channel, glass-laser systems that will each cost in excess of U.S. $\$10^9$ in pursuit of laser-fusion research.[1] A sizable portion of this price bears witness to the costs of optical materials and of the precision manufacturing methods for treating these materials at aperture scales that, up to now, were the domain of astronomers. There is strong incentive for developing lower-cost, high-throughput manufacturing technology and materials engineering, yielding devices that meet all the performance challenges typically demanded by such lasers.

One key constraint to limiting laser-system cost by aperture downscaling is the so-called *laser-damage threshold*.[2] The higher the damage threshold for given system-operating conditions (wavelength, pulse length, etc.), the more photons per cm^2 and seconds may be passed through a given device without incurring permanent performance penalties. In the asymptotic limit of an infinite laser-damage threshold, one could build infinitely powerful lasers having very affordable, small apertures. Short of this elusive condition, however, the quest for higher thresholds is both a material-design and device-processing imperative. It must be kept in mind, though, that any enhanced laser-damage threshold is useful only if no other optical performance parameters are sacrificed in the process.

Among such parameters are *wavefront quality*, absence of, or at least control of, *birefringence*, and long-term environmental and photolytic stability of the material. The latter assuages the need for reworking, replacing, or swapping devices frequently and thus affects the *operating* costs of large-clear-aperture lasers. The former two parameters are essential to transporting beams both with minimum static phase-front error and without polarization error. Both are pivotal to efficient higher-harmonic frequency conversion and to good focusability of beams onto the fusion targets.

With these demands in mind, we recently set out to test the utility of thin polymer membranes (pellicles) in high-peak-power, UV lasers. Scale-up of such membranes, and their preparation under ultraclean conditions, has been spurred by advances in UV lithography[3] of both semiconductor wafers and liquid crystal displays. The specific aim in these applications is to prevent particulate from falling onto, or settling on, the lithographic photomasks. As these primary applications call for excellent material homogeneity and low UV-absorption loss in pellicles, key prerequisites for successful pellicle use on high-peak-power UV lasers seemed already met. In this article, we will present an account of initial tests of such pellicles under 351-nm irradiation conditions significantly higher in fluence than in normal, photolithographic use.

In the following sections, the foil materials will be defined, the test procedures explained, and test results presented.

Sample Characterization

During this screening samples from three vendors[4] were sorted according to whether or not they were offered for *i*-line lithography, i.e., transmittance tuned for a maximum at 365 nm and prepared from a polymer with 280-nm cutoff (cellulose derivative), or for 248-nm, deep-UV lithography. In the following, we will sidestep reporting on cellulose derivatives since these foils are, in the current context, not noteworthy. They do find use, however, in optical-fuse (i.e., "must fail"), power-limiting applications where defined or downward-adjustable laser-damage thresholds are a key performance requirement.

Vendors offer two pellicle options: bare, single-layer foils or multilayer combinations with antireflective properties. In either implementation, pellicles are thin enough to act as both optically self-referencing etalons and freestanding samples in Fourier-transform IR spectroscopy. As will be shown here, the latter method is a simple and effective analysis tool for specifying the chemical similarities and differences in the samples from various vendors.

For these tests, vendors were not required to supply samples of a *prescribed thickness*, but only of a thickness *typically supplied for lithography applications*. Data, including those in Fig. 73.42, are therefore results from slightly different-thickness films (between 0.9 μm and 2.9 μm).

Figure 73.42 shows an overlay of three samples' IR absorption over the 4000 cm^{-1} to 400 cm^{-1} spectral range. From the general features it becomes immediately apparent that there is prominent overlap among the samples, i.e., largely similar addition polymers are used by the various suppliers. All samples show a weak "waviness" in their spectra—a manifestation of the samples' etalon effect in this wavelength range. Note the absence of any signal in the 2800-cm^{-1} area, the characteristic band for alkyl signatures, as well as the absence of signal around 3200 cm^{-1} for alkenes. There are, instead, strong, overlapping peaks between 1200 and 1400 cm^{-1}, characteristic for condensed system carbon–fluorine *Q* vibrations.[5] This permits identification of the materials as highly fluorinated (*perfluorinated*) homo- or copolymers. A widely known example of such a compound is tetrafluoroethylene.

After expanding the "fingerprint region" (see Fig. 73.43), subtle differences between samples become noticeable. Transmittance dips at 1030 cm^{-1} and 980 cm^{-1} in sample 2 (throughout this article, samples will be simply identified with numerals 1, 2, and 3 corresponding to sources in Ref. 4) and absent in sample 1 can be assigned to CF_2–CO vibrations found in perfluorinated 1,3-dioxolanes.[6] This sample thus belongs to the group of copolymers of perfluorinated dioxolane and tetrafluoroethylene. For certain weight ratios between the two members,[7] this copolymer remains amorphous over a wide temperature range and becomes solvent-processable—an important advantage for manufacturing low-scatter-loss, low-birefringence optical films.

It must be mentioned here that fluoropolymers are not the only deep-UV lithography materials. As early as 1985, a U.S. patent granted to Duly *et al.*[8] disclosed a polymethylmethacrylate pellicle for deep-UV lithography. We did not prepare

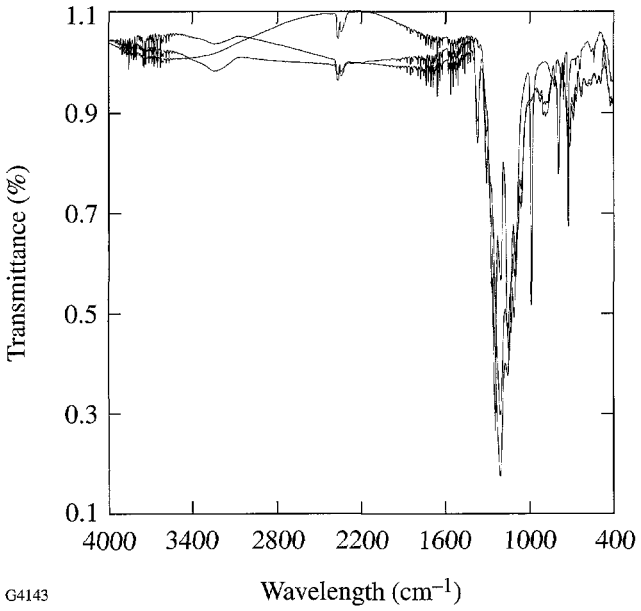

Figure 73.42
Infrared transmittance spectra (400 cm^{-1} to 4000 cm^{-1}) of the three sample types used in these measurements show the absence of alkyl and alkene characteristics (2900 cm^{-1} to 3200 cm^{-1}), while displaying strong carbon–fluorine vibrations.

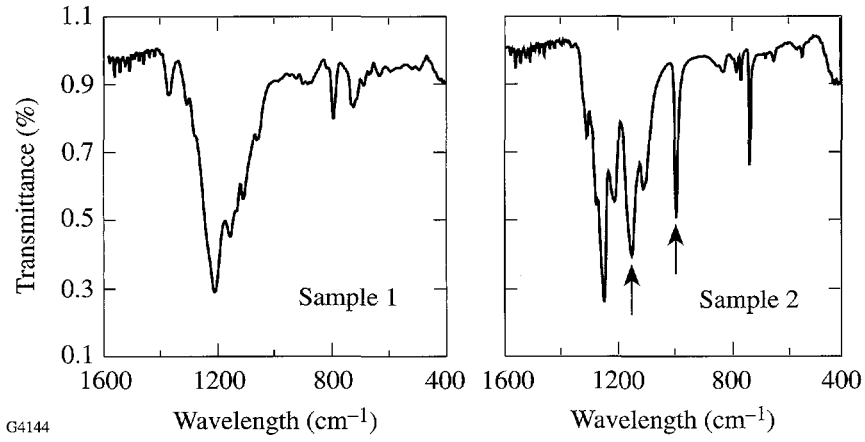

Figure 73.43
The "fingerprint" region (400 cm^{-1} to 1900 cm^{-1}) of the spectrum in Fig. 73.42. The fluorodioxolane signatures at 1030 cm^{-1} and 980 cm^{-1} are absent in sample 1 and highlighted in sample 2.

or obtain a pellicle from this material for comparison purposes; however, the issue of acrylates in high-peak-power laser use will be revisited during the discussion of current results.

Test Procedures

1. Damage-Threshold Measurements

A 7-s-repetition-rate, frequency-tripled Nd:glass laser in a standard laboratory environment is used for laser-damage testing. Its pulse length is 0.5 ns at the third harmonic, produced by Fourier-transform spectral narrowing through intracavity etalons, and the UV interaction spot size at the pellicle surface is 600 μm, produced by a 2-m-focal-length, fused-silica lens. The pulse length is sporadically monitored by a combination of a vacuum photodiode[9] and a 6-Ghz oscilloscope.[10] Each sample site is imaged under 110× dark-field microscopy both before and after laser irradiation. Any permanent, observable sample change is identified as damage.

At each irradiation instance, a digital record of the fluence distribution in a sample-equivalent plane is used to calculate the maximum shot fluence on target. Two irradiation modes are practiced: 1-on-1 and *N*-on-1. Samples are first tested in 1-on-1 mode and subsequently in *N*-on-1 mode. Mounted on a raster stage, random sample sites are moved into the irradiation position and irradiated by either one exposure (1-on-1 mode) or a sequence of increasingly intense pulses (*N*-on-1). The purpose of 1-on-1 irradiation lies in finding an *average damage threshold* averaged over a statistical number of sample sites. Backing off from this single-exposure average value by about a factor of 2, one may in subsequent *N*-on-1 testing start a fluence sequence at each *N*-on-1 site that ramps up until the damage fluence for each specific site has been found. Again this is carried out over a statistical number of sites. *N*-on-1 testing offers the more *realistic* threshold values as it simulates multishot, in-system-use conditions and accounts for various material-hardening effects known from the literature.[11]

In the case of 1-on-1 measurements, the average threshold value is the mean between the *highest nondamaging fluence* and the *lowest damaging fluence*, with the error derived from summing over all data points within the interval bracketed by these two fluences.

2. Photolysis Characterization

Long-term photolytic stability, i.e., change in sample absorbance in response to a large number of irradiations (1000) by *below-average-damage-threshold fluences* (nominally 3 J/cm^2, i.e., the maximum 351-nm system-design fluence on the OMEGA laser), is monitored by a calorimeter pair that samples the ratio of incident to transmitted pulse energy. To save time, a 5-s pulse repetition period is chosen. As a consequence, the unequal decay times of the two calorimeters introduce a constant bias that is measured under "sample absent" conditions over several hundred shots. Its slope is subsequently compared with that obtained under "sample in" conditions. Any observable *slope* differences are manifestations of sample photolysis effects.

This qualitative procedure is preferred over spectrophotometric measurements that offer quantitative results because of the small irradiation spot size (see previous section) and the associated registration accuracies involved in moving samples from one instrument to another. Even after registration issues are resolved, the task becomes one of microspectrophotometry, i.e, special effort has to be made to probe only the prior irradiated sample area if measurement sensitivity is to be kept acceptable.

3. Birefringence

Sample birefringence was evaluated by two methods: (1) a facile, low-contrast, visual check across the entire aperture between crossed sheet polarizers (100:1 contrast), and (2) a spot-by-spot measurement using a laser ellipsometer at 1053 nm. In this instrument, the sensitivity limit is 1/40 of a wave retardance averaged across a 0.8-mm spot size.

4. Interferometry in Transmission

A commercial interferometer[12] at $\lambda = 633$ nm was used to measure *transmission* wavefront errors in a double-pass mode. The interferometer is housed in a vibration-isolated, temperature- and air-draft–controlled enclosure.

Results

Even a decade ago, serious attempts at strengthening the laser-damage threshold of polymers[13] pointed out the critical importance of removing trace impurities from the (polyacrylic) polymer matrix. With the absorbance criterion having been made more rigorous since then by lithography demands, materials and processes for pellicles in 248-nm KrF excimer-laser lithography undergo strict optical-loss control,[3] both in terms of particulate as well as dissolved absorbers. It is thus not fully unexpected that we are able to report here the highest, 351-nm-laser-damage thresholds in our records covering tests on inorganic and organic optical materials for more than 15 years. The results are summarized in Fig. 73.44.

In Fig. 73.44, 1-on-1 and N-on-1 thresholds for the three vendors' foils are displayed. Although there is considerable variation among the thresholds for pellicles from different vendors, even the lowest reported threshold among them at 20 J/cm^2 is well above any operational 351-nm fluence on any large-scale glass laser in use or under design to date. Regarding these values, an important distinction must be made. In the **Test Procedures** section, the methodology for arriving at damage-threshold values was described. The thresholds marked with an asterisk in Fig. 73.44, i.e., those above 42 J/cm^2, *do not strictly comply* with this methodology for the following reason: The laser in use is *unable to generate the fluences at the given interaction spot size*, necessary to ascertain the *highest nondamaging fluence*. Thresholds marked with an asterisk represent the lowest damaging fluence obtainable from our laser at this spot size *for this given material*. In this regard, the perfluorinated pellicles are unique among the 1780 samples damage tested at this facility to date. They may also be unique at still shorter wavelengths.[14]

An additional challenge in determining these extraordinarily high thresholds derives from the interaction of the laser beam with air: at the stated fluences, particulates in air may get ionized near the sample surface and, pellicles being excellent dielectrics, locally charge the polymer. It becomes a daunting task to distinguish the electrostatically adhering particulates from "genuine damage" scatter sites. The threshold for vendor 3 at 69 J/cm^2 is an average over two sites on two films, both sites exhibiting a single detectable scatterer that remains uncertain as to whether or not it attracted dust.

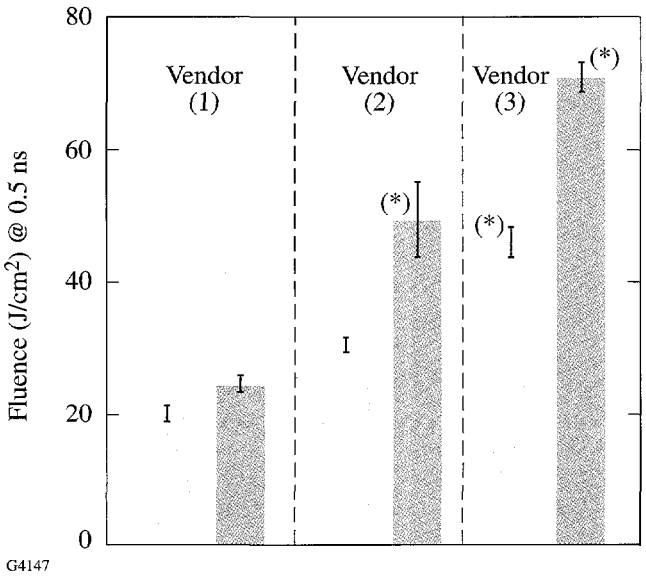

Figure 73.44
1-on-1 (light gray) and N-on-1 (dark gray) average damage thresholds for the three sample types identified as (1), (2), and (3) and tested at 351 nm (0.5-ns pulse length). Different sample types were received from different vendors. For the meaning of the asterisks, consult the text.

Figure 73.44 also reveals a consistent hardening in all samples upon multiple irradiation, i.e., the N-on-1 thresholds exceed the 1-on-1 thresholds by up to 30%. While this effect is neither new nor unique to these samples, it must be noted that the just-mentioned charging by air ionization may provide the basis for photorefractive effects in these polymers. In this instance, charge-separation time constants are critical, and the damage thresholds measured at the very-low repetition governing the current N-on-1 measurements, i.e., the sample is investigated after *each* exposure, are expected to be different from those that one would obtain under *high-repetition-rate* conditions. Such tests are still to be carried out.

For comparison, 351-nm bulk damage fluences for KDP (potassium dihydrogen phosphate) frequency-conversion crystals, as acquired for the OMEGA laser during the last five years, are lower by factors of 3 to 5 (with current crystal-growth technology, the canonical number is 10 J/cm^2 @ 351 nm, 1 ns). Three factors seem responsible for this remarkable superiority in damage-threshold values: (1) There is the already-mentioned attention to purity in starting materials and cleanliness in membrane processing. (2) More importantly, these pellicles intrinsically do not have to suffer the violent intrusions by grinding and polishing, typical for conventional optical elements, in order to achieve the transmission-wavefront uniformity reported below. (3) Being freestanding, frame-supported films, they expose very little bulk to the transiting laser pulse. Since thermodynamics requires that a finite density of defects must exist, even in very pure materials, this last property may be the pellicles' greatest asset in laser applications.

These advantages are further illustrated by data in Table 73.V, where 351-nm damage-threshold values are listed for a 240-nm-thick, inorganic, SiO_x film simultaneously vacuum-deposited on three different substrates and damage tested concurrently with the pellicles, i.e., under similar irradiation conditions. (The film stoichiometry is identified with only x here since no effort was made to accurately ascertain its value. We believe that $x = 2$.) This comparison shows how severe a price is paid for grinding and polishing: the damage threshold for the same film drops by an order of magnitude, depending on whether it is deposited on a conventionally

Table 73.V: Comparison of 351-nm, 0.5-ns laser-damage thresholds in J/cm^2 for a 240-nm-thick SiO_2 film concurrently vacuum deposited on three select surfaces: conventionally polished and cleaned fused silica,[15] freshly cleaved fused silica,[15] and freshly cleaved float glass.

Substrate Material and Surface Condition	Damage threshold (J/cm^2)	
	1-on-1	N-on-1
Polished fused silica	6.9±0.3	9.7±1.1
Cleaved fused silica	22.8±2.5	34.6±2.0
Cleaved float glass	27.7±1.3	24.5±2.0

prepared and cleaned fused silica[15] surface or on a freshly cleaved, otherwise untreated surface of either fused silica or inexpensive float glass. A lift-off technology, as is applied to the preparation of pellicles, can avoid this downside of conventional manufacturing.

As the sample films are homogenous, single-material layers, the *E*-field distributions of the transiting laser pulse inside the polymer are expected to *not exceed* the corresponding magnitudes *in vacuo*. No *E*-field *enhancement* needs to be considered in determining laser-damage thresholds for these films.

Next, we address sample *birefringence* results. Figure 73.45 shows a side-by-side comparison of parallel polarizers and crossed polarizers. Also included in the images is an extruded, 5-μm-thick Mylar® foil[16] whose intrinsic birefringence pattern in the two cases offers an instructive reference. Similar data exist, but are not shown here, for all vendors' pellicles. In quantitative terms (ellipsometry), no pellicle, including those with clear apertures as large as 30 cm, offered a single site in which the local birefringence exceeded the instrument sensitivity (λ/40 @ 1053 nm). Moreover, by applying uniaxial stress to square-frame–mounted pellicles of 0.9-mm thickness, even at stresses that visibly (unaided eye) distorted the frame, induced film birefringence remained below instrument sensitivity. In accordance with vendor specifications,[17] the stress-optic coefficient for perfluorinated-pellicle materials lies within 10% of that of the widely used stress-modeling material polymethacrylate. Owing to their short pathlength, however, pellicle films, even if nonuniformly stressed by, for instance, mounting or temperature biases, respond with retardance excursions tolerable in most high-peak-power laser systems.

Long-term photolytic stability, as measured by energy ratiometry, shows no measurable increase in absorptance in perfluorinated foils after 1000 exposures at nominally 3-J/cm^2 fluences per given site. The data shown in Fig. 73.46 represent ten-shot average values per data point for two cases: solid circles are data for beams passed through samples; open circles for "no-sample" conditions. The horizontal axis marks a cumulative number of shots. The offset between the two similarly sloped curves corresponds to the Fresnel insertion loss for this particular sample (16%, includes etalon reflectance and absorption). The slope itself is a result of unequal amounts of energy being deposited in each calorimeter at a repetition rate shorter than the thermal decay time of the calorimeter(s). Since any long-term increase (or decrease) in sample absorbance would have to manifest itself in a *change* in this slope,

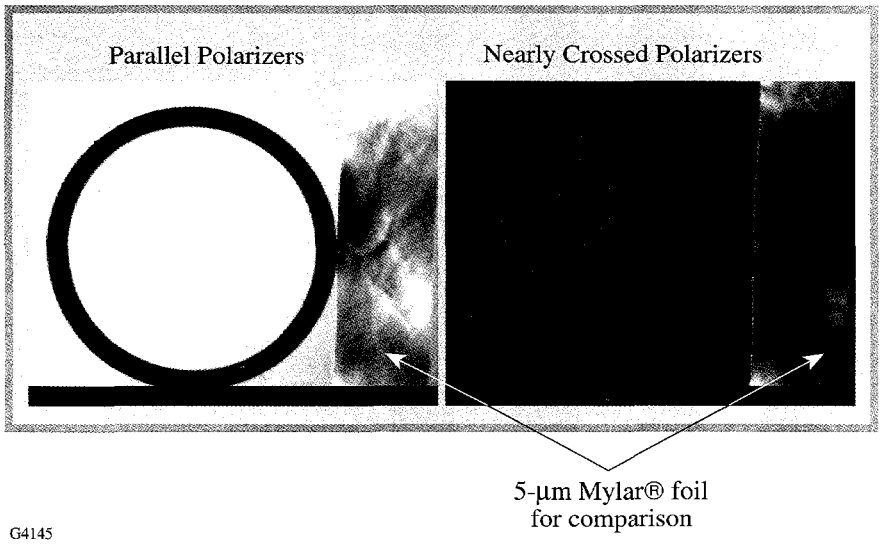

Figure 73.45
Comparison of birefringence between a 5-cm-clear-aperture, perfluorinated pellicle and an extruded, 5-μm-thick Mylar® foil placed between (a) parallel and (b) nearly crossed polarizers. Note the extensive stress birefringence imparted onto the Mylar® foil by the manufacturing process.

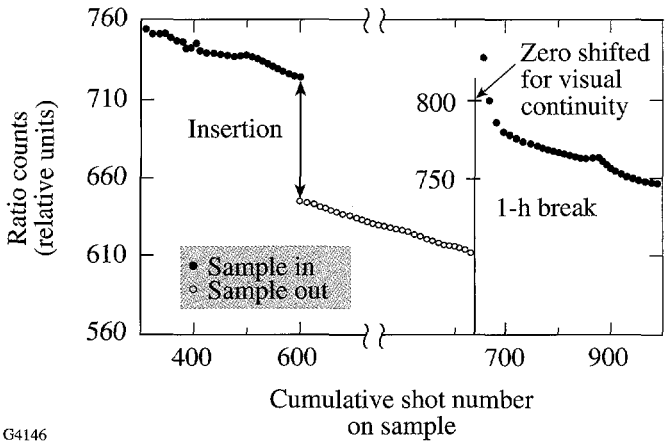

Figure 73.46
Calorimetric ratios of incident over transmitted energy (each data point is a ten-shot average) as a function of accumulated exposure. Nominal fluences on each shot were 3 J/cm^2. Full circles: sample in the beam; open circles: sample out.

the good agreement among slopes in Fig. 73.46 is taken as evidence for sufficient absence of such a cumulative absorbance increase. For a much smaller number of exposures per site, this is further corroborated by the distinction between 1-on-1 and *N*-on-1 thresholds depicted in Fig. 73.44. If there was substantial photolytic activity present in these samples, the evidenced "hardening" trend among all three sample types would be reversed.

We note here in passing that this absence of photolytic processes distinguishes the perfluorinated foils from cellulose-derivative ones, which, owing to such "photorefractive" response, give rise to interesting nonlinear scattering phenomena.[18] We note further that future large-scale laser systems are designed for >3-J/cm^2 maximum 351-nm fluence. Long-term photolytic stability in the 10- to 20-J/cm^2 fluence range still remains to be tested.

We also note that within the limited laser-output-power/spot-size phase space of our setup, i.e., a limited-range intensity gainlength test, a special effort to detect transverse stimulated Brillouin scattering yielded only *null results* in perfluorinated samples.

Interferometric tests of *thickness uniformity* (wavefront uniformity) pose a genuine challenge: the phase error measured between two consecutive, *empty-cavity* scans taken 10 min apart *is larger than* the phase error detectable *after the pellicle is inserted.* This result is true for pellicles up to 40 cm long (longest dimension). Thus, pellicle uniformity is better than can be measured with current state-of-the-art interferometers. This was independently verified by spectrophotometric scans at select sites across the pellicle aperture (all at 0° incidence). The objective in this test was to discern site-dependent wavelength peak shifts in the etalon spectral peaks in response to path-length differences. Again, within instrument resolution, only null results were obtained. As one would expect, such pellicles "ring" under all realistic mounting conditions—interferometry in *reflection* is a fruitless exercise, even if the sample film is mounted on a lapped frame that, by itself, is interferometrically flat.

System-Integration Considerations

From a systems-integration viewpoint, these perfluorinated films offer advantages but also a few drawbacks. Although highly elastic, the membranes are only a few microns thick and, accordingly, vulnerable to mechanical attack. Rapidly changing air-pressure differentials across the membranes, or directed air bursts typical of procedures for dust removal from optical surfaces, may cause membrane rupture. Another challenge is the still-limited clear-aperture size available commercially. The laser systems mentioned at the outset are designed for near-40-cm clear aperture: to date no perfluorinated pellicle measuring *40 cm in every direction* has been made. The largest pellicles available to this laboratory are 30 cm × 40 cm and 30 cm in diameter (circular).

Owing to the "drumhead" vibrations, pellicles are not suitable for image-quality, *reflective* applications. If the requirement, however, is simply one of getting photon energy into a certain direction, such as toward spatially integrating detectors or sensors, this drawback will be irrelevant.

Another challenge is posed by the *very low surface energy* of perfluorinated polymers (well-known "Teflon® effect"). There is not great latitude in choosing materials for multilayer designs, as poor wettability of perfluorinated surfaces makes uniform spin deposition of other materials nearly impossible.

Summary

The advantages of freestanding polymer film pellicles, apparent from the foregoing discussion, are rapid fabrication (spin on, lift off, mount on frame), robustness against 351-nm laser damage, photolytic stability, chemical inertness, amorphous structure, excellent transmitted-wavefront uniformity, and absence of birefringence. The best pellicles tested to date show UV damage thresholds up to five times higher than the frequency-conversion crystals (KDP) required for converting glass-laser output to the UV.

ACKNOWLEDGMENT

We thank our contacts at the three vendors for their prompt and enthusiastic support: Dr. K. Itoh, Shin-Etsu; Dr. C. B. Wang, MicroLithography, Inc.; and Joseph. S. Gordon, DuPont Photomasks. We also thank William Castle for help with interferometry and Jay Anzelotti for assistance in refractive-index calculations and field-distribution evaluation. Evaporated thin films were prepared under the direction of D. Smith. This work was supported by the U.S. Department of Energy Office of Inertial Confinement Fusion under Cooperative Agreement No. DE-FC03-92SF19460 and the University of Rochester. The support of DOE does not constitute an endorsement by DOE of the views expressed in this article.

REFERENCES

1. *Energy and Technology Review*, Lawrence Livermore National Laboratory, Livermore, CA, UCRL-52000-94-12, 1 (1994).

2. Many empirical as well as fundamental research results on laser damage can be found in the series of proceedings from the Annual Symposia on High-Power-Laser Materials (Boulder Conferences) published by the U.S. Government Printing Office as Special NBS Publications (until 1990) and by SPIE (after 1990).

3. T. Shirasaki *et al.*, in *Photomask and X-Ray Mask Technology*, edited by H. Yoshihara (SPIE, Bellingham, WA, 1994), Vol. 2254, pp. 392–400.

4. Shin-Etsu Chemicals, New Functional Materials Department, Research Center, Annoka, Gunma, Japan; DuPont Photomasks, Inc., Danbury, CT 06810; MicroLithography, Inc., Sunnyvale, CA 94089.

5. L. M. Sverdlov, M. A. Kovner, and E. P. Krainov, *Vibrational Spectra of Polyatomic Molecules* (Wiley, New York, 1974), p. 397.

6. J. R. Throckmorton, J. Org. Chem. **34**, 3438 (1969).

7. E. N. Squire, U.S. Patent No. 4,948,851 (14 August 1990); U.S. Patent No. 4,973,142 (27 November 1990).

8. D. L. Duly, H. Windischmann, and W. D. Buckley, U.S. Patent No. 4,523,974 (18 June 1985).

9. Hamamatsu U1381R-01, Hamamatsu Photonic Systems, Bridgewater, NJ 08807-0910.

10. Tektronix 7250, Tektronix, Inc., Beaverton, OR 97077.

11. M. R. Kozlowski *et al.*, in *Laser-Induced Damage in Optical Materials: 1990*, edited by H. E. Bennett *et al.* (SPIE, Bellingham, WA, 1991), Vol. 1441, pp. 269–282.

12. Zygo Mark IV-XP, Zygo Corporation, Middlefield, CT 06455-0448.

13. K. M. Dyumaev *et al.*, Bull. Acad. Sci. USSR Phys. Ser. **53**, 194 (1989).

14. While this manuscript was completed, 248-nm test results (15 ns) on select samples became available, buttressing the results listed here: T. Lehecka, U.S. Naval Research Laboratory (private communication). Request further information at lehecka@nemesis.nrl.navy.mil.

15. Corning 7940, Corning, Inc., Technical Products Division, Corning, NY 14831.

16. DuPont Mylar®, DuPont Packaging and Industrial Polymers, D-5100, Wilmington, DE 19898.

17. DuPont AF-1600, DuPont Fluoroproducts, Wilmington, DE 19880-0702.

18. S. Papernov, A. Schmid, and F. Dahmani, "Laser Damage in Polymer Waveguides Driven Purely by a Nonlinear, Transverse-Scattering Process," to appear in *Optics Communications*.

Subsurface Damage in Microgrinding Optical Glasses

In cold processing of optical glasses by microgrinding,[1,2] the resulting brittle-material-removal rate induces a cracked layer near the glass surface, referred to as subsurface damage (SSD). [Editor's note: The acronym for subsurface damage (SSD) used in this article should not be confused with its more common use as an acronym for smoothing by spectral dispersion.] In addition, there is a corresponding surface microroughness (SR), often found to increase in proportion to SSD, as originally observed by Preston.[3] SSD is a statistical measure and not necessarily equal to the flaw depth that may control mechanical strength of the brittle surface.

Direct measurement of SSD is tedious: The dimple method is often used[4,5] as well as wafering methods. Aleinikov[6] showed that SSD induced by lapping of glasses and other brittle ceramics (with hardness changing 30-fold, fracture toughness 6-fold, and Young's modulus 20-fold) was 3.9±0.2 times SR for SiC abrasives (100 to 150 μm), thus indicating that SSD may be estimated from SR. Aleinikov also found that SSD increased with increasing size of microindentation cracks (see Fig. 73.47). Thus, microindentation may be used to evaluate propensity to damage in lapping.

More recently, Edwards and Hed[8] studied the relation of SSD to SR under bound-diamond-abrasive conditions (53 to 65 μm and 180 to 250 μm in size) and found that for the three glasses studied (borosilicate crown BK7, zerodur, and fused silica) the average SSD was 6.4±1.3 times the peak-to-valley surface roughness (measured by a profilometer). The factor of 6.4 was arrived at by dividing SSD by SR for each glass. This proportionality factor becomes identical to that of Aleinikov[6] when all three materials tested by Edwards and Hed[8] are treated together (see Fig. 73.48). Similar observations have been reported for deterministic microgrinding of optical glasses with bound-abrasive-diamond tools of smaller size (2 to 4 μm) (see Lambropoulos *et al.*[9]).

In addition to correlating SSD with SR, it is possible also to correlate SSD for brittle materials with the materials' mechanical properties. Zhang[10] used metal bond wheels with bound diamond abrasives (40 to 230 μm in size) to grind structural ceramics under fixed infeed conditions and reported a subsurface damage depth (consisting of voids induced by the grinding) that correlated with the ductility index $(K_c/H_V)^2$ of these materials (see Fig. 73.49). The ductility index[9] is

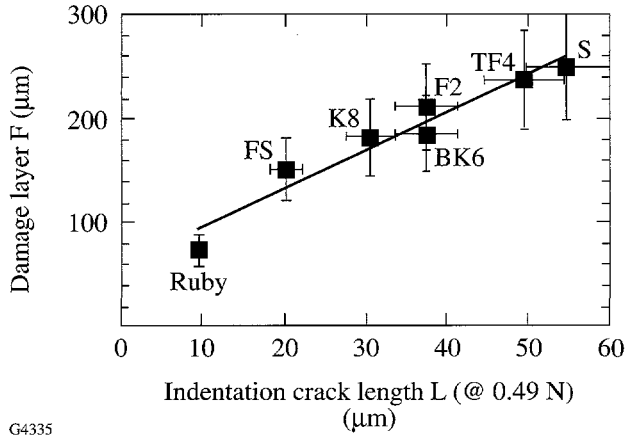

Figure 73.47
SSD in lapping versus indentation crack size (0.49 N) for brittle materials, based on Aleinikov.[6] Russian glass K8 is equivalent to Schott BK7 (Hoya BSC7, Ohara S-BSL7).[7]

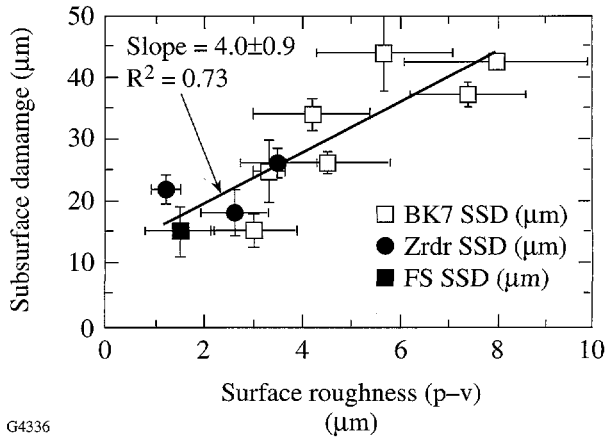

Figure 73.48
Relation of SSD to SR, as measured in bound-diamond-abrasive grinding by Edwards and Hed.[8]

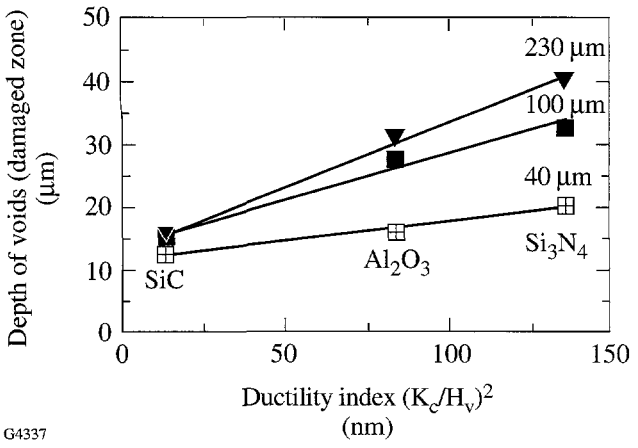

Figure 73.49
Subsurface damage versus mechanical properties of structural ceramics (SSD data from Zhang[10].)

inversely related to the brittleness H/K_c originally introduced by Lawn *et al.*[11,12]

In our notation, H denotes hardness, or resistance to plastic, irreversible deformation, measured by estimating the area of an indentation impressed under load P. Hardness is defined in terms of either projected area or actual area of contact. Specifically, H_K denotes Knoop hardness, extracted from measuring the long diagonal of a rhomboidal pyramid impression under load P by P/(projected contact area) = (constant) P/(long diagonal)^2, with the (constant) dependent on the rhomboidal pyramid geometry. H_V denotes Vickers indentation, extracted from measuring the average diagonal of a square pyramid impression under load P by P/(actual contact area) = (constant) P/(average diagonal)^2, with the (constant) dependent on the square pyramid geometry. For the same measured diagonal, Knoop indentations penetrate about half as much into the surface as Vickers indentations; thus, H_K more closely measures near-surface hardness. Generally, Knoop hardness H_K increases with Vickers hardness H_V. This correlation has been described in detail by Lambropoulos *et al.*[9]

Microgrinding Experiments

1. Lapping: Surface Roughness (SR) versus Subsurface Damage (SSD)

In all the following experiments, surface roughness was measured by a white-light interferometer (NewView 100, 0.35 × 0.26 mm^2, 20× Mirau, five measurements per surface) and subsurface damage by the dimple method (typically three to five dimples per surface[4,5]).

The goal of the lapping experiment was to investigate whether surface roughness can provide information about subsurface damage. Loose-abrasive lapping experiments were conducted on two glasses: the soft phosphate laser glass LHG8 (63% P_2O_5, 14% BaO, 12% K_2O, 7% Al_2O_3, 4% Nd_2O_3/Nb_2O_5) and the harder borosilicate crown optical glass BK7 (68.9% SiO_2, 10.1% B_2O_3, 8.8% Na_2O, 8.4% K_2O, 2.8% BaO, 1% As_2O_3, % by weight) (see Table 73.VI).

Five separate LHG8 blocks were lapped on both sides with Al_2O_3 abrasives (median size 30, 9, 5, 3, 1 μm). Measured SSD and SR, after grinding with each abrasive, are shown in Fig. 73.50.

Table 73.VI: Thermomechanical properties of optical glasses. Data for density ρ, glass transition temperature T_g, coefficient thermal expansion α, Young's modulus E, and Poisson ratio ν are from manufacturers' glass catalogs. Hardness H and fracture toughness K_c are from Schulman *et al.*[16] Knoop hardness is at 1.96 N. The fracture toughness of LaK9 was estimated from that of LaK10.

Glass	ρ (g/cm^3)	T_g (°C)	α (10^{-6} °C^{-1})	E (GPa)	ν	H_K (GPa)	K_c (MPa m$^{1/2}$)
LHG8	2.83	485	12.7	50	0.26	2.3	0.43
FS-C7940	2.20	1,090	0.52	73	0.17	5.6	0.75
SF58	5.51	422	9.0	52	0.26	2.7	0.46
SF7	3.80	448	7.9	56	0.23	3.4	0.67
BK7	2.51	559	7.1	81	0.21	5.1	0.82
K7	2.53	513	8.4	69	0.21	4.6	0.95
KzF6	2.54	444	5.5	52	0.21	3.7	1.03
LaK9	3.51	650	6.3	110	0.29	5.7	(0.90)
TaFD5	4.92	670	7.9	126	0.30	7.3	1.54

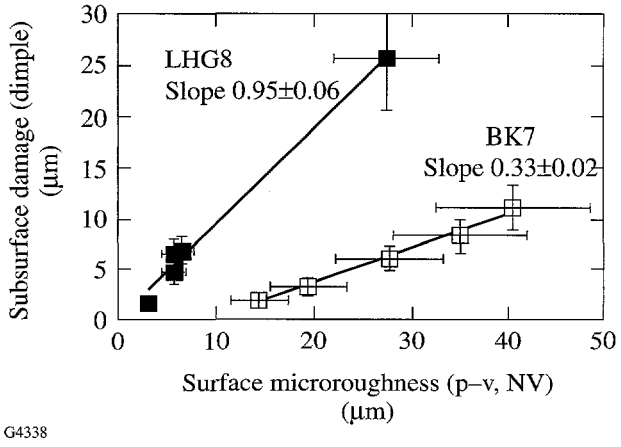

Figure 73.50
Correlation of SR (p–v) with SSD for loose-abrasive lapping of optical glasses (Al_2O_3 abrasives).

A similar experiment used BK7 with a wider abrasive size range (median size 40, 30, 20, 9, 5, 3, 1 μm). A single BK7 part was first lapped by 40-μm abrasives, then with 30-μm abrasives, and finally with 20-, 9-, 5-, 3-, and 1-μm abrasives. SSD and SR were measured at each step. Each lapping step removed between 0.3 to 1 mm of material and thus removed all the residual SSD from the previous abrasives used in the sequence. Larger abrasives typically led to higher SSD and higher SR.

The correlations of the subsurface damage to the peak-to-valley surface roughness for lapped LHG8 and BK7 are shown in Fig. 73.50. For LHG8 the p–v SR is equal to the measured SSD, whereas for BK7 the p–v SR is about 3 to 5 times the measured SSD. We conclude from these experiments that the p–v SR measured with the white-light interferometer provides an upper bound for the SSD measured by the dimple method.

2. Deterministic Microgrinding: Surface Roughness (SR) versus Subsurface Damage (SSD)

A series of multicomponent optical glasses, as well as fused silica,[13] were also ground under fixed infeed deterministic microgrinding conditions on the Opticam SM CNC machining platform,[14,15] which can manufacture planar and spherical surfaces, as well as aspheres.[9,14,15] Table 73.VI summarizes some of the glass properties.

Three metal-bonded diamond-abrasive ring tools were sequentially used on each surface (aqueous coolant Loh K-40, relative speed of work and tool of about 30 m/s): 70 to 80 μm, 10 to 20 μm, and 2 to 4 μm at infeed rates of 1 mm/min, 50 μm/min, and 5 μm/min, respectively. Three cuts were done with each tool. After each cut, SR of the optical surface was measured for microgrinding with all three tools, and SSD (three dimples for each cut) for the 2- to 4-μm and 10- to 20-μm tools.

Figure 73.51 shows the correlation between the measured p–v and rms SR for the three tools used, with each point representing one of the glasses ground and measured. Figure 73.52 shows the correlation of SSD (dimple method) and the p–v SR. It is seen that, as in lapping, the p–v SR may be used as an upper bound for the SSD for the 10- to 20-μm and 2- to 4-μm tools, within the uncertainty in the measurement of SSD and SR.

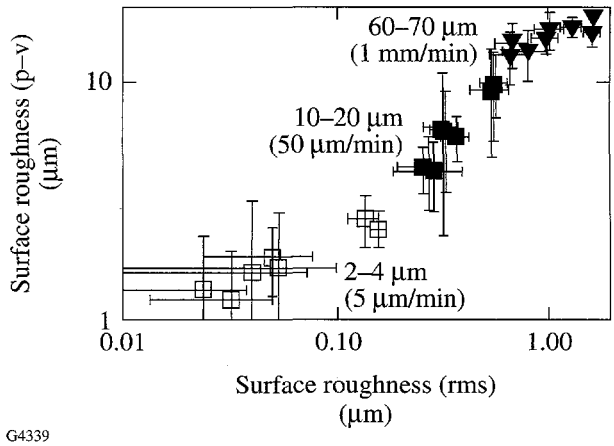

Figure 73.51
Correlation of p–v and rms SR under fixed infeed deterministic microgrinding of various optical glasses.

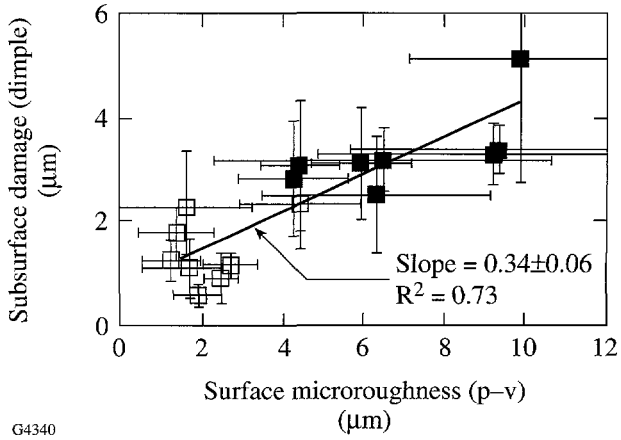

Figure 73.52
SSD (dimple method) versus p–v SR (via NewView 100 white-light interferometer) for fixed infeed deterministic microgrinding.

The effect of glass mechanical properties on SSD is shown in Fig. 73.53, where we have used the ductility index as the correlating parameter.[9] It is seen that, under fixed infeed grinding conditions, increasing ductility produces higher SSD, as observed in structural ceramics (Fig. 73.49). Correlations of measured SSD with the critical depth of cut discussed by Bifano *et al.*[17] or the critical load for fracture initiation discussed by Chiang *et al.*[18,19] gave similar trends.

The dependence of SSD on the ductility index is interpreted by a simple model of residual tensile stresses $\sigma \approx \beta\sigma_y$ (parallel to the surface), where $\beta \approx 0.08$[20] and σ_y is glass uniaxial yield stress ($\sigma_y \approx H_V/2$, see Ref. 9). Thus, crack depth a in the presence of such tensile stresses is estimated as

$$K_c = \Omega(\beta\ \sigma_y)\sqrt{\pi a} \Rightarrow a = \frac{1}{\pi}\left(\frac{K_c}{\Omega\beta\sigma_y}\right).$$

$\Omega \approx 1.1$ is a geometric factor accounting for the proximity of the free surface. Typical data for, say, BK7 give a crack depth of 2.1 to 4.3 μm, i.e., quite comparable to the measured SSD (see Fig. 73.52).

3. Comparison of Surface Quality Induced by Lapping and Deterministic Microgrinding

Figure 73.54 compares the surface quality of the optical glass BK7 (commonly used in many optical designs) resulting from loose-abrasive lapping with Al_2O_3 abrasives (seven sizes spanning 1 to 40 μm) and from deterministic microgrinding (three sizes spanning 3 to 75 μm) with bound diamond abrasives, over a wide range of abrasive sizes. The infeed rates for deterministic microgrinding were 5 μm/min (2- to 4-μm tool), 50 μm/min (10- to 20-μm tool), and 1 mm/min (70- to 80-μm tool). For both lapping and deterministic microgrinding, larger abrasives lead to deeper SSD and higher SR. The lapping results apparently become insensitive to abrasive size for abrasives in the 1- to 3-μm range.

For a given abrasive size, deterministic microgrinding results in surfaces with lower subsurface damage and lower surface microroughness (p–v or rms). Such surface features are in addition to any "figure" features extending over the whole aperture of the ground optical surface.

Conclusions

The quality of a manufactured optical surface can be characterized in a variety of ways, including surface microroughness[9] subsurface damage, surface figure error, residual stresses induced by the grinding process,[20,21] the rate of material removal,[22] and the rate of tool wear. In our work we have concentrated on subsurface damage and surface microroughness and addressed the following questions:

How can subsurface damage in a given brittle material be estimated from the measured surface microroughness? How can subsurface damage among brittle materials be correlated to their near-surface mechanical properties? How is the resulting

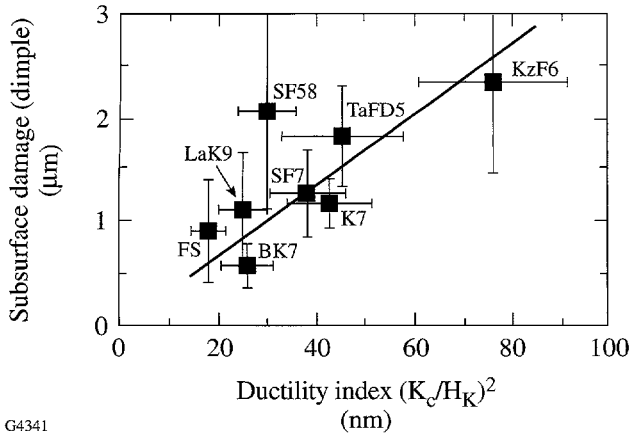

Figure 73.53
Dependence of subsurface damage SSD on glass mechanical properties via the ductility index $(K_c/H_K)^2$.

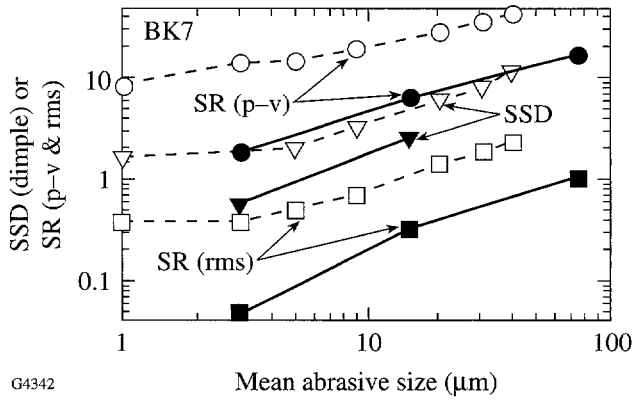

Figure 73.54
BK7 surfaces: lapping at fixed pressure (open symbols) versus deterministic microgrinding at fixed infeed with metal bonded-diamond-abrasive ring tools (solid symbols).

surface quality affected by material removal under loose-abrasive microgrinding at fixed nominal pressure (lapping) or by deterministic microgrinding under fixed infeed rate?

We have performed a series of loose-abrasive microgrinding (lapping at fixed nominal pressure) and deterministic microgrinding (at fixed infeed) experiments on various optical glasses. We summarize our results as follows:

- Peak-to-valley surface microroughness for the optical glasses tested (measured by the white-light interferometer, a relatively easy measurement to perform) provides an upper bound to the subsurface damage measured by the more-time-consuming dimple method;
- Subsurface damage in optical glasses under deterministic microgrinding conditions with 2- to 4-μm bound-diamond-abrasive tools scales with the glass ductility index $(K_c/H)^2$ in a manner similar to that reported for fixed infeed grinding of structural ceramics;[10] and
- For a given abrasive size, deterministic microgrinding produces lower subsurface damage and lower surface microroughness as compared to lapping.

The issue of residual stresses induced by grinding is also important and often referred to as the Twyman effect.[21] Although we have not measured residual stresses in this work, our previous work on optical glasses[20] and glass ceramics[23] shows that, for comparable abrasive sizes, deterministic microgrinding induces lower residual stresses than loose-abrasive lapping, while maintaining a higher material-removal rate and producing a lower surface roughness.

ACKNOWLEDGMENT

We acknowledge many helpful discussions with and insights from Mr. Don Golini of QED Technologies, LLC (Rochester, NY) and with Profs. Paul Funkenbusch and Stephen Burns of the Mechanical Engineering Department at the University of Rochester. We also acknowledge surface-roughness measurements provided by Mr. Ed Fess from the Center for Optics Manufacturing and microgrinding data by Mr. Bryan Reed from the Department of Mechanical Engineering and Ms. Yuling Hsu from the Center for Optics Manufacturing at the University of Rochester.

REFERENCES

1. T. S. Izumitani, *Optical Glass*, American Institute of Physics Translation Series (American Institute of Physics, New York, 1986), Chap. 4, pp. 91–146.
2. H. H. Karow, *Fabrication Methods for Precision Optics* (Wiley, New York, 1993), Chap. 5.
3. F. W. Preston, Trans. Opt. Soc. **XXIII**, 141 (1921–22).
4. A. Lindquist, S. D. Jacobs, and A. Feltz, in *Science of Optical Finishing*, 1990 Technical Digest Series (Optical Society of America, Washington, DC, 1990), Vol. 9, pp. 57–60.
5. Y. Zhou *et al.*, J. Am. Ceram. Soc. **77**, 3277 (1994).
6. F. K. Aleinikov, Sov. Phys. Tech. Phys. **27**, 2529 (1957).
7. L. B. Glebov and M. N. Tolstoi, in *CRC Handbook of Laser Science and Technology*, Vol. V: Optical Materials, Part 3, Supplement 2: Optical Materials, edited by M. J. Weber (CRC Press, Boca Raton, FL, 1995), pp. 823–826.
8. D. F. Edwards and P. P. Hed, Appl. Opt. **26**, 4677 (1987).
9. J. C. Lambropoulos, T. Fang, P. D. Funkenbusch, S. D. Jacobs, M. J. Cumbo, and D. Golini, Appl. Opt. **35**, 4448 (1996).
10. B. Zhang, in *Proc. ASPE*, 1996 Spring Topical Meeting on Precision Grinding of Brittle Materials (ASPE, Raleigh, NC, 1996), Vol. 13, pp. 76–81.
11. B. R. Lawn, T. Jensen, and A. Arora, J. Mater. Sci. **11**, 573 (1976).
12. B. R. Lawn and D. B. Marshall, J. Am. Ceram. Soc. **62**, 347 (1979).
13. Corning 7940, Corning, Inc., Technical Products Division, Corning, NY 14831.
14. H. M. Pollicove and D. T. Moore, Laser Focus World, March 1991, 145.
15. H. M. Pollicove and D. T. Moore, in *Optical Fabrication and Testing Workshop Topical Meeting*, 1992 Technical Digest Series (Optical Society of America, Washington, DC, 1992), Vol. 24, pp. 44–47.
16. J. Schulman, T. Fang, and J. Lambropoulos, *Brittleness/Ductility Database for Optical Glasses*, ver. 2.0, Department of Mechanical Engineering and Center for Optics Manufacturing, University of Rochester, Rochester, NY (1996).
17. T. G. Bifano, T. A. Dow, and R. O. Scattergood, Trans. ASME, B, J. Eng. Ind. **113**, 184 (1991).
18. S. S. Chiang, D. B. Marshall, and A. G. Evans, J. Appl. Phys. **53**, 298 (1982).
19. *ibid.*, 312.
20. J. C. Lambropoulos, S. Xu, T. Fang, and D. Golini, Appl. Opt. **35**, 5704 (1996).
21. J. C. Lambropoulos, S. Xu, and T. Fang, Appl. Opt. **36**, 1501 (1997).
22. F. Twyman, *Prism and Lens Making: A Textbook for Optical Glassworkers*, The Adam Hilger Series on Optics and Optoelectronics (Hilger & Watts, London, 1952), p. 318.
23. J. C. Lambropoulos, B. E. Gillman, Y. Zhou, S. D. Jacobs, and H. J. Stevens, in *Optical Manufacturing and Testing II*, edited by H. P. Stahl (SPIE, Bellingham, WA, 1997), Vol. 3134, pp. 178–189.

Bound-Abrasive Polishers for Optical Glass

Optical finishing of glass consists of generating (grinding) and polishing stages. In grinding, brittle fracture is performed on a workpiece using a series of two or three bound-abrasive grinding tools. These tools are composed of diamonds in a metal or resin matrix. The generating process starts with a coarse (~60 μm) diamond tool, and concludes with a medium (~15 μm) and (optional) a fine (~3 μm) tool. Reliable, repeatable, deterministic microgrinding with ring tools using Opticam CNC machining platforms developed at the Center for Optics Manufacturing (COM) produces spherical surfaces with rms surface microroughness of ~10 nm,[1] subsurface damage with a depth of less than 3 μm,[2] and peak-to-valley (p–v) surface shape errors less than 0.3 μm ($\lambda/2$).[3] On blanks to 100 mm in diameter, the process takes minutes per surface. Bound-diamond-abrasive ring tool generating has been adopted by many optics manufacturing companies in the U.S. as part of a modern finishing strategy when small quantities of prototype lenses are required with rapid turnaround. No specialized tooling is required, and diamond ring tools may be obtained from many suppliers.[4]

Determinism in the polishing stage of optics manufacturing continues to be elusive. As it is traditionally employed, polishing is a full-contact operation between a polishing lap, or *polisher*, and the workpiece. An aqueous abrasive slurry is introduced to the contact zone to hydrate the glass surface, and removal of the softened near-surface layer is achieved by chemomechanical effects and plastic scratching.[5] Loose-abrasive slurries are typically composed of cerium oxide (CeO_2) in water.[6] The polisher is composed of pitch or polyurethane on a cast iron backing plate.[7] Pitch is the preferred lapping surface for achieving subnanometer surface finishes on glass with high precision. Although much progress has been made in understanding slurry fluid chemistry,[8] slurry-workpiece electrostatics,[6] and the interaction among polishing abrasive, the polisher, and the part,[5] the conventional pitch polishing process continues to be heavily iterative in nature. Pitch is chemically unstable and loses organic volatiles with time.[9] Its compliance is also very sensitive to temperature.[10] As a reference template against which the part is continuously worked, a pitch lap must be frequently checked and corrected. The polishing step is the main bottleneck to reducing finishing time in rapid prototyping. Sub-aperture processing technologies using small pitch-surfaced tools[11] or ion beams[12,13] have found utility in selected applications. A newly developed process, magnetorheological finishing, has demonstrated the ability to rapidly and automatically polish out flats, concave/convex spheres, or aspheres on a magnetic fluid lap with no specialized tooling.[14]

An optics manufacturing company invests in excess of $200K to purchase, install, and operate a CNC diamond ring tool generating machine that can produce a *nearly* finished glass part. There is strong economic incentive to devise ways that would permit the use of such a machine to complete the finishing process by polishing out the part, thereby eliminating the need for any further processing steps and machines. One possible approach is to develop a bound-abrasive ring tool polisher, resident in the on-board automatic tool changer, to act as a final surface-finishing tool. The use of a bound-abrasive polisher has several potential advantages: Confinement of the abrasive in a binder enables finishing to be performed on a CNC machine platform. Large quantities of loose abrasives would destroy the guideways of the machine. A bound-abrasive polisher is less likely to deform under load and changes in temperature. Significantly less abrasive is required in the finishing process, thereby reducing the cost of consumables. Removal rates can be high. Issues of concern are the physical integrity of the polishing tool in use at ~1000 rpm (e.g., resistance to dissolution from the aqueous coolant, or fracture/crumbling under load), the ability to efficiently smooth the glass surface without ruining the surface figure, and the polisher's performance for different glass types.

Information in the Russian literature, primarily from V. V. Rogov and colleagues, addresses the use of bound polishing abrasives in the form of pellets affixed to a cast iron plate. They investigated pellet composition, tool rotation rate, and load for a variety of glasses.[15–17] The resulting pellet media, called Aquapol®,[18] are described as dimensionally stable from 10°–80°C. By introducing a superfine diamond grinding stage

to their process, a Moscow manufacturing enterprise was able to use Aquapol pellet polishing in distilled water to finish parts with some success. They noted, however, that the Aquapol materials "are rather brittle and possess low mechanical strength, which inevitably results in debris and crumbling at the edges of elements during operation and makes the tool unusable."[19] To avoid this problem, a form of nearly full contact Aquapol lap with a central hole was conceived and tested.[20] This concept proved successful for commercial-quality (e.g., figure accuracy tolerances to ~1 μm, rms surface roughness levels less than 10 nm) flat and spherical parts up to 50 mm in diameter. It was implemented at a number of factories throughout the former Soviet Union.

No information is available in the open literature regarding the use of bound-abrasive polishers in a ring tool geometry on CNC machine platforms. In this article we describe the development and testing of bound-abrasive compositions in three geometries: pellet, ring tool, and full-contact lap. We show that for several glass types, our compositions reduce rms surface roughness of initially fine ground surfaces to less than 2 nm in ~30 min. We demonstrate that bound-abrasive ring tools are compatible with CNC machine platforms, although maintaining or reducing surface figure errors is a problem that requires more study. We find, however, that it is feasible to use bound abrasives in *prepolishing* operations to remove grinding tool marks and dramatically shorten the time required for pitch polishing.

Key Performance Criteria, Variables, and Choices

There are five principle performance criteria for the successful development of a bound-abrasive polisher: First, the polisher must maintain its physical integrity during use at moderate to high velocities, in an aqueous environment, and under light to moderate load. Second, the polisher must release particles of polishing abrasive at a rate that promotes efficient removal of glass from the workpiece surface, but not so rapidly as to cause excessive tool wear, or so slowly that the tool surface "glazes" over with a solid film of binder. Third, the polisher must be manufactured in such a way that it exhibits reproducible performance under constant operating conditions. Fourth, the polisher must be capable of removing artifacts from grinding (e.g., tool marks, shallow scratches) to achieve an rms surface microroughness of less than ~2 nm in a reasonable period of time. Fifth, required surface figure tolerances must be met with the polisher.

Experiments on bound-abrasive polishers are complex because of the large number of variables and choices available in terms of polisher composition, manufacturing method, polisher geometry, workpiece glass type/shape, and polishing machine platform. The variables involved and the choices made for this work are summarized below.

1. Composition

Based upon the Russian work,[15] a successful bound-abrasive polisher consists of (in wt%) ~60 to 90/polishing agent, 5 to 25/binder, and 5 to 15/erosion promoter. Relative concentrations of abrasive/binder/erosion promoter are investigated here. Because of its high polishing efficiency for many soft and moderately hard glasses,[8] CeO_2 is the polishing abrasive of choice. An impure CeO_2/rare earth oxide blend, known as Polirit,[21,22] is used in the Aquapol media. It has a particle size of approximately 2 μm and is nominally 50% CeO_2. Polirit is available from several sources, and the variations in its composition from batch to batch have been noted.[23] We use three CeO_2 products with similar particle-size distributions and a range of purity levels from 50%–90%[24] (see Table 73.VII). The binder can be a polyimide, a phenolic (used in the Aquapol media), or an epoxy. From our earlier work[25] we have identified and use a low-viscosity, two-part epoxy[26] that can be readily impregnated with a high percentage of solids. The final ingredient in the polisher is an additive to promote erosion. Two types are studied here, separately and in combination, and their behavior is illustrated in Fig. 73.55. Ammonium chloride (NH_4Cl)[15] dissolves in the aqueous coolant during polishing to expose fresh abrasive particles to the work zone. Hollow alumina spheres[27] crush under mechanical loading and act as a form of controlled porosity to break up the binder material.

2. Manufacturing Method/Geometry

Because commercial mixing machines are costly and require large batch sizes, hand mixing was used to prepare all compositions according to a fixed methodology and cure schedule. Hand mixing has been found reliable and repeatable. The documentation given in this article is sufficient to transfer the manufacturing method to others. Mold geometry is limited to three forms in this work: pellet arrays (individual pellets waxed into arrays, or monolithic molded pellet arrays), rings, and full-contact laps.

3. Workpiece Glass Type/Shape

We concentrate on polishing commonly used optical glasses BK7,[28] SF7,[29] SK7,[29] SK14,[29] LaFN21,[29] TaFD5,[30] and fused silica,[31] whose Knoop hardness values fall in the range of ~3.4 to 6.7 GPa (350 to 680 kgf/mm^2) @ 200 gf.[32] Part shape is fixed at 35- to 50-mm diameter by 10 mm thick. Worked surfaces are either flat or spherical (convex 70-mm

Table 73.VII: Compositions and physical properties of Aquapol and selected experimental polishers.

ID#: Composition, wt%*	Shore D Hardness air	Shore D Hardness water**	Young's Modulus GPa	Shear Modulus GPa	Density (g/cm^3)	Form Used***
Polirit CeO_2 50% pure[22] / 2.0-μm size[42]						
#AS: Aquapol standard unknown composition	90	66	18.0	7.8	3.99	spa rt
CeRite 415K CeO_2 75% pure[43] / 2.0-μm size[44]						
#1: 94 CeO_2 6 epoxy 0 e.p.	88	11	12.1	4.8	3.99	rt
#2: 93 CeO_2 7 epoxy 0 e.p.	78	23	11.3	4.5	3.96	mpa rt
#3: 75% CeO_2 10% epoxy 15% e.p. (all h.al.s.)	88	81	14.1	5.7	3.20	rt
CeRite 4251 CeO_2 50% pure[43]/1.5-μm size[44]						
#4: 75% CeO_2 10% epoxy 15% e.p. (all h.al.s.)	73	63	na	na	2.53	mpa rt
CeRox 1663 CeO_2 90% pure[43]/1.0-μm size[44]						
#5: 63% CeO_2 25% epoxy 12% e.p. (10 h.al.s. + 2 a.cl.)	75	na	12.4	4.7	2.64	mpa rt
#6: 85% CeO_2 10% epoxy 5% e.p. (all a.cl.)	70	60	na	na	3.40	mpa rt

* e.p.–erosion promoter (h.al.s.–hollow alumina spheres; a.cl.–NH_4Cl)
** 60-min soak @ 25°C in buffered pH 10 DI water with gentle agitation
*** spa–single-pellet array; mpa–molded-pellet array; rt–ring tool

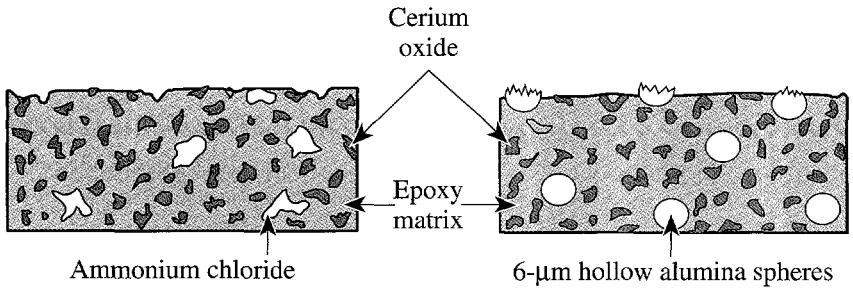

Figure 73.55
Ammonium chloride and hollow alumina spheres help promote erosion of the binder to expose fresh cerium oxide grains.

radius of curvature). Initial surface finish varies, depending on the method of preparation (loose abrasive grinding or ring tool generating).

4. Polishing Platforms

We evaluate polishing efficiency on three testbeds. A single-spindle polishing machine[33] is used for pellet polisher work with flat parts. This geometry is the easiest to implement and can be done with student assistants. Ring tool polishing trials are conducted on an Opticam SX CNC generating machine.[34] A collaborating company's[35] results from trials with full-contact polishers on semi-automated equipment are also reported.

Polisher Preparation and Bound-Abrasive Properties

To prepare a polisher, the abrasive and erosion promoter are dry mixed by hand and divided in half by weight. One portion is dispersed into two parts by weight of epoxy resin A, and the other is dispersed into one part by weight of epoxy hardener B. Once loaded with solids, A and B are separately hand mixed for 5 min, combined into a single batch, and hand mixed for an additional 10 min. A typical batch varies in weight from 50 g to 250 g. To prepare individual pellets similar in shape to the Aquapol media, the batch is poured into several 15-ml-capacity, plastic centrifuge tubes.[36] These tubes are tapped and mechanically vibrated to remove any entrapped air and cured at room temperature for 24 h. After curing, tubes are sliced open, and the cylindrical plugs are cut on a diamond saw[37] into 17.5-mm-thick pellets (12-mm diameter) with parallel surfaces. The individual pellets are mounted onto an aluminum plate with pitch or wax. Figure 73.56 illustrates the individual pellet polisher configuration. An alternative method uses an RTV silicone mold[38] containing an array of holes. The mold is treated with a mold-release agent,[39] and the batch is spread into it and cured. The 12-mm-diam pellets emerge in the form of a monolithic array (see Fig. 73.57), which is waxed to an aluminum plate. Other mold geometries are used to make solid rings. Full-contact laps are made by first creating a silicone mold master with a sample product part acting as a reference template.

For compositions containing >90-wt% solids, a small amount (10 ml per 100 g) of methanol[40] is added to resin A and hardener B to further reduce initial viscosities prior to loading in and mixing the solids. The use of methanol causes some cracking and fracture in molded rings during curing. This presents no problem since broken segments are glued together when being mounted onto a supporting ring tool chuck.

Mechanical properties testing for hardness and density verify the ability of different people to produce polishers with the same properties (±5%) when using our manufacturing method.[41] Table 73.VII gives property information for some experimental compositions. All six formulations function as bound-abrasive polishers, as will be demonstrated in the following sections. It is instructive to compare their physical properties with those of the standard hardness Aquapol media.

The Aquapol composition #AS is the hardest (Shore D) and least compliant (Young's modulus) material in Table 73.VII. It is brittle and easily fractured during routine handling and loading against a glass surface. By using an epoxy instead of a phenolic binder, we reduce hardness and increase compliance to improve handling. All experimental compositions show this feature. The CeO_2 concentration is so high in #1 and #2 that an erosion promoter is not necessary. A potential disadvantage to such a high abrasive concentration is the reduction of material resistance to disintegration in water. Measurements of hardness after soak tests in pH 10 water (a typical coolant requirement for CNC glass grinding machines[45]) show that compositions #1 and #2 are less robust.

A 1% increase in epoxy concentration (#1 to #2) improves soak test durability for a modest sacrifice in hardness. A further 3% increase to 10 wt% (#3, #4, #6) and higher (#5) greatly enhances soak test durability to that seen for Aquapol. (Soak

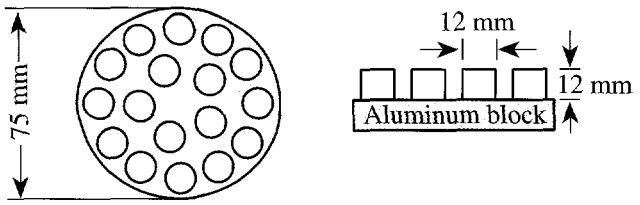

Figure 73.56
Setup for pellet array polisher manufactured from single pellets.

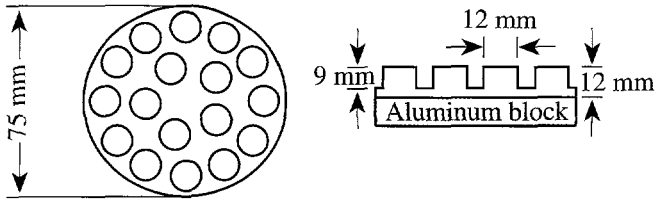

Figure 73.57
Setup for molded pellet array polisher.

tests, however, are not necessarily the best measure of a bound-abrasive polisher's durability in use as discussed later.) In addition to acting as erosion promoters, hollow alumina spheres in #3, #4, and #5 help to maintain high hardness and stiffness at high epoxy concentrations. Table 73.VII shows that, from a fabrication perspective, viable polishers may be manufactured from any of the three commercial CeO_2 abrasives.

Experimental Results for Pellet Laps

The objective was to evaluate the ability of flat, pellet array laps to reduce rms surface roughness of loose-abrasive–ground, flat glass parts to <2 nm in a fixed 30-min polishing cycle. Work reported is for compositions #5 and #6. Freshly made pellet array laps were dressed to expose the abrasive by working against a cast iron plate with ~9 μm alumina.[46] This also trued the surface. Glass parts of differing composition and physical properties were conditioned in the same manner to establish an initial ground surface whose rms surface roughness values were between 300 and 500 nm.[47] Work was carried out on a single-spindle machine,[33] lap on bottom, with the following setups: spindle speed, 35 rpm; eccentric speed, 58 rpm; front center adjustment, 0 mm; back center adjustment, 25 mm; load, 17.2 kPa (2.5 psi). The coolant was DI water, directed onto the lap and recirculated without filtration at a rate of ~200 ml/min. Results, summarized in Table 73.VIII, show that composition #5 works well for polishing out glasses with moderate hardness values. Composition #6 (higher CeO_2 concentration, less erosion promoter) works well for harder glasses, but twice as much time is required to polish down to below 2 nm rms. Other work (not reported here) shows that these polishers do not perform as well for crystalline materials (Si, Ge, CaF_2, ZnSe) whose hardness values fall outside the test range.

Table 73.VIII: Polishing results for bound-abrasive pellet array laps after 30 min.

Composition	Glass	(Hardness*)	Final rms[47] (nm)
#5	SF7	(3.4)	1
	SK7	(4.8)	1
	BK7	(5.1)	1
#6	fused silica	(6.5)	1.5 (60 min)
	TaFD5	(6.7)	1.5 (60 min)

*Knoop hardness, GPa @ 200 gf[32]

Molded Ring Tool Polishers

Several molded ring tool polishers were evaluated on the Opticam SX CNC generating machine.[34] Figure 73.58 shows the schematic of a ring tool polisher against a glass part. Major differences exist between the single-spindle machine used for flat pellet array polishing studies and the Opticam SX. The single-spindle machine utilizes a constant force approach for the lapping process. The Opticam SX uses a constant infeed rate for the cutting process with metal-bonded, diamond ring tools. The single-spindle machine operates at relatively low speeds and pressures, and experiments can be conducted with any desired coolant. Minimum tool and part speeds on the Opticam SX are 1000 rpm and 150 rpm, respectively. The coolant used for the SX polishing experiments is a filtered, high-viscosity grinding coolant, complete with corrosion inhibitors, defoamers, and fungicides.[48]

All compositions except #5 were manufactured in the form of solid and segmented ring tools for testing on the Opticam SX. Both flat and convex surfaces on either BK7 or SK14 glass (similar in hardness to SK7) were polished. All parts were prepared for polishing with the ring tool grinding strategy

summarized at the beginning of this article. Initial values of rms surface roughness were from 25 to 35 nm,[47] and the presence of residual grinding tool marks was noted (see below) on all parts. The programmed depth of cut (DOC) for each trial varied, but most trials had a 60-μm DOC and required ~15 min to complete. (It was not possible to measure the actual amount of glass material removed in a trial, due to the slightly compliant nature of the tools.) A wear path ~1 mm wide was typically observed on a tool surface after a trial. Tool wear was observed to be higher for compositions with higher CeO_2 concentrations. Table 73.IX shows that these polishers can reduce rms surface roughness to ≤1 nm. All in-house polishers maintained their mechanical integrity at speeds of 1000 rpm. There were no adverse effects noted on the guideways of the machine. In contradiction to the soak test results, compositions #1 and #2 held up well in the coolant spray, possibly because the time of exposure is reduced by 4× compared to that of the soak test. The Aquapol AS composition tool exhibited serious erosion problems in the commercial coolant, so it was therefore used for shorter, 5-min runs with a DOC of 30 μm. For these short runs, the standard Aquapol material performed well.

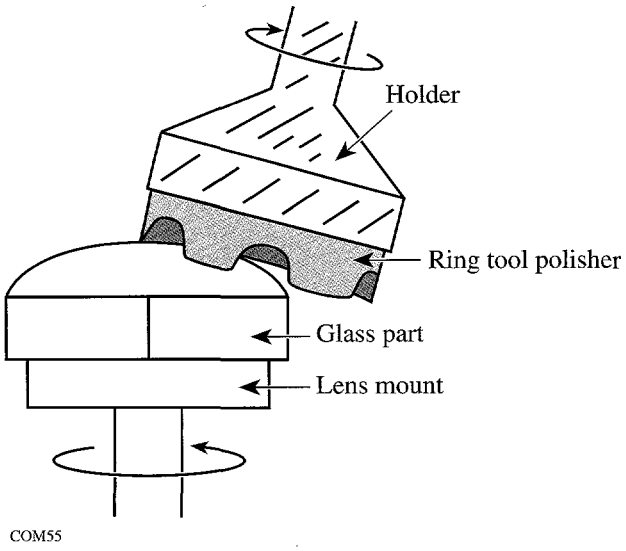

Figure 73.58
Schematic of bound-abrasive ring tool polisher.

It is useful if, as part of the polishing process, the polisher can remove diamond ring tool grinding marks. Referred to as "cutter" marks, they are produced on the part surface as a result of relative vibrations between the machine and the part and exhibit a circumferential periodicity that varies from 2 mm near part center to 10 mm near part edge. Figure 73.59 shows a radial profile scan[49] of a BK7 surface ground with a 10- to 20-μm diamond ring tool. The cutter marks have an amplitude of ~1000 Å and an edge periodicity of ~10 mm. Pitch laps and the high-cerium-oxide-concentration compositions #1 and #2 are very effective at removing cutter marks, as shown in Fig. 73.60. Other polisher compositions are similarly effective.

Attempts to reduce surface figure errors with bound-abrasive ring tools were not successful. Initial p–v surface figure values of 0.3 μm ($\lambda/2$) were seriously degraded by the tendency of the ring to polish a 0.5- to 2.0-μm-deep hole into the part center, regardless of shape (flat or convex sphere). A bound-abrasive ring tool polisher causes degradation to the surface figure when it does not wear rapidly enough to expose fresh CeO_2. The result is constant-force polishing similar to conventional polishing, on a machine designed to remove material at a constant infeed using diamond ring tools. The constant-force polishing causes excessive dwell in the part center. This can be avoided by going to a different bound-abrasive polishing tool shape and contact configuration.

Table 73.IX: Results for bound-abrasive ring tool polishing on the Opticam SX.

Composition	Part Shape	Glass	Programmed DOC (μm)	Final rms[47] (nm)	Tool Wear	Tool Marks Removed
#AS	flat	BK7	30	0.8	higher	yes
#1	flat	BK7	60	1.8	higher	no
#2	flat	BK7	120	1.10	higher	yes
	convex	SK14	60	0.6		yes
#3	flat	BK7	90	1.0	lower	yes
#4	flat	BK7	60	1.1	lower	yes
#6	convex	SK14	60	0.9	lower	no

An alternative polishing configuration, called contour mode polishing, is illustrated in Fig. 73.61. In this geometry, the peripheral face of the tool is used to remove material by following a tool path that traverses over the surface of the rotating workpiece (see infeed path motion in Fig. 73.61). A new aspheric generating machine, the Opticam AG, was recently delivered to the COM.[50] It possesses the correct configuration for use as a testbed for future trials of bound-abrasive polishers in a new form, that of a contour tool. Our expectation is that it should be possible to significantly reduce figure degradation when polishing in this manner.

Molded Full-Contact Polishers

Several full-contact polishers were molded from composition #6 for a local optics company[35] to test on LaFN21 glass (Knoop hardness, 6.18 GPa @ 200 gf). The polishers were made to a specified 11.48-mm radius of curvature and 22-mm diameter by using a sample lens as the mold master. After release from the mold, the polishers were modified by carving grooves in their centers to reduce center contact and help maintain the optical figure of the part during the polishing cycle. Due to constraints on the semiautomated machines at the company, the polishers were used with a cerium oxide polishing slurry instead of deionized water. Results indicate that the company can reduce overall finishing time by 50% by using full-contact molded polishers in a prepolishing stage. Due to the stiffer nature of these polishers compared to pitch, they can be used at higher pressures and spindle speeds to increase material-removal rates without degrading surface figure.

A microlens manufacturer[51] used molded bound-abrasive polishers made from the compositions and manufacturing methods described in this paper to aid in the production of $\lambda/4$ surfaces. Opticians preferred these polishers because their stiffness helped in maintaining figure.

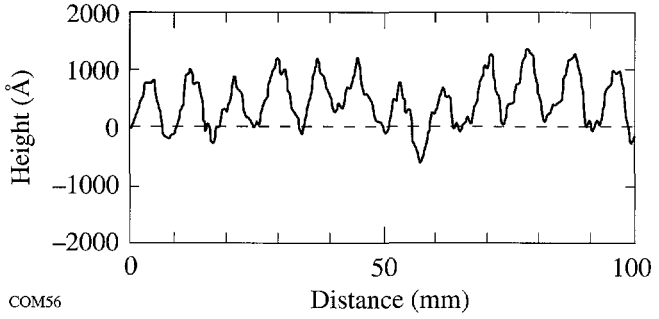

Figure 73.59
Radial profile scan showing tool marks remaining on a part surface from ring-tool-generating process.

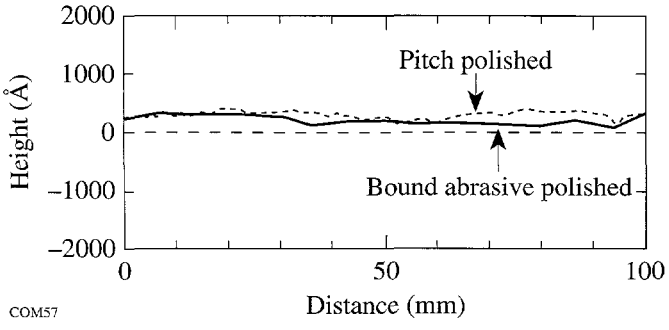

Figure 73.60
Removal of tool marks by either pitch polishing or bound-abrasive ring tool polishing.

Conclusions

We describe the development of bound-abrasive polishers using any of three commercial CeO_2 abrasives in six compositions. An epoxy is used as the binder. Useful polishing is achieved without an erosion promoter by using very high concentrations of abrasive. An erosion promoter is required to help break up the epoxy binder and expose abrasive grains at lower abrasive concentrations. Performance results are given for three polisher configurations: pellet array, ring tool, and full contact. All compositions work well, but the ones with higher CeO_2 concentration appear best for harder glasses.

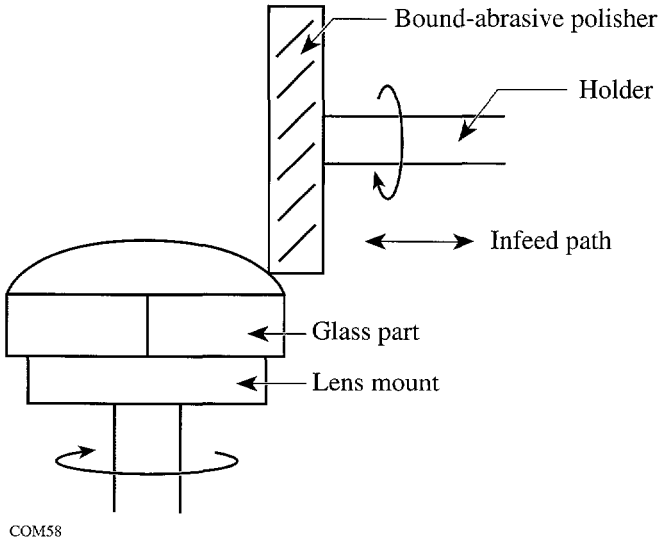

Figure 73.61
Concept for bound-abrasive contour polishing.

These polishers meet most of the performance criteria established for them. They maintain their physical integrity in aqueous coolants, under moderate loads, and at moderate to high velocities. They polish efficiently and are capable of reducing rms surface roughness of optical glasses from ~400 nm to ~1 nm in 30 min. The polishers are readily manufactured using simple process steps and have reproducible properties. They are compatible with Opticam-type CNC generating machines and can act as a fourth tool in an automatic tool changer to remove tool marks left from the last diamond ring tool grinding operation.

The issue of surface figure correction during polishing has not been successfully resolved with the bound-abrasive *ring* tool configuration, but a bound-abrasive *contour* tool mode of polishing is proposed as a solution. Finally, industry trials have demonstrated that the technology is transferable and helps to reduce overall production times when incorporated into the manufacturing process.

ACKNOWLEDGMENT

Funding for this work was provided by the U.S. Army Materiel Command and DARPA. The authors gratefully acknowledge the support of the students that have worked on the project: Shane Snyder, Amy Schneider, Jason Martin, Rich Andre, Caitlin Dickinson, and Willy Ng. We also acknowledge the support we have received from the UR Mechanical Engineering Department—specifically, Professors Paul Funkenbusch and John Lambropoulos for technical discussions and Professor Sheryl Gracewski for mechanical (Young's and Shear modulus) measurements. The authors acknowledge V. V. Rogov for suggestions regarding the optimal use of Aquapol and comments from the reviewers, which helped to narrow the focus of results reported here.

REFERENCES

1. J. C. Lambropoulos, T. Fang, P. D. Funkenbusch, S. D. Jacobs, M. J. Cumbo, and D. Golini, Appl. Opt. **35**, 4448 (1996).
2. J. C. Lambropoulos, S. D. Jacobs, B. E. Gillman, F. Yang, and J. Ruckman, "Subsurface Damage in Microgrinding Optical Glasses," to be published in the *Proceedings of the Fifth International Conference on Advances in the Fusion and Processing of Glass*, Toronto, Canada, 27–31 July 1997.
3. D. Golini and W. Czajkowski, Laser Focus World, July 1992, 146.
4. Our vendors include Scomac, Inc., Bergen, NY 14416 and H & C Tool Supply, Rochester, NY 14611, a distributor for Norton Superabrasives.
5. T. S. Izumitani, *Optical Glass*, American Institute of Physics Translation Series (American Institute of Physics, New York, 1986), Chap. 4, pp. 91–146.
6. M. J. Cumbo, D. Fairhurst, S. D. Jacobs, and B. E. Puchebner, Appl. Opt. **34**, 3743 (1995).
7. H. H. Karow, *Fabrication Methods for Precision Optics* (Wiley, New York, 1993), Chap. 5, p. 463.
8. L. M. Cook, J. Non-Cryst. Solids **120**, 152 (1990).
9. G. W. Fynn and W. J. A. Powell, in *Cutting and Polishing Optical and Electronic Materials*, The Adam Hilger Series on Optics and Optoelectronics, 2nd ed. (A. Hilger, Bristol, England, 1988), Chap. 3, p. 83.
10. N. J. Brown, Lawrence Livermore National Laboratory, Livermore, CA, UCRL-80301 (1977).
11. M. Ando *et al.*, Nanotechnology **6**, 111 (1995).
12. A. P. Bogdanov *et al.*, J. Opt. Technol. **61**, 474 (1994).
13. T. W. Drueding *et al.*, Opt. Eng. **34**, 3565 (1995).
14. D. Golini, S. Jacobs, W. Kordonski, and P. Dumas, in *Advanced Materials for Optics and Precision Structures*, edited by M. A. Ealey, R. A. Paquin, and T. B. Parsonage, Critical Reviews of Optical Science and Technology (SPIE, Bellingham, WA, 1997), Vol. CR67, pp. 251–274.
15. A. P. Denisenko *et al.*, Russian Patent No. SU 1263513 A1 (October 1986), USSR certificate No. 88333, trademark rights.
16. V. V. Rogov *et al.*, Sov. J. Opt. Technol. **56**, 33 (1989).
17. V. V. Rogov, Sov. J. Opt. Technol. **58**, 366 (1991).
18. Aquapol® product literature, Institute for Superhard Materials, Academy of Sciences of the Ukranian SSR, Kiev, Ukraine (1992).
19. V. M. Al'tshuller, S. A. Gerasimov, and V. P. Pushechnikov, J. Opt. Technol. **61**, 470 (1994).
20. S. I. Zakharov and O. V. Tapinskaya, Sov. J. Opt. Technol. **58**, 519 (1991).
21. N. L. Kudryavtseva *et al.*, Sov. J. Opt. Technol. **44**, 347 (1977).
22. N. L. Kudryavtseva, N. E. Khar'kov, and G. S. Khodakov, Sov. J. Opt. Technol. **50**, 378 (1983).
23. M. Yu. Konyukhov *et al.*, Sov. J. Opt. Technol. **58**, 798 (1991).
24. Transelco CeRite 415K, CeRite 4251, and Rhone Poulenc Cerox 1663, distributed by Universal Photonics, Inc., Hicksville, NY 11801.
25. W. Ng, B. E. Puchebner, S. D. Jacobs, J. L. Currin, B. McAvoy, D. Yungk, S. M. Gracewski, and P. D. Funkenbusch, in *Optical Fabrication and Testing Workshop*, Vol. 13, 1994 OSA Technical Digest Series (Optical Society of America, Washington, DC, 1994), pp. 114–116.
26. Epo-Tek B9131-2®, two-component "power laser adhesive," Epoxy Technology, Inc., Billerica, MA 01821.
27. Plasma alumina, low-density, microporous, hollow aluminum oxide spheres, 6-μm diameter, P.Q. Corporation, Conshohocken, PA 19428.
28. Ohara Corporation, Somerville, NJ 08876-3519.

29. Schott Glass Technologies, Inc., Duryea, PA 18642.

30. Hoya Optics, Inc., Fremont, CA 94538.

31. Fused silica, Code 7940, Corning Inc., Corning, NY 14831.

32. Schott Optical Glass Catalog (1989); Hoya Optical Glass Catalog (1989); Corning fused-silica product literature (1997).

33. R. Howard Strasbaugh (Model 6DE-DC-1), Woodbury, CT 06798.

34. Opticam® SX (renamed OptiPro 150), OptiPro Systems Inc., Ontario, NY 14519.

35. Optimax Systems, Inc., Ontario, NY 14519.

36. Catalog #21008-089, VWR Scientific Products, West Chester, PA 19380.

37. Buehler Isomet low-speed saw, Buehler Ltd., Lake Bluff, Il 60044.

38. Dow Corning RTV 3110, distributed by Wolcott-Park, Rochester, NY 14617.

39. ReleasaGen®, paintable ester mold release spray, IMS Inc., Chagrin Falls, OH 44022.

40. MX0485-7 methanol GR (anhydrous), EM Science, Gibbstown, NJ 08027.

41. B. E. Puchebner and S. D. Jacobs, in *Optical Manufacturing and Testing*, edited by V. J. Doherty and H. P. Stahl (SPIE, Bellingham, WA, 1995), Vol. 2536, pp. 256–264.

42. N. L. Kudryavtseva *et al.*, Sov. J. Opt. Technol. **46**, 478 (1979).

43. Universal Photonics Product Catalog (1996), p. 14.

44. Measurements performed on a Horiba LA 900 Laser Scattering Particle Analyzer®, Horiba Instruments, Inc., Irvine, CA 92714.

45. B. E. Gillman, B. M. Reed, M. A. Atwood, J. L. Ruckman, D. J. Quesnel, T. T. Ochinero, and S. D. Jacobs, in *Optical Manufacturing and Testing II*, edited by H. P. Stahl (SPIE, Bellingham, WA, 1997), Vol. 3134, pp. 198–204.

46. Microgrit Abrasives Corporation, Westfield, MA 01086.

47. NewView 100®, white-light interferometer, 0.25 mm × 0.35 mm, areal, 20X Mirau, Zygo Corporation, Middlefield, CT 06455. Each roughness measurement reported is an average of measurements made at three sites over the part surface, avoiding center and edges.

48. LOH K-40 Coolant, LOH Optical Machinery, Inc., Germantown, WI 53022.

49. Mark IV xp phase shifting interferometer, Zygo Corporation, Middlefield, CT 06455. Using a high-pass, fast Fourier transform filter, the software options allow a line scan to be taken around the part at a fixed radius from the part center (14 mm), defined as a radial scan.

50. Moore Tool Company, Bridgeport, CT 06607.

51. Model, Inc./Integrated Endoscopy, Irvine, CA 92618.

Color Gamut of Cholesteric Liquid Crystal Films and Flakes by Standard Colorimetry

Ever since cholesteric liquid crystals (CLC's) were discovered in 1888,[1] CLC colors have been noted for their qualitative vividness and luminosity;[2] however, there have been few quantitative colorimetric studies examining CLC's as colorants. We will describe how CLC's produce color, what colorimetric studies have been done on them, and how we have extended and improved on these previous studies.

CLC molecules generally have a large aspect ratio and are often modeled as long thin rods. These rods orient along an average preferred direction in a given plane. This preferred direction, indicated by a unit vector called the director, **n**, rotates slightly from one plane to the next, forming a helix structure that may be right-handed or left-handed depending on the constituents of the molecule.[3] In a typical model (shown in Fig. 73.62) the periodicity of the helix leads to the constructive interference colors of CLC's. The distance it takes the director to rotate through 360° is called the pitch P of the CLC helix. The pitch multiplied by $\bar{n}_n$, the average refractive index of the molecular layers, gives the wavelength of selective reflection, λ_0, which may range from the ultraviolet through the visible to the infrared.[4] The width of the reflected wavelength band for visible-reflecting CLC's (λ_0 ranging from 380 to 780 nm) can typically range from 10 to 100 nm.[5]

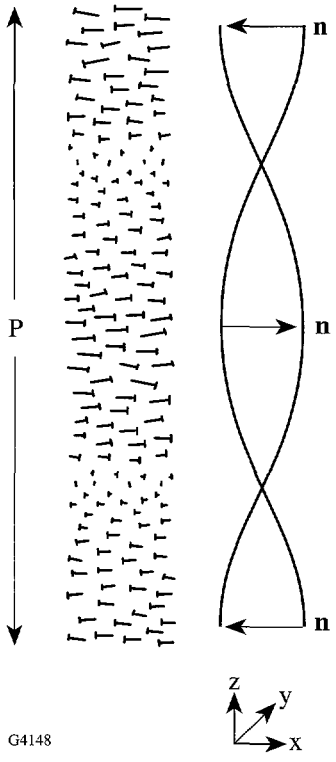

Figure 73.62
Schematic model of CLC structure.

In addition to the selectivity of reflected wavelength, the CLC helix is also selective with respect to polarization. Incident light that is superimposable on the helix, i.e., of the proper wavelength *and* the proper circular polarization, will be reflected.[4] Figure 73.63 shows schematically how randomly polarized white light incident parallel to the CLC helix is selectively reflected by wavelength and polarization.

In the ideal CLC structure, there is no discontinuity in any given plane. In real CLC structures, there may be defects in molecular orientation similar to dislocations in solid crystals. The regions of perfect structure between the defects or other discontinuities are referred to as *domains*.[6] Samples that are defect-free are called *monodomain*. Samples with discontinuous domains are referred to as *polydomain*.

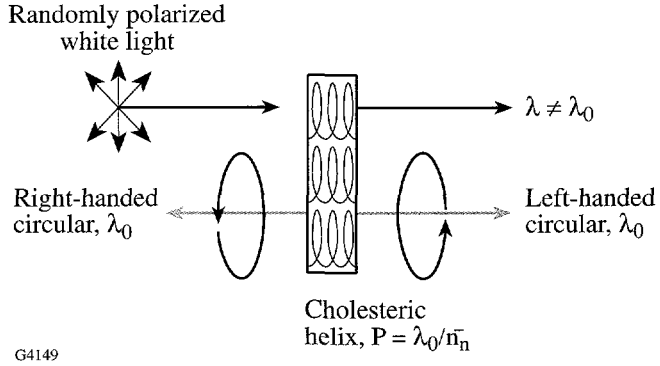

Figure 73.63
Schematic diagram of the wavelength and polarization selectivity of CLC's.

The CLC's that have been used for actively controlled color display purposes are usually polydomain: *polymer dispersed* in which the CLC molecules are found in microdroplets (~0.1 μm to ~10 μm in diameter)[7] distributed in an isotropic polymer matrix[8] and *gels* in which the CLC's form a more continuous phase with a small amount of either isotropic or anisotropic polymer to form a network that contributes to CLC molecular orientation.[9] Voltage and frequency are used to control the orientation of the CLC helices within the microdroplets or in the support polymer network; thus the ability to selectively reflect specific wavelength bands can be controlled electro-optically. Kitzerow *et al.*[10] calculated the chromaticities from the reflectivity spectra of a polymer-dispersed CLC system as a function of temperature. Although the chromaticity plot appears to indicate a color gamut covering almost the entire chromaticity diagram, many of the measurement details are unspecified, including the illuminant, the measurement angles, the actual chromaticity and luminosity values, and the voltage required for selective reflection. They indicate, however, that 2 to 3 V/μm are required to see some reflection, with intensity of the selective reflection increasing with increasing field strength to reach a plateau at 125 V/μm.

A third form of polydomain CLC that has been used for color display is called *encapsulated*. It is similar to polymer-dispersed CLC except for preparation method and has been used for decorative art[11] and for thermally controlled displays.[12] In the latter, temperature changes twist or untwist the CLC helix, shortening or lengthening the pitch and thereby controlling the reflected color. Makow and Sanders[11] used encapsulated CLC's to elucidate the qualitative color additivity of encapsulated CLC's of different colors in separate layers.

A fourth form of CLC's, *continuous film*, has been used for color filters,[13] optical notch filters,[14,15] polarization isolators,[16] and decorative art.[17] Even CLC continuous films may be polydomain unless some care is taken in the sample preparation.[18] The continuous films may be low-molecular-weight CLC's (LMCLC's) or higher-weight oligomer/polymer materials.

LMCLC's require two support substrates to promote the formation and maintenance of the helix structure across a continuous film. Makow[19] showed that, as with the encapsulated CLC's, layering different colors produces color additivity. Layering of LMCLC films, however, requires separating the layers by thin transparent sheets to prevent physico-chemical mixing that causes pitch averaging/blending.[20,21]

The oligomer/polymer type of CLC is more temperature stable than LMCLC's.[22] Oligomers/polymers can be physically manipulated at temperatures above a certain threshold called the *glass transition temperature* and retain molecular orientation below this temperature. One class of oligomers—cyclic polysiloxanes—has been particularly widely investigated.[23,24]

Cyclic polysiloxanes have been the subject of several colorimetric studies. Makow[25] demonstrated the artistic beauty of CLC polysiloxane films and showed that any spectral color could be produced by simply physico-chemically mixing a short-pitch with a long-pitch CLC. He also suggested that CLC polysiloxane films exhibit chromaticities outside the gamut of available colorants determined by Pointer,[26,27] although Makow actually compared CLC films measured in an 8/*d* geometry of an integrating sphere to Pointer's real surface colors measured by a 45/0 colorimeter. Nevertheless, he did initiate the possibility of comparing CLC's to other colorants. Makow also introduced the qualitative use of isoluminous contour lines as theoretical limits of saturation. As early as 1916, Ostwald[28] had concluded that there was some maximum attainable saturation for any given color. The reflection profile that would yield such a maximally pure or optimal color requires that the spectral reflectance have values of only zero or 100%, with no more than two discontinuous transitions between these values. The reflection profiles of most normal absorptive pigments do not meet these criteria. MacAdam[29] later used the CIE 1931 diagram to define limits of maximum attainable purity for a given luminosity Y and plotted these isoluminosity loci as contour lines within the CIE 1931 diagram. A sample with a given Y can be no purer than its associated isoluminous line.

One other chromaticity study on CLC polysiloxanes was done by Eberle *et al.*[30] They examined CLC polysiloxanes dissolved with dyes and CLC polysiloxanes on colored (paper) substrates, at many combinations of incident and reflection angles. The color additivity of a CLC and a traditional colorant (dye or paper) was quantified, but layers of CLC's of different colors were not examined. In that study, chromaticity and luminosity were shown to be simple averages of the components involved in any pair combination. Although not explicitly stated, Eberle *et al.* used the Center-of-Gravity Color-Mixing Principle.[31]

In its standard form, the Principle describes how two colors, C_1 and C_2, designated by chromaticity and luminosity coordinates $x_1y_1Y_1$ and $x_2y_2Y_2$ in the CIE 1931 chromaticity system are additively mixed. Using MacAdam's notations,[32] if

m_1 units of color C_1 are mixed with m_2 units of color C_2 (where $m_1 = Y_1/y_1$ and $m_2 = Y_2/y_2$), the chromaticity of the mixture color C_3 lies on a line connecting C_1 and C_2 on a CIE 1931 chromaticity diagram and has the following chromaticity values:

$$x_3 = \frac{m_1 x_1 + m_2 x_2}{m_1 + m_2}, \tag{1}$$

$$y_3 = \frac{m_1 y_1 + m_2 y_2}{m_1 + m_2}, \tag{2}$$

$$Y_3 = Y_1 + Y_2 . \tag{3}$$

The distance ratio of the line segments $\overline{C_1C_3}$ and $\overline{C_2C_3}$ shows the center-of-gravity relationship:

$$\frac{|C_1C_3|}{|C_2C_3|} = \frac{Y_2/y_2}{Y_1/y_1}. \tag{4}$$

If each of the two colors occupies a discrete fractional area designated A_1 or A_2 respectively, Eqs. (1)–(3) may be written as

$$x_3 = \frac{A_1 m_1 x_1 + A_2 m_2 x_2}{A_1 m_1 + A_2 m_2}, \tag{5}$$

$$y_3 = \frac{A_1 m_1 y_1 + A_2 m_2 y_2}{A_1 m_1 + A_2 m_2}, \tag{6}$$

$$Y_3 = A_1 Y_1 + A_2 Y_2 . \tag{7}$$

Since the CLC's with dyes or the CLC's on colored substrates occupied the same area, the form of the Center-of-Gravity Color-Mixing Principle used by Eberle *et al.* invoked Eqs. (1)–(3) and showed good agreement with experiment for their systems. They concluded that the CLC contributed to the measured color significantly near specular geometries (illumination angle ≈ reflection angle), but otherwise the substrate color dominated. This contribution of a colored substrate to the measured color of a CLC confirmed quantitatively what earlier artistic[17] work with CLC's had found: a black backing, contributing no color to the CLC appearance, produces truer CLC color effects.

To date, no *standard* colorimetry has been conducted on continuous CLC films or on discrete CLC domains, that is, at 45/0 and such that all conditions of measurement are explicitly known. No colorimetric experiment has quantified the color additivity of layering CLC's. No deterministic method has been developed for the color additivity of discrete CLC domains. No comparison has been made of CLC's as colorants and traditional absorptive colorants under similar conditions of measurement.

In this article, we address each of these issues. The CLC's used are cyclic polysiloxanes in two forms: continuous film and a new form called *flakes*. These two forms allow us to compare the color of CLC films to other colorants and to compare the large domains of a continuous film to the small domains of flakes. Further, flakes dispersed in a host will serve as a model for polymer-dispersed, gel, and encapsulated CLC forms. Principally, this article will show how the color gamut of CLC's can be affected by the form of the CLC, the size of the domains, and the method of mixing CLC's. Other aspects of CLC colorimetry including CLC flake production, polarization issues, the shape of the selective reflection profile, mixing CLC's with traditional absorptive dyes, and CLC's modeled as optimal colors are addressed elsewhere.[33]

Sample Preparation and Measurement Methods

The liquid crystal phase of the CLC cyclic polysiloxanes used in this study exists between 50°C and 200°C. At temperatures below this range, the molecular orientation is "frozen." At temperatures higher than this range, these materials are isotropic, noncolored liquids that decompose in the presence of oxygen. Three polysiloxanes were used: CLC670 (red reflecting), CLC535 (green reflecting), and CLC450 (violet reflecting). The number refers to λ_0, the wavelength in nanometers that is the center of the reflected wavelength band.

Continuous films are prepared by a process referred to as "knife-coating." A sample of CLC on a microscope slide or silicon wafer is heated to ~130°C. Another microscope slide is used on edge as a "knife" to spread the CLC into a thin film ~30 μm thick. This process produces the proper molecular orientation that results in brilliant reflective color.

A second form of CLC is produced by knife-coating continuous films on silicon wafers[34] and submerging them into liquid nitrogen. The films fracture into smaller pieces called *flakes*.[35] Flakes are collected by rinsing into a methanol slurry. The slurry is washed with methanol through a stack of sieves[36] into four size-groups: 90 to 180 μm, 45 to 90 μm, 20 to 45 μm, and <20 μm. The average refractive indices of the unfractured films are measured on an Abbe refractometer.[37] The flakes made from the films are mixed into a slurry (12%±3% by

weight) with an enamel, filtered[38] from a commercially available paint,[39] providing a very closely index-matched, transparent colorless host. This enamel-and-flake slurry is painted into a 1-cm × 2-cm color patch on black toner paper from a laser printer.[40] A schematic diagram of the typical orientation of CLC flakes brushed onto paper is shown in Fig. 73.64.

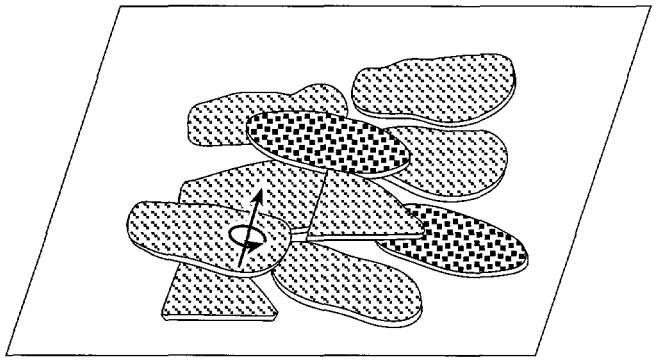

G4150

Figure 73.64
Schematic diagram of CLC flakes painted onto paper.

The chromaticity and luminosity (x,y,Y) of CLC samples were measured with two colorimeters, each using the CIE 1931 basis with D_{65} illuminant. CLC flake samples in enamel painted directly onto black toner paper were measured using the Gretag SPM 100-II colorimeter.[41] Due to the motor action of the Gretag detection head, the measurement of slides was unstable so CLC films on microscope slides with black toner paper backing were measured using the ColorTron II colorimeter.[42] Each sample was measured in five evenly spaced spots along the length of the color patch. These values were averaged, and a standard deviation due to variation across the sample was determined. Inter-instrument agreement was within this standard deviation.

The color of CLC's is angle dependent, following a Bragg-like law;[43] however, since most commonly available colorimeters use the 45/0 geometry, this article will address color effects for this fixed geometry only.

Experiments and Results

Since this article deals primarily with the nature of the color gamut of CLC's, we will discuss the six main features we have elucidated regarding techniques to access regions of CIE 1931 x,y,Y color space with CLC's as the colorants:

1. The Color Gamut of the Three Original CLC Films

Table 73.X lists the x,y,Y values and Fig. 73.65 illustrates the chromaticity positions of the original three CLC films. Geometric color additivity on the CIE 1931 chromaticity diagram ensures that an additive mixture of any two points yields a third chromaticity point *on* the line connecting the two components.[31] Using only the original three CLC's as continuous films, the chromaticities we can access are limited to those *on* the triangle of Fig. 73.65.

Table 73.X: The measured chromaticities and luminosities, x,y,Y, of the three original CLC polysiloxane films.

CLC ID	x	y	Y
CLC670	0.5153	0.3459	8.83
CLC535	0.2306	0.4803	26.26
CLC450	0.1777	0.0777	4.33

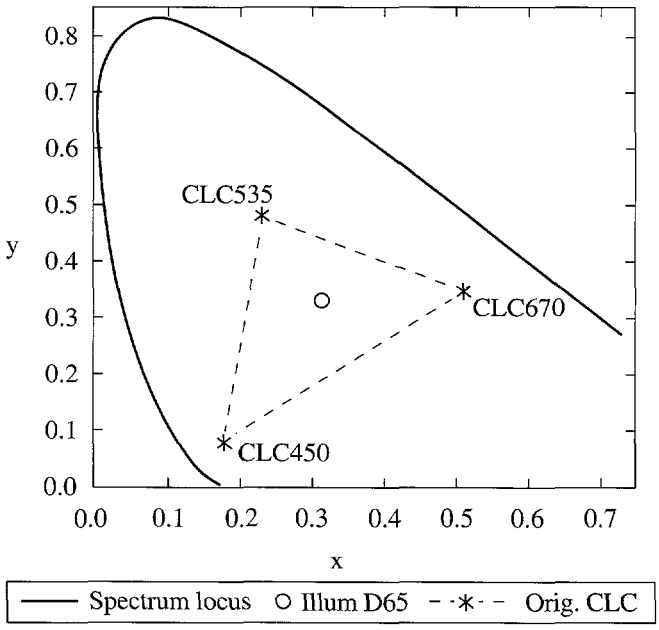

G4151

Figure 73.65
Chromaticities of the three original CLC polysiloxanes as knife-coated films on microscope slides with black toner paper backing.

2. Color Additivity by Layering

Unlike traditional inks in which absorption produces subtractive color combination of layers, CLC's are reflective.

Provided that each layer allows reflection from other layers (i.e., each reflecting layer is transparent to the others), the color mixing of CLC layers is *additive*. The knife-coated slides of CLC670, CLC535, and CLC450 were stacked in pairs with black toner paper at the bottom. Chromaticity and luminosity were recorded using the ColorTron II. Table 73.XI lists the results and Fig. 73.66 illustrates that the additive combination does fall on the line connecting the two components. The CIE color gamut is still limited to the triangle formed by CLC670, CLC535, and CLC450.

The color additivity was not a simple 1:1 averaging of the two layers as Eberle *et al.*[30] had found for CLC's layered with colored substrates. In fact, we found a clear difference in chromaticity of layered CLC's based on stacking order. For example, "670 over 450" (meaning the slide with CLC670 was on top and the slide with CLC450 was underneath) is closer to pure CLC670 than "450 over 670," which is closer to pure CLC450. These layers were made by placing the microscope slides together, both face up. This resulted in a layer-to-layer separation of one microscope-slide thickness. The presence of the microscope slide reduced the intensity of the light reaching the detector. The 45/0 geometry of the ColorTron II is designed to illuminate the sample *at* the measurement aperture. The 1-mm-thick microscope slide, displaced one layer from the ideal position, reducing incident intensity and therefore reflected intensity. An alternate way of stacking was to place the CLC layers in contact but separating both layers from the colorimeter by the thickness of a slide. There was virtually no difference in chromaticities from those of Table 73.XI using this alternate method of stacking. The combination chromaticity point fell closer to whichever sample was closest to the colorimeter, even when both films were subjected to the same displacement error from the measurement aperture. This indicated that the upper layer prevented the full reflection of the lower layer due to an imperfect helical structure and some overlap of the reflection bands.

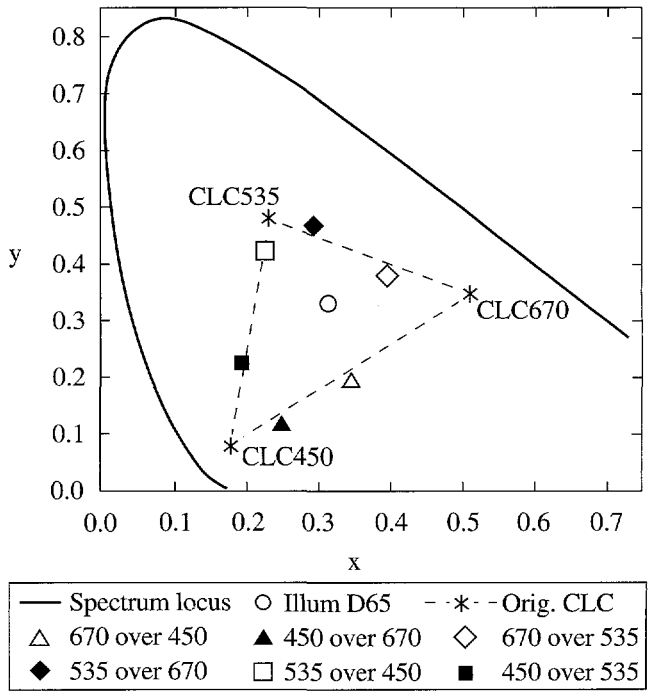

Figure 73.66
Chromaticity plot of layered CLC polysiloxane films.

Table 73.XI: *x,y,Y* of layered CLC polysiloxane films.

Sample		*x*	*y*	*Y*
Upper	Lower			
---	CLC670	0.5153	0.3459	8.83
---	CLC535	0.2306	0.4803	26.26
---	CLC450	0.1777	0.0777	4.33
CLC670	CLC535	0.3972	0.3839	16.81
CLC535	CLC670	0.2958	0.4659	30.84
CLC670	CLC450	0.3446	0.1984	9.69
CLC450	CLC670	0.2491	0.1264	8.67
CLC535	CLC450	0.2257	0.4240	27.77
CLC450	CLC535	0.1953	0.2320	18.21

3. New Hues by Mixing the Original CLC Polysiloxanes

In this section, we extend Makow's earlier qualitative work[25] by quantifying the chromaticities and luminosities of hues produced by physico-chemically mixing the original CLC polysiloxanes.

Two techniques were used to mix the polysiloxanes. The first technique was simply to place two CLC polysiloxanes in proximity, elevate the temperature to ~130°C, and stir them together with a microspatula. A second technique, which ensured more complete, homogeneous mixing, was mutual dissolution of the two components in dichloromethane, stirring, and evaporation. The resulting mixtures from this second technique were then prepared as knife-coated slides. The chromaticities and luminosities are listed for various weight ratios in Table 73.XII and illustrated in Fig. 73.67. Each mixture has produced a new chromaticity outside the original triangular color gamut, effectively increasing the region of color space that can be accessed by the CLC polysiloxane films.

4. Color Gamut of CLC Flakes Made from the Three Original CLC Polysiloxanes

In addition to using the continuous-film form of CLC's, we have also prepared samples of CLC flakes from each of the four different size-groups.

The *x,y,Y* measurements for the CLC flake colorant samples are listed in Table 73.XIII and illustrated in Fig. 73.68. For each of the original materials, decreasing flake size leads to more desaturation of the hue, finally allowing access to the chromaticities *within* the original triangular color gamut. As flake size decreases, the orientation of the periodic molecular planes, responsible for the color, becomes more and more disordered. As a result, the reflection spectrum of CLC flake samples becomes wider and more shallow. This is consistent with the desaturation seen for encapsulated CLC's[20] whose helices are disordered due to the presence of the confining wall.

5. Mixing CLC Flakes of Different Colors

Layering CLC films produced an additive color by simultaneous reflection. The use of CLC flakes makes it possible to invoke another kind of color additivity: spatial averaging. By mixing two different colors of flakes and painting the mixture,

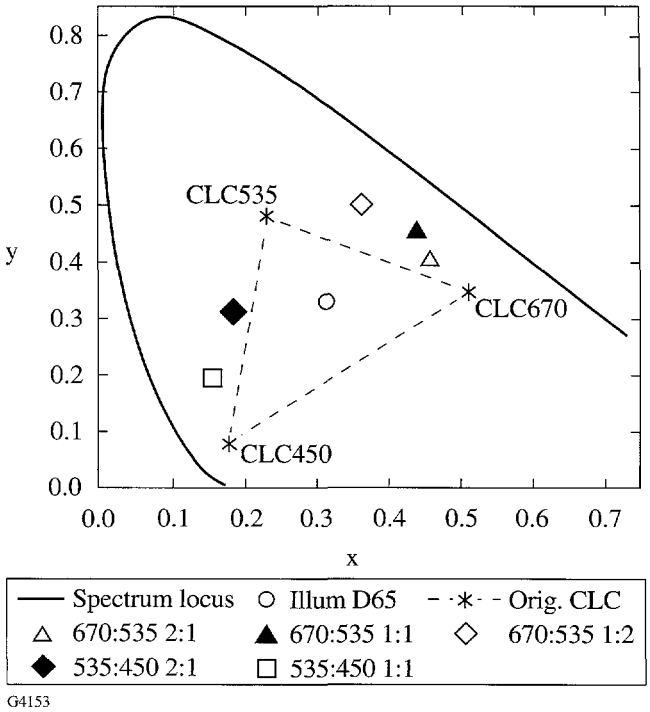

Figure 73.67
Chromaticity plot of CLC polysiloxane mixtures.

Table 73.XII: *x,y,Y* of CLC polysiloxane mixtures. Mixtures of pairs are listed with their mass ratios.

Sample	*x*	*y*	*Y*
CLC670	0.5168	0.3541	11.83
CLC535	0.2270	0.4738	24.69
CLC450	0.1775	0.0777	4.19
CLC670:CLC535::2:1	0.4582	0.4088	10.26
CLC670:CLC535::1:1	0.4409	0.4580	35.99
CLC670:CLC535::1:2	0.3607	0.5057	31.19
CLC535:CLC450::2:1	0.1822	0.3086	18.58
CLC535:CLC450::1:1	0.1562	0.1920	10.55

a color mosaic is produced. The resultant chromaticity of such a color mosaic can be determined by the fractional-area-weighted version of the Center-of-Gravity Color-Mixing Principle. For CLC flakes, instead of using the fractional areas, which are difficult to determine, we used the fractional masses of each type of flake in the mixture as the A_1 and A_2 factors in Eqs. (5)–(7). Provided the mixture is made with flakes from the same size-group so that the flakes behave similarly, the surface coverage by each color corresponds to the fractional masses and in turn follows the Center-of-Gravity Color-Mixing Principle very well.

Mixtures were made of CLC670, CLC535, and CLC450, in pairs, in weight ratios of 1:0, 3:1, 1:1, 1:3, and 0:1, for each of the flake size-groups separately. Weighting the chromaticities of the unmixed flake samples by these fractional masses, the x,y,Y of the mixtures were predicted and compared to the measured values. The comparison was made by converting the x,y,Y measurement to CIEL*a*b* coordinates through ColorTron II software. The color-difference function[44] ΔE^*_{ab} was also calculated for each predicted/measured pair, with a difference of 1 ΔE^*_{ab} unit corresponding approximately to a just-discernible color difference. The ΔE^*_{ab} values for each size-group were then averaged. The averages and ranges are shown in Fig. 73.69.

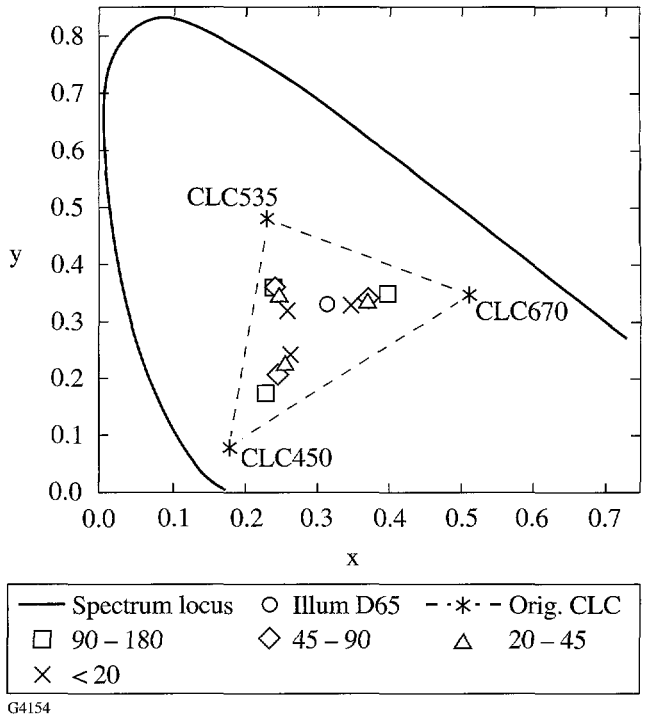

Figure 73.68
Chromaticity of CLC flakes of various size-groups (indicated in microns).

Table 73.XIII: x,y,Y of CLC flakes as a function of size. The film samples are knife-coated microscope slides measured with the ColorTron II. The flake samples are in enamel on black toner paper measured with the Gretag SPM 100-II.

CLC ID	Size	x	y	Y
CLC670	Film	0.5153	0.3459	8.83
	90 to 180 μm	0.3961	0.3504	5.73
	45 to 90 μm	0.3770	0.3468	5.86
	20 to 45 μm	0.3710	0.3443	6.85
	<20 μm	0.3510	0.3345	6.67
CLC535	Film	0.2306	0.4803	26.26
	90 to 180 μm	0.2402	0.3603	7.43
	45 to 90 μm	0.2419	0.3615	9.16
	20 to 45 μm	0.2472	0.3507	8.25
	<20 μm	0.2580	0.3241	7.27
CLC450	Film	0.1777	0.0777	4.33
	90 to 180 μm	0.2306	0.1823	3.73
	45 to 90 μm	0.2460	0.2111	3.86
	20 to 45 μm	0.2563	0.2315	4.51
	<20 μm	0.2629	0.2473	4.86

The 20- to 45-μm size-group had the lowest ΔE^*_{ab} values, i.e., the best agreement with the center-of-gravity predictions. This is attributed to an optimization of the two factors required for the center-of-gravity principle to hold:

(a) The flakes must be oriented with the normal to the periodic molecular planes normal to the paper. This ensures that all the flakes contribute their full reflection profiles to the combination color. Brushing accomplished this readily except for the <20-μm flakes. Under a microscope the latter appeared essentially cube-like with no preferred orientation.

(b) The flakes must completely hide the paper support. Samples of the two largest size-groups did not completely cover the measured area, whereas the two smaller size-groups covered it readily. Since the chromaticity of the exposed paper support was not included in the center-of-gravity calculations based on fractional masses, surface hiding was essential.

Figure 73.70 shows the measured x,y,Y values listed in Table 73.XIV for the 20- to 45-μm size-group. The Y values were very close in magnitude so the distribution of chromaticity points gives approximately the right spacing for 1:0, 3:1, 1:1, 1:3, and 0:1 mass-ratio mixtures for each color pair.

CLC flake mixtures behave like pixels or pointillist painting. The flakes may be mixed in any proportion, unlike films that can only be layered. Even the layering does not produce a 1:1 weighting of chromaticities as we showed earlier. So use of CLC flakes as colorants allows a range of hues, a range of saturation, and a deterministic method for predicting the resulting chromaticity of a quantifiable mixture. Further, CLC flakes in mixtures of red with violet can be used to predictably produce the nonspectral, that is, purple to magenta, region of x,y,Y color space. Finally, CLC flakes do not require elevated temperature or high voltages for painting since the reflecting molecular orientation is already present and "frozen in" at room temperature.

6. CLC Films Compared to Traditional Colorants

In this section, we compare CLC colors to some representative dyes, paints, and inks, i.e., traditional absorptive colorants. We compare these traditional colorants to the most saturated form of CLC, the continuous film, noting that CLC flakes are more versatile, if less saturated, than films.

The CLC film samples included in this comparison are knife-coated samples of CLC670, CLC535, CLC450, and the mixtures CLC670:CLC535::2:1, CLC670:CLC535::1:1, CLC670:CLC535::1:2, CLC535:CLC450::2:1, and CLC535:CLC450::1:1.

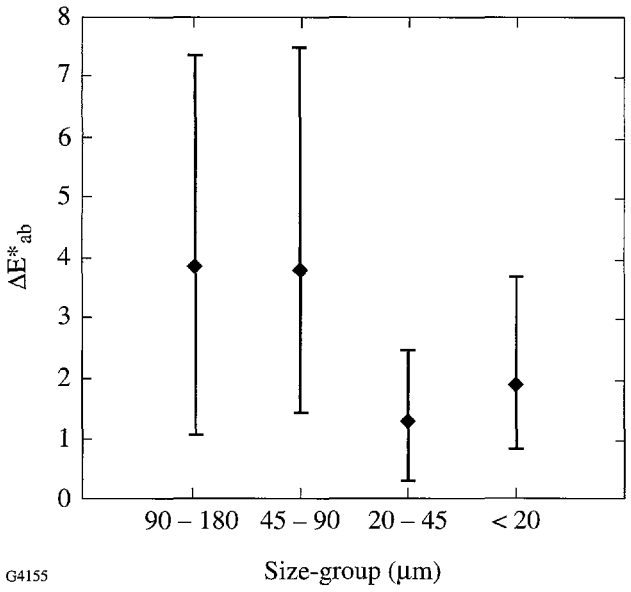

Figure 73.69
ΔE^*_{ab} averages and ranges for measured versus predicted chromaticity of CLC flakes mixtures.

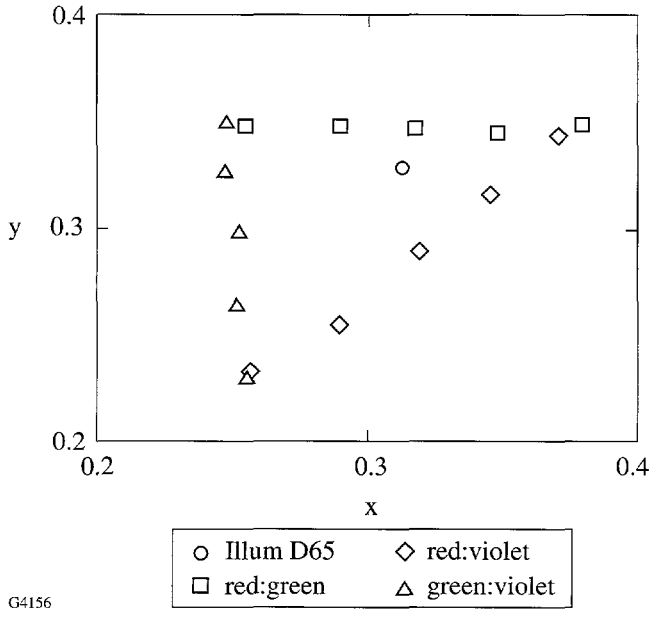

Figure 73.70
CIE diagram illustrating the Center-of-Gravity Color-Mixing Principle for 20- to 45-μm CLC flakes.

The colorants selected for comparison to these CLC films are (a) commercially available enamel-based paints[45] selected for their subjective vividness, (b) color samples from the Optical Society of America[46] selected for their subjective hue similarity to CLC film samples, and (c) three dyes: sudan III[47] (appears red), malachite green oxalate[48] (appears green), and crystal violet[49] (appears violet). Each dye was mixed with a nonchromatic polysiloxane, CLC850 ($\lambda_0 = 850 \pm 100$ nm), in a 2% by weight mixture. After mutual dissolving in dichloromethane, each dye/CLC850 mix was knife-coated onto a slide. Since CLC850 reflects only near-infrared at normal incidence and is only pale pink, very weakly saturated at 45/0, it is essentially invisible to standard colorimeters (Gretag range = 380 to 730 nm; ColorTron II range = 390 to 700 nm). CLC850 offers the advantage of providing a host for each dye without any significant chromatic contribution.

The CLC films were measured on the ColorTron II under the CIE 1931 D_{65} basis, using black toner paper backing. The dye samples were measured with the same instrument and instrumental settings but with white paper backing. The OSA samples are ink on cardboard, uniquely identified by a sequence of numbers[50,51] no longer in general use (approximately correspondent with brightness, yellowness-blueness, magenta-green-ness). The paint samples were prepared by brushing onto microscope slides until the coating was opaque to the naked eye under ambient room light. They were measured with the same instrument and instrumental settings as the other samples and used a white paper backing behind the slide.

The chromaticities, luminosities, and purities are listed in Table XV. Since CLC's have a definite bandwidth, they can never be as pure as the monochromatic points comprising the spectrum locus. A more practical measurement of purity $\mathcal{P}$ is to take the following ratio: the distance from the white point (the D_{65} chromaticity) to the chromaticity of the sample and the distance from the white point along the same line to the isoluminous (same Y value) contour line.

Table 73.XIV: Measured versus calculated x,y,Y of flake mixtures of size-group 20 to 45 μm. The abbreviations listed under "color" are R ≡ CLC670, G ≡ CLC535, and V ≡ CLC450 with the approximate mass ratios. The actual masses are listed and were used as the A_1 and A_2 values in Eqs. (5), (6), and (7) of the Center-of-Gravity Color-Mixing Principle.

Color	Mass (g) Color 1	Mass (g) Color 2	Meas x	Meas y	Meas Y	Calc x	Calc y	Calc Y	ΔE^*_{ab}
R			0.3710	0.3443	6.85				
V			0.2563	0.2315	4.51				
R:V 1:1	0.0051	0.0050	0.3197	0.2895	5.27	0.3148	0.2891	5.69	1.43
R:V 1:3	0.0042	0.0126	0.2892	0.2556	4.68	0.2854	0.2601	5.10	2.12
R:V 3:1	0.0046	0.0015	0.3454	0.3169	6.19	0.3432	0.3170	6.27	0.49
G			0.2472	0.3507	8.25				
V			0.2556	0.2300	4.52				
G:V 1:1	0.0049	0.0049	0.2517	0.2990	6.48	0.2510	0.2958	6.39	0.80
G:V 1:3	0.0027	0.0081	0.2512	0.2638	5.80	0.2532	0.2644	5.45	1.11
G:V 3:1	0.0100	0.0033	0.2469	0.3270	8.18	0.2490	0.3246	7.32	2.48
R			0.3794	0.3493	7.75				
G			0.2546	0.3488	6.79				
R:G 1:1	0.00862	0.00859	0.3179	0.3478	7.62	0.3212	0.3491	7.27	1.00
R:G 1:3	0.00514	0.01504	0.2896	0.3483	6.95	0.2896	0.3489	7.03	0.26
R:G 3:1	0.03152	0.01066	0.3484	0.3452	6.84	0.3508	0.3492	7.51	1.86

All the x,y,Y values are plotted for comparison in Fig. 73.71 with a dotted line representing the color gamut provided by CLC polysiloxane films.

Several observations from Table 73.XV and Fig. 73.71 are worth noting. First, we note that there are existing pigments more saturated and less saturated than CLC films. Overall, then, CLC films are not limiting cases in either direction of color purity. For commercial graphic arts applications, this means that CLC films as colorants are as capable of color depth as any other intermediate-saturation colorant.

Secondly, CLC films are more luminous than comparably hued pigments in the blue-violet region of the color gamut. In the lower left "corner" of the CIE diagram in Fig. 73.71, the purities are very similar (86%–96%). The chromaticity points are also very close for the CLC450 film, crystal violet dye, and dark blue paint. The CLC film, however, has a Y value four times greater than the dye and 24 times greater than the paint. Recall that the units for tristimulus values such as Y are lumens/m^2/sr = candelas/m^2—in other words, units of luminous flux. The blue-violet CLC film has more light reflecting from it than do pigments of comparable hue. CLC films reflecting in the red-to-green spectral range may show luminosity values comparable to similarly hued pigments; however, the purity values are not as similar. For comparable luminosities, red-to-green pigments are, in general, more saturated than red-to-green CLC films.

Summary

We have shown that CLC films and flakes can be measured by standard colorimetry. The color gamut of CLC's as colorants, measured by standard techniques, may be accessed by four techniques: layering of continuous films, physico-chemical

Table 73.XV: Chromaticities and purities of CLC films compared to other colorants. The purities are calculated with respect to the isoluminous curve corresponding to each sample's Y value.

Sample Form	Sample ID	Visual color	x	y	Y	$\mathcal{P}$ (%)
CLC	670	red	0.5043	0.3462	9.39	59
	670:535::2:1	gold	0.4582	0.4089	8.83	63
	670:535::1:1	butterscotch	0.4409	0.4580	35.99	73
	670:535::1:2	yellow-green	0.3607	0.5057	31.19	64
	535	green	0.2257	0.4732	24.31	37
	535:450::2:1	turquoise	0.1822	0.3086	18.58	56
	535:450::1:1	light blue	0.1562	0.1920	10.55	76
	450	violet	0.1793	0.0778	4.07	88
Dyes	sudan III	red	0.6836	0.3130	4.13	99
	malachite	green	0.1643	0.3902	3.68	52
	crystal violet	violet	0.1748	0.0341	0.94	96
Testor's gloss paints	1103	red	0.6445	0.3170	8.01	89
	1114	yellow	0.4961	0.4646	56.14	90
	1124	green	0.2335	0.6501	9.51	73
	1111	dark blue	0.1696	0.0688	0.17	86
OSA color samples	(-1,1,-1)	pink	0.4362	0.3113	24.86	48
	(-1,5,-5)	orange	0.4753	0.3833	26.64	59
	(-1,5,5)	green	0.2991	0.4917	28.72	43
	(-1,-5,3)	blue	0.2150	0.2387	22.88	54
	(-1,-5,-1)	violet	0.2698	0.2381	22.03	47

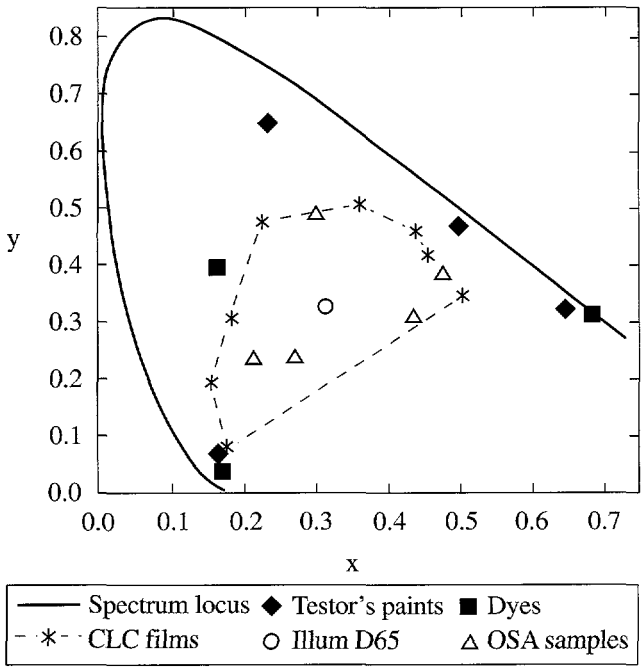

Figure 73.71
Chromaticity plot of CLC films, dyes, paints, and OSA ink samples.

mixing of CLC's, varying the size of the CLC domains, and spatial averaging of mixed domains. Layering and physicochemical mixing produce new hues, but these new hues can be determined only empirically. The Center-of-Gravity Color-Mixing Principle allows the deterministic prediction of hues of mixed flakes based on their fractional masses in the mixture. Despite their angle dependence and selective polarization behavior, the color gamut of CLC's can be successfully examined with standard colorimetry.

ACKNOWLEDGMENT

The authors thank Dr. F.-H. Kreuzer and Dr. Robert Maurer of the Consortium für elektrochemische Industrie GmbH, Munich, for the CLC polysiloxanes; Dr. Nicholas George, Dr. Brian Stossel, and Dr. Shen-ge Wang of the University of Rochester's Institute of Optics for the use of the Gretag SPM 100-II colorimeter; Robert Hutchison, Cormac Merle, and Curt Corum of Lucid Technologies, Inc., Henrietta, NY, for the loan of the ColorTron colorimeter and software. This work was supported by the U.S. Department of Energy Office of Inertial Confinement Fusion under Cooperative Agreement No. DE-FC03-92SF19460, the University of Rochester, and the New York State Energy Research and Development Authority. The support of DOE does not constitute an endorsement by DOE of the views expressed in this article. Funding was also provided by Reveo, Inc.

REFERENCES

1. F. Reinitzer, Monatsch. Chem. **9**, 421 (1888).
2. Y. Charnay, Leonardo **15**, 219 (1982).
3. C. W. Oseen, Trans. Faraday Soc. **29**, 883 (1933).
4. Hl. De Vries, Acta Cryst. **4**, 219 (1951).
5. L. B. Leder and D. Olechna, Opt. Commun. **3**, 295 (1971).
6. C. Viney and C. M. Dannels, Mol. Cryst. Liq. Cryst. **196**, 133 (1991).
7. P. S. Drzaic, *Liquid Crystal Dispersions*, Series on Liquid Crystals, Vol. 1 (World Scientific, Singapore, 1995), p. 12.
8. H.-S. Kitzerow, J. Rand, and P. P. Crooker, J. Phys. II France **2**, 227 (1992).
9. R. A. M. Hikmet and B. H. Zwerver, Liq. Cryst. **12**, 319 (1992).
10. H.-S. Kitzerow, P. P. Crooker, and G. Heppke, Liq. Cryst. **12**, 49 (1992).
11. D. M. Makow and C. L. Sanders, Nature **276**, 48 (1978).
12. R. M. Christie and D. Bryant, J. Oil and Colour Chemists' Assoc. **78**, 332 (1995).
13. N. Häberle *et al.*, in *1991 International Display Research Conference* (IEEE, Piscataway, NJ, 1991), pp. 57–59.
14. S. Ishihara *et al.*, Polymer **29**, 2141 (1988).
15. M. L. Tsai, S. H. Chen, and S. D. Jacobs, Appl. Phys. Lett. **54**, 2395 (1989).
16. S. D. Jacobs, K. A. Cerqua, K. L. Marshall, A. Schmid, M. J. Guardalben, and K. J. Skerrett, J. Opt. Soc. Am. B. **5**, 1962 (1988).
17. R. Lemberg, Leonardo **2**, 45 (1968).
18. J. Adams, W. Haas, and J. Wysocki, Mol. Cryst. Liq. Cryst. **8**, 9 (1969).
19. D. M. Makow, Appl. Opt. **19**, 1274 (1980).
20. D. Makow, Leonardo **15**, 257 (1982).
21. S. Nakano, U.S. Patent No. 5,508,068 (16 April 1996).
22. S.-H. Chen, H. Shi, J. C. Mastrangelo, and J. J. Ou, Prog. Polym. Sci. **21**, 1211 (1996).
23. H. Finkelmann *et al.*, Makromol. Chem. **179**, 829 (1978).
24. F.-H. Kreuzer *et al.*, Mol. Cryst. Liq. Cryst. **199**, 345 (1991).
25. D. Makow, Color Res. Appl. **11**, 205 (1986).
26. D. Makow, Mol. Cryst. Liq. Cryst. **123**, 347 (1985).

27. M. R. Pointer, Color Res. Appl. **5**, 145 (1980).

28. W. Ostwald, Physik. Zeits. **17**, 328 (1916) cited in D. L. MacAdam, J.O.S.A. **25**, 249 (1935).

29. D. L. MacAdam, J.O.S.A. **25**, 249 (1935).

30. H.-J. Eberle, A. Miller, and F.-H. Kreuzer, Liq. Cryst. **5**, 907 (1989).

31. R. W. G. Hunt, *Measuring Colour*, 2nd ed. (Ellis Horwood, London, 1995), pp. 66–68.

32. D. L. MacAdam, *Color Measurement: Theme and Variations*, 2nd rev. ed., Springer Series in Optical Sciences, Vol. 27 (Springer-Verlag, Berlin, 1985), p. 49.

33. E. M. Korenic, "Colorimetry of Cholesteric Liquid Crystals," Ph.D. thesis, University of Rochester, 1997.

34. Silicon epiprime, 100-mm-diam wafers, Wacker Siltronic Corporation, Portland, OR.

35. S. M. Faris, U.S. Patent No. 5,364,557 (15 November 1994).

36. Newark Wire Cloth Company, Newark, NJ 07104.

37. Bellingham and Stanley Model 60/HR refractometer, Bellingham and Stanley Ltd., North Farm Industrial Estate, Tunbridge Wells, Kent TN2 3EY, England.

38. Millex®-FG_{13} filter unit, 0.2 μm, Millipore Corporation, Bedford, MA 01730.

39. Testor's gloss enamel gold (#1144), The Testor's Corporation, Rockford, IL 61104.

40. Hewlett Packard LaserJet 4m, Hewlett Packard. The printing options used were the default settings: resolution = 300 dpi, halftone frequency = 60.0, and halftone angle = 45.0.

41. Gretag Imaging, Chicopee, MA 01022.

42. LightSource, Larkskpur, CA 94939 through Lucid Technologies, Inc., Henrietta, NY 14467.

43. J. L. Fergason, Mol. Cryst. **1**, 293 (1966).

44. G. Wyszecki and W. S. Stiles, *Color Science: Concepts and Methods, Quantitative Data and Formulae*, 2nd ed. (Wiley, New York, 1982), p. 829.

45. Testor's gloss enamel, red (#1103), yellow (#1114), green (#1124), and dark blue (#1111), The Testor's Corporation, Rockford, IL 61104.

46. Provided by Dr. D. L. MacAdam, The Institute of Optics, University of Rochester, Rochester, NY 14623.

47. Sudan III, CAS #85-86-9, certified, dye content 88%, C.I. 26100, Solvent Red 23, Aldrich Catalog #19,811-0, Aldrich Chemical Company, Milwaukee, WI 53223.

48. Malachite green oxalate, CAS #2437-29-8, certified, dye content 98%, Basic Green 4, Aldrich Catalog #86,121-9, Aldrich Chemical Company, Milwaukee, WI 53223.

49. Crystal violet, CAS #548-62-9, C.I. 42555, Basic Violet 3, No. C-3886, Sigma Chemical Company, St. Louis, MO 63178.

50. G. Wyszecki and W. S. Stiles, *Color Science: Concepts and Methods, Quantitative Data and Formulae*, 2nd ed. (Wiley, New York, 1982), Chap. 6.

51. D. L. MacAdam, *Color Measurement: Themes and Variations*, 2nd rev. ed., Springer Series in Optical Sciences, Vol. 27 (Springer-Verlag, New York, 1985), pp. 165–174. Optical Society of America color subcommittee uniform color scales (L, j, g) introduced in 1974.

The Development of Ion-Etched Phase Plates

Laser-driven implosion experiments on the OMEGA laser depend on optical phase conversion to provide uniform irradiation onto a target. Phase errors that accumulate as a wavefront propagates through the laser produce a nonuniform irradiance when focused into the target far field. The distributed phase plate (DPP) introduces a quasi-random phase front that produces a high-spatial-frequency, uniform pattern with a controlled energy envelope.[1] DPP's are used in conjunction with smoothing by spectral dispersion (SSD) and distributed polarization rotation to provide very smooth intensity distribution on the target when integrated over the full pulse duration of the laser.[2]

The continuous DPP is an improvement over earlier binary designs.[3] The binary phase plates used on the 24-beam OMEGA produced a uniform irradiation with limited control over the intensity envelope and a maximum of 78% efficiency with much of the lost energy coupled into higher diffractive orders. In OMEGA's target chamber geometry this diffracted light would cause catastrophic damage in the opposing beam optics, especially the frequency-conversion cell. The more recent continuous phase design offers better control of the speckle distribution and the envelope function while increasing the total energy impinging on the target to 96%. In addition to a continuous profile, the newer DPP design requires a deeper surface relief of approximately 5 μm. The binary DPP required only a surface relief of 0.3 μm between diffractive cells.

The principle of the continuous DPP's has been demonstrated and tested using a replication process.[3,4] The required pattern is generated as an amplitude modulation in photographic film and used to expose a photoresist-coated substrate. When developed, the relief pattern in the resist is coated with a release layer and then molded in epoxy supported by another silica substrate. After curing, the epoxy is separated from the master, the remnants of the release layer are removed, and the final epoxy negative relief is coated with a water-based sol-gel antireflection coating. Unfortunately, after exposure to many high-energy laser pulses, the epoxy material developed a high absorption peak near 351 nm and after 100 laser shots began to show a high level of damage. The ion-etched DPP was developed as a remedy to the failed, replicated epoxy phase plates. Much of the technology developed for the epoxy phase plates was successfully transferred to the newer etching method. This article emphasizes the technology developed exclusively for the ion-etched phase plate and will not delve into the details of phase-plate design, methods for making a master, testing methods, or target performance results with DPP.

Key Technical Issues for Ion Etching

The problems posed in etching DPP's are unique. While ion-etching methods are commonly used in the semiconductor industry, they are typically used for binary patterns with etch depths rarely exceeding 1 μm. Diffractive optics, which do have continuous profiles, are made typically on substrates much smaller than the required 30-cm aperture of the OMEGA laser, and once again usually have smaller etch depths. Experience with large optics, familiarity with broad-beam ion sources, and a short development period led to an intensive internal development program.

The ion-etch scheme used by LLE is shown schematically in Fig. 74.1. A positive image of the photoresist master will result after etching, unlike the negative image produced with replication. This does not affect the performance of the DPP; positive and negative profiles have the same far-field performance. The positive image does have an effect on the type and number of near-field defects (discussed in detail later).

An inert ion process was used for etching the DPP's. Inert ion etching (or ion milling) depends on molecular impacts (sputtering) for materials and is a purely physical process. Reactive processes were developed for high material-removal rates in a high-production environment, production of steep edges for semiconductor interconnects, and material selectivity to preserve masks. The intensity exposure mask for continuous DPP design in Fig. 74.2 has low gradient (no steep edges), and material selectivity is not as important as faithful reproduction of the photoresist surface. This last requirement demands that the etch depth be linear with time for both materials, which

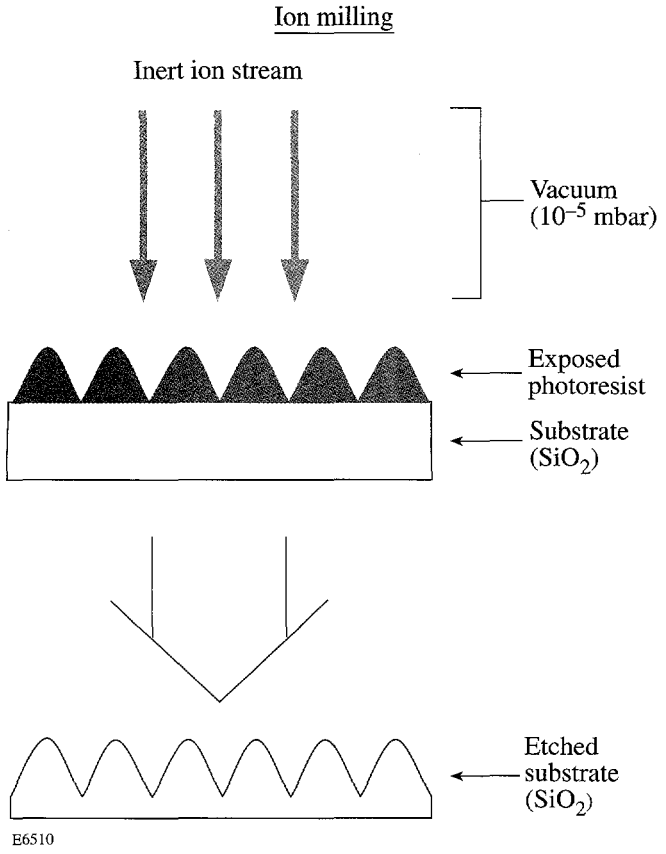

Figure 74.1
A surface-relief phase plate can be directly etched from a photoresist pattern into a silica substrate. The photoresist is completely removed after etching is complete. The etching molecule in this work is an inert gas, argon, so removing the photoresist and silica is purely a physical process.

is more likely in a purely physical process. Complete erosion of the mask is necessary since any remnant photoresist could be the potential site for laser damage in the 351-nm radiation. Since LLE has had little previous experience with reactive processes, inert ion etching was the method of choice.

A number of key technical issues had to be resolved before DPP's could be produced:

1. Uniformity

The uniformity of etch across the 280-nm beam aperture had to vary less than 6% after 5 μm of material was removed. This was accomplished by first using two 8-cm ion sources with the substrate in single rotation and, later in the project, a single 16-cm ion source, also with single rotation. After establishing the correct operating parameters for the guns, all were profiled at different beam voltages and total ion currents using a biased ion probe. The profiles were used to calibrate a model

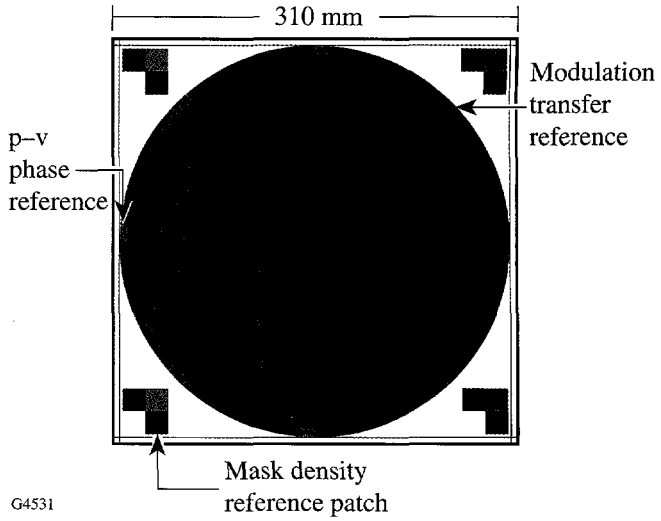

Figure 74.2
The continuous DPP for the third-order super-Gaussian profile used on OMEGA was designed using simulated annealing. The amplitude variation of the mask is transferred into phase variation by exposing the photoresist to the mask. The central portion of the mask was modified after design to provide a high point in the resist for in-process optical monitoring.

of etch uniformity that was developed to determine the best source location and pointing for high uniformity and reasonable etch rate. It is well known that the sputtering yield varies considerably with the ion incidence angle in inert ion etching.[5] The relationship between etch rate and incidence angle had to be determined for the two etch materials: silica and photoresist.

2. Surface Texturing

Surfaces are often textured after a high level of ion bombardment.[6,7] Silica surfaces have been observed to become rougher or smoother depending on the type of ion, ion energy, incidence angle, and ion density.[8,9] Texturing occurs predominantly in crystalline materials and is most often caused by the varying sputter rate of different crystal planes. Resputtering and defects in the surface preparation of a substrate have also caused texturing.[10] During development of etched DPP's, severe roughing of the surface was often observed but it was primarily caused by the overlying photoresist. Although surface texturing by ions was often suspected, the true cause appears to be excessive heating of the resist in almost all cases.

3. Linearity

An accurate representation of the photoresist master in silica can only be realized if the process remains linear throughout the etch. Proper processing of the resist and careful control of the substrate thermal cycle produced adequate linearity.

4. Near-Field Defects

Near-field defects are caused by small and steep surface variations in the photoresist layer, which cause diffraction and high intensities downstream of the DPP. These defects have a strong potential to damage the final focus lens and blastshields on the target chamber. Near-field defects were first observed in the fabrication of the first set of continuous epoxy DPP's for OMEGA. Methods for detecting and removing the defects were established for the epoxy DPP's and then modified for the ion-etched devices.

5. Production Tooling

Resputtering of tooling materials will cause higher absorption and scatter on the ion-etched surface. In addition the tooling must allow a clear view of the rear surface to radiate heat to the cooled cryopanels. The tooling design offered a unique solution to these requirements.

6. Laser-Damage Threshold

When measured at 351 nm, some ion-etched samples have shown a decrease in damage threshold. This could be caused by resputtering of ion sources, tooling, or chamber materials onto the optics. The damage threshold of the DPP's had to meet a 2.6 J/cm^2 @ 1-ns peak fluence requirement for the 351-nm OMEGA beam. The damage threshold of the DPP surfaces increased after etching, probably due to careful control of redeposition of tooling and removal of subsurface damage in the silica.

Each of the technical issues listed above is discussed in detail below.

Uniformity of Ion Etching with a Kaufman Source

The Kaufman[11] ion source, originally developed as a propulsion source for NASA, has since seen wide use in materials processing.[12] The source, shown schematically in Fig. 74.3, consists of a discharge chamber with a multipole magnetic field and a hot filament, two dished molybdenum extraction grids, and a neutralizer filament. Two 8-cm ion sources were used for prototype demonstration, and a 16-cm ion source was used for the production phase of this work.

Ion-source parameters are set depending upon the application, type of working gas, and performance of the source in a given pumping system. Argon was used as a working gas because the sputter yields for SiO_2 and photoresist are similar for this gas. The maximum gas flow rate, maximum beam current, and accelerator voltage range for the sources were determined using standard methods.[13] The beam voltage (ion energy) was kept below 500 V to avoid ion implantation, surface damage to the photoresist, and overheating.

The etch profiles of each source were tested using a unique profiling method: A large sheet of inexpensive float glass was coated with an optical multilayer that had a highly visible, 13-layer oxide coating (see Fig. 74.4). The coated plate was placed normal to the ion beam at a distance of 60 cm. The source was run long enough to etch to the last layers of the coating; the coating was then removed and inspected. The erosion pattern could then be discerned as contours in the multilayer surface (see Fig. 74.5). This method gave a very quick appraisal of the gun operation and indicated whether the profile would be suitable for highly uniform etching. For

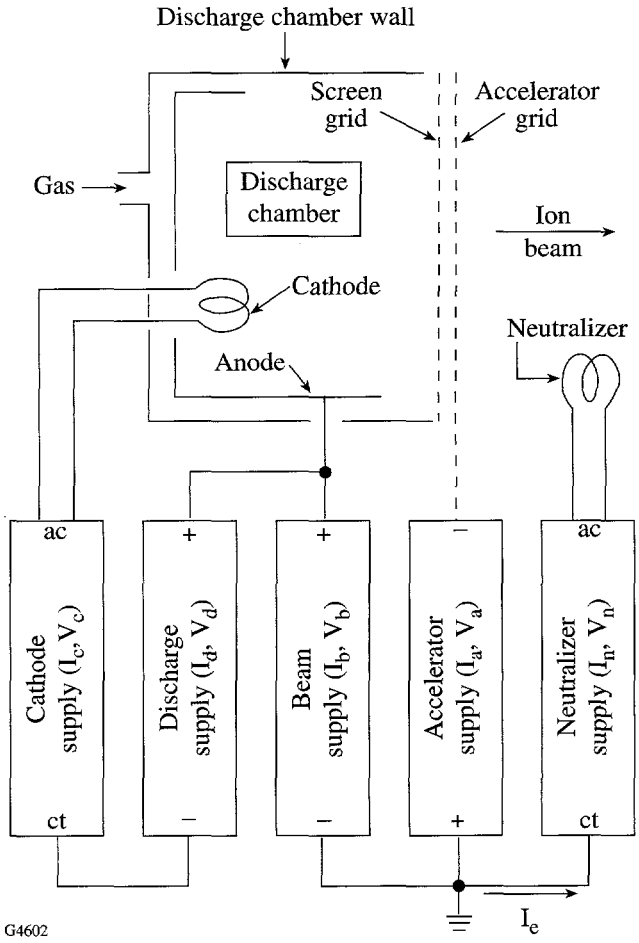

Figure 74.3
A typical broad-beam Kaufman ion source with power supplies is represented schematically. This type of source provides excellent control of ion energy and density. The source's condition during etching can be monitored by logging the voltage and current of each supply.

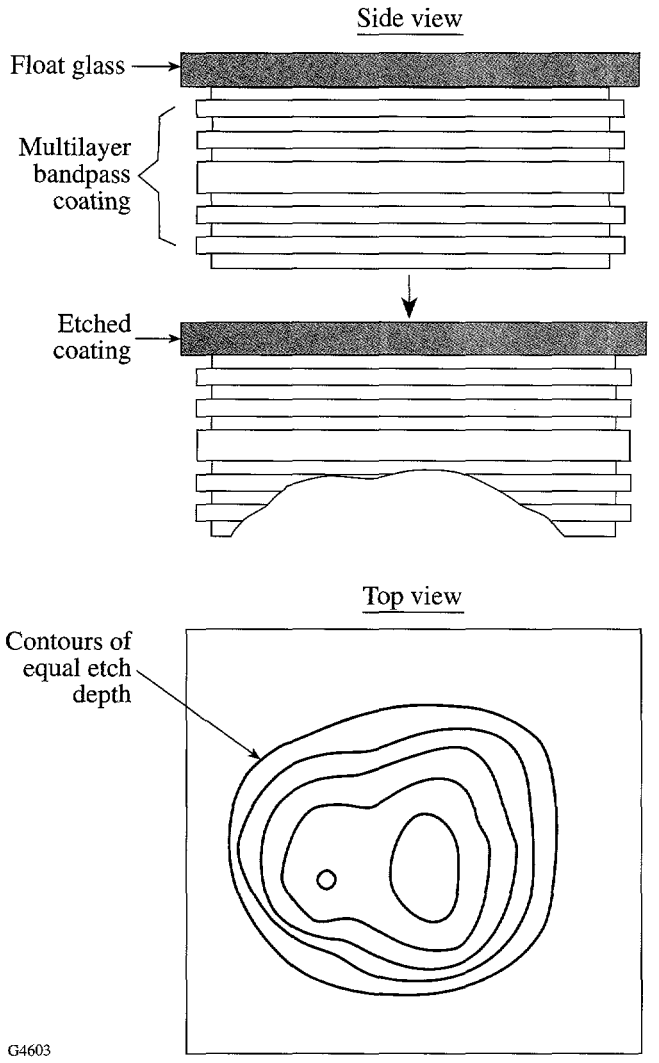

Figure 74.4
Ion-beam profiles can be monitored with a small probe or by etching into a visible interference filter deposited on inexpensive float glass as shown. The beam contours are formed by the eroded layer of the coating. After etching, the layers in an appropriately designed multilayer provide visible isothickness contours, indicating the beam profile of the ion source.

example, the etched profile of the 8-cm source operating at a beam current of 100 mA is shown in Fig. 74.5(a). Even though the source was within the normal electrical limits (low ion impingement of the grids), the profile has significant structure. The same source produced a low-structure symmetrical profile when operated at 50 mA [Fig. 74.5(b)] and was subsequently used with beam currents (I_b) no larger than 75 mA. The condition of the source anode also had a significant effect on the beam profile. The anode can be run in excess of 60 h before a discharge becomes difficult to maintain, as seen in Fig. 74.5(c); however, the beam profile again shows structure with the older anode. If the anode is abrasively cleaned, the structure in the beam profile disappears. The 16-cm source was later characterized in the same manner. Figure 74.5(d) shows the symmetrical beam profile of the source when operated with I_b = 300 mA and a beam voltage of 150 V.

The gun profiles were quantitatively measured with an open stainless steel probe after the initial gun characterization to determine the operational limits of the sources. For these measurements the ion probe was negatively biased with 18 V to repel the low-energy electrons in the beam. Both the 8-cm and the 16-cm sources were characterized at heights from the source grids ranging from 20 cm to 85 cm. The 8-cm source profiles were observed under varying conditions to determine which parameters affected the beam profile. Certain parameters, such as low neutralization current and high chamber pressure, had little effect on the profile. The most significant effect was a buildup of an insulating film on the anode, as noted above with the multilayer etch profiles. Significant differences seen in profiles between the two 8-cm sources were attributed to differences in the magnetic field surrounding the discharge chamber.

The 16-cm source beam profile is exceptionally immune to changes in the operating parameters. Profiles taken under a range of operating conditions and normalized at the on-axis center (r = 0) are compared in Fig. 74.6 for a fixed height above the source. In practice, the similarity in profiles allows use of the source over a wide range of ion energies and densities without making large changes in the geometry established to produce uniform etching. A single model, independent of source parameters, was used in the uniformity code discussed below.

Etching Model

Processes that use energetic ions for large substrates require that the time-averaged erosion effects from the ion flux be uniform across the surface. A numerical model has been developed to determine this flux and its effects on surface etching of a silica/photoresist combination. The geometries of the source and substrate are very similar to typical deposition geometries with single or planetary substrate rotation. The model was used to tune an inert ion-etching process that used single or multiple Kaufman sources[14] to less than ±3% uniformity over a 30-cm aperture after etching 5 μm of material. The same model can be used to predict uniformity for ion-assisted deposition (IAD).

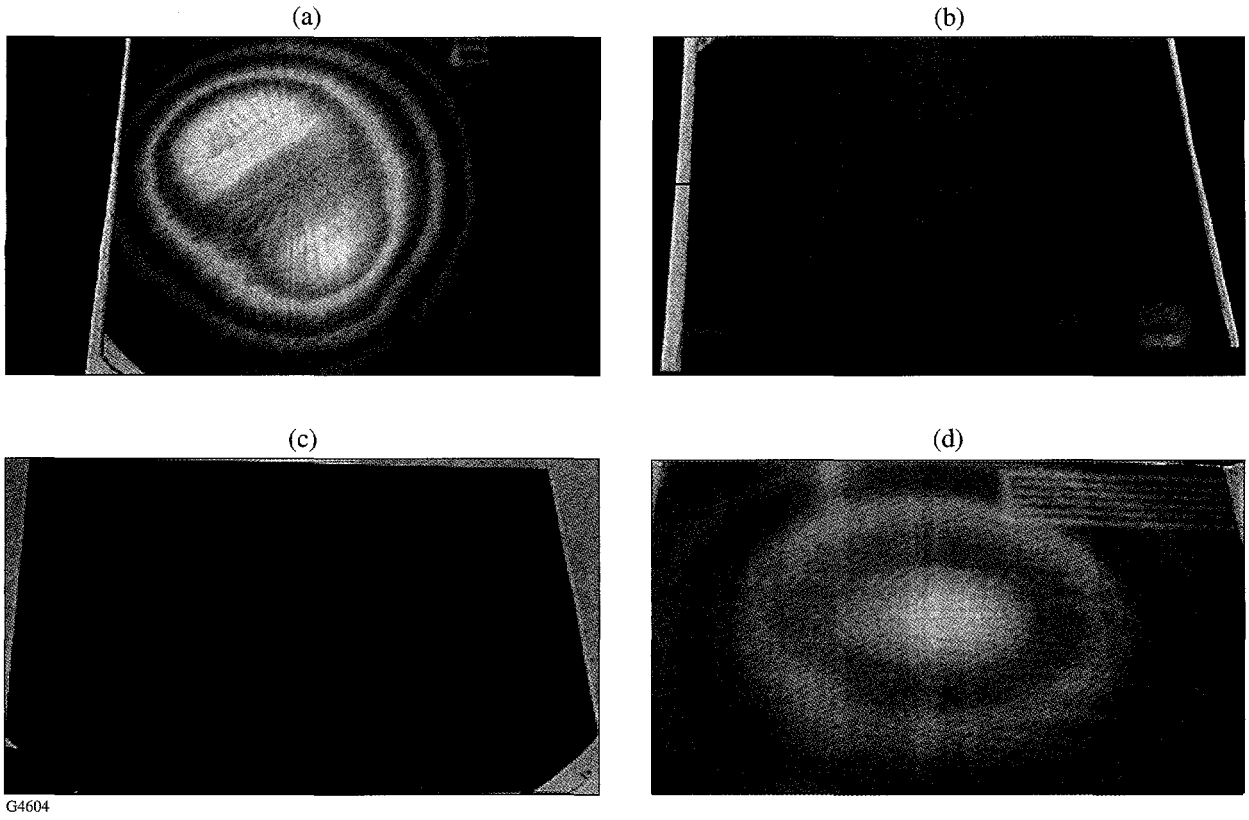

Figure 74.5
The beam profiles formed in the etched multilayers provide rapid feedback to determine correct operating limits and procedure with the ion sources. (a) Profile of a nonuniform etch obtained with the 8-cm source at an excessive beam current (I_b = 100 mA). The structure is a partial image of the spiral filament for the discharge chamber. (b) A profile from the same source as in (a) at lower beam current (I_b = 50 mA). (c) The 8-cm source operated at low current but with a contaminated anode, which had been used previously for 30 h without cleaning. The thin dielectric film that forms on the anode has an obvious effect on the discharge and beam uniformity. (d) The 16-cm source etched uniformly even when used at beam currents as high as 300 mA.

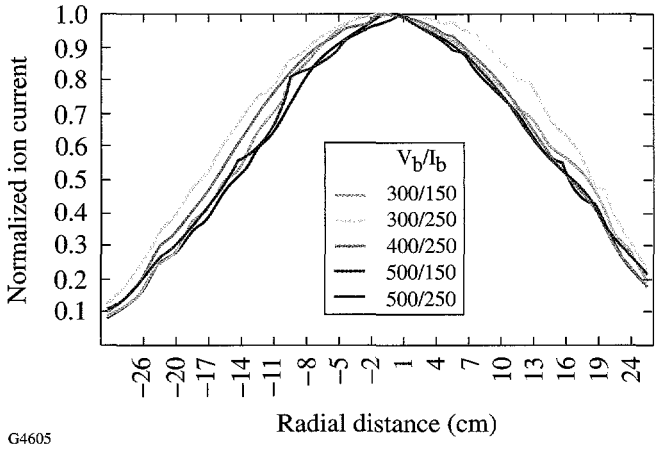

Figure 74.6
The 16-cm source had a stable profile over a wide operating range. The first number in the key is the beam voltage, and the second number is the beam current (in mA). All curves are normalized at $r = 0$.

In Fig. 74.7 an ion source is placed in some arbitrary location and orientation with a substrate rotating in a horizontal plane above the source. The total ion beam flux seen by a point P on a substrate at some radius r from the center can be approximated by

$$E(r) = \sum_{\phi=0}^{\phi_{max}} I(\phi, r)\, R(\phi, r)\, \Delta\phi, \qquad (1)$$

where $I(\phi, r)$ is the ion flux intensity determined at point ϕ, r and $R(\phi, r)$ is the sputter yield at the same point. R is actually a function of a single variable, the incidence angle of the ion,[15] but both ϕ and r are required to determine this angle. In reality, point P will see a range of incidence angles due to the broad nature of the source. Here, a point source is assumed using the top center of the ion-source grid as the origin of ions, and a single incidence angle is used for the approximation. The example in the diagram shows a simple single rotation of the substrate. For this case, $\phi_{max} = 2\pi$ represents one full rotation of the substrate and is adequate to model the uniformity. A more complex double rotation (planetary) can also be modeled. In that case the point P traces out an epicycloid instead of a circle.

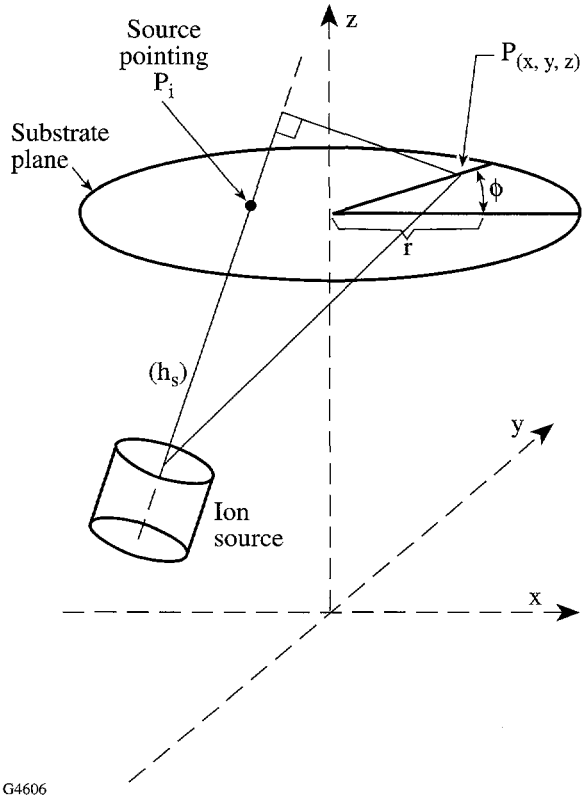

Figure 74.7
Geometry for ion etching with substrate rotation in the horizontal plane. To adjust the uniformity the source pointing was fixed, and then the source was moved on a rail along the x axis.

The model described by Eq. (1) can be broken down into three major parts:

1. summation and location routine: simulates the position of a point on a substrate, finds all position and angular parameters, and integrates the calculated flux through some amount of substrate rotation;

2. expression for $I(\phi, r)$: a model for the expected ion flux that is determined from measured values of the ion source; and

3. expression for $R(\phi, r)$: a relationship between the incident ion angle and energy and the sputtering yield (or etch rate) of the substrate. This also must be determined experimentally.

The model for $I(\phi, r)$ assumes a rotational symmetry of ion density about the axis normal to the ion-source grids.[16] This is a reasonable assumption if the discharge chamber in a hot-cathode source is maintained and cleaned regularly as discussed previously. At a given height h_s above the source, the data can then be fitted to a 1-D super-Gaussian equation

$$I = a + be^{\left(-\left|\frac{r-c}{d}\right|\right)^e}, \qquad (2)$$

where I = ion flux/area for a given r, a = dc offset (usually set to zero), b = amplitude factor at $r = 0$, c = offset for r (set to zero for well-centered beams), d = width factor, and e = shape factor.

The factors b, d, and e all vary with the height above the source. In practice, the beam profile is measured at various heights, and each profile is fitted to Eq. (2). The values found for b, d, and e at various heights are then fitted to curves using a commercial curve-fitting program. The resulting equations and associated coefficients can then be written into a concise code for modeling. Some results of the measured values and the model are given in Figs. 74.8(a) and 74.8(b). The model provides a smoother profile than the actual measured data. This is reasonably accurate since smoothing would also occur in the actual source data if the profile was an average of measurements at some fixed radial distance around the source.

The expression for $R(\phi, r)$, the etch rate as a function of ion incidence angle, was also determined experimentally. Small silica plates with binary photoresist patterns were mounted on miniature rotation drives with the axes set at 20°, 30°, 40°, 50°, 60°, and 0° to the beam axis (see Fig. 74.9). The center of each substrate was placed on a circle, and the entire assembly was rotated in the horizontal plane during the etch; thus, with the ion source on axis, the ion-etch rate for silica and photoresist could be determined simultaneously for six incidence angles by measuring step heights and photoresist thickness. Data were obtained for different operating source parameters and

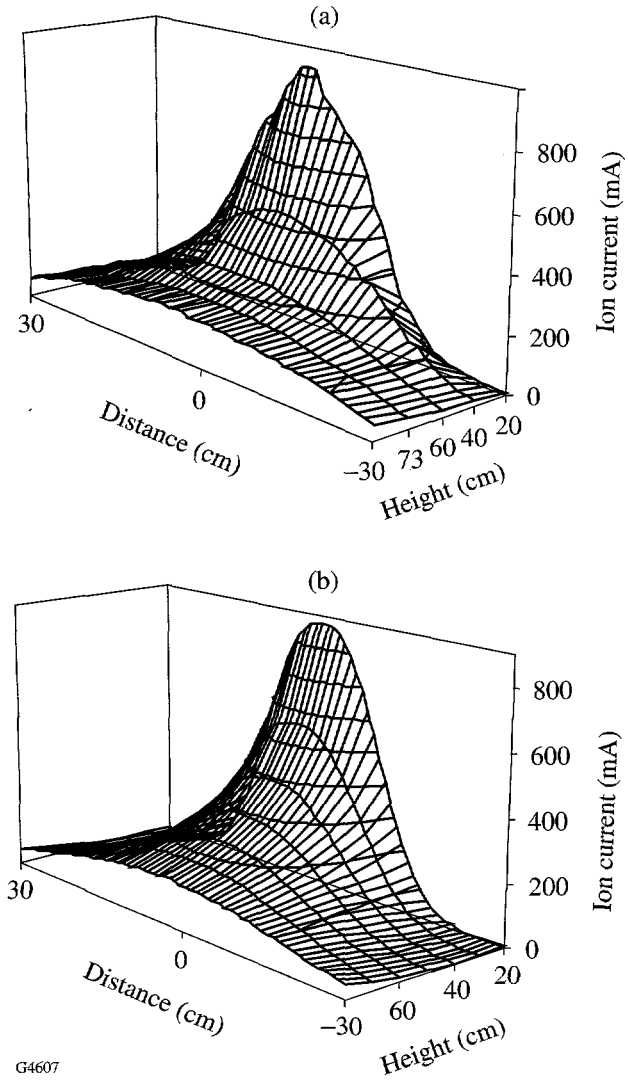

Figure 74.8
(a) Measured profile of the 16-cm ion source operating at 300-V beam voltage and 250-mA beam current at different heights above the grids. (b) Model of measured profile in (a). This model was used in the uniformity program to determine placement of the ion sources.

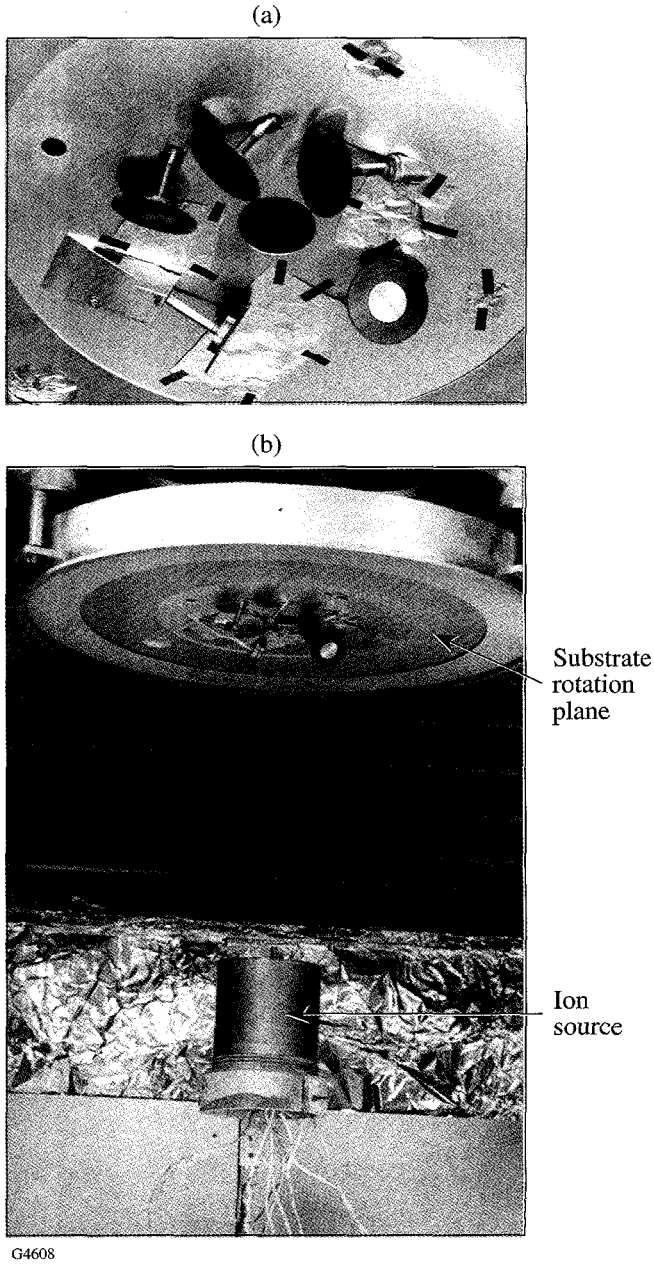

Figure 74.9
(a) The apparatus to measure the etch rate for silica and photoresist simultaneously for several ion incidence angles. Each substrate has a binary pattern of photoresist and is attached to the shaft of a motor. (b) The ion source was placed directly below the apparatus while the entire substrate apparatus above was rotated to obtain a uniform average ion flux density on all test pieces. Substrate heating affected the consistency of results in this experiment.

photoresist preparation processes. The data were often obscured by measurement errors and problems with surface roughening. The original intent was to generate curves for different photoresist annealing conditions (see Fig. 74.10) and to pick the curve that most closely matched the silica curve. In practice, the measurement was flawed by the inability to cool the samples during etching, which increased the apparent etch rate on photoresist. Thus, from these results, the etch rate of photoresist appeared higher than that of silica, but later, on cooled substrates, the etch rate of resist proved to be lower than that of silica.

Since the two materials did etch at different rates but appeared to follow the same curve, the curve for the photoresist annealed at 110°C was selected for the model. The normalized data from this measurement experiment were fitted to a polynomial of the form $y = l + m\theta^2 + n\theta^{2.5} + o\theta^3$. The data and the fitted curve are shown in Fig. 74.11. The accuracy of this data (due to thermal effects) is the largest source of error for the model.

The results for the full uniformity model using the 16-cm source demonstrated that the source should be able to etch a 30-cm aperture uniformly without requiring a supplemental 8-cm source for fine adjustments. Typical results from the full model are shown in Fig. 74.12. The array of curves demonstrates what effect moving the source on a path parallel to the

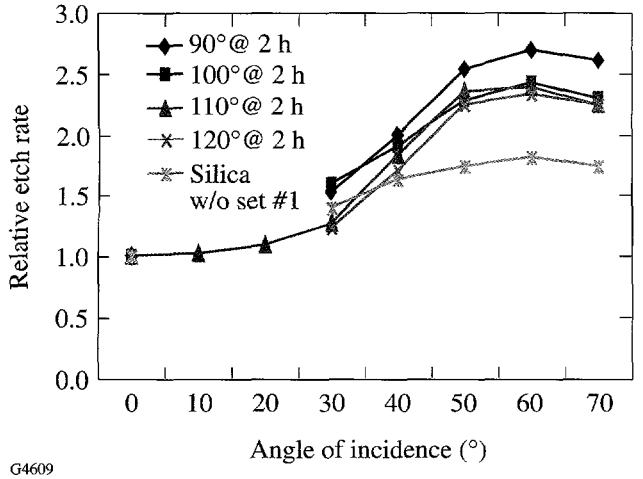

Figure 74.10
The measured etch rate versus ion incidence angle for photoresist anneal after development at different temperatures. Substrate heating affected the consistency of results for photoresist in this experiment. The silica measurements, which are more consistent, are included for comparison. All etch rates have been normalized at 0° for comparison.

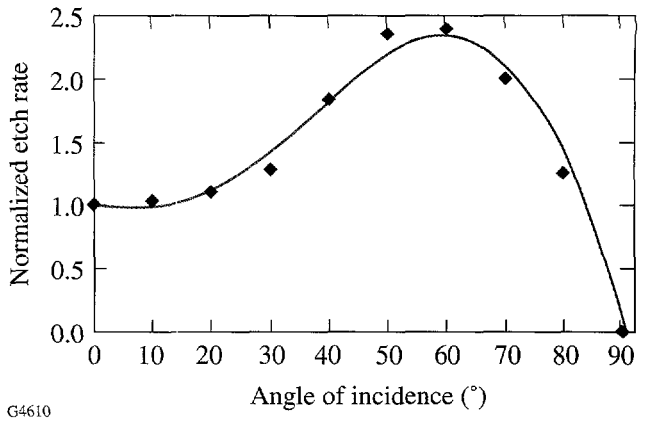

Figure 74.11
The photoresist data for resist baked at 110°C were fitted to the equation $r = \ell + m\theta^2 + n\theta^{2.5} + o\theta^3$ for the uniformity model. Some data were assumed based on other results investigating angular dependence of sputtering.[15] A zero rate was assumed for 90° and values were estimated for 10° and 20°, which satisfies the condition for an increasing positive first derivative.

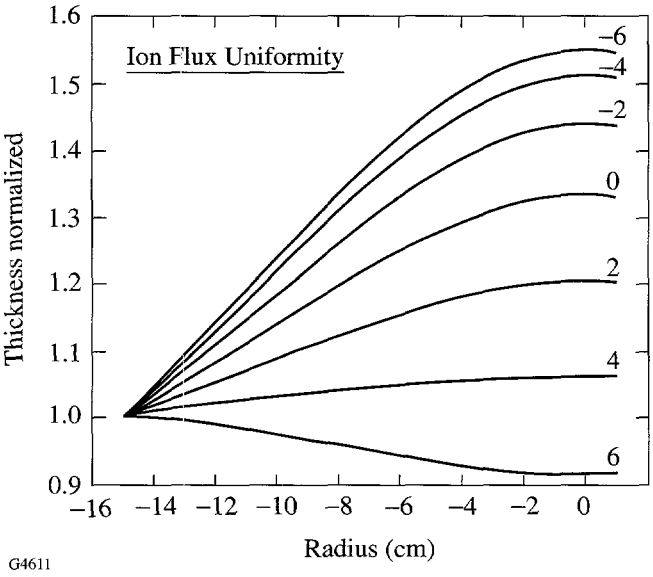

Figure 74.12
The uniformity model is used to evaluate gun positions for one or several ion sources. The graph shows the thickness of material removed, normalized to the first value at −15 cm, as a function of the radius along a DPP-sized substrate. The axis of the source struck the substrate plane at a 30° angle, and the ion-source grid center was placed 34 cm below the substrate. The source was pointed −11.5 cm from the x axis, and the curves represent the change in uniformity as the source is moved along the x axis (*x*-pointing value in centimeters is shown with the curve). This model was reflected in the hardware arrangement with the source on a rail that could easily duplicate the movement along the x axis. The model revealed that a uniform solution could be achieved with the single 16-cm ion source and indicated the sensitivity of positioning. The final position of the source was finally adjusted empirically for best uniformity.

x axis and away from the substrate has on uniformity. The ion-source axis is at 30° with respect to the substrate's normal axis, and the source is pointed away from the center. The model also tracks total integrated current for the starting point, which is used to determine the efficiency of a given geometry. Figure 74.12 shows that a uniformity of better than 7% could be achieved with careful pointing of the source. In practice, etch uniformity of less than 2.5% was measured and, during production of 60 optics, was kept below 6% across the 30-cm clear aperture.

The model was also used early in development to optimize the uniformity of two 8-cm sources etching simultaneously. The model did not always fit the exact results from the chamber; however, it did offer guidance in selecting which direction to move a source while final tuning was completed empirically. The best uniformity results were obtained with the source pointing outside the clear aperture. In this case, most of the ions did not strike the substrate, and the process made inefficient use of the generated ions. A double-source arrangement with a 16-cm and an 8-cm source could have greatly decreased the total etch time but only at the expense of decreased reliability and possible overheating of the photoresist. The 14-h etch time required for the approximately 5-μm etch into fused silica meshed well with the production rate for exposed photoresist-coated plates.

Uniformity Testing

The most reliable test of etch uniformity is to etch directly in silica or photoresist and measure the change in surface profile using interferometry. This method requires a surface that is flat enough to accurately test both before and after the etch. A uniform photoresist coating was applied to a flat-polished substrate, then was partially etched and measured. The substrate could then be stripped of the photoresist and reused without repolishing. The surface measurement prior to etching was stored and subtracted from the post-etch measurement to provide the true etch profile. One sample, if coated with 7 μm of photoresist, could be used several times for uniformity tests during development and as a quality check during production. A sample result of interferometry after etching a photoresist surface is seen in Fig. 74.13. The flat is measured in transmission by placing it in a Fizeau cavity and observing the change in wavefront. The height variation in the resist surface layer is then found from

$$d = \frac{\mathrm{OPD}}{(n-1)} \bullet \frac{\lambda}{2}, \tag{3}$$

where OPD is the optical path difference in waves and n is the refractive index of the photoresist at the test wavelength λ. The factor of 2 compensates for the round-trip path the wavefront travels when transmitting through the optic in the cavity.

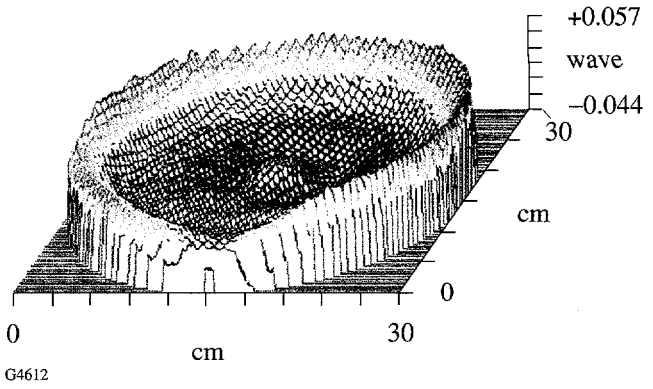

Figure 74.13
The surface figure of an etched photoresist coating measured in a phase-shifting interferometer. The surface figure prior to etching is subtracted from this measurement. The peak-to-valley and rms height values are 0.107 and 0.011 waves, respectively, measured at 633 nm. The overall power is removed from the data. Data from these measurements are combined with the total etch depth measured in the center to determine the etch uniformity in the following figures.

The plate is also tested at the center of the etched surface with a spectrometer to determine the total thickness of the photoresist coating before and after the etch. The total etch depth is found for the center and is combined with the interferometric data to generate a profile of the material removed by etching. This profile is divided by the average thickness of the etched material to provide a normalized etch uniformity for run-to-run comparison. Several profiles from the development and production phases are seen in Fig. 74.14. Figure 74.14(a) shows the convergence toward a good uniformity during the development phase. At the end of tuning the uniformity had a variation of less than 4%. Figure 74.14(b) shows the short-term stability (run-to-run) of uniformity attained during the final calibration sequence prior to etching the phase plates. The plots in Fig. 74.14(c) demonstrate the long-term stability of the etch uniformity over the 6-month production sequence of the phase plates. Stability was maintained by accurate positioning and pointing of the ion source and careful monitoring of the discharge electrical characteristics during source operation. Plots from the model in Fig. 74.12 suggest that maintaining pointing and position of the source to within a few millimeters should be adequate to limit variation in the uniformity to ±1%.

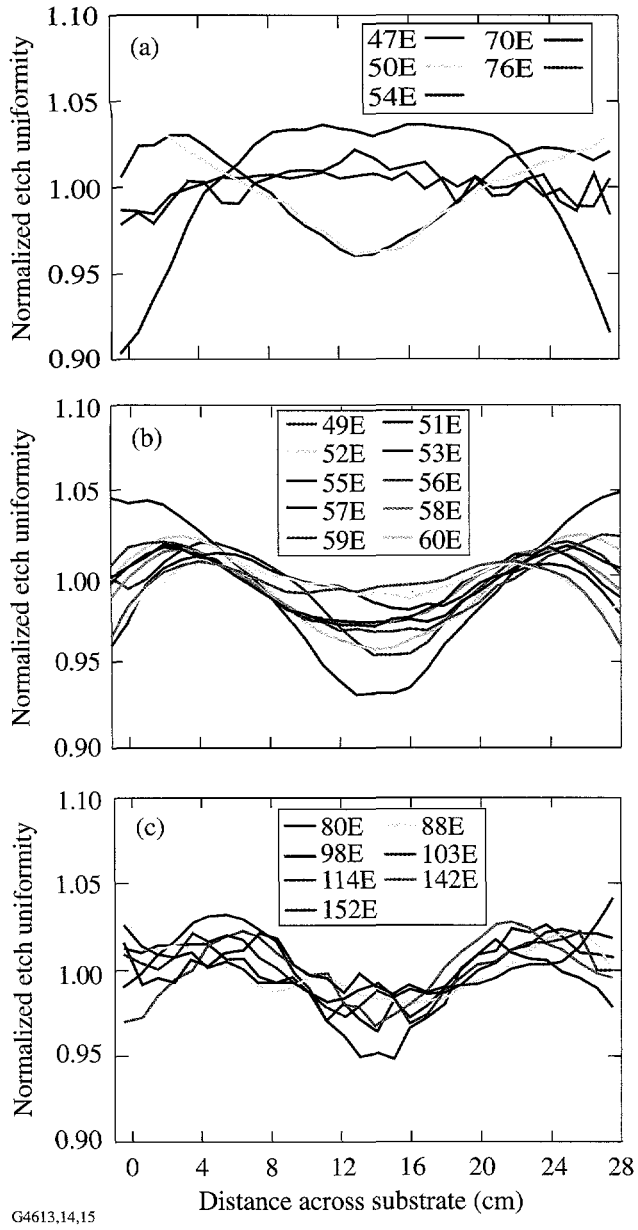

Figure 74.14
Plots of the normalized etch uniformity over the optic clear aperture during different phases of the project. (a) Good uniformity was achieved fairly quickly during the development stage as the ion source was adjusted to its final geometry. (b) The uniformity of sequential etch runs prior to production (calibration sequence) demonstrated the high repeatability of the process. The one run that deviated from ±2% was etched with a slightly different geometry. (c) The etch uniformity was very stable over the 8-month production period. The uniformity was periodically checked by etching flat, unexposed plates of photoresist. Gun position was checked frequently during production to maintain this uniformity. The numbers labeling the curves correspond to the sequential etch run for a given year.

Texturing Problems

Increasing surface roughness and scatter potentially limit the usefulness of ion-etch methods in optical applications. Surface texturing is well documented in ion-beam applications and has been attributed to several erosion-induced morphological changes including

a. development of cones and pyramids due to the angular dependence of the sputter yield;

b. faceting of different crystal planes in a polycrystalline material; and

c. redeposition of contaminating materials onto the mask and substrate. This causes local regions of different sputter yield that evolve into a structure surface.

The incidence angle tests were designed in part to test the effects of texturing from cause (a) listed above for silica and photoresist. Faceting (b) should not occur in either material since both are amorphous. Redeposition of metals, especially from tooling, was a concern and is addressed later. Other texturing effects in silica have been studied[9] but are generally found to occur at high incidence angles and at ion energies an order of magnitude higher than those used in this study.

The first experiments to probe the angle dependence on sputter yield tended to develop scatter on samples held normal to the ion beam and less so on the samples oriented at 60°, 50°, 40°, and 30° with respect to the incoming ion beam. The broad range of morphologies of the scatter in photoresist are seen in Fig. 74.15. The scanning electron micrographs (SEM) showed blistering in one view [Fig. 74.15(a)], while the other view [Fig. 74.15(b)] gave the impression of melting and flowing resist. Atomic force microscopy (AFM)[17] revealed high spatial frequencies in some areas of the photoresist scatter in Fig. 74.16(a). Areas where the photoresist had been fully eroded showed a different morphology [Fig. 74.16(b)]. The high spatial frequency component was absent here, and the surface was dominated by smooth, shallow depressions. The change of morphology of the silica surface is probably due to some planarization associated with the angular dependence of ions. This morphology occurred only in silica that was underneath the textured photoresist. Areas covered by only a very thin layer of resist showed no scatter related to etching. This evidence led to the conclusion that the photoresist was heating up, nearing its softening point, and beginning to flow during the etch.

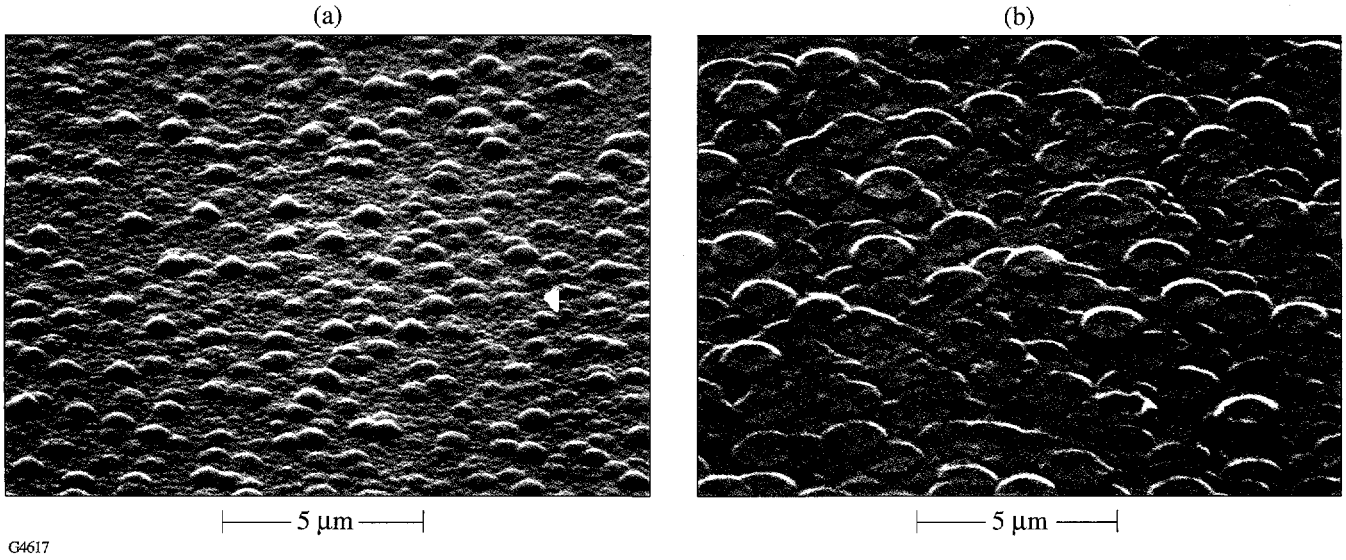

Figure 74.15
Scanning electron micrographs showing the different morphologies of high-scatter photoresist areas after etching. (a) and (b) are samples from ion-etch experiments to determine angular dependence of sputter (Fig. 74.9). The surface in (b) shows distinct signs of flow as the photoresist temperature rose during etching.

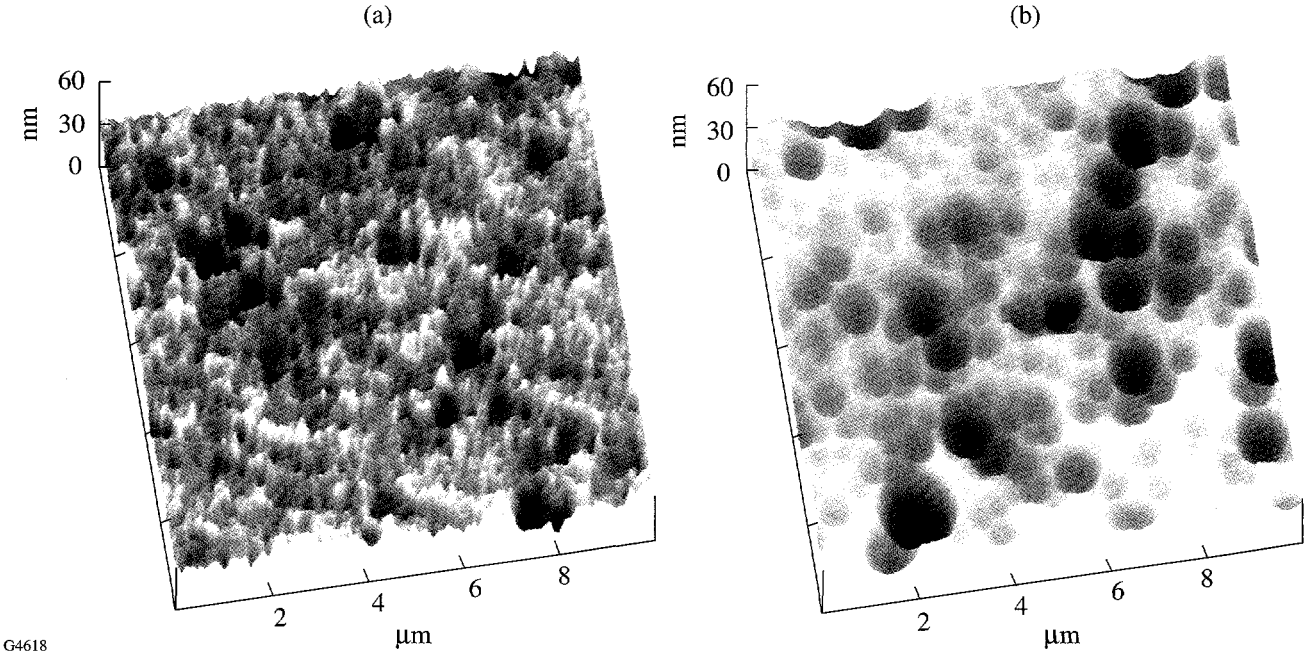

Figure 74.16
AFM scans of the surface of a 30-cm, partially etched substrate. High-scatter areas where photoresist remained (a) were measured as well as areas where photoresist was completely eroded away and only silica remained (b). The roughness in the resist area (a) seeded the topology of the SiO_2 surface (b). The morphology in the silica was then modified further by classical sputtering effects of angular dependence of sputtering, ion reflection, and redeposition.

The primary radiative thermal load during ion etching is the hot ion source and associated filaments. A secondary thermal load comes from the ion impingement, which provides an average energy of 0.1 W/cm^2 directly onto the surface of the resist; however, much of that energy is transferred by momentum to the etched molecule. In the angular dependence experiment the heat load would be largest for the substrate that had the largest amount of surface area exposed to the heat source, e.g., the normal incidence sample that typically had the highest scatter. To test this hypothesis a thermal sensor was placed directly above a rotating DPP master (a substrate with a full-thickness photoresist coating) to sense the temperature of the back of the substrate during etching. The temperature was monitored while the ion source was operated intermittently to allow the substrate to cool after a period of etching [Fig. 74.17(a)]. When the substrate was prevented from going above 50°C, the photoresist did not develop a textured surface. The surface of the photoresist layer must be significantly hotter

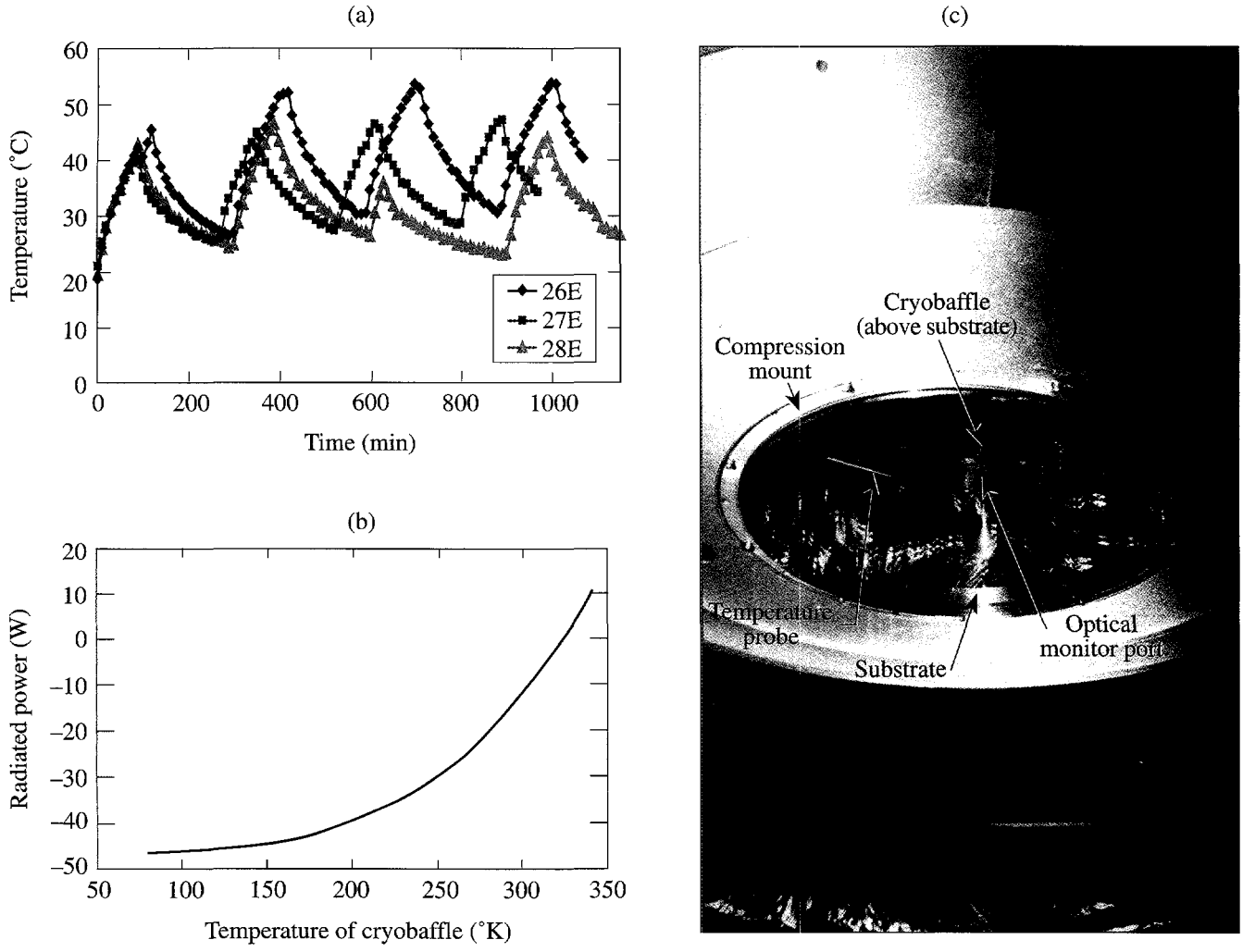

G4619,20

Figure 74.17

(a) The ion sources were operated intermittently in this test to allow the substrate to cool between etch cycles. The temperature of a probe close to the substrate is plotted versus time for several intermittent etch runs. Surface scatter in the resist became prominent when the measured probe temperature exceeded 50°C. A thermal load of 15 W (from the ion source) was calculated from the rate of temperature rise of the substrate. (b) The radiative heat transfer power of the cryobaffle on the back of the substrate has the capacity to cool the substrate if the baffle is cooled at liquid nitrogen temperatures. The calculation assumes the DPP is at 323°K and the emissivity of both the cryobaffle and the substrate are unity. (c) The DPP substrate is seen in the compression chuck. The cryobaffle is above the substrate with a temperature probe near the optical monitor port. The optic is held so it is the closest object to the ion source to prevent resputtering and redeposition from any metal hardware onto the optic surface.

than this measured temperature since softening temperatures for most resists exceed 120°C. This could not be confirmed because the front surface temperature of the rotating substrate could not be measured easily without disturbing other concurrent experiments. This test confirmed the suspicion that the texturing effect was due entirely to overheating of the resist during etching.

The immediate solution to the heating problem was to cryogenically cool the substrate from the back (top) surface. A 15-W heat load on the substrate was determined from the rate of temperature rise in the intermittent etch tests. The heat load could be reduced only by moving the ion source away from the substrate, which would result in excessively long etch runs. The thermal radiative power for two flat surfaces was found from the relationship

$$Q(T) = \sigma * \frac{T^4 - S^4}{\left[\left(\frac{1}{\varepsilon_1} + \frac{1}{\varepsilon_2}\right) - 1\right]} * A, \qquad (4)$$

where $\sigma = 5.6697 \times 10^{-8}$ W°K/m^2, T is the temperature of the cryobaffle, S is the maximum allowable temperature of the substrate (323°K), A is the substrate area, and ε_1 and ε_2 are the emissivity of the substrate and the cryobaffle. Both emissivity values were assumed to be unity since the peak wavelength of radiation will be in the 5- to 10-μm range. The cooling power of the cryobaffle as a function of the baffle temperature is given in Fig. 74.17(b). A cryobaffle was designed and fabricated[18] that had temperature regulation provided by a proportioning valve for liquid nitrogen and internal heaters [see Fig 74.17(c)]. The cryobaffle could be rapidly heated after the etch completion to prevent condensation on the substrate and excessive cooling of photoresist in partially etched plates. Temperatures of probes near the front surface and between the back surface and the cryobaffle were recorded for all etch runs.

The design of the substrate mount was driven by the need to thermally cool the optic from above, to hold the optic through a wide temperature range in case of ion-source failure, and to prevent redeposition onto the back of the substrate from scattered ions. In addition, resputtering of hardware onto the front surface of the substrate was to be avoided since it would both increase localized scatter and lower the damage threshold of the optic. The mount functioned as a compression chuck and used a polyetherimide[19] material to hold the optic [see Fig. 74.18(a)]. The optic surface was located well below all other hardware, which prevented resputtering of hardware material onto the surface. A conductive metal apron dropped down around the mount from the cryobaffle above to improve cooling of the mount.

The compression mount was tightened enough to prevent the optic from releasing during a worst-case condition where, if the cryobaffle failed, the optic and mount would heat to 80°C. The stresses of the mount on the optic were modeled using finite element analysis [Fig 74.18(b)] to ensure that the optic would not fracture when placed in the cold extreme of −80°C. The compressive stresses did not exceed 400 kg/cm^2, and the tensile stresses were less than 80 kg/cm^2 [SiO_2 strength is 11,000 kg/cm^2 (compressive) and 500 kg/cm^2 (tensile)].[20] The mount with an optic can be seen in Fig.74.18(c).

The surface scatter was visibly reduced in all etch runs that were cryocooled. The only exception occurred on some DPP's that were rotated too slowly during the etch cycle and others that did not cool well enough directly under the optical monitor port in the cryobaffle. (This caused local hot spots in the optic and very light scatter.) The total scatter from any plate never exceeded a loss of more than 1% at 351 nm. AFM scans of a typical and a worst-case surface are illustrated in Fig. 74.19. The typical low-scatter silica surface after removal of 5 μm of material had an rms roughness of 3.7 nm with peaks of 24 nm, and the worst-case area had an rms roughness of 4.14 nm with peaks of 60.8 nm. The isolated peaks in the worst case are assumed to be seeded by blisters in the photoresist.

Linearity

In a continuous profile optic, a linear removal rate between the photoresist and the silica is essential. If the process were not linear, it would be necessary to modify the original mask to compensate for the nonlinearity, and to tightly control the nonlinear process from run to run. Linearity was tested by using a calibration mask designed by LLE's Optical Imaging and Sciences Group [Fig. 74.20(a)]. This mask produces a linear ramp in resist, a stepped ramp, and several steps in different locations in the aperture. It also has a flat region across the center that can be used to measure etch uniformity. The ramp region, which was the most useful, was measured on an interferometer[21] before and after etching. A typical result from the measurement is seen in Fig. 74.20(b).

The ion-etch pattern faithfully reproduced the ramp in the photoresist master. The normalized measured ramps of the photoresist ramp and the etched silica ramp from this master are compared in Fig 74.20(c). The departure from the photore-

sist curve for the thicker resist is due to some residual spatial nonuniformity that existed in the process at the time of the test. The ratio of the slopes of the silica ramp to the photoresist ramp was approximately 1.3 during a calibration sequence just before production. This value represents the etch ratio of the two materials and depends on the photoresist type, resist bake parameters, ion incidence angle, and ion energy. The higher etch rate in the silica allowed for the use of lower thickness photoresist coatings and reduced exposure times to the mask for a given desired spot size of the DPP. The final resist thickness for this design was 3.5 μm, which produced a 5-μm peak-to-valley pattern in the silica. The ramp of the silica is plotted against the straight line target in Fig 74.20(d). The linearity seen in this graph is a result of careful compensation for nonlinearities in all stages of mask manufacture, including film response and photoresist response.

Near-Field Defects

Near-field defects are small-scale regions of high slope in the surface of the distributed phase plate. They are caused by either defects in the photoresist spinning process or imperfections in the mask used to expose the photoresist. Near-field defects produce regions of high intensity fairly close to the DPP surface, which could damage other optics in the vicinity.

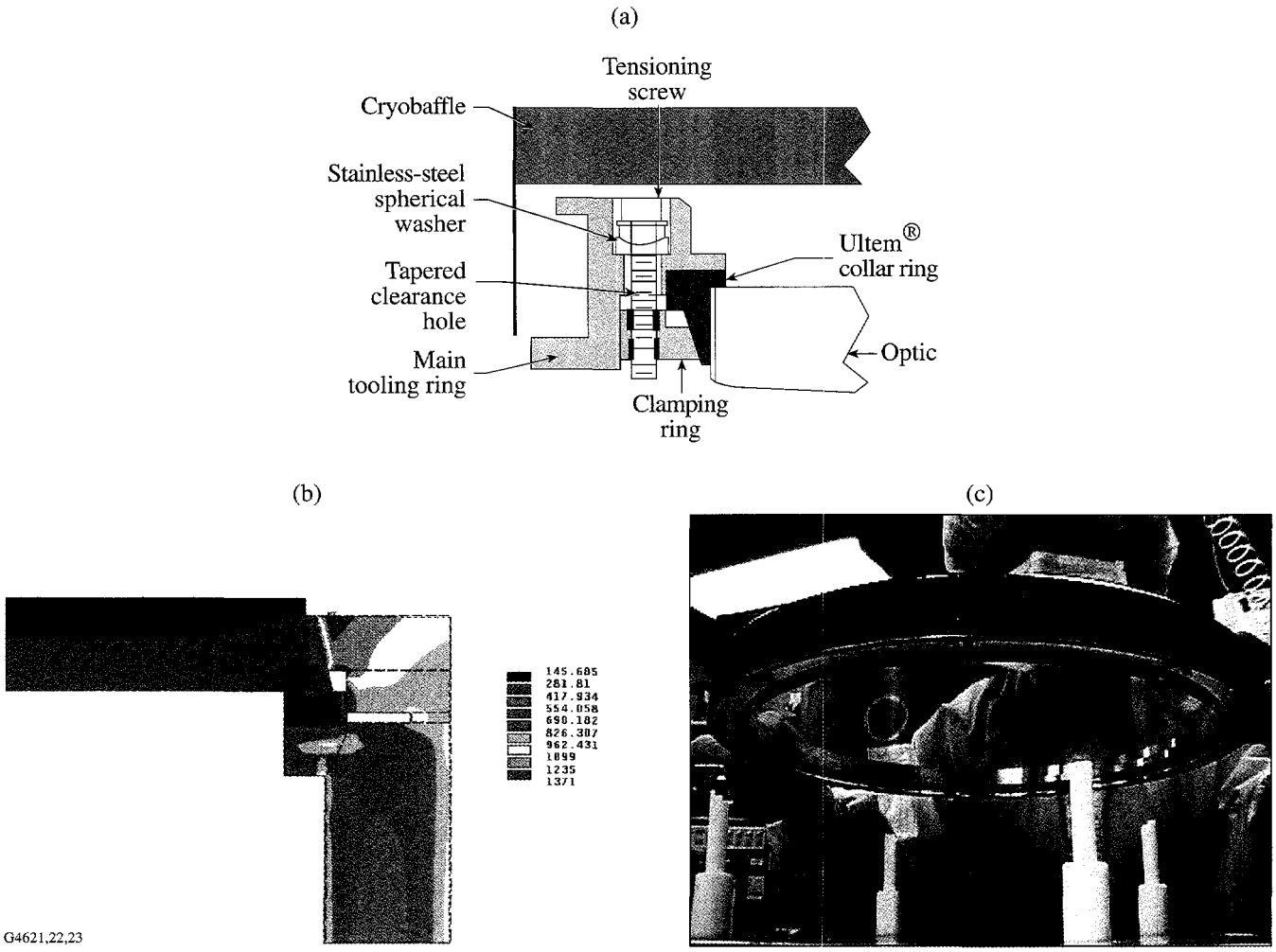

Figure 74.18
(a) The vacuum chuck holds the optic in compression with a Ultem® polyetherimide collar. The substrate mount acts as a barrier for ions traveling to the back surface; it also allows rear radiative cooling and optical monitoring through the optic. (b) Finite element analysis of the substrate in a fully tightened and cooled (−80°C) chuck determined that stresses in the optic would be well below the tensile strength of fused silica. The chuck is tightened enough to prevent the optics from falling out at the high-temperature extreme (+80°C). (c) A close-up view of the chuck on a mounting jig shows the optic, the Ultem® ring, and the tensioning screws. The mount is painted black to increase the infrared emissivity of the aluminum.

In OMEGA, near-field defects could damage the aspheric focusing lens, which is approximately 150 mm in front of the DPP. This lens is both expensive and difficult to replace.

During the production of the first set of replicated DPP's made in epoxy, the near-field defects were removed by locally altering the topography around the defect. Several methods for achieving this were attempted and tested by placing a repaired DPP and a surrogate focus lens in a full beam of OMEGA. The technique that prevailed in both the epoxy and the photoresist materials was to use a hot, blunt point to change the topography of the epoxy by melting. In these cases, the light striking the repaired area is scattered into a wide angular area. The repaired defect areas appear as small holes in the propagating beam.

For etched DPP's, near-field defects were repaired by altering either the photoresist master prior to etching or the fused-silica surface after etching. In silica the near-field defects were repaired by localized grinding with a small dental grinder. Since the etch ratio of silica to the photoresist is 1.3:1, a defect that causes a small modulation in photoresist will turn into a defect with a larger modulation in silica. For this reason, when making etched DPP's, it was preferable to inspect and repair the final etched surface.

DPP's were first inspected for near-field defects in a collimated beam at $\lambda = 442$ nm, which is fairly close in wavelength to the 351-nm wavelength of the OMEGA laser but still visible to the unaided eye. A shadow image of the collimated beam was examined against a white background at a distance of ~150 mm beyond the part. After mapping out the near field for regions of high intensity, a quantitative measure of intensity from each defect was obtained with a CCD camera in the near-field plane (see Fig. 74.21). If the near-field defect caused a peak intensity that exceeded the background by a factor of 3, the defect was marked and removed by grinding [see Fig. 74.21(c)]. During production, plates typically exhibited five to ten defects. Plates with as many as 20 defects were repaired and used on OMEGA. Near-field defect repair was one of the most time-consuming and labor-intensive operations in the manufacturing of DPP's. After being repaired, the optic was cleaned and sol-gel coated by dip coating.

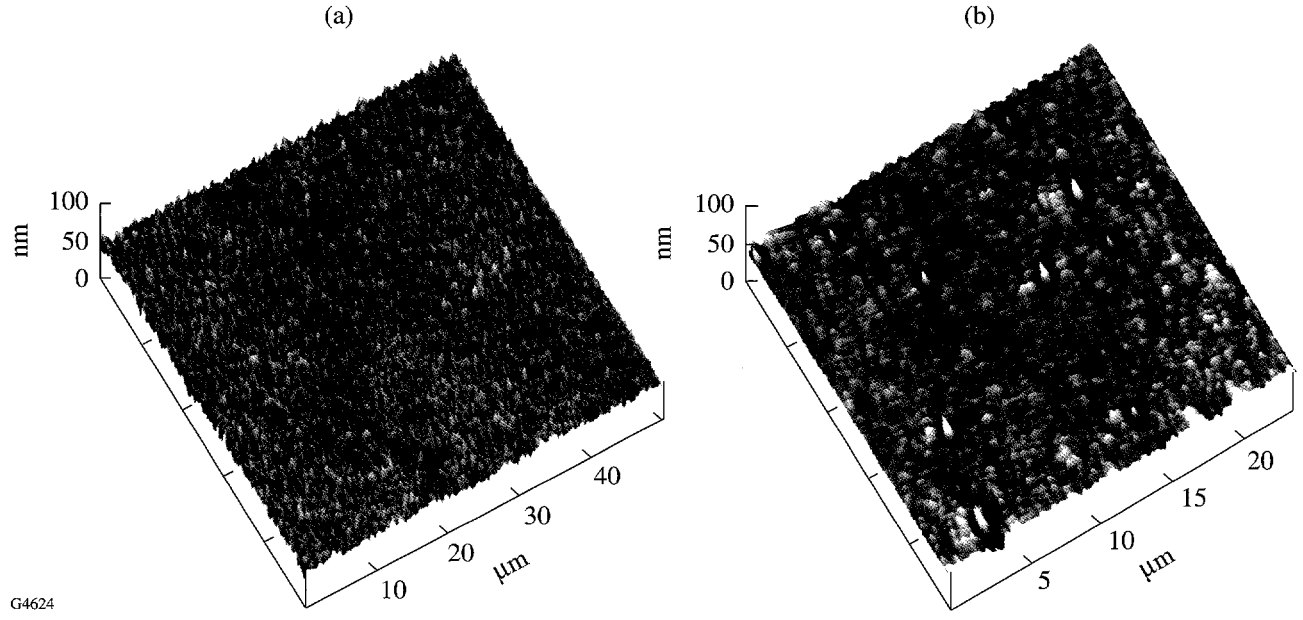

Figure 74.19
(a) The improved surfaces of a DPP cooled during etching can be seen in this AFM scan of a low-scatter area. The rms roughness = 3.4 nm; the P–V roughness = 24.5 nm. (b) AFM scan of worst-case scatter on a production DPP. Scatter was associated with a region that would not have been effectively cooled by the cryobaffle, such as the optical monitor port. The rms roughness = 4.1 nm; the P–V roughness = 60.8 nm. Isolated defects cause most of the scatter losses from this surface. Note the different scale lengths in the two AFM images.

Production Process/Results

A schematic of the full ion-etch system is shown in Fig. 74.22(a). The geometry of the ion source and the substrate can be seen in the photograph of the vacuum chamber's interior [Fig 74.22(b)]. A control program that would shut off the source after a set interval monitored the ion source. The program would terminate the etch if the ion source operated outside the prescribed parameter space for the ion-beam neutralizer emission current and the accelerator (grid) current. The chamber was loaded during the day and operated at night. A typical 14-h etch run included time to heat up the *cryobaffle* and the substrate to room temperature before removing the part for testing the next morning.

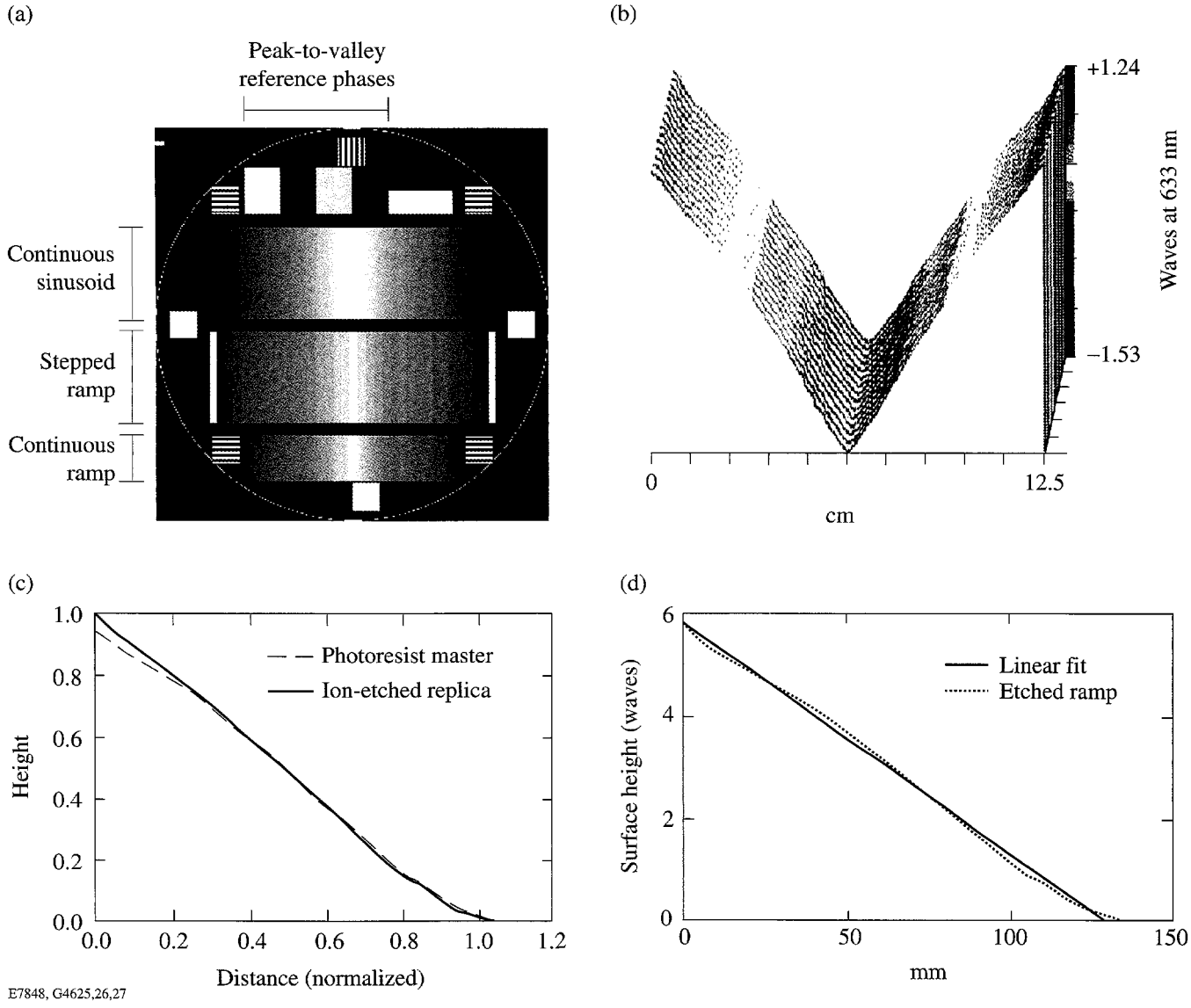

Figure 74.20

(a) The calibration mask is used to characterize both lithographic and etch nonlinearities. (b) A typical interferometric measurement of a continuous calibration ramp. (c) The measured continuous ramps for both silica and photoresist are closely matched and therefore indicative of a highly linear process. The heights are normalized for easy comparison. (d) The etched ramp is compared to a desired linear ramp. The final result includes errors of the entire DPP process, including the film errors from several stages of mask writing and enlarging, photoresist errors, and final etching.

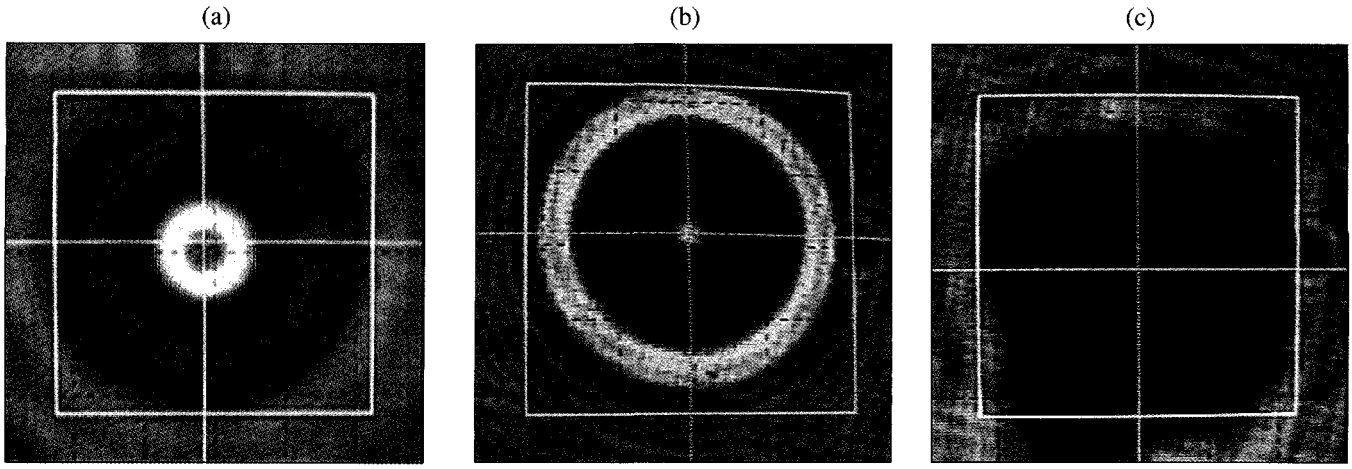

Figure 74.21
A CCD camera is used to analyze individual defects. Several type of near-field defects are found in the DPP's, including lenslets (a), comets (b), goobers, worms, and dirt (last three not illustrated). The final frame (c) shows the near-field result after repair.

An optical monitor measured the thickness of photoresist during an etching run to determine the etch rate and assist in endpoint determination. The DPP design was modified to produce the thickest area of photoresist in the center of the substrate, which was made to coincide with the center of the substrate rotation. A white-light beam was co-aligned with this point to allow for continuous monitoring by interference through the photoresist. The beam entered a monochromator/detector combination, and the signal was fed into a strip chart recorder. The etch rate derived from this measurement proved to be a good indicator of ion-source performance. Ion etching would continue for 30 min after the interference signal ceased to ensure that all the photoresist was removed.

The full production process for DPP's is summarized in the flowchart in Fig. 74.23. The process requires that a photoresist master be made for each etched phase plate. The DPP's for OMEGA were produced over a period of 19 weeks. During this time 79 successful etch runs—66 DPP's and 13 calibration or uniformity checks—were completed. Maintenance occurred on 9 days, and 5 etch runs resulted in failures. A high level of preventive maintenance was performed on the vacuum pumping system and the mechanical components just prior to the final calibration sequence.

Laser-induced-damage thresholds of ion-etched silica always increased when care was taken to prevent the occurrence of redeposition from sputtered tooling. Ion-etched samples of Corning 7940 fused silica were damage tested at 1ω and 3ω with 1-ns pulses. The results are compared to polished and cleaved surfaces in Fig. 74.24. The damage thresholds of the ion-etched surfaces increased over polished surfaces but were less than those for a freshly cleaved surface. The current explanation for the increase is that polishing processes produce both a hydrated layer and a layer of subsurface fractures that can trap absorbing contaminants during the polishing process. The ion-etch process removes the hydrated layer and the layer of fractures and associated contaminants, while the relatively low-energy ions do not penetrate and disrupt the structure near the surface.

A DPP's optical performance can be evaluated by examining the minimum spot size it produces when used in a focusing system similar in aperture and focal length to that found on OMEGA (265-mm aperture, 1800-mm focal length). The spot size is measured at the width corresponding to 5% of the maximum energy. A Gaussian function is fit to the measurement, and the order n (shape) of the function is found. The results for both the replicated epoxy and ion-etched DPP's are given in Table 74.I, and histograms for both DPP types are given in Fig. 74.25. The etched DPP's had a more consistent spot size than the replicated DPP's. Note that the target size had changed between the time the two sets were made. The Gaussian order for the ion-etched set was lower that the target value of 3, but most of those variations were probably due to errors in the mastering process and are not inherent to etching.

(a)

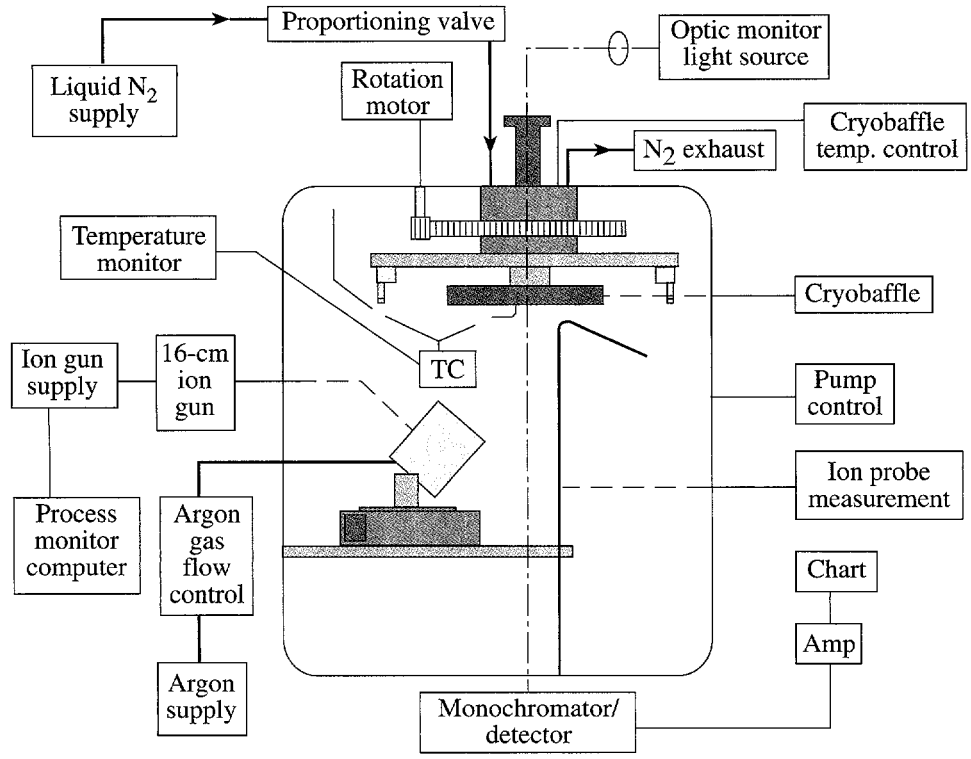

(b)

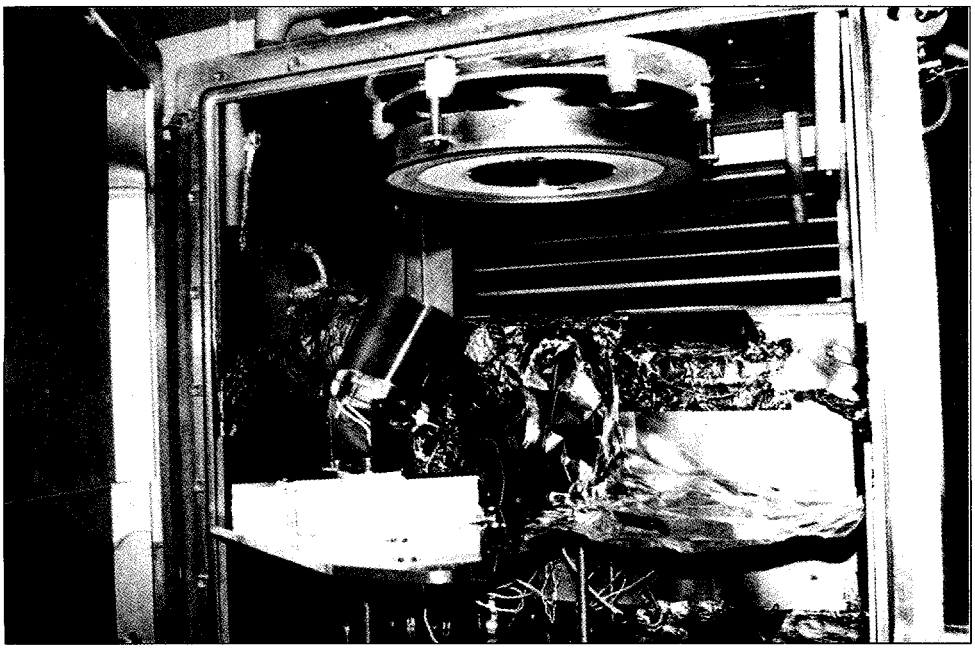

G4629,30

Figure 74.22
(a) Schematic of the LLE/OMAN 16-cm-ion-source etching system. The system was operated continuously for 14 h during each etch. (b) The 16-cm ion source (below) is shown on a rail in the 54-in. chamber with a substrate in the rotation fixture (above).

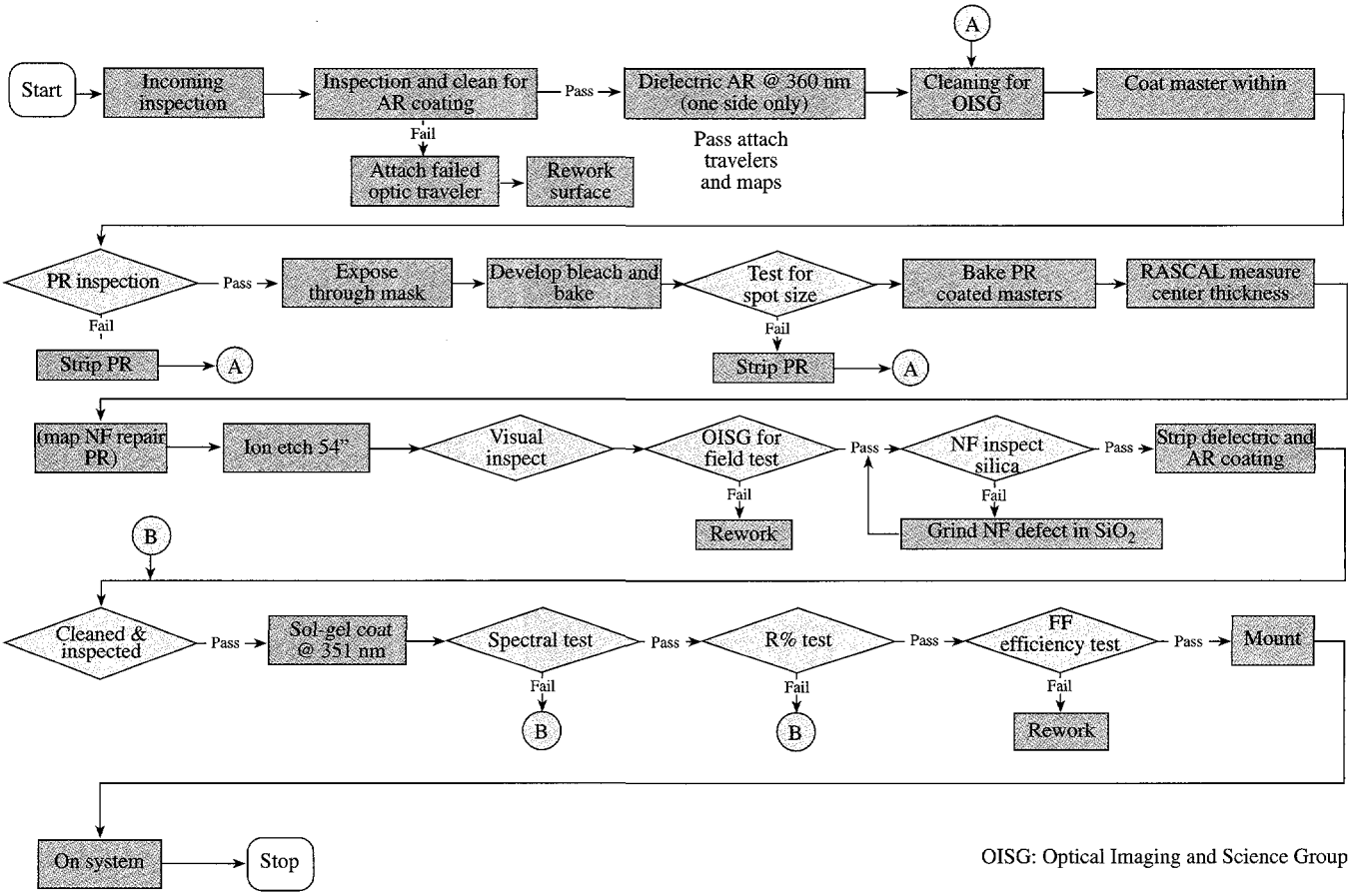

Figure 74.23
Flowchart of etched DPP production steps. The substrates were coated initially with a durable antireflection coating to reduce interference effects during exposure of the photoresist.

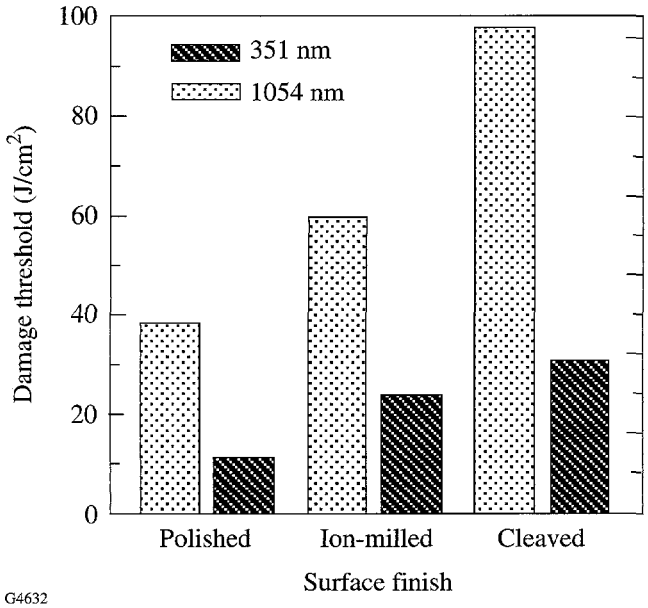

Figure 74.24
Ion etching improves the damage threshold at both 1ω and 3ω for 1-ns pulses.

The transmission through a DPP was measured by collecting all of the energy in the spot using an oversized detector and then reducing the aperture of the detector to 1 mm. The first measure indicates the performance of the sol-gel coatings and scatter characteristics of the piece. The second measure gives the energy likely to impinge on a target and is more relevant to performance on OMEGA. The distribution of the 1-mm aperture measurements for the 60 DPP's used on OMEGA is seen in Fig. 74.26. The plates are near the theoretical maximum transmission for the Gaussian order of $n = 2.44$.

Conclusion

Inert ion etching is a powerful tool for use in manufacturing DPP's for high-peak-power lasers. In concert with gray-level photoresist methods developed at LLE, it provides a method of transferring any continuous function onto an optical surface. The development and production time of 15 months was relatively short given the excellent performance of the devices.

The inert-ion-etching process may be invaluable as a tool for increasing the damage threshold of silica surfaces in both

Table 74.I. Comparison of performance results for 60 etched DPP's manufactured for OMEGA and earlier replicated epoxy DPP's.

	Etched DPP's		Epoxy DPP's	
	Mean	1 σ	Mean	1 σ
Minimum spot size, μm	936.7	14.1	635.8	37.6
Gaussian order	2.44	0.07	~	~
Full transmission	0.994	0.004	Degraded	~
T @ 1-mm aperture	0.959	0.006	~	~

~ no data available.

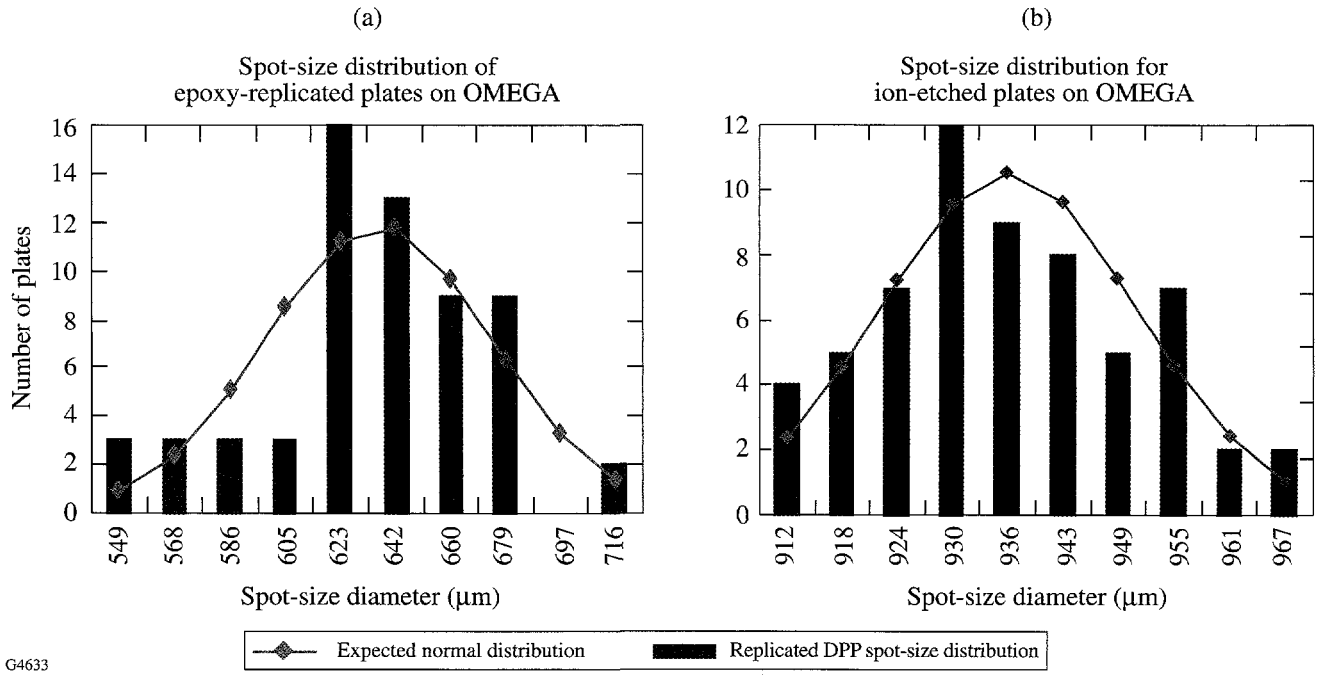

Figure 74.25
The far-field spot size (at the 5% of maximum width) was measured for each DPP. The distribution of spot sizes for the epoxy-replicated DPP's (a) was much broader than in the ion-etched DPP's (b).

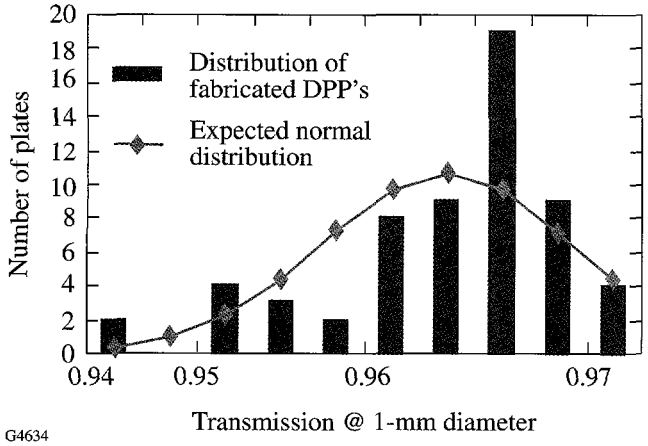

Figure 74.26
Despite some loss due to the near-field defect repairs and slight scatter, the transmission was near the maximum value possible for this Gaussian order. The DPP design requires that some of the energy be sent outside the target.

the infrared and the UV. Ion etching will be tested on other components of OMEGA to assess its capabilities for raising laser-damage thresholds.

ACKNOWLEDGMENT

This work was supported by the U.S. Department of Energy Office of Inertial Confinement Fusion under Cooperative Agreement No. DE-FC03-92SF19460, the University of Rochester, and the New York State Energy Research and Development Authority. The support of DOE does not constitute an endorsement by DOE of the views expressed in this article.

REFERENCES

1. Laboratory for Laser Energetics LLE Review **65**, 1, NTIS document No. DOE/SF/19460-117 (1995). Copies may be obtained from the National Technical Information Service, Springfield, VA 22161.

2. Laboratory for Laser Energetics LLE Review **71**, 101, NTIS document No. DOE/SF/19460-186 (1997). Copies may be obtained from the National Technical Information Service, Springfield, VA 22161.

3. Laboratory for Laser Energetics LLE Review **64**, 170, NTIS document No. DOE/SF/19460-99 (1995). Copies may be obtained from the National Technical Information Service, Springfield, VA 22161.

4. Y. Lin, T. J. Kessler, and G. N. Lawrence, Opt. Lett. **20**, 764 (1995).

5. G. K. Wehner and G. S. Anderson, in *Handbook of Thin Film Technology*, edited by L. I. Maissel and R. Glang (McGraw-Hill, New York, 1983), p. 3-17; G. C. Schwartz, in *Handbook of Semiconductor Interconnection Technology*, edited by G. C. Schwartz, K. V. Srikrishnan, and A. Bross (Marcel Dekker, New York, 1998), pp. 1–76.

6. O. Auciello and R. Kelly, eds., *Ion Bombardment Modification of Surfaces: Fundamentals and Applications*, Beam Modification of Materials, Vol. 1 (Elsevier, Amsterdam, 1984).

7. B. A. Banks, in *Handbook of Ion Beam Processing Technology: Principles, Deposition, Film Modification, and Synthesis*, edited by J. J. Cuomo, S. M. Rossnagel, and H. R. Kaufman (Noyes Publications, Park Ridge, NJ, 1989), pp. 338–361.

8. E. Chason and T. M. Mayer, Appl. Phys. Lett. **62**, 363 (1993).

9. T. Motohiro and Y. Taga, Thin Solid Films **147**, 153 (1987).

10. S. R. Wilson *et al.*, in *Science of Optical Finishing*, Vol. 9, 1990 Technical Digest Series (Optical Society of America, Washington, DC, 1990), p. 73.

11. H. R. Kaufman, R. S. Robinson, and W. E. Hughes, *Characteristics, Capabilities, and Applications of Broad-Beam Sources* (Commonwealth Scientific Corporation, Alexandria, VA, 1987).

12. J. M. E. Harper, J. J. Cuomo, and H. R. Kaufman, J. Vac. Sci. Technol. **21**, 737 (1982).

13. H. R. Kaufman, *Fundamentals of Ion-Source Operation* (Commonwealth Scientific Corporation, Alexandria, VA, 1984).

14. Commonwealth Scientific Corporation, Alexandria, VA 22314-1974.

15. O. Auciello, in *Ion Bombardment Modification of Surfaces: Fundamentals and Applications*, edited by O. Auciello and R. Kelly, Beam Modification of Materials, Vol. 1 (Elsevier, Amsterdam, 1984), Chap. 1; G. Carter and M. J. Nobes, *ibid.*, Chap. 5.

16. M. Jin, "Numerical Estimation for 8-cm Ion Source Distribution," Internal Memo, Laboratory for Laser Energetics, University of Rochester (8 August 1991).

17. Atomic force microscope contact mode, Model NS3, Digital Instruments, Inc., Santa Barbara, CA 93117.

18. Vacuum Process Technology, Pembroke, MA 02359.

19. Ultem®-Polyetherimide, available from Design Engineering Plastic Products, Reading, PA 19612-4233.

20. Fused silica available from Technical Products Division, Advanced Products Department, Corning Glass Works, MP-21-4, Corning, NY 14831.

21. Zygo Mark IVxp, Zygo Corporation, Middlefield, CT 06455.

A High-Resolution X-Ray Microscope for Laser-Driven Planar-Foil Experiments

A soft x-ray microscope ($E \lesssim 3$ keV) with high spatial resolution (~3 μm) has been characterized at LLE and used for initial experiments on the OMEGA laser system to study the hydrodynamic stability of directly driven planar foils. The microscope, which is an optimized Kirkpatrick-Baez (KB)–type design, is used to obtain four x-ray radiographs of laser-driven foils. Time-resolved images are obtained with either custom-built framing cameras (time resolution ~80 ps) or short-pulse backlighter beams ($\Delta t \lesssim 200$ ps). In the former case, a spatial resolution of ~7 μm was obtained (limited by the framing camera), while in the latter case a resolution of ~3 μm was obtained. This article details the testing, calibration, and initial use of this microscope in the laboratory and on OMEGA.

Recent experiments studying the hydrodynamic stability of laser-driven planar foils[1–7] have relied on the technique of time-resolved x-ray radiography as a method of diagnosis. The short time scales (~ ns) require the use of a laser-generated x-ray backlighter, while the small spatial scale lengths (~ μm) require a high-spatial-resolution imaging system. In a radiograph of a perturbed driven foil undergoing unstable growth, the modulation depth (the desired observable) is affected by the resolution (modulation transfer function) of the imaging system.[8] This is typically limited by the imaging system itself (pinhole resolution in the case of pinhole imaging) or additionally by the recording system blurring (as is typically the case when using framing camera or streak camera imaging). Systems used to record radiographs of laser-driven foils range from simple pinhole cameras coupled to x-ray framing cameras to Wolter microscopes coupled to streak cameras. A good example of the resolution obtainable with a pinhole–framing camera combination is described in Robey *et al.*,[9] where 5- to 10-μm-diam pinholes in combination with framing cameras at magnifications up to 12× yield a spatial resolution approaching 10 μm. Remington *et al.*[10] describe the measured resolution of the Nova 22× Wolter microscope, which has an ultimate resolution of ~2 to 3 μm but is not easily adaptable to multiple-frame, two-dimensional imaging. More recently, monochromatic imaging using bent crystals as the imaging device has been applied to flat-foil experiments.[7] Resolution approaching ~3 μm has been reported. Kodama *et al.*[11] report on an advanced Kirkpatrick–Baez (AKB) microscope, which consists of four mirrors producing a single image. This microscope has a quoted resolution of ~3 μm or better over an ~1-mm-diam region.

This work describes the characterization of a KB microscope configured to provide high-spatial-resolution (~3-μm), low-energy (≲3-keV), multiple framed images ($\Delta t \sim 80$ ps) of x-ray-backlit, laser-driven foils. This KB microscope optical assembly consists of glass reflecting surfaces assembled without an additional metal coating. As will be shown below, the uncoated reflecting surfaces provide a convenient high-energy cutoff at ~3 keV, which is appropriate to both the backlighter spectrum and the subjects of the radiography (plastic foils). The detailed design is further described in Marshall and Su.[12] Time resolution can be obtained by either custom framing cameras (developed at the Los Alamos National Laboratory[13]) or a novel, multibeam, short-pulse (~100-ps) backlighter irradiation scheme. This KB microscope will be used in future planar-foil stability experiments on the University of Rochester's OMEGA laser system.[14]

Characterization of the Microscope

The microscope used for these experiments was built and assembled by Sydor Optics.[15] It consists of four mirrors arranged in a stack of two perpendicular pairs (Fig. 74.27) that produce four images of laser–plasma x-ray emission. Images are formed by two perpendicular reflections at a mean grazing angle of ~0.70°. The super-polished reflecting surfaces (surface roughness < 4 Å) are concave with radii of curvature r = 26 m and a thickness along the optical axis of 4.5 mm. [Previously reported mirror assemblies (Ref. 12) had a thickness of 9 mm, resulting in a larger solid angle but also larger measured and calculated off-axis aberrations.] The surfaces perpendicular to the reflecting surfaces are also super polished and are used to optically contact the mirrors into a fixed, stable assembly. The images formed by the KB microscope obey the focus equation[16]

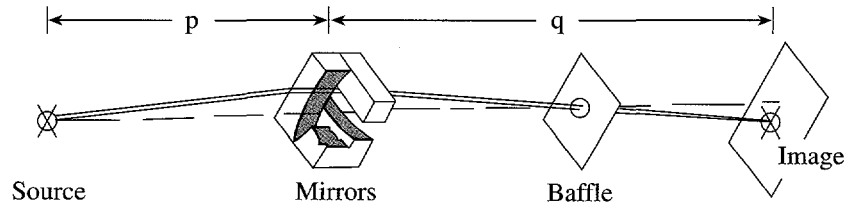

Figure 74.27
Schematic of the KB microscope optical assembly.

$$\frac{1}{p}+\frac{1}{q}=\frac{2}{R\sin i}, \tag{1}$$

where p is the distance from the object to the mirror assembly, q is the distance from the mirror assembly to the image, i is the grazing angle, and R is the radius of curvature of the mirrors. The distances p and q in Eq. (1) refer to the distance from the center of the assembly, i.e., between the pairs of perpendicular mirrors. The mirror separations have been adjusted (as described in Ref. 12) so that the focus of the first reflecting surface is coincident with the second reflecting surface. The best-focus distance at a magnification of 13.6 was found to be p = 179.3 mm. The solid angle subtended by each reflecting pair as seen from the source is $\sim 9\times 10^{-8}$ sr for this case.

After assembly the KB microscope was first characterized in the laboratory using a cw, e-beam-generated x-ray source. The e-beam impinged on a water-cooled tungsten target after passing through a bending magnet whose purpose was to prevent ion contamination of the target area. Typical e-beam voltage settings of 10 kV were used in all tests, producing a continuum x-ray source up to 10 keV. Images were recorded on Kodak DEF direct-exposure film after passing through a 1-mil (25.4-μm) Be window placed near the optic baffle. Figure 74.28(a) shows one of four such images taken of a 500-mesh Cu grid (0.001-in.-diam Cu wires spaced by 0.002 in., i.e., 500/in.) placed at the best focus of the microscope. A hole was placed in the grid [visible in Fig. 74.28(a) as a dark irregularly shaped region] as a position reference from image to image. The resolution as a function of position was determined from photomicrodensitometer (PDS)-digitized grid images. A Perkin–Elmer PDS with a 0.25 NA lens, and a scanning aperture of 10 μm, was used to digitize the images. Figure 74.28(b) shows a horizontal lineout through the image of Fig. 74.28(a) and just below the reference hole. The values are computed intensity in ergs/cm^2 versus position in μm [assuming a photon energy of 2 keV (see the energy response calibration later in this section) and using the semi-empirical formula of Henke *et al.*[17]]. The lineout has been averaged over the width of the space between the wires and median filtered to reduce point-to-point noise. The remaining pattern shows the overall resolution of the image near best focus. Figure 74.28(c) shows an enlargement of the lineout at the edge of the shadow of one wire. The width of the shadow is ~3.7 μm. This measurement was repeated across the image, yielding the resolution as a function of position [Fig. 74.28(d)]. The resolution thus measured closely follows that computed by ray tracing (solid line). Diffraction of soft x rays ($\lesssim$1.5 keV) will contribute to image blurring at best focus. The dotted line in Fig. 74.28(d) indicates the approximate effect of diffraction on the resolution for an assumed energy of 1.25 keV (worst case, i.e., lowest practical energy to be used). Diffraction is seen to limit the resolution to ~2 μm for such soft x rays. The measured resolution of 3 μm at best focus indicates that the optical system is limited to $\geq$1.5 times the diffraction limit. For comparison the resolution that would have been obtained if 9-mm-thick mirrors had been used is shown in Fig. 74.28(d) as a dot–dashed line. The smaller mirrors clearly provide a more optimum on-axis and off-axis resolution at the expense of solid angle.

The edge response function ε of the microscope (image of the shadow of the edge of a wire) is given by

$$\varepsilon(x)=\int_{-\infty}^{x}\ell(x')dx', \tag{2}$$

where ℓ is the line spread function, which is itself a function of x and y, but assumed to vary slowly. We can make the simplifying assumption that the point spread function (PSF) is given by the product of the line spread functions in the two perpendicular directions x and y. This is a good assumption provided the axes x and y are aligned along the axes of the microscope mirrors, as is the case for all of the images analyzed in this article. The PSF is thus computed from the observed edge response function by differentiation. The result of one such computation from the image of Fig. 74.28(a) near best focus is shown in Fig. 74.29(a). The computed PSF has a full width at half-maximum of 3.0 μm. Figure 74.29(b) shows the modulation transfer function (MTF)

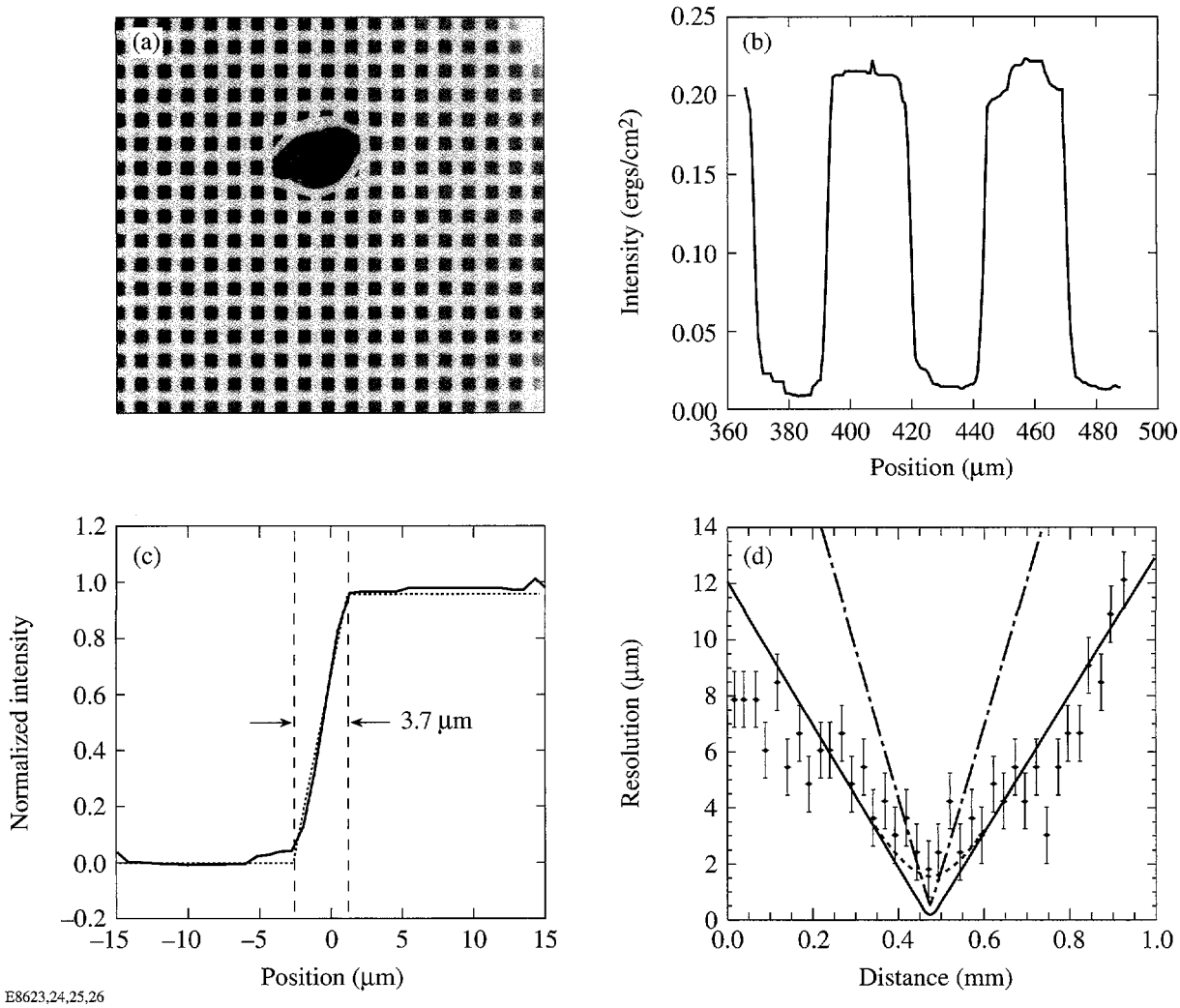

Figure 74.28
Laboratory tests of imaging with the KB microscope. (a) Image of a backlit Cu mesh taken with a cw x-ray source; (b) lineout below hole in grid passing through best focus; (c) enlargement of lineout near best focus; (d) width of the shadow of each wire versus position in the object plane of (a). The solid line is the resolution computed by ray tracing; the dotted line includes the effect of diffraction by 1.25-keV x rays. The dot–dashed line is the resolution computed by ray tracing for 9-mm-thick mirrors (as used in Ref. 12).

$$\mathrm{MTF} = F\left[\mathrm{PSF}(x)\right], \tag{3}$$

computed from the PSF by Fourier transform as a function of position about best focus. The ideal MTF of a pinhole camera with a 10-μm aperture at comparable magnification is shown for comparison.

Framed imaging with the KB microscope is accomplished with a pair of custom microchannel plate (MCP)–based cameras built at the Los Alamos National Laboratory[13] and originally designed to be used in the gated monochromatic x-ray imager[18] (GMXI), which also uses a KB optic for imaging. The GMXI vacuum housing and KB microscope chassis with the uncoated KB microscope optic were used to obtain framed images on the OMEGA target chamber. Each camera consists of a pair of 25-mm-diam MCP's proximity focused to P-11 phosphor-coated fiber-optic faceplates. Two such cameras record the four images of the KB microscope on Kodak TMAX 3200 film. A frame time of ~80 ps results when the cameras are electrically gated. Each camera can be independently triggered, while the separation of the images (~48 mm) results in a time between images on a camera of ~320 ps. Laboratory tests of the framing camera/KB microscope combination were

performed with the cw x-ray source described above, prior to its use on OMEGA. Figure 74.30(a) shows one such image. The resultant MTF is shown in Fig. 74.30(b) and is compared to the MTF's of the KB microscope without a framing camera and the MTF of a 10-μm pinhole at comparable magnification. As is evident, some amount of spatial resolution is lost when using the framing cameras with the KB microscope. The framing camera allows flexibility, however, in choosing the time of the radiograph when not using a short-pulse backlighter.

The energy dependence of the KB optic reflectivity was measured with the same tungsten x-ray source described above using the method described in Dhez *et al.*[19] The spectrum of both the reflected and unreflected x rays were recorded with a AMPTEK XR-100T Si(Li) detector.[20] The reflectivity was computed from the ratio of the two observed spectra and is shown in Fig. 74.31 along with the reflectivity computed from the tabulated values of the atomic scattering factors[21] and assuming a grazing angle of 0.70°. Both the ideal calculated response and the response convolved with the Si(Li) detector energy resolution are shown. The measurements were taken through a path that contained 38 μm of Be, which limited the sensitivity below 1.5 keV. The difference between the measured and computed reflectivities is small and may be due to

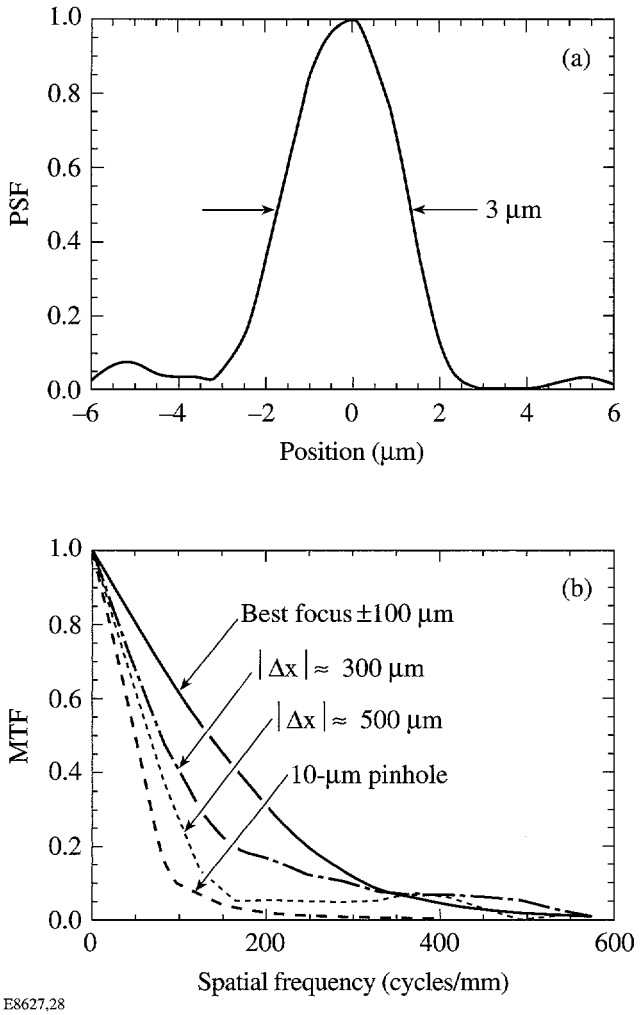

Figure 74.29
The PSF and MTF of the KB microscope recorded with DEF film. (a) The PSF near best focus; (b) the MTF versus position compared to that of a 10-μm pinhole at comparable magnification.

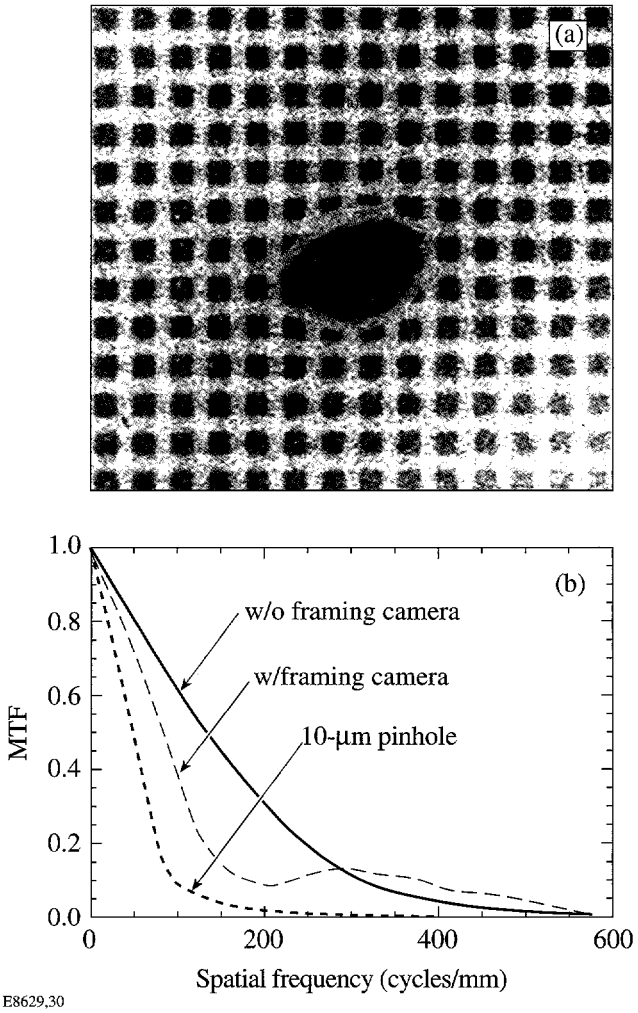

Figure 74.30
Laboratory test of the KB microscope with images recorded by a framing camera. (a) Image of the grid taken with a framing camera and a cw x-ray source; (b) the MTF of the KB microscope with framing camera–recorded images compared to the same obtained without framing cameras. The MTF of a 10-μm-pinhole-camera–based framing camera is also shown for comparison (dotted line).

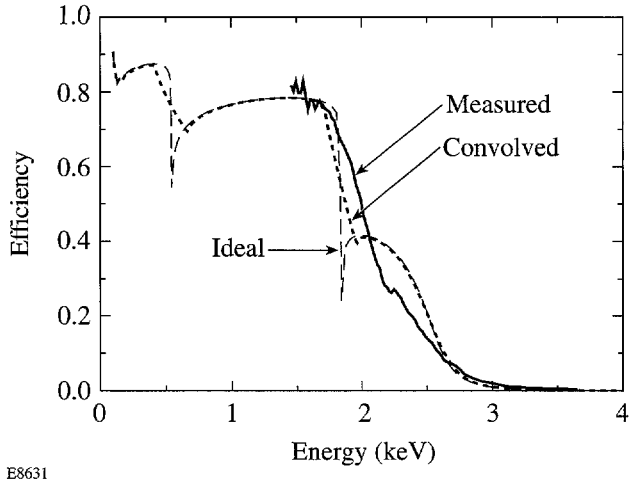

Figure 74.31
The reflectivity of the KB microscope versus energy. The solid line is the measured reflectivity, the dashed line is the reflectivity computed using tabulated values of the atomic scattering constants, and the dotted line includes the convolved response of the Si(Li) detector.

imprecise knowledge of the energy resolution of the Si(Li) detector at the low energies involved. The reflectivity is seen to fall at the Si edge (1.8 keV) and cut off at ~3 keV as expected due to the usual grazing-angle dependence of the x-ray reflectivity.

The choice of uncoated glass as the reflecting surface for planar-foil radiography is further elucidated by the following spectral analysis: A typical backlighter used for these experiments is a uranium foil illuminated at intensities of ~3 × 10^{14} W/cm^2. The spectrum of x rays emitted by such a backlighter[22] is shown in Fig. 74.32(a). Most of the emission comes from the uranium *N*-band (which is unresolved in this measured spectrum) with an additional peak at 3.5 keV due to *M*-band emission. A sensitivity weighted toward the low-energy end of the spectrum (<1.5 keV) is desired since the radiography is to be performed on a plastic (CH) foil. The uncoated-glass optic has a sharp dip in the reflectivity at 1.8 keV followed by a gradual decrease to nearly zero from 2 to 3 keV. The cutoff above 3 keV provides for complete rejection of *M*-band x rays (which would decrease the contrast of the radiography). The response to the U-backlighter spectrum can be further optimized with filtration. Figure 74.32(b) shows the computed efficiency of the KB optic when a 25.4-μm-thick Be plus a 6-μm Al filter is used. Figure 74.32(c) shows the spectral flux density seen at the image plane calculated for 10 J in a 300-μm-diam spot in a 100-ps interval (~1.5 × 10^{14} W/cm^2). This combination of microscope reflectivity and filter transmission is seen to result in a spectrum of x rays in a narrow band from ~1 to ~1.5 keV. The 1/*e* depth of x rays through plastic (such as parylene) in the midpoint of the band (1.25 keV) is ~9 μm. Conversely, a 0.5-μm variation in thickness through the foil would produce a modulation in the x-ray signal of ~5%. The calculated flux density is more than adequate to produce a good exposure on Kodak DEF (as would be the case when using a short-pulse backlighter).

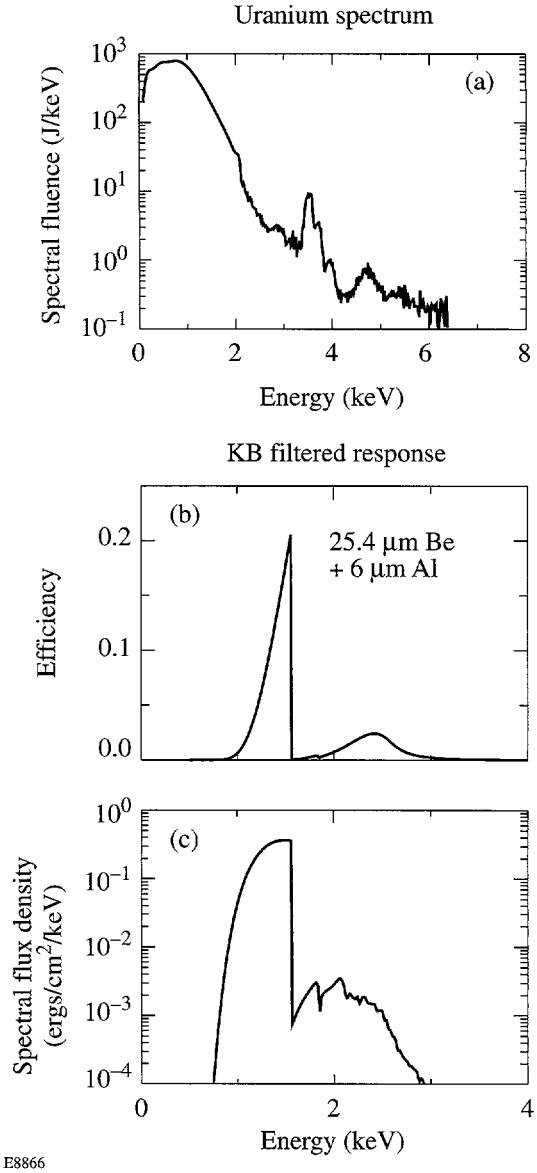

Figure 74.32
The response of the KB microscope to a uranium backlighter. (a) U-backlighter spectrum;[22] (b) the KB microscope response with a 25.4-μm Be plus 6-μm Al filter; (c) spectral flux density at the image plane calculated from the spectrum in (a) and the filter in (b).

Experiments on the OMEGA Laser Facility

Experiments were performed on the OMEGA 60-beam, UV (351-nm) laser system[14] using the soft x-ray KB optic to image laser–plasma x-ray emission. The KB microscope arrangement and the target-illumination method are shown in Fig. 74.33. Targets consisted of test grids and/or driven modulated foils backlit by U foils, illuminated by up to six beams of OMEGA at an intensity of up to 2.5×10^{14} W/cm^2. Figure 74.34 shows a set of such images of backlit grids. [The grids in this case were 25-μm-thick electroetched Ni mesh with a 500/in. pattern (e.g., 50-μm pattern) and 10-μm-square holes.] Grid shots were used to verify the system alignment and provide an *in-situ* measurement of the resolution. Figure 74.34(a) is a DEF-recorded image of a long-pulse (~3-ns) backlit grid, Fig. 74.34(b) is a DEF-recorded image of a short-pulse (~200-ps FWHM Gaussian) backlit grid, and Fig. 74.34(c) is a framing camera–recorded image of a long-pulse backlit grid. Analysis of the images yields MTF's indistinguishable from those shown in Fig. 74.30(b), verifying that the resolution of the microscope is maintained when using a laser–plasma source as a backlighter. Again, spatial resolution of 3 μm is obtained when the radiographs are recorded without the aid of a framing camera.

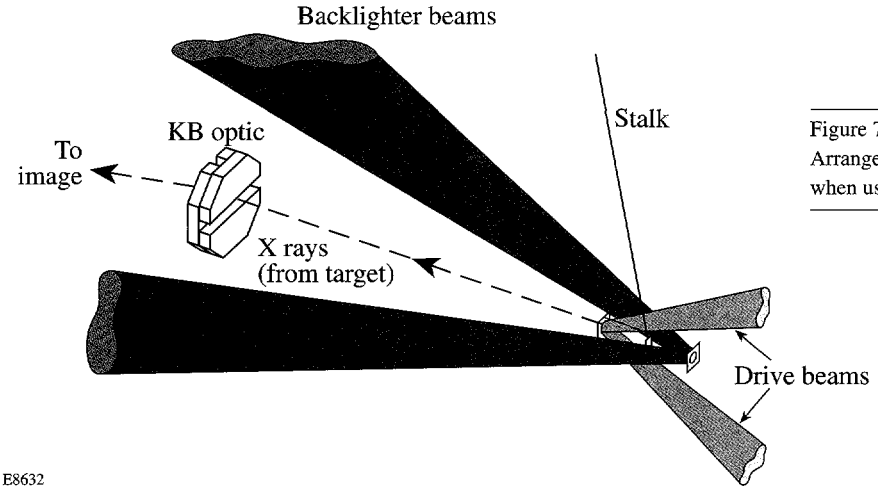

Figure 74.33
Arrangement of KB microscope, target, and beams of OMEGA when used for backlit flat-foil imaging.

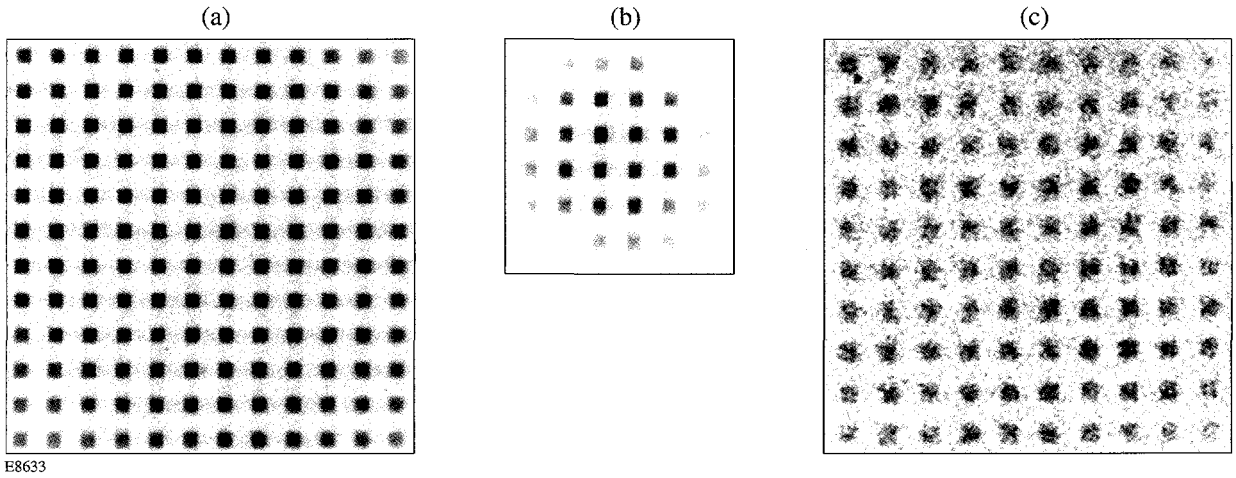

Figure 74.34
Resolution tests performed on the OMEGA laser system. (a) DEF-recorded image of a long-pulse backlit grid; (b) DEF-recorded image of a short-pulse backlit grid; and (c) framing camera–recorded image of a long-pulse backlit grid.

The framing cameras were used to image radiographs of driven perturbed foils. The overall experiments to observe Rayleigh–Taylor (RT) growth are more completely described in Knauer *et al.*[6] Figure 74.35(a) shows a framed image of one such driven foil, which consisted of a 20-μm-thick plastic foil with a 1.0-μm peak-to-valley, 20-μm period modulation on the driven side. The drive intensity was $\sim 2 \times 10^{14}$ W/cm^2. An intensity-converted lineout taken vertically through the image is shown in Fig. 74.35(b). (The values are deviations from the local average intensity.) An observed variation of ~6% peak-to-valley is evident, which is consistent with early-time ($t < 0.5$ ns) modulation, assuming the average energy of the x rays producing the modulation is ~1.25 keV. The image shown in Fig. 74.35 serves as an example of the microscope's capabilities.

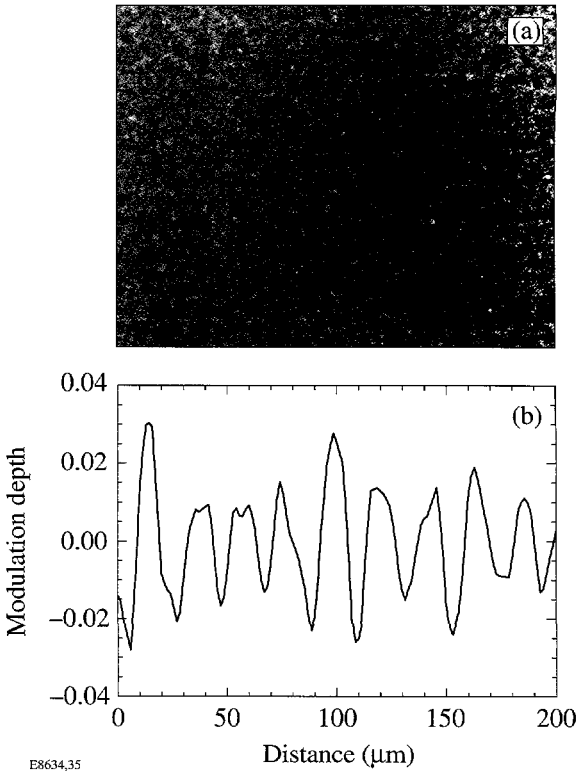

Figure 74.35
Radiograph of driven modulated foil. (a) Framed image of driven foil having an initial modulation depth of 1.0 μm and a 20-μm period; (b) lineout through the image.

Multiple-Beam, Short-Pulse Backlighting

The best possible method for utilizing the high spatial resolution of the KB microscope is to record the radiographs directly with x-ray sensitive film, or with a solid-state device having comparable spatial resolution, as was demonstrated in the preceding section. Since it is necessary to observe the time evolution of the object being radiographed in this instance (i.e., the modulated driven foil), a short-pulse (~100 ps or less) backlighter is required. This can be accomplished on OMEGA with up to six beams, as shown schematically in Fig. 74.36. The short pulses are staggered in time to arrive at the backlighter, spaced by the desired delay, and arranged to backlight the target from separate but nearby directions as seen from the microscope. Since the microscope, as installed in the OMEGA target chamber, is surrounded by six beams, a natural arrangement is for the beams to backlight the driven target in a hexagonal pattern. Tests are currently underway to provide for this experimental configuration on OMEGA.

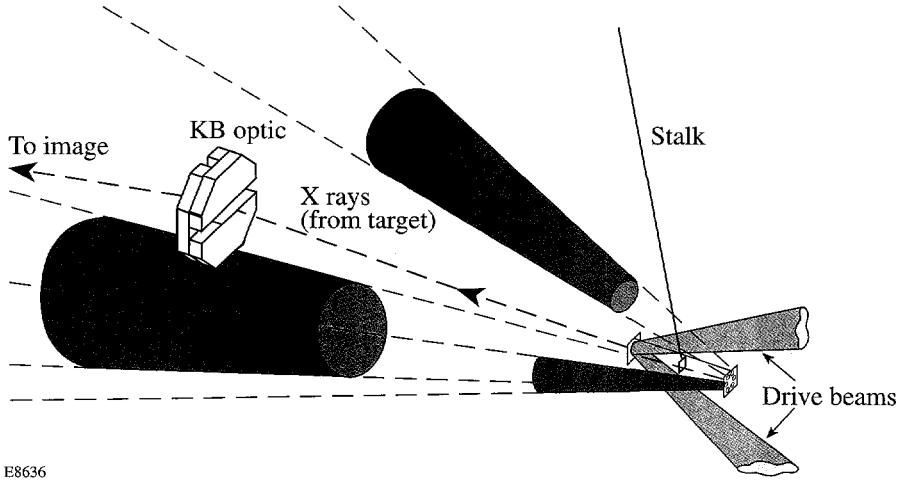

Figure 74.36
Configuration for obtaining multiframe radiographs by multibeam, short-pulse backlighter irradiation.

Conclusions

The KB microscope described in this article has a demonstrated resolution of ~3 μm at optimum focus and a sensitive energy range of ~1 to 3 keV dependent on filtration. When used with a framing camera, the obtainable resolution is degraded to ~7 μm, but with the benefit of ~80-ps time resolution afforded by the cameras. Both high-spatial (~3-μm) and temporal resolution can be obtained by using a multiple-beam, short-pulse backlighter configuration. In conclusion, the KB microscope described here as used in the GMXI is a flexible diagnostic of laser-driven, planar-foil experiments, providing the desired time-resolved, high-spatial-resolution x-ray radiographs.

ACKNOWLEDGMENT

The authors acknowledge the support of the staffs at the Laboratory for Laser Energetics and the Los Alamos National Laborabory. This work was supported by the U.S. Department of Energy Office of Inertial Confinement Fusion under Cooperative Agreement No. DE-FC03-92SF19460, the University of Rochester, and the New York State Energy Research and Development Authority. The support of DOE does not constitute an endorsement by DOE of the views expressed in this article.

REFERENCES

1. J. Grun *et al.*, Phys. Rev. Lett. **58**, 2672 (1987).
2. M. Desselberger *et al.*, Phys. Rev. Lett. **65**, 2997 (1990).
3. S. G. Glendinning, S. V. Weber, P. Bell, L. B. DaSilva, S. N. Dixit, M. A. Henesian, D. R. Kania, J. D. Kilkenny, H. T. Powell, R. J. Wallace, P. J. Wegner, J. P. Knauer, and C. P. Verdon, Phys. Rev. Lett. **69**, 1201 (1992).
4. K. Shigemori *et al.*, Phys. Rev. Lett. **78**, 250 (1997).
5. S. G. Glendinning, S. N. Dixit, B. A. Hammel, D. H. Kalantar, M. H. Key, J. D. Kilkenny, J. P. Knauer, D. M. Pennington, B. A. Remington, R. J. Wallace, and S. V. Weber, Phys. Rev. Lett. **78**, 3318 (1997).
6. J. P. Knauer, C. P. Verdon, D. D. Meyerhofer, T. R. Boehly, D. K. Bradley, V. A. Smalyuk, D. Ofer, P. W. McKenty, S. G. Glendinning, D. H. Kalantar, R. G. Watt, P. L. Gobby, O. Willi, and R. J. Taylor, in *Laser Interaction and Related Plasma Phenomena*, edited by G. H. Miley and E. M. Campbell (American Institute of Physics, Woodbury, NY, 1997), Vol. 406, pp. 284–293.
7. C. Brown *et al.*, Phys. Plasmas **4**, 1397 (1997).
8. S. G. Glendinning *et al.*, Rev. Sci. Instrum. **63**, 5108 (1992).
9. H. F. Robey, K. S. Budil, and B. A. Remington, Rev. Sci. Instrum. **68**, 792 (1997).
10. B. A. Remington *et al.*, Rev. Sci. Instrum. **63**, 5080 (1992).
11. R. Kodama *et al.*, Opt. Lett. **21**, 1321 (1996).
12. F. J. Marshall and Q. Su, Rev. Sci. Instrum. **66**, 725 (1995).
13. J. A. Oertel, T. Archuleta, C. G. Peterson, and F. J. Marshall, Rev. Sci. Instrum. **68**, 789 (1997).
14. T. R. Boehly, D. L. Brown, R. S. Craxton, R. L. Keck, J. P. Knauer, J. H. Kelly, T. J. Kessler, S. A. Kumpan, S. J. Loucks, S. A. Letzring, F. J. Marshall, R. L. McCrory, S. F. B. Morse, W. Seka, J. M. Soures, and C. P. Verdon, Opt. Commun. **133**, 495 (1997).
15. Sydor Optics, Inc., Rochester, NY.
16. P. Kirkpatrick and A. V. Baez, J. Opt. Soc. Am. **38**, 766 (1948).
17. B. L. Henke *et al.*, J. Opt. Soc. Am. B **3**, 1540 (1986).
18. F. J. Marshall and J. A. Oertel, Rev. Sci. Instrum. **68**, 735 (1997).
19. P. Dhez, H. Duval, and J. C. Malaurent, J. X-Ray Sci. Technol. **3**, 176 (1992).
20. A. C. Huber, J. A. Pantazis, and V. T. Jordanov, Nucl. Instrum. Methods Phys. Res. B **99**, 665 (1995).
21. B. L. Henke, E. M. Gullikson, and J. C. Davis, At. Data Nucl. Data Tables **54**, 181 (1993).
22. S. G. Glendinning *et al.*, in *Applications of Laser Plasma Radiation II*, edited by M. C. Richardson and G. A. Kyrala (SPIE, Bellingham, WA, 1995), Vol. 2523, pp. 29–39.

Measurements of Core and Pusher Conditions in Surrogate Capsule Implosions on the OMEGA Laser System

The primary objective of the experimental program at LLE is to evaluate the direct-drive approach to laser-driven inertial confinement fusion (ICF). In particular, its central goal is to validate, by using the 30-kJ, 351-nm, 60-beam OMEGA laser system,[1] the performance of high-gain, direct-drive target designs planned for use on the National Ignition Facility (NIF). This will be achieved by diagnosing the implosion of cryogenic, solid-DT-shell capsules that are hydrodynamically equivalent to the ignition/high-gain capsules planned for use on the NIF with a 1- to 2-MJ drive. In the direct-drive approach to fusion, the capsule is directly irradiated by a large number of symmetrically arranged laser beams, as opposed to the indirect approach in which the driver energy is first converted into x rays, which then drive the capsule. Direct drive has the potential to be more efficient since it does not require this intermediate x-ray conversion step. In both cases the high densities and core temperatures necessary for ignition require that the capsules must be imploded with minimal departures from one-dimensional behavior. For direct-drive capsules, the dominant effect contributing to degradations in capsule performance is believed to be the development of Rayleigh–Taylor (RT) unstable growth,[2] seeded by either laser-irradiation nonuniformities or capsule imperfections.

In a direct-drive capsule implosion, the development of hydrodynamic instabilities occurs in a number of stages. In the start-up, or imprinting, phase the laser is directly incident on the solid capsule surface. Eventually, a plasma is created due to either dielectric breakdown or other processes, a critical surface is formed, and the absorption of laser light sends a series of shocks into the target, eventually causing the shell to move and begin to accelerate. During this initial phase, nonuniformities present in the laser will cause nonuniform shocks to be launched into the target, resulting in imposed modulations and a certain amount of unstable growth during the shock transit period due to Richtmyer–Meshkov[3] (shock-driven) or RT (acceleration-driven) instability. During the subsequent acceleration phase of the implosion, RT growth continues to grow at the ablation surface with a growth rate that can be approximated by[4,5]

$$\gamma = \alpha\sqrt{[kg(t)]} - \beta k V_a(t), \tag{1}$$

where k is the unstable wave number, $g(t)$ is the acceleration, and $V_a(t)$ is the ablation velocity. The distortions that grow at the ablation surface can eventually feed through to the inner surface of the shell, where they add to any existing mass perturbations, thus seeding an instability that can grow at that surface as the target begins to decelerate during stagnation. If the resultant distortions are large enough, the performance of the capsule will be severely compromised. An integrated understanding of hydrodynamic instabilities, fuel–pusher mix, and their effect on capsule performance requires quantitative data and a study of the processes involved in each phase.

In this article we present the results of direct-drive experiments carried out on OMEGA to investigate each of the stages described above. First, we summarize the results of experiments designed to study the imprint and acceleration stages, in both planar and spherical geometries. Next we present the first phase of the investigation of the deceleration stage. [This stage has previously been investigated in indirectly driven targets at the Lawrence Livermore National Laboratory (LLNL) using plastic targets with an inner layer of Ti-doped CH and an Ar-doped D_2 fill.[6–8]] The goal of our initial experiments was to ensure that our diagnostics could measure the conditions in both the core and the shell during shell deceleration and stagnation and that they had enough sensitivity to observe differences in core conditions under various RT-growth conditions. The RT growth was modified by varying the temporal pulse shape (Gaussian or square) and by doping the outer 6 μm of the CH shell with chlorine.

The deceleration stage was studied by irradiating ~1-mm-diam, 20-μm-thick CH shells with 30 kJ of 351-nm, 1-ns laser pulses. No smoothing techniques were applied to the laser beams. The one-dimensional simulations of the experiments were carried out with the hydrodynamic code *LILAC*,[9] which includes ray tracing of the laser light, SESAME[10] equations of state, multigroup radiation transport, and non-LTE average-

ion capability. A few simulations were carried out with the two-dimensional code *ORCHID*[11] to investigate qualitatively the effect of the RT growth on the target during the acceleration, deceleration, and stagnation of the shell.

Imprint and Acceleration Phases

Direct measurements of laser imprinting are extremely difficult, although Kalantar *et al.*[12] have reported measurements of imprint in thin Si and Al foils using an x-ray laser as a backlighter. Measurements on OMEGA to date have relied on the technique of x-ray radiography of laser-accelerated CH foils in planar geometry,[13–17] using a uranium backlighter with an average photon energy of ~1.3 keV. Modulations in the optical depth of the driven foil measured at different times by an x-ray framing camera are used to observe the growth of perturbations seeded by imprinting. However, since the initial perturbations created by the laser imprint are too small to be measured directly by this method, the optical-depth measurements are not taken until the foil has accelerated and undergone a significant amount of RT growth in order to amplify the initial perturbation to detectable levels. This measurement therefore incorporates the combined effects of the imprint phase, shock transit phase, and a portion of the acceleration phase. Despite the complication added by the RT growth, such measurements are invaluable for comparing the effects of irradiation-uniformity changes, beam-smoothing techniques, and other mitigation schemes.

Face-on radiography of foils with intentionally imposed single-mode, sinusoidal mass perturbations were used to compare calculated RT-growth rates with experimental measurements. (These experiments are a continuation of the collaboration between LLE and LLNL.[14] Similar experiments have also been performed in indirect drive.[18]) In these measurements an x-ray streak camera or framing camera is used to measure the optical depth of the imposed mode as a function of time in much the same way as in the imprint measurements. In addition, side-on measurements of foil trajectory were used[19] to confirm that coupling of laser energy into the foils was in agreement with simulations. Results from single-mode experiments carried out on OMEGA are shown in Fig. 74.37. In these plots, the optical depth of the observed modulation of the backlighter, as seen through the accelerated foil, is plotted as a function of time, together with predictions from the 2-D hydrodynamic code *ORCHID*. (A more detailed description of this data can be found in Ref. 19.) The excellent agreement between the experimental data and the simulations is strong evidence that, for polymer materials, the RT unstable growth can be calculated accurately.

In spherical target experiments, where there is no diagnostic access to the rear surface of the shell, we have inferred the development of instability growth at the ablation surface during the acceleration phase through use of the so-called "burnthrough" technique.[20] In this method, time-resolved

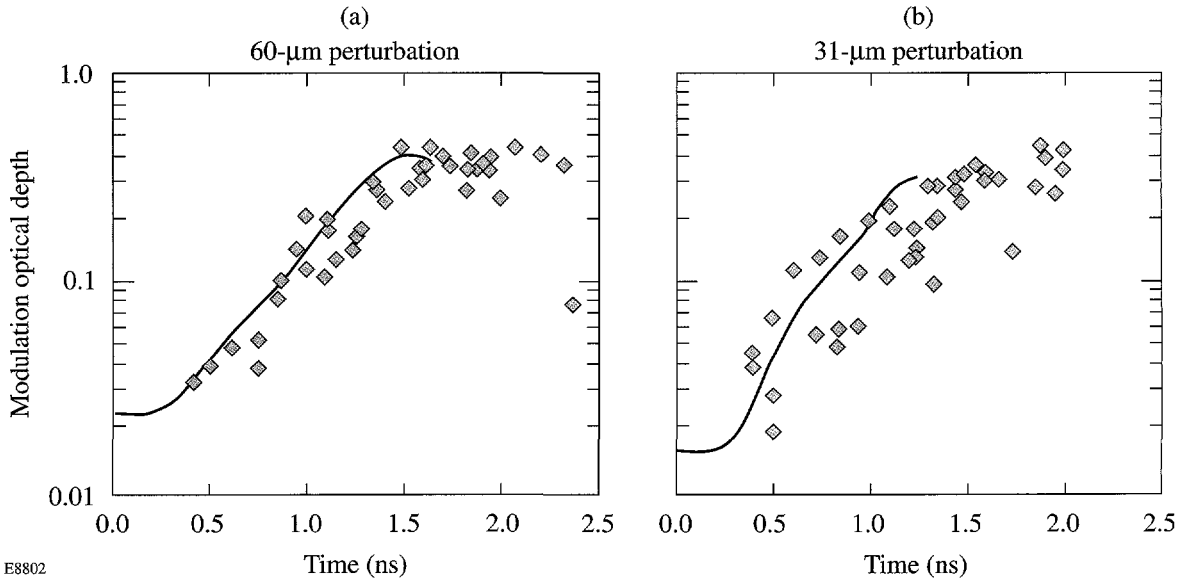

Figure 74.37
Results from the single-mode planar experiments (◆) conducted on the OMEGA laser compared to *ORCHID* simulations (solid line) for (a) 60-μm and (b) 31-μm perturbation wavelengths.

spectroscopy, using a spectrally dispersing x-ray streak camera, is used to detect the onset of x-ray emission from a buried signature layer. In the absence of any unstable growth or perturbation, the heat front propagates uniformly through the CH ablator until it reaches the signature layer and heats it, resulting in characteristic x-ray line emission. The presence of unstable growth, however, produces a mix region that can leach signature layer material out to the heat front, causing early emission. This method has been shown to be very sensitive to initial beam uniformity[21] and to target acceleration and effective Atwood number.[20] As with the planar-foil imprint measurements, this method measures the combined effects of imprint coupled with RT growth.

We conducted a series of burnthrough experiments with unsmoothed laser beams to provide a baseline for subsequent uniformity improvements scheduled for the OMEGA laser system. The targets used chlorinated plastic (C_8H_7Cl) as the signature layer, with CH ablator overcoats ranging from 8 to 12 μm. The target diameters were 900 to 950 μm, and in all cases the total shell thickness was 20 μm. The capsules were overcoated with a 1000-Å Al barrier layer to act as a timing reference mark and to prevent shinethrough[22] of the early part of the laser pulse into the target before formation of the critical surface. In these experiments, the targets were imploded by 60 beams, focused tangentially to the target, with a 1-ns full-width-at-half-maximum (FWHM) Gaussian temporal profile and a total of 20 to 25 kJ. Spectral dispersion for the x-ray streak camera was provided by a flat rubidium acid phthalate (RbAP) crystal, providing coverage of the *K*-shell spectrum of the Al overcoat in first-order Bragg diffraction, simultaneous with coverage of chlorine lines in second order. The data from these experiments, together with a typical streak camera image, are shown in Fig. 74.38(a). The time-resolved spectrum [Fig. 74.38(a)] shows Al lines, formed when the laser is initially incident on the outside of the capsule, and, after a delay of several hundred picoseconds, emission from the buried C_8H_7Cl layer. The measurements have been modeled using a postprocessor to *LILAC* that calculates the mix thickness using the Haan[23] method from an experimentally measured initial perturbation spectrum. (Full details of the model are given in Ref. 20.) Figure 74.38(b) shows a comparison of the experimental burnthrough times and those predicted by the model, as a function of CH ablator thickness. The two cases were normalized for one of the 9-μm cases. Variations in burnthrough time for a given ablator thickness are caused primarily by laser energy variations between shots. The burnthrough times predicted by *LILAC* for the uniform 1-D case are also shown and

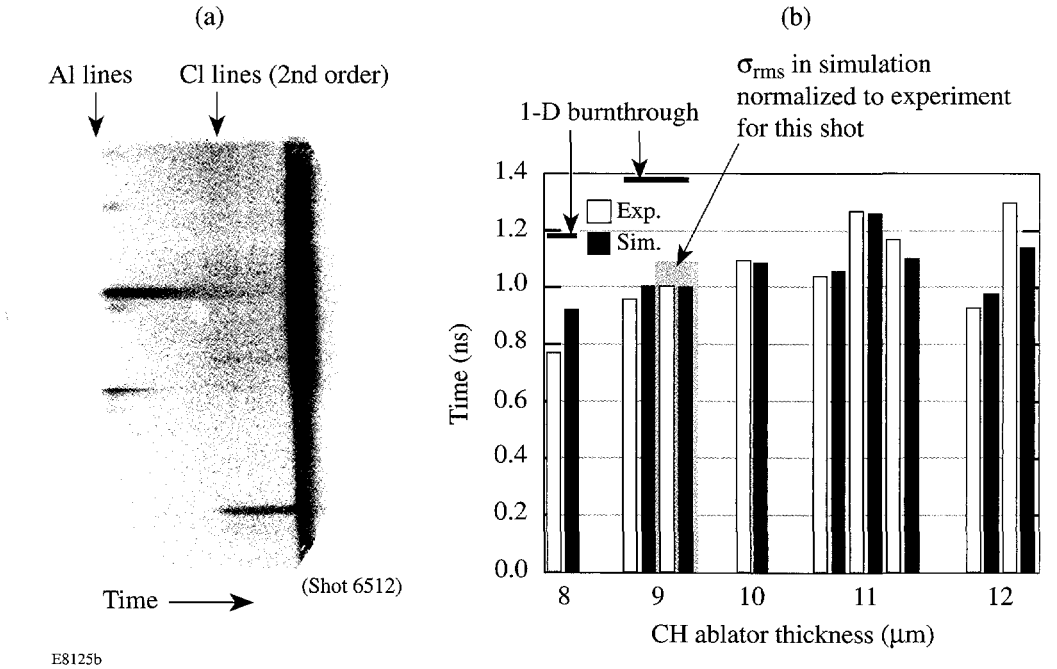

Figure 74.38
Results from burnthrough experiments carried out on the 60-beam OMEGA laser. (a) The streak camera spectrum shows the onset of the Cl lines from the Cl-doped substrate at the time of burnthrough. (b) Burnthrough times from the mix postprocessor to *LILAC* are compared to the experimental data for targets with increasing ablator thickness.

indicate that much-later-than-observed burnthrough would be expected for the 8- and 9-μm ablators, with no burnthrough expected for the thicker cases. The good agreement between the simulations and the experiment over a range of target parameters confirms our confidence in the model and shows that we are now well placed to diagnose planned improvements to laser uniformity.

Deceleration Phase

Initial measurements on deceleration-phase instability utilized a series of surrogate capsules, consisting of a CH shell filled with deuterium gas. These targets are designed to mimic the behavior of future OMEGA cryogenic DT capsules (and, by extension, NIF ignition capsules) by approximating their gross hydrodynamic behavior (e.g., similar in-flight aspect ratio and convergence). For the purposes of these experiments, the CH shell represents the main-fuel-layer region in a cryogenic ignition target, and the D_2 gas represents the fuel hot spot. Figure 74.39 shows the standard capsule we have used to investigate these two regions. The hot spot, or in our case the gas region, consists of 20 atm of D_2, doped with 0.25% Ar as a spectroscopic signature. The shell consists of a 20-μm CH layer in which is buried a 1-μm layer of (1%–4%) Ti-doped CH. The doped layer can be positioned at various distances from the shell/D_2 interface, allowing the study of conditions at different positions inside the shell/main fuel layer. This differs from the method described in Ref. 6, in which the Ti-doped layer was situated only at the pusher/fuel interface.

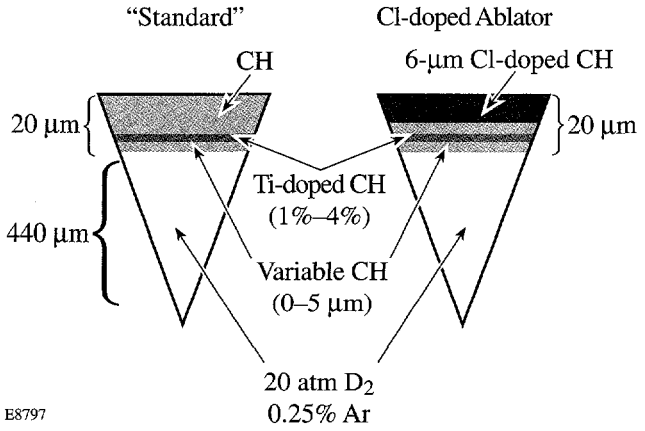

Figure 74.39
"Standard" and Cl-doped-ablator targets used during the deceleration phase experiments. The distance from the Ti-doped layer and the inner surface of the shell can be varied from 0 to 6 μm.

For future experiments the single-beam uniformity on the OMEGA laser system will be improved such that the on-target irradiation uniformity will be <1% σ_{rms}. This will be achieved through the use of distributed phase plates (DPP's),[24] 2-D smoothing by spectral dispersion (2-D SSD),[25] and distributed polarization rotators (DPR's).[26] However, current uniformity levels using unsmoothed beams are predicted to be in the region of 20% or more. To predict the effect these nonuniformities might have on capsule implosions, simulations were performed using the 2-D hydrodynamic code *ORCHID*. The simulations used the actual laser-beam nonuniformity spectrum, measured from single-beam, equivalent-target-plane (ETP) images mapped onto a sphere with the appropriate overlap parameters. Even modes 2 to 200 were consistent with each mode multiplied by $\sqrt{2}$ to account for the odd modes. Figure 74.40 shows predicted mass-density profiles at a time when the shell has reached half its initial radius for two cases: a 1-ns square pulse and a 1-ns FWHM Gaussian. In each case the shell is already showing signs of severe disruption, with the structure in the Gaussian case exhibiting longer-wavelength structures. For both cases the outside of the shell is more perturbed than the inside. As a check on the *ORCHID* predictions, we carried out a number of planar-target radiography experiments, using unmodulated foils of similar thickness (20 μm) and driven with similar intensities to the spherical targets. Figure 74.41 shows radiographs recorded on the x-ray framing camera for both the 1-ns square pulse and the 1-ns Gaussian, together with the predicted foil trajectories in each case. The radiographs show qualitative agreement with the *ORCHID* simulations in Fig. 74.40, both in terms of the type of structure seen and the fact that the Gaussian pulse shows longer-wavelength structure. Note that the Gaussian case is significantly more nonuniform despite having undergone less displacement. This is primarily due to the fact that the Gaussian pulse is predicted to imprint a factor of about 2.5 larger than the square pulse. The growth rates in the two cases are similar since the higher acceleration resulting from the square pulse is compensated by a higher ablation velocity. For an imploding target the growth factor will be larger for a Gaussian pulse because the shell will take longer to reach the same radial position.

Clearly implosions driven by these levels of nonuniformity are expected to be severely disrupted. For comparison purposes only, we investigated a series of targets in which the outer 6 to 7 μm of the ablator was replaced with C_8H_7Cl. The presence of chlorine in the ablator serves to radiatively heat the shell, causing it to decompress. The resultant reduction in peak shell density causes an increase in the ablation velocity V_a, thereby reducing the RT growth [see Eq. (1)]. (It should,

however, be pointed out that the radiation preheat in such a target does reduce the convergence ratio and 1-D performance of the implosion.) Figure 74.42 shows the *ORCHID* simulation for a target with a Cl-doped ablator. Comparison with Fig. 74.40 shows a clear improvement in the shell uniformity. This improvement is also in agreement with experimental measurements detailed in Ref. 20, in which delayed burnthrough times were observed for targets with Cl-doped ablators. *ORCHID* simulations near the time of peak compression are shown in Fig. 74.43. The undoped shell in Fig. 74.43(a) shows that although the core region appears to form relatively uniformly, the shell is clearly severely disrupted. In contrast, Fig. 74.43(b) shows a shell that is still relatively intact, although still not entirely uniform.

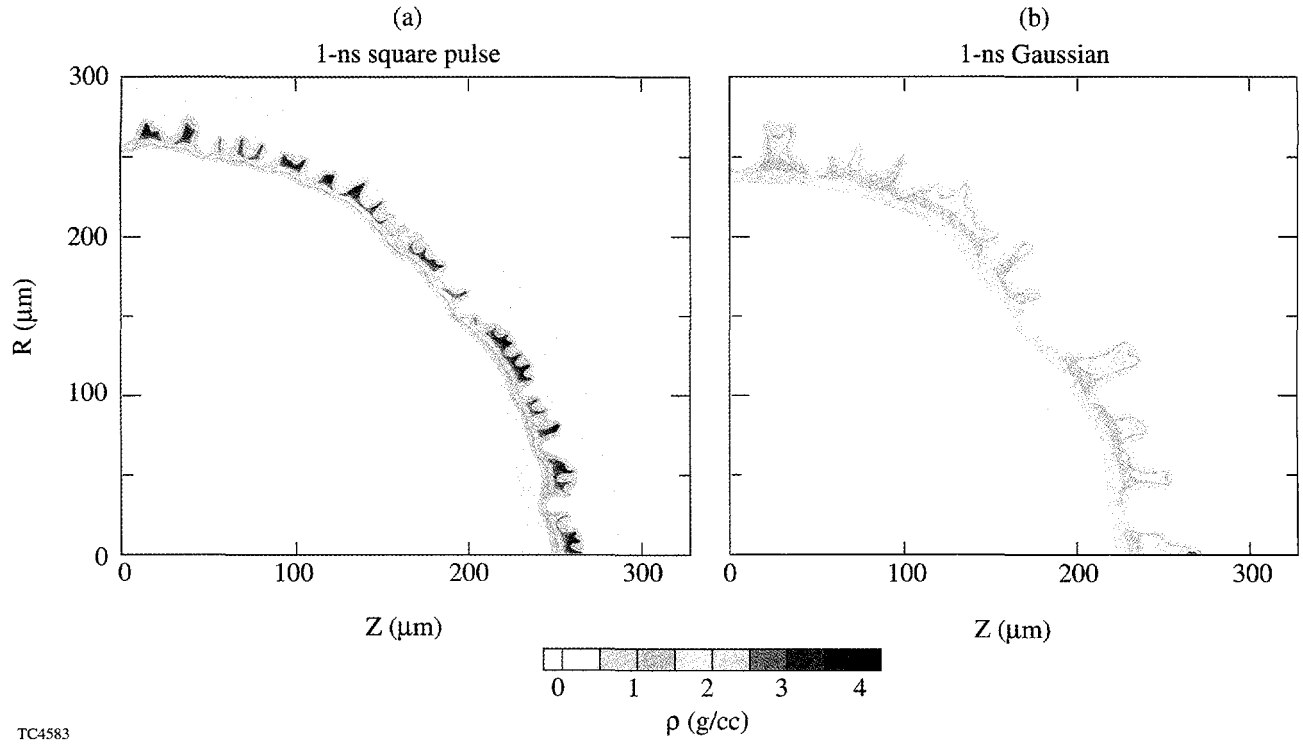

Figure 74.40
Shell conditions from *ORCHID* simulations compared for (a) a 1-ns square pulse and (b) a 1-ns Gaussian pulse irradiating the standard target. The actual laser beam nonuniformity measured from ETP images was used. The contours are for the mass density.

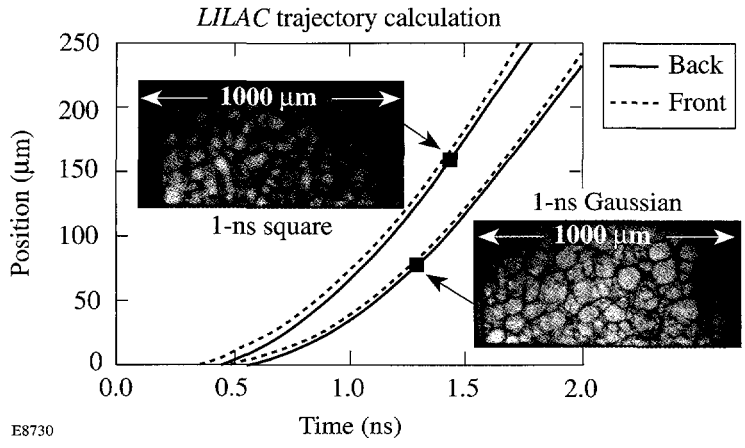

Figure 74.41
Backlit images from an experiment in which five unsmoothed OMEGA beams were focused on a planar 20-μm CH target confirm qualitatively the *ORCHID* simulation results in Fig. 74.40. The zero time for the Gaussian pulse is at 10% of peak intensity.

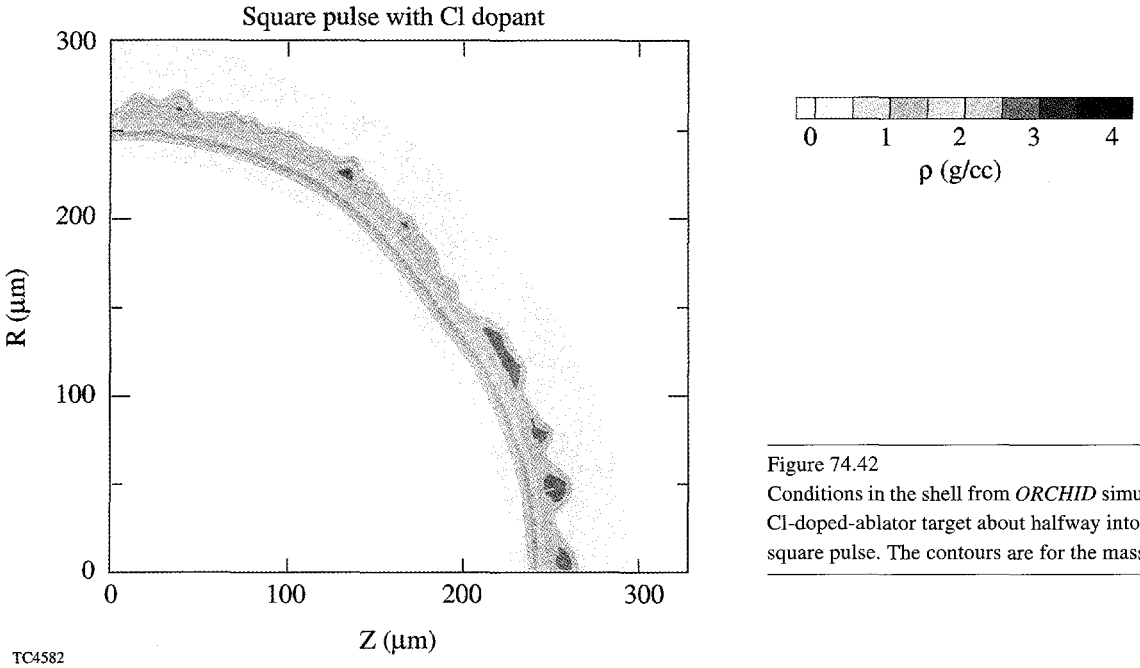

Figure 74.42
Conditions in the shell from *ORCHID* simulations compared for the Cl-doped-ablator target about halfway into the implosion for a 1-ns square pulse. The contours are for the mass density.

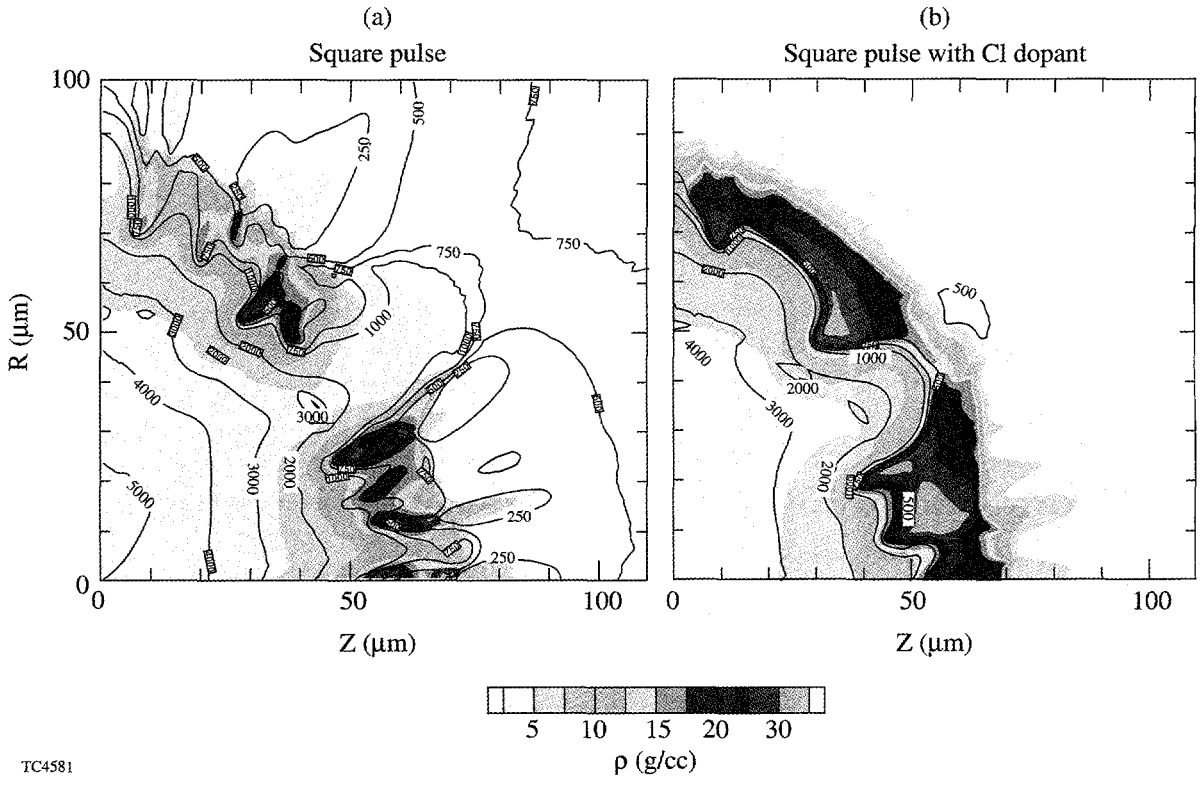

Figure 74.43
Core conditions from *ORCHID* simulations compared for (a) the standard target and (b) the Cl-doped target near time of peak core density for a 1-ns square pulse. The filled contour areas denote the mass density levels and the contour lines denote the electron temperature levels.

The experimental implosions were analyzed using a large number of diagnostics. Time-resolved imaging of the later stages of the shell trajectory and the core formation was recorded using a gated x-ray pinhole camera,[27,28] filtered to record emission >2 keV. Figure 74.44 shows a comparison of the measured shell and core radii as a function of time, compared with 1-D *LILAC* simulations. This comparison demonstrates our ability to reproduce the zeroth-order hydrodynamics of the implosion. Time-resolved x-ray spectra from the targets were recorded using a pair of streaked spectrographs. Both instruments used a RbAP crystal to disperse the spectrum onto a 250-Å Au photocathode. One spectrometer was set up with a wavelength range of ~2.8 to 4.3 Å to cover the Ar *K*-shell emission from the core, with the other spectrometer covering Ti and Ar emission in the approximate range of 1.9 Å to 3.4 Å. In each case the spectral resolution was approximately $E/\Delta E \sim 500$. Temporal resolution was 20 to 30 ps, depending on the camera used. The data were recorded on Kodak T-max 3200 film, digitized using a PDS microdensitometer and then corrected for film sensitivity and streak-camera–induced temporal curvature.[29] The sweep speed of each streak camera was measured using a temporally modulated fiducial pulse, although no absolute timing reference was used during actual target shots. The spectrometer dispersion was calculated using published wavelengths for the Ar and Ti lines.

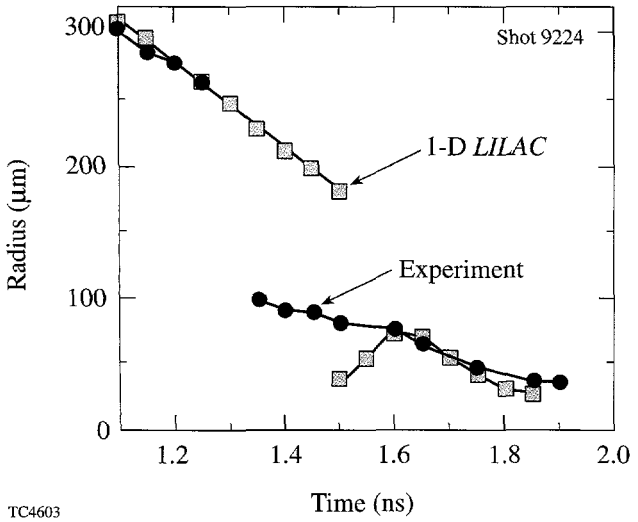

Figure 74.44
Trajectories of the peak emission from the framing camera images and from simulated images. The jump in the middle of the trajectories occurs when the peak emission moves from the heat front to the core.

Figure 74.45 shows a pair of time-resolved x-ray spectra recorded from the doped target implosions, one from a target with the Ti-doped layer at the gas/shell interface and the other with the Ti-doped layer situated 4 μm from the interface. In both streaks, Ar line emission, resulting from the initial shock heating of the core gas, appears first, followed by continuum emission from the stagnation. In Fig. 74.45(a), Ti He-like and H-like line emission from the inside surface of the shell can be seen a short time after the Ar emission, whereas the Ti in the buried layer is observed only in absorption. This absence of line emission occurred even when the Ti-doped layer was as close as 0.5 μm from the interface. Targets with a Cl-doped ablator showed little or no Ti emission, regardless of the position of the layer, in agreement with *LILAC* predictions.

The absorption feature seen in Fig. 74.45(b) around 4.6 keV corresponds to unresolved transitions of the type $1s$–$2p$ in titanium ions with incomplete L shells: Ti^{+13} to Ti^{+20}, formed when continuum from the core traverses the cold titanium layer. The envelope of the absorption feature, which changes as a function of time, indicates the ion specie of maximum abundance. The amount of absorption depends primarily on the areal density of the absorption region, but also on its temperature T and density ρ. It has been shown, however, that the measured integral over the absorption feature, together with the knowledge of the ion of peak absorption (which also depends on both T and ρ) can yield the areal density to within ±25% without knowing the temperature or the density.[30,31] Typical data is plotted in Fig. 74.46, together with the $\rho\Delta R$ predicted by *LILAC* for both a CH and a Cl-doped ablator. The measured areal density for the "standard" capsule case approximately follows the continuum emission and falls well below the *LILAC* prediction. This is not entirely surprising, based on the shell disruptions seen in Fig. 74.43(a). It is also possible that for such a severely distorted shell, low-density "holes" in the shell will cause the inferred areal density to be underestimated because the unabsorbed background signal distorts the spectrum. In contrast, the $\rho\Delta R$ measurements in Fig. 74.46(b) approach more closely to the 1-D simulations. In this shot, the timing of the density peak, delayed relative to the continuum emission, shows one of the limitations to this method since in the absence of any continuum emission we are unable to measure the $\rho\Delta R$ by absorption methods.

Measurements of the core/hot-spot region were carried out using both neutron-based and x-ray spectroscopic measurements. The burn history of these capsules was measured using the neutron temporal diagnostic (NTD).[32,33] Neutron collisions with a BC-422 plastic scintillator convert neutron kinetic

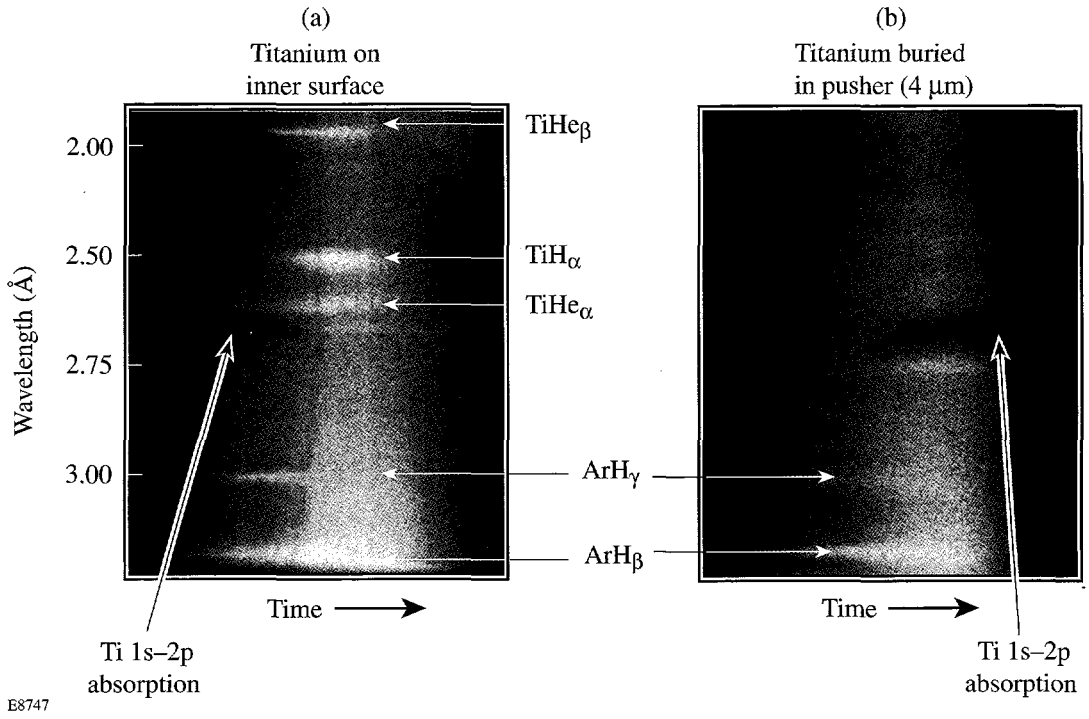

Figure 74.45
Time-resolved spectra for two positions of the Ti-doped layer for a standard target and a 1-ns square pulse: (a) at the inner surface and (b) 4 μm from the inner surface.

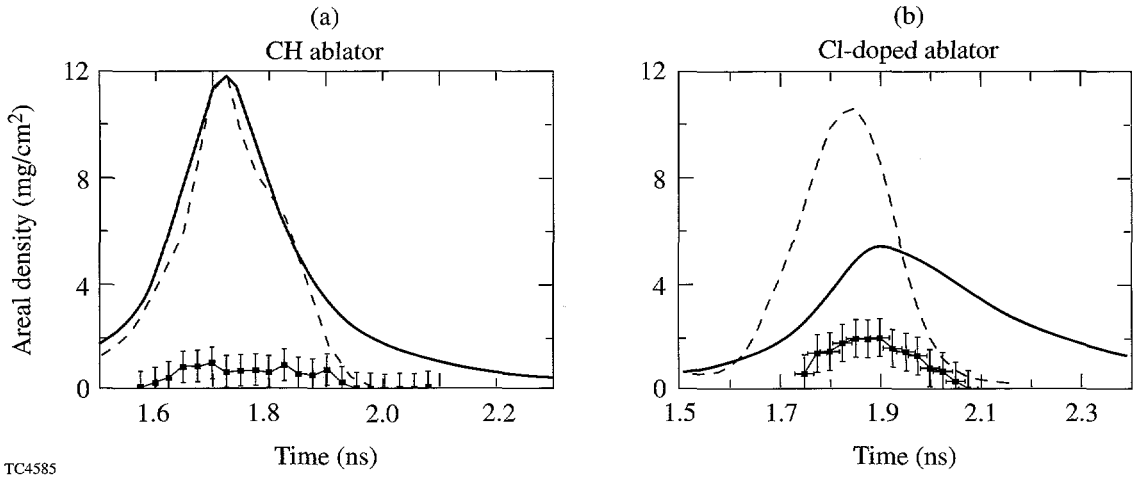

Figure 74.46
Areal densities obtained from the Ti absorption band (curve with error bars) and from the 1-D *LILAC* simulation (solid line) as a function of time for (a) the standard target and (b) the Cl-doped-ablator target. In both cases the Ti-doped layer was 4 μm from the inner surface. Also shown is the integrated continuum emission (dashed line) from the measured spectrum. Timing was made by matching the measured and predicted continuum peaks. The areal density can be measured only when the core emits continuum radiation.

energy to 350- to 450-nm-wavelength light, which is relayed to the photocathode of a fast streak camera whose output image is recorded by a charge-coupled device (CCD) camera. The temporal distribution of the emitted light is the convolution of the neutron emission history with the scintillator response; thus, the burn history is encoded in the leading edge of the light pulse. (The streak camera also records an optical fiducial signal to provide an absolute time base.) The shape of the neutron temporal distribution is obtained by deconvolving the effect of the scintillator decay rate from the recorded neutron signal. The quality of each deconvolution is checked by comparing the recorded signal with the convolution of the burn history and the exponential decay of the scintillator. Streak camera flat-field and time-base corrections are included in the signal processing. On OMEGA, NTD has demonstrated sensitivity to DD neutrons at yields above 1×10^8 and a temporal resolution of 25 ps. Figure 74.47(a) shows the measured neutron-production rate for a shot with a CH ablator, together with the rate predicted by *LILAC*. The rates agree fairly well early in time, when neutron production is dominated by the initial shock heating and compression, but as the implosion progresses toward full stagnation, where neutrons will be produced mainly by compression heating of the core, the measured rate falls significantly short of the 1-D predictions by a factor of about 20 to 30. We are, however, able to see a significant difference for implosions with the Cl-doped ablator [Fig. 74.47(b)]. In this case the predicted yield is lower due to radiative losses and preheating of the core. The measured neutron-production rates, however, come much closer to the simulations (a factor of 4 to 5 at peak production), although the experimental yield still cuts off earlier than the simulations.

Additional measurements of conditions inside the core were carried out by spectroscopic analysis of the *K*-shell line emission from the argon dopant.[34,35] For temperature and density regimes typically found in these implosions close to stagnation, the line shapes emitted by the *K*-shell argon ions depend strongly on electron density, while remaining relatively insensitive to changes in temperature. This fact combined with the temperature and density dependence of the relative intensity of the *K*-shell lines and their associated *L*-shell satellites allows the use of the argon line spectrum as an indicator of electron density and temperature. The effects of opacity broadening on the utility of this diagnostic are mitigated by the small concentration of argon in the fuel.

Stark-broadened line profiles for the argon He-γ, He-δ, and Ly-β resonant transitions and associated Li-like satellites were calculated using a second-order quantum mechanical relaxation theory.[36,37] These line profiles were combined using relative intensities derived from a detailed non-LTE kinetics code[38] corrected for the effects of radiative transfer using an escape-factor approximation.[39] The final state populations of the lines in the model were also derived from the results of the kinetics code. Source size was derived by assuming the emission was that of a homogeneous spherical region whose size was determined consistently with the electron number density. The Stark-broadened line profiles were cor-

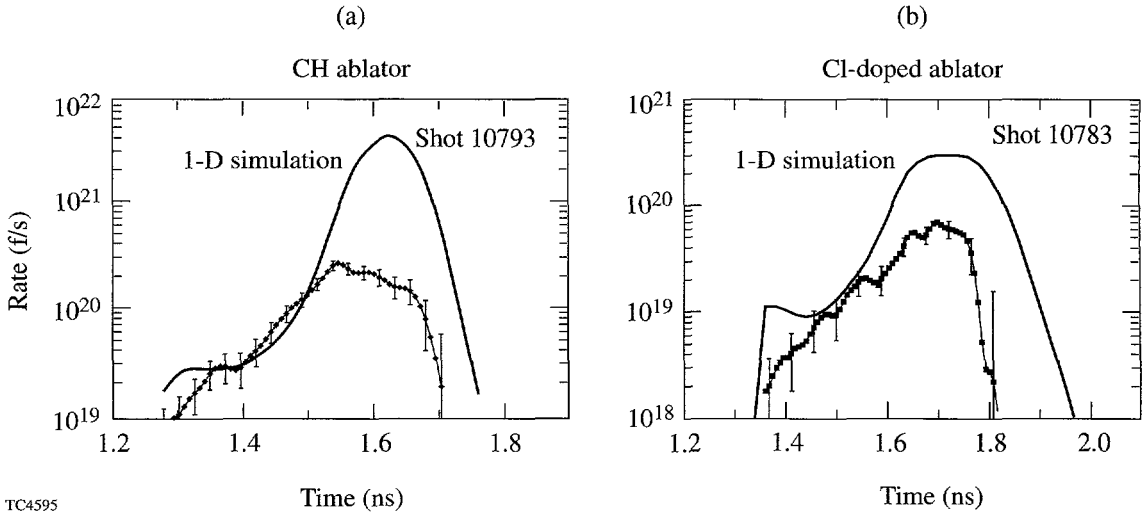

Figure 74.47
Neutron production rate obtained from the neutron temporal diagnostics (NTD) (curve with error bars) and from 1-D *LILAC* simulations (solid line) for (a) the standard target and (b) the Cl-doped-ablator target.

rected for the effects of opacity using a slab opacity model.[40] A similar theoretical spectrum was used in the analysis of the argon He-β line and its associated lithium-like satellites in Ref. 35. An example of the fits for shot 10778 is shown in Fig. 74.48. Comparison of the theoretical spectrum, after convolution with an appropriate instrumental response function, with time-resolved experimental spectra leads to an inference of the emissivity-averaged plasma electron temperature and density. Differences between the best-fitting theoretical spectrum and the experimental spectrum indicate the possible existence of gradients in the strongly emitting region of the plasma.

Figure 74.49 shows inferred electron temperature and density measurements as a function of time for the CH ablator target, imploded with the 1-ns square pulse. The temperatures and densities agree fairly well with the 1-D *LILAC* predictions at early times, but as the stagnation progresses, both parameters fall well short of the ideal case. These results are in qualitative agreement with the fusion-rate measurements. For the Cl-doped ablator (Fig. 74.50), the agreement between experiment and 1-D simulation is much closer, although the temperature still reaches only 75% of predicted.

Discussion and Conclusion

We have presented results that are part of an integrated program to investigate the physics of direct-drive ICF capsule implosions. Imprint and RT growth have been investigated in planar geometry using radiography of accelerated foils. The growth rates measured for CH foils are in excellent agreement with hydrocode simulations. The physics of the deceleration phase has been studied using a series of doped surrogate capsules. The main goal of these experiments was to develop techniques to diagnose the conditions in the shell (main fuel layer) and in the core (hot spot). The shell has been diagnosed using time-resolved spectroscopy of a Ti-doped tracer layer. With unsmoothed beams, experiments and simulations indicate that the shell is severely disrupted at time of shock convergence. When a Cl-doped ablator was used, the $\rho\Delta R$ inferred from the Ti absorption feature was much closer to 1-D predictions, confirming our diagnostic sensitivities to changes in target performance. These observations support the *ORCHID* simulations, which predict that the addition of a Cl-doped ablator results in a more intact shell.

The core has been diagnosed by both time-resolved neutron diagnostics and time-resolved spectroscopy of the Ar fuel dopant. From the analysis of the Ar line emission we find that the core conditions (electron densities and temperatures) just after the shock has reached the target center are close to those predicted by 1-D *LILAC* simulations. The same conclusion is reached from the analysis of the neutron-production rate. These conclusions are in qualitative agreement with *ORCHID* simulations, which predict near-spherical temperature profiles in the core. Conditions in the core deteriorate during compression and stagnation: both the electron temperature and density fail to reach *LILAC* predictions. This deterioration in core conditions occurs for both the square pulse and the Gaussian

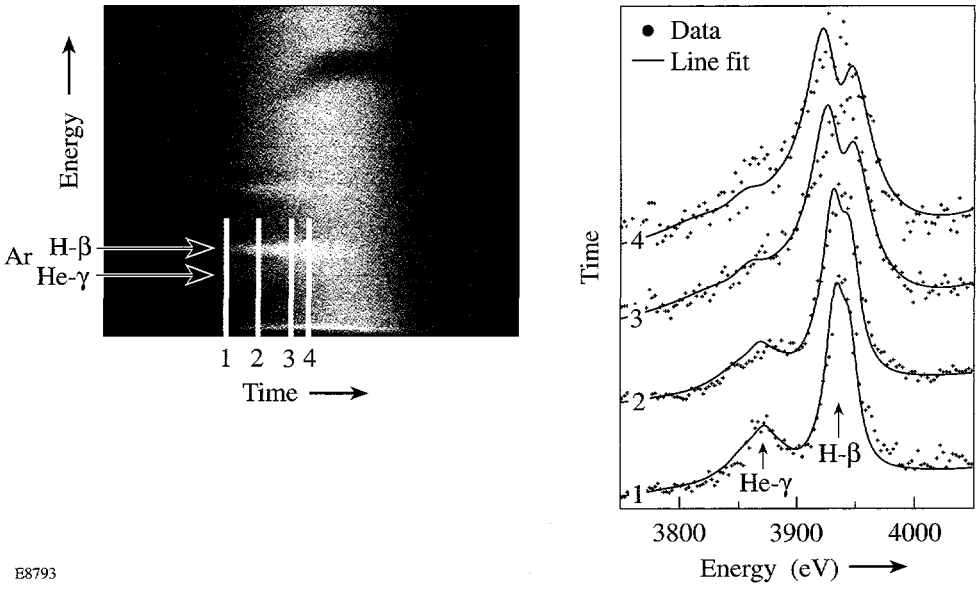

Figure 74.48
Time-resolved experimental spectrum and lineouts of the Ar H-β and He-γ lines for four times. The dots are the experimental values, and the lines are best fits from a quantum theory model combined with a non-LTE kinetics code[36–39] for a given electron temperature and density.

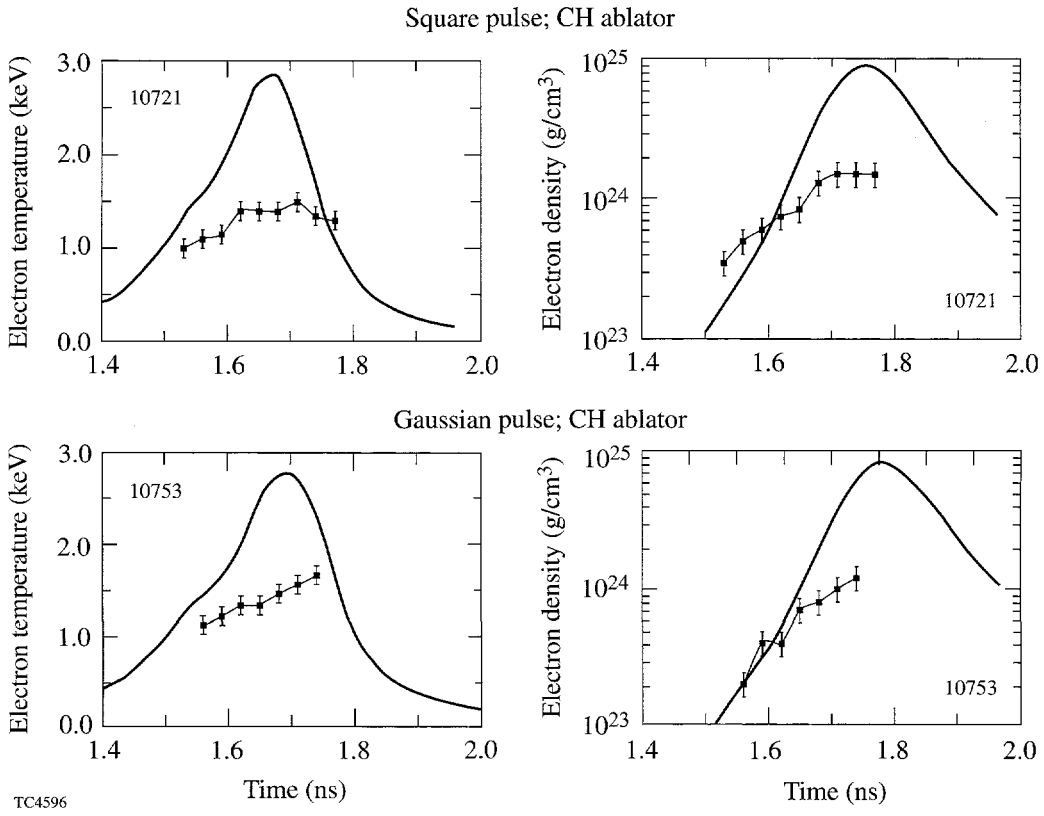

Figure 74.49
Measured and predicted electron temperatures and densities for the standard target for 1-ns square and Gaussian pulses. The predicted temperatures are mass-averaged temperatures from 1-D *LILAC* simulations (solid line).

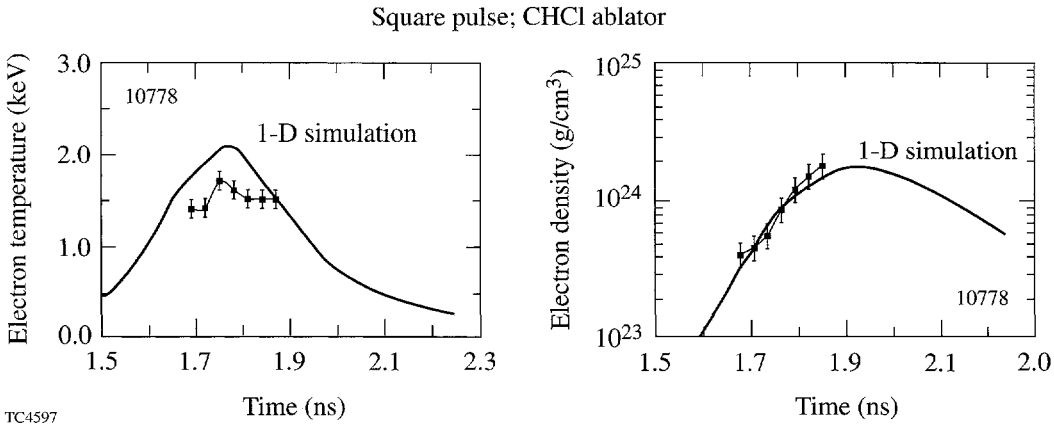

Figure 74.50
Measured and predicted electron temperatures and densities for the standard target and a Cl-doped-ablator target for a square pulse. The predicted temperatures are mass-averaged temperatures from 1-D *LILAC* simulations (solid line).

pulse. These observations indicate that final compression and resulting PdV work are not effective because the shell is probably not integral. Both diagnostics—time-resolved spectroscopy and neutron time detector—showed results that were closer to 1-D predictions when a Cl-doped ablator was used in agreement with simulations that predict reduced RT growth for those targets. The agreement between neutron and x-ray diagnostics is encouraging since cryogenic targets will be diagnosed primarily by neutron and charged-particle methods.

In conclusion, we have carried out initial mix implosion experiments with the unsmoothed OMEGA laser system to establish a base-line database for comparison with upcoming experiments in which full beam smoothing will have been implemented. We have also ascertained that the set of diagnostics used in these experiments can measure shell and core conditions and will enable us to study the effect of the RT instability on the main fuel layer (shell) and hot spot (core) in cryogenic targets.

ACKNOWLEDGMENT

This work was supported by the U.S. Department of Energy Office (DOE) of Inertial Confinement Fusion under Cooperative Agreement No. DE-FC03-92SF19460, the University of Rochester, and the New York State Energy Research and Development Authority. The support of DOE does not constitute an endorsement by DOE of the views expressed in this article.

REFERENCES

1. T. R. Boehly, D. L. Brown, R. S. Craxton, R. L. Keck, J. P. Knauer, J. H. Kelly, T. J. Kessler, S. A. Kumpan, S. J. Loucks, S. A. Letzring, F. J. Marshall, R. L. McCrory, S. F. B. Morse, W. Seka, J. M. Soures, and C. P. Verdon, Opt. Commun. **133**, 495 (1997).
2. Lord Rayleigh, Proc. London Math. Soc. **14**, 170 (1883); G. Taylor, Proc. R. Soc. London Ser. A **201**, 192 (1950).
3. R. D. Richtmyer, Commun. Pure. Appl. Math. **XIII**, 297 (1960); E. E. Meshkov, Izv. Akad. Nauk. SSSR Mekh. Zhidk. Gaza **4**, 33 (1970).
4. H. Takabe *et al.*, Phys. Fluids **28**, 3676 (1985).
5. R. Betti, V. N. Goncharov, R. L. McCrory, P. Sorotokin, and C. P. Verdon, Phys. Plasmas **3**, 2122 (1996).
6. O. L. Landen *et al.*, J. Quant. Spectrosc. Radiat. Transfer **54**, 245 (1995).
7. C. J. Keane *et al.*, J. Quant. Spectrosc. Radiat. Transfer **54**, 207 (1995).
8. O. L. Landen *et al.*, Phys. Plasmas **3**, 2094 (1996).
9. M. C. Richardson, P. W. McKenty, F. J. Marshall, C. P. Verdon, J. M. Soures, R. L. McCrory, O. Barnouin, R. S. Craxton, J. Delettrez, R. J. Hutchison, P. A. Jaanimagi, R. Keck, T. Kessler, H. Kim, S. A. Letzring, D. M. Roback, W. Seka, S. Skupsky, B. Yaakobi, S. M. Lane, and S. Prussin, in *Laser Interaction and Related Plasma Phenomena*, edited by H. Hora and G. H. Miley (Plenum Press, New York, 1986), Vol. 7, pp. 421–448.
10. B. I. Bennett *et al.*, Los Alamos National Laboratory Report LA-7130 (1978). Copies may be obtained from the National Technical Information Service, Springfield, VA 22161.
11. R. L. McCrory and C. P. Verdon, in *Inertial Confinement Fusion*, edited by A. Caruso and E. Sindoni (Editrice Compositori, Bologna, Italy, 1989), pp. 83–124.
12. D. H. Kalantar, M. H. Key, L. B. Da Silva, S. G. Glendinning, B. A. Remington, J. E. Rothenberg, F. Weber, S. V. Weber, E. Wolfrum, N. S. Kim, D. Neely, J. Zhang, J. S. Wark, A. Demir, J. Lin, R. Smith, G. J. Tallents, C. L. S. Lewis, A. MacPhee, J. Warwick, and J. P. Knauer, Phys. Plasmas **4**, 1985 (1997).
13. C. J. Pawley *et al.*, Phys. Plasmas **4**, 1969 (1997).
14. S. G. Glendinning, S. N. Dixit, B. A. Hammel, D. H. Kalantar, M. H. Key, J. D. Kilkenny, J. P. Knauer, D. M. Pennington, B. A. Remington, R. J. Wallace, and S. V. Weber, Phys. Rev. E **54**, 4473 (1996).
15. H. Azechi *et al.*, Phys. Plasmas **4**, 4079 (1997).
16. R. J. Taylor *et al.*, Phys. Rev. Lett. **76**, 1643 (1996).
17. T. R. Boehly, V. A. Smalyuk, D. D. Meyerhofer, J. P. Knauer, D. K. Bradley, C. P. Verdon, and D. Kalantar, in *Laser Interaction and Related Plasma Phenomena*, edited by G. H. Miley and E. M. Campbell (American Institute of Physics, Woodbury, NY, 1997), Vol. 406, pp. 122–129.
18. B. A. Remington *et al.*, Phys. Fluids B **4**, 967 (1992).
19. J. P. Knauer, C. P. Verdon, D. D. Meyerhofer, T. R. Boehly, D. K. Bradley, V. A. Smalyuk, D. Ofer, P. W. McKenty, S. G. Glendinning, D. H. Kalantar, R. G. Watt, P. L. Gobby, O. Willi, and R. J. Taylor, in *Laser Interaction and Related Plasma Phenomena*, edited by G. H. Miley and E. M. Campbell (American Institute of Physics, Woodbury, NY, 1997), Vol. 406, pp. 284–293.
20. J. Delettrez, D. K. Bradley, and C. P. Verdon, Phys. Plasmas **1**, 2342 (1994).
21. D. K. Bradley, J. A. Delettrez, and C. P. Verdon, Phys. Rev. Lett. **68**, 2774 (1992).
22. D. K. Bradley, T. Boehly, D. L. Brown, J. Delettrez, W. Seka, and D. Smith, in *Laser Interaction and Related Plasma Phenomena*, edited by H. Hora and G. Miley (Plenum Press, New York, 1991), Vol. 9, pp. 323–334.
23. S. W. Haan, Phys. Rev. A **39**, 5812 (1989).
24. Y. Lin, T. J. Kessler, and G. N. Lawrence, Opt. Lett. **20**, 764 (1995); Laboratory for Laser Energetics LLE Review **65**, 1, NTIS document No. DOE/SF/19460-117 (1995). Copies may be obtained from the National Technical Information Service, Springfield, VA 22161.
25. S. Skupsky, R. W. Short, T. Kessler, R. S. Craxton, S. Letzring, and J. M. Soures, J. Appl. Phys. **66**, 3456 (1989).

26. Laboratory for Laser Energetics LLE Review **45**, 1, NTIS document No. DOE/DP40200-149 (1990). Copies may be obtained from the National Technical Information Service, Springfield, VA 22161.

27. O. L. Landen, P. M. Bell, J. A. Oertel, J. J. Satariano, and D. K. Bradley, in *Ultrahigh- and High-Speed Photography, Videography, and Photonics '93*, edited by P. W. Roehrenbeck (SPIE, Bellingham, WA, 1993), Vol. 2002, pp. 2–13.

28. D. K. Bradley, P. M. Bell, J. D. Kilkenny, R. Hanks, O. Landen, P. A. Jaanimagi, P. W. McKenty, and C. P. Verdon, Rev. Sci. Instrum. **63**, 4813 (1992).

29. D. H. Kalantar *et al.*, in the *22nd International Congress on High-Speed Photography and Photonics*, edited by D. L. Paisley, and A. M. Frank (SPIE, Bellingham, WA, 1997), Vol. 2869, pp. 680–685.

30. B. Yaakobi, R. S. Craxton, R. Epstein, and Q. Su, J. Quant. Spectrosc. Radiat. Transfer **58**, 75 (1997).

31. B. Yaakobi, F. J. Marshall, D. K. Bradley, J. A. Delettrez, R. S. Craxton, and R. Epstein, Phys. Plasmas **4**, 3021 (1997).

32. R. A. Lerche, D. W. Phillion, and G. L. Tietbohl, in *Ultrahigh- and High-Speed Photography, Videography, and Photonics '93*, edited by P. W. Roehrenbeck (SPIE, Bellingham, WA, 1993), Vol. 2002, pp. 153–161.

33. T. J. Murphy and R. A. Lerche, *ICF Quarterly Report* **3**, 35, Lawrence Livermore National Laboratory, Livermore, CA, UCRL-LR-105821-93-1 (1992). Copies may be obtained from the National Technical Information Service, Springfield, VA 22161.

34. H. R. Griem, Phys. Fluids B **4**, 2346 (1992).

35. D. A. Haynes, Jr., D. T. Garber, C. F. Hooper, Jr., R. C. Mancini, Y. T. Lee, D. K. Bradley, J. Delettrez, R. Epstein, and P. A. Jaanimagi, Phys. Rev. E **53**, 1042 (1996).

36. R. C. Mancini *et al.*, Comput. Phys. Commun. **63**, 314 (1991).

37. L. A. Woltz and C. F. Hooper, Jr., Phys. Rev. A **38**, 4766 (1988).

38. Y. T. Lee, J. Quant. Spectrosc. Radiat. Transf. **38**, 131 (1987).

39. R. C. Mancini, R. F. Joyce, and C. F. Hooper, Jr., J. Phys. B: At. Mol. Phys **20**, 2975 (1987).

40. N. D. Delamater *et al.*, Phys. Rev. A **31**, 2460 (1985).

Accurate Formulas for the Landau Damping Rates of Electrostatic Waves

Laser–plasma instabilities[1] are important in the field of inertial confinement fusion[2] because they scatter laser light away from the target, which reduces the laser energy available to drive the compression of the nuclear fuel, or generate energetic electrons that preheat the fuel, which makes the fuel harder to compress. In stimulated Raman scattering an incident, or pump, light wave (0) decays into a frequency-downshifted, or Stokes, light wave (1) and an electron-plasma wave (2). In stimulated Brillouin scattering a pump light wave decays into a Stokes light wave and an ion-acoustic wave (2). The initial evolution of both instabilities is governed by the linearized equations[3]

$$\left(\partial_t + v_1\partial_z\right)A_1 = \gamma_0 A_2\,, \tag{1}$$

$$\left(\partial_t + \nu_2\right)A_2 = \gamma_0 A_1\,, \tag{2}$$

where A_1 and v_1 are the amplitude and group speed of the Stokes wave, respectively, A_2 and ν_2 are the amplitude and damping rate of the plasma wave (electron-plasma or ion-acoustic), respectively, and the coupling constant γ_0 is proportional to the amplitude of the pump wave. The convective amplification of an existing Stokes wave and the generation of a Stokes wave by plasma fluctuations are both characterized by the gain exponent[3]

$$g = \gamma_0^2 l/v_1\nu_2\,, \tag{3}$$

where l is the plasma length. Because the aforementioned parametric instabilities are important only when $g >> 1$, a small error in the damping rate of the plasma wave can produce a large error in the predicted amplitude of the Stokes wave. For this reason, it is important to determine accurately the Landau contribution to the damping rates of plasma waves.[4]

The properties of electrostatic plasma waves are determined by the dielectric function

$$\varepsilon(\omega,k) = 1 + \chi_e(\omega,k) + \chi_i(\omega,k), \tag{4}$$

where χ_e and χ_i denote the electron and ion susceptibilities, respectively. For each species s

$$\chi_s(\omega,k) = -\frac{\omega_s^2}{2v_s^2k^2}\,Z'\left(\frac{\omega}{\sqrt{2}v_sk}\right), \tag{5}$$

where ω_s is the plasma frequency, v_s is the thermal speed, and Z is the plasma dispersion function.[5] The electrostatic dispersion equation is simply

$$\varepsilon(\omega,k) = 0. \tag{6}$$

The solution of this dispersion equation has two branches: the high-frequency (electron-plasma) branch and the low-frequency (ion-acoustic) branch, both of which are studied in this article. In both cases our approximate analytical solution of the dispersion equation is compared to the numerical solution. Our analytical solutions are more accurate than the standard analytical solutions found in textbooks.[6–8]

Electron-Plasma Waves

The electron Debye length $\lambda_e = v_e/\omega_e$. For the case in which $k\lambda_e << 1$, Krall and Trivelpiece,[6] Ichimaru,[7] and Chen[8] all assert that

$$\omega_r \approx \omega_e\left[1 + 3\left(k\lambda_e\right)^2\right]^{1/2}, \tag{7}$$

$$\omega_i \approx -\left(\frac{\pi}{8}\right)^{1/2}\frac{\omega_e}{\left(k\lambda_e\right)^3}\exp\left[-\frac{1}{2\left(k\lambda_e\right)^2} - \frac{3}{2}\right]. \tag{8}$$

To gauge the accuracy of these formulas, we considered a numerical example. When $(k\lambda_e)^2 = 0.1$, formula (7) predicts that $\omega_r/\omega_e \approx 1.140$. The correct value of this frequency ratio, obtained by solving Eq. (4) numerically, with the ion term omitted, is 1.179. Formula (8) predicts that $\omega_i/\omega_e \approx 0.02979$, whereas the correct value is 0.01845. Although the predicted frequency is in error by only 3.3%, the predicted damping rate is in error by 61%. Clearly there is room for improvement.

In the aforementioned parameter regime $\omega \approx \omega_e$ and $\omega/v_e k \approx 1/(k\lambda_e) >> 1$. The electron-plasma dispersion function has the asymptotic expansion[5]

$$Z(\zeta) \sim i\sigma\pi^{1/2}\exp(-\zeta^2) - \sum_{n=0}^{\infty}\Gamma(n+1/2)/\left[\Gamma(1/2)\zeta^{2n+1}\right], \quad (9)$$

where

$$\sigma = \begin{cases} 0, & \text{if } \zeta_i > 1/|\zeta_r|, \\ 1, & \text{if } |\zeta_i| < 1/|\zeta_r|, \\ 2, & \text{if } \zeta_i < -1/|\zeta_r|, \end{cases} \quad (10)$$

$\Gamma(n+1/2) = (n-1/2)\Gamma(n-1/2)$ and $\Gamma(1/2) = \pi^{1/2}$. It is convenient to introduce the dimensionless parameters $K = k\lambda_e$ and $\Omega = \omega/\omega_e$. If one neglects the ion term in Eq. (4), the electron-plasma dispersion equation can be written as

$$D_r(\Omega) + iD_i(\Omega) = 0, \quad (11)$$

where

$$D_r(\Omega) = 1 - \sum_{n=1}^{\infty}(2n-1)!!K^{2n-2}/\Omega^{2n}, \quad (12)$$

$(2n-1)!! = (2n-1)(2n-3)\ldots(3)(1)$, and

$$D_i(\Omega) = \left(\frac{\pi}{2}\right)^{1/2}\frac{\Omega}{K^3}\exp\left(-\frac{\Omega^2}{2K^2}\right). \quad (13)$$

Because the exponent in Eq. (13) is proportional to $1/K^2$, $|D_i/D_r|$ and $|\Omega_i|/\Omega_r$ are exponentially small when $K^2 << 1$.

If one assumes that $|\Omega_i|/\Omega_r$ is less than any power of K required for an accurate solution of Eq. (11), then Ω_r is determined by the equation

$$D_r(\Omega_r) = 0 \quad (14)$$

and Ω_i is given by the formula

$$\Omega_i \approx -\left.\frac{D_i}{\partial D_r/\partial\Omega}\right|_{\Omega_r}. \quad (15)$$

By using Eq. (12) to evaluate the derivative in Eq. (13), one finds that

$$\Omega_i \approx -\left(\frac{\pi}{8}\right)^{1/2}\frac{C(\Omega_r)}{K^3}\exp\left(-\frac{\Omega_r^2}{2K^2}\right), \quad (16)$$

where the coefficient function

$$C(\Omega) = \Omega^4\Big/\left[\sum_{n=1}^{\infty} n(2n-1)!!K^{2n-2}/\Omega^{2n-2}\right]. \quad (17)$$

It is clear from Eqs. (12) and (17) that the dispersion equation (14) is an equation for Ω_r^2 that involves the small parameter K^2, and formula (16) depends on Ω_r^2. The efficient way to proceed is to solve Eq. (14) and evaluate formula (16) perturbatively, by expanding Ω_r^2 and D_r in powers of K^2. We chose to expand Ω_r and D_r in powers of K^2 to facilitate the analysis in the **Ion-Acoustic Waves** section. Specifically, we made the third-order expansions

$$\Omega \approx 1 + K^2\Omega_1 + K^4\Omega_2 + K^6\Omega_3, \quad (18)$$

$$D(\Omega) \approx D_0(\Omega) + K^2D_1(\Omega) + K^4D_2(\Omega) + K^6D_3(\Omega), \quad (19)$$

where $D_0(\Omega) = 1 - 1/\Omega^2$, $D_1(\Omega) = -3/\Omega^4$, $D_2(\Omega) = -15/\Omega^6$, and $D_3(\Omega) = -105/\Omega^8$, and

$$D_n(\Omega) \approx D_n(1) + D_n'(1)(\Omega-1) + D_n''(\Omega-1)^2/2 + D_n'''(1)(\Omega-1)^3/6. \quad (20)$$

We substituted these expansions in Eq. (14) and collected terms of like order.

The zeroth-order equation is satisfied identically. The first-order equation is

$$D_0'\Omega_1 + D_1 = 0, \tag{21}$$

from which it follows that

$$\Omega_1 = 3/2. \tag{22}$$

The second-order equation is

$$D_0'\Omega_2 + D_0''\Omega_1^2/2 + D_1'\Omega_1 + D_2 = 0, \tag{23}$$

from which it follows that

$$\Omega_2 = 15/8. \tag{24}$$

The third-order equation is

$$D_0'\Omega_3 + D_0''\Omega_2\Omega_1 + D_0'''\Omega_1^3/6 + D_1'\Omega_2 + D_1''\Omega_1^2/2 + D_2'\Omega_1 + D_3 = 0, \tag{25}$$

from which it follows that

$$\Omega_3 = 147/16. \tag{26}$$

By combining Eqs. (22), (24), and (26), one finds that

$$\Omega_r \approx 1 + 3K^2/2 + 15K^4/8 + 147K^6/16, \tag{27}$$

from which it follows that

$$\Omega_r^2 \approx 1 + 3K^2 + 6K^4 + 24K^6. \tag{28}$$

Since the exponent in Eq. (16) is proportional to $1/K^2$, the third-order formula for Ω_r^2 determines the exponential term correct to second order. Consequently, one need only determine C correct to second order.[9] The result is

$$C \approx 1 - 6K^4. \tag{29}$$

It follows from Eqs. (16), (28), and (29) that

$$\Omega_i \approx -\left(\frac{\pi}{8}\right)^{1/2}\left(\frac{1}{K^3} - 6K\right) \times \exp\left(-\frac{1}{2K^2} - \frac{3}{2} - 3K^2 - 12K^4\right). \tag{30}$$

We refer to formulas (27) and (30) as the third-order formulas, even though the latter formula is only accurate to second order. In a similar way, one could refer to the textbook formulas as the first-order formulas. Notice, however, that the textbook formula $\Omega_r \approx (1+3K)^{1/2}$ is less accurate than the true first-order formula $\Omega_r \approx 1 + 3K/2$.

The approximate analytical solutions of the electron-plasma dispersion equation are compared to the numerical solution in Fig. 74.51. The dashed lines represent the textbook solution, the solid lines represent the third-order solution, and the dotted lines represent the numerical solution. For $K^2 = 0.1$ the third-order formulas predict that $\Omega_r \approx 1.178$ and $\Omega_i \approx 0.01840$. These values of Ω_r and Ω_i differ from the correct values by 0.085% and 0.27%, respectively. For the displayed range of K^2 the maximal error associated with the third-order formula for Ω_r is 0.57% and the maximal error associated with the third-order formula for Ω_i is 14%. The third-order formulas are more accurate than the textbook formulas, even though the assumption on which they are based, that $|\Omega_i|/\Omega_r << K^6$, is only valid for $K^2 < 0.04$. Neither pair of formulas is accurate when K^2 is significantly larger than 0.1.

Ion-Acoustic Waves

The electron contribution to the ion-acoustic speed $c_e = (ZT_e/m_i)^{1/2}$, where Z is the ionization number. For the case in which $k\lambda_e << 1$ and $T_i/ZT_e << 1$, we define the baseline formulas

$$\omega_r \approx c_e k\left(1 + 3T_i/ZT_e\right)^{1/2}, \tag{31}$$

$$\frac{\omega_i}{c_e k} \approx -\left(\frac{\pi}{8}\right)^{1/2}\left[\left(\frac{Zm_e}{m_i}\right)^{1/2} + \left(\frac{ZT_e}{T_i}\right)^{3/2}\exp\left(-\frac{ZT_e}{2T_i} - \frac{3}{2}\right)\right]. \tag{32}$$

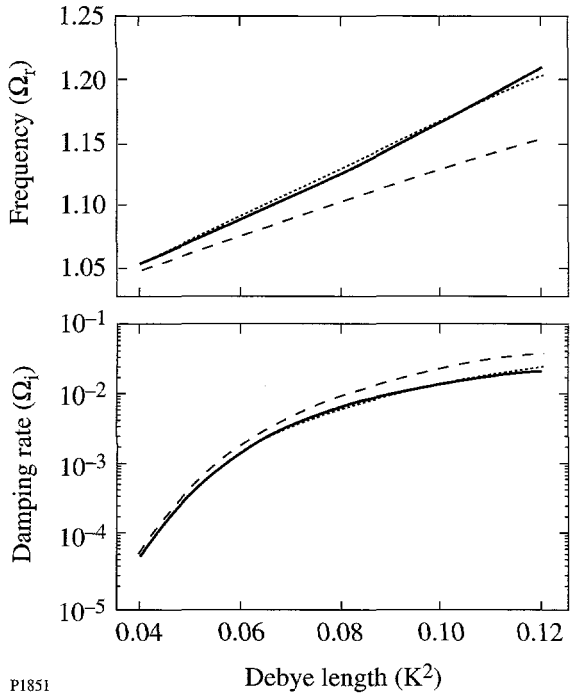

Figure 74.51
(a) Normalized frequency (ω_r/ω_e) and (b) damping rate (ω_i/ω_e) of an electron-plasma wave plotted as functions of the square of the normalized Debye length $(k\lambda_e)$. The dashed lines represent the textbook formulas (7) and (8), the solid lines represent the third-order formulas (27) and (30), and the dotted lines denote numerical solutions of the electron-plasma dispersion equation.

Krall and Trivelpiece[6] omit the ion-temperature contribution to the frequency (31) and the associated factor of exp(−3/2) in the ion contribution to the damping rate (32). Ichimaru[7] and Chen[8] retain these ion-temperature contributions. They agree on formula (31) for the frequency but differ on the formula for the damping rate. Ichimaru multiplies formula (32) by a factor of $\left(1+3T_i/ZT_e\right)^{1/2}$, whereas Chen, who considers only the ion contribution to the damping rate, multiplies the ion term in formula (32) by a factor of $1+3T_i/ZT_e$. In a recent paper[10] we showed empirically that Ichimaru's formula for the damping rate is the better of the two. To gauge the accuracy of Ichimaru's formulas, we considered a numerical example: When $T_i/ZT_e = 0.1$, formula (31) predicts that $\omega_r/c_e k \approx 1.140$. The correct value of the frequency ratio, obtained by solving Eq. (4) numerically with $k\lambda_e = 0.001$, is 1.181. Formula (32), multiplied by $\left(1+3T_i/ZT_e\right)^{1/2}$, predicts that $\omega_i/c_e k \approx 0.05064$, whereas the correct value is 0.03219. Although the predicted frequency is only in error by 3.4%, the predicted damping rate is in error by 57%. [For comparison, the damping rate predicted by formula (32) is in error by 38%.] Clearly there is room for improvement in the accuracy of the formula for the damping rate and the self-consistency of the method by which it is derived.

In the aforementioned parameter regime $\omega \approx c_e k$, $\omega/v_e k \approx \left(Zm_e/m_i\right)^{1/2} << 1$, and $\omega/v_i k \approx \left(ZT_e/T_i\right)^{1/2} >> 1$. One can use the expansion[5]

$$Z(\varsigma) = i\pi^{1/2}\exp\left(-\varsigma^2\right) - \varsigma\sum_{n=0}^{\infty}\left(-\varsigma^2\right)^n \Gamma(1/2)/\Gamma(n+3/2) \quad (33)$$

for the electron-plasma dispersion function and expansion (9) for the ion-plasma dispersion function. It is convenient to introduce the dimensionless parameters $T = T_i/ZT_e$ and $\Omega = \omega/c_e k$.

If one makes the assumption that $Z'(\varsigma_e) \approx -2$, which omits the electron contribution to the ion-acoustic damping rate, the ion-acoustic dispersion relation can be written in the form of Eq. (11), where

$$D_r(\Omega) = 1 + K^2 - \sum_{n=1}^{\infty}(2n-1)!!\,T^{n-1}/\Omega^{2n}, \quad (34)$$

$$D_i(\Omega) = \left(\frac{\pi}{2}\right)^{1/2}\frac{\Omega}{T^{3/2}}\exp\left(-\frac{\Omega^2}{2T}\right). \quad (35)$$

Since the dispersion functions can be rewritten as

$$\frac{D_r(\Omega)}{\left(1+K^2\right)} = 1 - \sum_{n=1}^{\infty}\frac{(2n-1)!!\left[T\left(1+K^2\right)\right]^{n-1}}{\left[\Omega^2\left(1+K^2\right)\right]^n}, \quad (36)$$

$$\frac{D_i(\Omega)}{\left(1+K^2\right)} = \left(\frac{\pi}{2}\right)^{1/2}\frac{\left[\Omega^2\left(1+K^2\right)\right]^{1/2}}{\left[T\left(1+K^2\right)\right]^{3/2}}\exp\left[-\frac{\Omega^2\left(1+K^2\right)}{2T\left(1+K^2\right)}\right], \quad (37)$$

Ω_r and Ω_i satisfy the equation

$$\Omega[K,T] = \Omega\left[0, T\left(1+K^2\right)\right]\Big/\left(1+K^2\right)^{1/2}. \quad (38)$$

Thus, one need only solve the ion-acoustic dispersion equation for the case in which $K^2 = 0$. In this case Eq. (34) has the same

form as Eq. (12), with K^2 replaced by T. It follows from this observation, and Eqs. (27) and (30), that the third-order solution is

$$\Omega_r \approx 1+3T/2+15T^2/8+147T^3/16, \tag{39}$$

$$\Omega_i \approx -\left(\frac{\pi}{8}\right)^{1/2}\left(\frac{1}{T^{3/2}}-6T^{1/2}\right) \times \exp\left(-\frac{1}{2T}-\frac{3}{2}-3T-12T^2\right). \tag{40}$$

Equations (38)–(40) apply to all values of K^2 that satisfy the inequality $T(1 + K^2) << 1$.

If one makes the approximation $Z'(\zeta_e) \approx -2 - i\pi^{1/2}\zeta_e$, which retains the electron contribution to the ion-acoustic damping rate, one must add to Eq. (35) the term

$$D_i(\Omega) = i\left(\frac{\pi}{2}\right)^{1/2}\Omega M^{1/2}, \tag{41}$$

where $M = Zm_e/m_i$ and Z is the ionization number. Since

$$\frac{D_i(\Omega)}{1+K^2} = i\left(\frac{\pi}{2}\right)^{1/2}\frac{\left[\Omega^2\left(1+K^2\right)\right]^{1/2}M^{1/2}}{\left(1+K^2\right)^{3/2}}, \tag{42}$$

Ω_r and Ω_i satisfy the equation

$$\Omega[K,M,T] = \Omega\left[0, M/\left(1+K^2\right)^3, T\left(1+K^2\right)\right]\Big/\left(1+K^2\right)^{1/2}. \tag{43}$$

Thus, one need only solve the ion-acoustic dispersion equation for the case in which $K^2 = 0$.

Unlike the ion contribution to D_i, the electron contribution is not exponentially small when $T << 1$, so one cannot evaluate formula (15) correct to an arbitrary power of T. This formula suggests, however, that the electron contribution to Ω_i is of order 0.01. It follows from Eq. (40) and Fig. 74.51(b) that the ion contribution to Ω_i is much smaller than the electron contribution for $T \le 0.06$ and is comparable to the electron contribution for $0.08 \le T \le 0.12$. In the latter range, both contributions to Ω_i are of order T^2. To make a perturbation expansion based on this ordering, we defined the damping parameters

$$\Gamma = \left(\frac{\pi}{8}\right)^{1/2}\frac{M^{1/2}}{T^2}, \tag{44}$$

$$\Delta = \left(\frac{\pi}{8}\right)^{1/2}\frac{1}{T^{7/2}}\exp\left(-\frac{1}{2T}-\frac{3}{2}\right) \tag{45}$$

and made the approximation

$$\exp\left(-\frac{\Omega^2}{2T}\right) \approx \exp\left(-\frac{1}{2T}-\frac{3}{2}\right)\left[1-T\left(\Omega_2+\frac{\Omega_1^2}{2}\right)\right], \tag{46}$$

which allowed us to write the real dispersion function as

$$D_r(\Omega) \approx D_{0r} + TD_{1r} + T^2D_{2r} + T^3D_{3r}, \tag{47}$$

where D_{0r}–D_{2r} were defined after Eq. (19) and

$$D_{3r} = -105 - 2\Delta\Omega_{2i}, \tag{48}$$

and the imaginary dispersion function as

$$D_i(\Omega) \approx T^2D_{2i} + T^3D_{3i}, \tag{49}$$

where

$$D_{2i} = 2(\Gamma + \Delta), \tag{50}$$

$$D_{3i} = 2\left[\Omega_{1r}(\Gamma+\Delta) - \Delta\left(\Omega_{2r} + \Omega_{1r}^2/2\right)\right]. \tag{51}$$

We then proceeded as described in the **Electron-Plasma Waves** section.

The zeroth-order and first-order equations are identical to the corresponding equations of the previous section, so $\Omega_{1r} =$

3/2 and $\Omega_{1i} = 0$ as we assumed in Eq. (46). The second-order equation is

$$D'_{0r}(\Omega_{2r} + i\Omega_{2i}) + D''_{0r}\Omega_{1r}^2/2 + D'_{1r}\Omega_{1r} + D_{2r} + iD_{2i} = 0, \quad (52)$$

from which it follows that

$$\Omega_{2r} = 15/8, \quad (53)$$

$$\Omega_{2i} = -(\Gamma + \Delta). \quad (54)$$

Formula (54) is equivalent to the base-line formula (32). The third-order equation is

$$\begin{aligned} &D'_{0r}(\Omega_{3r} + i\Omega_{3i}) \\ &+D''_{0r}(\Omega_{2r} + i\Omega_{2i})\Omega_{1r} \\ &+D'''_{0r}\Omega_{1r}^3/6 \\ &+D'_{1r}(\Omega_{2r} + i\Omega_{2i}) \\ &+D''_{1r}\Omega_{1r}^2/2 + D'_{2r}\Omega_{1r} + D_{3r} + iD_{3i} = 0, \end{aligned} \quad (55)$$

from which it follows that

$$\Omega_{3r} = 147/16 + \Delta(\Gamma + \Delta), \quad (56)$$

$$\Omega_{3i} = \Delta(\Omega_{2r} + \Omega_{1r}^2/2). \quad (57)$$

By combining Eqs. (53) and (56), one finds that

$$\Omega_r \approx 1 + 3T/2 + 15T^2/8 + [147/16 + \Delta(\Gamma + \Delta)]T^3. \quad (58)$$

By combining Eqs. (54) and (57), one finds that

$$\Omega_i = -T^2\{\Gamma + \Delta[1 - T(\Omega_{2r} + \Omega_{1r}^2/2)]\}. \quad (59)$$

It is clear from Eq. (46) that the Δ terms represent the exponential $\exp(-\Omega_r^2/2T)$, with the exponent evaluated correct to first order; thus, one can rewrite Eq. (59) as

$$\Omega_i \approx -\left(\frac{\pi}{8}\right)^{1/2}\left[M^{1/2} + \frac{1}{T^{3/2}}\exp\left(-\frac{1}{2T} - \frac{3}{2} - 3T\right)\right]. \quad (60)$$

Notice that the algebraic factors of Ichimaru and Chen are both absent. We refer to formulas (58) and (60) as the third-order formulas, even though the exponent in the latter formula is only accurate to first order.

The approximate analytical solutions of the ion-acoustic dispersion equation are compared to the numerical solution in Fig. 74.52. The dashed lines represent Ichimaru's solution, the solid lines represent the third-order solution, and the dotted lines represent the numerical solution. For $T = 0.1$ formula (58) predicts that $\Omega_r \approx 1.191$, which differs from the correct value of Ω_r by 0.85%. It is clear from Figs. 74.51(a) and 74.52(a) that the additional third-order term improves the accuracy of the formula in the range $T \leq 0.09$ but decreases the accuracy in the

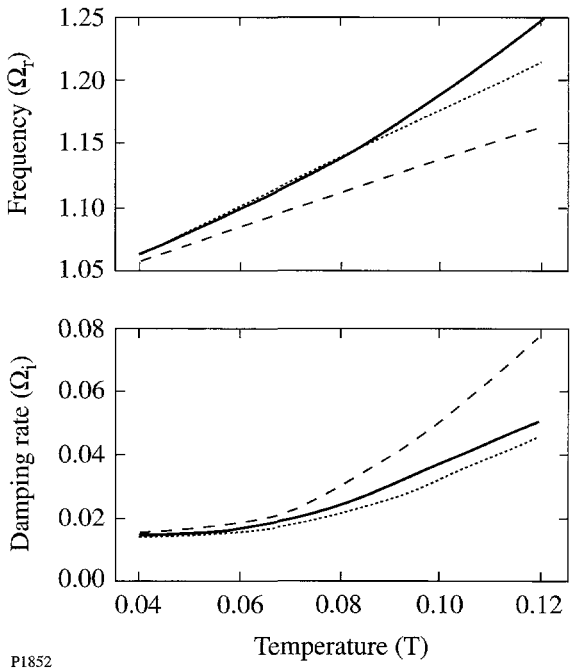

Figure 74.52
(a) Normalized frequency $(\omega_r/c_e k)$ and (b) damping rate $(\omega_i/c_e k)$ of an ion-acoustic wave plotted as functions of the temperature ratio (T_i/ZT_e). The dashed lines represent Ichimaru's formulas (31) and (32) multiplied by $(1 + 3T_i/ZT_e)^{1/2}$, the solid lines represent the third-order formulas (58) and (60), and the dotted lines denote numerical solutions of the ion-acoustic dispersion equation.

range $T > 0.09$. Formula (60) predicts that $\Omega_i \approx 0.03670$, which differs from the correct value of Ω_i by 14%. For the displayed range of T the maximal error associated with the third-order formula for Ω_r is 2.7% and the maximal error associated with the third-order formula for Ω_i is 14%. The third-order formulas are more accurate than Ichimaru's formulas. Neither pair of formulas is accurate when T is significantly larger than 0.1.

Summary

We used systematic perturbation methods to derive formulas for the Landau damping rates of electron-plasma waves [Eq. (30)] and ion-acoustic waves [Eq. (60)]. The predictions of these formulas were compared to the predictions of the textbook formulas[6–8] and numerical solutions of the electrostatic dispersion equation. When $(k\lambda_e)2 \le 0.1$ (for electron-plasma waves) and $T_i/ZT_e \le 0.1$ (for ion-acoustic waves), our formulas are more accurate than the textbook formulas. When $(k\lambda_e)^2 > 0.1$ and $T_i/ZT_e > 0.1$, no pair of formulas is accurate and the electrostatic dispersion equation must be solved numerically.

ACKNOWLEDGMENT

This work was supported by the U.S. Department of Energy Office of Inertial Confinement Fusion under Cooperative Agreement No. DE-FC03-92SF19460, the University of Rochester, and the New York State Energy Research and Development Authority. The support of DOE does not constitute an endorsement by DOE of the views expressed in this article.

REFERENCES

1. W. L. Kruer, *The Physics of Laser Plasma Interactions*, Frontiers in Physics, Vol. 73, edited by D. Pines (Addison-Wesley, Redwood City, CA, 1988), Chaps. 7 and 8.

2. R. L. McCrory and J. M. Soures, in *Laser-Induced Plasmas and Applications*, edited by L. J. Radziemski and D. A. Cremers (Dekker, New York, 1989), pp. 207–268.

3. R. E. Giacone, C. J. McKinstrie, and R. Betti, Phys. Plasmas **2**, 4596 (1995) and references therein.

4. L. Landau, J. Phys., USSR **X**, 25 (1946).

5. J. D. Huba, NRL Plasma Formulary, Naval Research Laboratory, NRL/PU/6790—94-265 (1994) and references therein.

6. N. A. Krall and A. W. Trivelpiece, *Principles of Plasma Physics* (McGraw-Hill, New York, 1973), pp. 385 and 390.

7. S. Ichimaru, *Basic Principles of Plasma Physics* (W. A. Benjamin, Reading, MA, 1973), p. 71.

8. F. F. Chen, *Introduction to Plasma Physics and Controlled Fusion*, Vol. 1, 2nd ed. (Plenum Press, New York, 1984), pp. 270–273.

9. For the record, the third-order contribution to C is $-48K^6$. The fourth-order equation is $D_0'\Omega_4 + D_0''\Omega_3\Omega_1 + D_0''\Omega_2^2/2 + D_0'''\Omega_2\Omega_1^2/2 + D_0''''\Omega_1^4/24 + D_1'\Omega_3 + D_1''\Omega_2\Omega_1 + D_1'''\Omega_1^3/6 + D_2'\Omega_2 + D_2''\Omega_1^2/2 + D_3'\Omega_1 + D_4 = 0$, from which it follows that $\Omega_4 = 9531/128$. The fourth-order correction to Ω_r^2 is $180K^8$. For $K^2 \le 0.1$ the fourth-order formulas for Ω_r and Ω_i are more accurate than the third-order formulas. As K^2 increases beyond 0.1, however, the predictions of the fourth-order formulas diverge from the numerical results more rapidly than the predictions of the third-order formulas.

10. R. E. Giacone, C. J. McKinstrie, and R. Betti, Phys. Plasmas **5**, 1218 (1998).

Efficient, End-Pumped, 1053-nm Nd:YLF Laser

Diode-pumped lasers offer better stability and higher reliability than flashlamp-pumped laser systems. Most of the diode-pumping schemes can be divided into two major categories: end pumping and side pumping. High efficiency and good beam quality are potential advantages of end-pumped solid-state lasers over side-pumped ones. Practical realization of these advantages depends upon the possibility of reshaping a strongly astigmatic diode-laser beam into a beam with a circular symmetry. Recently, several practical schemes were suggested[1,2] that make it possible to effectively re-image the 1-μm × 10-mm emitting area of a high-power, cw laser diode bar into a few-hundred-micron spot size. These techniques have been used successfully for direct cw end pumping of solid-state lasers[1] and the efficient coupling of high-power, cw laser-diode radiation into the optical fiber.[2] Using a transport fiber to deliver the pump beam to the end-pumped active medium has a number of practical advantages: (a) the pump beam at the transport fiber output has a high-quality, centrally symmetric energy distribution; (b) the radial size of the pump beam can be easily up- or down-scaled by using simple and virtually lossless optics; (c) a transport fiber provides a simple and transparent interface between the pump source and the active medium, which greatly simplifies the whole diode-pumped laser characterization and maintenance; and (d) both the pumping source and the active medium can be changed simply by reconnecting transport fibers. Therefore, it seems very attractive to couple the high-power, quasi-cw diode laser into the optical fiber and to use this fiber-coupled, quasi-cw, high-power laser diode to end pump a solid-state laser.

In this article we report on an efficient Nd:YLF laser operated at 1053 nm that was end pumped by fiber-coupled, high-power, pulsed diode arrays. Two quasi-cw 100-W linear arrays[3] were used in this experiment. The emitting area of these diodes was 1 μm × 10 mm with ~100% aperture fill factor. The diode laser's 3.6-nm-wide output spectrum was centered at 805 nm. The output from the laser-diode arrays was coupled into 0.6-mm-diam, 0.22-numerical-aperture step-index fibers in a manner similar to that reported in Ref. 2. Fiber-coupling efficiencies of >50% were measured at the maximum diode-laser output (Fig. 74.53). At the transport fiber output the laser-diode radiation was re-imaged with 1.6× magnification into the Nd:YLF rod through a beam splitter that was HR coated for 1053 nm ($R > 99\%$) and AR coated for 805 nm ($R < 1.5\%$). In the course of our experiments we investigated a Nd:YLF rod pumped from one side by a single diode array and pumped from both sides by two arrays simultaneously. The pump energy that reached each of the Nd:YLF rod surfaces was ≥25 mJ for the 0.5-ms pump duration. This represents ~50% transport efficiency from the emitting surface of the laser diode to the input surface of the Nd:YLF active element. The active laser element was a 5-mm-diam, 20-mm-long Nd:YLF rod with 1.1 atm% of Nd and AR coated for 805 nm and 1053 nm on both sides. The focused pump beam formed a circularly symmetric spot on the input faces of the Nd:YLF rod with a pump beam cross section of ≤1.3-mm FWHM over the entire 20-mm length of the laser crystal (Fig. 74.54). More than 95% of the pump energy was absorbed in the Nd:YLF crystal. We found that for this pumping scheme the Nd:YLF lasing threshold at 1053 nm is insensitive to pump-wavelength variation within at least ±2 nm. We attribute this to the fact that Nd:YLF has a broad and almost–polarization-insensitive absorption

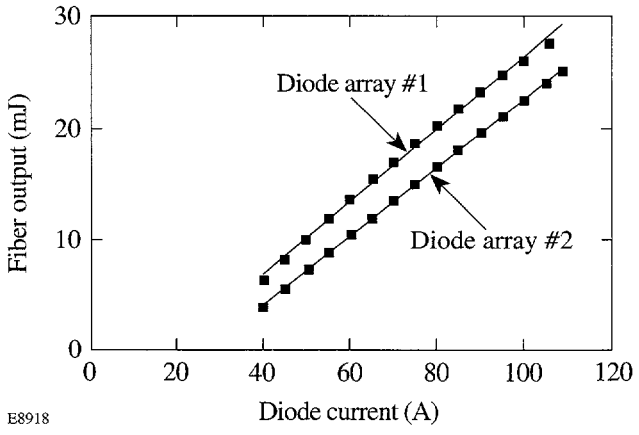

Figure 74.53
Fiber-coupled, 100-W, quasi-cw diode-array output versus diode current. Data presented are for the 0.6-mm-diam, 0.22-NA step-index fiber.

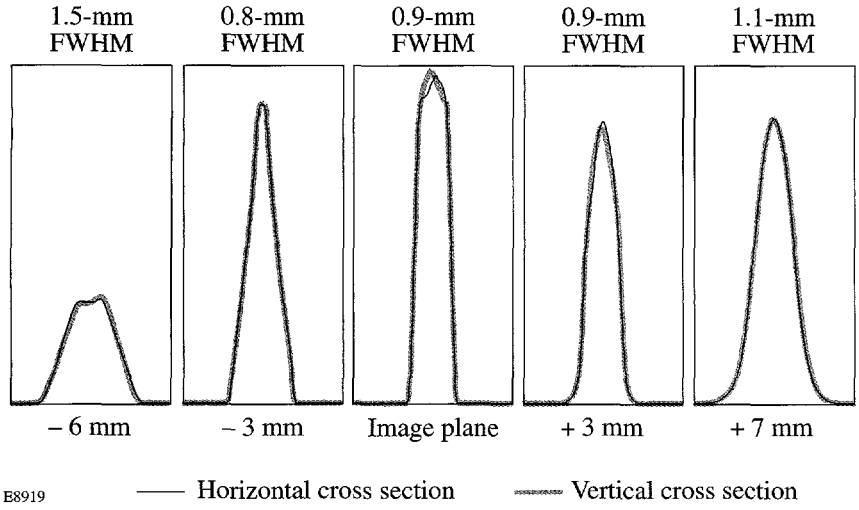

Figure 74.54
Pump-beam cross section along the axis of the active medium.

peak around 805 nm, which eliminates the need for the laser diode to be precisely wavelength tuned and externally cooled when the laser repetition rate is below 5 Hz. It should be pointed out that although all data presented here were taken at a 5-Hz repetition rate, we believe that a higher repetition rate can easily be achieved with proper heat removal from the diode laser and the active element.

The gain of the end-pumped rod was determined using a cw mode-locked Nd:YLF laser operated at 1053 nm that was collimated and apertured so that the probe beam used was ~1 mm in diameter. The single-pass, small-signal gain G_{ss} for the probe beam was observed with an analog oscilloscope[4] and measured with a digital oscilloscope.[5] The measured small-signal, single-pass gain for the ~1-mm beam at 1053 nm was 2.2 for pumping from one side and 4.2 for pumping from both sides (Fig. 74.55).

For the end-pumped Nd:YLF laser demonstration and characterization the following setup was used (Fig. 74.56): The cavity was 3.78 m in length and used a flat output coupler and a high reflector with a 5-m radius of curvature. Output couplers with reflectivity R = 85%, 70%, and 50% were tested. The 1053-nm wavelength for the Nd:YLF lasing was insured by the intracavity thin-film polarizer and appropriate Nd:YLF rod orientation in respect to this polarizer. The polarization of the output laser radiation was monitored by the extra-cavity Glan–Taylor polarizer. At the maximum one-sided pumping energy of ~27 mJ, the free-running output was 8.8 mJ in the multilongitudinal, fundamental TEM_{00} mode, which is 33% of the pump energy delivered to the Nd:YLF rod surface. At the maximum two-sided pump energy of 50 mJ, the free-running output was 20 mJ in the multilongitudinal fundamental TEM_{00} mode, which is 40% of the pump energy delivered to the Nd:YLF rod surface (Fig. 74.57). We believe that this is the highest TEM_{00} energy output reported to date for an end-pumped Nd:YLF laser operated at 1053 nm. The measured optical-to-optical differential efficiency was 54%. The spatial profile for the output beam was measured with a scientific-grade, cooled CCD camera.[6] The highly symmetric output beam has an intensity distribution very close to the intensity distribution calculated for our laser resonator parameters at 6.4-mJ output energy for the one-side pumping scheme (see Fig. 74.58). It should be emphasized that we observed the TEM_{00} output beam without any transverse mode control aperture in the cavity for the entire range of the pumping energies up to six times the threshold. We believe that this is attributed to the fact that the end-pumped volume cross section was smaller than the fundamental-mode cross section.[7]

The Q-switched mode of operation was also tested. To convert the Nd:YLF laser from the free-running mode to the Q-switching mode, a standard combination of the quarter-wave plate and Pockels cell was introduced into the laser cavity between the thin-film polarizer and the end mirror (Fig. 74.56). The reflectivity of the output coupler used for the Q-switched-mode operation was R = 70%. A high-voltage, step-function pulse was applied to the Pockels cell at the end of the pumping cycle to initiate the Nd:YLF laser Q-switching. The amplitude of this high-voltage pulse adjusted for maximum output energy at the highest pumping level (both ends pumping) was found to be 4.5 kV. The measured output energy in the Q-switched mode was 13.6 mJ (Fig. 74.59), and the Q-switched output pulse has a TEM_{00}-mode profile. The measured temporal FWHM of the Q-switched output pulse was 140 ns, which is less than six laser-resonator-cavity round-trips (Fig. 74.60).

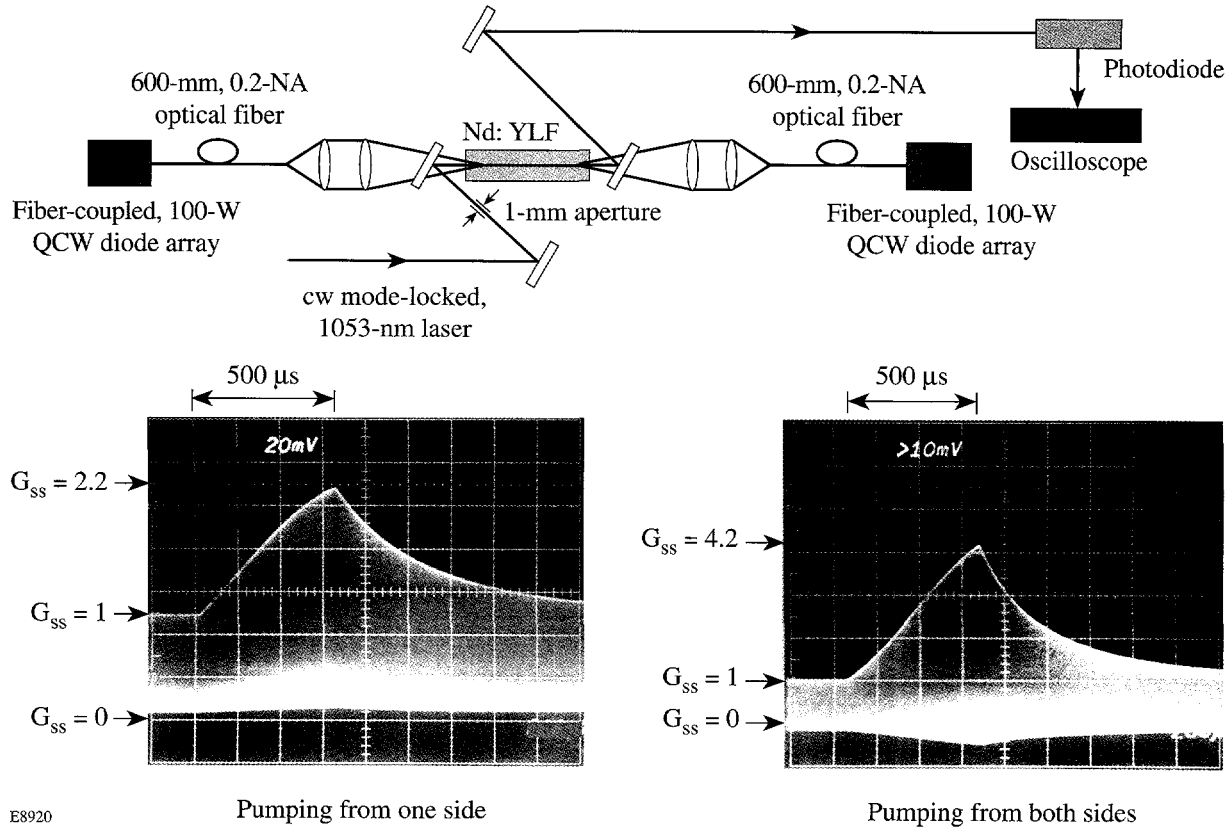

Figure 74.55
Small-signal-gain measurements: setup and experimental results.

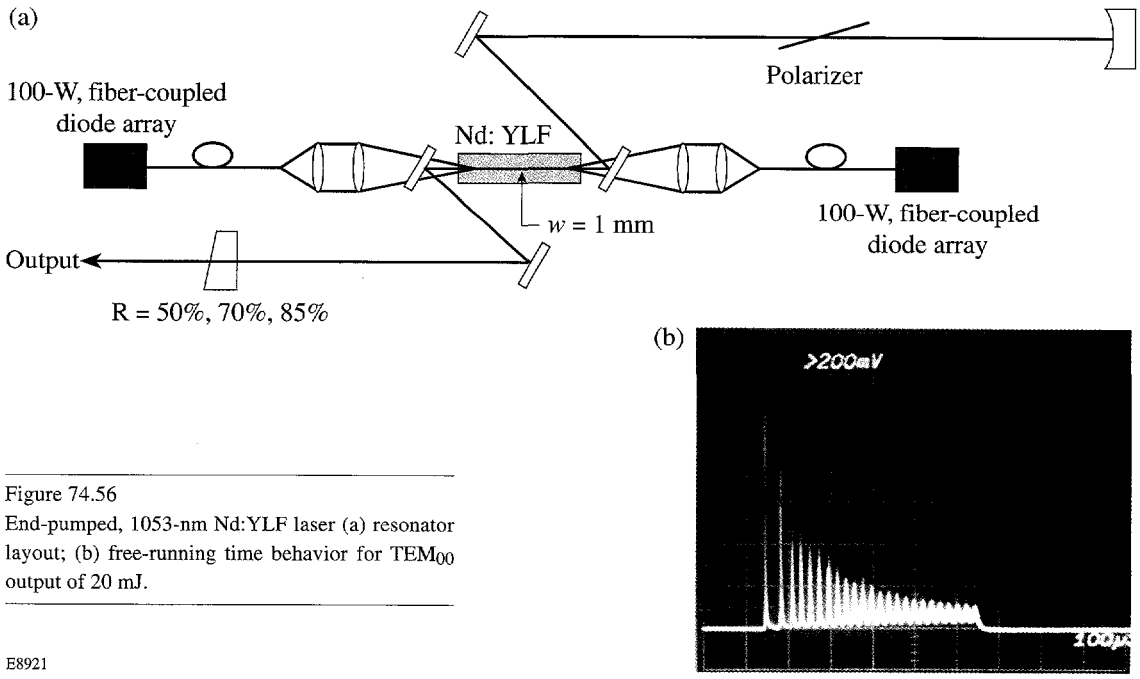

Figure 74.56
End-pumped, 1053-nm Nd:YLF laser (a) resonator layout; (b) free-running time behavior for TEM_{00} output of 20 mJ.

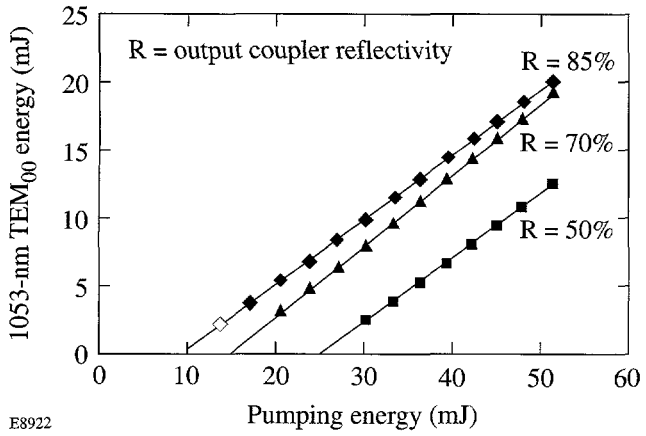

E8922

Figure 74.57
Measured, free-running, laser TEM_{00}-mode energy output at 1053 nm versus pump energy.

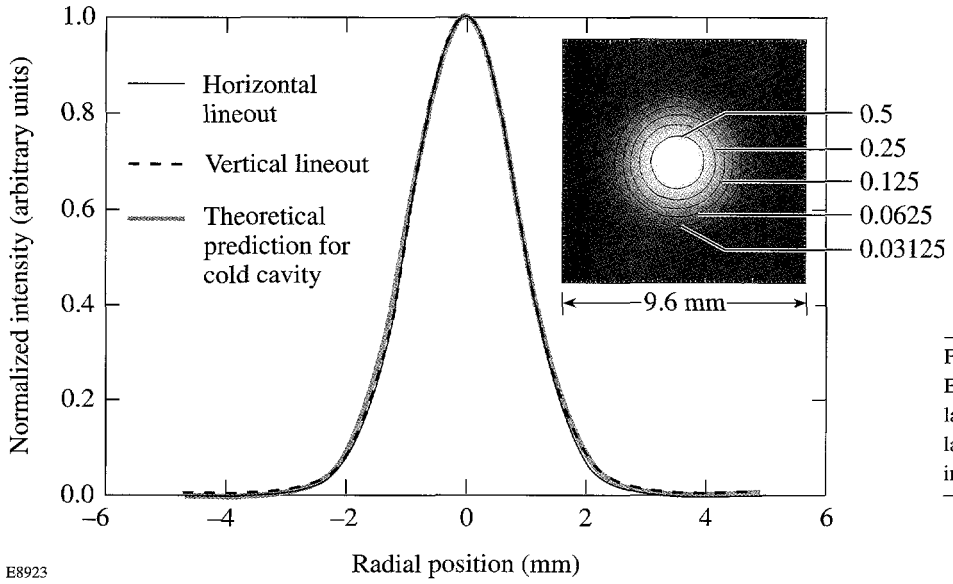

E8923

Figure 74.58
Experimentally measured and calculated output laser intensity beam profiles. An image of the laser beam on the logarithmic scale with superimposed contour lines is shown in the inset.

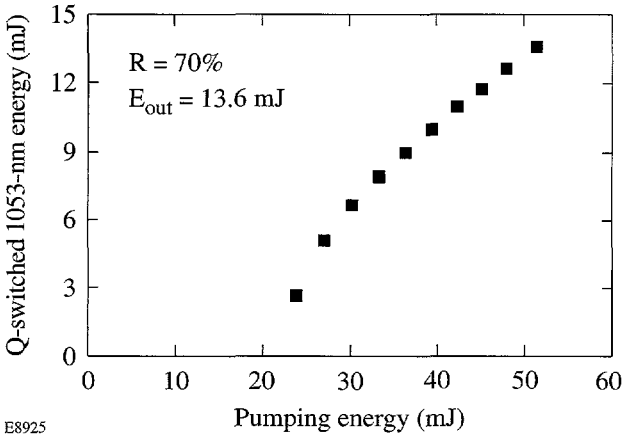

E8925

Figure 74.59
Measured Q-switched TEM_{00}-mode energy output versus pump energy.

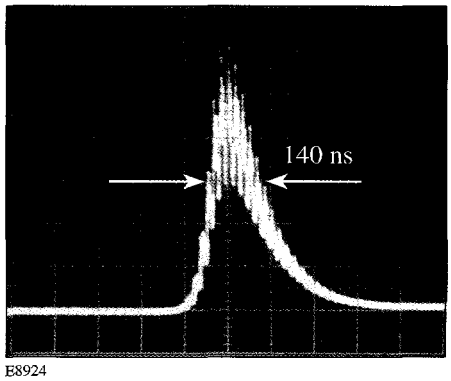

E8924

Figure 74.60
Q-switching pulse temporal profile for TEM_{00} output of 13.6 mJ.

In conclusion we developed an efficient Nd:YLF laser at 1053 nm that was end pumped by two fiber-coupled, 100-W, quasi-cw diode arrays. A 20-mJ TEM_{00} energy output with 54% differential efficiency for a free-running mode and 13.6-mJ TEM_{00} energy output for Q-switched operation were demonstrated. We believe that this is the highest TEM_{00} energy output reported to date for the efficient end-pumped Nd:YLF laser operated at 1053-nm wavelength.

ACKNOWLEDGMENT

This work was supported by the U.S. Department of Energy Office of Inertial Confinement Fusion under Cooperative Agreement No. DE-FC03-92SF19460, the University of Rochester, and the New York State Energy Research and Development Authority. The support of DOE does not constitute an endorsement by DOE of the views expressed in this article.

REFERENCES

1. W. A. Clarkson and D. C. Hanna, Opt. Lett. **21**, 375 (1996).
2. K. Du *et al.*, in *Advanced Solid State Lasers, 1997*, edited by C. R. Pollock and W. R. Bosenberg, OSA Trends in Optics and Photonics Series, Vol. 10 (Optical Society of America, Washington, DC, 1997), pp. 390–393.
3. Diode array SDL 3251-A1, SDL, Inc., San Jose, CA 95134-1365.
4. Tektronix oscilloscope 7104, Tektronix, Corporate Office, Wilsonville, OR 97070-1000.
5. Hewlett-Packard oscilloscope HP54720A, Hewlett-Packard, Test and Measurement Organization, Palo Alto, CA 94303-9512.
6. 5122 CCD detector model 1530-PUV, EG&G Instruments, Princeton Applied Research, Princeton, NJ 08543-2565.
7. F. Salin and J. Squier, Opt. Lett. **17**, 1352 (1992).

Self- and Cross-Phase-Modulation Coefficients in KDP Crystals Measured by a Z-Scan Technique

In the interaction of strong fields with matter, considerable interest has been shown in the development of high-efficiency frequency up-conversion of ultrashort laser pulses. One important area of interest is in ultrafast laser–solid interactions where up-conversion can lead to higher absorption due to higher-density interactions[1] and to an enhancement of the pulse-intensity contrast by many orders of magnitude, allowing the high-intensity pulse to interact with the solid-density material.[2] Efficient second-harmonic generation in KDP has been reported for ultrafast laser beams at intensities up to 400 GW/cm^2.[3] In this intensity region, nonlinear effects such as self- and cross-phase modulation[4,5] (SPM, XPM) originating from third-order nonlinear susceptibility $\chi^{(3)}$ may limit the efficiency of ultra-intense frequency-conversion processes that involve co-propagation of two beams with different wavelengths. SPM and XPM are responsible for spectral broadening in optical fibers and have been used in pulse compression to produce ultrashort laser pulses.[6] XPM has been observed in fiber Raman soliton lasers[7,8] and has proven to be important in optical parametric oscillators, optical parametric amplifiers,[9] and the harmonic-generation process in bulk nonlinear crystals.[10,11] Nonlinear phase changes can destroy the phase coherence required for efficient conversion. Z-scan,[12,13] four-wave mixing,[14,15] ellipse rotation,[16] and nonlinear interferometer[17,18] techniques have been used to measure the nonlinear refractive index $n_2\left[n_2 = 3/8n\chi^{(3)}\right]$ associated with SPM. Nonlinear refractive index coefficients associated with SPM in KDP crystals, which are widely used in frequency conversion,[19,3] were measured by degenerate three-wave mixing[20] and time-resolved interferomery[21] at 1 μm. In this article we report on the results of the single-beam Z-scan measurement[12,13] of the nonlinear refractive index associated with SPM at wavelengths of 1.053 μm, 0.527 μm, and 0.351 μm and two-color Z-scan[22] to measure the nonlinear coefficients of XPM between 1.053 μm and 0.527 μm in a KDP crystal. In the two-color Z-scan measurement, two collinear beams with different wavelengths are used; a weak probe beam can be defocused by the action of the strong pump beam in a thin sample.[22] The far-field intensity variation is used to determine the optical nonlinearity from XPM as the sample is moved along the propagation direction (z axis) of the focused beams.

A schematic of the setup is shown in Fig. 74.61. Infrared (IR) laser pulses (λ_1 = 1.053 μm), second-harmonic (SH) pulses (λ_2 = 0.527 μm), or third-harmonic (TH) pulses (λ_3 = 0.351 μm) are transmitted through an aperture A1 and can be treated as top-hat beams. Second-harmonic pulses are generated using a KDP type-I crystal, and third-harmonic pulses are generated using two KDP type-II crystals.[23] We use the top-hat spatial profile because it increases the measurement sensitivity.[24] This top-hat beam then co-propagates through a lens with focal length f_1 for IR, f_2 for SH, and f_3 for TH. The focal lengths f_1, f_2, and f_3 are slightly different due to the dispersion of the lens. The electric-field distribution near the focal point $E_i(r,z,t)$ $(i = 1,2,3)$ is described by Lommel functions.[25] It has an Airy radius at the focal spot of $1.22\,\lambda_i F_i$, where $F_i = f_i/2a$ and $2a$ is the diameter of aperture A1. The beam waist (w_{0i}) is defined as $w_{0i} = \lambda_i F_i$. The Rayleigh range (z_{0i}) is $\pi w_{0i}^2/\lambda_i$. A nonlinear crystal located in the focal region will introduce phase modulation proportional to the intensity. The single-beam Z-scan is performed when only one wavelength beam passes through A1. In these cases, if the sample thickness is much less than the Rayleigh range z_{0i} and the nonlinear absorption can be ignored, the field distribution at the exit surface of the sample can be expressed simply by

$$E_{ei}(r,z,t) = E_i(r,z,t)\,\exp\left\{ik_i L_{\mathrm{eff}_i}\left[\gamma_i\left|E_i(r,z,t)\right|^2\right]\right\}, \quad i = 1,2,3 \tag{1}$$

where $k_i = 2\pi/\lambda_i$, $L_{\mathrm{eff}_i} = \left[1-\exp(-\alpha_i L)\right]/\alpha_i$ is the effective sample thickness, α_i is the linear absorption coefficient, and γ_i is the nonlinear refraction coefficient, which is related to n_{2i} by $n_{2i} = \left(cn_0/40\pi\right)\gamma_i\left(m^2/\mathrm{W}\right)$, where $c(m/s)$ is the speed of light in vacuum and n_0 is the linear index of refraction. The incident electric field $E_i(r,z,t)$ is normalized so that $I_i = \left|E_i(r,z,t)\right|^2$.

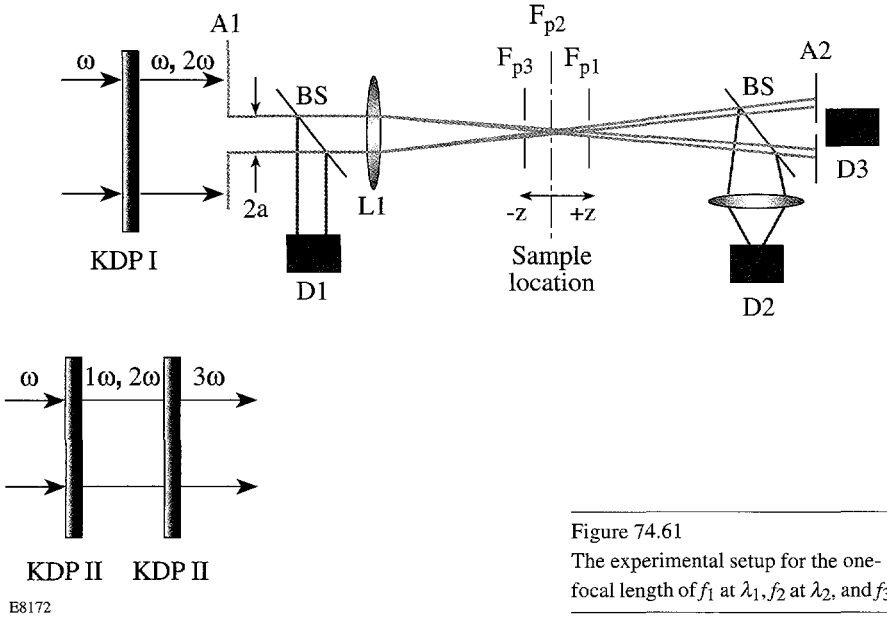

Figure 74.61
The experimental setup for the one- and two-beam Z-scans. A1, A2: aperture; L1: lens with focal length of f_1 at λ_1, f_2 at λ_2, and f_3 at λ_3; D1, D2, D3: photon detectors; BS: beam splitter.

In the two-color Z-scan, we measured the cross-phase-modulation coefficients between optical waves at λ_1 and λ_2. The output unconverted IR (pump beam) and SH pulses (probe beam) from a frequency doubler co-propagate through A1 (Fig. 74.61). The field distribution at the exit surface of the sample is

$$E_{e1}(r,z,t) = E_1(r,z,t) \exp\left\{ik_1 L_{\text{eff}_1}\left[\gamma_1 |E_1(r,z,t)|^2 + 2\gamma_{21}|E_2(r,z,t+\tau)|^2\right]\right\}, \quad (2)$$

$$E_{e2}(r,z,t+\tau) = E_2(r,z,t+\tau) \exp\left\{ik_2 L_{\text{eff}_2}\left[\gamma_2 |E_2(r,z,t+\tau)|^2 + 2\gamma_{12}|E_1(r,z,t)|^2\right]\right\}, \quad (3)$$

where τ is the time delay between IR and SH pulses introduced in the KDP type-I frequency-doubling crystal. In the exponent of Eqs. (2) and (3), the first term reflects the impact of self-phase modulation, and the second term reflects the phase modulation induced by an optical wave of the other wavelength. If the optical wave intensity at wavelength λ_2 is weak enough that $\gamma_2|E_2|^2 << \pi$, the second term in the exponential of Eq. (2) and first term in Eq. (3) can be ignored. Therefore, as the nonlinear crystal is moved along the z axis, the transmittance of the electric field at wavelength λ_1 through a finite aperture in the far field is determined by the self-phase modulation of the λ_1 optical wave, while the transmittance of the electric field at wavelength λ_2 is determined by the cross-phase modulation due to the λ_1 optical wave.

When the Fresnel number $w_{0i}/\lambda_i D$ is much smaller than unity, where D is the distance from sample to the aperture A2, the field distribution $E_{A2}(\rho,z,t)$ at the sampling aperture A2 (Fig. 74.61) is proportional to the Fourier transform of field at the exit surface of the sample.[26] The normalized Z-scan power transmittance is

$$T(z) = \frac{\int_{-\infty}^{\infty}\int_0^{r_a} |E_{A2}(\rho,z,t)|^2 \rho d\rho dt}{\int_{-\infty}^{\infty}\int_0^{r_a} |E_{i_{A2}}(\rho,z,t)|^2 \rho d\rho dt}, \quad (4)$$

where r_a is the radius of aperture A2 and E_{iA2} is the electric field at A2 without nonlinear crystal. Equation (4) gives the Z-scan fluence transmittance $T(z)$ as a function of crystal position.

Figure 74.62 shows numerical examples of the normalized transmittance as a function of sample positions in the presence of SPM and XPM, respectively. For all of the curves the on-axis nonlinear phase accumulation (either self- or cross-phase) is chosen to be $\Phi_0 = 0.4$, where $\Phi_0 = k_i L_{\text{eff}_i} \gamma_i I_0$ and I_0 is the on-axis peak intensity. The curves compare the effects of self- and cross-phase modulation on the transmittance of the two beams through the aperture. Even though the phase shifts are the same, the different focusing of the two beams means that transmittance as a function of crystal position will differ for the

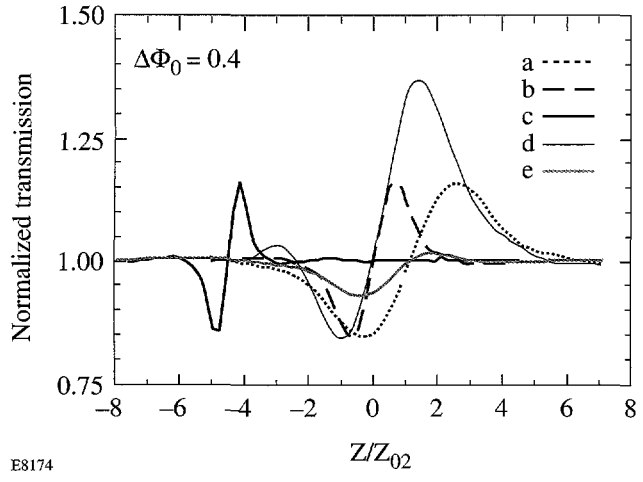

Figure 74.62
The effect of SPM and XPM on transmitting the beams at different wavelengths through the aperture (A2 in Fig. 74.61). In all cases, the nonlinear phase shift is $\Phi_0 = 0.4$. Curves (a), (b), and (c) are the transmittance of the single-color Z-scan at wavelengths of $\lambda_1 = 1053$ nm, $\lambda_2 = 527$ nm, and $\lambda_3 = 351$ nm. Curve (d) is the transmittance of the two-color (λ_1,λ_2) Z-scan with a strong λ_1 and weak λ_2. Curve (e) is the transmittance of the two-color (λ_1,λ_2) Z-scan for a strong λ_2 and λ_1. z/z_{02} is the position in terms of the Rayleigh range of the second-harmonic beam.

different physical processes. This can be beneficial in distinguishing the different effects, in particular, eliminating the contamination of SPM in the XPM measurements.

Curves (a), (b) and (c) in Fig. 74.62 show the effects of self-phase modulation on the transmittance for the beam at wavelengths of 1.053 μm (λ_1), 0.527 μm (λ_2), and 0.351 μm (λ_3), respectively. Since the f number of the system at λ_1 and λ_2 is about the same, the Rayleigh range z_{01} is twice z_{02}. The distance between peak and valley corresponding to the λ_2 optical wave is half that of the λ_1 optical wave. Curve (d) shows the effects of XPM of λ_1 on the transmittance of the weak λ_2 beam $(\lambda_2 = \lambda_1/2)$. The asymmetry in the relative decrease or increase in transmittance is mainly due to the dispersion of the focusing lens. The focal length is slightly longer for the λ_1 optical wave. The irradiance of electric field at 1.053 μm induces a positive lens for the λ_2 wave in the thin sample near its focus since $n_{21} > 0$. With the sample on the $-z$ side of the λ_1 focus (Fig. 74.61), the positive lensing effect tends to augment diffraction; therefore, the aperture transmittance is reduced. When the sample moves on the $+z$ side of the λ_1 focus, the positive lensing effect tends to collimate the beam and increase the transmittance through the aperture. The transmittance reaches a maximum when the sample is located approximately at the focal point of λ_1 (i.e, F_{p1} in Fig. 74.61) because the maximum intensity-dependent phase distortion takes place at F_{p1}. Curve (e) shows the effects of XPM of λ_2 on the transmittance of a weak λ_1 beam, which is opposite to curve (d). The asymmetry in the relative decrease or increase in transmittance is similar to curve (d) but the sensitivity is much smaller in this case. Because the pump beam's spot diameter is half that of the probe beam, only the center portion of the probe beam will experience nonlinear phase distortion.

In the experiment, 2.0-ps, 1-μm laser pulses are generated from a chirped-pulse-amplification laser system.[27] These 3-cm-diam pulses are incident on a 1-cm-thick, type-I KDP frequency-doubling crystal for cases where n_2 at 0.527 μm and a XPM coefficient between 1.052 μm and 0.527 μm were measured. These pulses are incident on two 1.6-cm-thick, type-II KDP crystals to generate TH when n_2 at 0.351 μm was measured. A half-wave plate placed before the doubler tunes the polarization of the IR to control the amount of SH or TH wave generated. A BG18 filter after doubler and UG11 filter after tripler were used respectively to block light at other wavelengths.[28] A 6.8-mm-diam aperture (A1 in Fig. 74.61) is placed after the crystal to select a small portion of the IR, SH, or TH waves. The spatial profile of the pulse passing through the aperture can be regarded as a top-hat pulse. The focal lengths of the lens after the A1 aperture were determined by a far-field spot-size scan using a CCD[29] camera. The measured focal lengths are $f_1 = 76.5 \pm 0.5$ cm at $\lambda_1 = 1.053$ μm, $f_2 = 74.3 \pm 0.5$ cm at $\lambda_2 = 0.527$ μm, and $f_3 = 65.4 \pm 0.5$ cm at $\lambda_3 = 0.351$ μm. The resulting beam waists (w_{01}, w_{02}, and w_{03}) were 118 μm, 58 μm, and 34 μm, respectively. The Rayleigh ranges (z_{01}, z_{02}, and z_{03}) were 4.2 cm, 2.0 cm, and 1.0 cm. For crystals with small n_2, a longer crystal is preferred as long as the thickness is less than one-third of the corresponding Rayleigh range. In all cases, the intensity is kept well below the damage threshold. Samples with different thicknesses and cuts were used for different wavelengths. The crystals were mounted on a translation stage. To simplify the experiment analysis, a 7.5-mm-thick KDP sample cut at 90° to the wave-propagation direction was used for measuring XPM coefficients to avoid generating additional second- and third-harmonic generation during the interaction. For other axis orientations, the **k**-vector spread due to focusing would allow part of the beam to satisfy the second- or third-harmonic phase-matching condition. The transmittance through the aperture would then be due to the combined effects from refractive index changes, second-, and third-harmonic generation.

The beam splitter after the aperture (A1 in Fig. 74.61) sends a small portion of the beam to a PIN diode[30] (D1 in Fig. 74.61),

which is used to monitor the top-hat IR energy. Part of the probe beam is reflected by the beam splitter before the analyzing aperture (A2 in Fig. 74.61) to a PIN diode (D2 in Fig. 74.61) and gives the open-aperture Z-scan curve. From the open-aperture scan the nonlinear absorption is measured. The change of transmission due purely to the nonlinear index of refraction is determined by dividing the closed-aperture transmittance by the one without the aperture. This has the advantage of compensating for the energy fluctuations during the experiment. The linear transmittance of aperture A2, defined as the ratio of power transmitted through A2 to the total power incident on the plane of the aperture, is 0.03. The incident IR temporal full width at half-maximum (τ_{FWHM}) was 2.0±0.2 ps as measured by a single-shot autocorrelator. The SH and TH pulse widths were calculated to be 1.41 ps and 1.45 ps, respectively, in the small-signal-gain region. The energy ε of the incident IR pulse was measured by an energy meter.[31] For a Gaussian temporal profile, the on-axis peak intensity I_0 within the sample is $I_0 = \sqrt{\pi \ln 2}\varepsilon / 2w_0^2 t_{FWHM}$.[32]

Figure 74.63 shows typical Z-scan results obtained to determine the SPM and XPM coefficients of KDP crystals. The parameters for each case are listed in Table 74.II. The peak-to-valley configuration of all these Z-scans indicates a positive nonlinearity. The solid line in each of the figures is the least squares fit to the experiment data using Eq. (3) to determine the total phase accumulation Φ_0. We use a temporal separation induced in the frequency-doubling crystal (KDP I), $\tau = 0.73$ ps in Eq. (2) in the case of XPM based on the predicted temporal walk-off between pulses at different wavelengths.[33] The extraordinary IR wave moves 0.73 ps ahead of the extraordinary SH wave at the exit of the 1-cm, KDP type-I doubler.

The nonlinear coefficient γ_2 can then be calculated from $\Phi_0 = kL_{eff}\gamma_{12}I_0$. There are several error sources in the measurement: the error in the curve fit, in measuring the crystal thickness, and in measuring the pulse width and energy that determine beam intensity. The least squares fit for the experiment data yields an error of 5%. The error for the crystal

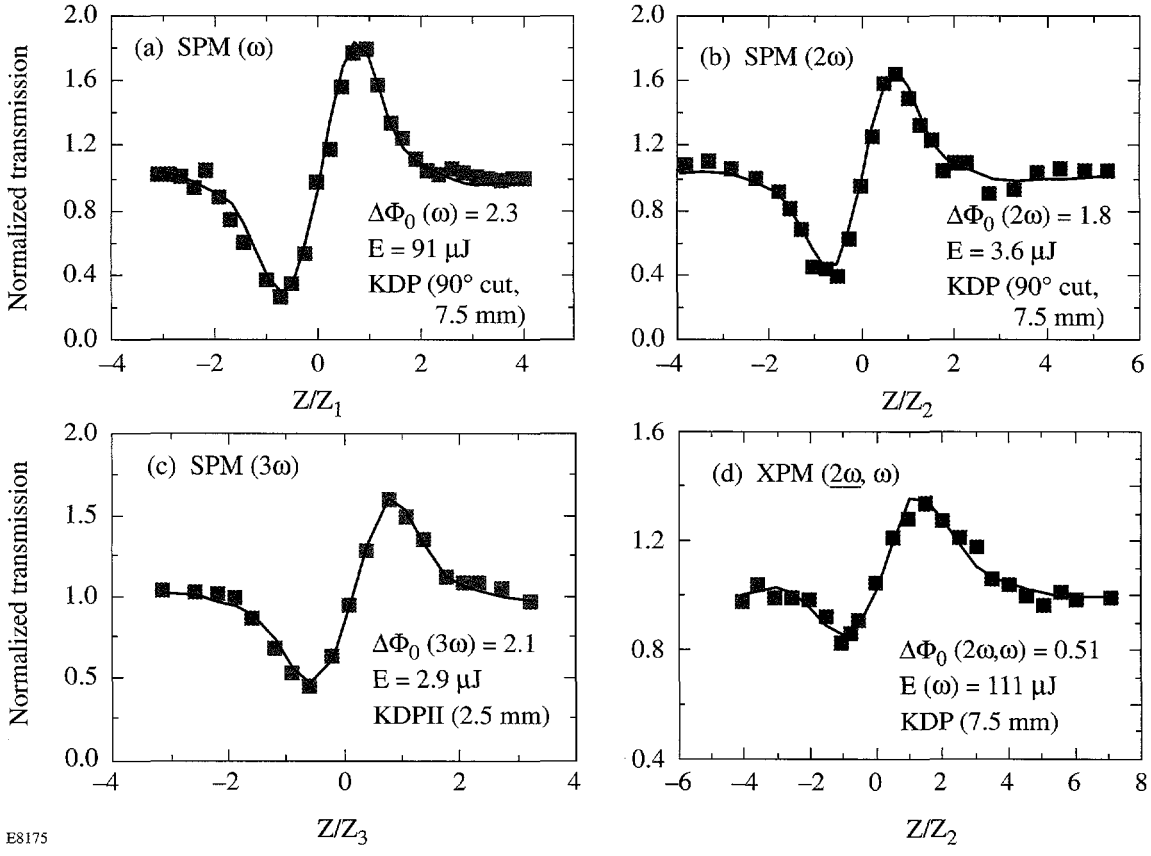

Figure 74.63
Experimental one- and two-beam Z-scans as a function of z/z_{0i}, $i = 1,2,3$. In all cases, the solid line is fit to determine the peak phase shift Φ_0. (a) Single beam, $\lambda_1 = 1.053$ μm, $\Phi_0 = 2.3$; (b) single beam, $\lambda_2 = 0.527$ μm, $\Phi_0 = 1.8$; (c) single beam, $\lambda_1 = 0.351$ μm, $\Phi_0 = 2.1$; and (d) two-color (λ_1,λ_2) beams, $\Phi_0 = 0.51$.

thickness is 1%. The errors for the beam waist coming from the measurement of focal length and diameter of the aperture are 1.6%. The largest error comes from measuring the IR pulse width and beam energy. The pulse widths of SH and TH were calculated based on the measurement of the IR pulse. The resultant error of the on-axis intensity is 12% for IR, 15% for SH, and 18% for UV. The nonlinear coefficients of SPM and XPM with different polarizations were measured, with the results presented in Table 74.III. Both n_2 and γ, which are related through the index of refraction, are presented. Our results for the nonlinear coefficient at 1.053-μm wavelength are in good agreement with the work reported in Refs. 20 and 21, which is shown in the last two columns of Table 74.III. To our knowledge, the nonlinear SPM coefficients at wavelengths of 0.527 μm, and 0.351 μm, and the XPM coefficient between 1.053 μm and 0.527 μm, are the first data set reported for KDP.

In the two-color Z-scan, there is a further temporal walk-off between the two colors with different wavelengths in the KDP sample. To measure $n_2(o\text{-}o)$, in which both the probe and the pump beams are ordinary waves, the optical axis of the sample KDP (90° cut) is perpendicular to the polarization of IR and SH pulses. Both the pump and probe beams are o-waves in the sample, and the pump pulse (IR) moves 0.51 ps ahead of the probe pulse (SH) after the sample. For measuring $n_2(e\text{-}e)$, both the pump (IR) and probe beams (SH) are e-waves in the sample, and the pump pulse moves 0.59 ps ahead of the probe pulse in the sample crystal. We include the walk-off effects in the theoretical fit by dividing the sample into segments and integrating the nonlinear phase experienced in each of the pieces. In each of the segments, the probe beam will experience a different nonlinear phase shift, which is due to the different time delay between the pump and probe; thus, the XPM can be

Table 74.II: The parameters of Z-scans for measuring SPM and XPM in KDP and the resultant phase shift Φ_0.

	λ (μm)	Pulse width (ps)	Energy (μJ)	Φ_0
(a)	1.053 (e) (SPM)	2.0	91±5	2.3±0.1
(b)	0.527 (o) (SPM)	1.41	3.6±0.4	1.8±0.1
(c)	0.351 (o) (SPM)	1.45	2.9±0.4	2.1±0.1
(d)	1.053 (e), 0.527 (e) (XPM) (pump) (probe)	2.0 (IR) 1.41 (SH)	111±7 (IR) <0.2 (SH)	0.51±0.04

Table 74.III: Measured values of n_2 and γ for KDP at 1.053 μm, 0.527 μm, and 0.351 μm for SPM and cross-phase coefficients between 0.527 μm and 1.053 μm. Also shown are results of previous work from Refs. 20 and 21.

	$n_2(10^{-13}$ esu)	$\gamma(10^{-16}$ cm^2/W)	$n_2(10^{-13}$ esu) other work	$\gamma(10^{-16}$ cm^2/W) other work
1.053 μm (o)	0.8±0.2	2.3±0.5	0.72[20]	2.9±0.9[21]
(e)	0.88±0.2	2.5±0.5	0.78,[20] 1.0±0.3[21]	
0.527 μm (o)	1.4±0.4	4.0±1.0		
	1.3±0.3	3.5±0.9		
0.351 μm (o)	2.4±0.7	7.0±2.0		
(e)	1.2±0.4	3.0±1.0		
0.527 (e); 1.053 (e) (weak; strong)	0.03±0.01	0.10±0.03		
0.527 (o); 1.053 (o) (weak; strong)	0.023±0.007	0.06±0.02		

well determined. We could improve the sensitivity of our measurement by putting a predelay crystal[34] before or after the frequency-doubling crystal to compensate for the walk-off introduced in the measured sample.

In conclusion, a top-hat Z-scan method was used to measure the phase shift caused by the self- and cross-phase nonlinearity in KDP crystals. The third-order nonlinear coefficient of KDP at different polarizations at wavelengths of 1.053 μm, 0.527 μm, and 0.351 μm was obtained. By considering the temporal walk-off between the pump and probe beams in the crystals, we are also able to estimate the nonlinear index of refraction due to the cross-phase modulation.

ACKNOWLEDGMENT

We thank R. Boni for providing several crystals, R. S. Craxton for performing pulse-width calculations, and both for many helpful discussions. This study was supported by the U.S. Department of Energy Office of Inertial Confinement Fusion under Cooperative Agreement No. DE-FC03-92SF19460, the University of Rochester, and the New York State Energy Research and Development Authority. The support of DOE does not constitute an endorsement by DOE of the views expressed in this article.

REFERENCES

1. W. L. Kruer, *The Physics of Laser Plasma Interactions*, Frontiers in Physics, Vol. 73, edited by D. Pines (Addison-Wesley, Redwood City, CA, 1988), Chap. 5.
2. J. C. Kieffer, P. Audebert, M. Chaker, J. P. Matte, H. Pépin, T. W. Johnston, P. Maine, D. Meyerhofer, J. Delettrez, D. Strickland, P. Bado, and G. Mourou, Phys. Rev. Lett. **62**, 760 (1989).
3. C. Y. Chien, G. Korn, J. S. Coe, J. Squier, G. Mourou, and R. S. Craxton, Opt. Lett. **20**, 353 (1995).
4. R. W. Boyd, *Nonlinear Optics* (Academic Press, Boston, 1992).
5. G. P. Agrawal, *Nonlinear Fiber Optics* (Academic Press, Boston, 1989).
6. K. J. Blow, N. J. Doran, and B. P. Nelson, Opt. Lett. **10**, 393 (1985).
7. M. N. Islam, L. F. Mollenauer, and R. H. Stolen, in *Ultrafast Phenomena V*, edited by G. R. Fleming and A. E. Siegman, Springer Series in Chemical Physics (Springer-Verlag, Berlin, 1986), pp. 46–50.
8. J. D. Kafka and T. Baer, Opt. Lett. **12**, 181 (1987).
9. R. H. Stolen and J. E. Bjorkholm, IEEE J. Quantum Electron. **QE-18**, 1062 (1982).
10. R. R. Alfano *et al.*, Phys. Rev. A **35**, 459 (1987).
11. L. Zheng, R. S. Craxton, and D. D. Meyerhofer, in *Conference on Lasers and Electro-Optics*, Vol. 15, 1995 OSA Technical Digest Series (Optical Society of America, Washington, DC, 1995), pp. 131–132; L. Zheng, "Third-Harmonic Generation of Intense Laser Pulses," Ph.D. thesis, University of Rochester, 1997.
12. M. Sheik-bahae, A. A. Said, and E. W. Van Stryland, Opt. Lett. **14**, 955 (1989).
13. M. Sheik-bahae *et al.*, IEEE J. Quantum Electron. **26**, 760 (1990).
14. S. R. Friberg and P. W. Smith, IEEE J. Quantum Electron. **QE-23**, 2089 (1987).
15. Y.-H. Chuang, Z. W. Li, D. D. Meyerhofer, and A. Schmid, Opt. Lett. **16**, 7 (1991).
16. A. Owyoung, IEEE J. Quantum Electron. **QE-9**, 1064 (1973).
17. M. J. Weber, D. Milam, and W. L. Smith, Opt. Eng. **17**, 463 (1978).
18. M. J. Moran, C.-Y. She, and R. L. Carman, IEEE J. Quantum Electron. **QE-11**, 259 (1975).
19. W. Seka, J. M. Soures, S. D. Jacobs, L. D. Lund, and R. S. Craxton, IEEE J. Quantum Electron. **QE-17**, 1689 (1981).
20. R. Adair, L. L. Chase, and S. A. Payne, Phys. Rev. B **39**, 3337 (1989).
21. D. Milam and M. J. Weber, J. Appl. Phys. **47**, 2497 (1976).
22. M. Sheik-Bahae *et al.*, Opt. Lett. **17**, 258 (1992).
23. R. S. Craxton, IEEE J. Quantum Electron. **QE-17**, 1771 (1981).
24. W. Zhao and P. Palffy-Muhoray, Appl. Phys. Lett. **63**, 1613 (1993).
25. M. Born and E. Wolf, *Principles of Optics: Electromagnetic Theory of Propagation, Interference and Diffraction of Light*, 6th ed. (Pergamon Press, Oxford, 1980), p. 435.
26. J. D. Gaskill, *Linear Systems, Fourier Transforms, and Optics* (Wiley, New York, 1978).
27. Y.-H. Chuang, D. D. Meyerhofer, S. Augst, H. Chen, J. Peatross, and S. Uchida, J. Opt. Soc. Am. B **8**, 1226 (1991).
28. Optical Glass Filters, Scott Glass Technologies, Inc., Duryea, PA 18642.
29. Model GP-MF 702, Panasonic, Secaucus, NJ 07094.
30. PIN 10D 4303, UDT Sensors, Inc., Hawthorne, CA 90250.
31. JD 1000 Joulemeter, Molectron Detector, Inc., Portland, OR 97224.
32. A. E. Siegman, *Lasers* (University Science Books, Mill Valley, CA, 1986).
33. Y. Wang and R. Dragila, Phys. Rev. A **41**, 5645 (1990).
34. Y. Wang, B. Luther-Davis, Y.-H. Chuang, R. S. Craxton, and D. D. Meyerhofer, Opt. Lett. **16**, 1862 (1991).

Micromechanics of Material-Removal Mechanisms from Brittle Surfaces: Subsurface Damage and Surface Microroughness

The cold processing of optical glasses usually involves rough grinding, microgrinding, and polishing. In microgrinding,[1,2] the resulting brittle-material-removal rate produces a cracked layer near the glass surface, referred to as subsurface damage (SSD). [Editor's note: The acronym for subsurface damage (SSD) used in this article should not be confused with its more common use as an acronym for smoothing by spectral dispersion.] Of course, the optical quality as well as the strength of the resulting surface is affected by such subsurface damage, so there is the need to understand the generation of subsurface damage as well as its measurement. Preston[3] was the first to observe that the damaged layer usually increases in proportion to the surface microroughness (SR). Preston measured a proportionality factor of 3 to 4, which seemed to be independent of the grinding conditions. We emphasize that subsurface damage is a statistical measure of the ground surface rather than a reflection of the deepest flaw that might control, say, the mechanical strength of the surface.

The direct measurement of SSD is tedious; therefore, fast and reliable techniques to measure subsurface damage are necessary: The dimple method, which is often used,[4,5] relies on the observation that a sufficiently deep spherical impression produced on the damaged optical surface must penetrate into and past the damaged layer. Wafering methods may also be used. The fact that SSD scales with SR was later confirmed, for example, by Aleinikov,[6] who showed that SSD induced by lapping of glasses and other brittle ceramics (with hardness changing 30-fold, fracture toughness 6-fold, and Young's modulus 20-fold) was 3.9±0.2 times SR for SiC abrasives (100 to 150 μm). This observation indicates that SSD may be estimated from SR, whose measurement is significantly simpler and less time consuming. Aleinikov also found that SSD increased with increasing size of microindentation cracks. Aleinikov's correlations between indentation crack length, subsurface damage, and surface roughness are summarized in Fig. 74.64.

Since the Preston[3] and Aleinikov[6] work showed the scaling of SSD with SR under loose-abrasive grinding conditions, it is interesting to extend their observations to bound-abrasive grinding. This issue was more recently examined by Edwards and Hed,[8] who studied the relation of SSD to SR under bound-diamond-abrasive conditions (53 to 65 μm and 180 to 250 μm in size). Edwards and Hed found that for the three glasses they studied (borosilicate crown BK7, zerodur, and fused silica) the average SSD exceeded the proportionality factor of about 4 found under loose-abrasive conditions: Specifically, they found that the average SSD was 6.4±1.3 times the peak-to-valley (p–v) surface roughness (as measured by a profilometer). The factor of 6.4 was arrived at by dividing SSD by SR for each glass. On the other hand, this proportionality factor becomes identical to that of Aleinikov when all three materials tested by Edwards and Hed are treated together (see Fig. 74.65). Similar observations have been reported for deterministic microgrinding of optical glasses with bound-abrasive-diamond tools of smaller size (2 to 4 μm to 70 to 80 μm) (see Lambropoulos *et al.*[9,10]).

In this article, we describe measurements of subsurface damage and surface roughness resulting from microgrinding optical glasses with metal-bonded diamond-abrasive ring tools and present a model for interpreting such data.

Experiments

To study the relation between surface microroughness (SR) and subsurface damage (SSD) in optical glasses, we selected eight glasses that are often used in optical design. The glasses included fused silica (Corning 7940), the borosilicate crown glass BK7, the crown glass K7, the lanthanum crown glass LaK9, the PbO containing dense flint glasses (SF7, SF58), the flint glass F7, the short (kurz) flint glass KzF6, and the dense tantalum flint glass TaFD5.

1. Glass Mechanical Properties

Glasses, like other brittle materials, are characterized by their hardness and fracture toughness.[11,12] Hardness was determined in air via the usual Vickers indentation method with loads ranging from 10 gf to 1 kgf. Fracture toughness was also determined from microindentation, via the model of Evans,[13] which, as we had previously shown,[9] is in good agreement with

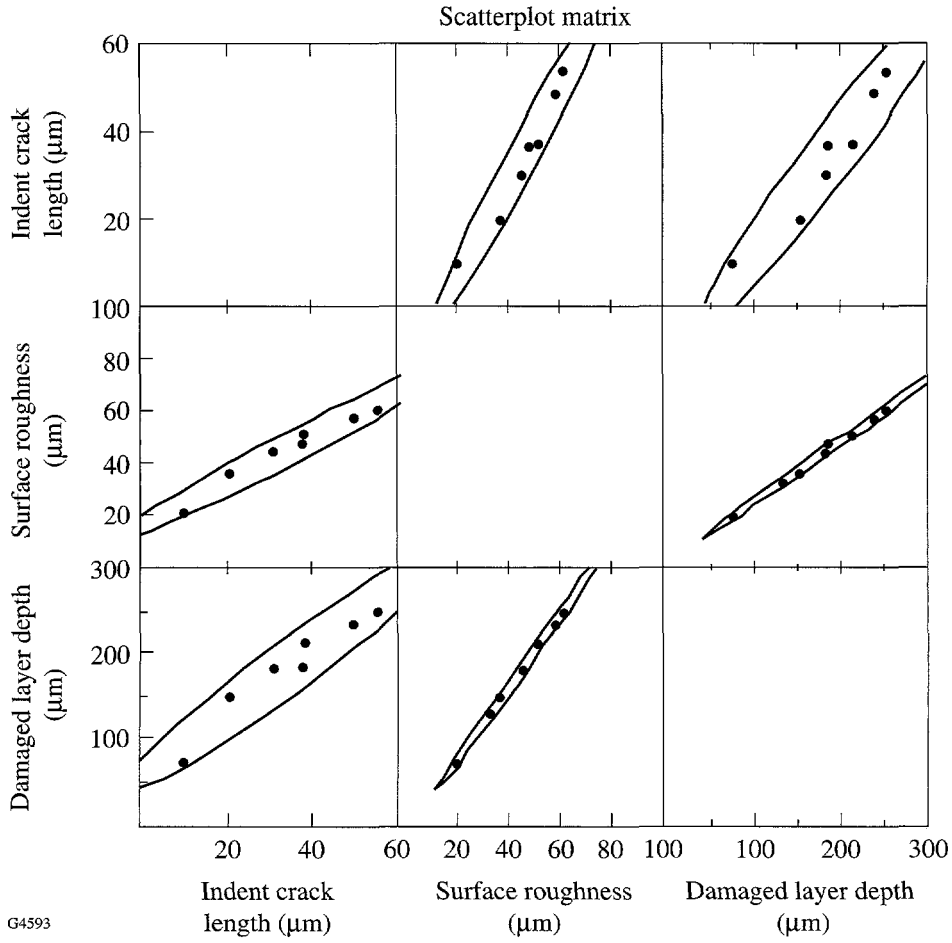

Figure 74.64
Correlations of indentation crack size, surface roughness, and subsurface damage under loose-abrasive conditions. Data are from Aleinikov.[6] Equivalents to Russian glasses can be found in Ref. 7. The individual brittle materials studied by Aleinikov are indicated in the work by Lambropoulos *et al.*[10]

the measurement of fracture toughness via bulk methods. Evans[13] used dimensional analysis and curve fitting over a range of $c/(D/2)$ from 1.5 to 7 and proposed

$$K_c = H\sqrt{D/2}\left(\frac{E}{H}\right)^{0.4} 10^{f(x)}, \quad x = \log_{10}\left(\frac{c}{D/2}\right), \tag{1}$$

$$f(x) = -1.59 - 0.34x - 2.02x^2 + 11.23x^3 - 24.97x^4 + 16.32x^5,$$

where K_c is fracture toughness, H hardness (Vickers), D indentation diagonal, E Young's modulus, and c the half-crack size. Microindentation of densifying glasses, such as fused silica, cannot be analyzed in this manner.[14–16]

In our notation, H denotes hardness, or resistance to plastic, irreversible deformation, measured by estimating the area of an indentation impressed under load P. Hardness is defined in terms of either projected area or actual area of contact.

Specifically, H_K denotes Knoop hardness, extracted from measuring the long diagonal of a rhomboidal pyramid impression under load P by P/(projected contact area) = (constant) P/(long diagonal)^2, with the (constant) dependent on the rhomboidal pyramid geometry.

H_V denotes Vickers indentation, extracted from measuring the average diagonal of a square pyramid impression under load P by P/(actual contact area) = (constant) P/(average diagonal)^2, with the (constant) dependent on the square pyramid geometry.

For the same measured diagonal, Knoop indentations penetrate about half as much into the surface as Vickers indentations; thus, H_K more closely measures near-surface hardness. Generally, Knoop hardness H_K increases with Vickers hardness H_V. This correlation has been described in detail by Lambropoulos *et al.*[9]

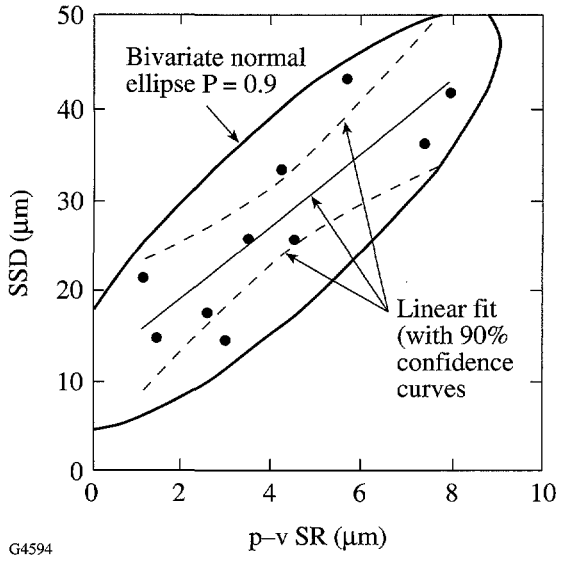

Figure 74.65
Relation of subsurface damage (SSD) to surface roughness (SR), measured in bound-diamond-abrasive grinding by Edwards and Hed.[8] Shown are the bivariate ellipse (at P = 90%, with aspect ratio of about 3.8) and the confidence curves at the level of 90% (dashed line). The straight line fit has a slope of 4.0±0.9 and an intercept of 11±4.

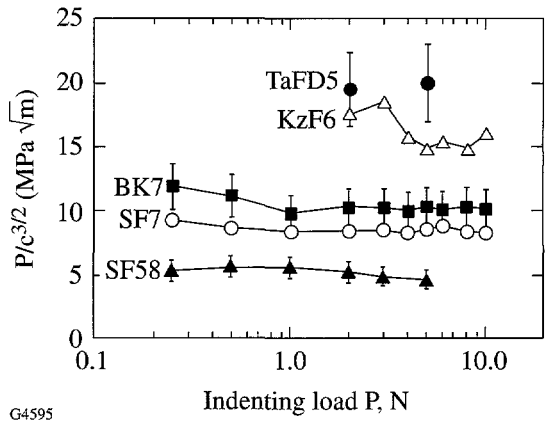

Figure 74.66
Correlation of the measured indentation crack length c (tip-to-tip surface trace length is $2c$) with applied load P shows essentially a constant value of the ratio $P/c^{3/2}$.

Figure 74.66 shows the measured values of $P/c^{3/2}$ versus the applied load P for some of our tested glasses, indicating that this ratio is essentially constant over the indenting loads used. Table 74.IV shows the glass thermomechanical properties. Data for density ρ, glass transition temperature T_g, coefficient of thermal expansion α, Young's modulus E, and Poisson ratio ν are from manufacturers' catalogs. Knoop hardness H_K and Vickers hardness H_V are at 1.96 N. K_c for fused silica was taken from the Corning catalog. H_V and K_c data of LaK9 were estimated from that of neighboring glasses LaK10, LaK11.[9,17] Data in Table 74.IV other than Vickers hardness have been reported previously.[10]

2. Deterministic Microgrinding Experiments

The surface-grinding experiments were done on a deterministic microgrinding platform, where infeed rate is imposed, thus resulting in surfaces of minimal figure errors, superior finish, and minimal damage. Imposing infeed rate leads to precise knowledge of the amount of removed material when microgrinding optical glasses. In the platform used, both the tool and work axis spin. The variable angle between these axes of rotation can be used to produce spherical surfaces of variable radius of curvature (from 5 mm to planar surfaces).

Table 74.IV: Thermomechanical properties of optical glasses.

Glass	ρ g/cm^3	T_g °C	α $10^{-6\circ}$ C^{-1}	E GPa	ν	H_K GPa	H_V GPa	K_c MPa $\sqrt{m}$
FS-C7940	2.20	1,090	0.52	73	0.17	5.6	8.5	0.75
SF58	5.51	422	9.0	52	0.26	2.7	3.5	0.46
SF7	3.80	448	7.9	56	0.23	3.4	5.3	0.67
BK7	2.51	559	7.1	81	0.21	5.1	7.2	0.82
K7	2.53	513	8.4	69	0.21	4.6	6.2	0.95
KzF6	2.54	444	5.5	52	0.21	3.7	5.5	1.03
LaK9	3.51	650	6.3	110	0.29	5.7	(5.5)	(0.95)
TaFD5	4.92	670	7.9	126	0.30	7.3	10.0	1.54

Pollicove and Moore have described progress in fabrication of precision optical components via deterministic microgrinding with rigid, computer-controlled machining centers and high-speed tool spindles.[18,19] Deterministic microgrinding has been used to manufacture convex and concave spherical surfaces, as well as aspheres. Specular surfaces, resulting after less than 5 min of deterministic microgrinding, have typical rms microroughness of less than 20 nm, 1 μm of subsurface damage, and a surface figure better than 1/2 wave peak-to-valley. Typical infeed rates are 5 to 10 μm/min with 2- to 4-μm bound-abrasive-diamond tools.

Three metal-bonded diamond-abrasive ring tools were sequentially used on each surface (aqueous coolant Loh K-40, relative speed of work and tool of about 30 m/s): 70 to 80 μm, 10 to 20 μm, and 2 to 4 μm at infeed rates of 1 mm/min, 50 μm/min, and 5 μm/min, respectively. Three cuts were done with each tool, all at a tool speed of about 30 m/s (tool rotation of 11,250 rpm, work rotation of 150 rpm).

After each cut, the surface roughness (SR) at three locations on the optical surface was measured using the Zygo New View 100 white-light interferometer (20× Mirau), a 3-D imaging surface structure analyzer. It uses coherence-scanning white-light interferometry for noncontact imaging and measurement of surface microstructure and topography. One portion of a light beam reflects from a test surface and the other portion from an internal high-quality reference surface. Both portions are then directed onto a solid-state camera with 320 × 240 pixels. Interference between the two light-wave fronts results in an image of light and dark interference fringes, indicating the surface structure of the test part. The test part is scanned by vertically moving the objective with a piezoelectric transducer. As the objective scans, a video system captures intensities at each camera pixel. Lateral resolution is determined by the microscope objective field of view and the number of pixels and is ultimately limited by the wavelength of the light source. With a 20× objective, the field of view is 0.35×0.26 mm^2.

Subsurface damage (SSD) was measured with the dimple method,[4,5] in which a steel ball is gently ground with fine diamond paste (0.25 μm) onto the optical surface, thus penetrating into and past the SSD zone. Optical measurement of the image reveals an outer ring of SSD surrounding an inner circle of damage-free surface. Measurement of the ring radii and knowledge of the steel sphere radius lead to the extraction of the SSD. Three dimples were done for each cut for the 2- to 4- and 10- to 20-μm tools. Because of the time required to produce dimples into and past the SSD of the surfaces ground with the 70 to 80 abrasives, no SSD measurements were done on these surfaces. Figures 74.67 and 74.68 summarize the roughness and subsurface damage measurements.

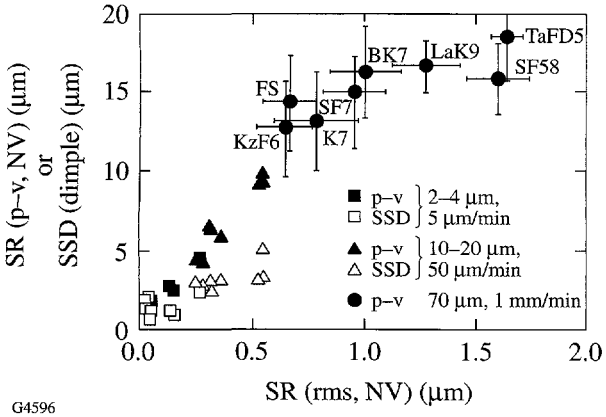

Figure 74.67
Summary of the measurements of peak-to-valley and rms surface roughness (SR) resulting from all three grinding tools used. Surface roughness was measured via the New View white-light interferometer, and subsurface damage (SSD) via the dimple method.

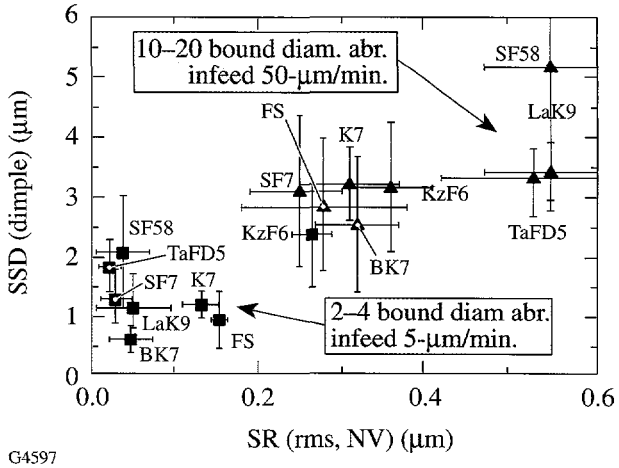

Figure 74.68
Summary of measurements for the rms surface roughness (SR) (white-light interferometry) and subsurface damage (SSD) (dimple method) for the deterministically microground surfaces with the 2- to 4-μm and 10- to 20-μm abrasives. A straight line correlation of all data has a slope of 5.5±0.9 and $R^2 = 0.73$.

Model for Ratio of Subsurface Damage to Surface Roughness

When a sharp indenter transmits normal load P into a brittle surface, the resulting indentation diagonal D is determined by the force P, the material hardness, and the sharpness of the indenting surface:

$$H = \frac{2P\sin\psi}{D^2} \tag{2}$$

with hardness defined via contact area between the indenter and the material (Fig. 74.69). Indentation mechanics can be simplified by considering the displaced material as occupying the volume of an equivalent half-sphere of radius a. Equating the volume displaced under the actual indenter (diagonal D) with that of the equivalent half-sphere volume $2\pi a^3/3$, we find

$$\frac{a}{D} = \left[\frac{3}{24\pi\sqrt{2}}\right]^{1/3}(\cot\psi)^{1/3} = 0.304(\cot\psi)^{1/3}. \tag{3}$$

Indentation induces a larger zone of plastically deformed material, approximately hemispherical with radius b. Length scales a (radius of indented half-sphere) and b (plastic zone size) can be correlated via the Hill model of the expanding cavity in a perfectly plastic material, discussed by Chiang *et al.*[20] This relation is further simplified to[20,21]

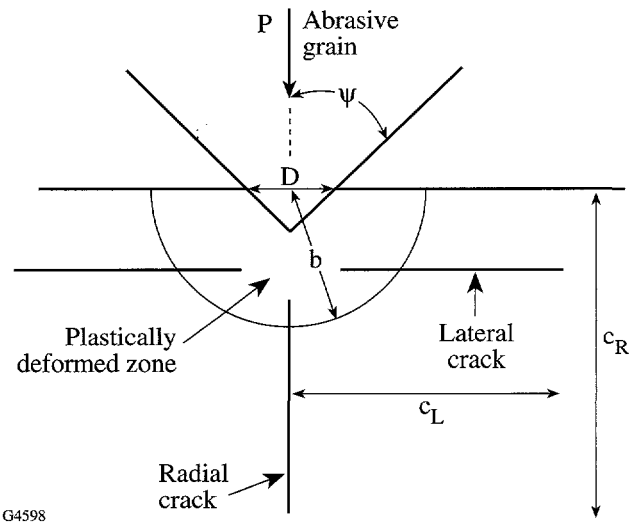

Figure 74.69
Schematic of sharp indentation shows indentation diagonal D, plastic zone size b, lateral and radial crack lengths c_L and c_R. Volume displaced by the indenter is equivalent to half-sphere of radius a.

$$\frac{b}{a} = \left(\frac{E}{H}\right)^m, \tag{4}$$

where m is a dimensionless constant in the range $m = 1/3$ to $1/2$. The more traditional approach in the fracture literature uses $m = 1/2$.[22–24] More recent data analysis suggests that $m = 1/3$ may be more appropriate.[25]

When the load P exceeds some threshold value, surface cracks appear.[21] The length c_R of radial cracks emanating from the indentation is related to fracture toughness K_c and load P by[22–25]

$$K_c = \alpha_K\left(\frac{E}{H}\right)^{1-m}(\cot\psi)^{2/3}\frac{P}{c_R^{3/2}}. \tag{5}$$

α_K is a dimensionless number, found from indentation data of Fig. 74.66 for the three glasses TaFD5 (high fracture toughness K_c), BK7 (intermediate K_c), and SF58 (low K_c). We fitted Eq. (5) to the measured fracture toughness K_c for $m = 1/2$ and $m = 1/3$, and found

$$\alpha_K(m) = 0.027 + 0.090\left(m - \frac{1}{3}\right). \tag{6}$$

Fracture mechanics analysis of microindentation shows that the residual stress field is tensile at the boundary of the elastic and plastic zones at the symmetry axis of the indentation, where any lateral cracking is expected to originate.[21,26] As lateral cracks remove material from the surface, we assume that the resulting SR is equal to the plastic zone depth b, following Buijs and Korpel–Van Houten.[27,28] Other assumptions may also be made, as by Lambropoulos *et al.*[29] Such assumptions have been compared and discussed by Lambropoulos.[30] We also assume that the depth SSD of the subsurface damage zone is equal to the depth of the radial cracks c_R; thus, the ratio of SSD to SR is

$$\frac{\text{SSD}}{\text{SR}} = \frac{c_R}{b} = 2.326\,\alpha_K^{2/3}\left(\frac{E}{H}\right)^{(2-5m)/3}$$

$$\frac{(\cot\psi)^{1/9}}{(\sin\psi)^{1/2}}\left[\frac{P}{\left(K_c^4/H^3\right)}\right]^{1/6}. \tag{7}$$

Indenting load P naturally scales with the material length scale K_c^4/H^3, as has been observed previously by Lawn,[31,32] Chiang *et al.*,[21] and Marshall *et al.*[26] The dependence of the ratio SSD/SR on the actual load P is rather weak (power of 1/6), which explains the experimental fact that over a wide range of abrasives, speeds, and pressures used there seems to be a constant ratio of SSD to SR (for example, Refs. 6 and 8).

Figure 74.70 shows the dependence of the SSD/SR on load P and sharpness angle ψ. For sharp abrasives ($\psi \to 0$), the ratio SSD/SR $\to \infty$, whereas for flat abrasives $(\psi \to \pi/2)$, SSD/SR $\to 0$. Figure 74.71 shows that by using typical material properties for optical glasses, intermediate values of ψ(20° to 80°), and typical indenting loads from 0.1 to 10 N, the ratio SSD/SR is in the range 4±2. Our range of indenting loads includes loads estimated to occur under lapping conditions. Chauhan *et al.*[33] estimated the maximum transmitted force to vary from 1.2 to 4.1 N as lapping abrasives ranged in size from 10 to 65 μm.

Guided by the model predictions for the dependence of ratio SSD/SR on glass mechanical properties, we have plotted in Fig. 74.72 the measured ratio SSD/SR versus the factor K_c^4/H^3 for grinding with the 10 to 20 abrasives under deterministic micro-grinding conditions (data from Fig. 74.68). Plotted in this manner, the experimental data show a dependence on K_c^4/H^3 like a power of –0.15±0.08, which is in general agreement with the model predictions of a power of –0.167. Of course, such a comparison is valid only as long as the force transmitted by the bonded abrasive grains is essentially constant among the various ground glasses.

The model discussed above also allows us to address the question: Under what circumstances can the depth of subsurface damage actually be less than the surface roughness? Such a condition would essentially mean that no subsurface damage would be present in the ground surface, thus resembling a condition of ductile grinding or polishing. Requiring that ratio SSD/SR < 1 leads to

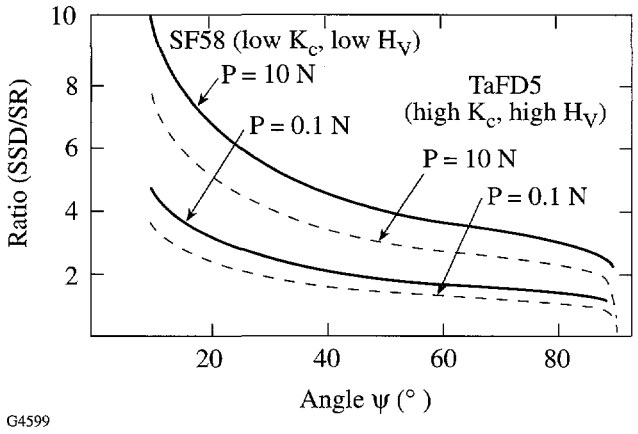

Figure 74.70
Ratio SSD/SR versus sharpness angle ψ for properties corresponding to glasses TaFD5 (hard, tough) and SF58 (soft, brittle). Indenting forces 0.1 or 10 N; factor $m = 0.40$.

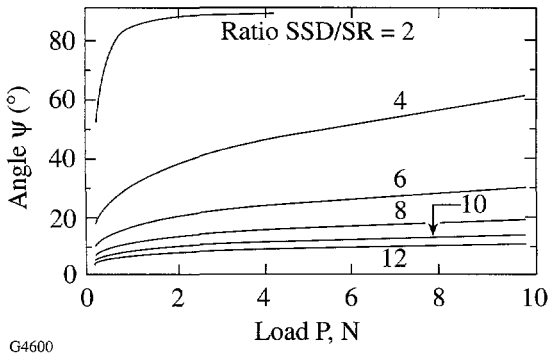

Figure 74.71
Ratio SSD/SR versus sharpness angle ψ and load P for typical optical glass (BK7). Factor $m = 0.40$.

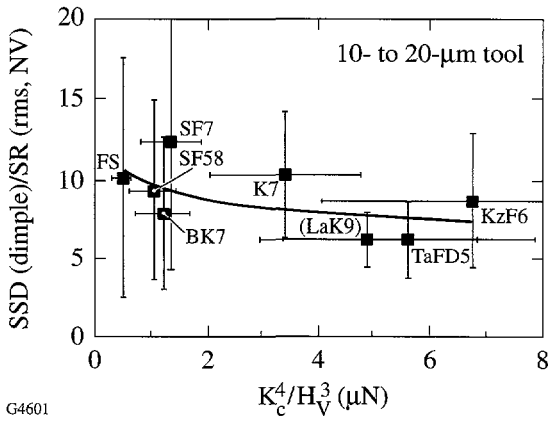

Figure 74.72
Measured ratio of subsurface damage (dimple method) to rms surface roughness (interferometry) versus the material-dependent load K_c^4/H^3 for the surfaces ground with the 10- to 20-μm metal-bonded diamond-abrasive tools. Hardness is H_V at 1.96 N. Datum for LaK9 is in parentheses since its K_c and H_V were estimated from neighboring glasses LaK10 and LaK11.

$$\frac{\mathrm{SSD}}{\mathrm{SR}} < 1 \Rightarrow P < \frac{\left(K_c^4/H^3\right)}{(2.326)^6\ \alpha_K^4 \left(\frac{\mathrm{E}}{H}\right)^{2(2-5m)}} \frac{(\sin\psi)^3}{(\cot\psi)^{2/3}}. \quad (8)$$

This result reveals that in order to promote more polishing-like conditions, the right-hand side of the above inequality must be made as large as possible to accommodate as large as possible a range of indenting forces P. Noticing that the dependence on the ratio (E/H) is rather weak (since m is in the range from 1/3 to 1/2), the polishing-like conditions can be achieved by a large value of the material-dependent load scale K_c^4/H^3, or by a large value of the angular factor $(\sin\psi)^3/(\cot\psi)^{2/3}$. This factor is a monotonically increasing function of the abrasive sharpness ψ; thus, polishing-like conditions are promoted by high fracture toughness K_c, low hardness H, and relatively flat abrasives contacting the manufactured optical surface. These effects are in addition to the chemical effects identified by Cook.[34] Notice, however, that other mechanical effects in polishing have been identified, both for polishing with traditional methods such as polyurethane pads[35,36] and for more recent polishing platforms that take advantage of subaperture material removal under computer–numerically controlled algorithms where the polishing slurry is a mixture of abrasive particles with a magneto-rheological fluid, as discussed by Jacobs *et al.*[37] and interpreted by Lambropoulos *et al.*[38]

Figure 74.67 shows that for those instances where both the p–v roughness and the subsurface damage (SSD) were measured, the p–v roughness was an upper bound to the subsurface damage. For the finer 2- to 4-μm bonded diamond abrasives, the measured p–v roughness is a good approximation to the actual SSD. For the intermediate 10- to 20-μm abrasives, the p–v roughness is a close upper approximation to the SSD. The reason is that the dimple method reveals a statistical measure of subsurface damage, without being able to identify the deepest flaw. On the other hand, the p–v roughness is dictated by the single deepest flaw detected within the measured area. Thus, we expect that the p–v roughness would exceed the SSD measurement by the dimple method, as indeed our measurements indicate. The usefulness of this observation becomes clear from the fact that, when the subsurface damage from a very rough ground surface is to be determined, the dimple method must produce a dimple into and past the damaged zone. This would be a very time-consuming and labor-intensive task for deep SSD, while requiring only a few minutes when subsurface damage is only a few microns in depth.

Conclusions

We have presented a micromechanics model based on the sharp indentation of a brittle surface to interpret the measured ratio of subsurface damage (SSD) to surface microroughness (SR). The measurements were done under deterministic microgrinding conditions where the imposed infeed rate produces surfaces with minimal figure error, and optimum surface roughness and subsurface damage. The glasses ground span a wide range of optical glasses.

We used 70- to 80-μm, 10- to 20-μm, and 2- to 4-μm abrasives at infeeds of 1 mm/min, 50 μm/min, and 5 μm/min, respectively. For the 70- to 80-μm abrasives, the rms SR, measured with white-light interferometry, ranges from 0.65 to 1.6 μm and the p–v roughness from 12 to 19 μm. For the 10- to 20-μm abrasives, rms SR ranges from 0.25 to 0.55 μm, p–v from 4 to 10 μm, and the SSD (measured with the dimple method) from 2.5 to 5.1 μm. For the 2- to 4-μm abrasives, rms SR ranges from 0.02 to 0.27 μm, p–v from 1.3 to 4.4 μm, and the SSD (measured with the dimple method) from 0.90 to 2.3 μm.

These measurements support the conclusion that peak-to-valley surface roughness measured by interferometry provides an upper bound to the subsurface damage measured via the dimple method. This observation is useful, and its applicability should be further explored for a wider range of optical materials under a large range of manufacturing processing conditions.

The micromechanics model predicts the ratio of SSD/SR in terms of the load transmitted by the abrasive grain, the sharpness of the abrasive, and the glass mechanical properties (Young's modulus E, hardness H, fracture toughness K_c). The dependence on load is rather weak, in agreement with our measurements and others. The effect of abrasive sharpness is more pronounced. In the limit of SSD/SR < 1, i.e., when polishing-like or ductile grinding conditions prevail, no SSD can be identified because it is enveloped within the surface microroughness. Such conditions are promoted for brittle materials with high fracture toughness and low hardness. Flat abrasive grains have the same effect.

ACKNOWLEDGMENT

We acknowledge many helpful discussions with and insights from Mr. Don Golini of QED Technologies, LLC (Rochester, NY) and with Profs Paul Funkenbusch, Stephen Burns, and James C. M. Li of the Mechanical Engineering Department at the University of Rochester.

REFERENCES

1. T. S. Izumitani, *Optical Glass*, American Institute of Physics Translation Series (American Institute of Physics, New York, 1986), Chap. 4, pp. 91–146.
2. H. H. Karow, *Fabrication Methods for Precision Optics* (Wiley, New York, 1993), Chap. 5.
3. F. W. Preston, Trans. Opt. Soc. **XXIII**, 141 (1921–22).
4. A. Lindquist, S. D. Jacobs, and A. Feltz, in *Science of Optical Finishing*, 1990 Technical Digest Series (Optical Society of America, Washington, DC, 1990), Vol. 9, pp. 57–60.
5. Y. Zhou *et al.*, J. Am. Ceram. Soc. **77**, 3277 (1994).
6. F. K. Aleinikov, Sov. Phys. Tech. Phys. **27**, 2529 (1957).
7. L. B. Glebov and M. N. Tolstoi, in *CRC Handbook of Laser Science and Technology*, Vol. V: Optical Materials, Part 3, Supplement 2: Optical Materials, edited by M. J. Weber (CRC Press, Boca Raton, FL, 1995), pp. 823–826.
8. D. F. Edwards and P. P. Hed, Appl. Opt. **26**, 4677 (1987).
9. J. C. Lambropoulos, T. Fang, P. D. Funkenbusch, S. D. Jacobs, M. J. Cumbo, and D. Golini, Appl. Opt. **35**, 4448 (1996).
10. J. C. Lambropoulos, S. D. Jacobs, B. Gillman, F. Yang, and J. Ruckman, in *Advances in Fusion and Processing of Glass II,* edited by A. G. Clare and L. E. Jones, Ceramic Transactions, Vol. 82 (The American Ceramic Society, Westerville, OH, 1998), pp. 469–474. See also Laboratory for Laser Energetics LLE Review **73**, 45, NTIS document No. DOE/SF/19460-212 (1997). Copies may be obtained from the National Technical Information Service, Springfield, VA 22161.
11. R. F. Cook and G. M. Pharr, J. Am. Ceram. Soc. **73**, 787 (1990).
12. I. J. McColm, *Ceramic Hardness* (Plenum Press, New York, 1990).
13. A. G. Evans, in *Fracture Mechanics Applied to Brittle Materials*, edited by S. W. Freiman (American Society for Testing and Materials, Philadelphia, 1979), Vol. ASTM STP 678, Part 2, pp. 112–135.
14. A. Arora *et al.*, J. Non-Cryst. Solids **31**, 415 (1979).
15. H. Li and R. C. Bradt, J. Non-Cryst. Solids **146**, 197 (1992).
16. J. C. Lambropoulos, S. Xu, and T. Fang, J. Am. Ceram. Soc. **79**, 1441 (1996).
17. J. Schulman, T. Fang, and J. Lambropoulos, *Brittleness/Ductility Database for Optical Glasses*, ver. 2.0, Department of Mechanical Engineering and Center for Optics Manufacturing, University of Rochester, Rochester, NY (1996).
18. H. M. Pollicove and D. T. Moore, Laser Focus World, March 1991, 145.
19. H. M. Pollicove and D. T. Moore, in *Optical Fabrication and Testing Workshop Topical Meeting*, 1992 Technical Digest Series (Optical Society of America, Washington, DC, 1992), Vol. 24, pp. 44–47.
20. S. S. Chiang, D. B. Marshall, and A. G. Evans, J. Appl. Phys. **53**, 298 (1982).
21. *ibid.*, 312.
22. A. G. Evans and E. A. Charles, J. Am. Ceram. Soc. **59**, 371 (1976).
23. B. R. Lawn, A. G. Evans, and D. B. Marshall, J. Am. Ceram. Soc. **63**, 574 (1980).
24. G. R. Anstis *et al.*, J. Am. Ceram. Soc. **64**, 533 (1981).
25. M. T. Laugier, J. Mater. Sci. Lett. **4**, 1539 (1985).
26. D. B. Marshall, B. R. Lawn, and A. G. Evans, J. Am. Ceram. Soc. **65**, 561 (1982).
27. M. Buijs and K. Korpel-van Houten, J. Mater. Sci. **28**, 3014 (1993).
28. M. Buijs and K. Korpel-van Houten, Wear **166**, 237 (1993).
29. J. Lambropoulos, M. J. Cumbo, and S. D. Jacobs, in *Optical Fabrication & Testing Workshop Topical Meeting* (Optical Society of America, Washington, DC, 1992), Vol. 24, pp. 50–53.
30. J. C. Lambropoulos, S. Xu, and T. Fang, Appl. Opt. **36**, 1501 (1997).
31. B. R. Lawn, T. Jensen, and A. Arora, J. Mater. Sci. **11**, 573 (1976).
32. B. R. Lawn and D. B. Marshall, J. Am. Ceram. Soc. **62**, 347 (1979).
33. R. Chauhan *et al.*, Wear **162–64**, 246 (1993).
34. L. M. Cook, J. Non-Cryst. Solids **120**, 152 (1990).
35. T. S. Izumitani, in *Workshop on Optical Fabrication and Testing: A Digest of Technical Papers* (Optical Society of America, Washington, DC, 1982), pp. 1–4.
36. J. C. Lambropoulos, in *Optical Fabrication and Testing*, 1996 Technical Digest Series (Optical Society of America, Washington, DC, 1996), Vol. 7, pp. 88–91.
37. S. D. Jacobs, D. Golini, Y. Hsu, B. E. Puchebner, D. Strafford, Wm. I. Kordonski, I. V. Prokhorov, E. Fess, D. Pietrowski, and V. W. Kordonski, in *Optical Fabrication and Testing*, edited by T. Kasai (SPIE, Bellingham, WA, 1995), Vol. 2576, pp. 372–382.
38. J. Lambropoulos, F. Yang, and S. D. Jacobs, in *Optical Fabrication and Testing*, 1996 Technical Digest Series (Optical Society of America, Washington, DC, 1996), Vol. 7, pp. 150–153.

Cholesteric Liquid Crystal Flakes—A New Form of Domain

The last 20 years have seen a growth of mixed-media systems in which cholesteric liquid crystals (CLC's) are one component. These include polymer-dispersed CLC's[1] in which the CLC's are confined to microdroplets within a continuous isotropic polymer and CLC's in gels[2] in which there is a small amount of polymer to stabilize the CLC structure. In either case, the continuity of the cholesteric texture is interrupted.

CLC's are characterized by a structure in which the average direction of molecules in a given plane, indicated by a unit vector called the director **n**, rotates about an axis. The continuously rotating director produces a helix. The length through which the director makes a complete 360° cycle is called the pitch P of the cholesteric. When the orientation of the helix axis is normal to the boundary surfaces, the texture produced is called Grandjean or planar.[3] This texture is responsible for the selective wavelength and polarization reflection unique to CLC's.[4] The center of the selective reflection wavelength band is given by

$$\lambda_0 = \bar{n}_n P, \tag{1}$$

where $\bar{n}_n$ = the average refractive index at a given plane perpendicular to the helix, calculated[5] from the ordinary and extraordinary cholesteric refractive indices.

The optical characterization of the CLC structure may be done by several methods. One of the simplest ways to evaluate the homogeneity of the Grandjean texture is with a polarizing microscope. A CLC sample aligned to the Grandjean texture is viewed between crossed polarizers. Dark areas indicate that the molecules through which the light has passed are either perfectly aligned with the polarizer or analyzer or isotropically distributed. In either case, for CLC's, dark spots and lines indicate deviations from cholesteric structure that are referred to as *disclinations*.[6,7] Regions between the disclinations are called *domains*, although there is some lack of consensus about the physical nature of a domain. There is some sense of a discrete area in which the director orientation is essentially constant, although this is usually subjectively determined by judging areas that appear homogeneous.[8,9] The term *monodomain* refers to regions that can be characterized by a single director. When directors characterize domains that are rather random with respect to each other, the region is considered *polydomain*.[10]

While domain boundaries may exhibit clear-cut disclinations, domains may not always be separated by a well-defined surface. Instead, there may be a discontinuity in the director orientation.[11] These discontinuities were first observed by Grandjean[12] and correctly described by Cano[13] as being caused by pitch deformations. The helix stretches or contracts to span the gap of the cell with an integer multiple of half-pitches. When the elastic limit is reached, the helix structure either inserts or removes a half-pitch. Although these discontinuities are called Cano *lines*, they do not actually appear as lines but as borders between regions differing in thickness by one half-pitch. Between crossed linear polarizers, this manifests as different retardances and therefore different colors.[14,15]

Other imaging techniques, including scanning electron microscopy (SEM), transmission electron microscopy (TEM), and atomic force microscopy (AFM), have been developed to image the periodic structure of CLC's in the planar/Grandjean texture. For example, a sample of low-molecular-weight (LM) CLC was frozen between metal sheets, the sheets were forced apart, and platinum-carbon replicas of the resulting fractured edges were examined by SEM.[16–18] Periodic striations corresponding to the half-pitch suggested that the fracturing occurred along the helix profile. Even disclinations could be viewed by this technique. Not only replicated samples but also the frozen CLC's themselves were examined using SEM.[19] Because of LMCLC samples unfreezing or ice building up on the surfaces, DeGennes[20] suggested the use of polymerized CLC's for SEM study. This experiment was conducted for the first time in 1993[21] to visualize the molecular distribution around a Cano line. The images showed that there were layers to the molecular distribution, but no additional quantitative analysis was done.

Atomic force microscopy, developed in 1985,[22] has been used to examine Langmuir–Blodgett and transferred freely-suspended liquid crystal films[23] as well as liquid crystal films on graphite.[24] Liquid crystal films have shown some two-dimensional structure and some cholesteric periodicity but are often deformed by contact with the cantilever tip.

Cyclic polysiloxane oligomers,[25,26] in particular, have been examined by Bunning *et al.*[27,28] with TEM and AFM. Samples for these studies were aligned to the Grandjean texture by shearing between Teflon sheets, cooled to below their glass transition temperatures, and microtomed, producing samples free of the effect of underlying support[29] substrates. Results indicate that the cyclic polysiloxanes do show corrugated fresh surfaces with a periodicity equal to one-half the pitch. From TEM and AFM results, in conjunction with x-ray diffraction studies, Bunning *et al.*[30,31] drew further conclusions regarding the structural morphology. Their proposed structure consists of interdigitated sidechains, the extent of association being dependent on the composition and temperature. The siloxane backbones form layers that twist into the helical structure of the cholesteric with the sidechains aligned along the director **n**.

Imaging the multiple domains of the CLC's within mixed-media systems by the techniques described above is complicated by the production methods of these mixed-media systems. Methods include (a) emulsification[32] of the liquid crystal with a polymer and (b) phase separation[33] of the liquid crystal from solution with a polymer. The CLC domains are produced at the same time as the mixed medium itself. As a result, the domains can be characterized only *within* the medium. The domains may be diluted or contaminated by other components of the mixture.[34] Polymer "walls" may affect molecular alignment at domain boundaries.[35]

In this article, we describe the production and characterization of a new form of CLC's called *flakes*, proposed by Faris.[36] We examine individual flakes by optical light microscopy, SEM, and AFM. We will show that flakes maintain many of the optical properties of the continuous films from which they are made. The CLC flakes can be embedded into a host to form a new type of mixed medium in which the flakes provide well-characterized CLC domains. We will show how the orientation of these CLC flakes can be evaluated quantitatively using Bragg's Law in the form of Fergason's Equation:[37]

$$\lambda_r = \lambda_0 \cos\left\{\frac{1}{2}\left[\sin^{-1}\left(\frac{\sin\theta_i}{\bar{n}_{ch}}\right) + \sin^{-1}\left(\frac{\sin\theta_r}{\bar{n}_{ch}}\right)\right]\right\}, \quad (2)$$

where λ_0 = the wavelength at the center of the selective reflection band at normal incidence, λ_r = the wavelength at the center of the selective reflection band at oblique incidence, θ_i = incidence angle, θ_r = observation angle in air, and $\bar{n}_{ch}$ = the approximate average cholesteric refractive index.

The orientation of CLC flakes can be further understood by using a function known as turbidity τ. This useful parameter has been developed[38] for nematic droplets dispersed in a matrix that does not absorb liquid crystal. It characterizes the extent of scattering as a function of incidence angle and refractive index mismatch in the anomalous diffraction regime. Turbidity has not yet been investigated for cholesteric materials, but for nematics has been defined as

$$\tau = -\ln\left[\frac{T_{sample}(\theta_i)}{T_{blank}(\theta_i)}\right]\frac{\cos\left[\sin^{-1}(\sin\theta_i/n_{med})\right]}{t}, \quad (3)$$

where $T_{sample}(\theta_i)$ = transmittance of a sample, $T_{blank}(\theta_i)$ = transmittance of a blank used to correct for reflection from the film and substrate, t = thickness of the sample, and n_{med} = the refractive index of the embedding medium.

Preparation of CLC Flakes

Two types of cyclic polysiloxanes were used in this study: (a) noncrosslinkable of the type shown in Fig. 74.73 (adapted from Ref. 26), obtained from Wacker–Chemie in Munich[39] and designated CLC670, which refers to its λ_0 in nm and (b) crosslinkable, designated CC3767 and similar to that of Fig. 74.73 but with terminal methacryl groups and crosslinked by UV curing in the presence of a photoinitiator.[40] The exact ratios of chiral to nonchiral side-chains and the amount of added monomer (to reduce viscosity for ease of workability) are proprietary to the manufacturer.

In a procedure referred to as "knife-coating," the noncrosslinkable material is applied onto a silicon wafer,[41] which is heated to 130°C on a hotplate;[42] polysiloxane is then melted onto the substrate surface. A microscope slide placed on edge and referred to as the "knife" is used to smear the polysiloxane across the surface. This knife-coating process causes the CLC to be aligned in the Grandjean texture as observed by reflective color. The substrate is then quickly removed from the hotplate, allowing the CLC to be quenched to room temperature, "freezing in" the helical structure of the Grandjean texture. The CLC films prepared in this way are ~30 μm thick.

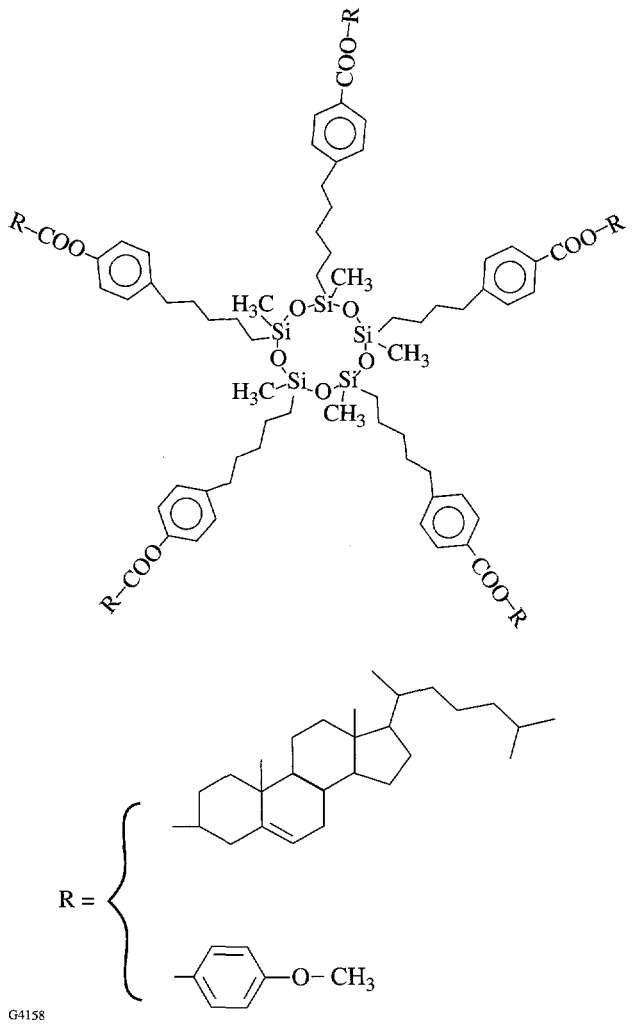

Figure 74.73
Structure of cyclic polysiloxane used in this study.

The crosslinked material is prepared by mixing the CLC with photoinitiator (1.5% by weight), sprinkling in 13-μm-sized glass fiber spacers,[43] and shearing the mixture between two 3-cm-diam, fused-silica substrates at 100°C. The sandwich cell, still at 100°C, is exposed for 2 min to ultraviolet light of $\lambda = 365$ nm and 15 mW/cm^2 at 5-cm distance.[44] After curing, the cell is pried open with a razor blade to expose the cured film.

For either method of preparation, the resulting "open-faced" film is placed in a Petri dish and covered with liquid nitrogen. The polymer CLC fractures and lifts slightly and temporarily off the silicon or glass surface. Methanol is used to wash the fractured CLC off the substrate.

Imaging Individual Flakes

1. Light Microscope

Viewed under a light microscope, flakes appear to be irregularly shaped with sharp corners. Figure 74.74 shows a micrograph of CLC670 flakes between crossed polarizers.[45] All samples show similar features. The flakes themselves appear to have few disclinations or Cano lines, suggesting that fracturing occurred along disclinations and discontinuities in the film, consistent with theoretical freeze-fracture models.[17]

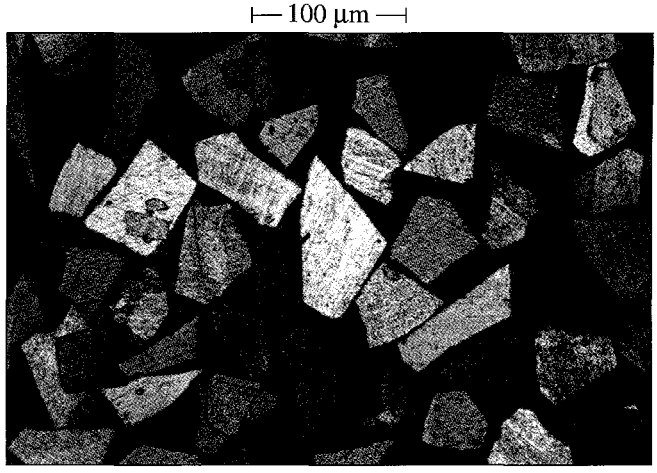

Figure 74.74
Photomicrograph of CLC670 flakes.

2. Scanning Electron Microscope

CC3767 (crosslinked) flakes were sputtered with silver and examined using scanning electron microscopy.[46] Samples like the one in Fig. 74.75 are seen to have an even more irregular structure than that which appeared under light microscopy. Some swelling is apparent at the edges of the flakes, which we attribute to absorption of the methanol used for the slurry. Periodic ridges are evident on many of the flakes. The freeze-fracture process appears to occur along the cholesteric helix profile, perpendicular to the director. From rough estimation of the magnitude of the pitch measured physically on the SEM observation screen, the pitch appears to be 486 nm. Based on Eq. (1) and prefracture measurements of λ_0 (= 712 nm) and $\bar{n}_n$ (= 1.5812 at 712 nm), the optically calculated pitch for this sample is 450 nm. The similar magnitude of the numbers suggests that the observed periodic ridges are, in fact, indicative of pitch. Due to parallax caused by the tilt of the sample and the SEM sample table, however, measurements from these photographs are only estimates.

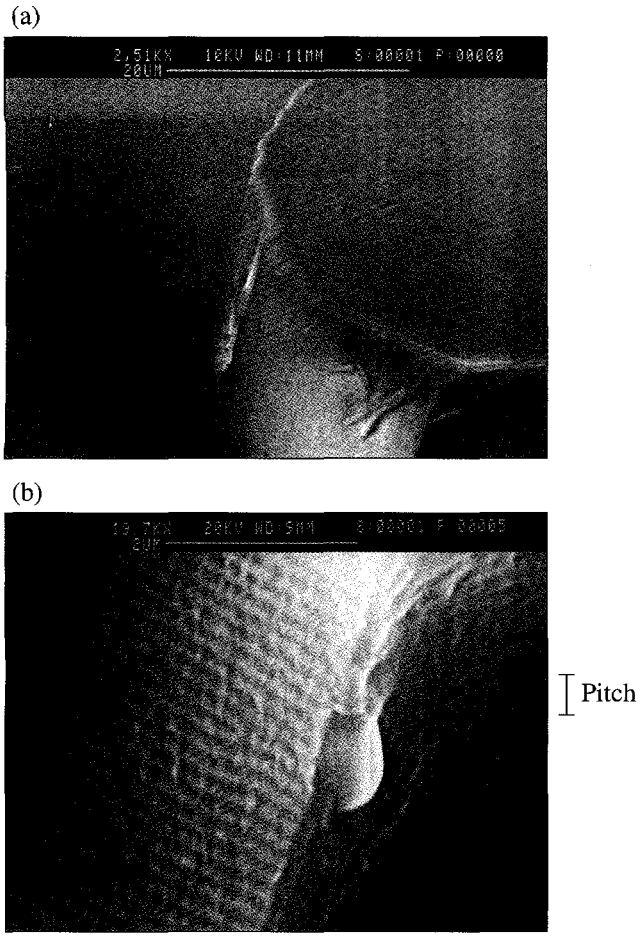

Figure 74.75
Scanning electron micrographs of a CLC flake (sample: CC3767). (a) There is slight swelling at the edges of a flake. (b) At higher magnification, periodic ridges corresponding to the pitch can be seen.

The noncrosslinked flakes were also examined with SEM. These also showed ridges consistent with half-pitch periodicity. Neither sputtering nor SEM voltage appeared to damage, melt, or decompose any of the flakes.

3. Atomic Force Microscope

To determine pitch physically and without parallax, a single CC3767 flake was mounted vertically against a small piece of glass using epoxy.[47] The flake was placed in an atomic force microscope[48] whose tip consisted of a pyramidal crystal of silicon nitride attached to a cantilever. The edge of the flake was rastered under this cantilever. Deflections of the cantilever by the surface resulted in an image profile of the surface like the one shown in Fig. 74.76. Our images are consistent with the microtomed and free-surface AFM images of cholesteric polysiloxanes obtained by Meister *et al.*[49] and provide a third unique view of the cholesteric corrugation due to pitch periodicity.

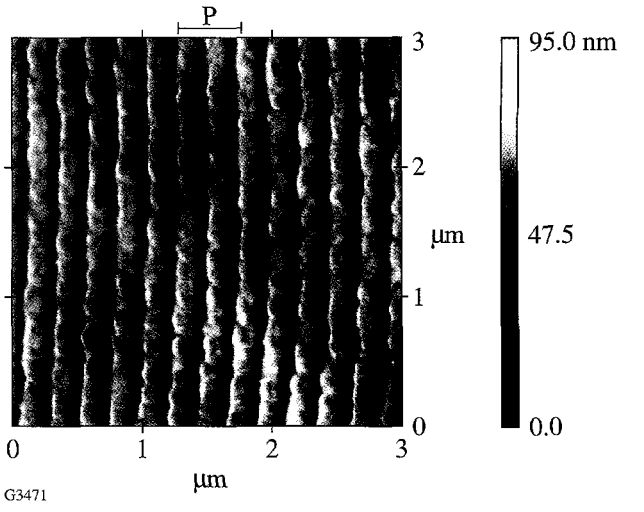

Figure 74.76
Atomic force micrograph of a CLC flake edge (sample: CC3767). The pitch measured from this image is 451 nm.

Since there is no parallax in this image, the pitch can be measured directly to be 451 nm. The pitch calculated from the prefracture optical measurements, listed in the **Scanning Electron Microscope** section, is 450 nm. The excellent agreement confirms that the ridges seen in both SEM and AFM images are those of the cholesteric helix profile exposed by freeze-fracturing. More importantly, the process of producing flakes from polymer CLC films maintains the pitch and, as we will show, the selective wavelength reflection capability of the original film.

AFM measurements of the noncrosslinkable CLC670 gave equally good agreement of physically measured and optically calculated pitch. The remaining tests described below used only the noncrosslinkable material to avoid the time-consuming process of preparing, curing, and splitting sandwich cells.

Sizing of CLC Flakes

To separate flakes by size, a stack of stainless steel screen sieves[50] is used. Table 74.V lists the mesh sizes and nominal particle-size ranges when stacked in order of increasing mesh number. Flakes in methanol slurry are dripped into the sieve stack, using methanol to wash the flakes through. Each stage is washed with methanol until the effluent appears visually clear. Material retained by each sieve is collected by methanol slurry and allowed to dry by evaporation. For a typical initial charge

Table 74.V: Sieve designations and measured ranges of CLC670 flakes.

Sieve designation (mesh size)	Nominal particle-size range (μm) that should be trapped in sieve	Median and standard deviation of each sieve group of CLC670 flakes measured by Horiba LA-900 (μm)
80	>180	218±204
170	90–180	124±28
325	45–90	66±26
635	20–45	35±16
Pan	<20	24±14

of about 5 g of flakes, the sieving process typically requires about 5 h to completely separate the larger-sized flakes (>45 μm) into three groups. The "20- to 45-μm" sieve cut takes an additional 4 h of sieving time. All separated samples are allowed to dry for 4 days.

To test whether the sieve separation technique was efficient, each sieve cut (what was trapped in the sieve as well as the final bottom collection pan) was tested for particle-size distribution using the Horiba LA-900 Particle Analyzer.[51] In this instrument, the particles are suspended in a fluid. For the CLC flakes, this fluid was methanol. No additional surfactant was used since initial testing with detergent as a surfactant led to the formation of bubbles, which interfered with particle detection. A small-fraction sample container of approximately 50-mL volume was used. In the small-fraction container, particles were kept in suspension in the instrument's light beam using a magnetic stirrer. The particles scattered and diffracted light from both a HeNe laser beam and a beam from a halogen lamp. The latter was equipped with two filters: one to pass 610-nm light and one to pass 480-nm light. Size distribution was determined based on an instrument algorithm that calculates the distribution of spherical particles that would give the same scattering pattern as the sample particles. The distribution of the algorithm's spherical particles is given as a percent frequency F%. The size range detectable by the Horiba LA-900 is 0.04 to 1000 μm. Plots are typically Gaussian in shape on a semilogarithmic scale for a natural distribution of particles.[52] For particles that are not uniform in shape, such as the CLC flakes, the particle analyzer detects the largest dimension,[53] so the median value of such a distribution lies on the high side of the sieve designation. The measured results are shown in Table 74.V.

Each size-group of CLC670 is plotted in Fig. 74.77 to show if the different size-group distributions are well or poorly separated. The vertical lines indicate the nominal ranges based on the sieve designations listed in Table 74.V. The medians and modes are well separated. In general, however, the ">180-μm" group contains flakes that exceed the Horiba LA-900 size-detection limits. The "<20-μm" group shows some agglomeration. Otherwise, each mode falls within the sieve-size designation. There is overlap among the groups within the standard deviations for each distribution, so we may expect to see trends in optical behavior related to size but probably no optical behavior unique to a particular size-group since each group contains some flakes whose sizes are common to adjacent groups.

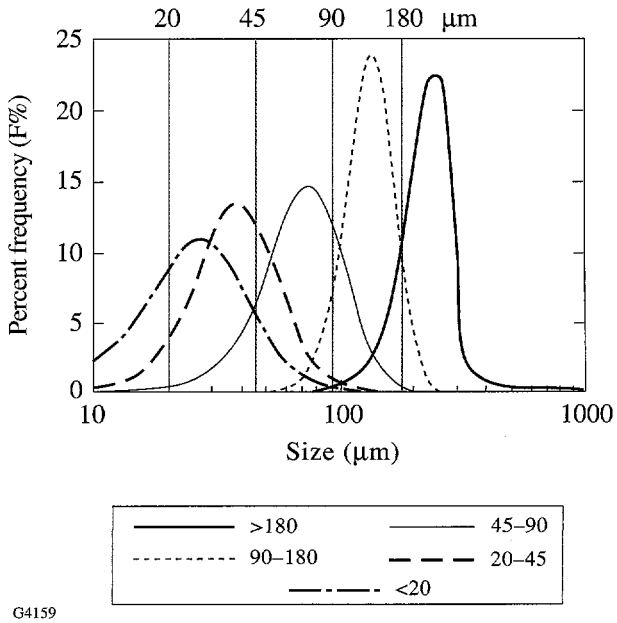

Figure 74.77
Effectiveness of sieving for separating size-groups. The vertical lines indicate the nominal size limits of the sieve designations.

Orientation of CLC Flakes

Glass disk substrates made from a conveniently available float glass ($n_{D,20} = 1.533$, 25-mm diameter, 1 mm thick) were weighed; then 1 mL of deionized water was dropped by graduated pipet onto each substrate to cover it to the edge. Flakes in methanol slurry were dripped onto the water bead by a medicine dropper. The flakes oriented themselves with their largest surface parallel to the meniscus. When the surface was visually covered with flakes, the underlying fluid was removed by medicine dropper. Each sample was allowed to dry. At regular intervals, each sample was weighed until three identical readings were obtained, indicating that the samples had completely dried (about 48 h total). After all the optical tests were completed for a given sample, its thickness was measured by contact gauge[54] in five spots and averaged. The gauge tip tended to disturb the flakes, so thickness measurements could not be made until optical testing was completed.

Since the >180-μm and <20-μm sieve groups for CLC670 were of anomalous size, they were excluded from optical testing so that comparisons of size effects on optical behavior could be drawn with more certainty by being based on the other three sieve groups. In addition, the >180-μm flakes, when oriented by water bead, did not completely cover the substrate. The <20-μm flakes, when oriented by water bead, tended to aggregate into visually observable inhomogeneities. Therefore, even qualitative comparisons involving these extreme sizes were not feasible.

Selective Reflection

Transmittance profiles of each size-group were determined by spectrophotometer[55] at 0° incidence. The results of three size-groups are shown in Fig. 74.78. There is a dramatic drop in overall transmittance with decreasing flake size; however, each size-group continues to show the selective wavelength reflection (manifested by a transmittance valley) characteristic of CLC's.

In addition, a CLC670 "45- to 90-μm" sample prepared by water-bead orientation was examined in transmission using right-hand circular and then left-hand circular incident polarization. Figure 74.79 shows that the CLC flakes continue to exhibit the selective polarization-handedness reflectivity also characteristic of CLC's.

Clearly, we have discrete CLC domains of prealigned Grandjean texture that continue to exhibit the selective wavelength and polarization of unfractured CLC films or of CLC polymer-dispersed or gel systems. These domains, however, are uncontaminated by any processing steps. The CLC flakes are also not subject to the alignment deformities that might be caused by confining walls.

The additional optical tests performed on these CLC flake samples will allow us to make comparisons by flake-size of orientation quality. In particular, we will look at the angle dependence of both the selective reflection wavelength and the scattering, considering CLC flakes as distributions of discrete cholesteric domains.

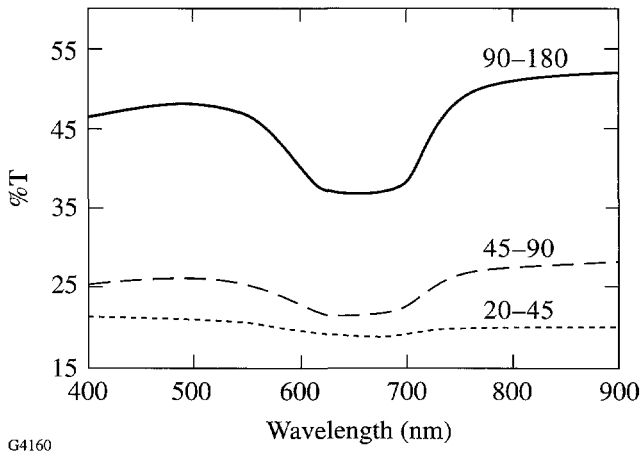

Figure 74.78
Transmittance profiles of three sieve groups.

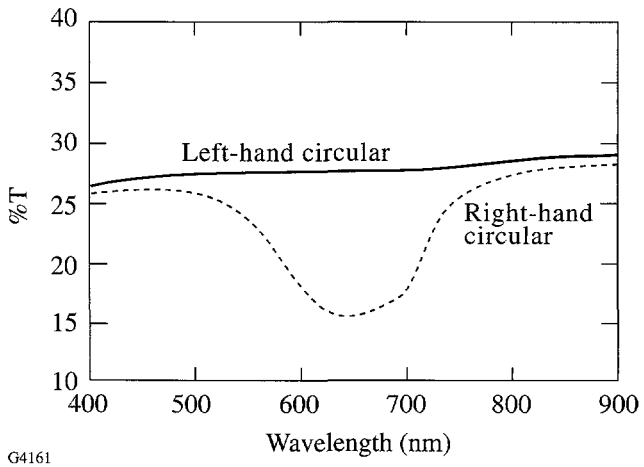

Figure 74.79
Selective polarization handedness of CLC flakes.

Angle Dependence of Selective Wavelength

Three to four samples from each size-group were prepared and examined in transmission at seven incidence angles (0°–60°). The center of the selective wavelength band was estimated by visual integration and recorded as λ_r-meas. The wavelength at 0° was recorded as λ_0. Equation (1) was used to calculate λ_r-theo. When measuring in transmission, the implicit assumption is $\theta_i = \theta_r$. The value of $\bar{n}_{ch}$ is 1.6, based on Abbe refractometer[56] measurements of the unfractured CLC films by a technique determined earlier for nematic liquid crystal polymers.[57] Figure 74.80 shows how well the average selective-reflection-wavelength measurements from each size-group agree with the calculated theoretical values.

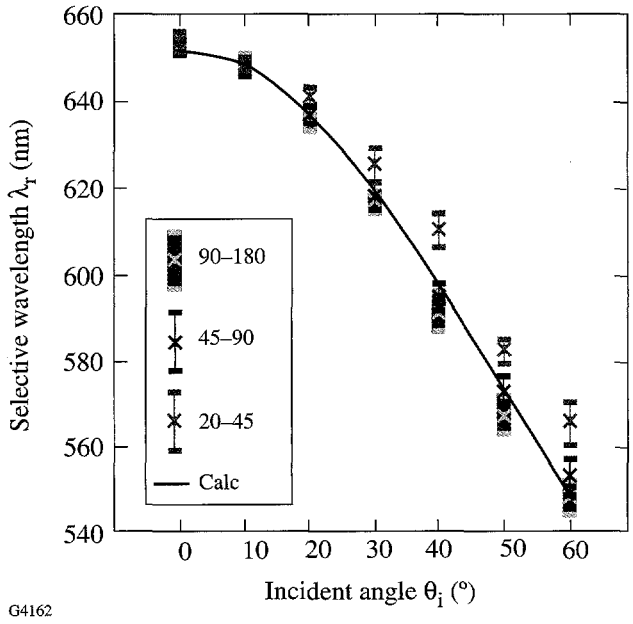

Figure 74.80
Angle dependence of selective wavelength reflection as a function of flake size.

The 45- to 90-μm flakes show better agreement with Bragg's Law in the form of Fergason's Equation than do the other two size-groups. We attribute this to a better orientation of the medium-sized flakes on the substrate. Their aspect ratio is large enough that the largest dimension is perpendicular to the thickness, so, during the water-bead orientation, the helix axis can align perpendicular to the substrate.

Scattering

We will interpret "scattering" here to refer to any redirection of light from its original path of propagation. As such, use of turbidity as a measure of scattering simply compares transmittance of samples, where lower transmittance corresponds to greater scattering. This section will show that the primary source of scattering by CLC flakes is the misalignment of the helix axes of individual flakes with respect to the substrate.

The same CLC670 samples prepared for angle-dependent wavelength studies were used for turbidity calculations. Turbidity was measured with a horizontal-pass HN32 Polaroid polarizing film[58] in the spectrophotometer as part of the background correction protocol. As incident angle was increased, the incident polarization remained *P*-polarized. The wavelength chosen for turbidity measurements needed to be well outside the selective reflection region, outside the region of substrate or CLC absorptivity, and part of a normal transmission scan that would not involve lamp, detector, or other voltage-dependent instrument changes; therefore, the chosen measurement wavelength was 900 nm.

The %T of a "blank" sample, i.e., a sample with everything but the liquid crystal, as well as the %T of the sample *with* liquid crystal were recorded at the same incident angle. Turbidity was calculated for all samples using Eq. (3) and averaged within each size-group at each incidence angle. Figure 74.81 shows the turbidity ranges of multiple samples of each group as well as for an unfractured continuous film. For each sieved size-group, the turbidity increases as the incident angle increases. The smaller the flakes, the higher the turbidity per unit thickness.

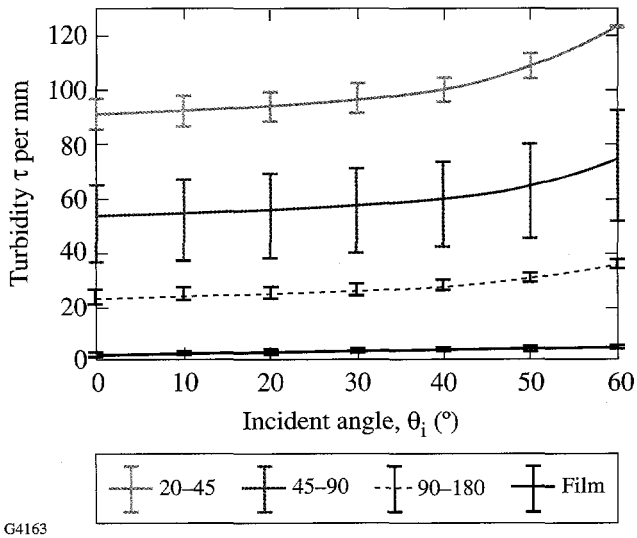

Figure 74.81
Turbidity ranges of multiple samples of each sieve group of CLC670 flakes.

As we saw in Fig. 74.78, transmission scans of flake samples of decreasing median size grow gradually wider and flatter with overall lower-percent transmittance. Due to their small aspect ratio, smaller flakes are not necessarily aligned with their helix axes perpendicular to the substrate. There will, then, be many angles of incidence and reflection for which some wavelength of a spectral scan will meet the Bragg/Fergason criterion of Eq. (2). Selective reflection may be expected to occur fairly uniformly across the spectrum as the variety of CLC flake orientations increases. As flake sizes get smaller, more flakes are required to cover the same sample area, resulting in this increase in orientation possibilities. Consequently, the turbidity increases as the disorder of the smaller flakes redirects more light out of the original propagation direction.

The flakes are still not small enough to be of the size of the measurement wavelength so we are examining the scattering geometrically. In anticipation of eventually being able to make CLC flakes as small as the domains of the other more common mixed-media systems,[59] the use of turbidity as a measure of scattering is used in this study even though it was developed originally for the so-called anomalous diffraction regime[60,61] in which the wavelength is only slightly smaller than the scatterers.

In analogy with mixed-media systems that employ index match or index mismatch to control scattering, the CLC flake samples were overcoated with one of two transparent hosts: (a) a silicone elastomer designated SE2061,[62] which has an ~0.2 index difference, *Dn*, from the average cholesteric index of CLC670 or (b) a transparent enamel filtered[63] from a commercially available paint[64] with a <0.04 index difference, *Dn*, from CLC670. In the overcoating process, 1 mL of host in a graduated medicine dropper was added dropwise to the center of the flake sample. Each host flowed uniformly and in its own time to the edge of the sample substrate. The overcoated flake samples were measured in the same way as the others, and turbidity was calculated for seven incident angles.

The turbidities of an uncoated sample, a sample overcoated with the moderate index match (SE2061), and a sample overcoated with the close index match (Testor's Enamel) are plotted for each size-group in Figs. 74.82(a), 74.82(b), and 74.82(c). In every case, overcoating with a host reduces the turbidity of the flake samples. There appears to be less of a difference between a moderate and a good index match than between a coated and an uncoated sample regarding turbidity of the larger flakes. In addition, the overcoated flakes show a narrower selective reflection band than uncoated flakes,[65] suggesting that the overcoating process improves the orientation of the flakes. This may explain why there was only a slight difference in turbidity between moderately and nearly index-matched CLC flakes: It is not the index match but rather

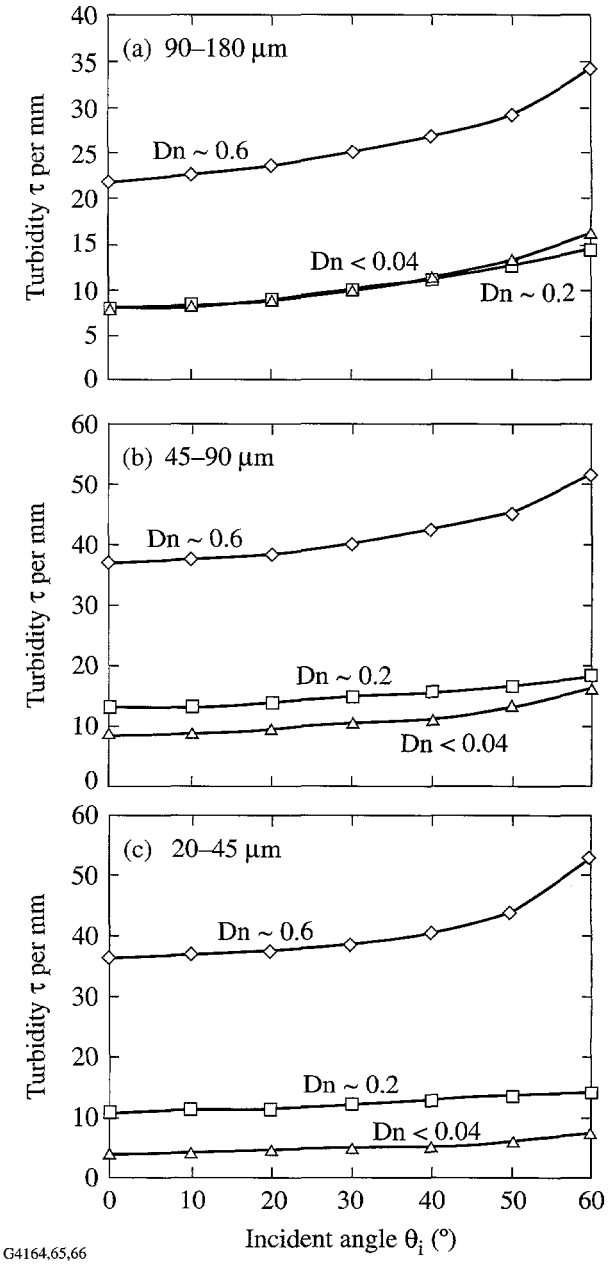

Figure 74.82
Comparison of turbidities of each flake size-group as a function of index match and incident angle. Each legend indicates the index mismatch of the flakes and host: 0.6 is air, 0.2 is SE2061, and <0.04 is enamel. The flake size-groups shown are (a) 90 to 180 μm, (b) 45 to 90 μm, and (c) 20 to 45 μm.

the flowing action of the hosts that reorients the flakes and reduces scattering.

Applications of Results

CLC flakes as part of a mixed medium can provide three main venues of use: decorative arts, document security, and models of other mixed-media systems. In the realm of decorative arts, we have shown elsewhere[66] that CLC flakes, with or without a host, can be successfully modeled and measured by standard colorimetric methods. As such, CLC flakes in a suitable host, such as the enamel used in this study, provide versatile paints and inks, which we have applied by brush, airbrush, and fountain pen to surfaces including paper, cloth, metal, and glass.

CLC flakes may also be considered for use in document security. Polymerized CLC films have been suggested for this purpose as overlays.[67] CLC flakes can be embedded into paper currency, for example, avoiding the problem caused by thin, brittle films. The use of CLC's allows angle-dependent color suitable for first-line identification. The unique polarized-reflection capability of CLC flakes provides a further deterrent to counterfeit reproduction.

Finally, CLC flakes are discrete cholesteric domains, which exhibit none of the limitations of polymer-dispersed and gel systems such as boundary deformations, high-voltage requirements, or domain contamination. With narrower sieve cuts to provide better flake-size uniformity, CLC flakes can provide an excellent physical model of the other mixed-media systems in which the domain is not so clearly characterized. Some work must be done to reduce CLC flake sizes for even closer modeling capability. Toward this end, small quantities of CLC flakes that are only 7 μm thick have been prepared.[68]

Conclusions

We have shown that CLC polysiloxane oligomer films can be fractured into smaller domains called flakes. These CLC flakes can be separated by size and oriented using flotation on an aqueous meniscus. CLC flakes maintain the wavelength and polarization selectivity of the original film. The CLC flakes can also be embedded into an isotropic polymer as a new kind of mixed medium in which the cholesteric domain structure is not contaminated, diluted, voltage dependent, or deformed. As work with this new mixed medium continues, we anticipate that narrower sieve cuts and smaller flakes will allow better use of CLC flakes as models for polymer-dispersed and gel CLC systems.

ACKNOWLEDGMENT

The authors thank Dr. F.-H. Kreuzer and Dr. Robert Maurer of the Consortium für elektrochemische Industrie GmbH and Munich for the CLC polysiloxanes. This work was supported by the U. S. Department of Energy, Office of Inertial Confinement Fusion under Cooperative Agreement DE-FC03-92SF19460, the University of Rochester, and the New York State Energy Research and Development Authority. The support of DOE does not constitute an endorsement by DOE of the views expressed in this article. Funding was also provided by Reveo, Inc.

REFERENCES

1. P. P. Crooker and D. K. Yang, Appl. Phys. Lett. **57**, 2529 (1990).
2. R. A. M. Hikmet, Liq. Cryst. **9**, 405 (1991).
3. G. S. Chilaya and L. N. Lisetski, Mol. Cryst. Liq. Cryst. **140**, 243 (1986).
4. HL. De Vries, Acta Cryst. **4**, 219 (1951).
5. W. U. Müller and H. Stegemeyer, Berichte der Bunsen-Gesellschaft. **77**, 20 (1973).
6. F. C. Frank, Faraday Discuss. Chem. Soc. **25**, 19 (1958).
7. M. Kléman, Rep. Prog. Phys. **52**, 555 (1989).
8. C. M. Dannels and C. Viney, Polymer News. **16**, 293 (1991).
9. C. Viney and C. M. Dannels, Mol. Cryst. Liq. Cryst. **196**, 133 (1991).
10. L. L. Chapoy, B. Marcher, and K. H. Rasmussen, Liq. Cryst. **3**, 1611 (1988).
11. A. Keller *et al.*, Faraday Discuss. Chem. Soc. **79**, 186 (1985).
12. M. F. Grandjean, Comptes Rendus Acad. Sci. **172**, 71 (1921).
13. R. Cano, Bull. Soc. fr. Minéral. Cristallogr. **92**, 20 (1968).
14. P. Kassubek and G. Meier, in *Liquid Crystals 2: Proceedings of the 2nd International Liquid Crystal Conference*, edited by G. Brown (Gordon and Breach, New York, 1969), pp. 753–762.
15. P. E. Cladis and M. Kléman, Mol. Cryst. Liq. Cryst. **16**, 1 (1972).
16. M. J. Costello, S. Meiboom, and M. Sammon, Phys. Rev. A. **29**, 2957 (1984).
17. D. W. Berreman *et al.*, Phys. Rev. Lett. **57**, 1737 (1986).
18. F. Livolant and Y. Bouligand, Mol. Cryst. Liq. Cryst. **166**, 91 (1989).
19. J. Voss and B. Voss, Z. Naturforsch. **31a**, 1661 (1976).
20. P. G. deGennes, *The Physics of Liquid Crystals*, 1st ed. (Clarendon Press, Oxford, 1974), p. 272.
21. I. Heynderickx, D. J. Broer, and Y. Tervoort-Engelen, Liq. Cryst. **15**, 745 (1993).

22. G. Binnig, C. F. Quate, and Ch. Gerber, Phys. Rev. Lett. **56**, 930 (1986).

23. R. M. Overney *et al.*, Langmuir **9**, 341 (1993).

24. H. Yamada, S. Akamine, and C. F. Quate, Ultramicroscopy **42–44**, 1044 (1992).

25. H. Finkelmann and G. Rehage, Makromol. Chem., Rapid Commun. **1**, 31 (1980).

26. F.-H. Kreuzer *et al.,* Mol. Cryst. Liq. Cryst. **199**, 345 (1991).

27. T. J. Bunning *et al.*, Liq. Cryst. **16**, 769 (1994).

28. T. J. Bunning *et al.*, Materials Directorate, Wright Laboratory, Wright-Patterson Air Force Base, OH, Interim Report #WL-TR-91-4089 (July 1989–June 1991).

29. C. Viney, G. R. Mitchell, and A. H. Windle, Mol. Cryst. Liq. Cryst. **129**, 75 (1985).

30. T. J. Bunning *et al.*, Mol. Cryst. Liq. Cryst. **231**, 163 (1993).

31. T. J. Bunning *et al.*, Liq. Cryst. **10**, 445 (1991).

32. J. L. Fergason, in *1985 SID International Symposium, Digest of Technical Papers*, edited by J. Morreale (Pallisades Inst. Res. Services, New York, 1985), pp. 68–70.

33. J. W. Doane *et al.*, Appl. Phys. Lett. **48**, 269 (1986).

34. M. Radian-Guenebaud and P. Sixou, Mol. Cryst. Liq. Cryst. **220**, 53 (1992).

35. D. K. Yang and P. P. Crooker, Liq. Cryst. **9**, 245 (1991).

36. S. M. Faris, U.S. Patent No. 5,364,557 (15 November 1994).

37. J. L. Fergason, Mol. Cryst. **1**, 293 (1966).

38. P. S. Drzaic and A. M. Gonzales, Appl. Phys. Lett. **62**, 1332 (1993).

39. F. Kreuzer, Wacker-Chemie, Consortium für Elektrochemische *Industrie GmbH*, Zielstattstrasse 20, D-81379 München, Germany.

40. The photoinitiator used is Irgacure-907, the trade name for 2-methyl-1,[4 methyl thiophenyl]2 morpholino propanone-1. Ciba Additives, Ciba-Geigy Corporation, Hawthorne, NY 10532-2188.

41. Silicon Epiprime, 100-mm-diam wafers, WaferNet, Inc., San Jose, CA 95131.

42. Dataplate digital hotplate/stirrer, PMC Industries, Inc., San Diego, CA 92121.

43. Ultra-Precision Glass Fibers, EM Industries, Inc., Advanced Chemical Division, Hawthorne, NY 10532.

44. UV Lamp Model B-100AP and Blak-Ray Ultraviolet Meter Model J-221, UVP, Inc., San Gabriel, CA 91778.

45. Photo used as October image in the American Institute of Physics 1996 "Beauty of Physics" calendar, Photographer: E. M. Korenic, Laboratory for Laser Energetics, University of Rochester, Rochester, NY 14623-1299.

46. In cooperation with Brian McIntyre, Scanning Electron Microscopist, The Institute of Optics, University of Rochester, Rochester, NY 14627.

47. Devcon® 5 Minute® Epoxy, ITW Devcon, Illinois Tool Works Company, Danvers, MA 01923.

48. Digital Instruments Nanoscope® III Scanning Probe Microscope, Digital Instruments, Inc., Santa Barbara, CA 93117.

49. R. Meister *et al.*, Phys. Rev. E **54**, 3771 (1996).

50. Newark Wire Cloth Company, Newark, NJ 07104.

51. LA-900 Laser Scattering Particle Size Distribution Analyzer, Horiba Instruments, Inc., Irvine, CA 92714.

52. T. Allen, in *Pigments—An Introduction to Their Physical Chemistry*, edited by D. W. Patterson (Elsevier, Amsterdam, 1967), Chap. 6, pp. 102–133.

53. M. Pohl, Horiba Instruments, Inc., Irvine, CA (private communication) (1994).

54. Digimatic indicator IDC Series 543, Mitutoyo Corporation, Paramus, NJ 07652.

55. Perkin-Elmer Model Lambda-9 spectrophotometer, Perkin-Elmer Corporation, Norwalk, CT 06859-0012.

56. Bellingham and Stanley Model 60/HR Abbe Refractometer, Bellingham and Stanley Ltd., North Farm Industrial Estate, Tunbridge Wells, Kent TN2 3EY, England.

57. E. M. Korenic, S. D. Jacobs, J. K. Houghton, A. Schmid, and F. Kreuzer, Appl. Opt. **33**, 1889 (1994).

58. HN32 Polaroid® linear polarizing film, Polaroid®, Polarizing Division, Norwood, MA 02062.

59. G. P. Montgomery, Jr., J. L. West, and W. Tamura-Lis, J. Appl. Phys. **69**, 1605 (1991).

60. S. Zumer, Phys. Rev. A **37**, 4006 (1988).

61. P. S. Drzaic, Mol. Cryst. Liq. Cryst. **261**, 383 (1995).

62. Petrarch Systems, Inc., Bristol, PA 19007.

63. Millex®-FG_{13} Filter Unit, 0.2 μm, Millipore Corporation, Bedford, MA 01730.

64. Testor's Gloss Enamel Gold (#1144), The Testor's Corporation, Rockford, IL 61104.

65. E. M. Korenic, "Colorimetry of Cholesteric Liquid Crystals," Ph.D. thesis, The Institute of Optics, University of Rochester, 1997, pp. 216–219.

66. E. M. Korenic, "Colorimetry of Cholesteric Liquid Crystals," Ph.D. thesis, The Institute of Optics, University of Rochester, 1997.

67. R. L. van Renesse, in *Optical Document Security*, edited by R. L. van Renesse (Artech House, Boston, 1994), Chap. 13, pp. 263–280.

68. S. D. Jacobs and T. Pfuntner, Laboratory for Laser Energetics, University of Rochester, Rochester, NY 14623-1299 (private communication) (1995).

Demonstration of Dual-Tripler, Broadband Third-Harmonic Generation and Implications for OMEGA and the NIF

A critical concern for Nd:glass fusion lasers such as OMEGA and the National Ignition Facility (NIF) is the uniformity of irradiation experienced by the fusion target. Uniform beams are generated by beam-smoothing schemes such as smoothing by spectral dispersion (SSD),[1] which vary the instantaneous speckle pattern on target on time scales that are short compared with relevant hydrodynamic time scales. In a simplified picture of beam smoothing, the laser presents a new speckle pattern to the target every coherence time, where the coherence time is given by the inverse of the bandwidth. The beam is smoothed because the target responds hydrodynamically to the average of a large number of independent speckle patterns. The ratio of the coherence time to the relevant hydrodynamic time is thus a key parameter. Alternatively stated, the time required to obtain a given level of uniformity is inversely proportional to the laser bandwidth.

Smoothing achieved using present fusion lasers is limited by the bandwidth acceptance of the KDP crystals that are used for third-harmonic generation (THG). Conventionally, THG involves frequency doubling in a first, "doubler" crystal followed by sum-frequency mixing in a second, "tripler" crystal.[2] Eimerl *et al.*[3] recently proposed, however, that broader-bandwidth THG can be achieved by using dual triplers, i.e., two tripler crystals in series with slightly different angular detunings from phase matching and appropriately chosen thicknesses. Oskoui[4] showed that by adding a second tripler to the existing conversion crystals in each beamline of the OMEGA laser system it is possible to increase the bandwidth acceptance by a factor of 3, and he developed an optimized design. Conversion of OMEGA to dual-tripler THG is now underway.

This article reports on what is believed to be the first experimental demonstration of dual-tripler THG. A second (type-II) KDP tripler, with 9-mm thickness, was added to a tripling cell (used on the former 24-beam OMEGA laser system) containing two type-II, 16-mm KDP crystals. All crystals were antireflection coated. The dual-tripler configuration was tested using a narrow-bandwidth, high-power laser beam whose angle of incidence on the crystals was varied. The THG conversion efficiency was measured as a function of this angle. Since an angular tilt of the incident IR beam is equivalent to a change in its wavelength (this relationship is linear to a good approximation, with ~ -160 μrad equivalent to 1 Å[5]), a measured increase in the angular acceptance of the THG conversion is equivalent to a proportional increase in the THG acceptance bandwidth.

One important parameter investigated in the experiment was the separation between the two triplers. The relative phase $\Delta\Phi$ between the three interacting waves (defined as $\Delta\Phi = \Phi_3 - \Phi_2 - \Phi_1$, where Φi is the phase of harmonic i) can change due to a number of factors, including dispersion in the air path between the triplers, dispersion in the windows of the crystal cell, and phase changes due to the coatings on the crystal surfaces. (The relative phase within a tuned crystal is zero by the definition of phase matching.) Using the formula $(n-1) \times 10^7 = 2726.43 + 12.288/\lambda^2 + 0.3555/\lambda^4$, where n is the refractive index and the wavelength λ is in μm,[6] 4.0 cm of air is predicted to be equivalent to a full cycle of phase shift [i.e., $(k_3-k_2-k_1)L=2\pi$, where k_i is the wave vector in air of harmonic i and L = 4 cm]. In the experiment, the relative phase $\Delta\Phi$ emerging from the first tripler was unknown due to dispersion in the output cell window; thus, to ensure the optimum $\Delta\Phi$ at the input to the second tripler, it was necessary to adjust the air gap to the optimum position within this 4-cm range.

This article extends the work of Ref. 7, which reports the experimental results, to include details of the dual-tripler design currently being implemented on OMEGA and a dual-tripler design that could provide a comparable bandwidth on the NIF.

Experiment

The laser beam used in the experiment originated from a Nd:YLF-based, diode-pumped, mode-locked oscillator that generated a train of bandwidth-limited, 100-ps-duration pulses. A single pulse was switched out and amplified in a flash-lamp-pumped, negative-feedback-controlled, regenerative amplifier[8] and two subsequent single-pass, flash-lamp-

pumped, Nd:YLF amplifiers separated by spatial filters. This produced a collimated beam with 100-ps time duration, up to 25 mJ of energy, and an approximately Gaussian spatial profile with a FWHM diameter of 4 mm.

The experimental setup is shown in Fig. 75.1. The input laser beam was reflected off an adjustable mirror, which was used to vary its angle of incidence on the crystals. Back-reflections from the crystal surfaces were transported through a 1-m focus lens onto a CCD camera to monitor the beam alignment relative to the crystals and the relative alignment between the crystals. The polarization of the incoming beam was adjusted using a half-wave plate to be 35° with respect to the *o* axis of the first crystal. The second tripler was mounted on a stage with a 5-cm translation range, which was required to optimize the relative phase between the three interacting waves incident on the second tripler. The crystals were set up using the converging-lens technique[9] with a separation of ~0.77 mrad between the phase-matching directions of the two triplers, this angle being the optimum predicted separation.

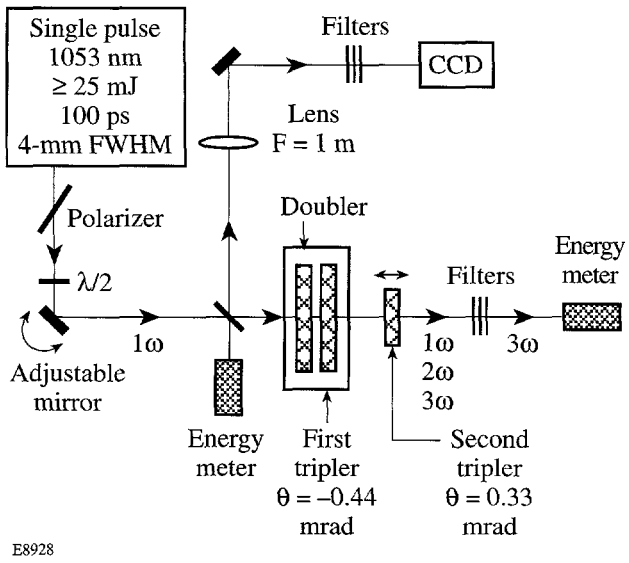

Figure 75.1
Experimental setup.

The experimental results are shown in Fig. 75.2 for five values of the air gap spanning the 4-cm range in 1-cm increments. The results are in excellent agreement with predictions of the plane-wave code Mixette (based on Ref. 2), which calculates the conversion averaged over the assumed Gaussian spatial and temporal beam profiles at a nominal intensity of 1.2 GW/cm^2.

The conversion efficiency was measured as the ratio of the energy of the third-harmonic beam at the output of the second tripler to the energy of the fundamental beam at the input to the doubler. For each angular position several measurements (typically 5 to 7) were made, and the averaged value was used as the measured conversion efficiency. Typically the averaged data had an uncertainty (standard deviation) of the order of 1% or less, although in a few cases the uncertainty was as large as ~5%.

Small scaling factors were applied to the experimental measurements (0.95 to the angle and 1.04 to the conversion) to account for systematic uncertainties in the accuracies with which the values of angles and intensities were measured. These scaling factors were determined from one data set and were then maintained constant for the remainder of the experiment. The calculations assumed that the first tripler was detuned to be phase matched for a beam tilt of –0.44 mrad on the horizontal axes of Fig. 75.2. The corresponding tilt for the second tripler was 0.33 mrad, all tilt angles quoted in this article being external to the crystals. (The absolute values of these angles were not known experimentally.) The optimum air gap [corresponding to Figs. 75.2(a) and 75.2(e)] was assumed to be 1.5 cm away from the point of no net dispersion [midway between that in Figs. 75.2(c) and 75.2(d)]. The sign of this distance depends on the orientations of the optic axes of the triplers, which were parallel in this experiment. The calculations shown in Fig. 75.2 assumed a 4.1-cm period, which was found to fit the data slightly better than the predicted 4.0-cm period; this small difference is ascribed to different temperatures, humidity, etc., from those of Ref. 6.

The nominal laser intensity I_{nom}, defined as

$$E/\left(\pi r_{\text{HW}}^2 \tau_{\text{FWHM}}\right),$$

where E is the laser energy and $2r_{\text{HW}}$ and τ_{FWHM} are the spatial and temporal FWHM's, respectively, was 1.2 GW/cm^2, corresponding to a peak intensity in space and time of 0.78 GW/cm^2. The low conversion efficiencies shown in Fig. 75.2 are primarily a result of the non-optimum beam profile (Gaussian in both space and time), for which 50% of the IR energy is incident at less than 30% of the peak intensity. This is illustrated in Fig. 75.3, which reproduces the data and calculated curve of Fig. 75.2(e) and adds predictions for what would have been obtained with different beam spatial and temporal profiles. It is seen that conversion efficiencies up to 80% would have resulted for beams flat in space and time.

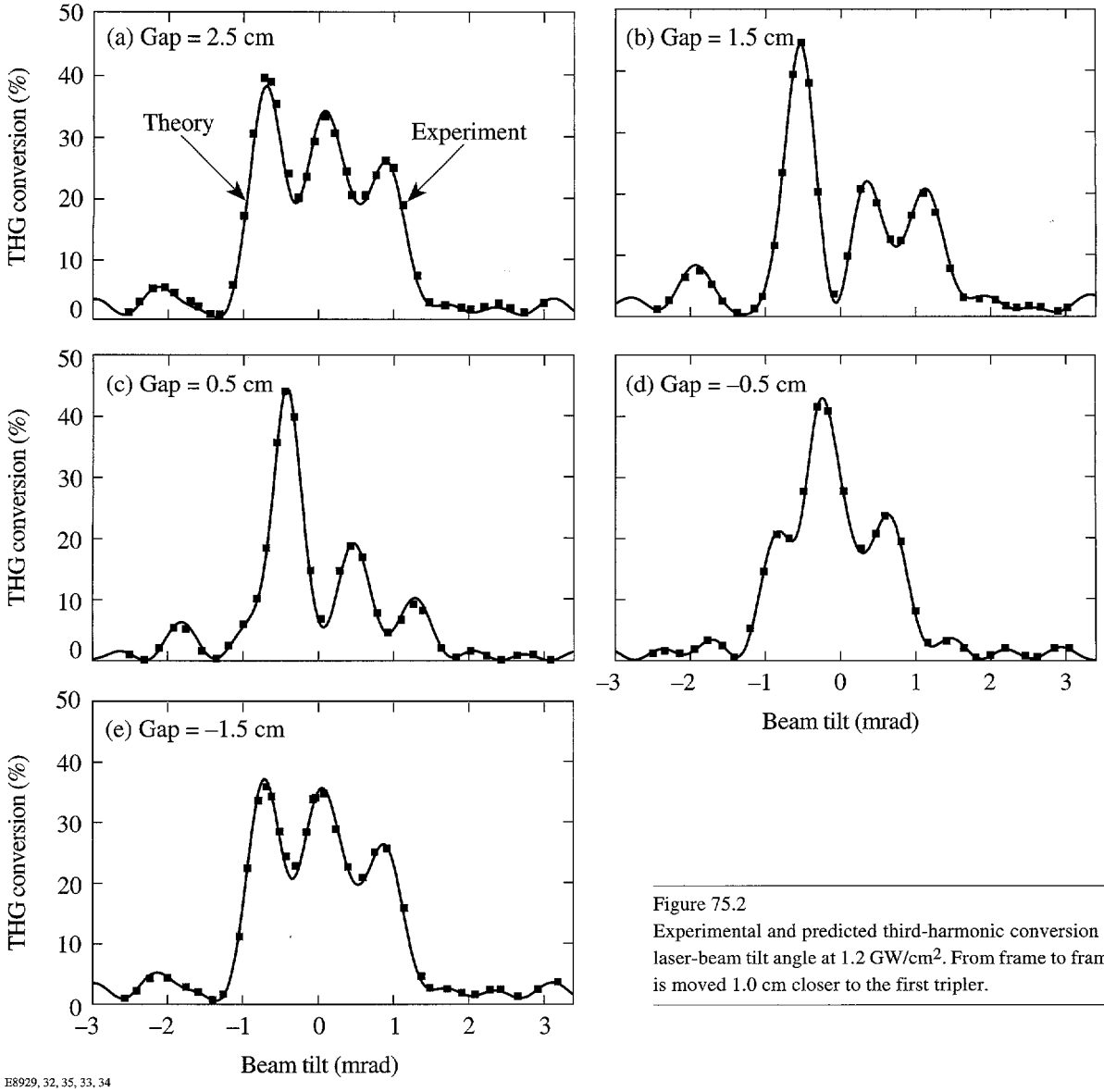

Figure 75.2
Experimental and predicted third-harmonic conversion as a function of the laser-beam tilt angle at 1.2 GW/cm^2. From frame to frame the second tripler is moved 1.0 cm closer to the first tripler.

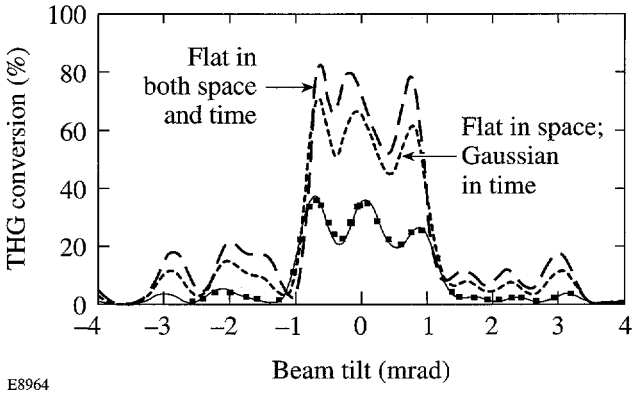

Figure 75.3
THG conversion versus beam tilt angle for the conditions of Fig. 75.2(e) (solid curve and data points) together with predictions for what would have been obtained if the beam were flat in space but Gaussian in time (dotted curve) and flat in both space and time (dashed curve). All curves are for a nominal intensity of 1.2 GW/cm^2.

Design for OMEGA

Figure 75.4 shows predictions for single rays (i.e., beams that are flat in space and time) for the OMEGA laser system, assuming that an 8-mm tripler crystal is added to each beam after the existing conversion crystals (which are both 12.2-mm, type-II KDP crystals). Here the first tripler is detuned 0.62 mrad (to phase match at –3.84 Å), and the second is detuned –0.38 mrad (to phase match at 2.36 Å). The air gap is 1.0 cm. Curves are shown for intensities from 0.5 to 1.5 GW/cm^2, spanning the range of normal operating conditions, and for small signal (0.1 GW/cm^2). At 1.5 GW/cm^2, the FWHM bandwidth is 13.8 Å, corresponding to 1.1 THz at 351 nm, and at lower intensities the bandwidth is slightly greater.

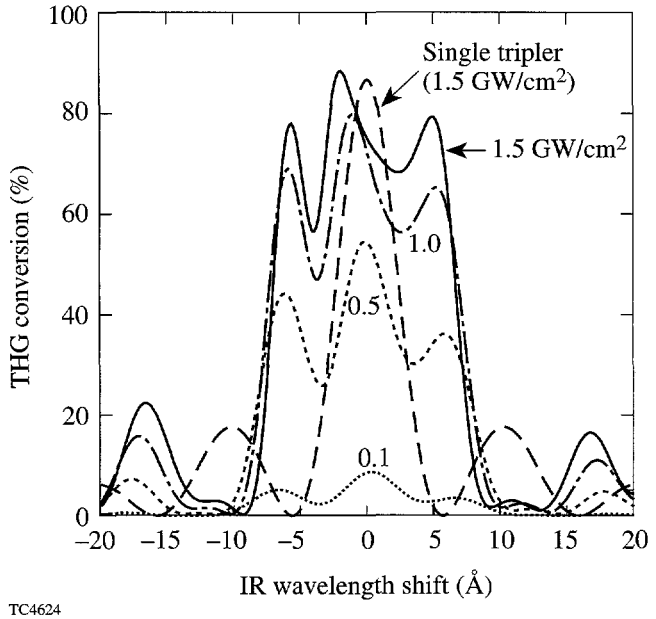

Figure 75.4
Predicted performance of the OMEGA laser system as a function of IR wavelength shift, for the addition of a second tripler of 8-mm thickness at a separation of 1.0 cm. The curves correspond to intensities ranging from 1.5 to 0.1 GW/cm^2. The dashed curve corresponds to the existing system at 1.5 GW/cm^2. At this intensity, the extra tripler increases the FWHM bandwidth from 4.9 Å to 13.8 Å (1.1 THz in the UV). The curves in this and similar figures are calculated for monochromatic beams with varying wavelength.

The shape of the dual-tripler curve at 1.5 GW/cm^2 is advantageous for the conversion of a broad-bandwidth phase-modulated beam. The THG conversion is maintained in the 60%–90% range as the IR wavelength varies through ±6 Å. In contrast, the single-tripler curve results in significant loss beyond ±2 Å. In a typical SSD laser beam, the instantaneous wavelength will vary in time through ±6 Å at any point in the beam cross section, and, at each time, it will exhibit a similar variation across the beam aperture. The net conversion integrated over the beam will then correspond to some average over wavelength of the curves of Fig. 75.4, depending on the specific parameters of the SSD design used.

The dual-tripler design being implemented on OMEGA calls for the triplers to be spaced 1.0 cm apart with a tolerance of ±0.1 cm, and for their relative angular separation to be accurate within 100 μrad. Curves illustrating the effects of these deviations are shown in Fig. 75.5 for the peak anticipated operating intensity of 1.5 GW/cm^2. In both cases, the variations in the predicted conversion curves are considered acceptable. The variations experienced in the spatially averaged conversion efficiency will be less (of the order of 1%–2%) because the curves resulting from deviations from the design lie above the design at some wavelengths and below the design at others.

It is worth noting that the alignment accuracy required by dual-tripler THG is no greater than that already in place on OMEGA. Currently the crystals are tuned to a much smaller tolerance than 100 μrad.

Design for the NIF

Very similar broadband conversion may also be obtained on the NIF. Two designs are considered here (see Table 75.I): The "11/8/10" design was suggested in Ref. 3, although with slightly different tuning angles. (It should be noted that all angles quoted in Ref. 3 are internal to the crystal, i.e., 1.5 times smaller than the external angles quoted here.) The "11/9/9" design is an alternative design that is compatible with the NIF two-crystal base-line design ("11/9").

A comparison between the two dual-tripler designs is shown in Fig. 75.6. The "11/8/10" design provides slightly more conversion and allows slightly more bandwidth; otherwise, the two designs are very similar. The curves are remarkably similar to those of the optimum OMEGA design of Fig. 75.4; again, the range of wavelengths that can be efficiently converted is increased from ±2 Å to ±6 Å.

Comparing either dual-tripler design with the two-crystal base-line design, shown superposed on both plots of Fig. 75.6 at the nominal operating intensity of 3.0 GW/cm^2, it is clear that there will be some loss in overall conversion when averaging over a broadband beam, but probably no more than 10% based on the 3.0-GW/cm^2 curve. (The loss at lower intensities is less.)

The effective beam uniformity resulting from dual-tripler conversion on the NIF may be even greater than that on OMEGA, based on the reasonable presumption that it is the ratio between the coherence time (1/bandwidth) and the relevant hydrodynamic time that is important. The coherence time is the same on each system, but the hydrodynamic time scales are a few times longer on the NIF.

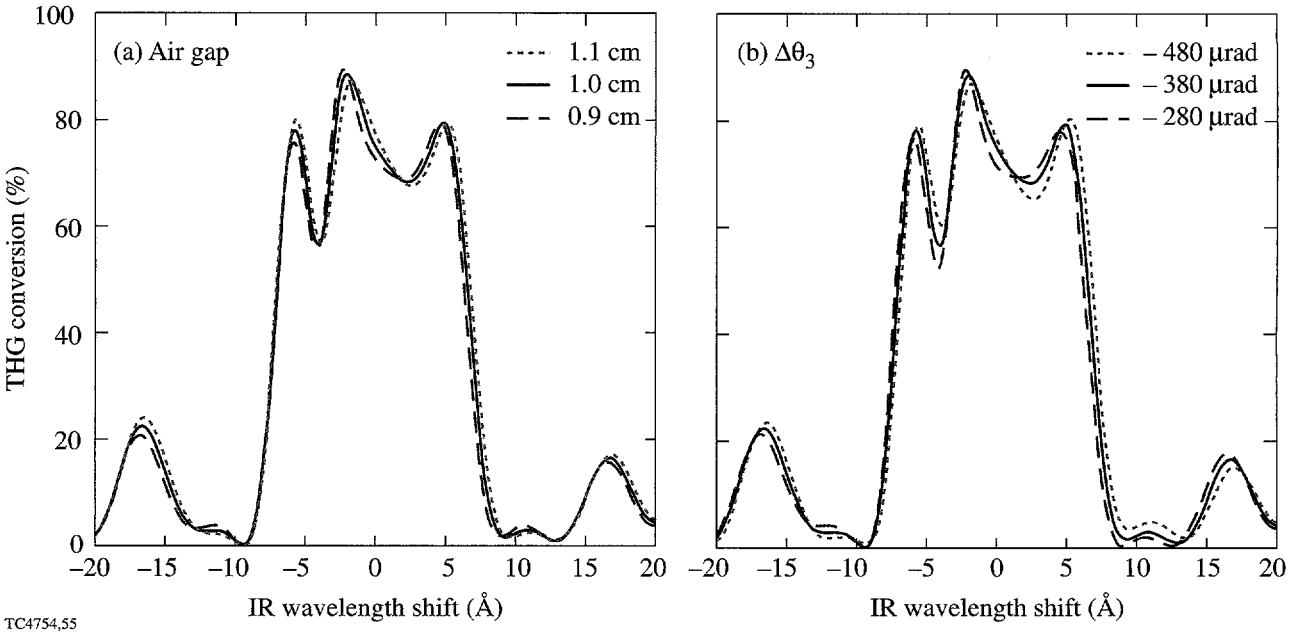

Figure 75.5
Sensitivity of the base-line design for dual-tripler THG on OMEGA to (a) deviations in the air gap between triplers from 1.0 cm and (b) deviations in the tilt angle of the second tripler from –380 μrad. All curves are for the maximum anticipated operating intensity of 1.5 GW/cm^2. Deviations of no greater than (a) ±0.1 cm and (b) ±100 μrad are acceptable.

Table 75.I: Existing and dual-tripler designs for OMEGA and the NIF. Tilt angles $\Delta\theta_i$ are external to the crystals, with a positive angle indicating an increase in the angle between the propagation direction and the optic axis. OMEGA crystals are all type-II KDP; NIF doublers are type-I KDP and triplers type-II KD*P. Subscript "1" indicates the doubler, "2" the first tripler, and "3" the second tripler.

	Crystal thickness (mm)			Crystal tilt (μrad)			Gap between triplers (mm)
	L_1	L_2	L_3	$\Delta\theta_1$	$\Delta\theta_2$	$\Delta\theta_3$	gap
OMEGA, present	12	12	–	0	0	–	–
OMEGA, dual tripler	12	12	8	0	620	–380	10
NIF "11/9" base line	11	9	–	350	0	–	–
NIF "11/8/10"	11	8	10	325	900	–1000	0
NIF "11/9/9"	11	9	9	325	750	–1000	0

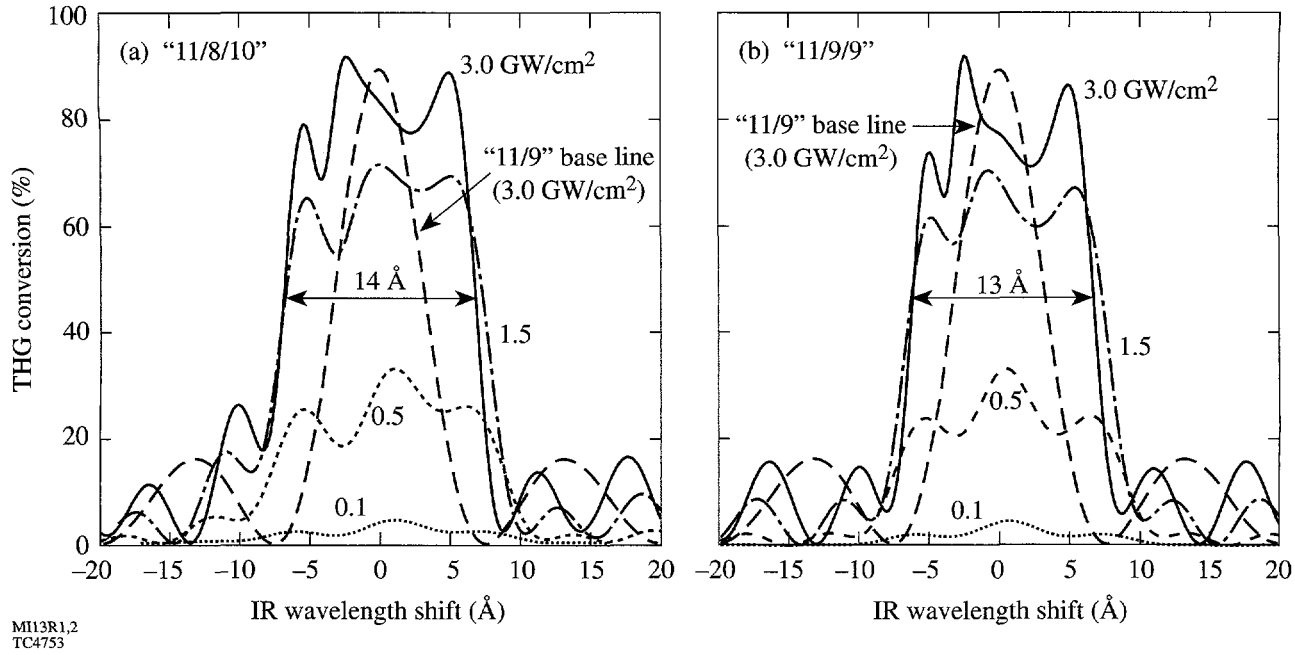

Figure 75.6
Predicted performance for two enhanced-bandwidth designs for the NIF: (a) the "11/8/10" design of Eimerl (Ref. 3) and (b) an alternative "11/9/9" design that leaves the base-line, two-crystal, "11/9" NIF design unchanged.

One important difference between OMEGA and the NIF is that the optimum "11/8/10" and "11/9/9" designs for the NIF require no relative phase change between the triplers. This will indeed be the case on the NIF since the base-line design calls for the crystals to be mounted in vacuum. It is anticipated that the antireflection (AR) coatings on the output of the first tripler and the input to the second tripler will not significantly affect the phase at any wavelength.

Transmission losses between crystal surfaces have not been included in the calculations presented here for OMEGA and the NIF since the AR coatings have not yet been designed. Small losses will be incurred since one cannot simultaneously eliminate reflections at all three wavelengths; however, this does not significantly affect the results presented here.

The sensitivity of the "11/9/9" dual-tripler design for the NIF to angular misalignments of the crystals is shown in Fig. 75.7. In each case, the ideal conversion curve was calculated together with eight variants. In each variant, each crystal was tilted by either $+\Delta\theta$ or $-\Delta\theta$. The shaded areas on the plots indicate the envelope of all eight of these variants, including the worst-case combinations. Again, less variation may occur in some cases for the average over a broadband beam since some curves lie below ideal at some wavelengths and above ideal at others. Results for a tolerance of ± 25 μrad are clearly better than those for ± 50 μrad.

At 1.5 GW/cm^2, the greatest deviations from ideal occur as a result of detunings of the doubler from the design orientation. These deviations are essentially the same that occur for the base-line, two-crystal NIF design and result from the sensitivity of the angle-detuned, type-I/type-II design to doubler orientation;[2] thus, the addition of a second tripler to the NIF does not require any greater angular alignment accuracy than is already included in the base-line design.

Conclusion

The dual-tripler scheme for broadband frequency conversion has been experimentally demonstrated. The close agreement between theory and experiment provides high confidence that the scheme will work on OMEGA and the NIF. On the basis of these results, plans are being made to convert the full OMEGA system. A similar design exists for the NIF. For both laser systems, an approximate threefold increase in bandwidth can be expected, which should result in a threefold reduction in smoothing time and correspondingly more-uniform target implosions.

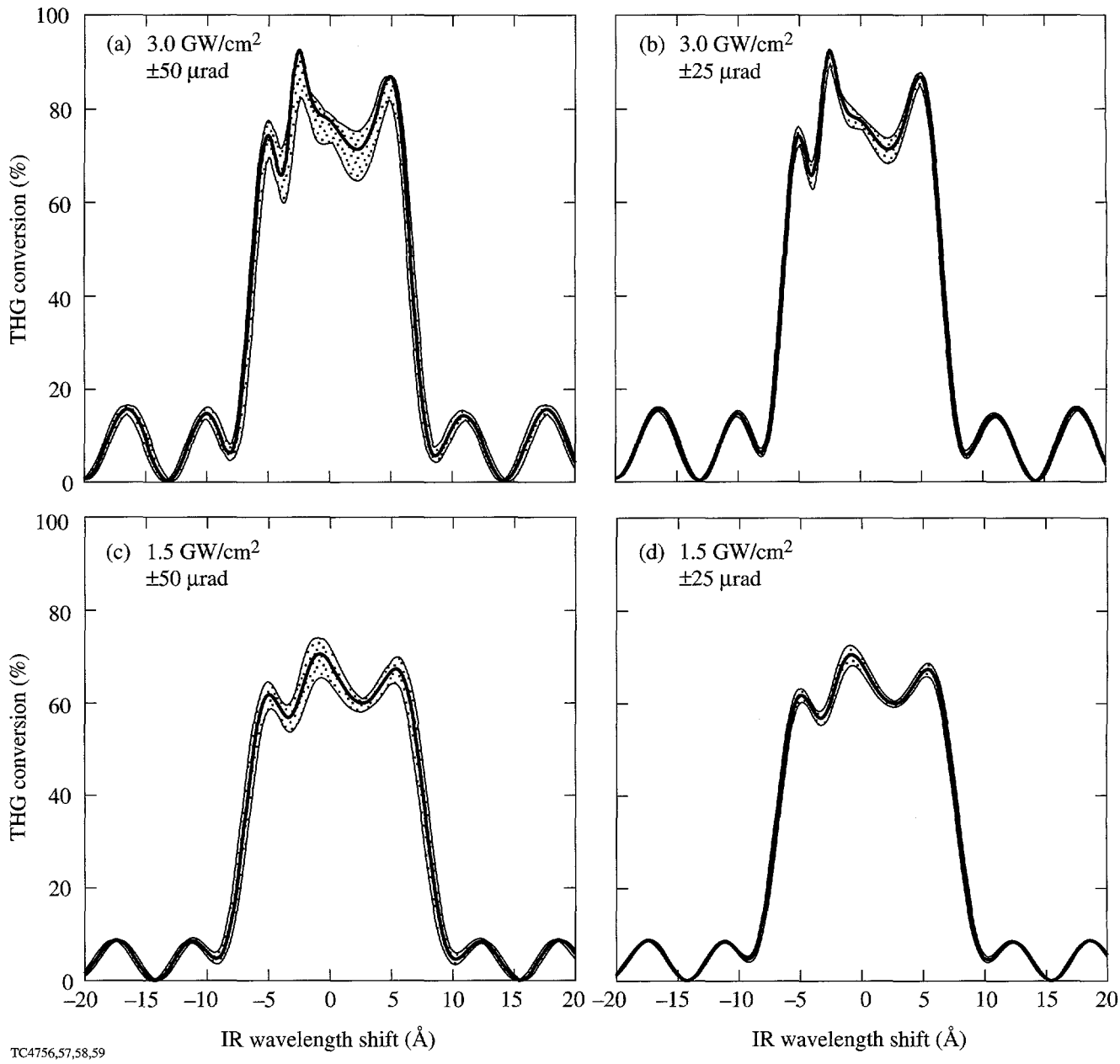

Figure 75.7
Sensitivity of the "11/9/9" NIF design to crystal alignment errors. In each case the solid line indicates the ideal conversion curve. The shaded area indicates the full range of possible curves (eight combinations) resulting from simultaneously applying errors of $\pm\Delta\theta$ (external) to each of the three crystals, where $\Delta\theta$ = 50 μrad [(a) and (c)] and 25 μrad [(b) and (d)]. The results for 3.0 GW/cm^2, the peak operating intensity [(a) and (b)], are not greatly different from those for 1.5 GW/cm^2 [(c) and (d)].

ACKNOWLEDGMENT

This work was supported by the U.S. Department of Energy Office of Inertial Confinement Fusion under Cooperative Agreement No. DE-FC03-92SF19460, the University of Rochester, and the New York State Energy Research and Development Authority. The support of DOE does not constitute an endorsement by DOE of the views expressed in this article.

REFERENCES

1. S. Skupsky, R. W. Short, T. Kessler, R. S. Craxton, S. Letzring, and J. M. Soures, J. Appl. Phys. **66**, 3456 (1989).
2. R. S. Craxton, IEEE J. Quantum Electron. **QE-17**, 1771 (1981).
3. D. Eimerl *et al.*, Opt. Lett. **22**, 1208 (1997).
4. S. Oskoui, Laboratory for Laser Energetics Report No. 277, NTIS document No. DOE/SF/19460-173 (1996). Copies may be obtained from the National Technical Information Service, Springfield, VA 22161.
5. R. S. Craxton, S. D. Jacobs, J. E. Rizzo, and R. Boni, IEEE J. Quantum Electron. **QE-17**, 1782 (1981).
6. R. C. Weast, ed. *CRC Handbook of Chemistry and Physics*, 58th ed. (CRC Press, Cleveland, OH, 1977), p. E-224.
7. A. Babushkin, R. S. Craxton, S. Oskoui, M. J. Guardalben, R. L. Keck, and W. Seka, Opt. Lett. **23**, 927 (1998).
8. A. Babushkin, W. Bittle, S. A. Letzring, A. Okishev, M. D. Skeldon, and W. Seka, in *Advanced Solid-State Lasers*, edited by C. R. Pollock and W. R. Bosenberg, OSA Trends in Optics and Photonics Series, Vol. 10 (Optical Society of America, Washington, DC, 1997), pp. 106–108.
9. W. L. Smith and T. F. Deaton, *Laser Program Annual Report 1979*, Lawrence Livermore National Laboratory, Livermore, CA, UCRL-50021-79, 2-209 (1980).

Ultrahigh Dynamic Range Measurement of High-Contrast Pulses Using a Second-Order Autocorrelator

In high-intensity, ultrafast laser–plasma interactions with solid targets, the intensity of prepulses with a typical time duration of ~1 ns, arriving before the main laser pulse, must be less than $\sim 10^{10}$ W/cm^2 to avoid having the high-intensity pulse interact with a preformed plasma.[1,2] Currently, the highest available peak laser intensities are $\sim 5 \times 10^{19}$ W/cm^2 with 30-fs pulses[3] for small-scale laboratory lasers and 10^{21} W/cm^2 with 500-fs pulses on a large-laboratory scale.[4] The development of optical parametric chirped-pulse amplification[5] may allow the construction of small-laboratory-scale, truly tabletop subpetawatt lasers with peak intensities in the range of 10^{21} to 10^{23} W/cm^2;[6] therefore, the dynamic range of temporal pulse measurements must exceed $\sim 10^{12}$ to predict if, where, and when a preformed plasma will be produced. Detailed knowledge of the temporal shape of the pulse is crucial to the study of high-density plasma physics.[7] The interaction of a high-contrast pulse with a high-density solid target or a high-density plasma is completely different from that of a low-contrast pulse. In particular, efficient production of the ultrafast x-ray emission[8,9] may require a high-contrast pulse.[10]

In some cases the intense pulse will contain a long, low-contrast prepulse with known temporal shape. The temporal shape of this prepulse must be known since it will affect the outcome of the interaction. At 10^{21} W/cm^2 intensities, a prepulse at the level of $\sim 10^{-12}$ below peak intensity produces a preformed plasma, while one at the 0.1% level of peak intensity can ionize atoms and ponderomotively accelerate electrons out of the focus before the main pulse arrives. A pulse of this kind is used in the fast ignitor,[11] where a long, low-contrast ($\sim 10^{-3}$ below peak intensity) prepulse bores a hole for the main pulse. The temporal history of the prepulse will critically affect the propagation of the intense laser pulse in a large-scale coronal plasma and the energy deposition process in the overdense region.

With current state-of-the-art, ultrashort, high-peak-intensity lasers, the ideal device for measuring the temporal profile of the pulse would be a device with temporal resolution of tens of femtoseconds and a dynamic range of 10^{12}.

Devices simultaneously possessing subpicosecond resolution and high dynamic detection range are noncollinear beam correlators based on frequency conversion. The pulse to be measured is split into two parts, one of which may be delayed by the time delay τ, attenuated, and perhaps modified in frequency. The two parts are recombined in a nonlinear medium. In high-dynamic-range autocorrelation (HDRA), the sum frequency is generated noncollinearly to avoid the direct exposure of the detector by each individual beam. In second-order (SO) HDRA, where the noncollinearly recombined replicas of the beam are identical, the second-harmonic energy $E_{2\omega}(\tau)$ as a function of delay is proportional to the second-order intensity correlation function[12] (autocorrelation function):

$$E_{2\omega}(\tau) \propto G^{(2)}(\tau) \propto \int I(t) I(t-\tau) dt,$$

where $I(t)$ is the intensity.

In third-order (TO) HDRA, one beam is frequency doubled before noncollinear recombination, and the resulting third-harmonic signal $E_{3\omega}(\tau)$ is proportional to the third-order intensity correlation function[13]

$$E_{3\omega}(\tau) \propto G^{(3)}(\tau) \propto \int I(t) I^2(t-\tau) dt.$$

The advantages of SO over TO HDRA are simplicity, longer wavelength of the recorded signal, and better temporal resolution. Deteriorated temporal resolution in TO HDRA can be due to the limited acceptance bandwidth of the tripler[14,15] and, for shorter pulses (~100 fs and shorter), due to the dispersion of the pulse in the doubler or relay optics of autocorrelator.[3,15] The main advantage of TO over SO HDRA is that it can distinguish prepulses from postpulses.

The required proportionality of $E_{2\omega}(\tau)$ on the square of the incident intensity, $E_{2\omega}(\tau = 0) \propto (I_\omega)^2$, is satisfied over many orders of magnitude of incident intensities, so no

modification in the optical part of the autocorrelator or in the attenuation of the input beam is required when the delay τ is increased. A square-law, slow detector (with nanosecond resolution) is usually attenuated with calibrated filters to keep the noncollinear, sum-frequency signal at approximately the same level. In addition, the detected signal can be electronically time gated (on a time scale of ~10 ns) to minimize any extraneous noise associated with long-time-scale optical or electrical background.

Ultrafast pin diodes or streak cameras possess neither the required temporal resolution nor the required high dynamic range. The typical dynamic range of a streak camera with picosecond resolution is 100. It can be boosted to 10^7 by nonlinear shutters, by operating at lower temporal resolutions, and, for stable laser systems, by averaging over many laser shots.[16] The main disadvantage of correlators is that they are an indirect method of detection, i.e., the transformation of the signal from $I(t)$ to $G^{(2)}(\tau)$ occurs nonlinearly, allowing the existence of multiple solutions during reconstruction of the primary signal from the correlation signal. Both streak cameras and autocorrelators lose important temporal-phase information of the pulse. Recently, several methods have been developed to completely characterize ultrashort pulses, i.e., to obtain the temporal-phase and intensity information about the most intense portion of the beam. This is done with autocorrelators that frequency resolve the autocorrelation signal. The single-shot technique, which is able to completely characterize the most intense portion of the pulse, such as frequency-resolved optical gating (FROG),[17] is well developed with SO and TO noncollinear autocorrelators. These techniques, however, have not demonstrated a dynamic range approaching 10^{12}.

For ultrashort intense pulses, it is necessary to perform additional high-contrast autocorrelation to obtain information about the temporal-energy distribution outside the most intense portion. In this article, we perform only high-contrast autocorrelation measurements, although the autocorrelator used is "FROG-ready" and can work in the single-shot regime if the on-crystal focusing lenses are removed. The phase-sensitive measurements were not performed because the measured pulse was close to its bandwidth limit.

Noncollinear Autocorrelator for Temporal-Pulse-Shape Measurements

The z coordinate (transverse) of the spatial profile of the wide second-harmonic (SH) beam[18,19] or third-harmonic beam[15] may be linearly mapped to the delay τ to obtain the corresponding autocorrelation function in a single shot, as shown on Fig. 75.8. Figure 75.8 illustrates type-I noncollinear phase matching for two wide beams of diameter D, represented by ordinary waves with carrier frequency ω, (o,ω) propagating in a doubling crystal with thickness L_c at angle Φ with respect to each other. The direction of the noncollinearly generated second-harmonic extraordinary $(e,2\omega)$ beam is determined by the phase-matching condition, $\vec{k}_{0_1,\omega} + \vec{k}_{0_2,\omega} = \vec{k}_{e,2\omega}$. To maintain the correspondence between the transverse signal profile $S_{2\omega}(z)$ and the autocorrelation function $G^{(2)}(\tau)$ over the most intense temporal portion of the pulse, the transverse sizes (D) of the interacting beams should be large to avoid distorting the shape of the SH beam due to the spatial shape of the fundamental beam. The following two conditions should be satisfied: the spatial walk-off of each beam along the z coordinate in the thickness of the crystal, $L_c \tan(\Phi/2)$, should be at least three times smaller than the beam diameter size along the z direction, $D\cos(\Phi/2)$, giving $L_c \tan(\Phi/2) \leq (D/3)\cos(\Phi/2)$, and the size of the interaction region (diamond-shaped region in Fig. 75.8) should be at least three times smaller than the transverse size of the beam D, giving $L_p/\tan(\Phi/2) \leq D/3$. $L_p \approx (c/n_{o,\omega})\tau_p$ is the physical length of the pulse inside the crystal, c is the speed of light, $n_{o,\omega}$ is the index of refraction, and

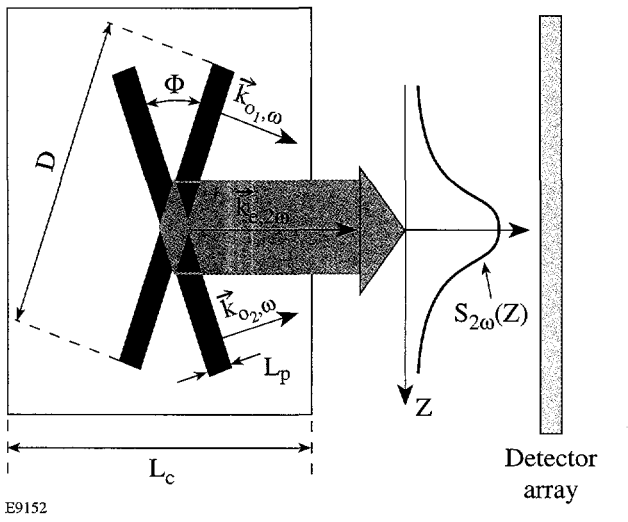

Figure 75.8
Single-shot setup for the noncollinear second-order autocorrelator. Two wide, ordinary beams with k-vectors $\vec{k}_{o_1,\omega}$ and $\vec{k}_{o_2,\omega}$, propagating in the nonlinear crystal at angle Φ with respect to each other, create a second-harmonic beam $\vec{k}_{e,2\omega}$. The width of the generated second-harmonic beam depends only on the duration of the pulses if beam diameters D are large. The shape of the second-harmonic beam, which is proportional to the second-order autocorrelation function $G^{(2)}(\tau)$, is recorded with a linear detector array.

τ_p is the pulse duration. The single-shot setup is limited to an ~10- to 100-ps range of delays (τ), due to the finite sizes of the crossing beams and/or the nonlinear crystal,[14] and to a dynamic range of ~10^6 to 10^7.[15,20] The finite dynamic range is due to the scattering of the intense portions of the noncollinearly generated beam into low-intensity portions.

To obtain a higher dynamic range with a delay of hundreds of picoseconds, one must work in the scanning regime when only one point of autocorrelation function (one τ) is recorded during a single shot. This is shown in Fig. 75.9, where the linear detector array is replaced by a single-point detector. In an experiment, the averaged autocorrelation function

$$\overline{G}(\tau,\Delta\tau)=\frac{1}{\Delta\tau}\int_{\tau-\Delta\tau/2}^{\tau+\Delta\tau/2}G(\tau')d\tau'$$

is recorded, instead of $G(\tau)$, due to finite sizes of the crossing beams. To avoid the effect of averaging $\overline{G(\tau)}=G(\tau)$, the transverse beam sizes at the intersection point inside the crystal must be reduced to one-third of the beam size obtained in a single-shot setup, or the time window determined by the crossing beams must be less than approximately one-tenth of the pulse duration $\Delta\tau\lesssim\tau_p/10$. Figure 75.9 can be compared to Fig. 75.8. In Fig. 75.9, the beam diameters are reduced by a factor of 10, and, consequently, the z width of the SH beam is reduced by factor of 3 with respect to the original single-shot size. The transverse size $D=2w_0$ of the crossing beams should satisfy $D/\{L_p/\sin(\Phi/2)\}\lesssim 0.3$. The sizes of the beams and their crossing angle will define the temporal resolution

$$\Delta\tau\approx(1.2/\gamma)(Dn_{o,\omega}/c)\tan(\Phi/2), \tag{1}$$

where γ is the form factor relating the FWHM of $I(t)$ to that of $G^{(2)}(\tau)$.

For ~100-fs and shorter pulses, dispersion may be a factor in the temporal resolution, or more correctly, dispersion will affect the width of the measured autocorrelation function because the lengths of interacting pulses, L_p, will be different upon arrival at the interaction point.

In the case of the finite transverse width of the probe pulse and negligible dispersion, the recorded autocorrelation function is proportional to the pulse shape $G(t)\propto I_\omega(t)$ at all times where $I_\omega(t)$ changes slowly, i.e., far from the most intense

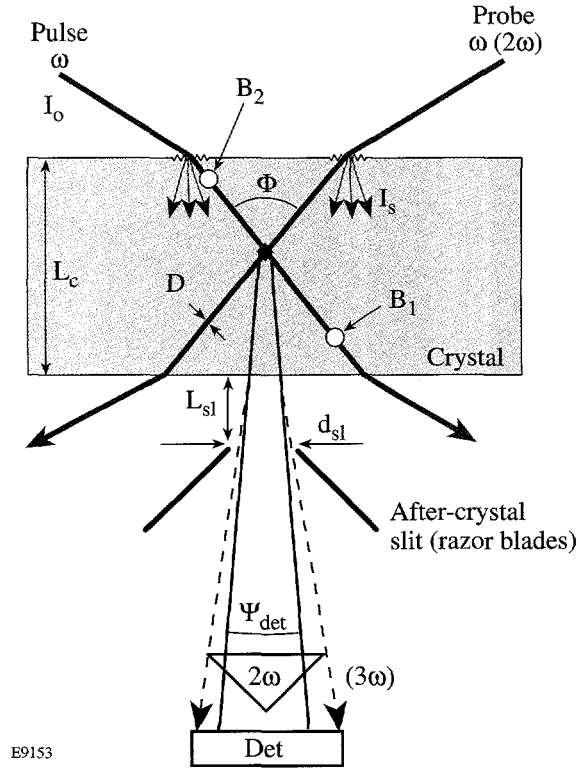

Figure 75.9
Geometry of the crossing beams in a noncollinear scanning autocorrelator. Two focused beams cross inside the crystal and generate the sum-frequency signal noncollinearly. For a particular delay between the pulse and the probe beams, the energy generated in the interaction region is proportional to the autocorrelation function. This geometry gives only one point of the auto-correlation function for a particular delay between the two beams (scanning regime) but allows one to obtain the higher dynamic range required for measurements of intense, ultrashort pulses. The light scattered from the first surface I_s (shown with arrows originating from the rough surface) can be frequency doubled during propagation through the bulk of the crystal and can reach the detector. An after-crystal slit is installed to reduce it. Each individual beam can be frequency converted along the passage through the crystal and then can scatter into the direction of the detector, producing a delay-independent background. We assume that only some portion of the beam path between points B_1 and B_2 is visible from the detector due to the presence of the after-crystal slit. We refer to this type of background as bulk-scattering noise.

region. The most intense portion is modified due to the autocorrelation transformation [integration of $I(t)I(t-\tau)$]. For example, for the temporal Gaussian/sech^2 pulse shape of $I(t)$ with a symmetric low-intensity pedestal, the $G^{(2)}(\tau)$ is 1.4 to 1.5 times wider than $I(t)$ and gives a pedestal intensity that is overestimated by factor of 2.8 to 3.

In several previous works, authors have measured 0.1- to 1-ps pulses with SO HDRA[21–25] with dynamic ranges of 10^5 to 10^8 and with TO HDRA[26–31] with dynamic ranges of 10^6 to 10^8. In two works,[3,13] the dynamic range with a TO autocorrelator is up to 10^{10} for 10-ps and 30-fs pulses with a temporal resolution of ~1 ps and ~0.1 ps, respectively (affected by dispersion). In the latter reference, the recorded autocorrelation function does not follow $G^{(3)}(\tau)$ over the most intense portion of the pulse, and additional second-order, single-shot, low-contrast autocorrelation is performed to complement the high-contrast measurements. In all of the cited references, there were no estimates of the factors that limit the available dynamic range.

In modern short-pulse laser systems, a contrast measurement of 10^8 may be insufficient. In a conventional CPA laser system, where a nanojoule-level oscillator determines the high-dynamic-range structure of the pulse, the contrast of optical background is ~10^8 or lower.[32–35] This optical background usually propagates through the CPA system and is present in the final amplified and compressed pulse. In addition, after stretching and relay losses, the amplified pulse may acquire a background associated with the amplified spontaneous emission (ASE) of the amplifier itself. As a rule of thumb, the contrast of the compressed pulse resulting from ASE noise of an amplifier can be expressed as the number of injected photons within the gain-narrowed spectrum, if the injected-pulse spectrum is wider than the gain-narrowed spectrum supported by this amplifier. Typically, with a pulse energy of ~100 pJ injected into the first regenerative or multipass amplifier, the ASE background may be of the order of 10^{-8} below the peak intensity in the compressed pulse.

In the case of insufficient pulse contrast, several schemes have been proposed to increase it. These include the use of the nonlinear birefringence of the fibers,[32] Pockels cells,[20] saturable absorbers,[21] frequency doubling of the amplified pulse,[36,37] degenerate optical parametric amplification (OPA),[38] amplification based on stimulated Raman scattering,[39] and self-induced plasma shuttering.[23] Using feedback-controlled mode-locked (FCM) lasers[40] with a saturable absorber inside the cavity makes it possible to create 1-ps pulses with ~10^8 contrast and ~1-μJ energy,[27] which effectively nullifies the influence of ASE of subsequent amplifiers to the level of 10^{-12}. For OPA CPA,[5] where co-propagating amplified and pumped pulses are timed and matched in duration, the long-duration ASE noise does not exist, due to the absence of an inverted medium. In many of the above-mentioned, experimentally realized schemes, the estimated contrast of picosecond and shorter pulses may be higher than 10^{12} but has not been measured.[36–39]

We have analyzed the factors that limit the dynamic range of the noncollinear autocorrelators and have systematically minimized them. The main physical factors are the finite energy of the pulse, scattering from the surface of the crystal, and bulk scattering. Minimizing or eliminating noise resulting from these factors dictates the geometry of the crossing beams in the autocorrelator and the size and quality of the crystal for a given pulse duration. Our estimate for the dynamic range is carried out for SO HDRA but can be applied to TO HDRA as well because both use the second-order nonlinearity $\chi^{(2)}$ of the medium [a cascaded $\chi^{(2)}{:}\chi^{(2)}$ process in the case of TO autocorrelation measurements] to produce the noncollinear signal.

The dynamic range of the autocorrelator can be conveniently defined as the ratio of the noncollinear signal at zero delay ($\tau = 0$) to the sum of signals E_1 and E_2 due to each beam, one at a time, sensed by the detector when the other beam is blocked:

$$DR = E_{\mathrm{nc}}(\tau = 0)/(E_1 + E_2). \tag{2}$$

This definition is independent of the temporal pulse shape and beam delay. Here E_{nc}, E_1, and E_2 are the energies that reach a detector from the noncollinear signal at zero delay and from each individual beam, respectively. It is assumed that $E_1, E_2 \ll E_{\mathrm{nc}}$, and that the detector is frequency filtered to detect only the sum of the frequencies. The noise signals E_1 and E_2 reaching the detector can be scaled according to the second-harmonic-generation (SHG) equation[41] with additional spatial averaging into the detector:

$$E_{1,2} \propto I_{1,2}(2\omega) \propto \int d_{\mathrm{eff}}^2 L^2 \,\mathrm{sinc}^2\left[\frac{\Delta k(\Omega)L}{2}\right] I_{1,2}^2(\omega,\Omega)\, d\Omega_{\mathrm{det}}. \tag{3}$$

Here $\mathrm{sinc}(x) = \sin(x)/x$, $d\Omega_{\mathrm{det}}$ is the solid angle subtended by the detector from a point in the interaction region, $I(\omega,\Omega)$ is the

fundamental harmonic intensity into the direction of the detector, L is the interaction length for SHG, Δk is the phase mismatch, and d_{eff} is standard shorthand for the effective second-order nonlinearity. Equation (3) assumes that the regions of the surface and of the bulk of the crystal traversed by the beams become weak secondary sources of light at the sum frequency (the frequency of noncollinear signal) due to the scattering followed by frequency conversion or due to the frequency conversion (of strong but SHG phase-mismatched beams) followed by scattering. The highly directional noncollinear (nc) signal is scaled with the same parameters:[18,42] $E_{\text{nc}} \propto d_{\text{eff,nc}}^2 L_{\text{nc}}^2 I_1 I_2$ (for $\Delta k = 0$). L_{nc} can be roughly estimated as the walk-off distance when one beam crosses the other. These equations allow an estimate of the amount of noncollinear signal produced by two beams and the background produced by each individual beam. With the known position of the entrance pupil of the detector and the scattering properties of the crystal, the noncollinear signal can be compared to the signal produced by the scattered light, and the dynamic range of the noncollinear autocorrelator can be estimated.

Finite Pulse Energy

When the energy of the amplified pulse exceeds several millijoules, the current state-of-the-art lasers can operate only at a low repetition rate—typically 1 to 10 Hz for the first amplification stage and less for the second and higher stages. In this case, a multipulse averaging technique (such as lock-in detection) is impossible. A detector signal corresponding to below 1 photon per pulse in the incident radiation is not practically extractable. If we assume that the equivalent noise level of the device is 10 photons per pulse, to obtain the dynamic range of 10^{12}, 10^{13} photons, or 3 μJ of energy, are required in the second-harmonic noncollinear signal at the peak ($\tau = 0$) for 1-μm fundamental light. The undepleted second-harmonic signal ($E_{\text{nc}} \propto I_1 I_2$) can be produced with ~10% efficiency; hence, a 30-μJ pulse is required at the entrance to the crystal. For high-repetition-rate lasers, such as oscillators, lock-in detection can reduce requirements for the energy of individual pulses by 3 or more orders of magnitude. For example, several types of ultrashort-pulse oscillators, with individual-pulse energy in the range of 1 nJ, have been characterized with dynamic ranges of 10^8.[32–35]

Surface Scattering

Light scatters from a rough surface according to[43]

$$\frac{I_s}{I_0} = \left(\frac{4\pi\delta}{\lambda}\right)^2, \tag{4}$$

where I_0 and I_s are the incident and scattered intensities, λ is the wavelength of the incident radiation, and δ is the rms surface roughness. Equation (4) is valid for near-normal incidence and relatively smooth surfaces, $\delta \ll \lambda$. It is assumed that light scatters from the surface isotropically. With typical numbers $\delta \approx 50$ Å and $\lambda = 1$ μm, we find $I_s/I_0 = 0.4\%$, which is very high. The fundamental light scattered from the surface can propagate through the crystal, be frequency doubled, and reach the detector, shown in Fig. 75.9 as arrows originating from the rough surface. The detector is assumed to be blocked against the fundamental light. Using the scaling of Eq. (3) with $I(\omega,\Omega) = (1/4\pi)I_s$, $d\Omega_{\text{det}} \approx 10^{-2}$ steradians, a mismatch factor $\text{sinc}^2(\Delta k L_c/2) \approx 10^{-5}$, and the SHG length of the surface-scattered noise equal to the crystal bulk length $L_c\left[L_{\text{scat}} = L_c \sim 1 \text{ mm}\left(L_{\text{scat}}/L_{\text{nc}} \approx 10\right)\right]$, the signal-to-noise level is approximately 10^8. This is about three to four orders of magnitude lower than required. The scattering in a particular direction can be enhanced if the surface is manufactured with a characteristic roughness period, which acts as a diffraction grating.

To reduce the surface-scattering effects, an aperture or slit can be placed just after the crystal to block the surface-scattered light from entering the detector. We refer to this slit as an "after-crystal" slit (see Fig. 75.9). It is evident that this is more effective at higher crossing angles, with smaller entrance-pupil angles of the detector, and/or with thicker crystals. For the two beams crossing halfway in the bulk of the crystal, the condition for reducing surface-scattering noise can be stated as follows: an observer at the detector should not see regions where the interacting beam hits the surface, or the backward image of the detector entrance-pupil angle onto the first surface of the crystal should be within the "dark area" (see Fig. 75.9),

$$d_{\text{sl}} + \Psi_{\text{det}}\left(L_{\text{sl}} + L_c/n_{2\omega}^e\right) < L_c \tan(\Phi/2) - 6w_0/\cos(\Phi_{\text{air}}/2). \tag{5}$$

The left-hand side of Eq. (5) is the size of the backward image of the detector onto the first surface of the crystal with slit size d_{sl}, crystal thickness L_c, and distance from second surface of the detector to the slit, L_{sl}. The right-hand side is the size of the "dark area" on the first surface of the crystal where the two beams, with waist size w_0, separated by the distance $L_c \tan(\Phi/2)$, are attenuated to $10^{-8} I_0$. This is due to the phase-matching and intensity effects on the conversion efficiency. Equation (5) determines the minimum crossing angle or

thickness of the crystal for efficient surface-noise filtering. It also fixes the optimal linear size of the detector Ψ_{det} in the crossing plane. The other dimension of the detector is determined purely by the divergence of the noncollinear SHG beam. To maximize the dynamic range, we must choose Ψ_{det} to be approximately equal to the divergence of the noncollinear SH beam, assuming that the detector is in the far field.

The following factors should be considered simultaneously with Eq. (5):

1. The size of the fundamental beams determines the resolution of the autocorrelator, the size of the SHG beam, and the size of the after-crystal slit.

2. The crossing angles are limited by the finite birefringence of the crystal. For example, for $\lambda = 1$ μm, the maximum crossing angle for $LiIO_3$ and BBO is 39°, while for KDP it is 20°.

3. The closer the slit is to the crystal, the better. The razor blades are positioned at an angle with respect to each other that minimizes L_{sl} while keeping the area of contact of the razor blade with the crystal as small as possible. Another reason for such positioning is to avoid blocking each fundamental beam because backwardly reflected light may give additional background.

4. Smaller waists $\left\{w_0 = D/2 \ll 0.3L_p/\left[2\sin(\Phi/2)\right]\right\}$ are impractical because the SHG conversion efficiency will decrease due to the reduced interaction length. Tighter focusing would require higher intensities to keep the energy of the noncollinear signal at the same level, which could result in damage or saturation of the crystal.

The following example illustrates these constraints. Focusing two identical $w_0 = 2$ mm beams with $f = 250$ mm lenses into a noncritically phase-matched $LiIO_3$ crystal (maximum possible $\Phi = 39.5°$) with $L_c = 5$ mm will produce a second-harmonic beam with size $w_{0,2\omega} \approx 100$ μm and divergence $\Psi_{2\omega}$ $\sim 10^{-2}$ rad. For 30-μJ total energy of the two beams, with $d_{eff,nc} = d_{31} = 4.2$ pm/V,[44] the estimated conversion efficiency will be ~10%, giving the required ~3 μJ per pulse of the noncollinear signal. The corresponding peak intensity of each fundamental beam will be ~500 GW/cm^2 for a 1-ps pulse duration. For a crystal–slit separation $L_{sl} = 10$ mm, one needs a slit width $d_{sl} \approx 400$ μm to transmit 99% of light and a linear angular size of the detector $\Psi_{det} \approx 3\Psi_{2\omega} \approx 3 \times 10^{-2}$ rad. The other linear angular size of the detector in the plane perpendicular to the crossing plane is approximately the same and is determined by the divergence of the SH beam. This gives a 340-μm size of the backward image of the detector onto the first surface of the crystal and the size of the "dark area" as 600 μm. A 2- to 3-mm-thick crystal is required to efficiently filter the surface-scattering noise. With a low-birefringence crystal such as KDP ($\Phi_{max} \approx 20°$), a 6- to 8-mm-thick noncollinear crystal is required to satisfy Eq. (4) and to filter out the surface-scattering noise. In all previously reported SO HDRA's utilizing a nonlinear crystal for frequency conversion,[21–25] the dynamic range at the level of 10^8 to 10^9 was probably limited by surface scattering.

Bulk Scattering

Bulk scattering is always present in the background and presents the fundamental limitation to the dynamic range of the autocorrelator. Each beam propagating through the crystal can be scattered into the direction of the detector and converted to SH noise or can be converted to the SH and then scattered. The latter process is more probable because the scattering is inversely proportional to the fourth power of wavelength $R \propto 1/\lambda^4$. R, expressed in cm^{-1}sr^{-1}, is the bulk-scattering intensity ratio I_s/I_0 per unit length traveled in the bulk of a solid material per unit solid angle. Bulk scattering depends on the macroscopic index-of-refraction inhomogeneities of a dielectric, Δn,[45]

$$R = \frac{C}{\lambda^4}(\Delta n)^2, \tag{6}$$

where λ is expressed in μm and $C \approx$ (2 to 4) $\times 10^3$ μm^4 cm sr^{-1}. The angular and polarization dependence of the scattered light is omitted for the purposes of these estimates. Well-manufactured amorphous glasses have $\Delta n \approx 10^{-4}$–10^{-5} cm^{-1} and follow the λ^{-4} laws.[46] Good-quality optical crystals may have $\Delta n \approx 10^{-6}$ cm^{-1} and $R \approx 10^{-8}$ for visible light. For the smaller bulk-scattering ratios ($R \le 10^{-8}$–10^{-9} cm^{-1} sr^{-1}), the scattering from a single molecule can be comparable to the scattering from macroscopic inhomogeneities.

Here we describe the level of noise scattered into the detector from a single beam converted to the second harmonic and then scattered. We assume that SHG occurs over a 1-mm length along the k-vectors ($\vec{k}_{o_1,\omega}$ and $\vec{k}_{o_2,\omega}$) of the beams. This gives the ratio of the bulk-generated to noncollinearly generated intensities:

$$I_{2\omega,bulk}/I_{2\omega,nc} = \left(L_{bulk}/L_{nc}\right)^2 \operatorname{sinc}^2\left(\Delta k L_{bulk}/2\right) \approx 10^{-3}.$$

Taking $\Delta n \sim 10^{-5}$ cm^{-1} gives $R_0 = 10^{-7}$ for $\lambda = 0.5$ μm. The highly fluctuating function $\text{sinc}^2(x)$ may be replaced on average with $1/2x^2$. With the solid angle of the detector $d\Omega_{\text{det}} \approx 10^{-2}$ steradian, the fraction $R_0 L_{\text{im}} d\Omega_{\text{det}} \approx 10^{-10}$ of the light will be scattered into the direction of the detector, giving background noise at the level $10^{-3} \times 10^{-10} = 10^{-13}$. Here, $L_{\text{im}} \sim 1$ mm is the length of the path of the single beam inside the crystal, which is visible from the detector as shown in Fig. 75.9 with end points B_1 and B_2 and with $L_{\text{im}} = |B_1 - B_2|$. This path segment is the secondary source of SHG noise, which creates delay-independent background into the detector. The noncollinear signal will be $\sim 5 \times 10^{12}$ times stronger than the bulk-scattering signal.

Here we discuss the bulk-noise level into the detector in the case where the fundamental beam first scatters in the bulk and where the scattered portion is converted into the second harmonic. The portion of the fundamental harmonic scattered into the direction of the detector from the segment path $[B_1 B_2]$ is $(R_0/16)\ L_{\text{im}} d\Omega_{\text{det}} \approx 10^{-11}$. The SHG (even perfectly phase matched) is the square of this expression. Even if the SHG length of this scattered beam is an order of magnitude higher than the effective SHG length of the main noncollinear signal, the estimated dynamic range is $\sim 10^{18}$, making this scattering process negligible.

Portions of the individual beams directly converted into the second harmonic and then scattered into the direction of the detector limit the dynamic range of the autocorrelator to the level of 5×10^{12} with the refractive bulk inhomogeneities in the 1-mm-thick crystal at the level of $\Delta n \sim 10^{-5}$ cm^{-1}.

Experimental Setup and Results

The experimental setup is shown in Fig. 75.10. The high-contrast pulse is generated in a chirped-pulse-amplification (CPA) system utilizing a chirping fiber. The system consists of

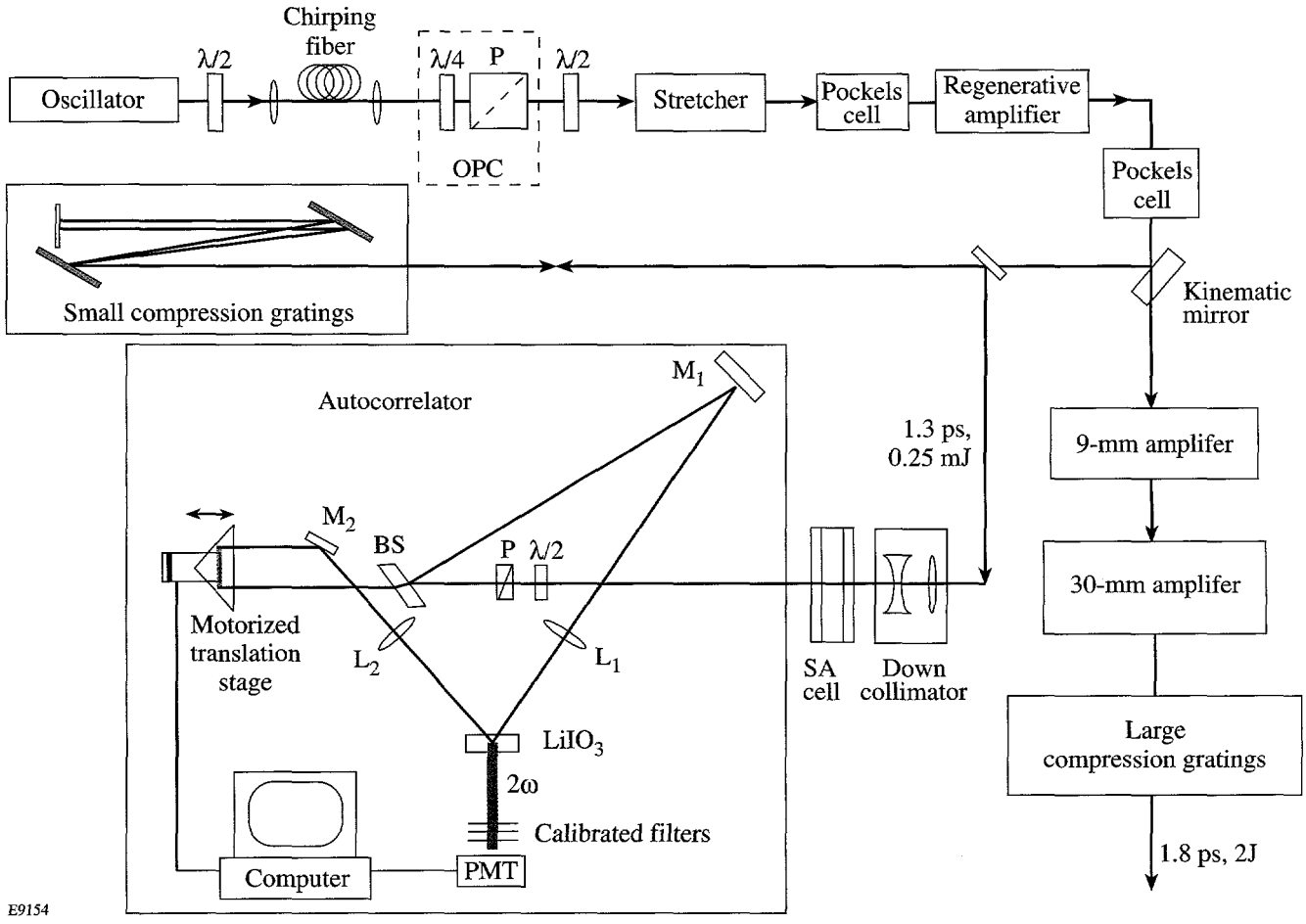

Figure 75.10
Experimental setup for production and measurement of ultrahigh-contrast, 1-ps pulses. OPC: the optical pulse cleaner; P: polarizer; $\lambda/2$ and $\lambda/4$: half- and quarter-wave plates, respectively; BS: beam splitter; M_1 and M_2: mirrors; L_1 and L_2: on-crystal focusing lenses; and PMT: photomultiplier tube.

a Nd:YLF oscillator followed by a fiber, a stretcher, three amplification stages, and a grating compressor. The pulse train from the Nd:YLF oscillator[47] is made up of 100-MHz, 45-ps bandwidth-limited pulses at a wavelength of 1053 nm. These pulses pass through an 800-m-long, single-mode optical fiber, which imposes a frequency chirp on the pulse with a bandwidth of up to 40 Å. A grating stretcher is then used to expand the pulse to 450 ps. After the stretcher, one pulse is selected with a Pockels cell for amplification.

The chirped pulse is amplified in three stages. All three amplifiers are flash-lamp-pumped, water-cooled rod amplifiers that have Nd^{3+}:glass as an active host. The first stage is a non-cavity-dumped, linear regenerative amplifier,[21,48] which provides most of the gain. It operates at a 1-Hz repetition rate. After about 85 passes, one pulse from the regenerative amplifier train with an output energy of ~0.5 mJ is switched out on the leading edge of the pulse-train envelope. The total cumulative *B*-integral of this pulse is ~0.7. This pulse then passes through a 9-mm-diam rod amplifier where its energy is raised to ~60 mJ. The 9-mm rod amplifier amplifies the pulse in one, two, or three passes. The energy of the pulse can be further boosted by 50 times in the third stage with a single-pass, 30-mm rod amplifier. The amplified pulse is compressed with a pair of compression gratings. The energetic parameters of the CPA system are listed in Table 75.II. When compressed, 1.6-ps pulses can carry energies in excess of 2 J and can be focused onto a target with peak intensities up to 10^{19} W/cm^2.

The amplified compressed pulse exhibits a pedestal consisting of two broad, equal-intensity satellite pulses separated from the main pulse by ~60 ps, as shown in Fig. 75.11, curve (a), with solid circles. The existence of two symmetric satellites was ascertained by performing TO HDRA measurements.[21] Their origin is the overlaid pedestal from the oscillator[13] and uncompensated phase distortions from the chirping fiber. The satellites and long pedestal can be suppressed by two and one-half orders of magnitude by using optical pulse cleaning (OPC) with the nonlinear birefringence of the chirping fiber.[49,50] A quarter-wave plate and a polarizer are inserted, as in Ref. 51, rather than an additional fiber, as in Ref. 32 (Fig. 75.10). The half-wave plate after the OPC is used to restore the polarization necessary for the grating stretcher. The spectrum leaving the chirping fiber was substantially reshaped, as shown in Fig. 75.12. The original spectrum, leaving the fiber without a quarter-wave plate is shown with a solid line. It has peaks at ±20 Å from the central frequency and two wave-breaking sidelobes[52] at ±30 Å. After rotating the wave plate and polarizer for maximum rejection of low-intensity light and maximum transmission of high-intensity light, the spectrum became centrally peaked with reduced peaks at ±20 Å and completely eliminated side lobes, as shown with the dashed line in Fig. 75.12. The spectral intensity of the amplified spectrum is primarily determined by the gain-narrowing in the regenerative amplifier and is almost independent of the injected spectrum. The pulses with contrast improved by OPC are shown in Fig. 75.11 with open diamonds. The seed energy contained within the shape of gain-narrowed spectrum is ~5 pJ. This imposes an ASE background with contrast ~10^7 when the pulse is compressed, as seen in Fig. 75.11 [curve (b)] for delays $\tau \geq 130$ ps. This background is very sensitive to the alignment of the seed and can be increased by one or two orders of magnitude by a slight mispointing of the seed pulse. The inset in Fig. 75.11 shows the amplified spectrum (solid curve) corresponding to the autocorrelation data (a) and the spectrum after OPC (dashed curve) corresponding to the autocorrelation data (b). The spectral width of the amplified OPC-modified pulse was 11.5 Å (FWHM), with the shape close to Gaussian. With a form factor $\gamma = 1.4$, the autocorrelation measurement gives a pulse duration of 1.4 ps and a corresponding time-bandwidth product of 0.44.

Table 75.II: Parameters of the CPA system

	In	Out	Total gain (gain in the active host)	Peak fluence	Output spectrum	*B*-integral
Oscillator		1 nJ/45 ps		–	0.4 Å	
Fiber	1 nJ	0.3 nJ/150 ps	0.5	–	30 Å	~100
Regenerative amplifier	3 pJ/450 ps	0.5 mJ/150 ps	10^{36}	0.1 J/cm^2	12 Å	0.7
9-mm amplifier (three passes)	0.3 mJ	60 mJ	400	0.1 J/cm^2	12 Å	0.2
30-mm amplifier	40 mJ	2 J	50	0.5 J/cm^2	12 Å	0.6

The contrast of the amplified compressed pulses was further boosted by a fast saturable absorber (SA) cell.[21] The compressed pulse was down-collimated to a waist of 0.7 mm before the SA cell to obtain a peak fluence of 25 mJ/cm^2 with 1.4-ps, 0.25-mJ pulses. The SA was Kodak dye #9860 in nitrobenzene with molar concentrations (n_M) varying from 50 to 75 μM. The relaxation time of this SA is ~4.2 ps.[53] The thickness of the cell was 1 cm, with ~12.5-mm wall thicknesses. Within the range of incident fluences between 0.01 and 20 mJ/cm^2, the incident-fluence-dependent absorption coefficient $[T = \exp(-\alpha L)]$, as measured with compressed 1.6-ps pulses, was

$$\alpha = \alpha_0 + \alpha_{sat}\left[1 + \left(J_{inc}/J_{sat}\right)^n\right]^{-1},$$

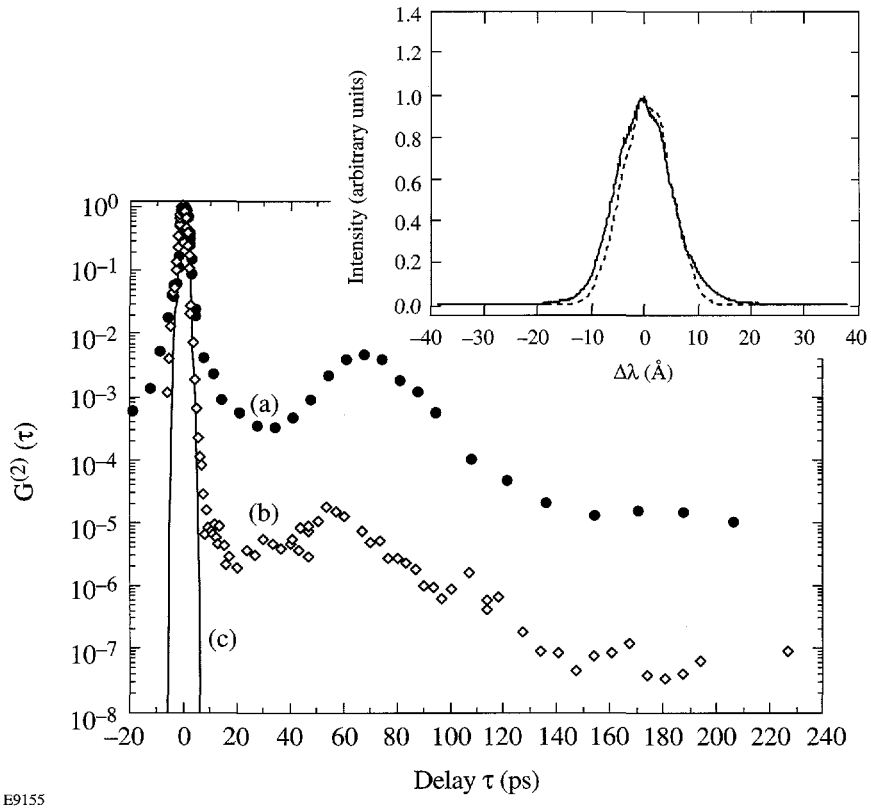

Figure 75.11
Normalized second-order autocorrelation functions of the compressed pulses leaving the regenerative amplifier: (a) original pulses, (b) OPC-cleaned pulses, and (c) the 1.4-ps Gaussian-curve fit to both of these autocorrelation functions. The origin of the pedestal and two symmetric satellites is the oscillator and the uncompensated (after compression with gratings) phase distortions from the chirping fiber. After OPC cleaning and amplification, the pedestal level is determined by the ASE from the regenerative amplifier, which is nearly equal in intensity to the residual pedestal from the oscillator and fiber.

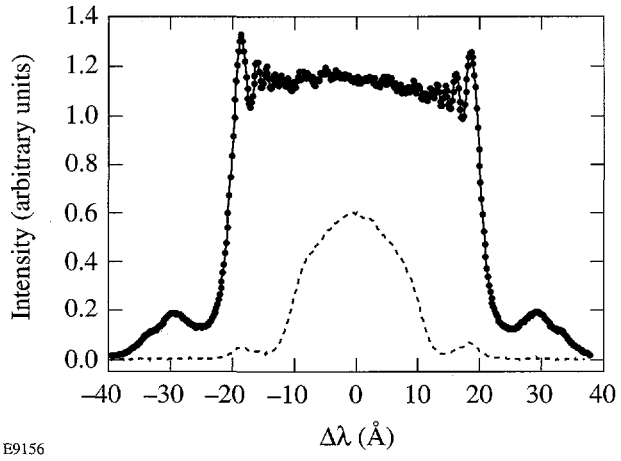

Figure 75.12
The spectrum leaving the chirping fiber. The spectrum measured without a quarter-wave in the OPC is shown with solid line. The OPC-cleaned spectrum is shown with dashed line.

with $\alpha_0/n_M = 0.02$ cm^{-1} μM^{-1}, $\alpha_{sat}/n_M = 0.16$ cm^{-1} μM^{-1}, $J_{sat} = 1.28\pm0.02$ mJ/cm^2, and $n = 1.50\pm0.04$. For incident fluences higher than ~30 mJ/cm^2, increased nonlinear absorption was observed instead of saturable absorption (decrease in transmission by 2%–3%). The operating incident intensity was chosen near 20 to 25 mJ/cm^2. The measured transmission of the cell was $\exp(-\alpha_0 L) = 22\%$ with a Kodak-dye concentration of ~75 μM, and the expected contrast boost was $\exp(\alpha_{sat} L) \sim 10^5$.

The autocorrelator was constructed as follows: A 10-mm × 10-mm, 4-mm-thick $LiIO_3$ crystal with rms surface roughness below 50 Å and bulk index-of-refraction inhomogeneities below 10^{-5} cm^{-1} was chosen as the noncollinear crystal. The two beams had a crossing angle $\Phi \approx 19°$ (~75° in the air). Without a down-collimator and on-crystal focusing lenses, the autocorrelator was used to measure the pulse duration in a single shot. The diameter of each individual beam was $2w_0 \sim 5.6$ mm. With a down-collimator before the saturable absorber cell and with the insertion of $f = 125$-mm lenses L_1 and L_2 (see Fig. 75.10), the two beams were focused onto the crystal with waist sizes of 40 μm. The crystal was cut for type-I noncritical phase matching. An after-crystal slit with a width of $d_{sl} \approx 300$ μm was placed $L_{sl} = 1$ mm behind the crystal, as shown in Fig. 75.9. The autocorrelator was carefully aligned with respect to any geometrical displacement of the probe beam inside the crystal when the translation stage is scanned. A photomultiplier tube (PMT), heavily filtered against the fundamental frequency and attenuated with variable-calibrated neutral-density filters to keep the signal on the same level, was used as the detector. The signal from the PMT was additionally time gated to avoid any noise associated with two-photon fluorescence, or any other long-time-scale optical noise. The signal from the PMT was an electrical pulse ~4 ns in duration. This electrical pulse was integrated within the gate time of 80 ns and converted into counts. One count from our acquisition system corresponded to 4 optical photons. The combined optical and electrical noise level with the PMT exposed to the experimental surroundings, without attenuating neutral-density filters and without blocking the noncollinear signal, was 2 counts.

The second-order autocorrelation measurements of pulses cleaned with OPC and SA are shown in Fig. 75.13. Each point of the autocorrelation curve in Fig. 75.13 corresponds to an average of five laser shots. The inset shows the measured spectrum before and after the SA cell. From the spectral measurements, it can be seen that the B-integral accumulated in the SA cell is ~1. The estimated B-integral in the rest of the autocorrelator optics is ~0.3. After transmission through the SA cell, the duration of the pulse was reduced from 1.4 ps to 1.0 ps. The peaks at 54, 100, and 125 ps are Fresnel reflections from optics in the autocorrelator. The pulse is measured to have an intensity contrast in excess of 10^{11}.

The dynamic range of the autocorrelator, measured as the ratio of the peak of the signal to the sum of the signals measured from each arm while the other arm was blocked, was 10^8 without the after-crystal slit and 10^{11} with it. Noise from each arm represented a constant addition to the signal, independent of the delay, but proportional to the square of the energy of the fundamental light at the input of the autocorrelator. That additional noise can be subtracted from the signal for each shot, leaving not the noise level from each arm, but rather the uncertainty of the noise level of each arm. The uncertainty of the noise level of each arm was 20% of the noise itself; thus, the system was able to resolve the signal with a dynamic range of 0.5×10^{12}. The signal at large delays was about twice as large as the noise.

The estimates based on the simple geometric layout shown in Fig. 75.9 with Gaussian beam profiles show that our approach can be applied to pulses as short as 100-fs duration. For pulses shorter than ~100 fs, both the geometry and the phase-matching conditions over the 10-nm spectrum may make it difficult to reduce the surface-scattering noise, which may decrease the dynamic range of an autocorrelator. The shorter pulses require higher temporal resolution (smaller $\Delta\tau$) and thus smaller crossing angles. Smaller crossing angles would require a longer crystal. Longer crystals would cause the distortion of the temporal shape of the pulse (due to material dispersion) before it reached the interaction region. Tighter focusing would bring noncollinear frequency conversion closer to saturation with lower energies of the crossing fundamental beams and would give smaller noncollinear beam energies. The after-crystal slit still might be a solution with 100-μm-thick crystals and tighter focusing for multikilohertz systems able to generate ~30-fs pulses[3] because one can utilize lock-in detection.

In conclusion, we have demonstrated for the first time second-order autocorrelation measurements of ultrashort picosecond pulses with dynamic ranges of $\sim 0.5 \times 10^{12}$. To our knowledge, this is the highest dynamic range obtained in time-resolved dynamic-range measurements with tens-of-femtoseconds resolution. To our knowledge, this is also the first consideration of dynamic-range limitations for noncollinear, high-dynamic-range autocorrelation measurements.

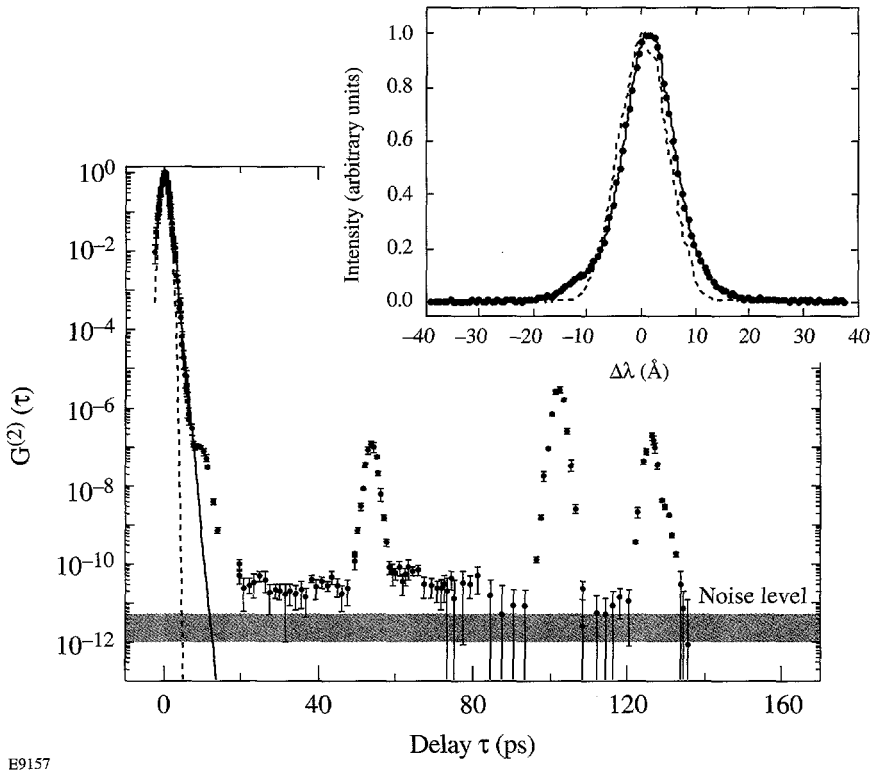

Figure 75.13
Normalized second-order autocorrelation of the OPC-cleaned pulses (as shown in Fig. 75.11 with open diamonds) after transmission through the SA cell. A 10^{-12} signal corresponds to ~4 photons per shot. The final autocorrelation function has peaks at 54 ps, 100 ps, and 125 ps at a level of 10^{-5} to 10^{-6} below the peak intensity. These are Fresnel reflections in the autocorrelator optics and in the SA cell. The 54-ps peak is associated with the reflection from the 5-mm-thick non-wedged mirror (M_2 in Fig. 75.10) in the translation-stage arm. It can be eliminated by using a wedged mirror. The 100-ps peak is the secondary reflection in the plano-convex ($f = 125$ mm, thickness = 10 mm) on-crystal focusing lenses (L_1 and L_2 in Fig. 75.10). This expected peak was at a different position when focusing lenses with a different thickness were used. It can be reduced and eliminated by better coating and with a slight misalignment of the focusing lenses. The 125-ps peak is the Fresnel reflection from the 1/2-in.-thick wall of the second SA cell. It disappeared but was replaced by a similar peak at 10 ps when a SA cell with 1-mm-thick walls was used. The inset shows the intensity spectrum of the pulses before (dashed line) and after (solid line) transmission through a SA cell for incident fluences of ~25 mJ/cm^2. After transmission through the cell, the pulse duration decreased from 1.4 ps to 1.0 ps. The dashed and solid curves are, respectively, 1.0-ps Gaussian and sech^2 fits to this autocorrelation data.

ACKNOWLEDGMENT

This work was supported by the U.S. Department of Energy Office of Inertial Confinement Fusion under Cooperative Agreement No. DE-FC03-92SF19460, the University of Rochester, and the New York State Energy Research and Development Authority. The support of DOE does not constitute an endorsement by DOE of the views expressed in this article.

REFERENCES

1. P. B. Corkum *et al.*, Phys. Rev. Lett. **61**, 2886 (1988).
2. B. C. Stuart *et al.*, Phys. Rev. B **53**, 1749 (1996).
3. A. Antonetti *et al.*, Appl. Phys. B **B65**, 197 (1997).
4. G. A. Mourou, C. P. J. Barty, and M. D. Perry, Phys. Today **51**, 22 (1998).
5. A. Galvanauskas *et al.*, Opt. Lett. **23**, 210 (1998).
6. I. N. Ross *et al.*, Opt. Commun. **144**, 125 (1997).
7. M. M. Murnane, H. C. Kapteyn, and R. W. Falcone, Phys. Rev. Lett. **62**, 155 (1989).
8. H. Chen, B. Soom, B. Yaakobi, S. Uchida, and D. D. Meyerhofer, Phys. Rev. Lett. **70**, 3431 (1993).
9. B. Soom, H. Chen, Y. Fisher, and D. D. Meyerhofer, J. Appl. Phys. **74**, 5372 (1993).
10. Throughout the text it is assumed that the contrast of some structure is the ratio of the peak intensity of the pulse to the intensity of this structure, while the intensity level of a structure is the inverse of the contrast.

11. M. Tabak *et al.*, Phys. Plasmas **1**, 1626 (1994).

12. E. P. Ippen and C. V. Shank, Appl. Phys. Lett. **27**, 488 (1975).

13. G. Albrecht, A. Antonetti, and G. Mourou, Opt. Commun. **40**, 59 (1981).

14. R. Wyatt and E. E. Marinero, Appl. Phys. **25**, 297 (1981).

15. P. Pax, J. Weston, and W. E. White, in *Femtosecond to Nanosecond High-Intensity Lasers and Applications*, edited by E. M. Campbell (SPIE, Bellingham, WA, 1990), Vol. 1229, pp. 82–86.

16. A.-C. Tien *et al.*, Opt. Lett. **22**, 1559 (1997).

17. R. Trebino and D. J. Kane, J. Opt. Soc. Am. A **10**, 1101 (1993).

18. J. Janszky, G. Corradi, and R. N. Gyuzalian, Opt. Commun. **23**, 293 (1977).

19. C. Kolmeder, W. Zinth, and W. Kaiser, Opt. Commun. **30**, 453 (1979).

20. K. Yamakawa *et al.*, Opt. Lett. **16**, 1593 (1991).

21. Y.-H. Chuang, D. D. Meyerhofer, S. Augst, H. Chen, J. Peatross, and S. Uchida, J. Opt. Soc. Am. B **8**, 1226 (1991).

22. L. Zhao *et al.*, in *Mode-Locked and Solid State Lasers, Amplifiers, and Applications*, edited by M. Piché and P. W. Pace (SPIE, Bellingham, WA, 1993), Vol. 2041, pp. 93–102.

23. D. M. Gold, Opt. Lett. **19**, 2006 (1994).

24. P. Beaud *et al.*, in *OSA Proceedings on Shortwavelength V: Physics with Intense Laser Pulses*, edited by M. D. Perry and P. B. Corkum (Optical Society of America, Washington, DC, 1993), Vol. 17, pp. 11–15.

25. O. A. Konoplev, Y. Fisher, and D. D. Meyerhofer, in *Conference on Lasers and Electro-Optics*, Vol. 15, 1995 OSA Technical Digest Series (Optical Society of America, Washington, DC, 1995), p. 216.

26. Y. Beaudoin *et al.*, Opt. Lett. **17**, 865 (1992).

27. R. S. Marjoribanks *et al.*, Opt. Lett. **18**, 361 (1993).

28. C. N. Danson *et al.*, Opt. Commun. **103**, 392 (1993).

29. C. Rouyer *et al.*, in *OSA Proceedings on Shortwavelength V: Physics with Intense Laser Pulses*, edited by M. D. Perry and P. B. Corkum (Optical Society of America, Washington, DC, 1993), Vol. 17, pp. 2–5.

30. M. P. Kalashnikov *et al.*, Phys. Rev. Lett. **73**, 260 (1994).

31. J. P. Chambaret *et al.*, Opt. Lett. **21**, 1921 (1996).

32. J.-L. Tapié and G. Mourou, Opt. Lett. **17**, 136 (1992).

33. P. F. Curley *et al.*, Opt. Commun. **120**, 71 (1995).

34. A. Braun *et al.*, Opt. Lett. **20**, 1889 (1995).

35. I. D. Jung *et al.*, Appl. Phys. B **B65**, 307 (1997).

36. K. Yamakawa *et al.*, IEEE J. Quantum Electron. **27**, 288 (1991).

37. C. Y. Chien, G. Korn, J. S. Coe, J. Squier, G. Mourou, and R. S. Craxton, Opt. Lett. **20**, 353 (1995).

38. Y. Wang and B. Luther-Davies, J. Opt. Soc. Am. B **11**, 1531 (1994).

39. L. L. Losev and V. I. Soskov, Opt. Commun. **135**, 71 (1997).

40. P. Heinz and A. Laubereau, J. Opt. Soc. Am. B **6**, 1574 (1989).

41. E. P. Ippen, and C. V. Shank, in *Ultrashort Light Pulses*, edited by S. L. Shapiro, Topics in Applied Physics, Vol. 18 (Springer-Verlag, Berlin, 1977), pp. 83–122.

42. S. Umegaki and S. Tanaka, Jpn. J. Appl. Phys. **16**, 775 (1977).

43. H. E. Bennett and J. O. Porteus, J. Opt. Soc. Am. **51**, 123 (1961).

44. D. A. Roberts, IEEE J. Quantum Electron. **28**, 2057 (1992).

45. L. D. Landau and E. M. Lifshitz, *Electrodynamics of Continuous Media*, Course of Theoretical Physics, Vol. 8 (Pergamon Press, Oxford, 1960), p. 385.

46. H. Bach and N. Neuroth, in *The Properties of Optical Glasses*, Schott Series on Glass and Glass Ceramics (Springer-Verlag, Berlin, 1995), p. 88.

47. P. Bado, M. Bouvier, and J. S. Coe, Opt. Lett. **12**, 319 (1987).

48. O. A. Konoplev and D. D. Meyerhofer, IEEE J. Sel. Top. Quantum Electron. **4**, 459 (1998).

49. R. H. Stolen, J. Botineau, and A. Ashkin, Opt. Lett. **7**, 512 (1982).

50. B. Nikolaus, D. Grischkowsky, and A. C. Balant, Opt. Lett. **8**, 189 (1983).

51. H. Roskos *et al.*, Opt. Commun. **61**, 81 (1987).

52. W. J. Tomlinson, R. H. Stolen, and A. M. Johnson, Opt. Lett. **10**, 457 (1985).

53. B. Kopainsky, W. Kaiser, and K. H. Drexhage, Opt. Commun. **32**, 451 (1980).

54. Y.-H. Chuang, J. Peatross, and D. D. Meyerhofer, in *Short-Pulse High-Intensity Lasers and Applications*, edited by H. A. Baldis (SPIE, Bellingham, WA, 1991), Vol. 1413, pp. 32–40.

Using Ion-Beam Techniques to Determine the Elemental Composition of ICF Targets

The precise elemental composition of any inertial confinement fusion (ICF) target (capsule, flat foil, or a package attached to a hohlraum) must be known to interpret the results of the implosion. The accuracy of this information was never an issue in earlier experiments: the composition was well known because the targets were straightforward designs (i.e., glass capsules and micro-encapsulated polystyrene shells) that were fabricated using well-characterized polymer chemistry methodologies that yield known compositions. Targets used today are more complicated than those used previously and are fabricated by new methods that are still in their infancy and, accordingly, are less understood.[1] These techniques involve the plasma-induced (a low-temperature, glow-discharge) polymerization of gas-phase monomers. The energy from the plasma and the presence of ions allow gas-phase and gas-surface interactions to occur that are otherwise unattainable using classical solvent chemistry because numerous reaction mechanisms are now thermodynamically and kinetically allowed. The resulting materials are amorphous solid-state solutions where the composition cannot be inferred *a priori* from the processing conditions. The overriding importance of this target-fabrication technique, however, is that thin-wall capsules, and capsules with discrete radial regions of the capsule wall doped with mid- to high-atomic-weight elements, can now be produced.[2] The associated uncertainty regarding the composition of these targets now requires the evaluation and application of suitable analysis techniques.

When a target is made of commercially available material, the material assay is accurately known. When targets are made using coating processes, only the composition of the source (precursor) material is well known; independent analysis of the as-deposited material is needed if the composition is to be accurately known. This analysis is done by many methods: The most common technique is electron microscopy using either energy-dispersive or wavelength-dispersive x-ray detection to identify the elements. These techniques are well established, and quantitative data can be obtained with the use of NIST standards. The diagnostic probe size is small (typically <1-μm diameter, 5 μm deep) and nondestructive, features that are desirable for analyzing ICF targets. Another technique adapted for ICF-sized shells—x-ray fluorescence—is also nondestructive and is used to identify dopants (chlorine, titanium, germanium, silicon) in individual shells according to their characteristic x-ray emission signal.[3] Carbon, hydrogen, oxygen, and nitrogen cannot be detected. Again, the actual elemental composition can be quantified if a suitable external calibration of the technique can be established. The techniques discussed here provide a third nondestructive method for assaying individual capsules, with the added virtue that they do not require external calibration. This eliminates several sources of uncertainty in the measurement.

In this article the capabilities and limitations of the ion-beam techniques along with the accuracy that can be achieved in the absence of external calibration are discussed. An analysis of current ICF capsules and some flat-foil targets is presented. This is not the only work that has used ion-beam techniques to characterize ICF targets: recently, Sandia National Laboratory reported on using ion tomography to measure the density and density uniformity of foam targets used in Sandia's ICF program.[4]

Rutherford Backscattering Spectroscopy

The first of two ion-beam techniques used to determine the elemental composition of ICF targets is Rutherford backscattering spectroscopy (RBS). This technique analyzes the energy of ions elastically recoiled off a surface. The stoichiometry, areal density, and presence of impurities in the top 5 to 20 μm of the material can be absolutely determined. Elements with atomic number $Z \geq 4$ can be identified at concentrations as low as 100 parts per million (the sensitivity depends on the atomic mass of the elements involved). The typical surface area of the analysis beam is 1×1 mm, although smaller probe dimensions (limit: 1-μm diam) are achievable by using quadropole electro-optics to focus the beam. The principal disadvantage of the RBS technique is that it cannot be used to detect elements at trace concentrations: it has moderate sensitivity to heavy elements in mid- to light matrices (threshold is 1 in $\sim 10^4$) and poor sensitivity to light elements in heavy matrices (threshold

~1 part in 10). Fortunately, these limitations do not apply to the ICF targets investigated for this article. A second limitation of the RBS technique is the logistical one of having ready access to the equipment. The equipment is expensive to purchase and operate and exists only in a few universities and commercial organizations.

RBS also quantifies the composition of the film at varying depths: the minimum resolvable depth increment is 5 to 10 nm, and the maximum depth the technique can probe depends on the material composition of the film and the ion beam. For example, a He^+ beam at 2.0 MeV can distinguish chlorine in a hydrocarbon matrix to a depth of ~ 6 μm; a H^+ beam at 1.4 MeV can distinguish chlorine in the same polymer down to 20 μm. These capabilities allow the location and concentration of dopants in a multilayered polymer capsule to be accurately characterized. (A concern in the fabrication process is that the dopant may diffuse out of its original layer when the capsules are processed after the vapor-phase, plasma-polymerization process is complete.)

Principles

Analysis ions are accelerated to a well-defined energy (typically 1 to 10 MeV) and are focused onto the target. Most ions lose energy through inelastic collisions with the target substrate and are implanted into, or are transmitted through, the substrate. A very small fraction of the incident ions elastically recoil off atoms in the target substrate, and a further fraction of the recoiled ions have sufficient energy to escape from the solid and be detected. The energy of the recoiled ions is measured using a surface-barrier detector, and the number of ions in a predefined energy range (referred to as a channel) is counted. The substrate atoms are identified by measuring the energy of the recoiled atom, allowing for the energy the ion loses traversing (both entering and exiting) the substrate. The number of atoms per cross-sectional area is determined from the total number of recoils detected.

A schematic representation of the recoil process is shown in Fig. 75.14(a), and the resulting backscattered spectrum, in Fig. 75.14(b). The abscissa displays the energy of the recoiled ions, where the bandwidth of each energy channel is the energy resolution of the detector (16 keV) and the highest channel number has the greatest energy. The abundance and distribution of elements A and B are calculated from the peaks A_A and A_B. The peak height depends on (1) the absolute number of identical substrate atoms at each resolvable discrete depth and (2) the kinematics of the ion–atom interaction. The peak width depends on the distribution of the identical substrate atoms through the film depth: ions that recoil from deeper within the solid possess lower recoil energies as they lose energy traversing the substrate. The ratio of the energy E_0 of the incident ion to the energy E_1^A of the high-energy side of peak A is the kinematic factor $K_A = E_1^A / E_0$, which is specific for the incident ion, the target atom, and the scattering angle. The kinematic factor is also given by

$$K = \left\{ \left[\left(M_2^2 - M_1^2 \sin^2 \theta \right)^{1/2} + M_1 \cos\theta \right] \Big/ \left(M_1 + M_2 \right) \right\}^2 ,$$

where θ is the laboratory angle through which the incident ion is scattered and M_1 and M_2 are the masses of the incident ion and target atom, respectively.[5] K, M_1, E_0, and θ are all known, allowing M_2 to be determined. (It is physically intuitive that the greater the mass of the substrate atom, the higher the energy of the recoiled He ion.) The physical basis for this equation is that the kinematic factor depends on the conservation of energy and momentum in a two-body collision, a realistic approximation at these energies (0.5 to 5 MeV for He^+) where the collisions are pure Coulombic and where relativistic and off-resonance nuclear reactions do not occur. Tables of the kinematic factors are available for many incident ions (including $^1H^+$ and $^4He^+$) and substrate atoms at discrete recoil angles (θ).[5] An added significance of the kinematic factor is that it influences the mass resolution of the technique; the incident ion and ion energy can be varied to resolve elements with similar masses. Other important factors affecting the accuracy and sensitivity of the technique are the resolution of the surface-barrier detector and energy straggling by the ion beam as it penetrates into the surface (i.e., statistical fluctuations that cause the initially monoenergetic ion beam to assume an increasingly wide energy range as the penetration depth increases).

The areal density of the ith element is determined from the knowledge of the experimental configuration [Fig. 75.14(a)]: the detector solid angle Ω; the integrated peak count A_i, for a known number of incident ions Q; and the measured, or calculated, cross section $\sigma_i(E,\theta)$:

$$N_i t = \frac{A_i \cos\theta}{Q \Omega \sigma_i (E,\theta)},$$

where N_i is the atomic density of the ith element and t is the film thickness. If the scattering is Rutherford, the cross section $\sigma(E,\theta)$ can be calculated:

$$\sigma(E,\theta) = \left(Z_1 Z_2 e^2/4E\right)^2 \times \frac{4\left[\left(M_2^2 - M_1^2 \sin^2\theta\right)^{1/2} + M_2 \cos\theta\right]^2}{M_2 \sin^4\theta\left(M_2^2 - M_1^2 \sin^2\theta\right)^{1/2}},$$

where Z_1 and Z_2 are the atomic numbers of the incident ion and target atom, respectively, and $e^2 = 1.44 \times 10^{-13}$ MeV-cm.

This analysis typically yields ±3% uncertainty for the areal density measurement and less than 1% uncertainty for the average stoichiometry. This precision decreases as deeper layers are analyzed because of energy straggling.

Material analyses using these techniques are typically done with ^{4}He ions and modest accelerator energies (0.5 to 2 MeV). At higher and lower energies, the elastic-scattering cross section departs from the Rutherford cross section (i.e., near Coulombic): at lower energies the deviation is due to the nuclear charges being partially screened by the electron shells of both nuclei; at higher energies the deviation is caused by the presence of short-range nuclear forces. Helium is typically used because the backscattering cross sections with all atoms larger than beryllium are nearly Rutherford in this energy region, and there is extensive experimental data regarding the kinematic factors and Rutherford-scattering cross sections.

Nuclear Resonance Analysis of Hydrogen

Accurately quantifying the amount of hydrogen in materials is extremely difficult. Most analytical techniques are unable to detect hydrogen. Those that can detect hydrogen quantify the atom indirectly by probing those atoms/complexes that incorporate hydrogen, i.e., classical spectroscopy looks at the absorption/emission of hydrogen-bonded complexes; electron-detection–based techniques (i.e., x-ray photoelectron spectroscopy and electron-energy-loss spectroscopy) quantify hydrogen from the electron-energy-loss spectrum. More conventional methods (i.e., combustion analysis) that can quantify the hydrogen content typically require a large sample size. This introduces an additional source of uncertainty when analyzing ICF targets since many (typically in excess of 100) capsules are required to obtain the necessary mass. The measured hydrogen content is thus an aggregate value that averages several processing batches and many capsules from the same batch. Consequently, it is impossible to know how much the hydrogen content varies from one target to the next.

Ion-beam–based techniques have been used for more than 10 years to measure hydrogen concentrations in thin films. Because these techniques are sensitive to small variations in hydrogen concentrations and require only a small sample size, they are convenient for analyzing ICF targets. Two ion-beam techniques exist: One technique, elastic recoil detection (ERD), is the reverse of classical RBS since heavy incident atoms forward-scatter lower-Z substrate atoms ($1 \le Z \le 9$) and are themselves kinematically recoiled.[5] The second technique is

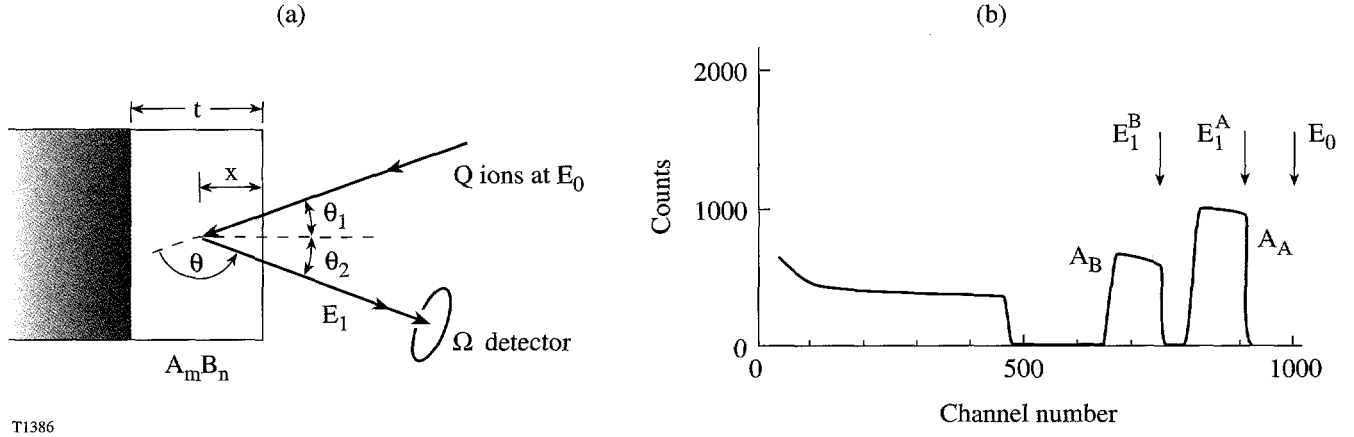

Figure 75.14
(a) Schematic of the experimental geometry used for RBS. (b) Associated Rutherford backscattered spectrum for a two-element material (A_mB_n) on a lower-mass substrate.

themselves kinematically recoiled.[5] The second technique is nuclear resonance analysis (NRA). This technique measures the gamma-ray product (γ) of a nuclear reaction[5]

$$^{15}N^{++} + {}^{1}H \rightarrow {}^{12}C + {}^{4}He + \gamma(4.43\ \text{MeV}).$$

The reaction cross section at the resonance energy (6.385 ±0.005 MeV) is large and decreases rapidly off resonance; the cross section is four orders of magnitude lower and 8 keV off resonance. The γ-ray yield is proportional to the hydrogen concentration at the resonant energy and is accurate to within 2 at.%. Depth profiling is achieved by varying the incident $^{15}N^{++}$ energy, and as the ion loses energy traversing the solid, a region develops within the solid where the ion energy is at resonance (6.385 MeV) and γ rays are produced. The detection "window" equates to a depth of ~7.5 nm in the solids analyzed for this article. This technique's advantage over ERD is greater depth resolution and sensitivity, and it is this latter technique that is used to analyze ICF targets.

Experimental Conditions

The ion-beam work was analyzed using the Dynamitron Accelerator (Model P.E.A.-3.0) at the Accelerator Laboratory at the State University of New York at Albany. The three ions used were $^{1}H^{+}$, $^{4}He^{+}$, and $^{15}N^{++}$ at energies of 1.4, 2, and 8 MeV, respectively. Three beamlines were used. One beamline was configured for standard RBS analysis (nominal 1-mm × 1-mm spot size). The laboratory geometry [Fig. 75.14(a)] was as follows: the angle between the beam and the detector, ($\theta_1 + \theta_2$), was 14°; the angle between the sample normal and the detector, θ_2 ,was 7°; the sample normal was 7° above the equator; and the solid angle Ω of the surface-barrier detector was 31 msr. The second beamline was configured for microprobe analysis (spatial spot size ~1-μm diam); the detector was above the incoming beam at $\theta_1 + \theta_2 = 23°$; the sample was perpendicular to the beam; and the solid angle was 87 msr. The third beamline used $^{15}N^{++}$ for hydrogen analysis. A NaI scintillation detector was positioned directly behind the incident ion beam.

Data recorded during the 5 to 10 min typically required to acquire a RBS spectrum are (1) the number of recoils at each discrete energy resolvable by the surface-barrier detector (FWHM resolution is 16 keV); (2) the total current and charge striking the target; and (3) a correction for the dead time of the pulse-height analyzer. The total charge and current incident on the surface were optimized to obtain a satisfactory signal-to-noise ratio while minimizing any ion-beam damage to the substrate. This latter effect is of special concern as most of the analyzed materials are plastics and are susceptible to bulk heating effects. Typically the total charge delivered to the substrate is less than 10 μC/cm^2. This threshold was chosen based on a related report that found that bombarding a teflon film with 6-MeV nitrogen ions decreased the fluorine concentration by only 1%.[6] Since carbon–hydrogen and carbon–fluorine bonds have comparable strengths, this ion-beam threshold is believed to have a minimal perturbation on the target's composition. This was confirmed by measuring the hydrogen content of solution-cast polystyrene films to be 50 at.%, the theoretically expected value. The total dead time of the detector is kept below 10% by controlling the ion-beam current. Finally, particle-induced x-ray emission (PIXE) data were acquired and used to help qualitatively identify the elements present in the material.

Data Analysis

The first step to determine whether ion-beam techniques are suitable for analyzing ICF targets is to calculate the behavior of an energetic ion in an ICF target. Of interest are the trajectory and penetration range of different ions, at specific energies, within the material. These data are available using "Stopping and Range of Ions in Materials"[7]—a software that uses the known collisional cross sections and stopping powers to perform a Monte Carlo simulation of an ion's path through the material. In this manner the divergence ("straggling") of the beam as a function of depth can be determined. Also, the energy lost by the ion to the substrate as it penetrates deeper into the material can be determined.

An example of this simulation is shown in Fig. 75.15. The modeled substrate is a multilayered polymer capsule, as provided by General Atomics, and analyzed by RBS (Fig. 75.16). The incident He ion is at 2 MeV and is defined as a point source on the surface of the substrate. The ion penetrates 9.44 μm into the plastic with a depth "straggle" of 0.18 μm and a radial divergence of ~0.3 μm [Figs. 75.15(a) and 75.15(b)]. Figure 75.15(c) shows the energy lost as a function of depth as the He ion penetrates the material; on average, the ion loses ~20 eV/Å. This information is useful for determining whether the ion beam is heating and possibly altering the substrate. These data confirm that a microprobe beam with a 2-μm-diam spot size will sample a cylindrical volume no greater than 3 μm in diameter and ~8 μm deep.

The Rutherford backscattering spectrum is analyzed using a standard code—Rump[8]—which uses known kinematic factors, Rutherford cross sections, and stopping powers to simu-

composition. The procedure is to first simulate the RBS spectrum using a "guessed" elemental composition and then compare the theoretical spectrum with the actual spectrum. The guessed composition is then refined and the theoretical spectrum recalculated. The process is iterated until the stimulated recoil spectrum corresponds with the actual spectrum. When the material is not isotropic, it is necessary to specify the composition of the material at discrete layers. Agreement between the theoretical and actual spectra of various ICF polymer targets is shown in Figs. 75.16–75.18. The accuracy of these analyses is ±2 at.% of the absolute value for the primary components (i.e., C, N, O) and 5% to 20% for trace (<10 at.% total concentration) dopants such as Cl, Si, Ge, and Ti.

RBS detects elements with atomic numbers greater than 4. As this excludes hydrogen, a major component of ICF polymer capsules (~50 at.%), its concentration was determined using nuclear resonance analysis. The hydrogen concentration (ρ_H) is related to the experimentally measured gamma-ray yield (Y) by

$$Y = \int Q\rho_H(x)\sigma(x)dx,$$

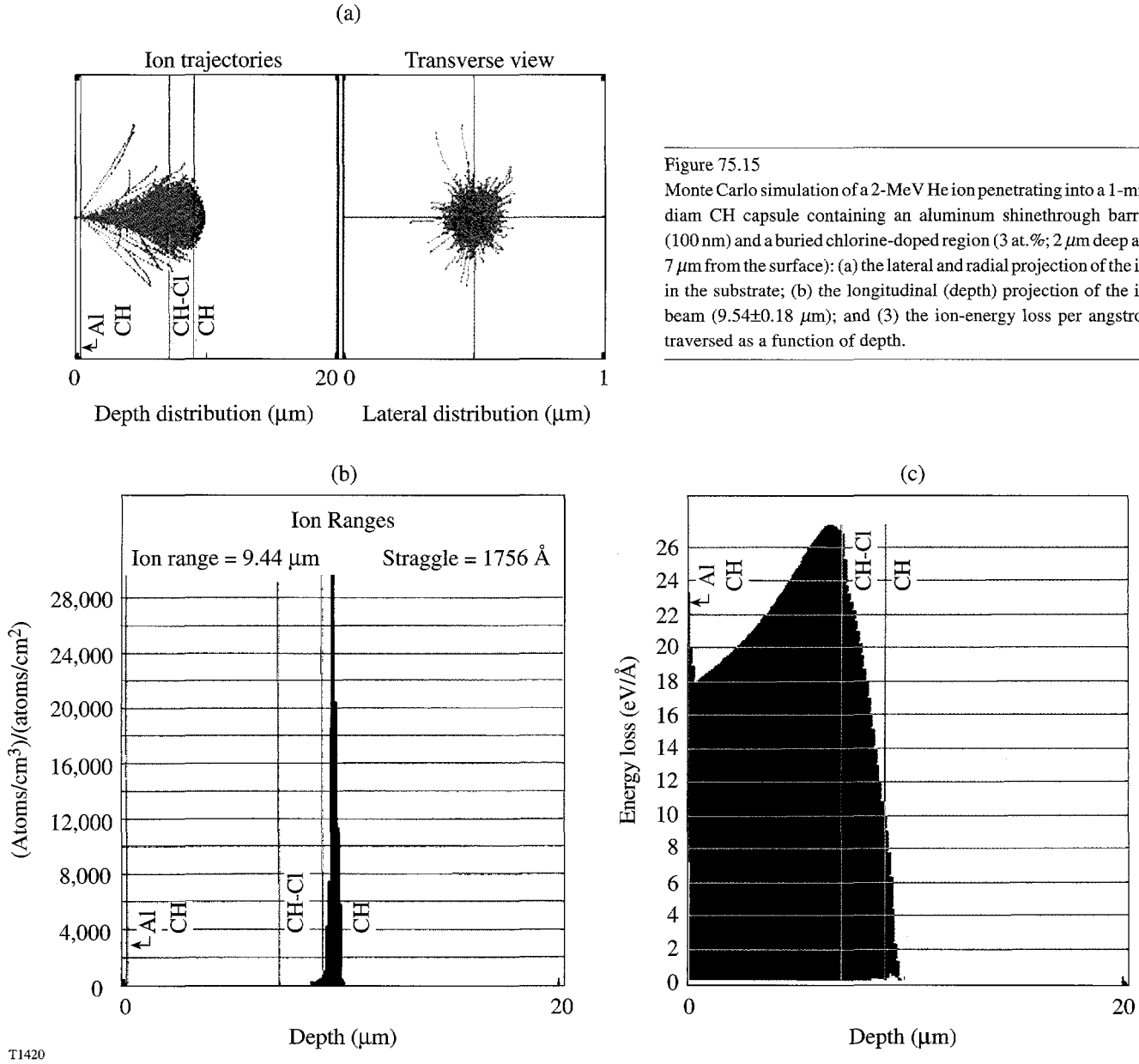

Figure 75.15
Monte Carlo simulation of a 2-MeV He ion penetrating into a 1-mm-diam CH capsule containing an aluminum shinethrough barrier (100 nm) and a buried chlorine-doped region (3 at.%; 2 μm deep and 7 μm from the surface): (a) the lateral and radial projection of the ion in the substrate; (b) the longitudinal (depth) projection of the ion beam (9.54±0.18 μm); and (3) the ion-energy loss per angstrom traversed as a function of depth.

where Q is the number of incident ions and σ is the cross section. Clearly, this cross-sectional dependency requires the film's elemental composition (elements other than hydrogen), film thickness, and density to be accurately known—information that is obtained from the RBS analysis.

Using $dx = dE/(dE/dx)$ gives

$$Y = Q\int \frac{\rho_H(E)\,\sigma(E)}{dE/dx}\,dE,$$

where

$$\sigma(E) = \frac{\sigma_0\Gamma^2/4}{(E - E_{res})^2 + \Gamma^2/4}$$

is the Breit–Wigner formula,[5] σ_0 is the cross section at the resonance energy, and Γ is the full width at half-maximum of the cross section. Integration yields

$$Y = \frac{Q\rho_H\pi/2\sigma_0\,\Gamma}{dE/dx}$$

or

$$\rho_H(x) = K(dE/dx)Y(x),$$

where K is a constant incorporating all the cross-section parameters (including detector efficiency). K is independent of the material being analyzed; for example, to calculate the amount of hydrogen in a hydrocarbon:

$$\rho_H(\text{at.\%}) = (0.45\times10^{19})(dE/dx)_{CH}$$
$$(\text{measured \# counts}/\ 0.5\text{–}\mu\text{C total charge}),$$

and

$$(dE/dx)_{CH} = \rho_{CH}\,\frac{\chi_C(dE/dx)_C + \chi_H(dE/dx)_H}{\chi_C MW_C + \chi_H MW_H},$$

where 0.45×10^{19} is the constant K, dE/dx is the stopping power of the CH substrate, MW is the molecular weight, and χ is the atomic fraction. The penetration depth is equal to

$$\left[E(^{15}N) - E_{reson}(6.385\ \text{MeV})\right]/(dE/dx)_{CH}.$$

Clearly, to completely analyze a polymer capsule, both RBS and NRA data sets must be obtained and iterated until each data set can be accurately simulated with the same elemental composition.

Results

1. Plasma Polymer Capsules

The elemental composition of all types of ICF capsules used at LLE are summarized in Table 75.III. For the most common type of ICF target, a hydrocarbon capsule made by plasma

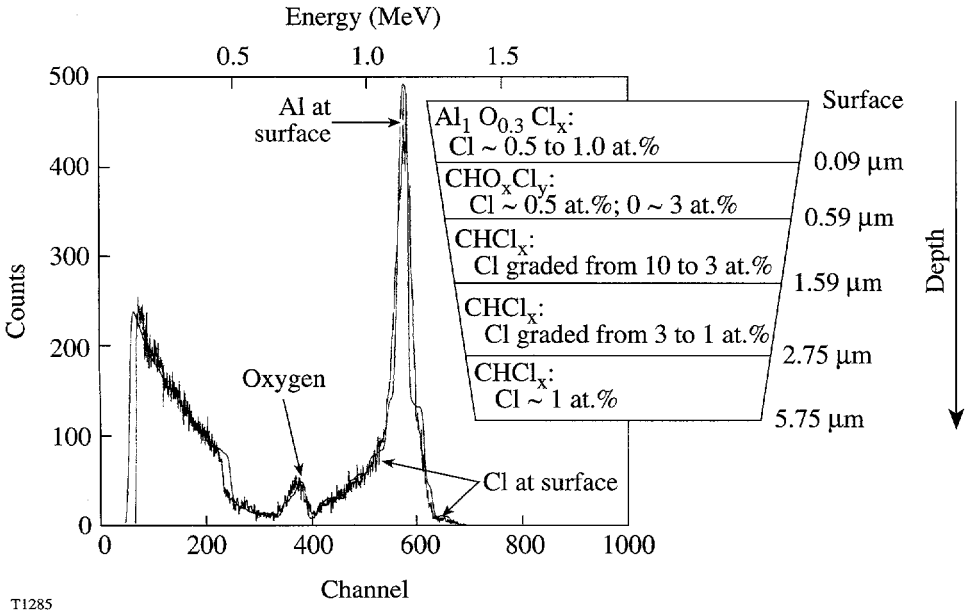

Figure 75.16
RBS spectrum of a 900-μm-diam capsule overlaid with the simulated spectrum. The Cl distribution of elements in the top 5.75 μm is inset.

Table 75.III: The range of composition of each element in capsules and flat films provided by GA, as measured using ion-beam analysis.

Composition (fractional-atom content)							
Film Material	Carbon	Hydrogen	Silicon	Germanium	Titanium	Chlorine	Oxygen
CH	0.4→0.48	0.5→0.55					0.02→0.06
CH-Cl	0.44→0.47	0.50→0.53				<0.01→0.1 (pyrolyzed) 0.02→0.03 (unpyrolyzed)	0.01→0.04
CH-Ti	0.33→0.43	0.42→0.62			0.015→0.067	0→0.015	0.02→0.08
CH-Si	0.40	0.47	0.06				0.07
CH-Ge	0.42→0.44	0.48→0.50		0.02→0.04			0.02→0.08

polymerization, the hydrogen concentration ranged from 50 to 55 at.%. There is insufficient data to determine statistically if this variation is inherent in the plasma-processing method or if the fluctuation is a measure of the repeatability of the process. Oxygen was also identified in the polymer; the quantity varied from <1 at.% to a maximum of ~6 at.%. It is speculated that oxygen is adsorbed from the environment and that the concentration depends on how long the capsule was exposed to air. (The maximum of 6 at.% was observed after the plastic had been stored in the laboratory for several months.)

Data obtained from analyzing capsules doped with high-atomic-number elements are summarized below.

a. Silicon-doped capsules. The concentration was constant at 6±1 at.% in all the shells and flat films analyzed. Moreover, silicon was uniformly distributed throughout the depth of the shell wall, as far as the ion beam could probe (6 μm). Figure 75.17 (spectrum 3) shows that the leading edge of the silicon signal was suppressed when a hydrocarbon plastic overcoat was applied (as was expected). Importantly, this signal remained suppressed when the capsule was pyrolyzed (a necessary processing step to remove the mandrel). The absence of any signal due to silicon having diffused to the outer surface of the capsule demonstrated the thermal stability of the silicon-doped plastic; hence, this material is suitable for processing by the current target-fabrication techniques. The oxygen content was 7 at.%.

b. Germanium-doped capsules. The germanium-doping fabrication process was evaluated by examining Ge-doped capsules made simultaneously in the same batch and also in different batches. As with the silicon-doped capsules, the germanium concentration was uniformly distributed throughout the wall of the capsule (shown in Fig. 75.18), and oxygen was present. The measured germanium concentrations varied from 2 to 4 at.% from one capsule to the next. The variation is a measure of the repeatability of the processing conditions: plasma polymer capsules fabricated at the same time varied by less than <1 at.% while those made in different batches varied by a factor of 2. Although the processing conditions were intentionally identical for all the batches analyzed, the varying germanium concentrations demonstrate the inherent control and repeatability of the process.

c. Titanium-doped capsules. The ion-beam analysis technique was used by LLE to assist GA in developing Ti-doped plasma polymer capsules. Capsules were produced using purposely varied processing parameters, and the resulting titanium concentrations varied from 1 to 8 at.%. High titanium concentrations (6 at.%) were accompanied by high oxygen levels (9 at.%) and lower hydrogen concentrations (41 at.%). Figure 75.19 shows this correlation; the depth-profiled hydrogen concentrations at 0.1, 0.28, and 0.44 μm are shown for two films containing different titanium concentrations. Currently, capsules with titanium concentrations of from 3 to 6 at.% are available.

d. Chlorine-doped capsules. The chlorine content was analyzed using both helium and hydrogen ion beams; the former provided greater sensitivity and accuracy while the latter provided greater penetration that allowed the complete 20-μm wall of the capsules to be profiled. The quantity and position of the chlorine were found to be strongly dependent on

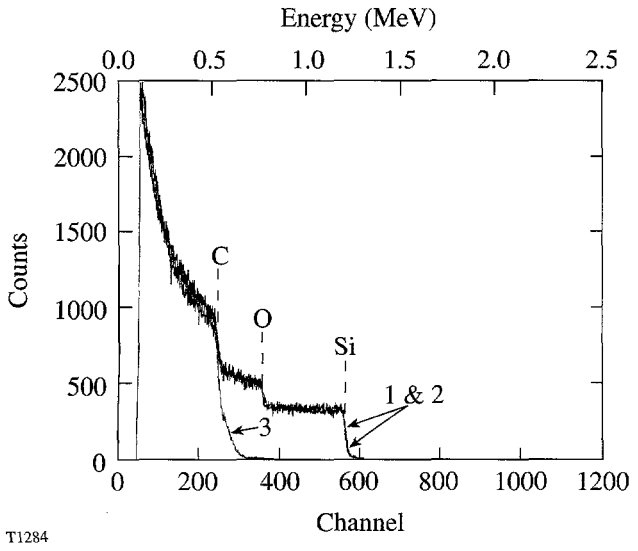

Figure 75.17
RBS spectra of three silicon-doped capsules show that the silicon is uniformly distributed through the capsule wall and is thermally stable: (1) Si-doped CH; (2) Si-doped CH after pyrolysis; and (3) Si-doped CH overcoated with CH and then pyrolyzed at 300°C.

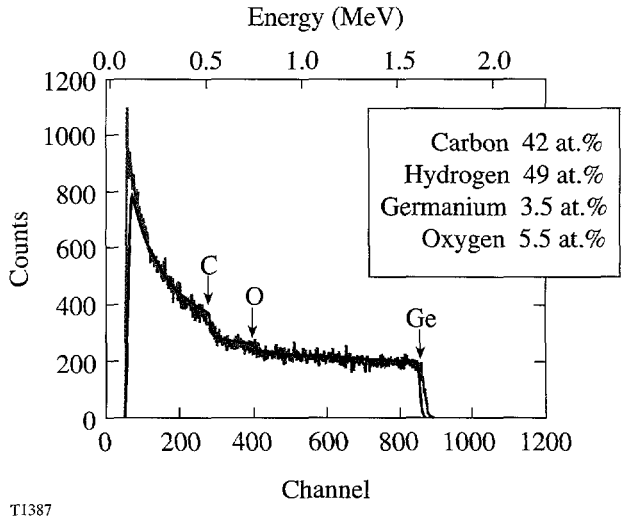

Figure 75.18
RBS spectrum of a Ge-doped capsule. Germanium is uniformly distributed through the first 5 μm of the capsule wall.

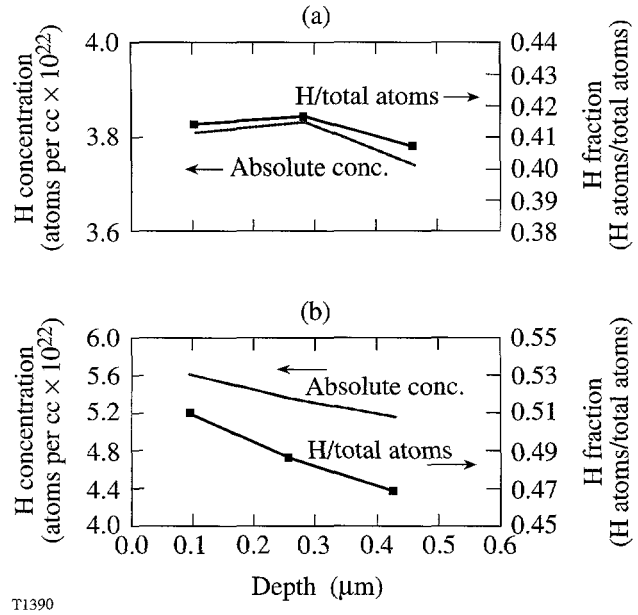

Figure 75.19
Depth-profiled hydrogen concentrations (expressed as an absolute density and an atomic fraction) in two Ti-doped plastic films: film (a) consists of 44-at.% carbon, 6-at.% titanium, and 9-at.% oxygen content, and film (b) consists of 42-at.% carbon, 2-at.% titanium, and 6-at.% oxygen.

how the polymer capsule was processed. When the capsule was pyrolyzed at 300°C after fabrication (as is typically done to remove the decomposable mandrel), chlorine diffused from the originally doped layer and was distributed throughout the shell wall. The chlorine concentration at any depth would vary from <1 to 10 at.%, with the higher concentration measured in a very thin band at the external wall of the shell. The distribution is shown in Fig. 75.16. Here, chlorine was intended to be located in a 2-μm region 7 μm beneath the surface. In reality, chlorine was detected throughout the top 5.75 μm of the capsule—the maximum depth at which the He ion at 2 MeV could detect chlorine in plastic. A hydrogen ion beam was used to extend the depth sensitivity to detect how far chlorine had diffused into the capsule's wall (a different capsule from the one analyzed above). The resulting spectrum is shown in Fig. 75.20. The chlorine-doped layer was intended to be 1 μm thick and 6 μm below the surface with a concentration of 6 at.%. Actually, the layer was distributed through the top 10 μm of the capsule with an average concentration of 0.05 at.%; no chlorine was detected at greater depths.

Analysis of many chlorine-doped capsules shows the chlorine concentration to be 2 to 3 at.% and thermally stable when the chlorine-doped layer is deposited after the pyrolysis is complete. The consequence of these results for designing targets for ICF experiments is that capsules with a chlorine-doped layer within 3 μm of the inner surface are not achievable; conversely, capsules with a chlorine-doped layer more than 3 μm from the inner surface are feasible.

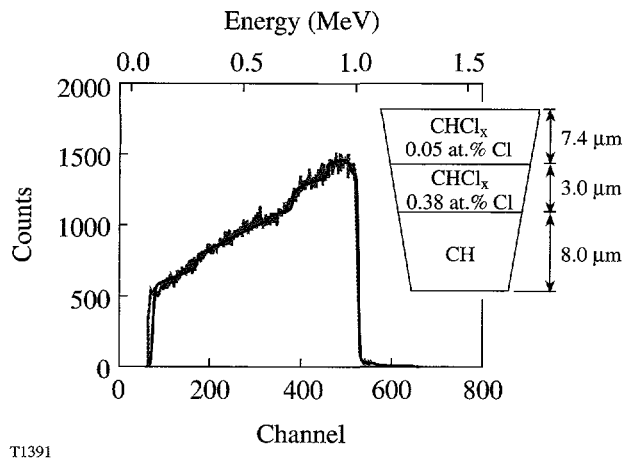

Figure 75.20
The experimental RBS spectrum of a Cl-doped CH capsule overlaid with the simulated fit. A 1.4-MeV H-ion beam profiled the entire 18.4-μm thickness of the capsule wall.

e. Deuterated capsules. The fully deuterated polymer capsule is an important type of ICF target. It is made by polymerizing deuterated-gas monomers onto a poly-α-methylstyrene mandrel and then pyrolyzing the composite to remove the mandrel. It is important that no hydrogen be present in the capsule wall after the process. [It is possible that the deuterium in the CD wall and the hydrogen in the poly-α-methylstyrene (PAMS) wall could exchange during the pyrolysis process.] Hydrogen was not detected in the CD capsule wall, which, given the threshold sensitivity of the NRA technique, limits the hydrogen content in the deuterated plastic to be below 1 at.%.

2. Flat-Foil Targets

A type of target used in plasma physics experiments consists of several layers of different elements used to spectroscopically diagnose the plasma temperature. The more accurately the number of atoms in each layer is known (from the measured film thickness, composition, and areal density), the more accurate is the temperature measurement.[9] Current sputter-deposition and evaporation techniques measure the deposition rate using quartz crystal monitors, a method that can measure the film thickness to within 3%–8% but cannot measure the elemental composition. An independent nondestructive method for analyzing targets after they are assembled is needed, and RBS is a suitable technique.

A target analyzed here consisted of a 1-mm-diam plastic (CH) film overcoated with two thin layers of Ti and KCl. The thickness was measured with 3% accuracy. The titanium layer consisted of 30-at.% oxygen (not surprising since titanium is an effective oxygen getter), and the stoichiometric ratio of K to Cl was 1 to 1. These data allowed the total number of titanium, potassium, and chlorine atoms to be determined.

A type of target used for hydrodynamic instability studies uses an open-cell foam (2- to 5-μm pore size; 1-mm diam and 100 μm thick) overcoat to help minimize the growth of the Rayleigh–Taylor instability. Whereas the target design called for a thin, gold overlayer on the foam, fabrication complexities made it impossible to ensure that the gold was confined to the foam's outer surface (given the open cell structure of the material). The RBS spectrum determined that the sputtered gold atoms had penetrated 30 μm below the surface (Fig. 75.21). These data demonstrated that the target, as-

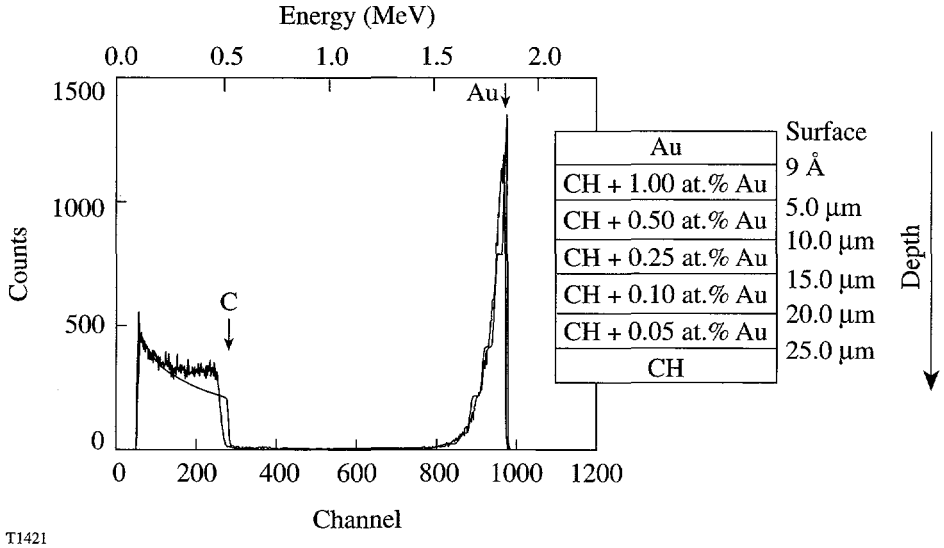

Figure 75.21
The experimental and simulated RBS spectra of a 30-mg/cm^3-polystyrene foam overcoated with 1 nm of gold.

fabricated, differed significantly from what was intended. This information helps define the capabilities and limitations of different target-fabrication methodologies, which is essential for building new types of targets.

3. Polyimide Shells

The ion-beam analysis technique has also been used to assist the polyimide-shell-development effort.[10] Compositions of films deposited by different processing conditions were determined using both RBS and NRA. Examples of the depth-profile data are shown in Fig. 75.22. These data show that both the elemental ratio in the polyamic acid precursor and the resultant polyimide material were very close to the expected stoichiometric values; however, both materials possessed excess nitrogen (~2 at.%). This information has allowed the processing parameters to be refined with the goal of optimizing the mass flux of the two precursor monomers.[11]

As discussed previously, RBS provides areal density information, and additional information about the actual (theoretical or measured) density is required to extract the film-layer-thickness information. Conversely, if the film thickness is known, then the actual density can be determined. This approach was used to determine the density of the precursor (polyamic acid) and final (polyimide) films. Films of measured thickness were analyzed, and the density of the

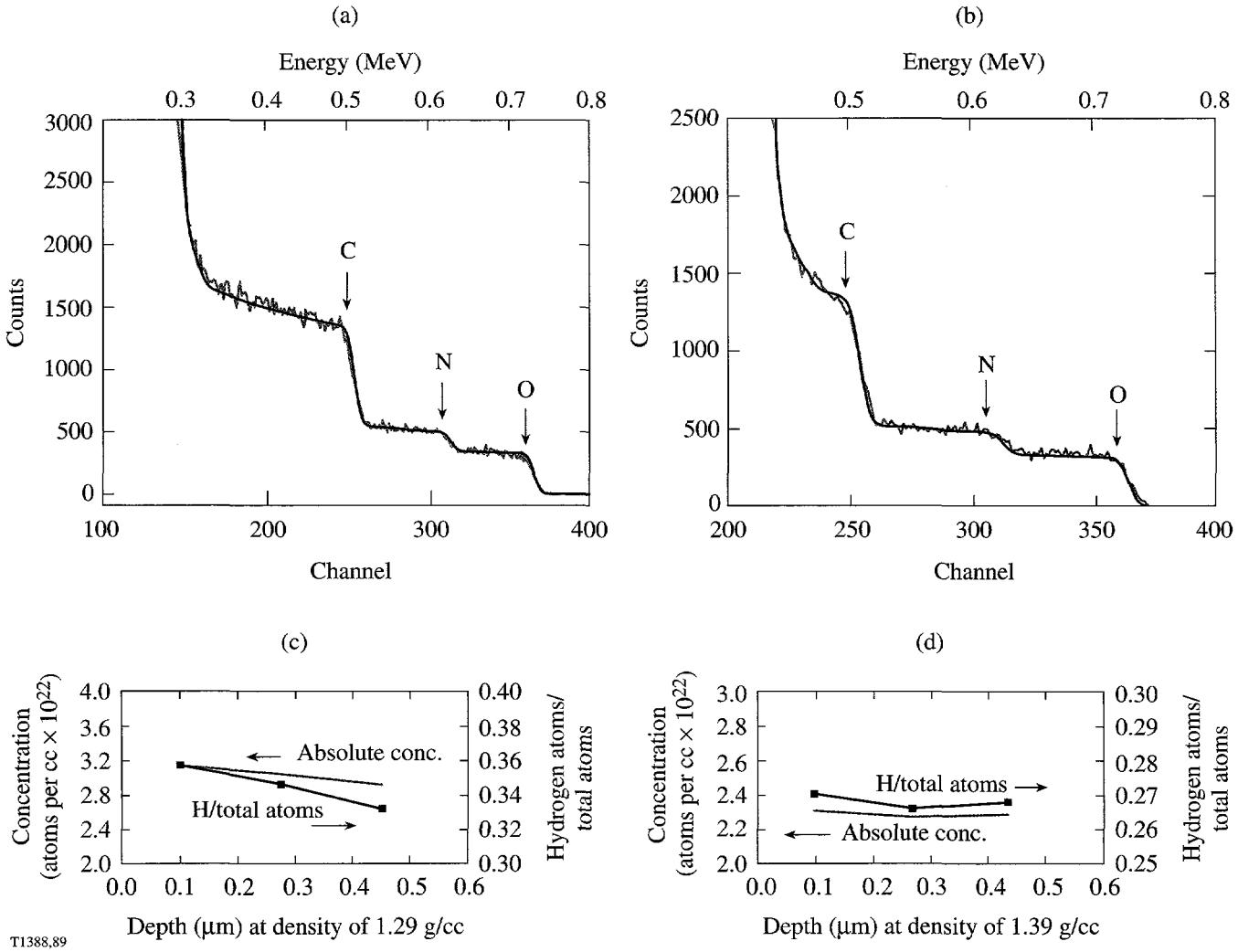

Figure 75.22

The experimental RBS spectra (with the simulated spectra overlaid) and NRA spectra of polyamic acid [(a) and (c)] and polyimide [(b) and (d)] films. The polyamic acid is 2.18 μm thick, consists of 47-at.% carbon, 35-at.% hydrogen, 7-at.% nitrogen, 11-at.% oxygen, and has a density of 1.28 g/cm^3. The polyimide film is 1.78 μm thick, consists of 55-at.% carbon, 26-at.% hydrogen, 7-at.% nitrogen, 12-at.% oxygen, and has a density of 1.44 g/cm^3.

polyamic acid and polyimide films was determined to be 1.29 ± 0.02 g/cm^2 and 1.44 ± 0.02 g/cm^2, respectively. The value of knowing these data is twofold: (1) the implosion dynamics can be more accurately modeled, and (2) significant changes in density and porosity can induce significant changes in the residual intrinsic stress that affects the survivability and ultimate strength of the material.

Summary

Two ion-beam techniques, Rutherford backscattering spectroscopy and nuclear resonance analysis of hydrogen, used in conjunction, provide an accurate method for analyzing the complete elemental composition of individual capsules. These data are used to interpret ICF data and to support the development of suitable targets. The strengths of these techniques are (1) they are absolute measurements that do not rely on external calibration to infer the composition of the substrate material, and (2) they provide depth-resolved information, essential data to confirm that the fabricated targets are what they were designed to be.

ACKNOWLEDGMENT

This work was supported by the U.S. Department of Energy Office of Inertial Confinement Fusion under Cooperative Agreement No. DE-FC03-92SF19460, the University of Rochester, and the New York State Energy Research and Development Authority. The support of DOE does not constitute an endorsement by DOE of the views expressed in this article.

REFERENCES

1. S. A. Letts, D. W. Myers, and L. A. Witt, J. Vac. Sci. Technol. **19**, 739 (1981).
2. N. Abbas, ICF Target Component Fabrication and Technology Development Support, FY96 Year-End Review, San Diego, CA (October 1996).
3. Internal Confinement Fusion Target Component Fabrication and Technology Development Support, General Atomic's Annual Report to the U.S. Department of Energy, 1 October 1996–30 September 1997.
4. A. Antolak, ICF Target Component Fabrication and Technology Development Support, FY97 Year-End Review, San Diego, CA (October 1997).
5. J. R. Tesmer and M. A. Nastasi, eds. *Handbook of Modern Ion Beam Materials Analysis* (Materials Research Society, Pittsburgh, PA, 1995).
6. P. Bodo and M. Schott, Thin Solid Films **286**, 98 (1996).
7. J. F. Ziegler, J. P. Biersack, and U. Littmark, *The Stopping and Range of Ions in Solids*, The Stopping and Ranges of Ions of Matter, Vol. 1 (Pergamon Press, New York, 1985).
8. L. R. Doolittle, Nucl. Instrum. Methods Phys. Res. B **B9**, 334 (1985).
9. D. D. Meyerhofer, presented at the 25th European Conference on Laser Interactions with Matter (25th ECLIM), Formia, Italy, 4–8 May 1998.
10. E. L. Alfonso, S.-H. Chen, R. Q. Gram, and D. R. Harding, "Properties of Polyimide Shells Made Using Vapor Phase Deposition," to be published in the Journal of Materials Research.
11. E. L. Alfonso, S.-H. Chen, R. Q. Gram, D. R. Harding, and F. Y. Tsai, "Fabrication of Polyimide Shells by Vapor Phase Deposition for Use as ICF Targets," presented at the Target Fabrication Meeting, Jackson Hole, WY, 19–23 April 1998, and to be published in Fusion Technology.

Kα Cold-Target Imaging and Preheat Measurement Using a Pinhole-Array X-Ray Spectrometer

Two-dimensional (2-D) monochromatic imaging of laser-imploded targets[1–6] is useful for diagnosing target compression and stability. Here we present a simple method for such imaging, using an array of about 300 pinholes placed in front of a flat-crystal x-ray spectrometer. The main advantage of this method (in addition to its simplicity) is the ability to simultaneously obtain a large number of images over a wide range of photon energies. This is particularly useful for imaging the emission region of a single spectral line from a doped target, where images around the wavelength of the line can be simultaneously obtained and subtracted from the image at the line. Imaging a spectral line of a dopant can be useful for studying mixing of target layers. *Here we use the array to image Kα fluorescence from a titanium-doped target (excited by core radiation) and thereby obtain an image of the cold layer at peak compression.* This image can otherwise be obtained only through backlighting. Using a flat crystal limits the field of view, but this limitation is shown not to be severe when imaging the compressed target core. On the other hand, the narrow field of view translates into improved spectral resolution. We show that sufficient intensity can be obtained in monochromatic imaging even without the gain in intensity when using a focusing crystal. In addition, the array provides spectra of high spectral resolution because of the reduction in the effective source size. Finally, we show that, in addition to the core-pumped Kα emission, a second Kα-emitting zone of a larger radius appears in the image. This Kα emission is pumped during the laser-irradiation pulse, indicating preheat by suprathermal electrons.

Figure 75.23 shows the geometry of the pinhole array placed in front of a crystal spectrometer. The dispersion direction indicated in Fig. 75.23 is determined by the orientation of the array with respect to the crystal. Rays from the target traversing different pinholes fall on the crystal at different angles; thus, different wavelengths are diffracted. The distance between adjacent pinholes (750 μm) is chosen so that adjacent images on the film are close but not overlapping. Rays from different parts of the target traversing the same pinhole also fall on the crystal at different angles; thus, the target image from continuum radiation is not monochromatic; rather, the photon energy across the image (in the dispersion direction) varies over a finite interval. A single spectral line will show the image of only a narrow section of the target (in the dispersion direction); however, the compressed core can be imaged by a spectral line of sufficient spectral width. In the direction of dispersion, the shift in the average photon energy between adjacent images is typically ~100 eV. The line of pinholes in a direction perpendicular to that of the crystal dispersion is slightly tilted, causing a small photon-energy shift (of the order of ~10 eV) between two adjacent images in that direction; thus, an array of 30 × 10 pinholes can produce 300 images with energies spread over the range of, say, 4 to 7 keV. The advantage due to the tilt in the vertical lines of pinholes can be viewed in two ways: (a) for a given target location, adjacent images correspond to slightly shifted photon energy, or (b) for a given spectral line, adjacent images correspond to slightly different sections of the target. The properties of array imaging,

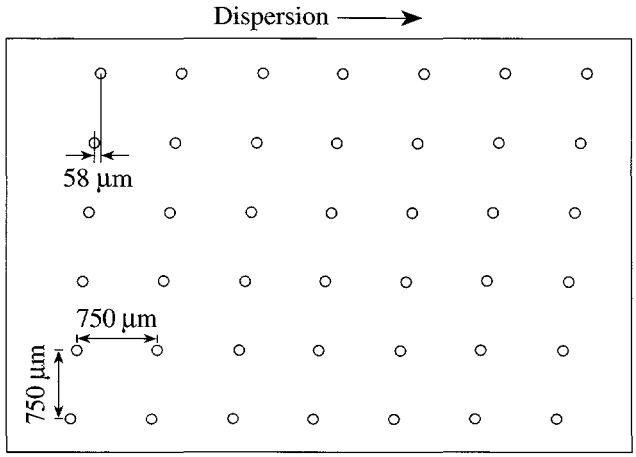

Figure 75.23
The geometry of the pinhole array placed in front of the spectrometer. Each of about 300 pinholes yields a narrow-band, 2-D image at a slightly shifted photon energy. The 58-μm shift due to the tilt in the vertical direction yields an energy shift between adjacent images of ~6 to 10 eV in the range of 4 to 5 keV.

in conjunction with the test results shown in Figs. 75.24 and 75.27, will be further discussed below.

Two arrays of the type shown in Fig. 75.23 were used to image targets imploded on the 60-beam OMEGA laser system.[7] In both cases, the target consisted of a polymer shell containing an embedded, titanium-doped layer. We show two examples of such tests: In the first shot (a) an array of 50-μm-diam pinholes (in 25-μm-thick Pt foil) was used, and the results are shown in Fig. 75.24 (this figure is used mostly to illustrate the properties of array imaging). In the second shot (b) an array of 25-μm-diam pinholes (in 12.5-μm-thick Pt foil) was used and the results are shown later in Fig. 75.27 (this figure is used mostly to illustrate the imaging of the cold, compressed shell through Kα-line fluorescence). Except for the pinhole size and foil thickness, the two arrays had the same geometry as in Fig. 75.23.

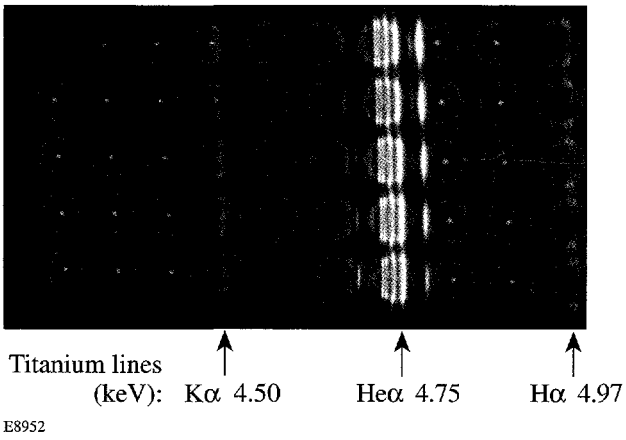

Figure 75.24
Part of the ~300 array-spectrometer images obtained with an array of 50-μm pinholes, from a titanium-coated target implosion [shot (a)]. Because of the vertical tilt in the array (see Fig. 75.23), the target section imaged by a given spectral line shifts for successive images in that direction. Lines (such as the Heα line) from a different target location can reappear on a neighboring image.

Properties of Array Imaging

In shot (a) a CH polymer shell of 867-μm inner diameter and 13.7-μm thickness was doped with titanium at 7% by atom number, overcoated by 13.9-μm-thick undoped CH. The fill gas was 10 atm deuterium. The laser pulse was a 1-ns flat pulse (to within ±5%) with 0.1-ns rise and fall times and 29.8 kJ of energy. Figure 75.24 shows part of the array images obtained with a Ge(111) diffracting crystal. The dispersion direction is horizontal—a tilt in the images in the vertical direction is evident. Both the Ti-Kα line and lines of Ti^{20+} (helium-like) and Ti^{21+} (hydrogen-like) ions are marked. The Ti^{20+} Heα line and its dielectronic satellites reappear on neighboring images. This is due to parallel rays emanating from different target locations and traversing adjacent pinholes. Without the array, these two groups of lines would be part of a broad spectral feature representing emission from the whole target. The array transmits rays from only two target slices.

Individual lines yield monochromatic images of only a section of the target (because rays from other target sections do not satisfy the Bragg diffraction condition for that line). On the other hand, the continuum radiation gives rise to complete target images; however, these images are not monochromatic—the photon energy shifts across the image in the direction of dispersion (by ~100 eV). The energy shift between adjacent images in the dispersion direction varies from ~80 eV (at 4 keV) to ~130 eV (at 5 keV). The tilt in the vertical direction causes a photon-energy shift between two adjacent images that varies from ~6 eV (at 4 keV) to ~10 eV (at 5 keV).

The narrow field of view for individual lines (in the direction of dispersion) can be remedied by replacing the flat crystal with a curved crystal in the Rowland-circle geometry;[2,3,5] however, Fig. 75.24 shows that typical lines can be spectrally wide enough for imaging the core even with a flat crystal. This is seen simply in the fact that the lines are about as broad as the target core (e.g., in the lowest image in the column marked "Kα"). The width of the lines in this context refers to their spectral width, transformed into a spatial width in the image. This transformation is obtained by differentiating the Bragg law for diffraction, from which the spatial extent Δx covered by a single spectral line of width ΔE (in the direction of dispersion) can be obtained. The result is $\Delta x = (\Delta E/E)L \tan \theta_B$, in terms of the Bragg angle θ_B and the target distance to the film (along the relevant ray). The spatial width of the Kα line in the direction of dispersion is ~130 μm. Part of it is due to the pinhole size (50 μm), but most of it is due to the spectral width of the Kα line (a larger pinhole size increases the field of view in the direction of dispersion but reduces the spatial resolution in both directions). Deconvolving the pinhole broadening from the total width shows that the spectral width of the line is ~5 eV and that the spatial width would be ~120 μm when using a very small pinhole. Thus, a flat crystal can yield 2-D Kα monochromatic images of only the core; however, there is no limitation on the field of view in the direction perpendicular to that of the dispersion. Furthermore, because the pinholes tilt in the vertical direction, the position of a given spectral line shifts across the target image for successive images in that direction, as is

clearly evident in Fig. 75.24; thus, the combination of successive images in the vertical direction delineates the total emission region of the line. This works particularly well for the Kα line since its linewidth (~5 eV) is about the same as the average energy shift between successive images in the vertical direction (~6 eV). In higher-performing implosions the shell temperature would be higher so that some *M*-shell electrons would be ionized; in that case, the Kα line would be broader due to the overlapping of shifted lines from various charge states, and the field of view would then broaden. Also, in such implosions the compressed core is smaller and would thus require a smaller field of view.

The Ti^{20+} and Ti^{21+} lines in Fig. 75.24 are seen to be emitted from the target periphery, i.e., the hot laser-absorption region. On the other hand, the Kα line is emitted by the cold part of the Ti-doped layer following the photoionization of *K*-shell electrons. The source of this radiation can be either the coronal emission during the laser irradiation or the core radiation during peak compression. The Kα line emission in Fig. 75.24 is seen to come from a layer inside the hot corona region: the diameter of the coronal rings is ~900 μm, whereas the length of the Kα emission region perpendicular to the dispersion direction is only ~750 μm, and it peaks near its extremities. Thus, the radiation from the laser-heated corona pumps the fluorescence of Kα in the cold shell underneath the coronal region. An additional peak can be seen at the target center, indicating the possible Kα emission pumped by core radiation. This point is discussed in more detail in the next section, where the results of shot (b) clearly indicate Kα fluorescence pumped primarily by core radiation.

An important advantage of this device is the ability to reliably subtract the continuum images off a spectral line from the image on the line, thus obtaining the image of the region emitting that line. This is further discussed in conjunction with Fig. 75.27, where the cold shell is imaged through its Kα fluorescence. Additionally, the core spectrum can be easily separated from the coronal emission and plotted over a wide spectral range with good spectral resolution. Additional useful information in Fig. 75.24 is the absence of target cores in the spectral range of ~4.5 to 4.7 keV and above ~4.9 keV due to absorption of core radiation in the cold titanium layer. This absorption is due to titanium $1s$–$2p$ absorption lines and absorption above the Ti *K* edge, respectively.[8]

The array spectrometer can be alternatively used for achieving high spectral resolution: in the case of a large emitting source (such as emission prior to peak compression) the pinholes limit the effective source size and thus improve spectral resolution. For example, the fine-structure splitting of the Hα line of titanium is clearly seen in Fig. 75.24, indicating a resolution higher than 500. Without the pinhole array the whole target would radiate the line and the spectral resolution would be less than 100. In Fig. 75.25 the lineout in the direction of dispersion shows that a high-resolution spectrum can be obtained from a large source for lines that are much stronger than the continuum. In that case, the images formed by the continuum can be subtracted and the net line emission obtained. In general, the lineout can be recorded as a function of target position (perpendicular to the direction of dispersion). To facilitate the continuum-image subtraction, the lineout in Fig. 75.25 was chosen to avoid the core emissions. To further illustrate the high spectral resolution, we compare (in Fig. 75.26) part of the spectrum of Fig. 75.25 with that obtained simultaneously by an identical spectrometer where the pinhole array has been replaced by a 50-μm-wide slit. In the latter spectrum, the lines are considerably broadened due to the source size (~0.8 mm). They are further affected by the spatial distribution of target emission; because of the limb effect, the spectral lines appear on film as partly overlapping rings, giving rise to spurious splits in the spectrum. An 0.8-mm source size corresponds in the present arrangement without the array to a spectral resolution $E/\Delta E$ of ~130, whereas the pinhole-array spectrum in Fig. 75.26 shows a spectral resolution $E/\Delta E$ higher than ~500.

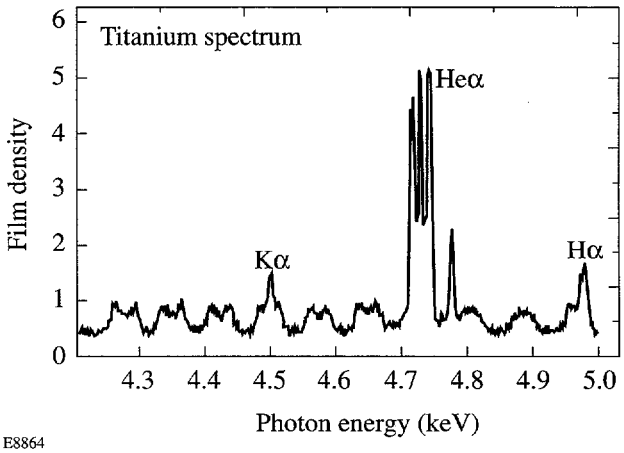

Figure 75.25
Lineout of Fig. 75.24 in the direction of dispersion (avoiding the cores), showing that a high-resolution spectrum from a large source can be obtained by using a pinhole-array spectrometer. For lines that are much stronger than the continuum, the images (that are due to the continuum) can be subtracted away. The line at ~4.8 keV is the Ti Heα line (from a different target location) transmitted though an adjacent pinhole.

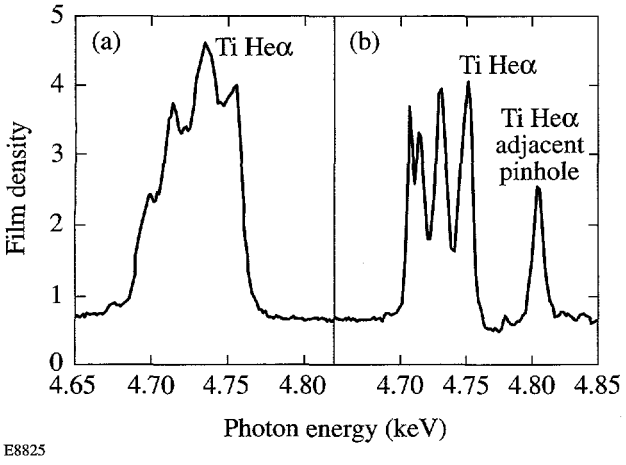

Figure 75.26
Comparison of the Ti Heα line manifold obtained simultaneously with and without the pinhole array. The Heα line ($2p^1P$–$1s$ transition in Ti^{20+}) is well resolved from its low-energy satellites when using the array. Without the array the lines are considerably broadened by the ~0.8-mm source size.

Imaging the Cold Shell with Kα Fluorescence

In shot (b), an empty CD polymer shell of 898-μm inner diameter and 5.9-μm thickness was coated with an 11.7-μm-thick layer of CH doped with titanium at 2% by atom number, overcoated by 13.5-μm-thick undoped CH. The laser pulse shape was the same as in shot (a), and its energy was 27.1 kJ.

Figure 75.27 shows part of the array images from target shot (b) obtained with a PET(002) diffracting crystal. The laser-irradiation uniformity in this shot was deficient, leading to a nonuniform implosion. We chose to display a section of the array images where the Kα line image is centered on the target core (second image from left). For images above and below this image the Kα line moves off target center toward the left and right, respectively. The Ti^{20+} lines (indicative of hot plasma) are seen to be emitted from the periphery of the target. On the other hand, a ring of emission at the wavelength of the Ti Kα line (indicative of a cold plasma) is seen to be emitted around the compressed core. This is evident when comparing the emission around the core in the second image from left to that in the other images. The nonsphericity of the Kα emission pattern is discussed below. The spatial features of these lines indicate that the Ti Heα line is emitted during the laser-irradiation time, whereas the Kα line is emitted around peak compression and is pumped by core radiation. These conclusions are consistent with the streaked spectra obtained for shot (b). Figure 75.28 shows lineouts of streaked spectra at three different times of the implosion: t_1– during the laser-irradiation period (lasting about ~1 ns); t_2–during the shell coasting when no radiation is emitted (lasting about 0.8 ns); and t_3–during peak compression, or stagnation (lasting about 0.2 ns). It is clearly seen that the Ti^{20+} Heα line is emitted during the laser irradiation; more precisely, the streak record shows that it is emitted toward the end of the laser pulse, when the burnthrough of the polymer overcoat has reached the doped layer. On the other hand, the Kα line is emitted during peak compression. This is entirely consistent with the conclusions drawn from the spatial patterns of these lines. In addition to the Kα line, the spectrum at peak compression also shows strong absorption above the Ti K edge. This is absorption of core radiation by the cold shell around the core and is precisely the source of photoionization leading to Kα fluorescence;[9] this observation provides an additional indication that the Kα line is pumped by core radiation at peak compression. The drop of intensity above the K edge can be used to estimate the areal density ($\rho\Delta r$) of the doped layer at peak compression and from here the total $\rho\Delta r$ of the compressed shell. It should be pointed out that there is very little change in the K-shell absorption at a given energy when M- or L-shell electrons are ionized.[10] In this case, however, the transmitted intensity above the K edge is too weak to determine the areal density, and only a lower limit of the $\rho\Delta r$ can be obtained. Assuming transmission of less than ~10% at the K edge, the areal density of the doped layer is $\rho\Delta r > 22$ mg/cm^2. The total areal density of the compressed shell (that includes the undoped mandrel) can be estimated[8] as $\rho\Delta r > 32(\pm 6)$ mg/cm^2.

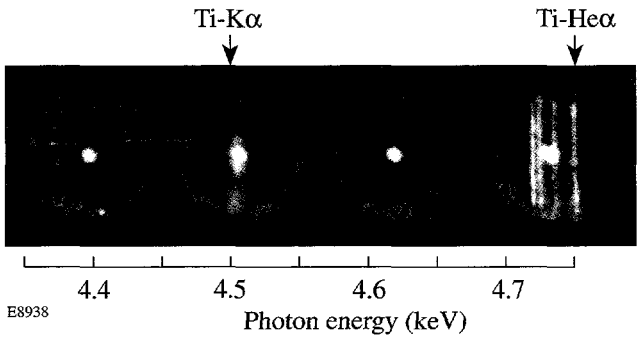

Figure 75.27
Part of the array images from target shot (b). The Ti^{20+} lines are seen to be emitted from the periphery of the target. On the other hand, a ring of emission at the wavelength of Ti Kα line is seen to be emitted around the compressed core. The Kα line is excited by core radiation, and its image delineates the cold shell at peak compression (see Fig. 75.28).

Figure 75.27 indicates that the Kα linewidth is insufficient for imaging the full extent of the cold shell in the dispersion direction. Since no limitation of field of view applies to the perpendicular direction, the Kα image is elliptically shaped. The vertical profile of the Kα emission shows the true dimension of the cold shell. By combining successive images in the vertical direction, we can obtain at least a qualitative view of the 2-D image of the cold shell. As mentioned above, in future high-performance implosions a single image may be sufficient for obtaining the 2-D image of the cold shell.

Using vertical lineouts in Fig. 75.27 we can obtain the dimensions of the cold shell in that direction. Figure 75.29(a) shows two such lineouts: (a) through the center of the second image from the left ("on Kα") and (b) an average of lineouts through the centers of the neighboring images on each side ("off Kα"). The peaks of the two profiles varied by about 10% (possibly due to fluctuations in pinhole sizes) and were normalized to the same height. The difference between these two curves [shown in Fig. 75.29(b)] delineates a ring-shaped layer of cold Ti-doped shell. Changing the relative intensity of the two profiles in Fig. 75.29(a) within the 10% uncertainty changes mostly the central minimum in Fig. 75.29(b), but not the overall shape and dimensions of the intensity ring. Alternative off-Kα profiles could be chosen by moving above and below the Kα image in Fig. 75.27 (sufficiently for the Kα emission to disappear); however, the closeness of peak intensity of the two profiles in Fig. 75.29(a) indicates that the choice adopted here is adequate. The nonuniformity of the implosion seen in the images of Fig. 75.27 is also evident in Fig. 75.29(b). Figure 75.29(a) also shows Kα emission at a ~300-μm radius. This delineates the position of the cold shell during the laser pulse, when it is pumped by radiation and suprathermal electrons from the laser-heated material; this is further discussed in the following section. Figure 75.29(a) shows higher Kα intensity around +300 μm than around −300 μm, again indicating nonuniformity. This nonuniformity mirrors the nonuniformity during peak compression: the peak of the Kα profile around +80 μm is higher than the peak around −80 μm. This is surely the result of the irradiation nonuniformity as evident in Fig. 75.27: The coronal emission in the four

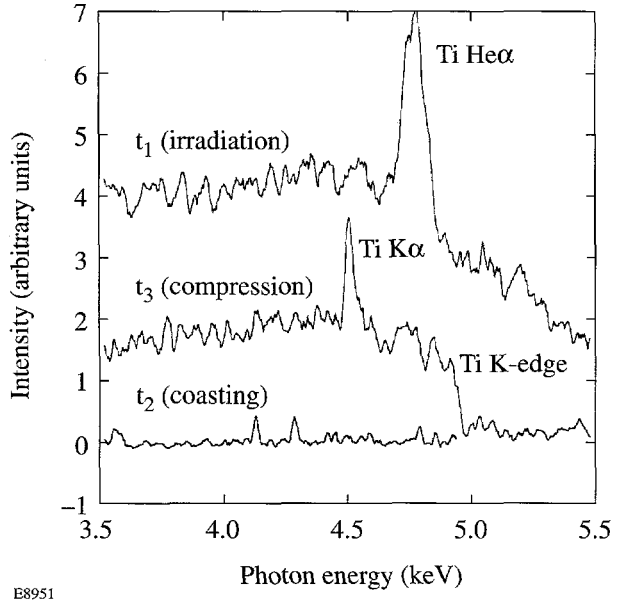

Figure 75.28
Spectra recorded by a streaked spectrograph at three times during the implosion of shot (b). The Ti^{20+} line emission occurs during the laser-pulse irradiation, t_1, whereas the *K*-edge absorption and the concomitant Kα line emission occur about ~1 ns after the end of the laser pulse, at the time of peak compression, t_3; t_2 is a time during the intervening coasting. These results confirm the conclusions from Fig. 75.27. Positive axis direction corresponds to downward direction in Fig. 75.27.

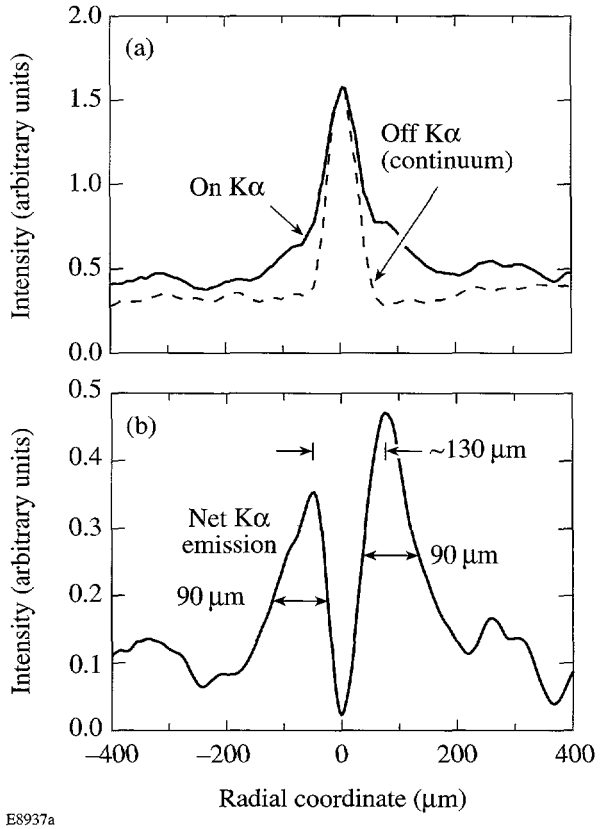

Figure 75.29
(a) Lineouts through images of Fig. 75.27, in the vertical direction (perpendicular to the direction of dispersion). The "on Kα" curve is through the center of the second image from the left; the "off Kα" curve is an average of lineouts through the centers of the two neighboring images on each side. (b) The difference between the two curves in (a) delineates the cold Ti-doped shell.

images is more intense on the lower half of the target, corresponding to a higher intensity of Kα (the positive axis in Figs. 75.29 and 75.30 corresponds to the downward direction in Fig. 75.27). Figure 75.29(b) indicates, for the cold shell, a ring of ~90-μm thickness and an average diameter of ~130 μm. In a previous experiment,[9] the Kα from a similar Ti-doped target was imaged in one dimension using a slit in front of a flat-crystal spectrometer. With one-dimensional (1-D) imaging, a ring-shaped source results in a flat-topped profile, and only the outer diameter of the ring can be reliably determined. The FWHM of the Kα profile in Ref. 9 (~250 μm) is similar to the FWHM in Fig. 75.29(b); however, the array yields an actual image of the ring of Kα emission (the profiles in Fig. 75.29 are slices through a 2-D image rather than 1-D images). The Kα emission profile and the *K*-edge absorption relate to the same target region, namely, the cold doped layer; thus, the ring thickness from Fig. 75.29(b) and the areal density derived from the *K*-edge absorption can be used to estimate the shell density. As noted above, the ablated part of the doped layer emits the Heα line of titanium, whereas the unablated doped layer emits the Kα line. The thickness of the doped layer (~90 μm) found in Fig. 75.29(b) is larger than the actual thickness at peak compression because of the time integration. Also, the areal density estimated above was only a lower limit; thus, a lower limit for the density of the doped layer can be obtained by dividing the estimated $\rho\Delta r$ of that layer (22 mg/cm^2) by its thickness (~90 μm) to yield $\rho > 2$ g/cm^3. This low density (albeit only a lower limit) is to be expected in view of the deficient symmetry of the laser irradiation in this experiment. A better determination of the shell density can be obtained by (a) lowering the level of doping to avoid complete *K*-edge absorption and (b) time-gating the spectrometer to avoid smearing due to time integration.

Preheat Measurement Using Early Kα Emission

In addition to Kα emission excited by core radiation at peak compression, Kα radiation is also emitted during the laser-irradiation pulse. The latter emission can be seen in Fig. 75.27 (second image from the left) and in Fig. 75.29 as a weak ring of emission at a radius of ~300 μm. To better understand the origin of this emission, we simulate the transport through the target of radiation giving rise to Kα emission, both the primary (or pumping) radiation and the secondary (or fluorescent) Kα radiation. We use profiles of target parameters calculated by the one-dimensional code *LILAC* to compute the transport of radiation of photon energy above the Ti *K*-edge, flowing radially outward and inward. The radiation is derived from the OPLIB astrophysical opacity tables[11] using the LTE approximation. To calculate the pumping of Kα fluorescence we must know the component of the total opacity (given by the tables) that is related to photoionization of *K*-shell electrons. At the *K* edge, this component is easily found from the *K*-edge jump in the opacity tables; for all higher photon energies we make use of its known dependence on photon energy. Finally, the Kα emission is transported along straight cords in the direction of observation, and the resulting profile is convolved with the instrumental broadening function (due to the pinhole's finite size).

Figure 75.30 compares the resulting Kα profile with the measured profile (from Fig. 75.29), normalized to the simulated profile. Two ring-shaped Kα emission zones are seen: an intense ring at a radius of ~80 μm and a weaker ring at a radius of ~300 μm. In the experiment (Fig. 75.27), only sections of each ring are observed (along the vertical axis) because the crystal limits the field of view in the direction of dispersion. The simulations show that the strong, inner ring is emitted around peak compression and is pumped by outgoing core radiation; on the other hand, the weak, outer ring is emitted during the laser-irradiation pulse and is pumped by ingoing coronal radiation. The nonuniformity in the measured image (higher intensity at positive radial distances) was discussed above. Figure 75.30 shows that the position of the cold shell during the laser pulse and during peak compression is in rough agreement with one-dimensional code predictions, in spite of the marked nonuniformity. It should be noted, however, that the inner, undoped shell is not detected by the Kα emission;

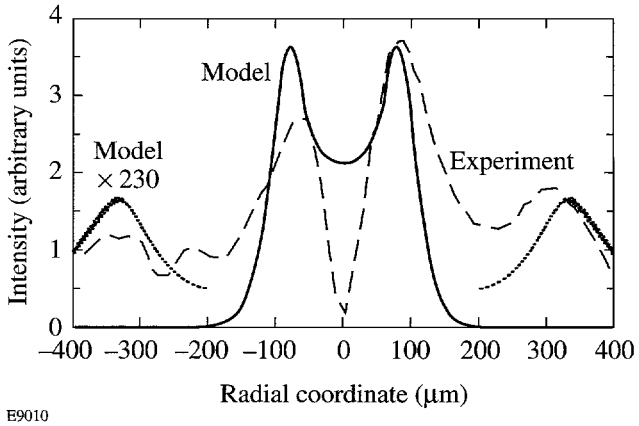

Figure 75.30
Measured and simulated radial profile of Kα emission for target shot (b). The inner ring of ~80-μm radius marks the position of the cold shell around the time of peak compression and is pumped by core radiation. The outer ring of ~300-μm radius marks the position of the shell during the laser pulse and is pumped by coronal radiation. The simulation includes only radiation transport, and the required multiplication by a factor of 230 shows that the outer ring is pumped by suprathermal electrons rather than by radiation.

the behavior of that segment of the shell is most indicative of target performance.

Whereas the position of the outer Kα emission ring is quite well predicted by the code, its intensity is not: we must multiply its calculated intensity by ~230 to match the experiment. The only obvious explanation is that the outer ring of Kα emission is mostly excited not by radiation but by suprathermal electrons, which are not included in the simulations. This question can be asked: How does the assumption of LTE in the radiation-transport calculations affect these conclusions? First, the LTE assumption affects mostly the intensity of the emission rings rather than their position. Second, departures from LTE would be more severe in the outer ring (of lower density) and would reduce the radiation available for pumping. Thus, the outer Kα ring would be even weaker with respect to the inner Kα ring than with the LTE calculations.

We now estimate the total preheat energy E_{ph} deposited in the target, based on the energy $E_{K\alpha}$ of electron-excited Kα emission. The total Kα energy of the outer ring, measured by a spatially integrating spectrometer, is $E_{K\alpha}$ ~10 mJ. For suprathermal-electron temperatures T_h above ~10 keV the ratio $R = E_{ph}/E_{K\alpha}$ tends to a constant independent of T_h. For medium-Z elements this constant is ~170;[12] thus, the preheat energy deposited in the titanium part of the shell is ~10 mJ × 170 = 1.7 J. To estimate the total preheat of the Ti-doped shell we note that the deposition rate for electrons in CH (over a very wide electron energy range) is ~10 times higher than that in Ti at 2% concentration;[13] thus, the preheat energy deposited in the doped shell is ~17 J. Since about half of the unablated shell is doped, this brings the total preheat energy to ~34 J. This estimate of preheat energy is independent of T_h; it only assumes that T_h is well above ~10 keV. The suprathermal electrons surmised from the Kα emission can give rise to fast (or suprathermal) ions. In fact, total fast-ion energies of the order of 10 J (and ion energies >> 10 keV) have been measured by the charged-particle spectrometer on similar OMEGA target shots; thus, the two measurements are consistent.

In conclusion, a simple imaging method for laser-fusion experiments has been demonstrated. Placing a multi-pinhole array in front of a flat-crystal spectrometer yields monochromatic, two-dimensional images with an ~100- to 150-μm field of view, sufficient for imaging cores of highly compressed targets. Images of the whole target are also obtained, with an ~100-eV bandwidth of the continuum. The method was applied to imaging the Kα fluorescence, shown to be excited by the core radiation at peak compression. This latter method yields the image of the cold shell at peak compression without using backlighting. Sufficient intensity has been shown to be obtained with 25-μm pinholes and a flat, nonfocusing diffracting crystal. Additionally, high spectral resolution was shown to be obtained with the array. This is particularly useful when measuring lines from the laser-interaction region, where the size of the target limits the spectral resolution to ~100, whereas with the array, the resolution can be five times higher. Finally, preheat in the amount of ~40 J was deduced from Kα emission during the laser pulse, which appears as an outer ring of ~300-μm radius.

ACKNOWLEDGMENT

This work was supported by the U.S. Department of Energy (DOE) Office of Inertial Confinement Fusion under Cooperative Agreement No. DE-FC03-92SF19460, the University of Rochester, and the New York State Energy Research and Development Authority. The support of DOE does not constitute an endorsement by DOE of the views expressed in this article.

REFERENCES

1. C. L. S. Lewis and J. McGlinchey, Opt. Commun. **53**, 179 (1985).
2. J.-C. Kieffer *et al.*, Appl. Opt. **28**, 4333 (1989).
3. C. Brown *et al.*, Rev. Sci. Instrum. **68**, 1099 (1997).
4. F. J. Marshall and J. A. Oertel, Rev. Sci. Instrum. **68**, 735 (1997).
5. M. Vollbrecht *et al.*, J. Quant. Spectrosc. Radiat. Transf. **58**, 965 (1997).
6. H. Azechi *et al.*, Appl. Phys. Lett. **37**, 998 (1980).
7. T. R. Boehly, R. S. Craxton, T. H. Hinterman, J. H. Kelly, T. J. Kessler, S. A. Kumpan, S. A. Letzring, R. L. McCrory, S. F. B. Morse, W. Seka, S. Skupsky, J. M. Soures, and C. P. Verdon, Rev. Sci. Instrum. **66**, 508 (1995).
8. B. Yaakobi, F. J. Marshall, D. K. Bradley, J. A. Delettrez, R. S. Craxton, and R. Epstein, Phys. Plasmas **4**, 3021 (1997).
9. B. Yaakobi and F. J. Marshall, J. Quant. Spectrosc. Radiat. Transfer **61**, in press.
10. D. J. Botto, J. McEnnan, and R. H. Pratt, Phys. Rev. A **18**, 580 (1978).
11. M. F. Argo and W. F. Huebner, J. Quant. Spectrosc. Radiat. Transfer **16**, 1091 (1976).
12. B. Yaakobi, J. Delettrez, L. M. Goldman, R. L. McCrory, W. Seka, and J. M. Soures, Opt. Commun. **41**, 355 (1982).
13. G. Knop and W. Paul, in *Alpha-, Beta- and Gamma-Ray Spectroscopy*, 1st ed., edited by K. Siegbahn (North-Holland, Amsterdam, 1965), Vol. 1, p. 12; L. V. Spencer, *Energy Dissipation by Fast Electrons*, National Bureau of Standards, Monograph 1 (U.S. Government Printing Office, Washington, DC, 1959).

Forward and Backward Stimulated Brillouin Scattering of Crossed Laser Beams

Stimulated Brillouin scattering (SBS) in a plasma is the decay of an incident (pump) light wave into a frequency-downshifted (Stokes) light wave and an ion-acoustic (sound) wave.[1] It is important in direct[2] and indirect[3] inertial confinement fusion (ICF) experiments because it scatters the laser beams away from the target, thereby reducing the energy available to drive the compressive heating of the nuclear fuel.

The SBS of an isolated beam has been studied in detail. Backward SBS was studied in numerous early papers, and near-forward, sideward, and near-backward SBS were studied in some recent papers.[4–8] Because beams overlap in the coronal plasma surrounding the nuclear fuel, it is also important to analyze SBS (and other parametric instabilities) driven by two (or more) crossed beams. For some scattering angles the SBS geometries allow the pump waves to share daughter waves.[9–11] Because the growth of these daughter waves is driven by two pump waves (rather than one), the growth rates associated with these scattering angles are higher than the growth rates associated with other scattering angles. Such is the case for forward and backward SBS, in which the Stokes wave vectors bisect the angle between the pump wave vectors.

The outline of this article is as follows: (1) We derive the equations governing forward and backward SBS. (2) We solve the linearized equations governing the transient phase of the instability. These equations differ from the linearized equations governing the SBS of an isolated beam[7] because the forward and backward SBS of crossed beams each involve one Stokes wave and two sound waves (rather than one). (3) We solve the nonlinear equations governing the steady state of the instability. These equations describe the nonlinear competition between forward and backward SBS. (4) We discuss the entire evolution of forward and backward SBS. Finally, (5) we summarize the main results of the article.

In the Appendix we show that, in steady state, the equations governing the simultaneous near-forward and near-backward SBS of an isolated beam are equivalent to the equations governing the simultaneous forward and backward SBS of crossed beams; thus, many results of this article also apply to the SBS of an isolated beam.

Governing Equations

The SBS of crossed beams is governed by the Maxwell wave equation[1]

$$\left(\partial_{tt}^2 + \omega_e^2 - c^2\nabla^2\right)A_h = -\omega_e^2 n_l A_h \qquad (1)$$

for the electromagnetic potential, together with the sound-wave equation[1]

$$\left(\partial_{tt}^2 + c_s^2 - \nabla^2\right)n_l = \frac{1}{2}c_s^2\nabla^2\left\langle A_h^2\right\rangle. \qquad (2)$$

The electromagnetic potential $A_h = \left(v_h/c_s\right)\left(m_e/m_i\right)^{1/2}$ is the quiver speed of electrons in the high-frequency electric field divided by a characteristic speed that is of the order of the electron thermal speed; n_l is the low-frequency electron density fluctuation associated with the sound wave divided by the background electron density; and the $\langle\ \rangle$ signify that only the low-frequency response to the ponderomotive force was retained.

The geometry associated with forward SBS is shown in Fig. 75.31(a). The forward SBS of beam 1 is subject to matching conditions of the form

$$\omega_1 = \omega_f + \omega_{s1}, \quad \mathbf{k}_1 = \mathbf{k}_f + \mathbf{k}_{s1}, \qquad (3)$$

where $(\omega_1, \mathbf{k}_1)$ and $(\omega_f, \mathbf{k}_f)$ satisfy the light-wave dispersion equation $\omega^2 = \omega_e^2 + c^2k^2$, and $(\omega_{s1}, \mathbf{k}_{s1})$ satisfies the sound-wave dispersion equation $\omega^2 = c_s^2k^2$. Similar matching conditions apply to the forward SBS of beam 2. Because the sound frequencies depend on the magnitudes of the sound-wave vectors, but not on their directions, $\omega_{s2} = \omega_{s1} = \omega_s$.

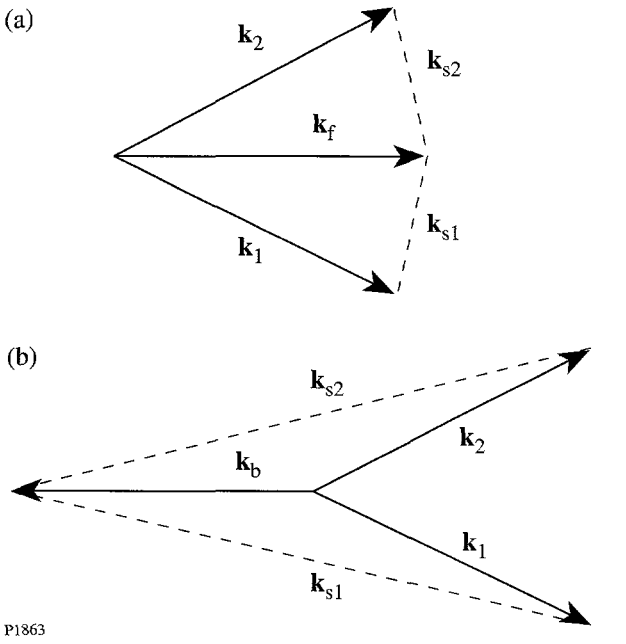

Figure 75.31
Geometry associated with the SBS of crossed laser beams: (a) forward SBS; (b) backward SBS.

By substituting the Ansätze

$$A_h = \left[A_1 \exp\left(i\mathbf{k}_1 \cdot \mathbf{x} - i\omega_0 t\right) + A_2 \exp\left(i\mathbf{k}_2 \cdot \mathbf{x} - i\omega_0 t\right) + A_f \exp\left(i\mathbf{k}_f \cdot \mathbf{x} - i\omega_f t\right)\right] + c.c. \quad (4)$$

and

$$n_l = N_1 \exp\left(i\mathbf{k}_{s1} \cdot \mathbf{x} - i\omega_s t\right) + N_2 \exp\left(i\mathbf{k}_{s2} \cdot \mathbf{x} - i\omega_s t\right) + c.c. \quad (5)$$

in Eqs. (1) and (2), one can show that

$$\partial_z A_f = i\left(\omega_e^2 / 2\omega_0 v_0\right)\left(A_1 N_1^* + A_2 N_2^*\right), \quad (6)$$

$$\left(\partial_t + \nu_{s1}\right) N_1^* = -i\left(\omega_s^2 / 2\omega_s\right) A_1^* A_f + \nu_{s1} n^*, \quad (7)$$

$$\left(\partial_t + \nu_{s2}\right) N_2^* = -i\left(\omega_s^2 / 2\omega_s\right) A_2^* A_f + \nu_{s2} n^*. \quad (8)$$

Because $\omega_s << \omega_0$, we made the approximation in Eq. (6) that the frequency and group speed of the scattered light wave equal the frequency and group speed v_0 of the pump waves, respectively. In Eqs. (7) and (8) $\nu_{s1} N_1^*$ and $\nu_{s2} N_2^*$ are phenomenological terms that model the Landau damping of the sound waves,[12] and $\nu_{s1} n^*$ and $\nu_{s2} n^*$ are phenomenological terms that maintain the density fluctuations associated with the sound waves at their common noise level n^* in the absence of instability. Because the Landau-damping rates depend on the magnitudes of the sound-wave vectors, but not on their direction, $\nu_{s2} = \nu_{s1} = \nu_s$.

Equations (6)–(8) describe the initial (transient) evolution of SBS. In steady state,

$$d_z A_f = \mu_f \left(\left|A_1\right|^2 + \left|A_2\right|^2\right) A_f, \quad (9)$$

where

$$\mu_f = \omega_e^2 \omega_s^2 / 4\omega_0 \omega_s \nu_s v_0. \quad (10)$$

Apart from a factor of $|A_1|^2$ or $|A_2|^2$, μ_f is the spatial growth rate of forward SBS in the strongly damped regime.[7] The forward-scattered intensity $F = |A_f|^2$ satisfies the equation

$$d_z F = 2\mu_f \left(P_1 + P_2\right) F, \quad (11)$$

where $P_1 = |A_1|^2$ and $P_2 = |A_2|^2$ are the pump intensities.

The geometry associated with backward SBS is shown in Fig. 75.31(b). The backward SBS of beam 1 is subject to matching conditions of the form

$$\omega_1 = \omega_b + \omega_{s1}, \quad \mathbf{k}_1 = \mathbf{k}_b + \mathbf{k}_{s1}, \quad (12)$$

where $(\omega_1, \mathbf{k}_1)$ and $(\omega_b, \mathbf{k}_b)$ satisfy the light-wave dispersion equation, and $(\omega_{s1}, \mathbf{k}_{s1})$ satisfies the sound-wave dispersion equation. Similar matching conditions apply to the backward SBS of beam 2: as in forward SBS, $\omega_{s2} = \omega_{s1} = \omega_s$.

By adding to Ansatz (4) the term

$$A_b \exp\left(i\mathbf{k}_b \cdot \mathbf{x} - i\omega_b t\right) + c.c. \quad (13)$$

and to Ansatz (5) the terms

$$N_1 \exp\left(i\mathbf{k}_{s1} \cdot \mathbf{x} - i\omega_s t\right) + N_2 \exp\left(i\mathbf{k}_{s2} \cdot \mathbf{x} - i\omega_s t\right) + c.c. \quad (14)$$

associated with backward SBS, one can show that

$$-\partial_z A_b = i\left(\omega_e^2/2\omega_0 v_0\right)\left(A_1 N_1^* + A_2 N_2^*\right), \quad (15)$$

$$\left(\partial_t + \nu_{s1}\right)N_1^* = -i\left(\omega_s^2/2\omega_s\right)A_1^* A_b + \nu_{s1} n^*, \quad (16)$$

$$\left(\partial_t + \nu_{s2}\right)N_2^* = -i\left(\omega_s^2/2\omega_s\right)A_2^* A_b + \nu_{s2} n^*. \quad (17)$$

As in forward SBS, $\nu_{s2} = \nu_{s1} = \nu_s$. In its transient (linear) phase, backward SBS is independent of forward SBS.

In steady state, the backward-scattered intensity $B = |A_b|^2$ satisfies the equation

$$-d_z B = 2\mu_b\left(P_1 + P_2\right)B, \quad (18)$$

where μ_b is given by Eq. (10) and the values of ω_s and ν_s associated with backward SBS. Apart from a factor of $|A_1|^2$ or $|A_2|^2$, μ_b is the spatial growth rate of backward SBS in the strongly damped regime.[7]

In the high-gain regime, the intensities of the scattered light waves as they exit the plasma are comparable to the intensities of the pump waves as they enter the plasma, and one must account for the depletion of the pump waves within the plasma. In steady state, the pump intensities satisfy the equations

$$d_z P_1 = -2\mu_f F P_1 - 2\mu_b B P_1, \quad (19)$$

$$d_z P_2 = -2\mu_f F P_2 - 2\mu_b B P_2, \quad (20)$$

where we made the approximation that the evolution of the pump waves is one dimensional. One can verify Eqs. (19) and (20) by applying the principle of power conservation to Eqs. (11) and (18).

Linear Analysis of the Transient Phase

The forward SBS of crossed beams consists of two mirror-image processes that share the same Stokes wave and, hence, are governed by the coupled equations (6)–(8). By making the substitutions $\omega_0^{1/2} A_f \to A_f$, $i\omega_e N_1^*/\omega_s^{1/2} \to N_1$, $i\omega_e N_2^*/\omega_s^{1/2} \to N_2$, $i\omega_e n^*/\omega_s^{1/2} \to n$, and $z/v_0 \to z$, one can rewrite these equations as

$$\partial_z A_f = \gamma_{f1} N_1 + \gamma_{f2} N_2, \quad (21)$$

$$\left(\partial_t + \nu_s\right)N_1 = \gamma_{f1} A_f + \nu_s n, \quad (22)$$

$$\left(\partial_t + \nu_s\right)N_2 = \gamma_{f2} A_f + \nu_s n, \quad (23)$$

where

$$\gamma_{f1} = \omega_e \omega_s |A_1|/2(\omega_0 \omega_s)^{1/2}, \quad (24)$$

$$\gamma_{f2} = \omega_e \omega_s |A_2|/2(\omega_0 \omega_s)^{1/2}. \quad (25)$$

A_f is proportional to the action amplitude of the Stokes wave, and N_1 and N_2 are proportional to the action amplitudes of the sound waves. In the absence of damping, γ_{f1} and γ_{f2} are the temporal growth rates of the forward SBS of beams 1 and 2, respectively, in an infinite plasma.

By using the combined amplitudes

$$N_+ = \left(\gamma_{f1} N_1 + \gamma_{f2} N_2\right)/\gamma_f, \quad (26)$$

$$N_- = \gamma_f\left(N_1/\gamma_{f1} - N_2/\gamma_{f2}\right), \quad (27)$$

where $\gamma_f = \left(\gamma_{f1}^2 + \gamma_{f2}^2\right)^{1/2}$, one can rewrite Eqs. (21)–(23) as

$$\partial_z A_f = \gamma_f N_+, \quad (28)$$

$$\left(\partial_t + \nu_s\right)N_+ = \gamma_f A_f + \nu_s n_+, \quad (29)$$

$$\left(\partial_t + \nu_s\right)N_- = \nu_s n_-, \quad (30)$$

where $n_+ = n\left(\gamma_{f1} + \gamma_{f2}\right)/\gamma_f$ and $n_- = n\gamma_f\left(1/\gamma_{f1} - 1/\gamma_{f2}\right)$. Equations (28) and (29) are equivalent to the equations governing the forward SBS of an isolated beam,[7] and Eq. (30) is simple. Consequently, the solutions of Eqs. (28)–(30) can be written in the form

$$A_f(z,t) = \int_0^t \int_0^z \nu_s n_+ G_f(z - z', t - t')\,dz'\,dt', \quad (31)$$

$$N_+(z,t) = \int_0^t \int_0^z \nu_s n_+ G_+(z - z', t - t')\,dz'\,dt', \quad (32)$$

$$N_-(z,t) = \int_0^t \int_0^z \nu_s n_- G_-(z - z', t - t')\,dz'\,dt', \quad (33)$$

where the Green functions

$$G_f(z,t) = \gamma_f I_0\left[2\gamma_f (zt)^{1/2}\right] \exp(-\nu_s t), \tag{34}$$

$$G_+(z,t) = \gamma_f (t/z)^{1/2} I_1\left[2\gamma_f (zt)^{1/2}\right] \times \exp(-\nu_s t) + \delta(z) \exp(-\nu_s t), \tag{35}$$

$$G_-(z,t) = \delta(z) \exp(-\nu_s t). \tag{36}$$

In Eqs. (34) and (35), I_m is the modified Bessel function of the first kind, of order m. The original amplitudes N_1 and N_2 are determined by Eqs. (32) and (33) and the inversion equations

$$N_1 = (\gamma_{f1}/\gamma_f)\left[N_+ + (\gamma_{f2}^2/\gamma_f^2)N_-\right], \tag{37}$$

$$N_2 = (\gamma_{f2}/\gamma_f)\left[N_+ - (\gamma_{f1}^2/\gamma_f^2)N_-\right]. \tag{38}$$

Solutions (31)–(33) describe the growth and dissipative saturation of forward SBS. By analyzing the time dependence of the Green functions, one can show that the saturation time

$$t_s \sim \gamma_f^2 z/\nu_s^2. \tag{39}$$

The steady-state limits of solutions (31)–(33) are

$$A_f(z,\infty) = (n_+\nu_s/\gamma_f)\left[\exp(\gamma_f^2 z/\nu_s) - 1\right], \tag{40}$$

$$N_+(z,\infty) = n_+ \exp(\gamma_f^2 z/\nu_s), \tag{41}$$

$$N_-(z,\infty) = n_-. \tag{42}$$

Notice that $\gamma_f^2/\nu_s v_0 = \mu_f(|A_1|^2 + |A_2|^2)$, in agreement with Eq. (9). If the interaction length exceeds a few gain lengths, one can model Stokes generation as Stokes amplification with an incident amplitude $A_f(0) = (n_+\nu_s/\gamma_f)$.

The backward SBS of crossed beams also consists of two mirror-image processes that share a Stokes wave and are governed by Eqs. (21)–(25), with f replaced by b and z replaced by l–z; thus, Eqs. (26)–(42), and the conclusions drawn from them, also apply to backward SBS. Equations (21)–(23) apply to other parametric instabilities driven by crossed pump waves, provided that one type of daughter wave is strongly damped.

Nonlinear Analysis of the Steady State

The simultaneous forward and backward SBS of crossed beams is governed by Eqs. (11) and (18)–(20). By making the substitution $P_1 + P_2 \rightarrow P$, one can rewrite these equations as

$$d_z F = 2\mu_f PF, \tag{43}$$

$$-d_z B = 2\mu_b PF, \tag{44}$$

$$d_z P = -2(\mu_f F + \mu_b B)P. \tag{45}$$

Equations (43)–(45) apply to other simultaneous parametric instabilities driven by crossed pump waves, provided that one type of daughter wave is strongly damped. For SBS, $\mu_b = \mu_f = \mu$,[7] and one can use the substitution $2\mu z \rightarrow z$ to rewrite Eqs. (43)–(45) in the simple form

$$d_z F = PF, \tag{46}$$

$$-d_z B = PB, \tag{47}$$

$$d_z P = -(F + B)P. \tag{48}$$

The substitutions $F/P(0) \rightarrow F$, $B/P(0) \rightarrow B$, $P/P(0) \rightarrow P$, and $P(0)z \rightarrow z$ nondimensionalize Eqs. (46)–(48) but leave them unchanged in form. Because the solutions of Eqs. (46)–(48) are complicated, it is instructive to review the limiting solutions that apply to forward and backward SBS separately.

1. Forward SBS

In the absence of backward SBS, Eqs. (46)–(48) reduce to

$$d_z F = PF, \tag{49}$$

$$d_z P = -FP. \tag{50}$$

It follows from these equations that

$$P + F = 1 + N_f, \tag{51}$$

where $N_f = F(0)$ is incident (noise) intensity of the forward-scattered wave. Since $P \geq 0$, it follows from Eq. (51) that

$$S_f \le 1 + N_f , \tag{52}$$

where $S_f = F(l)$ is the output (signal) intensity of the forward-scattered wave and l is the gain length of forward SBS. Equation (52) reflects the fact that the signal intensity cannot exceed the total input intensity.

By substituting Eq. (51) in Eq. (49), one can show that

$$(1 + N_f)z = \log\left[\frac{F}{N_f(1 + N_f - F)}\right]. \tag{53}$$

Equation (53) determines the interaction distance z required to produce the forward-scattered intensity F. By inverting this equation, one finds that

$$F(\zeta) = \frac{N_f(1 + N_f)}{N_f + \exp(-\zeta)}, \tag{54}$$

where $\zeta = (1 + N_f)z$. Solution (54) is consistent with Eq. (52).

The normalized intensities of the pump and Stokes waves in a semi-infinite plasma are plotted as functions of the gain distance z in Fig. 75.32, for the case in which $N_f = 10^{-6}$. As the Stokes intensity increases, the pump intensity decreases, in accordance with Eq. (51). For future reference, notice that the initial growth of the Stokes wave from noise is driven by an undepleted pump wave.

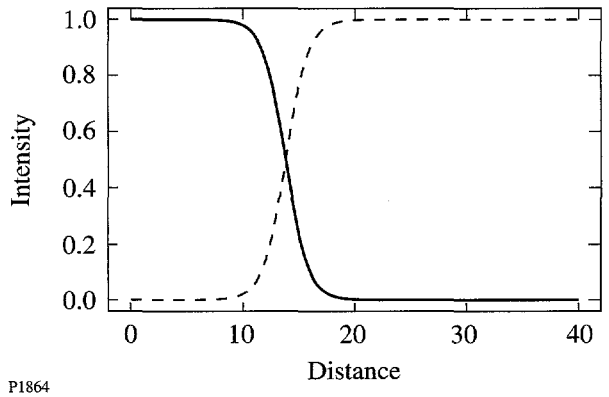

Figure 75.32
Normalized intensities plotted as functions of the gain distance for forward SBS in a semi-infinite plasma. The solid line represents the pump wave; the dashed line represents the Stokes wave. For forward SBS the output intensities from a finite plasma depend on the plasma length in the same way that the intensities within a semi-infinite plasma depend on the distance from the plasma boundary.

2. Backward SBS

In the absence of forward SBS, Eqs. (46)–(48) reduce to

$$-d_z B = PB, \tag{55}$$

$$d_z P = -BP. \tag{56}$$

It follows from these equations that

$$P - B = 1 - S_b , \tag{57}$$

where $S_b = B(0)$ is the output (signal) intensity of the backward-scattered wave. Since $P \ge 0$, it follows from Eq. (57) that

$$S_b \le 1 + N_b , \tag{58}$$

where $N_b = B(l)$ is the incident (noise) intensity of the backward-scattered wave and l is the gain length of backward SBS. Equation (58) reflects the fact that the signal intensity cannot exceed the total input intensity.

By substituting Eq. (57) in Eq. (55), one can show that

$$(1 - S_b)z = \log\left[S_b(1 - S_b + B)/B\right]. \tag{59}$$

The signal intensity is determined by Eq. (59) and the condition $B(l) = N_b$. By inverting Eq. (59), with S_b known, one finds that

$$B(\zeta) = \frac{S_b(1 - S_b)}{\exp(\zeta) - S_b}, \tag{60}$$

where $\zeta = (1 - S_b)z$. Solution (60), which was first obtained by Tang,[13] is consistent with Eq. (58).

The normalized output intensity of the Stokes wave is plotted as a function of the gain length l in Fig. 75.33(a), for the case in which $N_b = 10^{-6}$. The normalized intensities of the pump and Stokes waves within the plasma are plotted as functions of the gain distance z in Fig. 75.33(b), for the case in which $N_b = 10^{-6}$ and $l = 30$. Because the pump and Stokes waves propagate in opposite directions, the initial growth of the Stokes wave from noise is driven by a depleted pump wave [Fig. 75.33(b)]. Consequently, when pump depletion is important ($l > 10$), the rate at which the Stokes output intensity increases with gain length is slower for backward SBS [Fig. 75.33(a)] than for forward SBS (Fig. 75.32). Backward SBS scatters the pump power less efficiently than forward SBS.

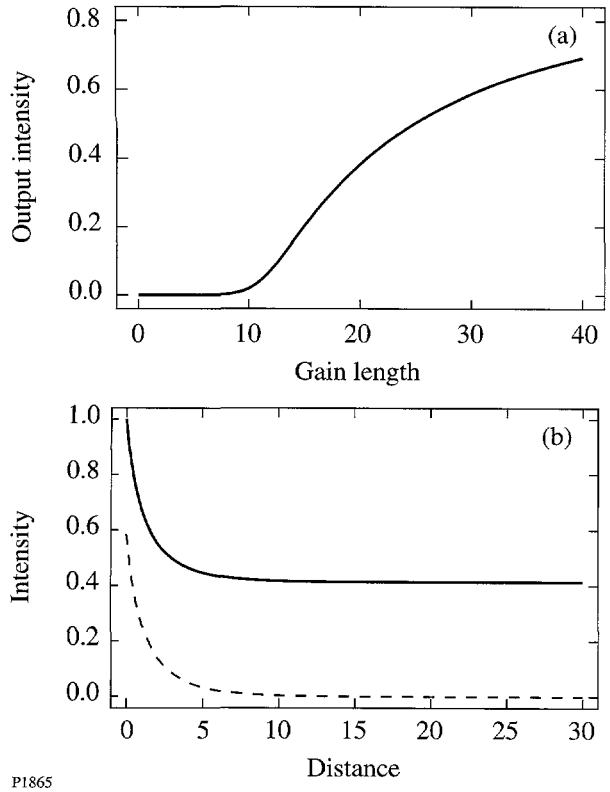

Figure 75.33
(a) Normalized output intensity of the Stokes wave plotted as a function of the gain length l for backward SBS. (b) Normalized intensities within the plasma plotted as functions of the gain distance for $l = 30$. The solid line represents the pump wave; the dashed line represents the Stokes wave.

3. Simultaneous Forward and Backward SBS

When forward and backward SBS occur simultaneously, it follows from Eqs. (46)–(48) that

$$P + F - B = 1 + N_f - S_b \tag{61}$$

and

$$FB = N_f S_b . \tag{62}$$

Equation (61) is a generalization of equations that apply to the forward and backward instabilities separately, whereas Eq. (62) is peculiar to the combined instability. Since $P \geq 0$, it follows from Eq. (61) that

$$S_f + S_b \leq 1 + N_f + N_b . \tag{63}$$

Equation (63) reflects the fact that the total signal intensity cannot exceed the total input intensity. It follows from Eqs. (62) and (63) that

$$S_f \leq N_f + \frac{N_f}{N_f + N_b}, \tag{64}$$

$$S_b \leq N_b + \frac{N_b}{N_f + N_b}. \tag{65}$$

By substituting Eqs. (61) and (62) in Eq. (46), one can show that

$$d_z F = (R_+ - F)(R_- + F), \tag{66}$$

where

$$\pm 2R_\pm = 1 + N_f - S_b \pm \left[(1 + N_f - S_b)^2 + 4N_f S_b\right]^{1/2}. \tag{67}$$

It follows from Eq. (66) that

$$(R_+ + R_-)z = \log\left[\frac{(R_+ - N_f)(R_- + F)}{(R_+ - F)(R_- + N_f)}\right]. \tag{68}$$

S_b is determined by Eq. (68) and the condition $B(l) = N_b$, which is equivalent to the condition $F(l) = (N_f / N_b) S_b$. By inverting Eq. (68), with S_b known, one finds that

$$F(\zeta) = \frac{R_+(R_- + N_f)\exp(\zeta) - R_-(R_+ - N_f)}{(R_- + N_f)\exp(\zeta) + (R_+ - N_f)}, \tag{69}$$

where $\zeta = (R_+ + R_-)z$. Solution (69) is consistent with Eq. (64). For the common case in which $1 - S_b >> N_f$, one can use the approximate roots

$$R_+ \approx 1 - S_b + N_f / (1 - S_b), \tag{70}$$

$$R_- \approx N_f S_b / (1 - S_b), \tag{71}$$

to rewrite Eqs. (68) and (69) as

$$(1 - S_b)z \approx \log\left\{\frac{(1 - S_b)\left[N_f S_b + (1 - S_b)F\right]}{(1 - S_b - F)N_f}\right\} \tag{72}$$

and

$$F(\zeta) \approx \frac{N_f (1 - S_b)\left[\exp(\zeta) - S_b\right]}{N_f \exp(\zeta) + (1 - S_b)^2}, \tag{73}$$

respectively, where $\zeta \approx (1 - S_b)z$.

The normalized (total) output intensity of the (forward and backward) Stokes waves is plotted as a function of the gain length l in Fig. 75.34(a), for the case in which $N_b = N_f = 10^{-6}$. When pump depletion is unimportant ($l < 10$), the Stokes output intensity of the combined instability is the sum of the Stokes output intensities of the forward and backward instabilities. The normalized intensities of the pump and Stokes waves within the plasma are plotted as functions of the gain distance z in Fig. 75.34(b) for the case in which $N_b = N_f = 10^{-6}$ and $l = 30$. The initial growth of both Stokes waves from noise is driven by a depleted pump wave. Consequently, when pump depletion is important ($l > 10$), the rate at which the Stokes output intensity increases with gain length is slower for the combined instability than for the forward instability [Fig. 75.34(a)].

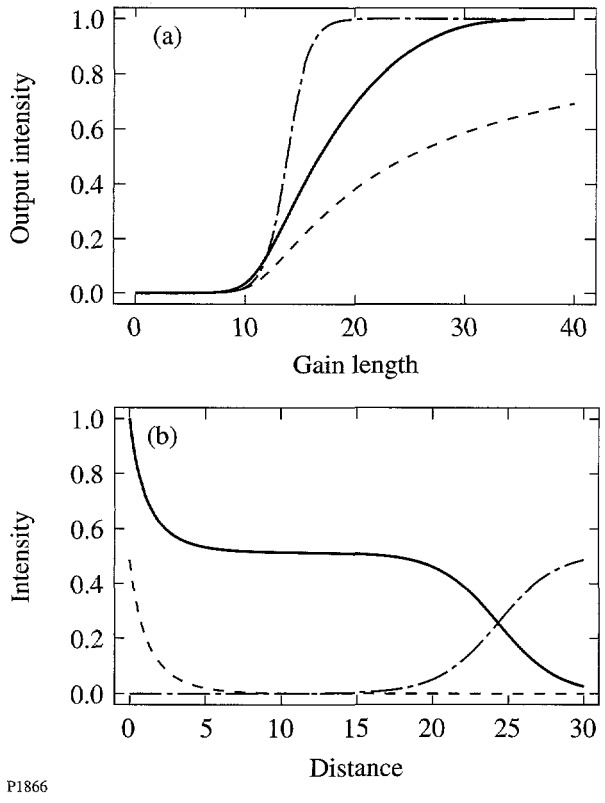

Figure 75.34
(a) Normalized output intensities plotted as functions of SBS gain length l. The forward and backward noise intensities are equal. The solid line represents the total output intensity for the combined instability. For comparison, the dot–dashed and dashed lines represent the output intensities when forward and backward SBS occur separately [Figs. 75.32 and 75.33(a), respectively]. (b) Normalized intensities within the plasma plotted as functions of the gain distance for $l = 30$. The solid line represents the pump wave, the dot–dashed line represents the forward Stokes wave, and the dashed line represents the backward Stokes wave.

In Figs. 75.32–75.34, the noise intensities for forward and backward SBS were equal. This choice made possible a fair comparison of the intrinsic scattering efficiencies of the two instabilities. The noise intensity for forward SBS is larger, however, than the noise intensity for backward SBS because the action sources that generate the light waves [Eq. (40) for forward SBS and its analog for backward SBS] are inversely proportional to the sound frequencies.[14] To illustrate how this imbalance affects the combined instability, the normalized output intensity of the Stokes waves is plotted as a function of the gain length in Fig. 75.35(a) for the case in which $N_f = 10^{-16}$ and $N_b = 10^{-7}$. The normalized intensities of the pump and Stokes waves within the plasma are plotted as functions of the gain distance in Fig. 75.35(b) for the case in which $N_f = 10^{-6}$, $N_b = 10^{-7}$, and $l = 30$. It is clear from the figures that forward SBS overwhelms backward SBS in steady state.

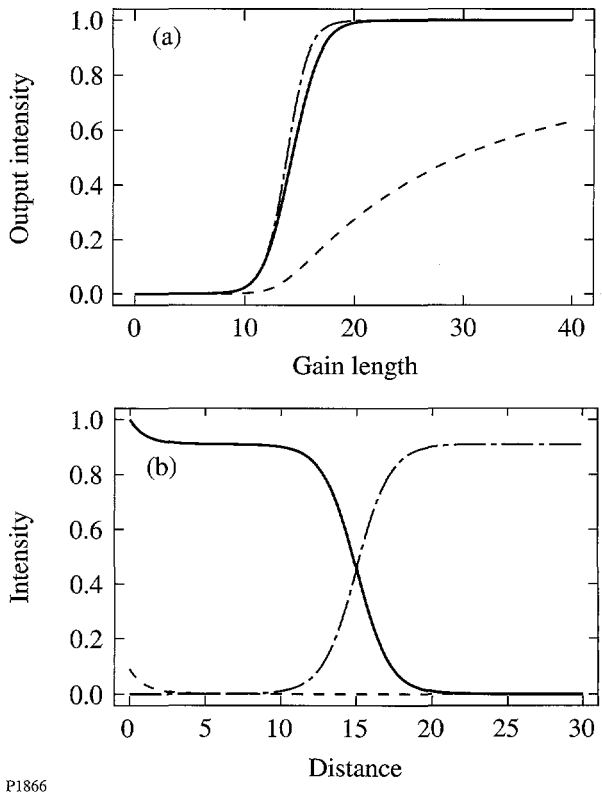

Figure 75.35
(a) Normalized output intensities plotted as functions of SBS gain length l. The forward noise intensity exceeds the backward noise intensity by a factor of 10. The solid line represents the total output intensity for the combined instability. For comparison, the dot–dashed and dashed lines represent the output intensities when forward and backward SBS occur separately. (b) Normalized intensities within the plasma plotted as functions of the gain distance for $l = 30$. The solid line represents the pump wave, the dot–dashed line represents the forward Stokes wave, and the dashed line represents the backward Stokes wave.

Discussion

Initially, pump depletion is unimportant, and forward and backward SBS grow independently. This (linear) spatiotemporal growth is described by Eqs. (28)–(30). Since the growth rate $\gamma_f \propto (\sin\phi)^{1/2}$ [Eqs. (24) and (25)], the sound-wave damping rate $\nu_s \propto \sin\phi$, and the saturation time $t_s \propto 1/(\sin\phi)$ [Eq. (39)], where 2ϕ is the scattering angle, backward SBS grows and saturates more quickly than forward SBS.[7] The steady-state (nonlinear) spatial evolution of backward SBS is described by Eqs. (57) and (60). In the high-gain regime, backward SBS depletes the pump wave significantly [Fig. 75.33(b)]; thus, the spatiotemporal growth of forward SBS is driven by a pump wave whose intensity varies with distance, and Eqs. (31)–(36) do not apply as written. By making the substitutions $N_\pm/\gamma_f \to N_\pm$, $n_\pm/\gamma_f \to n_\pm$, and $\int_0^z [\gamma_f(z')]^2 dz' \to z$ in Eqs. (28)–(30), however, one can show that

$$\partial_z A_f = N_+ , \tag{74}$$

$$(\partial_t + \nu_s) N_+ = A_f + \nu_s n_+ , \tag{75}$$

$$(\partial_t + \nu_s) N_- = \nu_s n_- . \tag{76}$$

Since Eqs. (74)–(76) contain no variable coefficients, their solution can be inferred from Eqs. (31)–(36). It follows that the (linear) saturation time of forward SBS is given by Eq. (39), with $\gamma^2 z$ replaced by $\int_0^z [\gamma_f(z')]^2 dz'$. Since the saturation time is proportional to the (integrated) gain distance, the reduction of the gain distance by pump depletion shortens the saturation time of forward SBS. Since the steady-state (nonlinear) Eqs. (46)–(48) have a unique solution, the spatial evolution of the combined instability is given by Eqs. (61), (62), and (69), even though forward and backward SBS grow at different rates and saturate at different times. It is clear from Figs. 75.34 and 75.35 that the output intensity of the backward Stokes wave is lower in the presence of the forward Stokes wave than in its absence; thus, the combined instability is characterized by a burst of backward SBS followed by the ascendance of forward SBS.

The major theme of the **Nonlinear Analysis of the Steady State** section and the preceding discussion is that forward and backward SBS coexist and compete for the pump energy. One should remember that several other processes also coexist and modify this competition. These processes include double SBS,[9] which is made possible by a sound wave whose wave vector is the sum of the pump-wave vectors, and the transfer of energy between the pump waves[15–21] and the Bragg scattering of the pump waves,[16] both of which are made possible by a sound wave whose wave vector is the difference of the pump-wave vectors; thus, the interaction physics is even richer than the physics discussed herein.

Summary

In this article we studied in detail the simultaneous forward and backward SBS of crossed laser beams. We obtained new analytical solutions for the linearized equations governing the transient phase of the instability [Eqs. (21)–(23)] and the nonlinear equations governing the steady state [Eqs. (46)–(48)]. In their transient phases, forward and backward SBS grow independently. Initially, backward SBS grows more quickly than forward SBS. As the backward Stokes wave grows, it depletes the pump wave and modifies the growth of the forward Stokes wave. In steady state, forward SBS dominates the combined instability because the forward Stokes wave has a larger noise intensity from which to grow and forward SBS scatters the pump power more efficiently.

In the Appendix we show that the equations governing the simultaneous near-forward and near-backward SBS of an isolated beam are equivalent to the equations governing the simultaneous forward and backward SBS of crossed beams; thus, the results of this article also apply to the SBS of an isolated beam.

ACKNOWLEDGMENT

This work was supported by the National Science Foundation under contract No. PHY-9415583, the U.S. Department of Energy Office of Inertial Confinement Fusion under Cooperative Agreement No. DE-FC03-92SF19460, the University of Rochester, and the New York State Energy Research and Development Authority. The support of DOE does not constitute an endorsement by DOE of the views expressed in this article.

Appendix A: Forward and Backward SBS of an Isolated Laser Beam

In this appendix we show that the equations governing the simultaneous forward and backward SBS of an isolated beam are equivalent to the equations governing the simultaneous forward and backward SBS of crossed beams. The geometry associated with the forward SBS of an isolated beam is shown in Fig. 75.36(a). Each forward-scattering process is subject to matching conditions of the form

$$\omega_0 = \omega_f + \omega_s , \quad \mathbf{k}_0 = \mathbf{k}_f + \mathbf{k}_s , \tag{A1}$$

where $(\omega_0, \mathbf{k}_0)$ and $(\omega_f, \mathbf{k}_f)$ satisfy the light-wave dispersion equation $\omega^2 = \omega_e^2 + c^2 k^2$, and $(\omega_s, \mathbf{k}_s)$ satisfies the sound-

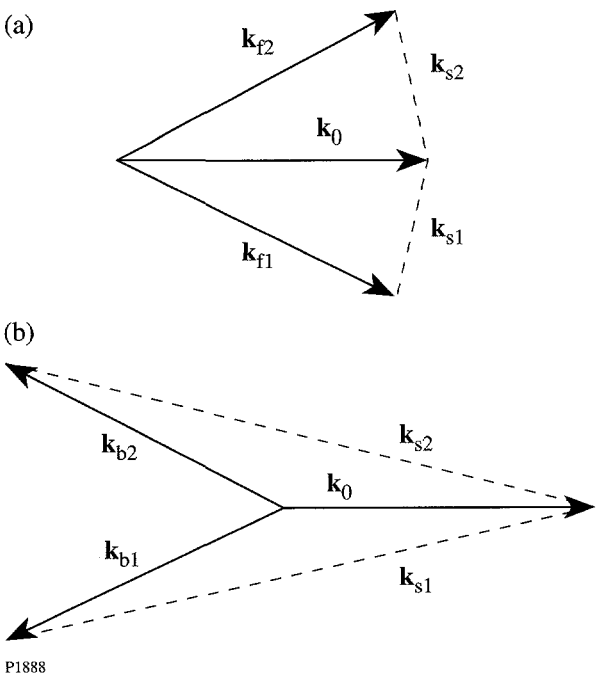

Figure 75.36
Geometry associated with the SBS of an isolated laser beam: (a) near-forward SBS; (b) near-backward SBS.

wave dispersion equation $\omega^2 = c_s^2 k^2$. Because the frequencies of the daughter waves depend on the magnitude of their wave vectors, but not on their directions, $\omega_{f2} = \omega_{f1} = \omega_f$ and $\omega_{s2} = \omega_{s1} = \omega_s$.

By substituting the Ansätze

$$A_h = \left[A_0 \exp\left(i\mathbf{k}_0 \cdot \mathbf{x} - i\omega_0 t\right) + A_{f1} \exp\left(i\mathbf{k}_{f1} \cdot \mathbf{x} - i\omega_f t\right) + A_{f2} \exp\left(i\mathbf{k}_{f2} \cdot \mathbf{x} - i\omega_f t\right)\right] + c.c. \quad \text{(A2)}$$

and

$$n_l = N_1 \exp\left(i\mathbf{k}_{s1} \cdot \mathbf{x} - i\omega_s t\right) + N_2 \exp\left(i\mathbf{k}_{s2} \cdot \mathbf{x} - i\omega_s t\right) + c.c. \quad \text{(A3)}$$

into Eqs. (1) and (2), and making the slowly varying envelope approximation, one can show that each forward-scattering process is governed by equations of the form

$$\partial_z A_f = i\left(\omega_e^2 / 2\omega_0 v_0\right) A_0 N^*, \quad \text{(A4)}$$

$$\left(\partial_t + \nu_s\right) N^* = -i\left(\omega_s^2 / 2\omega_s\right) A_0^* A_f + \nu_s n^*. \quad \text{(A5)}$$

In Eq. (A5), $\nu_s N^*$ is a phenomenological term that models the Landau damping of the sound wave, and $\nu_s n^*$ is a phenomenological term that maintains the density fluctuations associated with the sound wave at their noise level n^* in the absence of instability. Because the Landau-damping rates depend on the magnitudes of the sound-wave vectors, but not on their directions, $\nu_{s2} = \nu_{s1} = \nu_s$. By making the substitutions $\omega_0^{1/2} A_f \to A_f$, $i\omega_e N^* / \omega_s^{1/2} \to N$, $i\omega_e n^* / \omega_s^{1/2} \to n$, and $z/v_0 \to z$, one can rewrite Eqs. (A4) and (A5) as

$$\partial_z A_f = \gamma_f N, \quad \text{(A6)}$$

$$\left(\partial_t + \nu_s\right) N = \gamma_f A_f + \nu_s n, \quad \text{(A7)}$$

where

$$\gamma_f = \omega_e \omega_s |A_0| / 2\left(\omega_0 \omega_s\right)^{1/2}. \quad \text{(A8)}$$

Equations (A6) and (A7) are equivalent to Eqs. (28) and (29), the solution of which was described in the text.

Equations (A4) and (A5) describe the transient evolution of forward SBS. In steady state,

$$d_z A_f = \mu_f |A_0|^2 A_f, \quad \text{(A9)}$$

where

$$\mu_f = \omega_e^2 \omega_s^2 / 4\omega_0 \omega_s \nu_s v_0. \quad \text{(A10)}$$

Notice that $\mu_f |A_0|^2 = \gamma_f^2 / \nu_s v_0$ is in agreement with Eqs. (A6)–(A8). It follows from Eq. (A9) that the forward-scattered intensities $F_1 = |A_{f1}|^2$ and $F_2 = |A_{f2}|^2$ satisfy the equations

$$d_z F_1 = 2\mu_f P F_1, \quad \text{(A11)}$$

$$d_z F_2 = 2\mu_f P F_2, \quad \text{(A12)}$$

where $P = |A_0|^2$ is the pump intensity.

The geometry associated with the backward SBS of an isolated beam is shown in Fig. 75.36(b). Each backward-

scattering process is subject to matching conditions of the form

$$\omega_0 = \omega_b + \omega_s, \quad \mathbf{k}_0 = \mathbf{k}_b + \mathbf{k}_s, \tag{A13}$$

where $(\omega_0, \mathbf{k}_0)$ and $(\omega_b, \mathbf{k}_b)$ satisfy the light-wave dispersion equation, and $(\omega_s, \mathbf{k}_s)$ satisfies the sound-wave dispersion equation. As in forward SBS, $\omega_{b2} = \omega_{b1} = \omega_b$ and $\omega_{s2} = \omega_{s1} = \omega_s$.

By adding to Ansatz (A2) the terms

$$A_{b1}\exp\left(i\mathbf{k}_{b1}\cdot\mathbf{x} - i\omega_b t\right) + A_{b2}\exp\left(i\mathbf{k}_{b2}\cdot\mathbf{x} - i\omega_b t\right) + c.c. \tag{A14}$$

and to Ansatz (A3) the terms

$$N_1\exp\left(i\mathbf{k}_{s1}\cdot\mathbf{x} - i\omega_s t\right) + N_2\exp\left(i\mathbf{k}_{s2}\cdot\mathbf{x} - i\omega_s t\right) + c.c. \tag{A15}$$

associated with backward SBS, one can show that each backward-scattering process is governed by equations of the form

$$-\partial_z A_b = i\left(\omega_e^2/2\omega_0 v_0\right)A_0 N^*, \tag{A16}$$

$$\left(\partial_t + \nu_s\right)N^* = -i\left(\omega_s^2/2\omega_s\right)A_0^* A_b + \nu_s n^*. \tag{A17}$$

As in forward SBS, $\nu_{s2} = \nu_{s1} = \nu_s$. It follows from Eqs. (A16) and (A17) that the transient evolution of backward SBS is governed by Eqs. (A6)–(A8), with f replaced by b and z replaced by l–z. Equations (A6) and (A7) apply to other parametric instabilities driven by an isolated pump wave provided that one type of daughter wave is strongly damped. In steady state, the backward-scattered intensities $B_1 = |A_{b1}|^2$ and $B_2 = |A_{b2}|^2$ satisfy the equations

$$-d_z B_1 = 2\mu_b P B_1, \tag{A18}$$

$$-d_z B_2 = 2\mu_b P B_2, \tag{A19}$$

where μ_b is given by Eq. (A10), with f replaced by b.

In the high-gain regime, the intensities of the scattered waves as they exit the plasma are comparable to the intensity of the pump wave as it enters the plasma, and one must account for the depletion of the pump wave within the plasma. In steady state, the pump intensity satisfies the equation

$$d_z P = -2\mu_f\left(F_1 + F_2\right) - 2\mu_b\left(B_1 + B_2\right). \tag{A20}$$

By making the substitutions $F = F_1 + F_2$ and $B = B_1 + B_2$ in Eqs. (A11), (A12), (A18), (A19), and (A20), one can show that the simultaneous forward and backward SBS of an isolated beam is governed by the equations

$$d_z F = 2\mu_f P F, \tag{A21}$$

$$-d_z B = 2\mu_b P B, \tag{A22}$$

$$d_z P = -2\left(\mu_f F + \mu_b B\right)P. \tag{A23}$$

Equations (A21)–(A23) are equivalent to Eqs. (43)–(45), the solution of which was described in the text. It is clear from the derivation of Eqs. (A21)–(A23) that one can interpret F as the intensity scattered forward over the entire range of angles for which propagation in the z direction is a reasonable approximation, and one can interpret B as the intensity scattered backward over the entire range of angles for which propagation in the $-z$ direction is a reasonable approximation. Equations (A21)–(A23) apply to other parametric instabilities driven by an isolated pump wave, provided that one type of daughter wave is strongly damped. For SBS, $\mu_b = \mu_f = \mu$,[7] and one can use the substitution $2\mu z \rightarrow z$ to rewrite Eqs. (A21)–(A23) in the form of Eqs. (46)–(48).

REFERENCES

1. W. L. Kruer, *The Physics of Laser Plasma Interactions*, Frontiers in Physics, Vol. 73, edited by D. Pines (Addison-Wesley, Redwood City, CA, 1988).
2. R. L. McCrory and J. M. Soures, in *Laser-Induced Plasmas and Applications*, edited by L. J. Radziemski and D. A. Cremers (Dekker, New York, 1989), p. 207.
3. J. D. Lindl, Phys. Plasmas **2**, 3933 (1995).
4. M. R. Amin *et al.*, Phys. Rev. Lett. **71**, 81 (1993).
5. M. R. Amin *et al.*, Phys. Fluids B **5**, 3748 (1993).
6. C. J. McKinstrie, R. Betti, R. E. Giacone, T. Kolber, and J. S. Li, Phys. Rev. E **50**, 2182 (1994).
7. R. E. Giacone, C. J. McKinstrie, and R. Betti, Phys. Plasmas **2**, 4596 (1995); **5**, 1218 (1998).
8. C. J. McKinstrie, J. S. Li, and A. V. Kanaev, Phys. Plasmas **4**, 4227 (1997).

9. A. A. Zozulya, V. P. Silin, and V. T. Tikhonchuk, Sov. Phys. JETP **65**, 443 (1987).

10. D. F. DuBois, B. Bezzerides, and H. A. Rose, Phys. Fluids B **4**, 241 (1992).

11. C. J. McKinstrie and M. V. Goldman, J. Opt. Soc. Am. B **9**, 1778 (1992).

12. Laboratory for Laser Energetics LLE Review **74**, 113, NTIS document No. DOE/SF/19460-241 (1998). Copies may be obtained from the National Technical Information Service, Springfield, VA 22161.

13. C. L. Tang, J. Appl. Phys. **37**, 2945 (1966).

14. R. L. Berger, E. A. Williams, and A. Simon, Phys. Fluids B **1**, 414 (1989).

15. W. L. Kruer *et al.*, Phys. Plasmas **3**, 382 (1996).

16. V. V. Eliseev *et al.*, Phys. Plasmas **3**, 2215 (1996).

17. C. J. McKinstrie, J. S. Li, R. E. Giacone, and H. X. Vu, Phys. Plasmas **3**, 2686 (1996).

18. C. J. McKinstrie, V. A. Smalyuk, R. E. Giacone, and H. X. Vu, Phys. Rev. E **55**, 2044 (1997).

19. C. J. McKinstrie, A. V. Kanaev, V. T. Tikhonchuk, R. E. Giacone, and H. X Vu, Phys. Plasmas **5**, 1142 (1998).

20. R. K. Kirkwood *et al.*, Phys. Rev. Lett. **76**, 2065 (1996).

21. A. K. Lal, K. A. Marsh, C. E. Clayton, C. Joshi, C. J. McKinstrie, J. S. Li, and T. W. Johnston, Phys. Rev. Lett. **78**, 670 (1997).

Landau Damping and Transit-Time Damping of Localized Plasma Waves in General Geometries

The collisionless damping of electrostatic plasma waves, first predicted by Landau[1] in 1946 and since rederived in many ways and confirmed experimentally, has become perhaps the most well known phenomenon in plasma physics. Landau damping plays a significant practical role in many plasma experiments and applications but has continued to be of great interest to theorists as well. Much of this interest stems from the counterintuitive nature of the result itself (that waves carrying free energy dissipate with no increase in entropy) coupled with the rather abstruse mathematical nature of Landau's original derivation. For these reasons there was even some controversy over the reality of the phenomenon,[2] until it was actually observed in experiments.

The usual derivation of Landau damping[3] begins by linearizing the Vlasov equation for an infinite homogeneous collisionless plasma. The linearized Vlasov equation is Fourier transformed in space and Laplace transformed in time, and the resulting equations in transform space are then solved algebraically to yield a relation between the perturbing field and the perturbed distribution function. Alternatively, this relation may be obtained by directly integrating the linearized Vlasov equation in configuration space using the method of characteristics,[4] also known as "integration over unperturbed orbits," and then performing the Fourier and Laplace transforms. Integration of this relation over particle velocities then leads to the dielectric response function and a dispersion relation for the plasma waves. Performing the integration over velocities entails the avoidance of a pole on the real axis by deforming the integration contour into the complex velocity plane. (Details can be found in most introductory plasma physics texts.) While this derivation is mathematically elegant, it is physically rather obscure, especially in regard to the introduction of complex velocities. For this reason, many "physical" derivations of Landau damping have been published, employing only real physical quantities throughout.[5,6] In these derivations, the energy transferred from the wave to each particle is calculated directly and then integrated over the particle distribution function to give the damping. In these physical derivations, however, the perturbed particle orbit must be determined and the wave-particle energy transfer calculated to second order in the field amplitudes. (The reasons for this will be discussed below.) Calculation of the perturbed particle orbit in a time-varying field is rather complicated, even for a plane wave, involving as it does iterated time integrals of the equation of motion. Such complications are contrary to the motivation for a physical derivation of Landau damping, which is to provide a simple, physically intuitive explanation of the phenomenon. Furthermore, they ought to be unnecessary since the transform derivation requires only unperturbed orbits and first-order quantities. One of the results that will emerge below is a physical derivation of Landau damping based solely on unperturbed orbits.

Strictly speaking, the term "Landau damping" applies only to the damping of infinite plane waves in homogeneous plasmas. Localized electrostatic perturbations in inhomogeneous plasmas, however, are also damped by collisionless processes.[7] Particles transiting the region containing the wave exchange energy with it; for a thermal distribution of particles, this results in a net transfer of energy from the wave to the particles and a consequent damping of the wave. This process is usually referred to as "transit-time damping."[8,9] Since, in general, the Fourier transform method used by Landau is difficult to apply in inhomogeneous plasmas, transit-time damping calculations employ the physical approach described above: the energy transferred to each particle is calculated and then integrated over the particle distribution function. Again, however, this requires that the perturbed particle orbits be determined and the energy transfer be calculated to second order in the fields; for a localized field in an inhomogeneous plasma, this is much more complicated than for a plane wave. Since Landau damping can be calculated based solely on the unperturbed orbits, it is natural to inquire if transit-time damping could also be calculated without invoking the perturbed orbits. One of the main purposes of this article is to show how this can be done.

First, we give a physical derivation of transit-time damping in a plasma slab of finite width based on unperturbed orbits and investigate how the damping of a plasma wave confined to the

slab varies with slab width and mode number. We also show that the result reduces to the usual Landau-damping expression as the width becomes large. Next, we present a similar analysis for spherical geometry followed by a brief discussion of the cylindrical case, which is covered in more detail in a future article.[10] Finally, in an appendix, we show formally that in general geometries our approach gives results equivalent to those obtained by other methods that require the use of perturbed orbits and higher-order terms.

Transit-Time Damping in Slab Geometry

Our approach to transit-time damping may be outlined as follows: Consider a localized oscillating electrostatic field that may be regarded as stationary in time, i.e., its oscillation amplitude is unchanging. In practice, this may correspond to a situation of weak damping, where the damping rate is much smaller than the oscillation frequency (as is often the case for Landau damping), or to a situation where wave energy lost to damping is replenished by an external source, such as in the case of stimulated Raman or Brillouin scattering, where the electrostatic wave is driven by interaction with an electromagnetic pump wave. We assume that the particle distribution function f_0 depends solely on the particle energy E, and we further assume that collisional damping is negligible and take the plasma to be collisionless, so that $f_0(E)$ satisfies the Vlasov equation. Consider a six-dimensional phase-space volume element dV, which passes through the localization volume in time Δt and emerges as the volume element dV^*. Since the Vlasov equation conserves phase-space volume, we have $|dV^*| = |dV|$, though the shape of the volume element may change. Through interaction with the field, each particle in dV acquires an energy increment ΔE, which may be positive or negative. Since the situation is stationary and the Vlasov equation is invariant under time reversal, the time-reversed process must be occurring simultaneously. In the reversed process, the volume element dV^* enters the localization volume and emerges as dV, each particle in the volume *losing* the energy increment ΔE in time Δt. The net rate at which energy is transferred to the particles associated with dV is then

$$\Delta P = \left\langle \frac{\Delta E}{\Delta t}\left[f_0(E)dV - f_0(E+\Delta E)dV^* \right] \right\rangle$$

$$\cong -\frac{\left\langle (\Delta E)^2 \right\rangle}{\Delta t}\frac{\partial f_0}{\partial E}dV, \qquad (1)$$

where the angle brackets indicate averaging over the field phase. Integration of this quantity over the phase space within the localized volume then gives *twice* the collisionless power transfer to the electrons since the phase space is effectively included twice in the integration (both forward and backward in time).

To illustrate, we now calculate the average energy gain rate of electrons crossing a one-dimensional slab region containing a standing-wave electrostatic field. We will obtain a simple expression for the field damping rate as a function of the slab length (for fixed oscillation frequency and wavelength).

Consider a standing-wave electrostatic potential, ϕ, of real frequency ω:

$$\phi = -\frac{C}{k}\sin(kx)\cos(\omega t)$$

in the slab region with boundaries at $x = 0$ and $x = L$. Here C is a constant inside the slab and vanishes outside, and $kL = 2\pi j$ with j a positive integer so that the potential is continuous. The corresponding electrostatic field is

$$E(x,t) = C\cos(kx)\cos(\omega t).$$

We also assume that electrons with a constant number density n_0 and a velocity distribution $f_0(E)$ are streaming constantly and freely through this region from the left at $x = 0$ and from the right at $x = L$. The density and temperature are chosen such that $\omega_{pe}^2 >> 3k^2v_T^2$, where ω_{pe}^2 is the usual plasma frequency and v_T the thermal velocity, so that weak Landau damping and quasi-steady-state conditions obtain. The frequency ω and wave number k then satisfy the Bohm-Gross dispersion relation $\omega^2 = \omega_{pe}^2 + 3k^2v_T^2 \approx \omega_{pe}^2$. We can also treat the case of stronger damping, with $\omega_{pe}^2 \sim 3k^2v_T^2$, if we assume that the steady state of the field is maintained by an external source such as the stimulated Raman scattering instability.

To first order in the field amplitude C, the velocity increment obtained by an electron of initial velocity v crossing the slab is simply

$$\Delta v = -\int_0^T \frac{eC}{m}\cos(kvt)\cos(\omega t + \phi)dt,$$

where we have used the unperturbed orbit $x = vt$. Here ϕ is the phase of the field at the time of entrance of the particle, and $T = L/v$. To this order, the energy change ΔE is given by

$\Delta E = mv\Delta v$. It is a simple matter to carry out the integral and then average $(\Delta E)^2$ over the phase. Note that $kvT = kL = 2\pi j$ and hence $\exp(\pm kvT) = 1$. The result is

$$\left\langle (\Delta E)^2 \right\rangle = \frac{(evC)^2}{2} \sin^2\left(\frac{\omega T}{2}\right)\left[\frac{1}{\omega + kv} + \frac{1}{\omega - kv}\right]^2,$$

and Eq. (1) becomes

$$\Delta P = -\frac{(evC)^2}{2T} \sin^2\left(\frac{\omega T}{2}\right) \times\left[\frac{1}{\omega + kv} + \frac{1}{\omega - kv}\right]^2 n_0 \frac{df_0(v)}{dE} dv.$$

The net power transferred is obtained by integrating this expression over the phase space within the slab volume, noting that $T = L/|v|$. The result is

$$P = -\frac{\omega_{pe}^2 C^2}{16\pi} \int_{-\infty}^{\infty} \sin^2\left(\frac{\omega L}{2|v|}\right) \times\left[\frac{1}{\omega + kv} + \frac{1}{\omega - kv}\right]^2 v|v| \frac{df_0(v)}{dv} dv, \quad (2)$$

where we have divided by 2 to compensate for the double-counting of phase space, as noted earlier. Note also that although the familiar resonant denominators appear in the integrand, they do not represent poles because of the sine function, so the difficulties in dealing with poles in the velocity integration that arise in Landau's calculation do not appear here.

The energy damping rate follows by dividing this result by the total plasma-wave energy within the slab volume. This energy is

$$W = \int_0^L \left\langle \frac{E^2(x,t)}{4\pi} \right\rangle dx = \frac{C^2 L}{16\pi}, \quad (3)$$

where the angle brackets denote averaging over time; hence, the field *amplitude* damping rate is *half* of (2) divided by (3):

$$\gamma = -\omega_{pe}^2 \int_0^{\infty} \sin^2\left(\frac{\omega L}{2v}\right) \times\left[\frac{1}{\omega + kv} + \frac{1}{\omega - kv}\right]^2 \frac{v^2}{L} \frac{df_0(v)}{dv} dv. \quad (4)$$

It is easy to show that this reduces to the Landau value in the infinite slab-length limit. Without loss of generality, we may take ω and k positive. If $v \neq \omega/k$, the integrand is finite and thus gives no contribution to γ as $L \to \infty$ (keeping k fixed, which means increasing L in wavelength steps, or j in integral steps). For $v \to \omega/k$, the integrand varies directly as L and becomes infinite. Clearly, the integrand is proportional to $\delta(v - \omega/k)$ in this limit. Replacing nonresonant values of v by ω/k and defining the integration variable $q \equiv \pi(L/\lambda)(\omega/kv - 1)$, where $\lambda = 2\pi/k$ is the wavelength, yields

$$\gamma = -\omega_{pe}^2 \left(\frac{\omega}{k}\right)^2 \frac{df_0}{dv}\bigg|_{\frac{\omega}{k}} \frac{1}{2\omega} \int_{-\pi L/\lambda}^{\infty} \frac{\sin^2 q}{q^2} dq.$$

In the limit of an infinite homogeneous plasma $L/\lambda \to \infty$, we obtain

$$\gamma = -\frac{\pi\omega_{pe}^2 \omega}{2k^2} \frac{df_0}{dv}\bigg|_{\frac{\omega}{k}}, \quad (5)$$

which is the familiar Landau damping rate for electrostatic waves in a homogeneous plasma.

Colunga *et al.*[11] have also obtained an expression for transit-time damping in a slab and noted that it can be represented as the Landau damping of the Fourier components of the localized electric field, which also gives (5) as the size of the slab increases. Their derivation, however, requires calculation of the wave-particle energy transfer to second order (i.e., use of perturbed orbits.)

We next investigate the damping rate's dependence on the slab size and plasma parameters. Assuming a Maxwellian distribution for $f_0(E)$ and changing the integration variable to $z \equiv \omega/kv$, Eq. (4) becomes

$$\gamma = \frac{4F^3\omega_{pe}^2\lambda}{(2\pi)^{3/2} L\omega} \int_0^{\infty} \frac{\sin^2\left(\frac{\pi L}{\lambda} Z\right)\exp\left(-F^2/2z^2\right)}{\left(1 - z^2\right)^2 z^3} dz. \quad (6)$$

Here, $F = \omega/kv_T$, with v_T the electron thermal velocity. For values of F well above unity, we have $\omega \approx \omega_{pe}$ and $F \approx (k\lambda_D)^{-1}$. The integral above is readily evaluated, for fixed F, and its variation with j is shown in Figs. 75.37(a) and 75.37(b) for $F = 6$ and $F = 4$, respectively. What is actually plotted is the ratio of γ to γ_L, where γ_L is the infinite slab limit $(L/\lambda \to \infty)$ of Eq. (6),

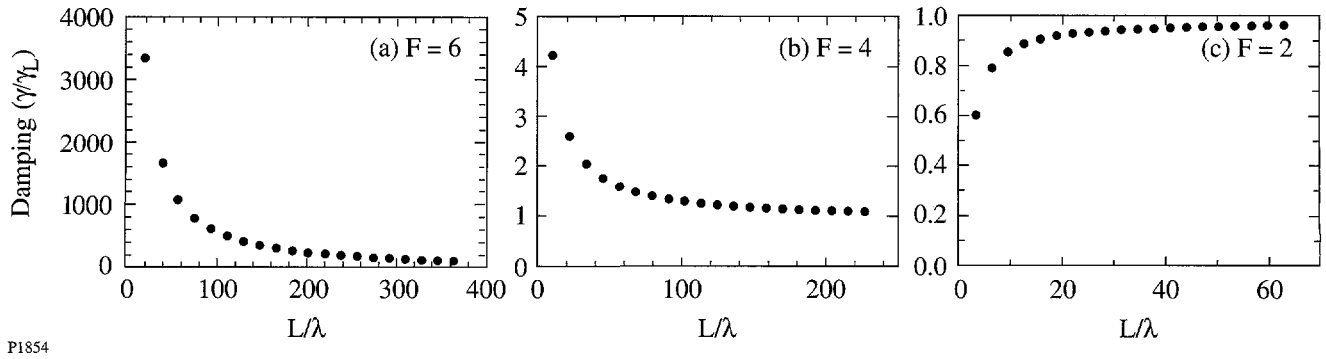

Figure 75.37
Damping rates for a standing plasma wave in a slab of length L, normalized to the Landau damping rate for an infinite homogeneous plasma γ_L. In (a)–(c) results are presented for three values of the parameter $F = \omega/kv_t$, with smaller values of F corresponding to stronger Landau damping.

$$\gamma_L = \left(\frac{\pi}{8}\right)^{1/2} \frac{F^3\omega_{pe}^2}{\omega} \exp\left(\frac{-F^2}{2}\right), \tag{7}$$

the usual Landau damping value. The Landau result arises from the resonant part of the integral; the nonresonant part gives rise to the finite geometry transit-time component of the damping.

Note the monotonic decrease in damping to the usual Landau value as L/λ increases. The value of the ratio at $L/\lambda = 1$ increases as F increases and can be quite large; hence, the transit-time damping can be much larger than the Landau rate for finite slabs. Note, however, that γ_L decreases exponentially with increasing F.

The nonresonant contribution does not always lead to augmentation of the Landau damping rate. As F decreases, the variation with L/λ reverses and the damping *increases* monotonically to the Landau value, as shown in Fig. 75.37(c) for $F = 2$. The general trend seems to be that the finite geometry increases the damping when the infinite geometry (Landau) limit of the damping is small (large F) and reduces damping when the infinite geometry limit is large. An analogous trend appears in the spherical and cylindrical cases, as discussed below, and a qualitative interpretation is presented in the **Conclusions** section.

Transit-Time Damping in Spherical Geometry

As an example of a finite three-dimensional calculation, we now examine the damping of electrostatic modes trapped in a sphere of radius R with a homogeneous internal density n_0. To illustrate the method as simply as possible, we consider only modes with no angular dependence (angular mode numbers $l = m = 0$); more complicated potentials and density profiles will give rise to more complicated forms of the function G, defined in Eq. (10) below, but can be handled by the same basic approach.

The potential inside the sphere is taken to be

$$\phi(r,t) = Aj_0(kr)\cos(\omega t + \alpha), \tag{8}$$

corresponding to a standing spherical wave, where $j_0(x) = \sin x/x$ denotes the spherical Bessel function of order zero, and α is an arbitrary constant representing the phase of the wave, to be averaged over below. The boundary condition is $j_0(kR) = 0$, so k may be any of a discrete set of wave numbers determined by the roots of the Bessel function.

Let $t = 0$ be the time when a particle is closest to the center of the sphere. We obtain its change in energy by integrating over the unperturbed orbit:

$$\Delta E = -e\int_{-t_0}^{t_0} \mathbf{v}\cdot\nabla\phi(\mathbf{r},t)\,dt.$$

Here $2t_0 = \sqrt{R^2 - b^2}/v$ is the time required to cross the sphere, where b is the distance of closest approach to the center of the sphere. The total derivative of the potential is

$$\frac{d}{dt}\phi[\mathbf{r}(t),t] = \mathbf{v}\cdot\nabla\phi[\mathbf{r}(t),t] + \frac{\partial}{\partial t}\phi[\mathbf{r}(t),t],$$

so the above integral can be written

$$\Delta E = -e\int_{-t_0}^{t_0}\left\{\frac{d}{dt}\phi[\mathbf{r}(t),t]-\frac{\partial}{\partial t}\phi[\mathbf{r}(t),t]\right\}dt.$$

The potential seen by the particle is the same before and after passing through the sphere, so

$$\int_{-t_0}^{t_0}\frac{d}{dt}\phi[\mathbf{r}(t),t]dt=0$$

and

$$\Delta E = e\int_{-t_0}^{t_0}\frac{\partial}{\partial t}\phi[\mathbf{r}(t),t]dt.$$

Substituting the form of the potential, changing the integration variable to $s = kvt$, and averaging over the phase α gives

$$\langle\Delta E^2\rangle = \frac{\omega^2e^2A^2}{2k^2v^2}G^2\left(kR,kb,\frac{\omega}{kv}\right), \tag{9}$$

where

$$G\left(kR,kb,\frac{\omega}{kv}\right)\equiv\int_{-k\sqrt{R^2-b^2}}^{k\sqrt{R^2-b^2}} \times j_0\left(\sqrt{k^2b^2+s^2}\right)\cos\left(\frac{\omega s}{kv}\right)ds, \tag{10}$$

a function that must be evaluated numerically.

Next we must integrate Eq. (1), the power loss in an element of phase-space volume, over the six-dimensional phase space inside the sphere. The total power being transferred to particles in the sphere is then

$$P=\int_0^{\pi}d\theta_r\sin\theta_r\int_0^{2\pi}d\phi_r \times\left\{\int_0^R drr^2\int_0^{\infty}dvv^2\int_0^{\pi}d\theta_v\int_0^{2\pi}d\phi_v\left[-\frac{1}{2}\frac{\langle\Delta E^2\rangle}{\Delta t}\frac{\partial f_0}{\partial E}\right]\right\}, \tag{11}$$

where the factor 1/2 in the integrand compensates for the double-counting of phase space, as noted earlier in the **Transit-Time Damping** section. Because of the spherical symmetry, the term in braces must be independent of θ_r and ϕ_r, so for convenience we can evaluate it at $\theta_r = \phi_r = 0$ and obtain

$$P = 4\pi n_0\left\{\int_0^R drr^2\int_0^{\infty}dvv^2\int_0^{\pi}d\theta_v\int_0^{2\pi}d\phi_v \times\left[-\frac{1}{2}\frac{\langle\Delta E^2\rangle}{\Delta t}\frac{\partial f_0}{\partial E}\right]\right\}\Bigg|_{\theta_r=\phi_r=0}. \tag{12}$$

For $\theta_r = \phi_r = 0$ we can use the relation $b/r = \sin\theta_v$ to convert the integral over θ_v to an integral over b:

$$\int_0^{\pi}d\theta_v\sin\theta_v\rightarrow 2\int_0^{\pi/2}d\theta_v\sin\theta_v\rightarrow 2\int_0^r db\frac{b/r}{\sqrt{r^2-b^2}}. \tag{13}$$

From Eqs. (9) and (10) we see that $\langle\Delta E^2\rangle$ is independent of r for fixed b, so using Eq. (13) and $\Delta t = 2\sqrt{R^2-b^2}/v$, we can perform the r and ϕ_v integrals in Eq. (12):

$$P=\frac{2\pi^2\omega^2e^2A^2n_0}{k^2} \times\int_0^{\infty}dvv\left[-\frac{\partial f_0(E)}{\partial E}\right]\int_0^R dbbG^2\left(kR,kb,\frac{\omega}{kv}\right). \tag{14}$$

The amplitude-damping rate is now given by $\gamma/\omega = P/2\omega W$, where W is the wave energy contained in the sphere:

$$W=\int_V\left\langle\frac{E^2}{4\pi}\right\rangle_t dV.$$

From Eq. (8) we have

$$\langle E^2\rangle_t=\frac{1}{2}k^2A^2j_0'^2(kr),$$

so

$$W=\int_V\frac{E_{\max}^2}{16\pi}dV=\frac{1}{2}k^2A^2\int_0^R r^2j_0'^2(kr)dr=\frac{1}{4}RA^2. \tag{15}$$

As $R\rightarrow\infty$ with k fixed, the electrostatic wave will locally come to look like a plane wave with wave number k throughout most of the volume of the sphere, so we might expect that in this limit Eq. (14) should give the usual Landau damping rate for such a wave. In Appendix A we show that this is indeed the case.

As in the slab geometry, we can characterize the wave parameters by the quantity $F = \omega/kv_T$ and calculate the damping rates obtained from Eqs. (14) and (15) as the radius of the sphere changes. Figures 75.38(a)–75.38(c) show the results for $F = 6$, 4, and 2, respectively. As in the slab case, we find that the results lie above the Landau limit when the damping is weak (F large), and below when the damping is strong (F small).

Cylindrical Geometry

The case of cylindrical geometry is somewhat more complicated than the slab and spherical geometries because there are two independent components of the wave vector: axial and radial. The cylindrical case is analyzed in detail in a forthcoming article,[10] where the results are applied to the problem of stimulated Raman scattering in a self-focused light filament in a laser-produced plasma. Here we merely note that the damping rate can be shown both analytically and numerically to approach the Landau value as the radius becomes large, and we show some results for the case of a purely radial wave vector for the same values of $F = \omega/kv_T$ as in the slab and spherical cases [Figs. 75.39(a)–75.39(c)]. Once again, we find that the finite radius results lie below the Landau value for F small and above for F large.

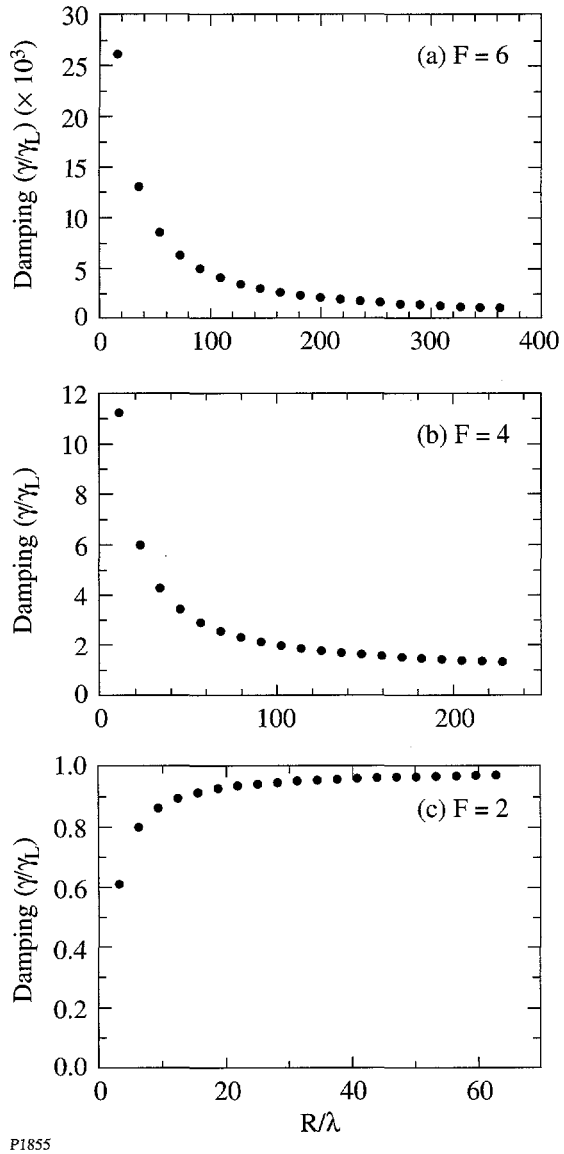

Figure 75.38
Same as Fig. 75.37, but for a sphere of radius R.

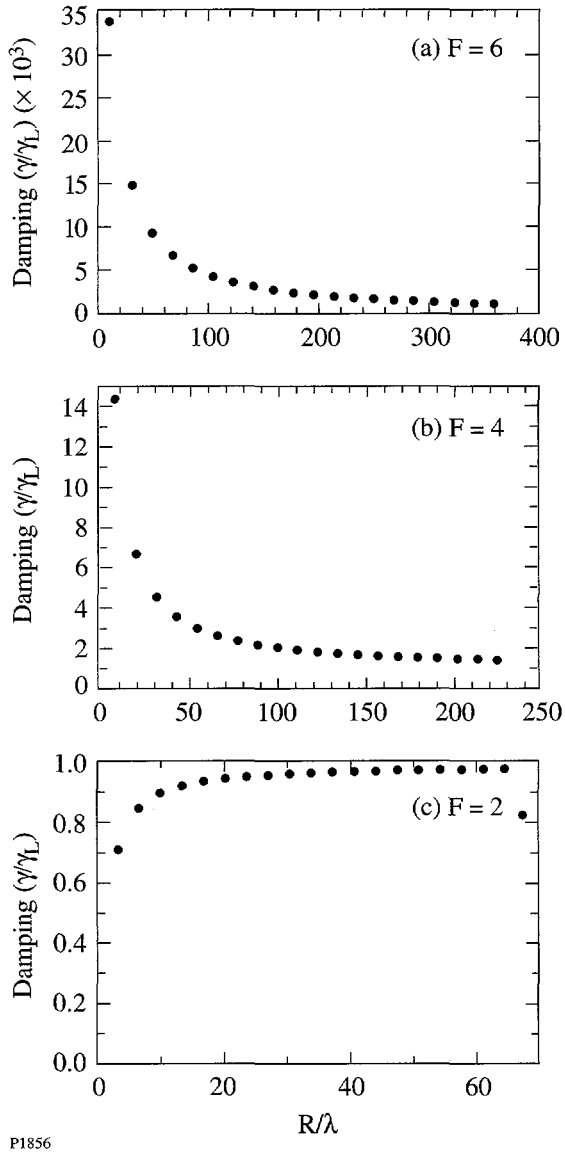

Figure 75.39
Same as Fig. 75.37, but for a cylinder of radius R. Here $F = \omega/kv_t$, where k is the radial wave number of the oscillation and the axial wave number is zero.

Conclusions

In summary, we have demonstrated a new, simplified approach to calculating transit-time damping. Our approach uses the time-reversal invariance of the Vlasov equation to avoid the necessity of calculating the wave–particle energy exchange to second order in the wave fields. We have illustrated the method by analyzing the damping of electrostatic oscillations in slab, cylindrical, and spherical geometries, both analytically and numerically. In general, our results seem to show that finite geometry effects tend to augment Landau damping when it would be small in an unbounded geometry, and reduce it when it would be large.

These results suggest a qualitative physical interpretation based on regarding the particles interacting with the electrostatic wave as falling into two classes: resonant and nonresonant. Resonant particles are those whose (unperturbed) motion keeps them in a constant phase relationship with the wave; depending on this phase they continuously either gain or lose energy from their interaction with the wave. As is well known, these are the particles responsible for Landau damping in infinite homogeneous plasmas. Nonresonant particles, on the other hand, see a varying wave phase as they propagate, and alternately gain and lose energy as this phase changes. In the case of an infinite geometry, these gains and losses cancel out over the infinite "transit time," and the nonresonant particles make no contribution to Landau damping. In the case of a finite system, the "resonant" particles can be regarded as those that do not get significantly out of phase with the wave while passing through the system; since their transit time decreases as the system becomes smaller, the number of particles that can be regarded as resonant increases as the confinement volume shrinks. It can be shown,[6] however, that the contribution of these nearly resonant particles to the damping goes as the fourth power of the time, so that the net contribution to the damping of the near-resonant particles diminishes as the confinement volume and the transit time become smaller. On the other hand, for a finite volume the energy gains and losses of the nonresonant particles no longer average to zero, and as the volume becomes smaller, the contribution of these nonresonant particles to the damping becomes larger. Thus, the damping in a finite system contains a smaller resonant component and a larger nonresonant component than in the corresponding infinite system. When the Landau damping is large in the infinite system (F small), the decrease in the resonant damping dominates the increase in the nonresonant damping, so that the damping in the finite system decreases from the Landau rate as the system size diminishes. When Landau damping is small (F large), the increase in nonresonant damping dominates, and the transit-time damping of the finite system is larger than the Landau damping of the corresponding infinite system. This picture is in qualitative agreement with the results we have obtained above for the slab, cylinder, and spherical geometries.

It should be noted that the essential advantage of the time-reversal invariance approach—the need to calculate the wave–particle energy transfer ΔE to only first order—is not dependent on the particular geometry of the system under consideration. For purposes of illustration, we have chosen simple geometries; in more complex geometries and inhomogeneous plasmas the phase-space integrals such as Eq. (13) will have to be carried out numerically, but the simplification in the calculation of ΔE will then be even more valuable. In Appendix B we show that the time-reversal invariance approach can be applied in quite general geometries, and verify that it gives results identical to the perturbed orbit approach.

ACKNOWLEDGMENT

This work was supported by the U.S. Department of Energy Office of Inertial Confinement Fusion under Cooperative Agreement No. DE-FC03-92SF19460, the University of Rochester, and the New York State Energy Research and Development Authority. The support of DOE does not constitute an endorsement by DOE of the views expressed in this article.

Appendix A: Large-Radius Limit of Collisionless Damping in Spherical Geometry

To evaluate the damping rate for large radii, we first investigate the nature of the function

$$S(kR,z) \equiv \frac{k}{R}\int_0^R dbbG^2(kR,kb,z), \tag{A1}$$

from which Eqs. (14) and (15) contain the R dependence of the damping rate (here $z \equiv \omega/kv$ and the factor k is included for convenience to make the function dimensionless). From Eq. (10) we have, using $j_0(x) \equiv \sin(x)/x$ and defining $t = s/kR$ and $x = b/R$,

$$G(kR,x,z) = 2\int_0^{\sqrt{1-x^2}} \frac{\sin kR\sqrt{t^2+x^2}}{\sqrt{t^2+x^2}}\cos(zkRt)dt$$

$$= \mathrm{Im}\left\{\int_0^{\sqrt{1-x^2}} \frac{1}{\sqrt{t^2+x^2}} \left[e^{ikR\left(\sqrt{t^2+x^2}-zt\right)} + e^{ikR\left(\sqrt{t^2+x^2}+zt\right)}\right]dt\right\}$$

$$= \mathrm{Im}\left\{\int_0^{\sqrt{1-x^2}} \frac{1}{\sqrt{t^2+x^2}}\left[e^{ikR\psi_-(t)} + e^{ikR\psi_+(t)}\right]dt\right\}, \tag{A2}$$

where

$$\psi_{\pm}(t) \equiv \sqrt{t^2 + x^2} \pm zt.$$

We next use the method of stationary phase to determine the dominant behavior of $G(kR,x,z)$ as $kR \to \infty$. Using the Riemann–Lebesgue lemma, it is readily shown that the integral in Eq. (A2) vanishes as $1/kR$ as $kR \to \infty$ unless the functions

$$\psi'_{\pm}(t) = \frac{d}{dt}\left[\sqrt{t^2 + x^2} \pm zt\right] = \frac{t}{\sqrt{t^2 + x^2}} \pm z$$

vanish at some point in the t integration interval $\left[0, \sqrt{1-x^2}\right]$, in which case the integral will vanish more slowly than $1/kR$ as $kR \to \infty$. Clearly $\psi'_{+}(t)$ cannot vanish in this interval, so the dominant behavior of G is given by

$$G(kR, x, z) \sim \mathrm{Im}\left\{\int_0^{\sqrt{1-x^2}} \frac{1}{\sqrt{t^2 + x^2}} e^{ikR\psi_{-}(t)} dt\right\}$$

$$\text{for } x^2 + z^2 \le 1. \qquad \text{(A3)}$$

The inequality in Eq. (A3) is the necessary and sufficient condition that $\psi'_{-}(t)$ vanish in $\left[0, \sqrt{1-x^2}\right]$. When this inequality is not satisfied, G vanishes more rapidly as $kR \to \infty$ and hence may be neglected; thus, the dominant behavior of Eq. (A1) as $kR \to \infty$ is given by

$$S(kR, z) \sim kR \int_0^{\sqrt{1-z^2}} dx\, x G^2(kR, x, z). \qquad \text{(A4)}$$

The dominant contribution to the integral in Eq. (A3) comes from the point in $\left[0, \sqrt{1-x^2}\right]$ where $\psi'_{-}(t)$ vanishes, so we may extend the upper limit of the range of integration without changing the leading behavior of G:

$$G(kR, x, z) \sim \mathrm{Im}\left\{\int_0^1 \frac{1}{\sqrt{t^2 + x^2}} e^{ikR\left(\sqrt{t^2+x^2} - zt\right)} dt\right\}$$

$$\text{for } x^2 + z^2 \le 1,$$

$$\sim 2\int_0^1 \frac{\sin\left(kR\sqrt{t^2 + x^2}\right)}{\sqrt{t^2 + x^2}} \cos(zkRt)\, dt.$$

Using $t = s/kR$ and $x = b/R$, this can be written

$$G(kR, kb, z) \sim 2\int_0^{kR} \frac{\sin\sqrt{k^2b^2 + s^2}}{\sqrt{k^2b^2 + s^2}} \cos(zs)\, ds$$

$$\sim 2\int_0^{\infty} \frac{\sin\sqrt{k^2b^2 + s^2}}{\sqrt{k^2b^2 + s^2}} \cos(zs)\, ds$$

$$= \pi J_0\left(kb\sqrt{1-z^2}\right) \text{ for } \left(\frac{b}{R}\right)^2 + z^2 \le 1.$$

Substituting in Eq. (A4), we obtain

$$S(kR, z) \sim \frac{1}{kR} \int_0^{kR\sqrt{1-z^2}} d(kb)(kb) G^2(kR, kb, z)$$

$$\sim \frac{\pi^2}{kR} \int_0^{kR\sqrt{1-z^2}} d(kb)(kb) J_0^2\left(kb\sqrt{1-z^2}\right)$$

for $z \le 1$. Using

$$\int x J_0^2(\alpha x)\, dx = \frac{x^2}{2}\left[J_0^2(\alpha x) + J_1^2(\alpha x)\right],$$

this becomes

$$S(kR, z) \sim \frac{\pi^2 kR}{2}\left(1 - z^2\right)$$

$$\left\{J_0^2\left[kR\left(1 - z^2\right)\right] + J_1^2\left[kR\left(1 - z^2\right)\right]\right\}$$

$$\sim \pi \text{ as } kR \to \infty \text{ for } z < 1,$$

where we have used the formula

$$\lim_{x \to \infty} x\left[J_0^2(x) + J_1^2(x)\right] = \frac{2}{\pi}.$$

For $z > 1$, since the condition $x^2 + z^2 \le 1$ cannot be satisfied, $S(kR,z)$ must vanish as $kR \to \infty$. Defining

$$T(z) \equiv \lim_{kR \to \infty} S(kR, z) = \begin{cases} \pi, z < 1 \\ 0, z > 1 \end{cases},$$

we see that $T(z)$ is a step function in z.

Thus, using Eqs. (14) and (15), the damping rate for large kR becomes

$$\lim_{kR\to\infty}\frac{\gamma}{\omega}=\lim_{kR\to\infty}\frac{P}{2\omega W}$$

$$=\frac{4\pi^2\omega e^2}{k^3}n_0\int_0^\infty dvv\left[-\frac{\partial f_0}{\partial E}\right]T\left(\frac{\omega}{kv}\right)$$

$$=\frac{4\pi^2\omega e^2}{k^3}n_0\pi\int_{\omega/k}^\infty dvv\left[-\frac{\partial f_0}{\partial E}\right]. \qquad \text{(A5)}$$

Note from Eqs. (12) that f_0 here is the normalized three-dimensional distribution function, assumed isotropic:

$$4\pi\int_0^\infty v^2 f_0(v)\,dv=1.$$

Using

$$\frac{\partial f_0}{\partial E}=\frac{1}{mv}\frac{\partial f_0}{\partial v},$$

the integral in Eq. (A5) is readily evaluated to give

$$\lim_{kR\to\infty}\frac{\gamma}{\omega}=\frac{4\pi^3\omega e^2}{k^3}n_0 f_0\left(\frac{\omega}{k}\right). \qquad \text{(A6)}$$

This result can be expressed in a more familiar form in terms of the one-dimensional velocity distribution g, defined by

$$g(u)\equiv 2\pi\int_0^\infty dvvf_0\left(\sqrt{u^2+v^2}\right)$$

$$=2\pi\int_u^\infty dvvf_0(v). \qquad \text{(A7)}$$

Differentiating this expression gives

$$\frac{dg}{du}=-2\pi uf_0(u),\ \text{or}\ f_0(u)=-\frac{1}{2\pi u}\frac{dg}{du}.$$

In terms of the one-dimensional distribution function, Eq. (A6) becomes

$$\lim_{kR\to\infty}\frac{\gamma}{\omega}=-\frac{2\pi^2e^2n_0}{k^2m}\left.\frac{dg(u)}{du}\right|_{u=\frac{\omega}{k}}$$

$$=-\frac{\pi\omega_p^2}{2k^2}\left.\frac{dg(u)}{du}\right|_{u=\frac{\omega}{k}},$$

which is just the Landau damping rate for plane waves of frequency ω and wave number k. This is to be expected since, as the radius of the sphere increases, an increasingly large fraction of the volume of the sphere contains waves that are locally planar, so that particles gain energy from them at the same rate as from a plane wave.

Appendix B: Equivalence of Perturbed Orbit and Time-Reversal Invariance Approaches to Transit-Time Damping

Transit-time damping of a confined electrostatic wave in a plasma arises from the transfer of energy from the wave to particles passing through the confinement region. In many cases of interest it may be assumed for purposes of calculating the damping that the wave properties (amplitude, frequency, etc.) are stationary in time. This means that background plasma properties such as the size and density of the confinement region are either constant or their variation is small during the wave period and the particle transit time. It also means that the wave energy lost to the damping is either replaced by another process, such as stimulated scattering, or again is small during the wave period and particle transit time.

Previous calculations of transit-time damping have taken a straightforward approach: the energy gained or lost by a particle transiting the confinement region is calculated, averaged over the phase of the wave, and integrated over the flux of particles weighted by the velocity distribution function. This approach can be represented in general by Fig. 75.40(a), and the power transferred from the wave to particles can be written

$$P=\int_0^\infty dv_x\,v_x\int d\mathbf{s}\,f_0(E)\left\langle\Delta E(E,0,\mathbf{s},\phi)\right\rangle_\phi$$

$$-\int_{-\infty}^0 dv_x\,v_x\int d\mathbf{s}\,f_0(E)\left\langle\Delta E(E,l,\mathbf{s},\phi)\right\rangle_\phi. \qquad \text{(B1)}$$

Here the angle brackets denote averaging over the phase ϕ of the wave, and $\mathbf{s}$ represents the coordinates and velocities perpendicular to the arbitrarily chosen x axis:

$$d\mathbf{s}=dydzdv_ydv_z.$$

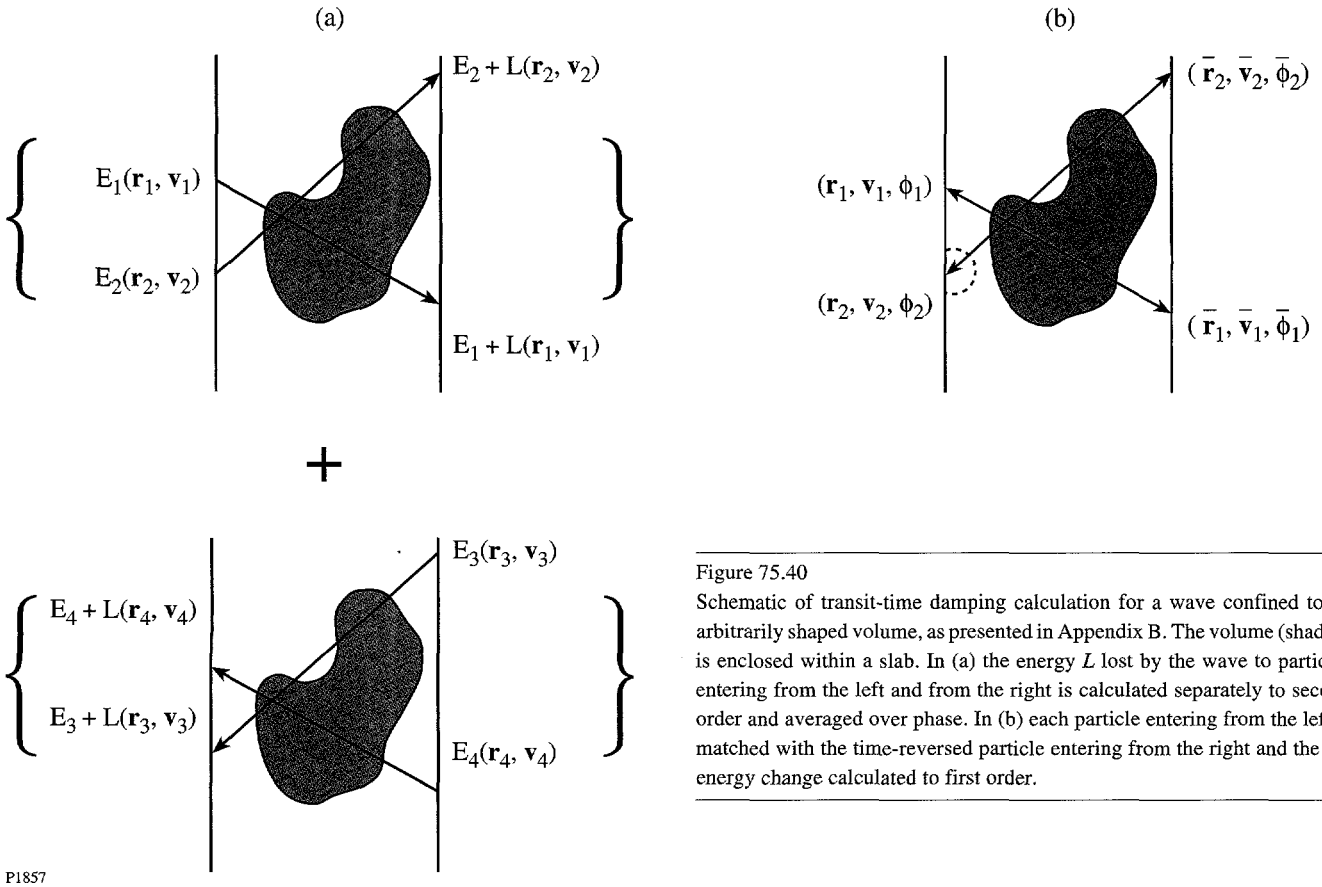

Figure 75.40
Schematic of transit-time damping calculation for a wave confined to an arbitrarily shaped volume, as presented in Appendix B. The volume (shaded) is enclosed within a slab. In (a) the energy L lost by the wave to particles entering from the left and from the right is calculated separately to second order and averaged over phase. In (b) each particle entering from the left is matched with the time-reversed particle entering from the right and the net energy change calculated to first order.

We include in our analysis all particles passing through a slab extending from $x = 0$ to $x = l$ and containing the confinement volume V. (Of course, only those particles following trajectories passing through V actually contribute to the damping, but describing only these trajectories is difficult for a volume of arbitrary shape. Including all trajectories passing through the slab greatly simplifies the representation of the particle flux in the general case and does not change the result since the additional trajectories do not contribute to the damping.) The functions $\Delta E\,(E,0,\mathbf{s},\phi)$ and $\Delta E\,(E,l,\mathbf{s},\phi)$ give the energy change for particles entering the slab at $x = 0$ and $x = l$, respectively, with energy E, phase ϕ, and other parameters $\mathbf{s}$. The distribution function f_0 is assumed uniform and isotropic and depends only on the energy $E = m\left(v_x^2 + v_y^2 + v_z^2\right)/2$.

The next step is to calculate the phase-averaged energy change:

$$L(E,0,\mathbf{s}) = \left\langle \Delta E\left(E,0,\mathbf{s},\phi\right)\right\rangle_\phi \text{ for } x = 0,\ v_x > 0;$$

$$L(E,l,\mathbf{s}) = \left\langle \Delta E\left(E,l,\mathbf{s},\phi\right)\right\rangle_\phi \text{ for } x = l,\ v_x < 0.$$

The energy ΔE gained or lost by a specific particle is first order in the field amplitude, but the gains and losses cancel to first order after phase averaging, so that the loss functions L are second order in the field. Evaluation of the loss functions thus requires that the energy changes ΔE also be calculated to second order, which in turn means that the perturbed trajectories must be determined and integrated over. This can lead to complicated calculations in general. Details of the calculation of the loss functions and the resulting damping rates are given for some simple cases in Robinson.[9]

Our purpose here is to show that the integrations in Eq. (B1) can be rearranged so that ΔE need only be calculated to first order, which can be accomplished by integration over the unperturbed orbits.

First we take the phase average outside the integrations and write it explicitly as an integral over ϕ:

$$P = \frac{1}{2\pi}\int_0^{2\pi} d\phi \int_0^\infty dv_x\, v_x \int d\mathbf{s}\, f_0(E)\,\Delta E\left(E,0,\mathbf{s},\phi\right)$$
$$-\frac{1}{2\pi}\int_0^{2\pi} d\bar{\phi} \int_{-\infty}^0 d\bar{v}_x\, \bar{v}_x \int d\,\bar{\mathbf{s}}\, f_0\left(\bar{E}\right)\Delta\bar{E}\left(\bar{E},l,\bar{\mathbf{s}},\bar{\phi}\right), \qquad \text{(B2)}$$

where we have also denoted the integration parameters for particles entering the slab from the right at $x = l$ by an overbar (this amounts only to a change of dummy variable at this point and has no physical significance). We could, however, just as well calculate the second integral in Eq. (B2) by integrating over the parameters with which these particles leave the slab at $x = 0$. Since we are dealing with a collisionless plasma, we can invoke Liouville's theorem to say that an element of phase-space volume is invariant on passing through the slab:

$$dxdydzdv_x dv_y dv_z = d\bar{x}\,d\bar{y}\,d\bar{z}\,d\bar{v}_x\,d\bar{v}_y\,d\bar{v}_z\,. \tag{B3}$$

Using $d\phi = \omega\,dt$, $d\bar{\phi} = \omega\,d\bar{t}$, $dx = v_x dt$, and $d\bar{x} = \bar{v}_x d\bar{t}$, where ω is the wave frequency, Eq. (B3) becomes

$$v_x dydzdv_x dv_y dv_z d\phi = \bar{v}_x\,d\bar{y}\,d\bar{z}\,d\bar{v}_x\,d\bar{v}_y\,d\bar{v}_z\,d\bar{\phi}$$

or

$$v_x dv_x d\mathbf{s}\,d\phi = \bar{v}_x d\bar{v}_x d\bar{\mathbf{s}}\,d\bar{\phi}\,. \tag{B4}$$

Thus, the transformation from the integration parameters at $x = l$ to those at $x = 0$ has unit Jacobian, and we can write Eq. (B2) as

$$P = \frac{1}{2\pi}\int_0^{2\pi} d\phi \int_0^{\infty} dv_x\, v_x \int ds\, f_0(E)\,\Delta E(E,0,\mathbf{s},\phi) - \frac{1}{2\pi}\int_0^{2\pi} d\phi \int_{-\infty}^{0} dv_x\, v_x \int ds\, f_0\left(\bar{E}\right)\Delta\bar{E}\left(\bar{E},l,\bar{\mathbf{s}},\bar{\phi}\right), \tag{B5}$$

where $\bar{E}$ is now a function of the $x = 0$ parameters:

$$\bar{E} = \frac{1}{2}m\left(v_x^2 + v_y^2 + v_z^2\right) + \Delta E(E,0,\mathbf{s},\phi) = E + \Delta E(E,0,\mathbf{s},\phi). \tag{B6}$$

Also, from the definitions of ΔE and $\Delta\bar{E}$, we have

$$\Delta\bar{E}\left(\bar{E},l,\bar{\mathbf{s}},\bar{\phi}\right) = E - \bar{E} = -\Delta E(E,0,\mathbf{s},\phi). \tag{B7}$$

Substituting Eqs. (B6) and (B7) in Eq. (B5), we get

$$P = \frac{1}{2\pi}\int_0^{2\pi} d\phi \int_0^{\infty} dv_x\, v_x \int ds\, f_0(E)\,\Delta E(E,0,\mathbf{s},\phi) + \frac{1}{2\pi}\int_0^{2\pi} d\phi \int_{-\infty}^{0} dv_x\, v_x \int ds\, f_0(E+\Delta E)\,\Delta E(E,0,\mathbf{s},\phi). \tag{B8}$$

Since the process is assumed to be stationary, Eq. (B8) must be invariant under time reversal. The only effect of the time-reversal operator on Eq. (B8) is to change the sign of v_x (strictly speaking, it also changes the phase by a constant, but since we are integrating over all ϕ, this is irrelevant). The time-reversed form of Eq. (B8) is thus

$$P = -\frac{1}{2\pi}\int_0^{2\pi} d\phi \int_{-\infty}^{0} dv_x\, v_x \int ds\, f_0(E)\,\Delta E(E,0,\mathbf{s},\phi) - \frac{1}{2\pi}\int_0^{2\pi} d\phi \int_0^{\infty} dv_x\, v_x \int ds\, f_0(E+\Delta E)\,\Delta E(E,0,\mathbf{s},\phi). \tag{B9}$$

Adding Eqs. (B8) and (B9) and dividing by 2 gives

$$P = \frac{1}{4\pi}\int_0^{2\pi} d\phi \int_{-\infty}^{\infty} dv_x |v_x| \int ds\left[f_0(E) - f_0(E+\Delta E)\right]\Delta E(E,0,\mathbf{s},\phi) = -\frac{1}{2}\int_{-\infty}^{\infty} dv_x |v_x| \int ds\left\langle \Delta E^2(E,0,\mathbf{s},\phi)\right\rangle_{\phi} \frac{df_0}{dE}. \tag{B10}$$

Note that although this expression is second order in the field, as it should be, it achieves second order only through the squaring of ΔE, so that ΔE itself need only be calculated to first order.

Equation (B10) is a surface integral, i.e., the values of v_x and $\mathbf{s}$ in the integral are evaluated on the $x = 0$ surface of the slab. It is useful to rewrite Eq. (B10) in a form involving a volume integral rather than a flux. The integration in Eq. (B10) is shown schematically in Fig. 75.40(b). Since we are calculating ΔE to first order, we can represent the particle trajectories by their unperturbed orbits. Consider the six-dimensional "flux tube" traced out by a phase-space volume element crossing the slab along an unperturbed orbit (which need not be a straight line). The rate at which phase-space volume enters the tube is $v_x d\mathbf{s}$, and since in a collisionless process phase-space volume is conserved, the volume of the flux tube is given by

$$\Delta V = t_0(E,\mathbf{s})\,v_x d\mathbf{s}, \tag{B11}$$

where $t_0(E,\mathbf{s})$ is the time taken for a particle following the orbit to cross the slab. Since phase-space volume moves as an

incompressible fluid, flux tubes cannot intersect, and a set of these flux tubes whose collective cross section comprises the $x = 0$ plane will exactly fill the phase-space volume within the slab. Furthermore, the (unperturbed) flux $v_x d\mathbf{s}$ through the tube is a constant, so we may deform the slab boundary as shown by the dotted contour in Fig. 75.40(b) without affecting the validity of Eq. (B11); the volume of the tube and the time taken to pass along it are reduced in the same proportion. As long as the deformed boundary is outside the volume V in which the potential is nonvanishing, ΔE is also unaffected, so we may deform the original slab boundary to conform to the boundary of V and use Eq. (B11) to convert Eq. (B10) to an integral over the phase space within V:

$$P = -\frac{1}{2}\int_V d^3\mathbf{r}\int d^3\mathbf{v}\,\frac{\left\langle \Delta E^2(\mathbf{r},\mathbf{v},\phi)\right\rangle_\phi}{t_0(\mathbf{r},\mathbf{v})}\frac{df_0}{dE}$$

$$= \frac{1}{2}\int d^3\mathbf{r}\int d^3\mathbf{v}\Delta P, \qquad \text{(B12)}$$

where ΔP is the expression for the energy loss for a volume of phase space we wrote down immediately on the basis of time-reversal invariance in Eq. (1) at the beginning of this article. We have derived Eq. (B12) from Eq. (B1) here to demonstrate the equivalence of our approach to earlier formulations of transit-time damping, which are also based on Eq. (B1).

REFERENCES

1. L. Landau, J. Phys., USSR **X**, 25 (1946).
2. J. Dawson, Phys. Fluids **4**, 869 (1961).
3. G. Schmidt, *Physics of High Temperature Plasmas* (Academic Press, New York, 1966), pp. 199–210.
4. R. C. Davidson, *Methods in Nonlinear Plasma Theory* (Academic Press, New York, 1972), pp. 57–62.
5. E. M. Lifshitz and L. P. Pitaevskifi, *Physical Kinetics*, Course of Theoretical Physics, Vol. 10, 1st ed. (Pergamon Press, Oxford, 1981), pp. 127–128.
6. D. R. Nicholson, *Introduction to Plasma Theory*, Wiley Series in Plasma Physics (Wiley, New York, 1983), pp. 87–92.
7. G. J. Morales and Y. C. Lee, Phys. Rev. Lett. **33**, 1534 (1974).
8. P. A. Robinson, Phys. Fluids B **1**, 490 (1989).
9. P. A. Robinson, Phys. Fluids B **3**, 545 (1991).
10. R. W. Short and A. Simon, "Collisionless Damping of Localized Plasma Waves in Laser-Produced Plasmas and Application to Stimulated Raman Scattering in Filaments," to be published in LLE Review **76**.
11. M. Colunga, J. F. Luciani, and P. Mora, Phys. Fluids **29**, 3407 (1986).

Highly Stable, Diode-Pumped Master Oscillator for the OMEGA Laser Facility

The OMEGA facility is a 60-beam, 30-kJ (UV) laser system for performing inertial confinement fusion (ICF) experiments. One of the main features of the OMEGA laser is an optical pulse–shaping system capable of producing flexible temporal pulse shapes[1] (Fig. 76.1). The recently developed diode-pumped Nd:YLF master oscillator[2] is capable of satisfying the basic OMEGA requirements, such as single-frequency, long-pulse, Q-switched operation with high amplitude stability. Some OMEGA operational issues (modulator minimization procedures, bandwidth characterization, increased repetition rate, and temporal diagnostic calibration), however, have motivated the development of a new diode-pumped, multipurpose laser. The new laser is capable of serving as the OMEGA master oscillator (stable, single-frequency, Q-switched operation), as well as a source of stable, single-frequency cw radiation (for modulator characterization and minimization) and stable, sinusoidally modulated radiation (for temporal diagnostics calibration).

OMEGA Pulse-Shaping System

The heart of the OMEGA optical pulse–shaping system is an integrated-optic (IO) modulator. To obtain high-contrast, high-precision, shaped optical pulses, the modulator must be biased to provide zero transmission in the absence of an electrical waveform (modulator minimization procedure). To accomplish this on OMEGA, cw laser radiation from a different laser source than the master oscillator (the cw mode-locked laser) is manually directed to the modulator. This operator intervention is time consuming and places unnecessary stress on fiber-optic connectors and components. This operator intervention is eliminated with a master oscillator that can be easily switched to cw operation.

By increasing the laser repetition rate in Q-switched operation, precision pulse-shape and bandwidth measurements can be made with a high-bandwidth sampling oscilloscope. In addition, with careful laser-cavity-length control the laser can

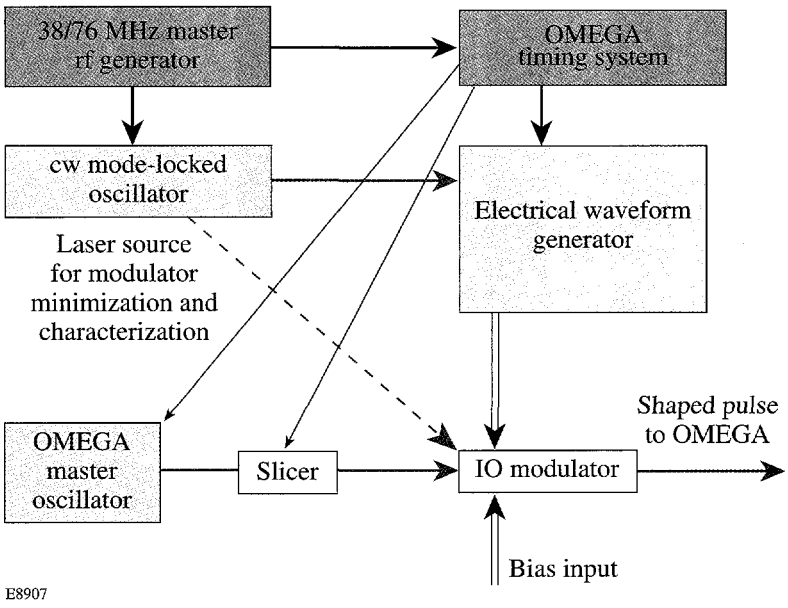

Figure 76.1
Block diagram of the OMEGA pulse-shaping system.

lase simultaneously on two adjacent cavity modes and provide a precise, temporally modulated signal for temporal diagnostics calibration (streak cameras, photodetectors, etc.).

Laser Characteristics

The basic design of the laser (Fig. 76.2) is similar to the one described earlier.[2] As a pump source we have chosen a single-stripe, 1.2-W, cw SDL-2326-P1 laser diode (a modification from the previous design) with a thermoelectric cooler that eliminates the need for water cooling. The diode wavelength is temperature tuned to 797 nm to provide maximum pump absorption in the active element. The polarization of the pump radiation is parallel to the *c*-axis of the active element, which increases pump absorption to approximately 80%.

Beam-conditioning optics for the diodes consist of an AR-coated aspherical lens (NA~0.68) and an AR-coated cylindrical lens. The pump radiation is focused into the active element through the dichroic end mirror. Transmission of the conditioning optics, focusing lens, and dichroic mirror is ~90% at 797 nm. The active element is a 4-mm-diam by 5-mm, 1.1% Nd:YLF wedged and AR-coated rod oriented with the Brewster prism to provide 1053-nm lasing. The acousto-optic modulator (AOM) used as *Q*-switch (GOOCH & HOUSEGO, QS080-2G-RU2) is wedged and AR coated for 1053 nm. In the cw operation regime (no rf power applied to the AOM) the laser generates a total of 260 mW of cw power (in both counter-propagating beams) with an optical-to-optical efficiency >21% at 1053 nm (Fig. 76.3).

Unidirectional single-frequency operation is achieved by applying a low (<200-mW) rf power to the AOM.[3] By removing the rf power from the AOM we obtain *Q*-switched, 50- to 200-ns (FWHM) pulses [Fig. 76.4(a)] at a repetition rate of up to 10 kHz. The energy content of the sliced, flat-top portion of the pulse [Fig. 76.4(b)] is 0.2 to 1.5 μJ, depending on the pulse width. Without removing the rf power to the AOM (*Q*-switch trigger off), the laser generates up to 100 mW of single-frequency cw power (optical-to-optical efficiency is ~13%).

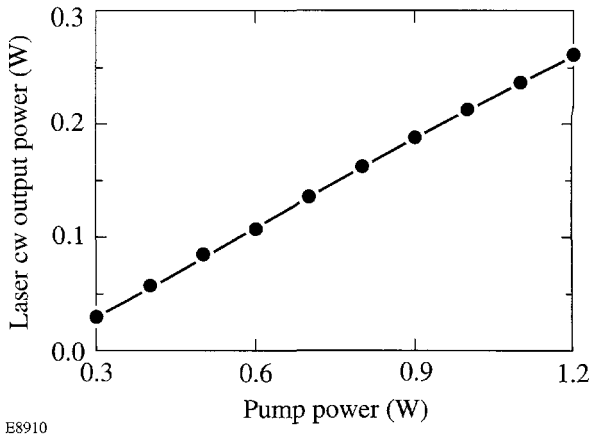

Figure 76.3
Laser cw output power versus diode pump power for bidirectional operation.

The spatial laser beam profile is close to TEM_{00} and is launched into a single-mode optical fiber delivery system for all our applications. We routinely achieve a single-mode fiber launching efficiency of the order of 85%, which indicates a high-quality beam profile.

Laser Parameter Control and Stabilization

To achieve single-frequency, highly stable (in terms of amplitude, timing jitter, wavelength) laser operation we employ several feedback loops:

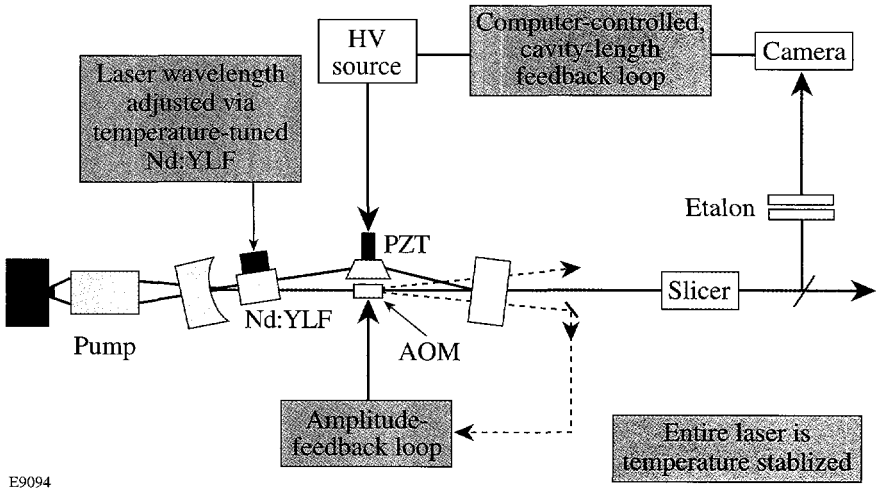

Figure 76.2
Block diagram of the multipurpose Nd:YLF laser.

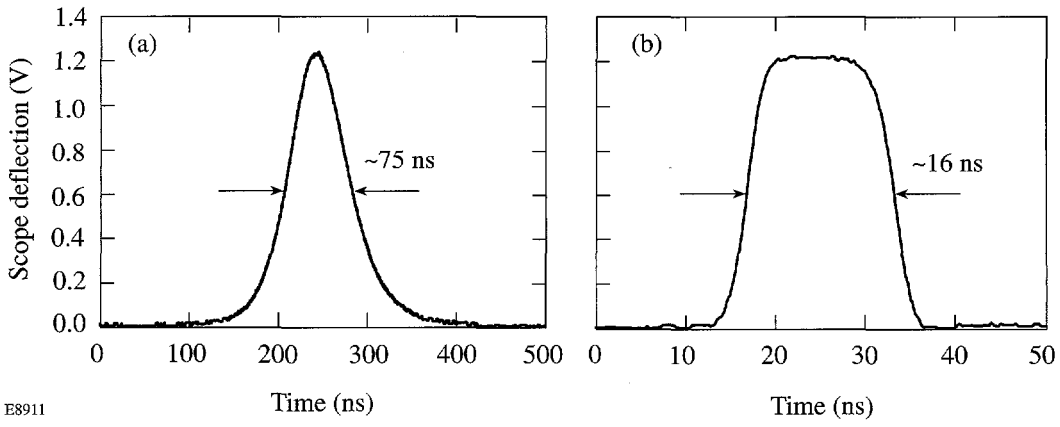

Figure 76.4
(a) The Q-switched pulse envelope and (b) sliced central flat-top portion of the pulse to be sent to the modulator.

- amplitude-feedback loop
- wavelength control and stabilization
- frequency-feedback loop
- overall laser temperature stabilization
- two-mode operation

1. Amplitude-Feedback Loop

To damp relaxation oscillations and stabilize the prelase phase, the rf power applied to the AOM is controlled with a circuit that provides negative amplitude feedback. One of the beams diffracted by the AOM is coupled into a 0.4-mm multimode fiber and sent to a diode that generates a feedback signal (Fig. 76.2). For a high (low) feedback signal the rf power to the AOM is increased (decreased), thus increasing (decreasing) the cavity losses and stabilizing the cw laser output power. With amplitude-feedback stabilization, a very smooth prelase phase with no relaxation oscillations is observed (Fig. 76.5), and the externally triggerable Q-switch leads to high amplitude stability and low temporal jitter of the output pulse. Amplitude fluctuations of the Q-switched pulse are 0.5% rms and the timing jitter is 3 to 5 ns rms depending on the Q-switched optical pulse duration.

2. Wavelength Control and Stabilization

Due to the large longitudinal mode spacing and the absence of wavelength-tuning elements (such as etalons, gratings, etc.) the laser is operating at the peak of the gain curve; thus, the only way to adjust and stabilize the lasing wavelength is to adjust the peak position of the Nd:YLF gain curve by changing and stabilizing the temperature of the active element. The operating temperature of the active element is 34°C to 36°C with no temperature control. Adjustment of the laser wavelength for OMEGA requires additional heating up to 39°C to 45°C. We have developed a miniaturized heater–sensor feedback loop that is mounted on the active element heat sink and can maintain its temperature to within 0.1°C. Figure 76.6 shows the wavelength tuning and stabilization by adjusting and maintaining the temperature of the active element. We have found the thermal wavelength coefficient $\Delta\lambda/\Delta T$ to be +0.08 Å/°C.

3. Frequency-Feedback Loop and Overall Temperature Stabilization

To ensure single-frequency operation we have developed a computerized wavelength-feedback loop. The laser spectrum is measured with an air-spaced etalon and analyzed by a computer equipped with a CCD camera and framegrabber. If the fringe peak moves, the computer produces a driving voltage to change the high voltage on the piezoelectric translator (PZT)

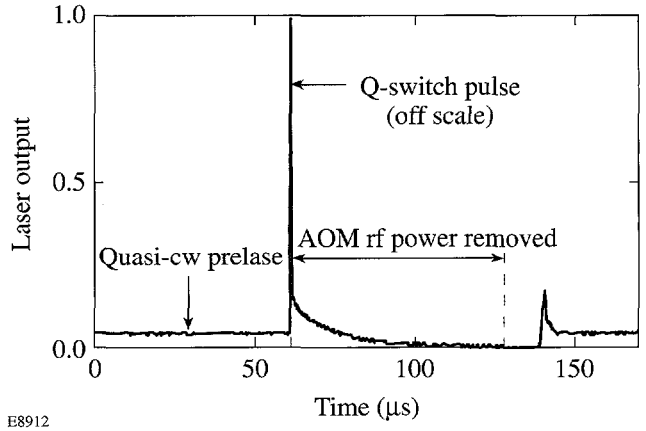

Figure 76.5
Amplitude feedback provides constant prelase for higher amplitude stability of the Q-switched pulse with lower timing jitter.

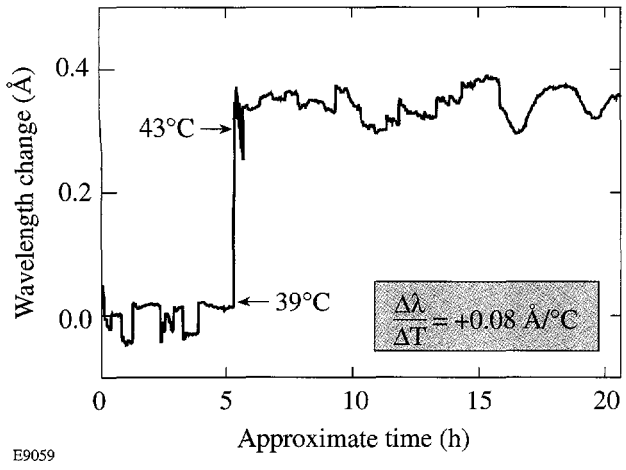

Figure 76.6
The laser output wavelength is adjusted and stabilized by controlling the temperature of the active element.

to correct the laser cavity length and bring the fringe peak to its initial position. The following procedure locates the correct fringe position (reset): The computer scans the PZT driver voltage until the two-mode operation is detected; it then reverses the scan to find the next two-mode operation voltage; and finally, it sets the voltage between these two-mode operation voltages. This reset procedure is repeated every 0.5 h and ensures single-frequency operation [Fig. 76.7(a)]. The thermal drift due to room-temperature changes, however, causes an undesirable wavelength drift. When the laser housing and active element are temperature stabilized [Fig. 76.7(b)], the laser runs single frequency with a residual wavelength drift of 0.01 Å rms over 15 h of operation (Fig. 76.8).

We have taken the envelope of the sliced flat-top pulse using a 20-ps-resolution streak camera. This envelope is extremely smooth (Fig. 76.9), indicating a high single-frequency contrast.

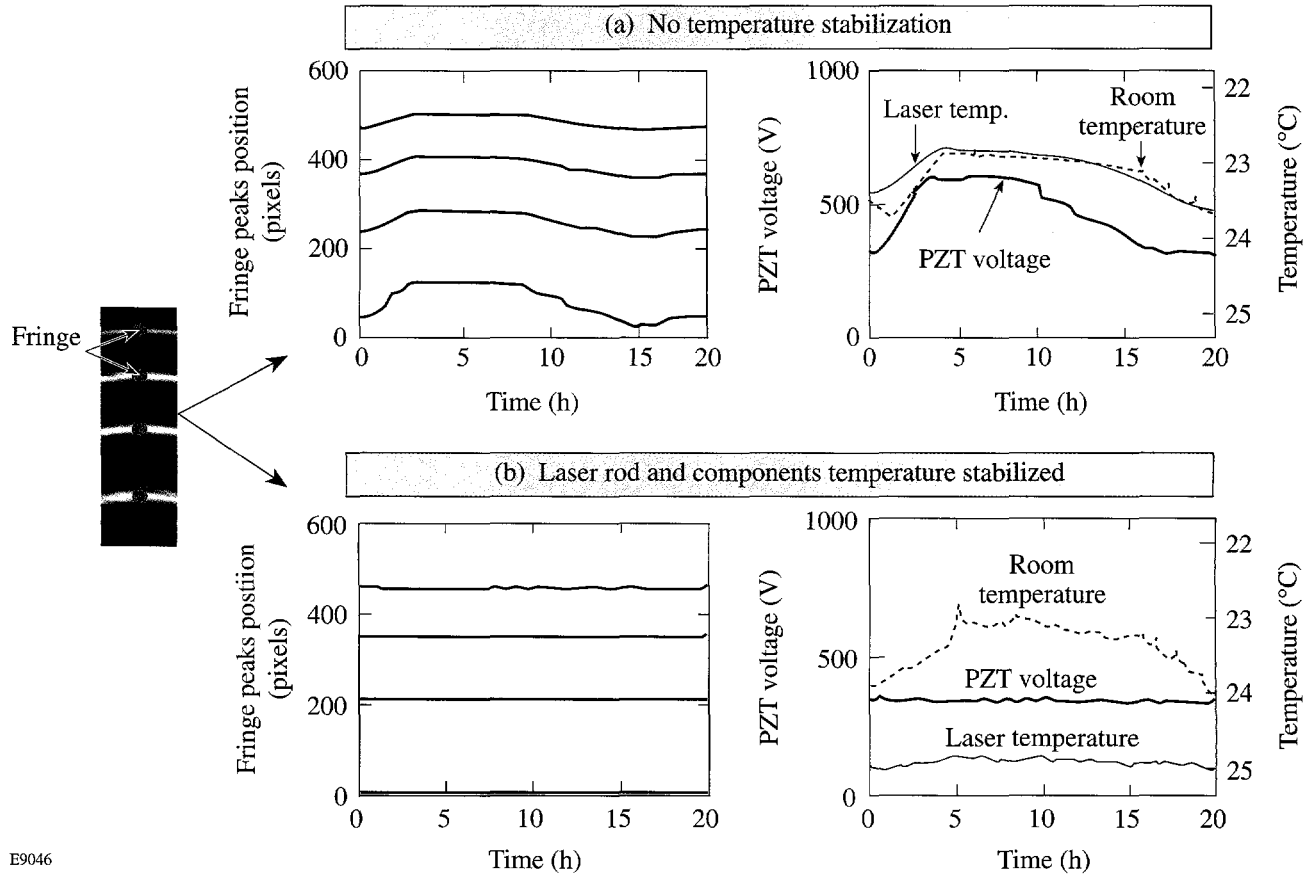

Figure 76.7
The laser operates with a single frequency; however, with no temperature stabilization the frequency drifts over time and follows the room temperature (a). Temperature stabilization of the active element and laser components significantly improves wavelength stability (b).

4. Two-Mode Operation

By applying the appropriate computer-controlled feedback to the PZT-mounted prism in the laser cavity, the laser can be forced to operate over many hours on two adjacent longitudinal modes with approximately equal amplitudes [Fig. 76.10(a)]. In this case the pulse's temporal structure is a deeply modulated sinusoidal signal with a 267-ps period [Fig. 76.10(b)]. This signal can be particularly useful for OMEGA temporal diagnostics calibration such as streak camera sweep speeds, etc.

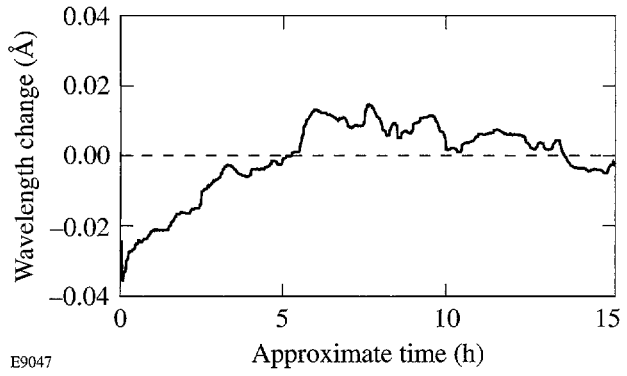

Figure 76.8
The laser wavelength stability is 0.01 Å over 15 h.

Conclusion

We have developed a diode-pumped, multipurpose Nd:YLF laser for the OMEGA laser facility that is suitable for our pulse-shaping applications, including modulator minimization and characterization, as well as temporal diagnostics calibration. The laser combines three functions without realignment:

- *Q*-switched, single-frequency master oscillator for the OMEGA laser,
- cw single-frequency operation for pulse-shaping applications, and
- the source of a stable sinusoidal optical signal for diagnostics applications.

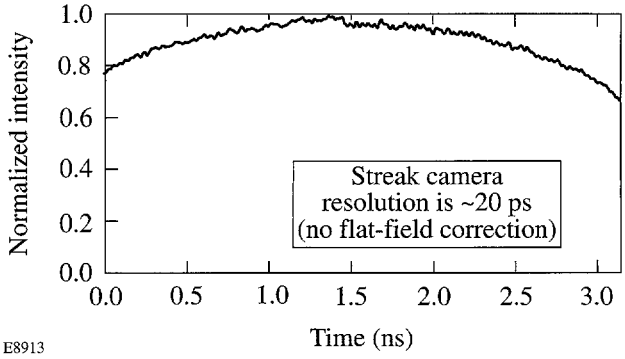

Figure 76.9
Streak camera measurement of the pulse envelope (no flat-field correction) showing high single-frequency contrast.

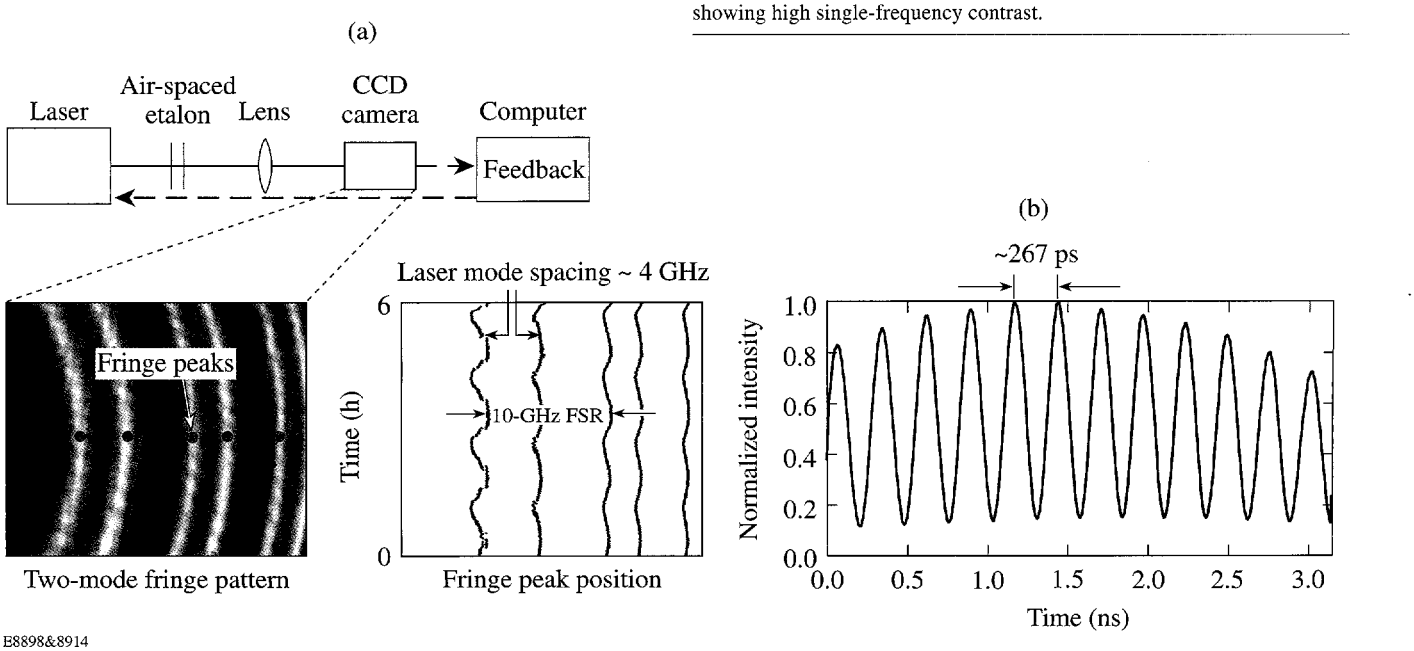

Figure 76.10
(a) Long-term, two-mode operation and (b) streak camera measurement of the optical sinusoidal signal (no flat-field correction).

The laser output is either up to 100 mW of cw single-frequency radiation or Q-switched pulses with a smooth or sinusoidally modulated envelope at a repetition rate of ≤10 kHz. Changeover requires no laser realignment.

ACKNOWLEDGMENT

This work was supported by the U.S. Department of Energy Office of Internal Confinement Fusion under Cooperative Agreement No. DE-FC03-92SF19460 and the University of Rochester. The support of DOE does not constitute an endorsement by DOE of the views expressed in this article.

REFERENCES

1. A. V. Okishev, W. Seka, J. H. Kelly, S. F. B. Morse, J. M. Soures, M. D. Skeldon, A. Babushkin, R. L. Keck, and R. G. Roides, in *Conference on Lasers and Electro-Optics*, Vol. 11, 1997 OSA Technical Digest Series (Optical Society of America, Washington, DC, 1997), p. 389.

2. A. V. Okishev and W. Seka, IEEE J. Sel. Top. Quantum Electron. **3**, 59 (1997).

3. W. A. Clarkson, A. B. Neilson, and D. C. Hanna, IEEE J. Quantum Electron. **32**, 311 (1996).

Regenerative Amplifier for the OMEGA Laser System

The 60-beam OMEGA Nd:glass laser is a direct-drive inertial confinement fusion (ICF) laser facility capable of achieving 30-kJ UV energy with an arbitrary temporal pulse shape predetermined by the target design. The initial low-energy, temporally shaped pulse is generated by the pulse-shaping system[1] (similar to a design developed at the Lawrence Livermore National Laboratory[2]), followed by multistage amplification with splitting, resulting in 60 laser beams with 1-kJ IR energy per beam. At the first amplification stage a negative-feedback-controlled, Nd:YLF regenerative amplifier (regen) is used. In this regen, the shaped pulse is amplified up to nine orders of magnitude to the submillijoule level.

In this article we present the requirements, design, and experimental results for the regens currently in use on OMEGA. These externally synchronizable regens boost the energy of the temporally shaped pulses to the submillijoule level with long-term energy variations of ~0.2% and with the output parameters of the amplified pulse insensitive to the injected pulse energy. The temporal distortions of the amplified pulse caused by the negative feedback are immeasurable. Four regenerative amplifiers equipped with this negative feedback system have operated flawlessly on OMEGA for the past two years.

Regenerative Amplifier Requirements for the OMEGA Laser System

The pulse-shaping system on OMEGA must meet a number of specifications[3] with a large safety margin to allow stable and reliable OMEGA operation. The low-energy pulses generated by this system must be amplified to an ~400-μJ energy with better-than-2% stability; the output pulses must be externally synchronizable; and the amplification process should introduce minimum and predictable temporal-pulse-shape distortions.

Multipass regens have been shown to provide high gains.[4,5] Flash-lamp-pumped regens, however, have typical output energy fluctuations[5,6] in the range of 5% to 10% for externally synchronized laser pulses. These fluctuations are caused primarily by an intrinsic flash-lamp instability. The relative variation in the flash-lamp output $\delta E_{\text{pump}}/E_{\text{pump}}$ leads to a variation of the amplified pulse energy $\delta E_{\text{out}}/E_{\text{out}}$ as[7]

$$\delta E_{\text{out}}/E_{\text{out}} \approx \ln(G_{\text{tot}})\,\delta E_{\text{pump}}/E_{\text{pump}}, \qquad (1)$$

where G_{tot} is the total small-signal gain. For a standard regen, $G_{\text{tot}} \approx 10^7$ to 10^9; therefore, for $\delta E_{\text{out}}/E_{\text{out}} \approx 2\%$, the pump energy variation must be $\delta E_{\text{pump}}/E_{\text{pump}} \leq 0.1\%$. For a standard flash-lamp–pumped regen, this is difficult, if not impossible, to achieve.[6,7] In addition, fluctuations in the pulse energy injected into the regen can also affect the regen output stability. For an externally synchronizable pulse, 2% regen output stability requires approximately the same stability for the injected pulse. This is difficult to achieve since the efficiency of injecting an optical pulse into the regen is affected by many factors that are difficult to control. A negative feedback can enhance the stability and external synchronizability of the regen,[8] but the time-dependent losses introduced by that negative feedback can cause undesirable temporal-pulse-shape distortions of the injected pulse during amplification. These distortions are difficult to model accurately, which seriously hampers the generation of a desired pulse shape at the regen output.

We developed a flash-lamp–pumped Nd:YLF regen with a redesigned negative-feedback system that completely satisfies OMEGA requirements. This feedback system introduces no temporal-pulse distortions, apart from pulse distortion due to gain saturation, that can be accurately modeled and compensated for. In the following sections we will discuss practical aspects of this regen design and present results of our numerical modeling and experimental measurements.

Negative-Feedback System for the Regenerative Amplification of Temporally Shaped Pulses

A negative feedback renders the regen output insensitive to input variations as well as to gain and loss fluctuations inside the regen cavity. The feedback signal is derived from the intracavity pulse energy and controls the intracavity losses. A block diagram of this regen is shown in Fig. 76.11. The

instantaneous intracavity pulse energy is sensed by a photodiode whose signal is amplified by feedback electronics and applied to the Pockels cell electrode; thus, the losses increase as the circulating pulse energy increases, resulting in a steady-state round-trip gain near unity. After the feedback (pre-lase) phase, all cavity losses are eliminated, and the pulse is amplified as in a standard Q-switched oscillator.

The pre-lase phase is crucial for stabilizing the output pulse energy. Pulses injected into the regen above the average energy reach the steady-state phase early in time, while injected pulses with less energy reach the steady-state phase later. In the steady-state phase, the circulating intracavity pulse energy is constant and independent of the injected pulse energy (Fig. 76.12); thus, the regen with negative feedback is very insensitive to input fluctuations, in contrast to a regen without feedback.

The steady-state phase also compensates for gain fluctuations caused by flash-lamp fluctuations. During the steady-state phase the circulating-pulse energy remains approximately constant while the gain continuously decreases due to the energy dissipated by the feedback losses. The rate at which gain is reduced after each round-trip depends on the ratio of the intracavity pulse fluence to the saturation fluence. The exact value of the intracavity pulse energy in the pre-lase phase can be controlled externally to minimize the regen output fluctuations due to gain or loss variations (Fig. 76.12).

Successful implementation of this distortionless negative-feedback system places stringent requirements on the feedback electronics. Our intracavity Pockels cells are KD*P crystals that require the feedback electronics to deliver high-voltage electrical signals in the 2- to 3-kV range in order to introduce noticeable intracavity losses. Past experience has

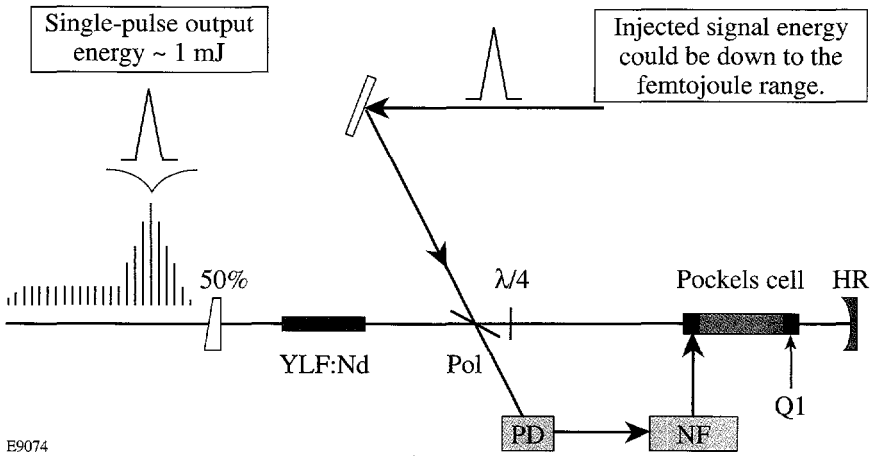

Figure 76.11
Block diagram of the regen with negative feedback.

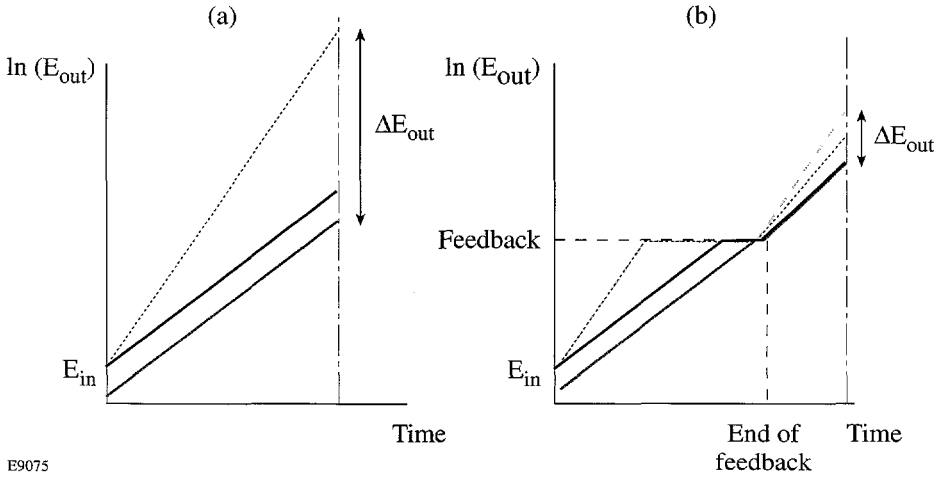

Figure 76.12
Semilog schematic plot of the energy evolution in the regen (a) without feedback and (b) with negative feedback. Negative feedback mitigates effects of shot-to-shot gain and loss fluctuations and injected-pulse energy variation. The solid curve represents the average injected energy and the average regen gain. The dotted curves represent the average injected energy and a regen gain higher than the average gain. The shaded curve represents a case where the injected energy is less than average and the regen gain is average.

shown[9] that the negative-feedback electronics must have a delay time shorter than 2 to 3 regen cavity round-trips. To stabilize the intracavity pulse energy, the feedback electronics must respond faster than the relaxation-oscillation frequency[10]

$$\omega_0 = \sqrt{(r-1)\gamma_c\gamma_{\mathrm{YLF}}}\,, \tag{2}$$

where γ_c is the inverse photon lifetime in the regen cavity, γ_{YLF} is the inverse relaxation time of the upper laser level of Nd:YLF, and r is the pumping rate. These feedback requirements are difficult, if not impossible, to fulfill with standard electronics.

Typical fast, high-voltage feedback electronics strongly distort the output pulse shape because of small feedback-induced intracavity loss variations during the time the circulating pulse propagates through the Pockels cell. Although the single-pass distortions are small, their effect is cumulative, and after many round-trips the distortions become severe. To eliminate these distortions the negative-feedback signal applied to the Pockels cell must be constant while the shaped pulse propagates through the Pockels cell. This requires that the negative-feedback signal have no fast-frequency components, which contradicts Eq. (2).

This problem can be circumvented with a two-component, negative-feedback signal. The first component is a high dc voltage that introduces a time-independent constant loss and brings the regen very close to the steady-state phase. In this phase the relaxation-oscillation frequency of the regen is very small [see Eq. (2) with $r \approx 1$]; thus, the circulating pulse energy can be held constant with a second low-voltage, low-frequency electrical-feedback signal. Due to the low voltage and slow temporal variation of the second feedback component, the temporal shape of the amplified pulse is not distorted.

Regen Modeling

The regen dynamics were modeled in a manner similar to that published in Ref. 11. Using an ideal four-level amplifying medium, neglecting fluorescence depumping, and assuming that the pulse fluence J is much smaller than the saturation fluence J_s of the gain medium ($J_{s,\mathrm{Nd:YLF}} \approx 0.8$ J/cm^2 at 1053 nm), one obtains a pair of simplified recurrent rate equations:[4]

$$J_{k+1} = T_k \exp(g_k) J_k\,, \tag{3}$$

$$g_{k+1} = g_k - \left[\exp(g_k) - 1\right] J_k / J_s\,. \tag{4}$$

Here k is the index for the resonator round-trip; T_k, g_k, and J_k are the resonator transmission, gain coefficient, and pulse fluence during the k^{th} round-trip, respectively; and $g_k = \ln(G^{\mathrm{ss}}{}_k)$, where $G^{\mathrm{ss}}{}_k$ is the small-signal gain of the k^{th} round-trip. We have also assumed that the $G^{ss}\, J_k / J_s << 1$. The gain coefficient at the time of injection, g_0, is proportional to the pump energy E_{pump}. The calculated intracavity fluence of the regen is shown in Fig. 76.13(a) for an initial net round-trip gain $G_0 = 2.1$, which is typical for OMEGA regens. The dependence of the output pulse train (pulse energy and build-

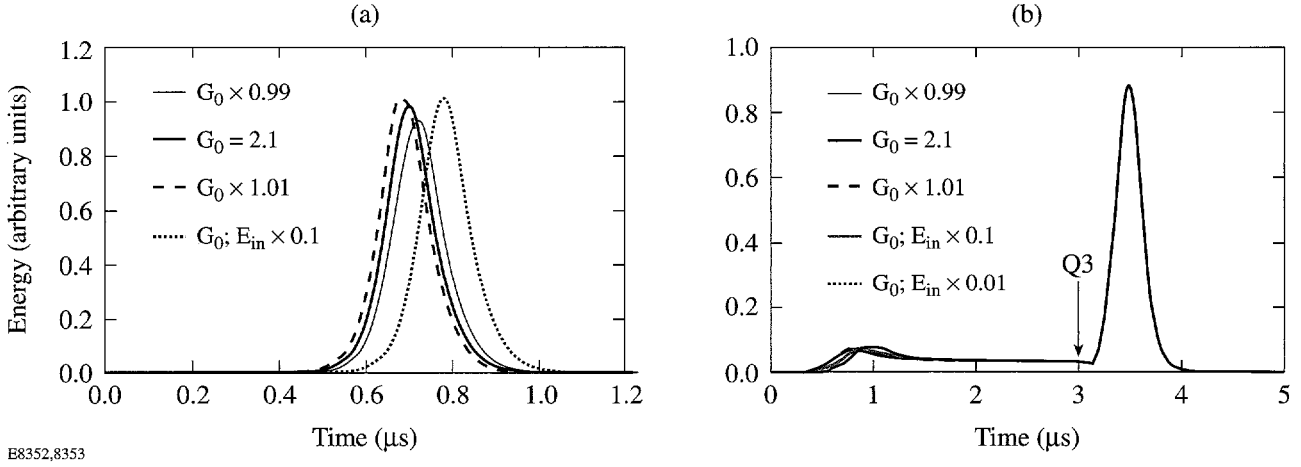

Figure 76.13
Numerical simulations clearly demonstrate the stabilizing effect of the negative feedback on the output energy of the regen: (a) thick solid line—standard regen output; dashed/thin solid lines—pumping energy varied by ±1%; dotted line—10× less injected pulse fluence; (b) same as (a) but with negative feedback.

up time) on variations in net round-trip gain G_0 and injected pulse energy E_{in} are also shown in this figure.

The two-component negative feedback is modeled by multiplying the right side of Eq. (3) by the transmission functions T_{dc} and T_{ac}. The former models the time-independent loss while the latter accounts for the modulated feedback losses required to maintain constant circulating pulse energy. The actual value of T_{dc} is adjusted in such a way that the regen operates just slightly above threshold. In the steady-state phase, T_{ac} is inversely proportional to the difference between the intracavity pulse fluence and the threshold fluence J_{th} of the pulse at the time when the dc feedback losses were introduced. In Fig. 76.13(b), modeling results for the regen with the feedback are presented for the same initial conditions as in Fig. 76.13(a). The negative-feedback stabilization of the regen output is clearly apparent by the insignificant variations in maximum amplitude of the train envelope as well as by the constant build-up time beyond the externally triggered Q-switch [Q3 in Fig. 76.13(b)].

Experimental Results

The block diagram for the regen with negative feedback is shown in Fig. 76.14. A temporally shaped optical pulse is injected into the regen through a polarization-maintaining, single-mode fiber and a Faraday isolator. At the time of injection, a step-like quarter-wave voltage (~4.1 kV) is applied to the Pockels cell, and the injected pulse experiences small losses and relatively high round-trip gain. When the energy of the amplified pulse reaches a predetermined level (~10 μJ), a second step of ~2 kV applied to the second Pockels cell electrode changes the differential voltage applied across the Pockels cell, adding a time-independent constant intracavity loss. As a result, the net round-trip gain is reduced to just slightly above threshold, preventing further rapid buildup of the laser pulse. At this time, a small feedback voltage applied to the Pockels cell is sufficient to control and maintain a constant steady-state pulse energy over periods of a few microseconds. Furthermore, since the regen operates close to the threshold, the response time of the regen (equal to the inverse of the relaxation-oscillation frequency) is very long compared to the regen round-trip time of 26 ns. This completely eliminates pulse distortions caused by the negative feedback. At a predetermined time [Q3 in Fig. 76.13(b)], a third Q-switch voltage step is applied to the Pockels cell, which compensates the losses caused by the previous loss-producing voltages. This process produces a train of highly stable pulses under a Q-switched envelope as shown in Fig. 76.15. Single shaped pulses of ~1 mJ and exceptional energy stability (~0.2% rms) have been generated over periods exceeding 4 h of continuous 5-Hz operation [~7.7×10^4 shots (see Fig. 76.16)]. A 0.5% rms energy stability was observed over a 9-h period (>1.6×10^5 shots). In addition to its excellent energy stability, the regen output is also very insensitive to the injected energy (see Fig. 76.17).

Injection of a square pulse confirms that the only measurable distortions of the temporal pulse shape are due to gain saturation. These distortions can be modeled precisely by simple rate equations[11] and can be effectively precompensated (see Fig. 76.18). With the present system we have experimentally demonstrated the generation of kilojoule-level laser pulses from the OMEGA laser system with prescribed temporal pulse shapes (see Fig. 76.19).

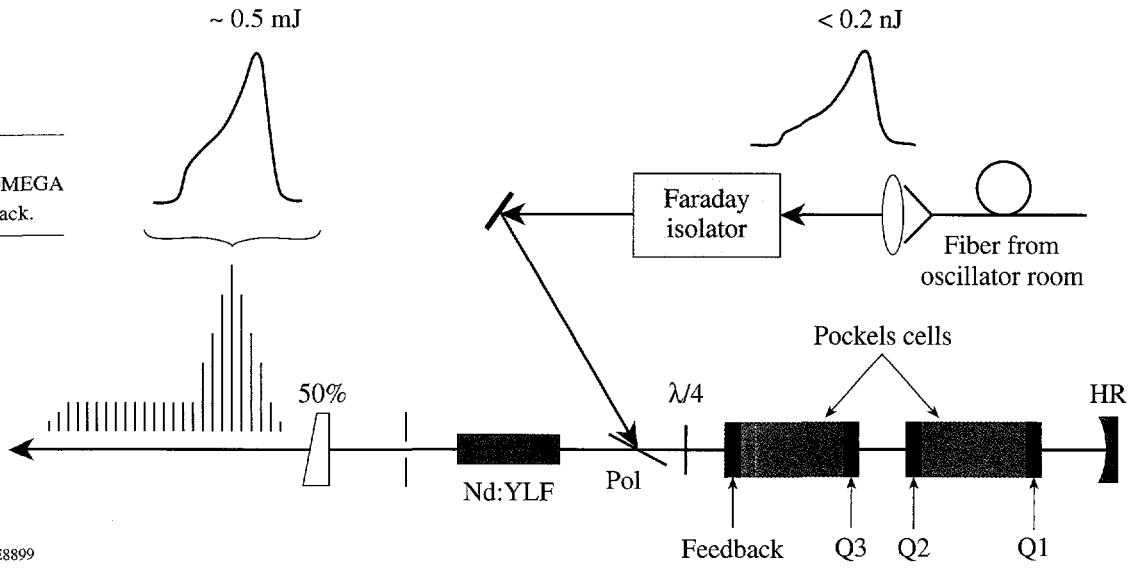

Figure 76.14
Block diagram of the OMEGA regen with negative feedback.

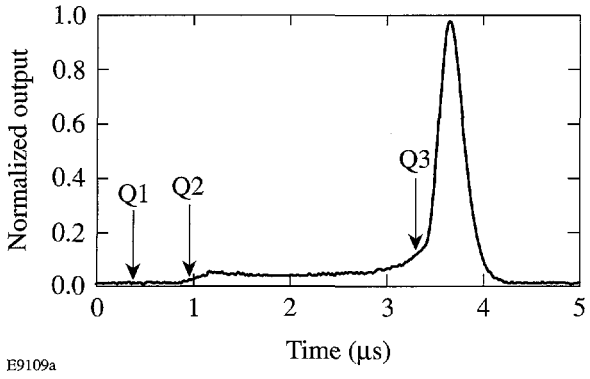

Figure 76.15
Measured envelope of the output pulse train from the regen with negative feedback.

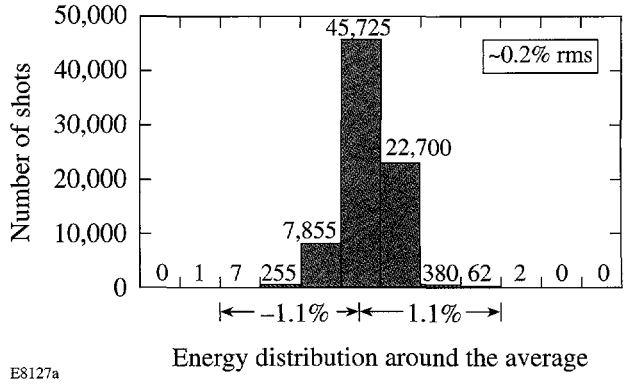

Figure 76.16
Stability histogram for the single-pulse energy distribution at the regen output. Data were collected over 4 h of continuous operation at a 5-Hz repetition rate.

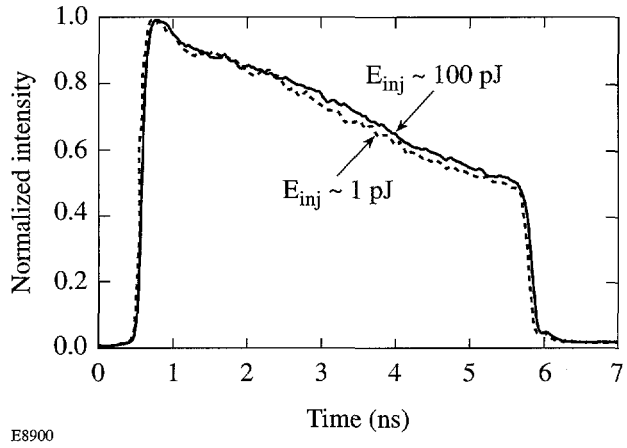

Figure 76.17
IR streak camera measurements of the regen output. Solid line—the injected pulse at nominal energy; dashed line—the injected pulse energy attenuated by a factor of 100.

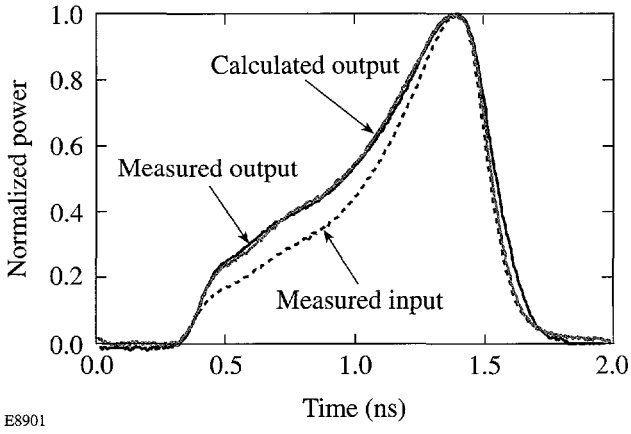

Figure 76.18
Measured and simulated regen output pulse shapes.

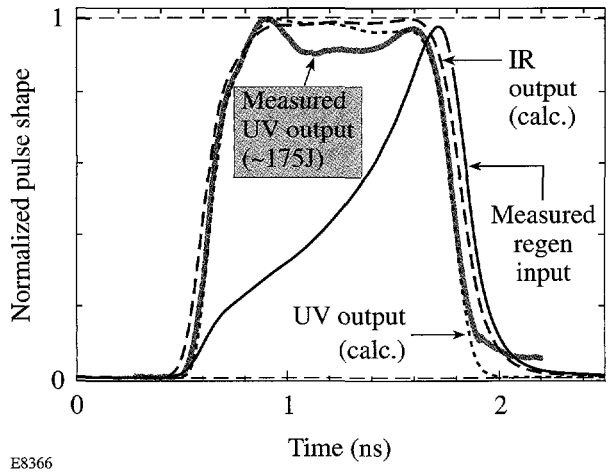

Figure 76.19
Measured and simulated UV output pulse shapes for a 10-kJ UV OMEGA laser shot. The simulated UV pulse shape uses the measured regen input pulse shape. The calculated IR pulse shape at the input to the frequency triplers is also shown.

Conclusion

In conclusion, we have developed a negative-feedback–controlled and externally synchronizable Nd:YLF regenerative amplifier capable of amplifying shaped optical pulses to the millijoule level. Long-term, shot-to-shot energy fluctuations of ~0.2% rms represent, to our knowledge, the best energy stability ever demonstrated for a millijoule-level laser system, either flash lamp pumped or diode pumped. In addition to superior stability and reproducibility, the current OMEGA regen output is very insensitive to the injected energy, and the temporal distortions due to the negative feedback are immeasurable. Four regens equipped with this negative-feedback system have operated flawlessly on OMEGA for over two years.

ACKNOWLEDGMENT

This work was supported by the U.S. Department of Energy Office of Inertial Confinement Fusion under Cooperative Agreement No. DE-FC03-92SF19460, the University of Rochester, and the New York State Energy Research and Development Authority. The support of DOE does not constitute an endorsement by DOE of the views expressed in this article.

REFERENCES

1. R. L. Keck, A. Okishev, M. D. Skeldon, A. Babushkin, and W. Seka, in *Laser Interaction and Related Plasma Phenomena*, edited by G. H. Miley and E. M. Campbell (American Institute of Physics, New York, 1997), Vol. 406, pp. 333–340.

2. R. B. Wilcox *et al.*, in *Laser Coherence Control: Technology and Applications*, edited by H. T. Powell and T. J. Kessler (SPIE, Bellingham, WA, 1993), Vol. 1870, pp. 53–63.

3. T. R. Boehly, D. L. Brown, R. S. Craxton, R. L. Keck, J. P. Knauer, J. H. Kelly, T. J. Kessler, S. A. Kumpan, S. J. Loucks, S. A. Letzring, F. J. Marshall, R. L. McCrory, S. F. B. Morse, W. Seka, J. M. Soures, and C. P. Verdon, Opt. Commun. **133**, 495 (1997).

4. W. H. Lowdermilk and J. E. Murray, J. Appl. Phys. **51**, 2436 (1980).

5. J. E. Murray and W. H. Lowdermilk, J. Appl. Phys. **51**, 3548 (1980).

6. S. C. Burkhart *et al.*, in *First Annual International Conference on Solid State Lasers for Application to Inertial Confinement Fusion*, edited by M. André and H. T. Powell (SPIE, Bellingham, WA, 1995), Vol. 2633, pp. 48–58.

7. B. M. Van Wonterghem, J. T. Salmon, and R. W. Wilcox, *ICF Annual Report 1995*, Lawrence Livermore National Laboratory, Livermore, CA, UCRL-LR-105821-95-1, 42 (1996).

8. D. L. Brown, I. Will, R. G. Roides, C. K. Merle, M. D. Skeldon, and W. Seka, in *1993 Optical Society of America Annual Meeting*, 1993 OSA Technical Digest Series, Vol. 16 (Optical Society of America, Washington, DC, 1993), p. 250.

9. I. M. Bayanov *et al.*, Sov. J. Quantum Electron. **19**, 994 (1989).

10. A. E. Siegman, *Lasers* (University Science Books, Mill Valley, CA, 1986).

11. M. D. Skeldon, A. Babushkin, W. Bittle, A. V. Okishev, and W. Seka, IEEE J. Quantum Electron. **34**, 286 (1998).

Transient Bandwidth Analysis of Photoconductive Microwave Switches Implemented in the OMEGA Pulse-Shaping System

The OMEGA laser fusion program at LLE calls for complex, temporally shaped optical pulses incident on fusion targets.[1] The pulse-duration and rise-time specifications of these optical pulses dictate an electrical pulse–shaping system bandwidth of approximately 0.1 to 10 GHz. The optical pulses are created by imprinting an electrical equivalent of the desired optical envelope onto an optical square pulse, using an integrated-optics Mach–Zehnder interferometric electro-optic modulator as shown in Fig. 76.20. The electrical pulse shape is generated by the reflection of an electrical square pulse from a distributed variable-impedance microstrip transmission line. The electrical square pulse is generated by illuminating a photoconductive semiconducting (PCS) switch in a series–gap configuration, which discharges a microstrip transmission line charged with a dc voltage. Assuming the PCS switch is saturated by the illumination, the rise time of the electrical pulse corresponds to the rise time of the optical illumination trigger pulse, and the switch conductivity remains roughly constant for the duration of the electrical pulse. The fall time is computed by convolving the rise time with the reflection impulse response of the second, unilluminated switch.[2] The resulting propagating square pulse has an amplitude of half the dc voltage and a duration of twice the charge-line's round-trip time.[3]

Measurements of the shaped electrical signal before and after the PCS switches, as shown in Fig. 76.21, indicate that the frequency response of the shaped laser pulse is strongly limited by the transmission of the shaped electrical pulse through the PCS switches. Time-gated microwave measurements of the switch attenuation did not reveal the source of the switch's bandwidth limitations.[4] In this latter case, however, the optical illumination conditions were significantly different from the actual OMEGA operating conditions, and the measurements were performed using a simple time-windowed,

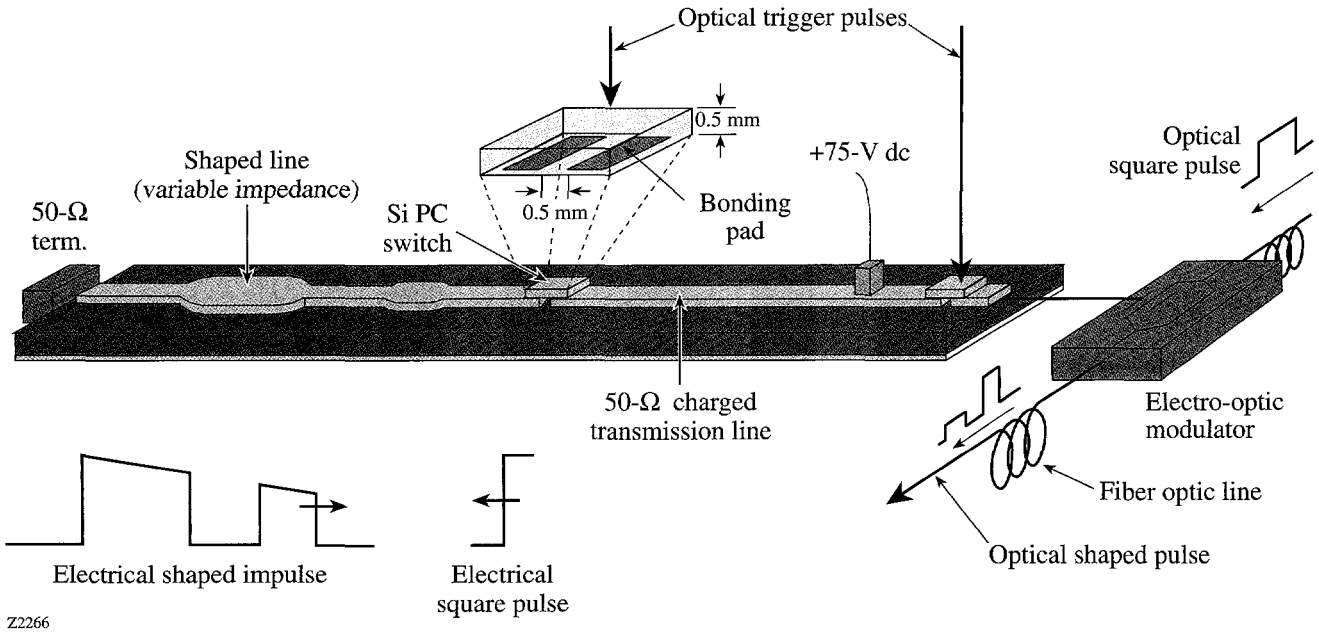

Figure 76.20
The microwave signal reflected from the shaped variable impedance line must pass through two PCS switches before reaching the electro-optic modulator.

power-detection technique. Also, phase/dispersion variations and decay of the PCS switch transmission within the measurement time window could not be detected with this technique. These limitations motivated the design and implementation of the improved measurement scheme described in this article.

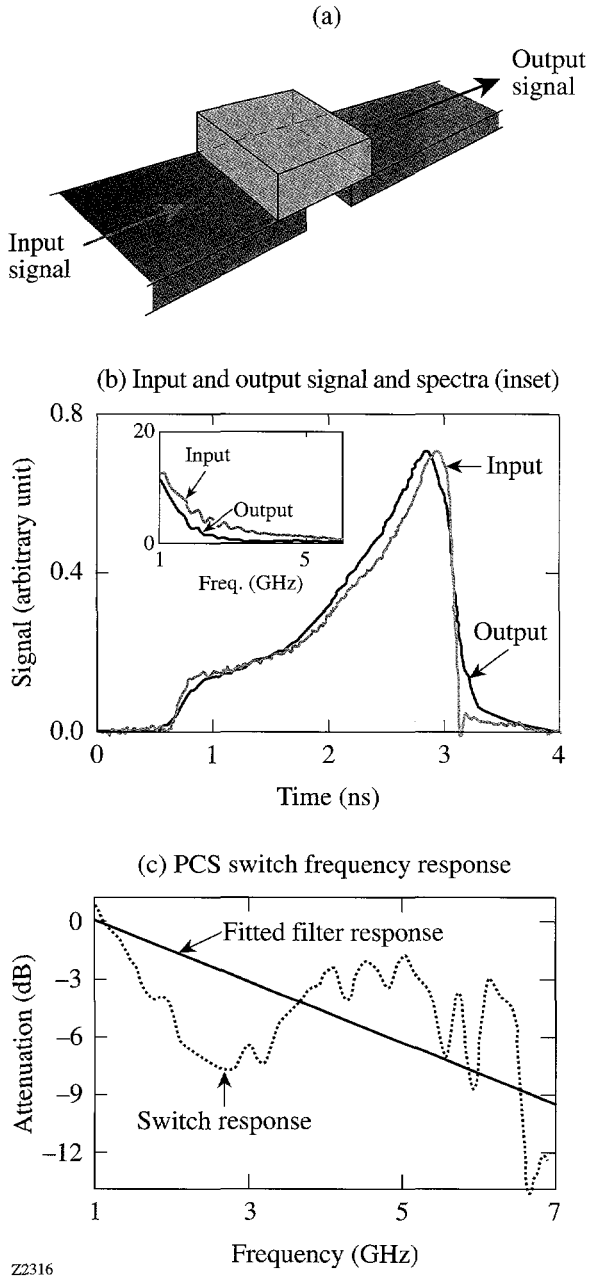

Figure 76.21
The PCS switch, microstrip line, and input and output signals are shown graphically in (a). These signals were (b) measured and their spectra found (inset). The (c) switch response was computed by a ratio of the spectra and compared to a single-pole low-pass filter.

PCS switches, unlike conventional diode or transistor microwave switches, do not operate in a steady-state "on/closed" condition. After optical illumination, the carrier recombination dynamics cause the switch transmission to decay to an "off/open" state. For example, the PCS switches used on OMEGA are typically driven to their highest (saturated) charge-carrier density by a 500-ps, 100-μJ optical pulse. After illumination, the carrier density decays monotonically, meaning that the PCS switch's on-state is transient in nature since it depends on the carrier recombination dynamics. This imposes requirements beyond the capabilities of conventional microwave test equipment (e.g., network analyzers, modulation analyzers): PCS switches as implemented in the OMEGA pulse-shaping system cannot be modeled as exclusively filters or modulators. The modulator model breaks down because PCS switches transmit signals with a bandwidth comparable to the transmission bandwidth of the switch, and they don't fit the filter model well because of their time-varying properties. Note that due to thermal damage issues at the metal–semiconductor (soldered-contact) interface, cw optical illumination for the purpose of creating a time-invariant device in the saturated regime is not possible.[5] This means that it is necessary to use transmission equations for a linear device that are more general than those for filters and modulators and to develop a measurement system capable of measuring a generalized transmission function.

We describe a method for measuring the transient complex (amplitude and phase) frequency response of a microwave device, and we give results for PCS switch measurements. These measurements were performed with PCS switch excitation conditions identical to those used on OMEGA, and over temporal durations and frequency ranges of interest to OMEGA pulse-shaping experiments. With this system, microwave devices whose transient bandwidths were previously only approximated can now be characterized and compared with a more general, multiport microwave device theory. This measurement scheme is compatible with triggerable microwave devices that have a deterministic time evolution; other examples aside from photoconductive devices are amplifier and active filter turn-on/turn-off transients and atmospheric multipath fading due to relative antenna motion.

Theoretical Background

From a linear-system viewpoint, the relationship between the input and output voltage signals of the device under test (DUT) shown in Fig. 76.22(a) is

$$V_n(\omega) = S(\omega) \cdot V_m(\omega), \tag{1}$$

where $V_m(\omega)$ and $V_n(\omega)$ are the total voltages across ports m and n and $S(\omega)$ is the DUT (filter) frequency response. Equation (1) can be Fourier transformed to

$$v_n(t) = \int_{\tau=-\infty}^{\tau=\infty} h(t-\tau)\cdot v_m(\tau)\,d\tau, \tag{2}$$

where $v_m(t)$ and $v_n(t)$ are the total instantaneous voltage signals and $h(t)$ is the impulse response.

Measurements of microwave devices conventionally involve either scalar or vector network analysis of scattering or S parameters, where $a_n(\omega)$ and $b_n(\omega)$ are the incident and scattered signals from a port n, which has a characteristic impedance Z_0, also shown in Fig. 76.22.[6] These microwave signals a and b are related to the total voltage across the port by the incident and reflected voltages V^+ and V^-:

$$a = \frac{V^+}{\sqrt{Z_0}}, \quad b = \frac{V^-}{\sqrt{Z_0}} \tag{3}$$

and are related to each other (for a two-port DUT) by the relationship

$$\begin{bmatrix} b_1 \\ b_2 \end{bmatrix} = \begin{bmatrix} S_{11} & S_{12} \\ S_{21} & S_{22} \end{bmatrix} \begin{bmatrix} a_1 \\ a_2 \end{bmatrix}. \tag{4}$$

Since the PCS switches operate in the transmission mode, we will focus on the S_{21} parameter. The S_{21} parameter relates the signal transmitted from port 2 (output) to the signal incident on port 1 (input) in the frequency domain; this relation is similar to Eq. (1) and is given by

$$b_2(\omega) = S_{21}(\omega)\cdot a_1(\omega). \tag{5}$$

The transmission parameter S_{21} is defined in the spectral domain because of the assumed linear time invariance of the DUT. The assumption of a linear time-invariant (LTI) device is only appropriate, however, when the DUT response approaches an ideal filter (i.e., does not vary in time).

A linear device such as an ideal amplitude or phase modulator is not time invariant. Modulators are typically measured with spectrum or modulation analyzers in the linear small-signal regime with narrow-band (cw) input signals, so that the assumption of an infinite-bandwidth ideal modulator introduces negligible error. The equations characterizing a modulator's input–output relationship is then exactly complementary to Eqs. (1) and (2):

$$v_n(t) = k(t)\cdot v_m(t) \tag{6}$$

$$V_n(\omega) = \int_{\xi=-\infty}^{\xi=\infty} K(\omega-\xi)\cdot V_m(\xi)\,d\xi, \tag{7}$$

where $k(t)$ and $K(\omega)$ are the modulation function and its transform.[7]

If a linear device cannot be approximated as either time invariant or as having infinite bandwidth, then none of the above equations is appropriate. Test systems that are based on these equations (such as spectrum, modulation, and network analyzers) are unable to measure the transfer function of such a device; therefore, a more general input–output relationship has been developed. This was done by recognizing that any linear device can be characterized by the generalized form of the filter and modulator Eqs. (2) and (7):

$$v_n(t) = \int_{\omega=-\infty}^{\omega=\infty} G(t,\omega)\cdot V_m(\omega)\,d\omega, \tag{8}$$

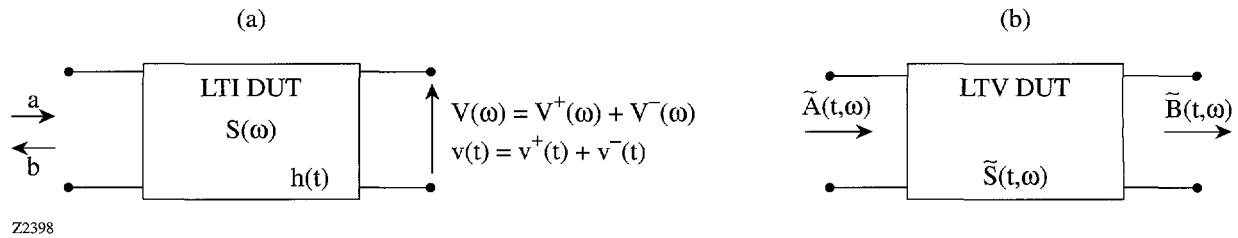

Figure 76.22
(a) Conventional LTI (filter) two-port microwave devices use a scattering matrix to define input–output relationships between the signals, while (b) LTV microwave devices relate input to output via a more general $\tilde{S}(t,\omega)$ matrix.

where $G(t,\omega)$ is the (more general) input–output relation, now a function of both time and frequency.[8] This function $G(t,\omega)$ has a simple extension to conventional microwave measurements if it is viewed as a generalized $S(\omega)$ parameter and renamed $\tilde{S}(t,\omega)$, as shown in Fig. 76.22(b). The input–output transmission function is similar to Eq. (5):

$$\tilde{B}_2(t;\omega) = \tilde{S}_{21}(t,\omega)\cdot\tilde{A}_1(t;\omega), \tag{9}$$

where $\tilde{A}$ and $\tilde{B}$ are joint time-frequency distributions of one-dimensional functions (indicated by the semicolon between the variables) related to v^+ and v^- by the Wigner time-frequency (WTF) distribution[9]

$$\tilde{A}(t;\omega) = \frac{1}{Z_0}\int_{-\infty}^{\infty} v^+(t+\tau/2)\,v^{+*}(t-\tau/2)\,e^{-j\omega\tau}d\tau, \tag{10}$$

and $\tilde{B}$ is defined similarly for v^-.

This input–output relationship of Eq. (9) is simpler than the integral function of Eq. (8) and has the further advantage that in the microwave regime the signals a and b are more easily measured than the total transmission-line voltages $V_m(\omega)$ and $v_n(t)$. Any $\tilde{S}$ parameter can be determined from Eq. (9) and from measurements of the input and output microwave signals at the appropriate ports. For example, in a two-port microwave device such as a PCS switch, if the microwave signal is incident on port 1 and the response measured at port 2, the $\tilde{S}_{21}$ parameter can be determined by dividing the WTF distribution of the output (port 2) signal by the WTF distribution of the input (port 1) signal. Comparing Eqs. (9), (1), and (5), the parameter $\tilde{S}_{21}(t,\omega)$ can be seen as a time-varying frequency response $S(\omega)$.

Note that $\tilde{S}$ is the (complex) time-varying frequency response of the microwave device and is to be distinguished from the time-varying spectrum of a signal $\tilde{A}$, a joint time-frequency distribution generated from a one-dimensional (complex) signal by Eq. (10). To make this difference between $\tilde{A}$ and $\tilde{S}$ apparent, one can Fourier transform $\tilde{S}$ in the second variable (ω to τ), which results in $\tilde{S}(t,\tau)$. A magnitude surface plot of this two-dimensional function shows the temporal change of the impulse response "$h(\tau)$" with time t. In contrast, transforming $\tilde{A}$ in either variable will result in a surface plot of a one-dimensional function multiplied by itself along each axis, i.e., if $\tilde{A}(t;\omega)$ was Fourier transformed in the second variable (ω to τ), the resulting function $\tilde{A}(t;\tau)$ would by definition be proportional to $v^+(t)\cdot v^+(\tau)$. This is simply $v^+(t)$ multiplied by itself in the second, dummy variable τ and therefore not a function of two independent variables, as $\tilde{S}(t,\tau)$ is. Thus, the time-varying bandwidth $\tilde{S}$ of a device is distinct from the time-varying spectrum of a signal $\tilde{A}$.[10,11]

Experimental Design

The system we created to measure the time and frequency variations of the switch's transfer function is based on a microwave interferometric measurement and is shown in block-diagram form in Fig. 76.23. The DUT for which we measure the two-dimensional transfer function $\tilde{S}(t,\omega)$ is shown at the center of the figure (in our case, a PCS switch). The DUT is triggered (in our case, by a laser pulse), causing a single-frequency microwave signal of known power and phase from the microwave generator to propagate through the DUT and also through a separate, parallel reference arm consisting of an amplifier and a phase shifter. The two arms, after splitting at the directional coupler, are recombined and compared to one another in amplitude (at the diode detectors) and phase (at the mixer/phase detector). Alternatively, the signal from each arm can be measured directly by an oscilloscope of sufficiently high bandwidth and subsequently compared. Both measurements are shown in Fig. 76.23. The timing system synchronizes the triggering of the DUT with the phase of the microwave signal incident on it, so that each trigger occurs at the same phase of the microwave signal. This allows sampling oscilloscope measurements, which improves the measurement resolution over single-shot digitizing oscilloscopes.

The signal-measurement process proceeds in the following step-and-dwell manner: The microwave generator is set to a single given frequency of known phase and amplitude. The DUT is then triggered, and the evolution of the transmitted signal is measured and compared with the reference arm signal for the temporal duration of interest. The microwave generator then steps to the next microwave frequency, and the process repeats for the range of frequencies of interest. The recorded data is then reduced to two sets of complex (amplitude and phase), two-dimensional arrays of incident and transmitted signals corresponding to $\tilde{A}$ and $\tilde{B}$. Using Eq. (9) we calculate the transfer function $\tilde{S}(t,\omega)$, which can then be analyzed for bandwidth and modulation features. For a PCS switch, the transfer function is expected to show an exponentially decaying modulation due to carrier recombination and a (possibly changing) bandwidth, which can be modeled by a lumped-element circuit consisting, in general, of a time-changing reactance and a time-changing resistance. The values of these elements can then be associated with switch properties such as carrier lifetime, non-ohmic contacts, thickness and gap length,

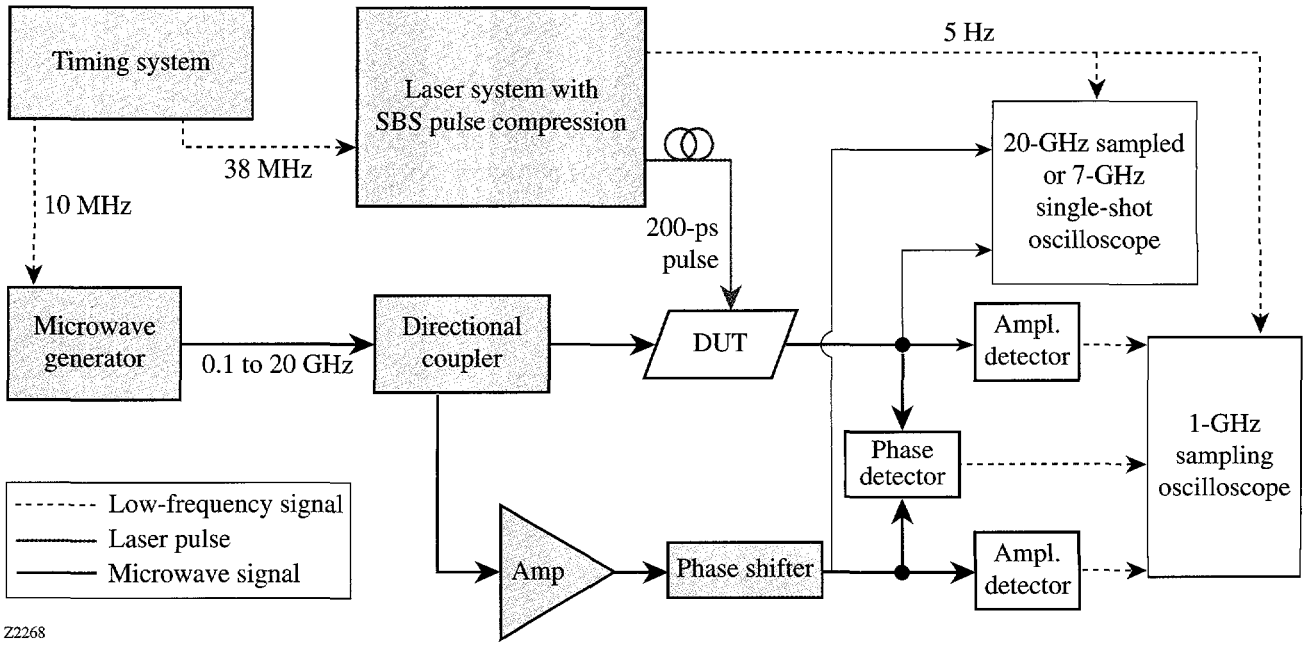

Figure 76.23
Signal flow of system capable of analyzing transient-bandwidth devices.

and the bandwidth of the switch can be optimized by appropriately modifying these switch properties. For example, the metal–semiconductor interface can be made Schottky or ohmic-like by selective ion implantation and dopant diffusion, which affects carrier recombination, surface velocity, trapping states, and contact resistance. Switch thickness and switch-gap width and length will affect capacitive coupling and series resistance and should be selected so as to minimize the switch RC time constant and maximize photon absorption.

Experimental Results

A representative magnitude plot of the two-dimensional transfer function $\tilde{S}(t,\omega)$ of a PCS switch is shown in Fig. 76.24. As explained in the **Theoretical Background** section, $\tilde{S}(t,\omega)$ is necessary to describe the transmission response of a PCS switch [$S(\omega)$ is inadequate] because the switch modulates a signal whose spectral content is comparable to its bandwidth. Features of the transfer function, such as the conductive carrier decay along the temporal axis and frequency-dependent attenuation along the spectral axis due to bandwidth limitations, are readily observed. By numerically fitting a linear lumped-element model having both filtering and modulating components to the measured transfer function, values of various microwave components can be extracted. The fitted model, shown in Fig. 76.25, is a simple low-pass filter in series with an exponentially decaying resistive element. The switch's 3-dB bandwidth is approximately 5 GHz, which agrees well with the observed bandwidth loss of shaped pulses propagating through the OMEGA pulse-shaping system (Fig. 76.26).

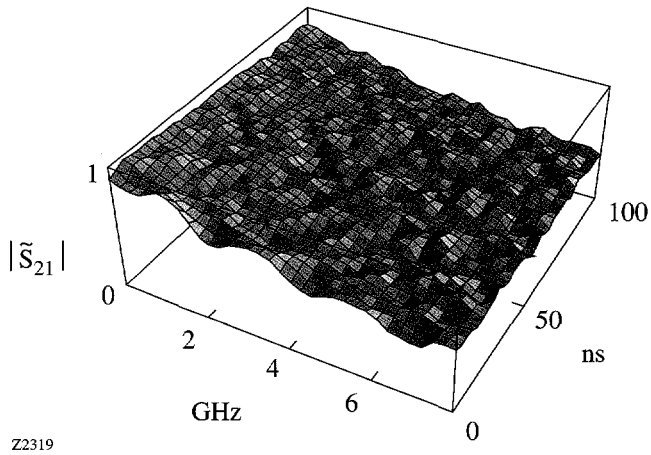

Figure 76.24
Measured $\tilde{S}_{21}(t,\omega)$ shows carrier decay along the temporal axis and bandwidth limitations along the spectral axis.

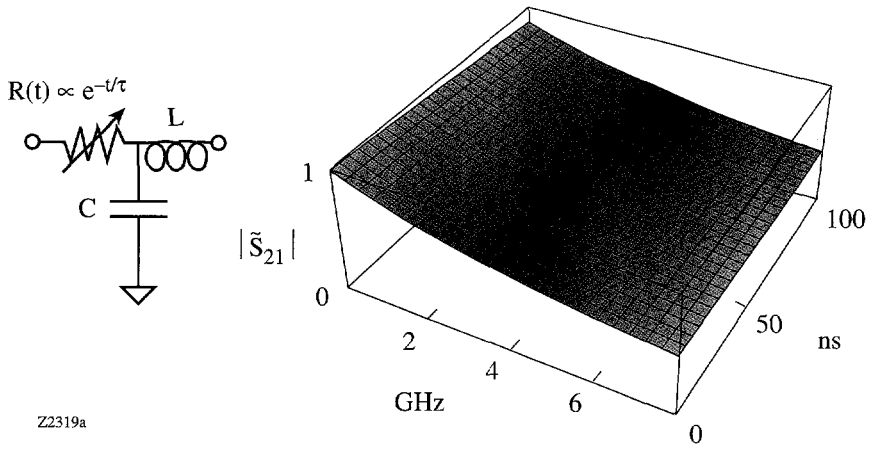

Figure 76.25
Modeled $\tilde{S}_{21}(t,\omega)$ accurately fits an exponentially decaying resistance in series with a low-pass filter to the measured data.

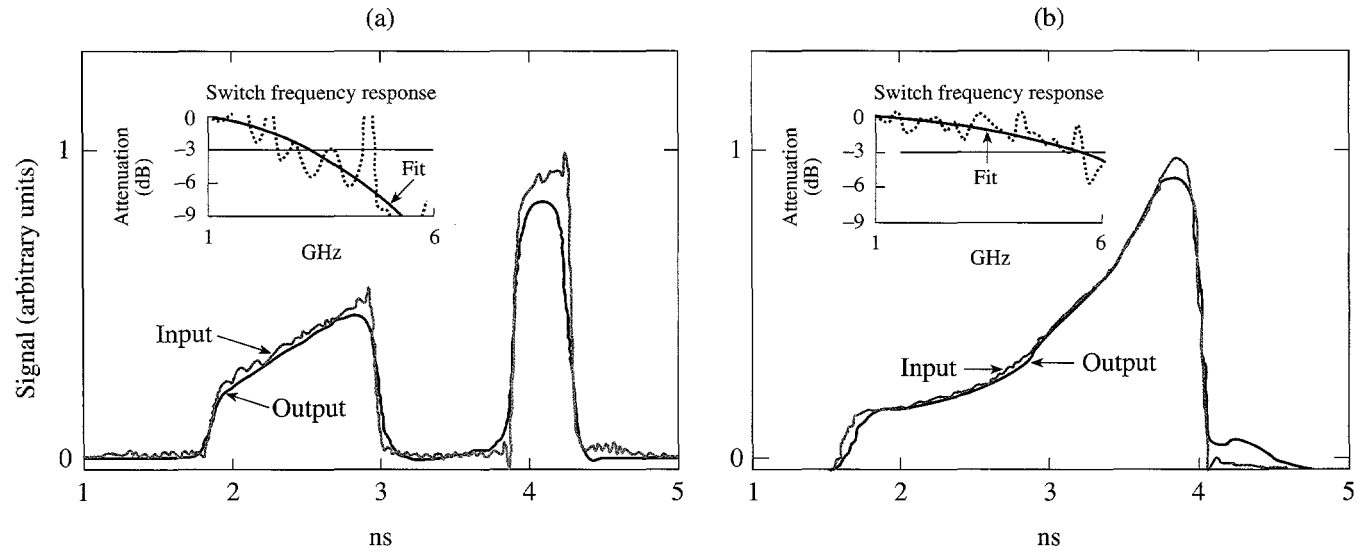

Figure 76.26
By optimizing switch parameters, transmission bandwidth on OMEGA pulse shaping has been improved from (a) mid-1995, the beginning of OMEGA's pulse shaping, to (b) early 1998.

Conclusions

Measurements of optical and electrical temporal pulse shapes at different locations in our pulse-shaping system indicate that the primary bandwidth limitations occur during transmission of our electrical pulse shapes through the PCS switches. When pulse shaping was first implemented on OMEGA, the measured attenuation at 10 GHz (corresponding to 30-ps pulse rise- and fall-times) was more than 12 dB through the switch, and the 3-dB bandwidth was near 3 GHz. This frequency response is significantly worse than the other components in the pulse-shaping system: e.g., microstrip transmission line, connectors, and electro-optic modulator. Modeling of photoconductive switches[12] indicates that a much larger bandwidth is theoretically possible; thus, efforts were taken to isolate and comprehensively measure the microwave transmission bandwidth of our PCS switches. This characterization made possible the systematic optimization of the many parameters of the switch, such as gap length, microwave skin depth versus optical absorption depth, and metal–semiconductor contact preparation. Since conventional network analyzers were incapable of determining the bandwidth of a device that varied in time, a measurement system was designed and built

tailored to such time-varying devices. This measurement system allowed determination of the relationship between the properties of the switch and its frequency response characteristics. By improving the physical switch properties, the 3-dB bandwidth of the OMEGA pulse-shaping PCS switches has been increased to over 5 GHz. The full bandwidth of the implemented PCS switches is now as broad as the next-most-limiting device in the pulse-shaping system (believed to be the electro-optic modulator) and is sufficient for current OMEGA optical-pulse-shape requirements.

ACKNOWLEDGMENT

This work was supported by the U.S. Department of Energy Office of Inertial Confinement Fusion under Cooperative Agreement No. DE-FC03-92SF19460 and the University of Rochester. The support of DOE does not constitute an endorsement by DOE of the views expressed in this article. The author also acknowledges the support of the Frank Horton Graduate Fellowship Program.

REFERENCES

1. M. D. Skeldon, A. Okishev, S. A. Letzring, W. R. Donaldson, K. Green, W. Seka, and L. Fuller, in *Optically Activated Switching IV*, edited by W. R. Donaldson (SPIE, Bellingham, WA, 1994), Vol. 2343, pp. 94–98.
2. G. H. Owyang, *Foundations for Microwave Circuits* (Springer-Verlag, New York, 1989).
3. S. C. Burkhart and R. B. Wilcox, IEEE Trans. Microwave Theory Tech. **38**, 1514 (1990).
4. K. Green, W. R. Donaldson, R. Sobolewski, A. Okishev, M. D. Skeldon, S. A. Letzring, and W. Seka, in *First Annual International Conference on Solid State Lasers for Application to Inertial Confinement Fusion*, edited by M. André and H. T. Powell (SPIE, Bellingham, WA, 1995), Vol. 2633, pp. 615–621.
5. W. C. Nunnally, in *High-Power Optically Activated Solid-State Switches*, edited by A. Rosen and F. Zutavern (Artech House, Boston, 1994), pp. 29–42.
6. K. Kurokawa, IEEE Trans. Microw. Theory Tech. **MTT-13**, 194 (1965).
7. H. D'Angelo, *Linear Time-Varying Systems: Analysis and Synthesis*, The Allyn and Bacon Series in Electrical Engineering (Allyn and Bacon, Boston, 1970).
8. L. A. Zadeh, J. Appl. Phys. **21**, 642 (1950).
9. M. A. Poletti, J. Audio Eng. Soc. **36**, 457 (1988).
10. D. J. Kane and R. Trebino, Opt. Lett. **18**, 823 (1993).
11. F. T. S. Yu and G. Lu, Appl. Opt. **33**, 5262 (1994).
12. S. S. Gevorgian, IEE Proc. J, Optoelectron. **139**, 153 (1992).

Simulations of Near-Field Intensity Modulations in High-Intensity Laser Beams due to Self- and Cross-Phase Modulation Between Orthogonally Polarized Laser Beams Emerging from a Diamond-Turned KDP Wedge

The near-field intensity modulation due to a diamond-turned KDP wedge is investigated through computer simulations within the framework of its application to LLE's OMEGA laser system. KDP wedges will be installed on each OMEGA beamline and mounted 12 m away from the final focusing optics. The wedges will improve the direct-drive inertial confinement fusion uniformity by a process known as polarization smoothing. Diamond turning is the finishing process of choice due to the greater cost incurred by installing polished KDP crystals on every beamline.

The Nova laser facility at the Lawrence Livermore National Laboratory (LLNL) reported blast-shield damage that was linked to the mid-range spatial wavelengths (1 to 4 mm) of scratch marks on diamond-turned KDP crystals in use at the time. This motivated LLE to employ polished KDP crystals for frequency tripling on OMEGA during its 24- to 60-beam upgrade (completed in 1995) because polishing produces a smoother distribution of spatial wavelengths of lower amplitude. While diamond-turning technology has improved recently, residual concern has existed regarding the potential damaging effects of installing diamond-turned KDP crystals. This has prompted an investigation, both theoretical and experimental, into the potential effects of the scratch or milling marks left behind by diamond turning.

This article represents part of the theoretical investigation of this problem. In particular, the simulations model the nonlinear effects that result from (1) the beam propagation through the 12 m of air that separates the KDP wedge from the final focusing optics, (2) the initial phase perturbation of the beam due to the residual scratch marks on the diamond-turned KDP surface, and (3) the nonlinear index's polarization dependence. The danger here is that small-scale self-focusing might develop high-intensity spikes leading to filamentation damage in the final focusing optics. The simulations reported here demonstrate that KDP wedges, diamond-turned or smooth, are not a significant source of intensity modulation under OMEGA laser conditions. In addition, for a beam with a varying polarization state, these simulations exhibit an intensity enhancement in the vicinity of linear polarization due to the nonlinear effect of cross-phase modulation.

Diamond-Turned KDP Wedge

1. Polarization Smoothing

The concept of polarization smoothing originated from Kato[1] who recognized the uniformity that would result from rotating the polarization through 90° on half of the individual phase-plate elements chosen at random. A more practical device, first described in Ref. 2, is a wedge of birefringent material such as KDP. A linearly polarized beam incident upon the KDP wedge is split into two orthogonally polarized beams of equal intensity when the incident beam's polarization vector is oriented at 45° with respect to the slow and fast axes of the crystal (see Fig. 76.27). The resultant two orthogonal beams co-propagate at a slight angle of separation with respect to each other, determined by the wedge angle and the refractive indexes for the slow and fast waves. The current requirements for OMEGA set the wedge angle to 4.5 min. This causes a separation angle of 44 μrad between the two orthogonal beams and a relative offset of 80 μm after focusing on target. The relative offset of 80 μm achieves an instantaneous theoretical $1/\sqrt{2}$ reduction of the nonuniformity through spatial averaging, which complements the uniformity achieved by SSD alone.[3]

As a consequence of the separation angle, the combined polarization state of the two orthogonally polarized beams continuously cycles through all elliptical states along any transverse plane. The rate of change is determined by the transverse components of the wave vectors. Since the separation angle is small, the wavelength of the cycle is given by

$$\lambda_{\mathrm{pol}} = \frac{\lambda}{\sin(\theta)} = \frac{351\ \mathrm{nm}}{\sin(44\ \mu\mathrm{rad})} = 8\ \mathrm{mm}, \qquad (1)$$

where $\lambda = 351$ nm is the UV operating wavelength of OMEGA. The resultant $\lambda_{\mathrm{pol}} = 8$ mm is the transverse distance required to cycle the polarization state from right-handed circular, to

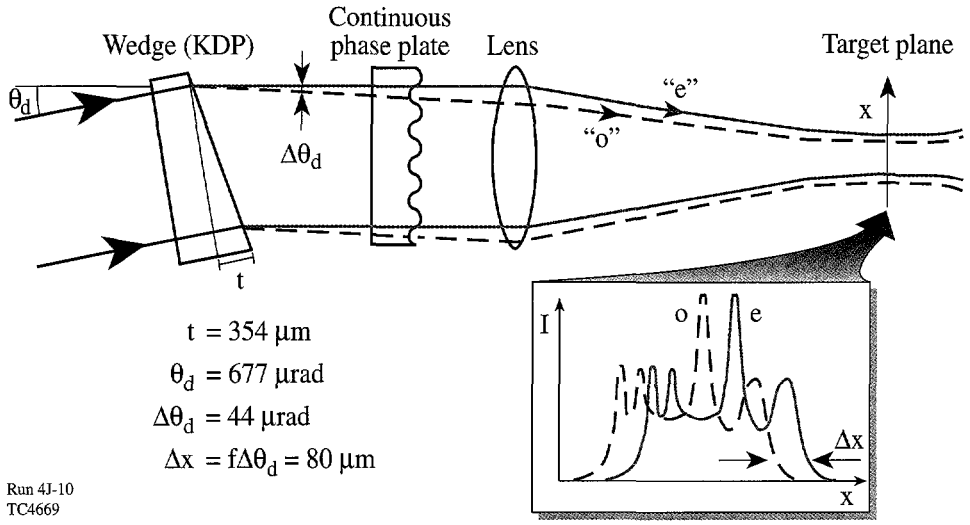

Figure 76.27
A birefringent KDP wedge achieves polarization smoothing and a theoretical $1/\sqrt{2}$ reduction in nonuniformity.

linear, to left-handed circular, back to linear, and returning to right-handed circular.

2. Induced Phase Perturbations

Two types of phase perturbation result from the introduction of a diamond-turned KDP wedge. The first is due to the residual scratch marks left behind by the diamond-turning process. The scratch marks cause a beam to acquire a pseudorandom phase perturbation as the beam passes through the front and back faces of the crystal. The pseudorandom phase perturbation can be described by a thin-optic transformation

$$\Phi_{\text{mill}} = k_0\left(n_{\text{KDP}} - 1\right) S(y), \tag{2}$$

where $S(y)$ is the depth of the scratch mark as a function of the transverse position y, $k_0 \equiv 2\pi/\lambda$ is the vacuum wave number, and n_{KDP} represents the refractive index for either the slow or fast wave.

The second type of phase perturbation arises during propagation because the nonlinear refractive index is a function of polarization state and intensity (see subsection 1 of the **Ellipticity** section) together with the fact that the KDP wedge produces a beam whose combined polarization state varies as a function of transverse position y. The nonlinear refractive index is a maximum for linear polarization and a minimum for circular polarization. Therefore, both orthogonally polarized beams accumulate a periodic phase perturbation during propagation that is greatest in the vicinity of linear polarization.

Both types of phase perturbation affect the beams by introducing spatial phase modulation that can then be converted into intensity modulation by virtue of the diffractive process that occurs during propagation. Intense beams can develop high-intensity spikes leading to filamentation damage through the coupled process of phase modulation and diffraction.

3. Model of Scratch Marks

The pseudorandom behavior of the residual scratch marks is modeled in this article by bandpass filtering a white noise source, viz.

$$S(y) = \mathcal{F}^{-1}\left\{\mathcal{F}\left[\Xi(y)\right] \bullet \text{rect}\left(\frac{k_y - k_{y_0}}{k_{y_{\max}} - k_{y_{\min}}}\right)\right\},$$

$$\text{rect}(x) = \begin{cases} 1; & |x| \le \dfrac{1}{2} \\ 0; & |x| > \dfrac{1}{2} \end{cases}, \tag{3}$$

where $\mathcal{F}$ represents the spatial Fourier transform, $\Xi(y)$ is the noise source, k_{y_0} is the central spatial wave number, and $k_{y_{\max}}$ and $k_{y_{\min}}$ represent the maximum and minimum passed spatial wave numbers. This result is sometimes referred to as "colored" noise.[4] Figure 76.28 illustrates an example in which the passband was set to $2\pi/(4\text{ mm}) \le k_y \le 2\pi/(2\text{ mm})$. These data are used in the subsequent illustrative numerical simulations given in the **Numerical Results** section. This passband was selected since it covers the troublesome spatial frequencies identified by LLNL. Also, these data closely resemble surface profile measurements on a qualitative basis. An alternative function that completely describes the power spectral density of the scratch marks could be used in place of the

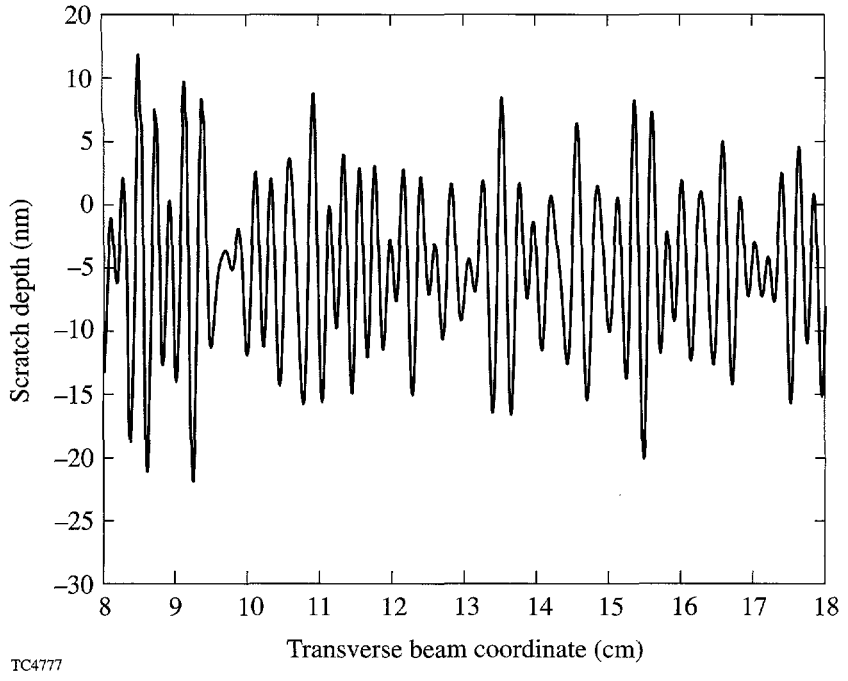

Figure 76.28
A bandpass-filtered pseudorandom noise source where the passband is set to $2\pi/(4\text{ mm}) \le k_y \le 2\pi/(2\text{ mm})$ and the peak-to-valley scratch depth is 40 nm.

rect(k_y) function. However, an adequate statistical description of the diamond-turned scratch marks is unavailable at this time. The rect(k_y) can be viewed as a worse-case situation that emphasizes the higher spatial frequencies since the actual power spectral density would go to zero in a continuous manner as the spatial frequency increases.

Nonlinear Wave Equation

The analysis of beam propagation for this problem assumes that the optical field is monochromatic and the bandwidth of the spatial spectrum is small relative to the vacuum wave number $k_0 = \omega_0/c$, where ω_0 is the angular frequency and c is the vacuum speed of light. This permits the slowly varying amplitude to be separated from the rapidly varying part, such that the electric field vector is given by

$$\mathbf{E}(y,z,t) = \frac{1}{2}\left[\hat{\mathbf{p}}E(y,z)e^{-i(\omega_0 t - k_0 n_0 z)} + c.c.\right], \tag{4}$$

where $E(y,z)$ is the slowly varying complex amplitude as a function of both the transverse distance y and propagation distance z, $\hat{\mathbf{p}}$ is the polarization vector, n_0 is the refractive index, and *c.c.* indicates the complex conjugate. An arbitrary elliptical polarization state decomposes naturally into a weighted vector sum of right-handed and left-handed circular polarization states, viz.

$$\begin{aligned}\mathbf{E}(y,z,t) &= \frac{1}{2}\left\{\left[\hat{\mathbf{p}}_{\mathrm{RH}}E_{\mathrm{RH}}(y,z) + \hat{\mathbf{p}}_{\mathrm{LH}}E_{\mathrm{LH}}(y,z)\right]e^{-i(\omega_0 t - k_0 n_0 z)}\right. \\ &\quad \left. + c.c.\right\},\end{aligned} \tag{5}$$

where $E_{\mathrm{RH}}(y,z)$ and $E_{\mathrm{LH}}(y,z)$ are the complex amplitudes of the right-handed and left-handed circular polarization states, which are defined in terms of Cartesian components as

$$\begin{aligned}E_{\mathrm{RH}}(y,z) &= \frac{1}{\sqrt{2}}\left[E_x(y,z) - E_y(y,z)\right], \\ E_{\mathrm{LH}}(y,z) &= \frac{1}{\sqrt{2}}\left[E_x(y,z) + E_y(y,z)\right],\end{aligned} \tag{6}$$

and the polarization vectors are defined as

$$\hat{\mathbf{p}}_{\mathrm{RH}} \equiv \frac{1}{\sqrt{2}}\left(\hat{\mathbf{x}} + i\hat{\mathbf{y}}\right), \qquad \hat{\mathbf{p}}_{\mathrm{LH}} \equiv \frac{1}{\sqrt{2}}\left(\hat{\mathbf{x}} - i\hat{\mathbf{y}}\right). \tag{7}$$

The optical field is assumed to propagate in a lossless, isotropic nonlinear Kerr-like medium, where the nonlinear refractive index is given by

$$n = n_0 + \Delta n. \tag{8}$$

The quantity Δn represents the change in the refractive index beyond the low-intensity value n_0 and exhibits a linear dependence on the optical field intensity. The scalar nonlinear wave equation for each vector component is then given by

$$\frac{\partial E_{\mathrm{RH}}(y,z)}{\partial z} = \frac{i}{2k}\nabla_T^2 E_{\mathrm{RH}}(y,z) + ik_0\,\Delta n_{\mathrm{RH}}\,E_{\mathrm{RH}}(y,z), \tag{9}$$

$$\frac{\partial E_{\mathrm{LH}}(y,z)}{\partial z} = \frac{i}{2k}\nabla_T^2 E_{\mathrm{LH}}(y,z) + ik_0\,\Delta n_{\mathrm{LH}}\,E_{\mathrm{LH}}(y,z), \tag{10}$$

where $k = k_0 n_0$ and[5]

$$\Delta n_{\mathrm{RH}} = \frac{3}{4n_0}\left[\chi^{(3)}_{xyxy}\left|E_{\mathrm{RH}}(y,z)\right|^2 + \left(\chi^{(3)}_{xyxy} + \chi^{(3)}_{xxyy}\right)\left|E_{\mathrm{LH}}(y,z)\right|^2\right], \tag{11}$$

$$\Delta n_{\mathrm{LH}} = \frac{3}{4n_0}\left[\chi^{(3)}_{xyxy}\left|E_{\mathrm{LH}}(y,z)\right|^2 + \left(\chi^{(3)}_{xyxy} + \chi^{(3)}_{xxyy}\right)\left|E_{\mathrm{RH}}(y,z)\right|^2\right], \tag{12}$$

and it has been assumed that $\partial^2 E(y,z)/\partial z^2 = 0$, i.e., the slowly varying envelope approximation. The first terms in Eqs. (11) and (12) represent self-phase modulation, and the second group of terms represents cross-phase modulation. The vector components are coupled through the cross-phase modulation terms. Due to the symmetry of centrosymmetric Kerr-like media and the fact that both vector components share the same frequency ω_0, there are only two independent third-order susceptibility constants $\chi^{(3)}_{xyxy}$ and $\chi^{(3)}_{xxyy}$ that obey the relation $\chi^{(3)}_{xxxx} = 2\chi^{(3)}_{xyxy} + \chi^{(3)}_{xxyy}$ and follow the frequency convention $\chi^{(3)}_{xyxy}(-\omega,-\omega,\omega,\omega)$. (Notice that it is this convention that causes the subtle notational deviation from that of Sutherland.[5]) Either scalar nonlinear wave equation, Eq. (9) or Eq. (10), can be written in operator form as[6]

$$\frac{\partial E(y,z)}{\partial z} = \left(\hat{D} + \hat{N}\right)E(y,z), \tag{13}$$

where the operator $\hat{D}$ accounts for diffraction and is defined as

$$\hat{D} \equiv \frac{i}{2k}\nabla_T^2, \tag{14}$$

the operator $\hat{N}$ governs media nonlinearities and is defined as

$$\hat{N} \equiv ik_0\Delta n, \tag{15}$$

the quantity $E(y,z)$ represents either the right-handed or left-handed complex amplitude, and Δn represents either Eq. (11) or Eq. (12). The formally exact solution of Eq. (13) is given by

$$E(y,z+\Delta z) = e^{i(\hat{D}+\hat{N})\Delta z}\,E(y,z).$$

An important merit of decomposing an arbitrary elliptical polarization state into right-handed and left-handed circular polarization states is that

$$\frac{\partial\left|E_{\mathrm{RH}}(y,z)\right|^2}{\partial z} = 0 \quad \text{and} \quad \frac{\partial\left|E_{\mathrm{LH}}(y,z)\right|^2}{\partial z} = 0.$$

This implies that the intensities of the vector components and therefore the quantity Δn are all constants of motion. This is not true for a Cartesian decomposition, due to the well-known cross-phase modulation effect of ellipse rotation, which causes the magnitudes along the Cartesian components to change with propagation distance.[7]

1. Ellipticity and the Nonlinear Refractive Index

The ellipticity parameter η covers the range $-\pi/4 \le \eta \le \pi/4$, where $\tan(\eta)$ describes the ratio of the minor and major axes of the polarization ellipse with the sign defining its handedness [positive (+) indicates right-handed and negative (–) indicates left-handed].[7] When $\eta = 0$, the polarization state is linear and, when $|\eta| = \pi/4$, the polarization state is circular. Equations to calculate the lengths of the major and minor axes can be found in Oughstun[8] (see Ref. 8, Sec. 4.2.1) and are governed by the complex amplitudes $E_{\mathrm{RH}}(y,z)$ and $E_{\mathrm{LH}}(y,z)$. Consequently, the ellipticity parameter η is also a function of the complex amplitudes $E_{\mathrm{RH}}(y,z)$ and $E_{\mathrm{LH}}(y,z)$. The quantities Δn_{RH} and Δn_{LH} depend on the magnitudes $\left|E_{\mathrm{RH}}(y,z)\right|$ and $\left|E_{\mathrm{LH}}(y,z)\right|$ and are indirectly functions of the polarization state.

The extrema of the quantities Δn_{RH} and Δn_{LH} occur when the polarization state is either linear or circular. If the polarization state is linear, then $|E_{lin}|^2 = 2|E_{LH}|^2 = 2|E_{RH}|^2$ (where the factor of 2 comes from the equal intensity split into both polarization states), and the change in the nonlinear refractive index becomes

$$\Delta n_{lin} = \frac{3}{8n_0}\left[\chi^{(3)}_{xxyy} + 2\chi^{(3)}_{xyxy}\right]|E_{lin}|^2 . \quad (16)$$

If the polarization state is circular, either right-handed or left-handed, then

$$\Delta n_{cir} = \frac{3}{4n_0}\chi^{(3)}_{xyxy}|E_{cir}|^2 . \quad (17)$$

In either of these two degenerate states $|E_{lin}|^2 = |E_{cir}|^2$ so that

$$\Delta n_{lin} > \Delta n_{cir} . \quad (18)$$

In a more general sense, the nonlinear refractive index is larger in the vicinity surrounding, or in the immediate neighborhood of, the points of linear polarization relative to the minimum values attained at the points of right-handed or left-handed circular polarization.

2. Angular Spectrum Representation

If nonlinear effects can be neglected, the vector components become decoupled and obey the scalar Helmholtz wave equations given by

$$\nabla^2 E(y,z) + k_0^2 n^2 E(y,z) = 0, \quad (19)$$

which has an exact solution at any exit plane $z + \Delta z$ given by the angular spectrum representation (see Ref. 9, Sec. 3.7), viz.

$$E(y, z+\Delta z) = \frac{1}{2}\pi \int_{-\infty}^{\infty} \tilde{E}(k_y, z) e^{i\Delta z\sqrt{k_0^2 n^2 - k_y^2}}\, e^{ik_y y} dk_y , \quad (20)$$

where $\tilde{E}(k_y, z)$ is the spatial Fourier transform at the entrance plane z and is defined by

$$\tilde{E}(k_y, z) = \int_{-\infty}^{\infty} E(y,z) e^{-ik_y y} dy . \quad (21)$$

3. Self- and Cross-Phase Modulation

If diffraction can be neglected, the scalar nonlinear wave equation for either vector component has the simple form

$$\frac{\partial E(y,z)}{\partial z} = \hat{N} E(y,z), \quad (22)$$

which has a solution given by

$$E(y, z+\Delta z) = E(y,z) e^{ik_0 \Delta n \Delta z} , \quad (23)$$

because the quantity Δn is not a function of the propagation distance for a circular-polarization decomposition. As a result, the nonlinear effects of self- and cross-phase modulation, acting alone, induce a simple phase accumulation that is a function of both the polarization state and intensity. This is a generalization of the well-known B-integral.

Numerical Approach

The numerical split-step Fourier method (see Ref. 6, Sec. 2.4.1) is used to solve the differential Eq. (13), where the total required distance of propagation is divided into small steps over which the linear effects of diffraction are treated separately from the nonlinear effects of self- and cross-phase modulation. This permits the solutions given by Eqs. (20) and (23) to be used if the chosen step size is sufficiently small that the linear and nonlinear effects are approximately independent over that step.

The numerical calculation over one small step Δz is referred to as a propagation step. One propagation step entails the independent calculation of diffraction using the results of Eq. (20) and the independent calculation of the nonlinear phase accumulation as described by Eq. (23). The detailed manner in which this is carried out greatly affects the overall error achieved and directly affects the required number of steps needed to obtain a suitable level of accuracy. For example, if a full diffraction step is followed by a full nonlinear step, the error is $O\{\Delta z^2\}$, which is equivalent to solving Eq. (13) as

$$E(y, z+\Delta z) \cong e^{i\Delta z \hat{D}} e^{i\Delta z \hat{N}} E(y,z). \quad (24)$$

However, if a half diffraction step is followed by a full nonlinear step and then by another half diffraction step, the error is $O\{\Delta z^3\}$, which is equivalent to solving Eq. (13) as

$$E(y, z+\Delta z) \cong e^{i\frac{\Delta z}{2}\hat{D}} e^{i\Delta z \hat{N}} e^{i\frac{\Delta z}{2}\hat{D}} E(y,z). \quad (25)$$

The errors associated with Eqs. (24) and (25) are found by comparing these approximate solutions to the formally exact

solution to Eq. (13) and applying the Baker–Hausdorff formula for two noncommuting operators.[6] The method described by Eq. (25), known as the symmetrized split-step Fourier method, is employed for the numerical simulations in the subsequent section. Figure 76.29 graphically represents this particular approach over two small steps of Δz.

Numerical Results

The intent of this investigation is to isolate the effects caused by the nonlinear propagation in air, the scratch marks, and the wedged shape of the KDP crystal, while ignoring the nonlinear index of KDP. To this end, only the exit face of the KDP crystal is considered to be scratched, and the initial beam shape is regarded as infinitely smooth. As a consequence, the nonlinear ripple growth within the KDP crystal can be neglected.

The beam shape is modeled by using spatially offset hyperbolic-tangent step functions, viz.

$$E(y) = \frac{1}{2}\left\{\tanh\left[100(y+0.14)\right] - \tanh\left[100(y-0.14)\right]\right\}, \quad (26)$$

which yields an infinitely smooth, 28-cm-diam beam. The nominal intensity level for OMEGA equal to 1.3 GW/cm^2 is used. Also, an unrealistic value of 10.3 GW/cm^2 is used to demonstrate a regime where the nonlinear effects dominate since, as it will be shown, the nonlinear effects are small for the nominal OMEGA intensity level. The measure of intensity modulation used in this paper is the contrast defined as

$$\text{Contrast} = \frac{\max\{I(y)\}}{\text{mean}\{I(y)\}}, \quad (27)$$

where the transverse position y, for this formula only, covers the region where $I(y)$ was initially at full value; thus, the region where the beam intensity tapers to zero is not considered for this statistic.

1. Material Parameters

The material parameters used in the simulations are given in this subsection. The linear refractive indices for the KDP crystal are $n_{\text{KDP}_o} = 1.532498$ for the ordinary wave and $n_{\text{KDP}_e} = 1.498641$ for the extraordinary wave, which propagates at 59° to the optic axis. The third-order nonlinear susceptibility constants for air are

$$\chi^{(3)}_{xyxy}(-\omega,-\omega,\omega,\omega) = 28.16 \times 10^{-19} \text{ esu}$$

and

$$\chi^{(3)}_{xxyy}(-\omega,-\omega,\omega,\omega) = 172.4 \times 10^{-19} \text{ esu}.$$

The third-order susceptibility constants are four times those given in Ref. 10, due to the particular definitions they used for the polarization vector and intensity, as noted by Sutherland [see Ref. 5, p. 298]. There is a compensatory factor of 1/4 in the definition of Δn used in this article, which effectively balances this deviation.

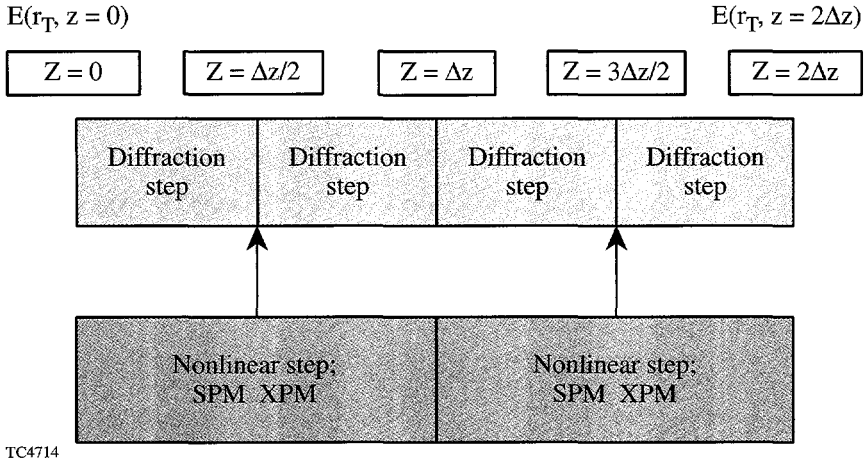

Figure 76.29
Two propagation steps of the symmetrized split-step Fourier method covering a distance of 2Δz.

2. Enhancement of Linear Polarization

As was mentioned in subsection 1 of the **Nonlinear Wave Equation** section, the phase accumulation is greatest in the vicinity surrounding points of linear polarization. When diffraction is included, these areas tend to focus and correspond to peaks of intensity modulation. To illustrate this effect, a simulation was carried out modeling a KDP wedge with an optically smooth surface, i.e., without an initial pseudorandom phase perturbation. Due to the wedge and the dependence of the nonlinear refractive index on the polarization state, a ripple is introduced with a wavelength 1/2 λ_{pol} (where the factor of 1/2 emphasizes that the overall phase perturbation of both orthogonal beams has extrema at the transverse positions corresponding to linear or circular polarization that are independent of the handedness), which can lead to small-scale self-focusing if the beam intensity is high enough. This is contrary to what would be expected in the absence of a wedge; with a perfectly smooth beam and an optically smooth KDP surface, one would observe only a rotation of the polarization ellipse (except in the degenerate cases when the whole beam is either linearly or circularly polarized) and possibly whole-beam self-focusing. This simulation was run with an input intensity of 10.3 GW/cm^2 and yielded a contrast of 1.31. These results are presented in Fig. 76.30, where a correlation between the peak intensities and the linear polarization is evident by the location of the square symbols. If the intensity were lowered to the nominal OMEGA level, a small contrast of only 1.04 would be calculated.

The enhancement of linear polarization may be amplified or seeded by the presence of scratch marks on the surface of the KDP wedge. This effect can be understood by running a simulation that accounts only for diffraction. In this situation there is, of course, no correlation between the intensity peaks that develop during propagation and the polarization state. Some intensity peaks, however, are inevitably located in the neighborhood of linear polarization. These intensity peaks seed the nonlinear growth by increasing the associated phase accumulation in these regions as described by Eq. (23) and, as a consequence, induce a greater intensity modulation than observed for the optically smooth wedge.

A simulation for the nominal OMEGA laser intensity, including both linear and nonlinear effects, yielded a contrast of 1.32 and is presented in Fig. 76.31(a). In this case, only a slight correlation exists between the intensity peaks and the linear polarization state due to the weak nonlinear effect. When the intensity level is increased to 10.3 GW/cm^2, however, an appreciable growth is observed in the vicinity of linear polarization [as shown in Fig. 76.31(b)], and, consequently, a

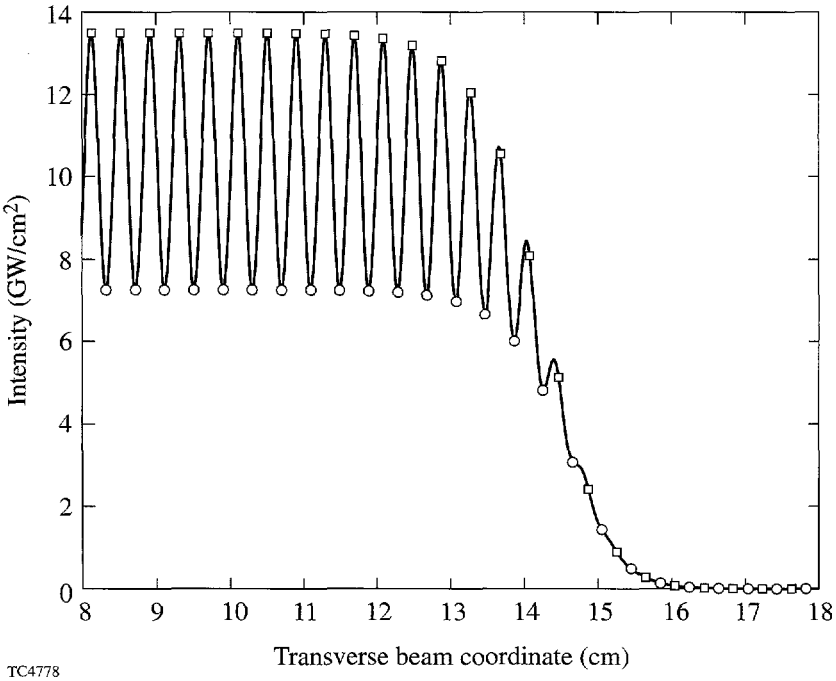

Figure 76.30
The simulation of propagating 12 m past an optically smooth KDP wedge with an incident intensity level of 10.3 GW/cm^2. A contrast of 1.31 is observed. Squares and circles indicate positions of linear and circular polarization, respectively.

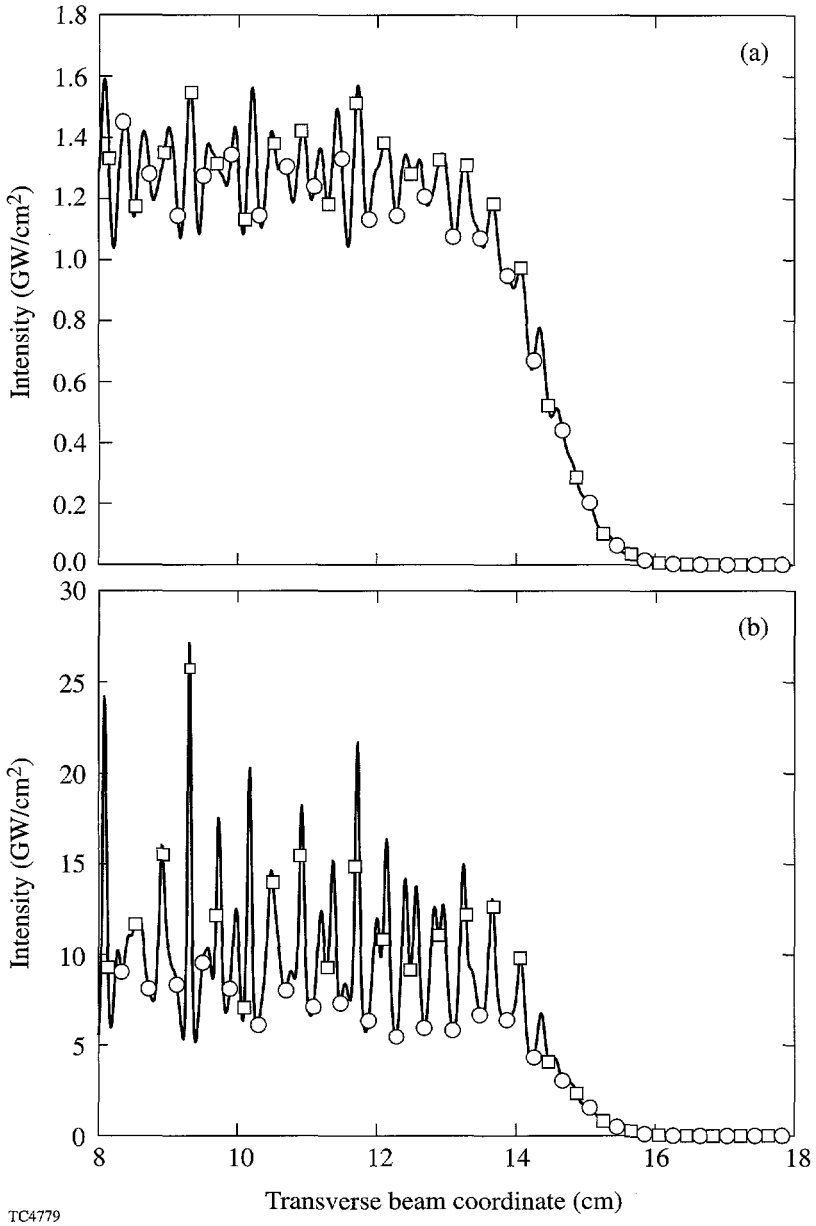

Figure 76.31
The simulation of nonlinear propagation through 12 m of air past a pseudorandomly scratched KDP wedge with 40-nm peak-to-valley scratch depth and a passband of $2\pi/(4\text{ mm}) \le k_y \le 2\pi/(2\text{ mm})$ (a) at 1.3 GW/cm^2 and (b) at 10.3 GW/cm^2. The resulting contrast is 1.32 in (a) and 2.63 in (b). Squares and circles indicate positions of linear and circular polarization, respectively.

significant correlation exists between the intensity peaks and these regions as indicated by the association of the majority of the square symbols with the intensity peaks.

3. Contrast Calculations at the Nominal OMEGA Intensity Level

Tables 76.I and 76.II contain contrast data calculated from simulations of linear and nonlinear propagation, respectively, in which the same scratch-depth data presented in Fig. 76.28 was scaled to cover the 10-nm to 50-nm range for an incident intensity level of 1.3 GW/cm^2. The scratch-depth range presented here was chosen to correspond to the range of surface profile measurements that were taken on diamond-turned KDP crystals, which yielded peak-to-valley scratch depths of 40 nm (worst case) and 15 nm (best case). These tables also include calculated contrast data for three additional passband configurations: the passband is narrowed to $k_y = 2\pi/(3\text{ mm})$, widened to $2\pi/(100\text{ mm}) \le k_y \le 2\pi/(1\text{ mm})$ and widened to a low pass of $k_y \le 2\pi/(1\text{ mm})$.

If the scratch mark model given in Eq. (3) is extended to include another spatial dimension, a 2-D colored noise source is modeled. A 2-D beam is then modeled by extending Eq. (26) to include another dimension. Both of these models are then

used to simulate 2-D nonlinear beam propagation in an analogous manner to the 1-D case. The plot presented in Fig. 76.32 shows three lineouts from a 2-D simulation (taken at the center and near the edges of the beam) for a beam with an intensity of 1.3 GW/cm^2, a scratch-mark passband of $2\pi/(4\text{ mm}) \le k_x, k_y \le 2\pi/(2\text{ mm})$, and a peak-to-valley scratch depth of 40 nm. The contrast calculated for the whole 2-D beam is 1.35, compared to the value of 1.32 given in Table 76.II for the corresponding 1-D case.

At the nominal OMEGA intensity level of 1.3 GW/cm^2, a contrast ratio of 1.8:1 represents the damage threshold of the final optics. The data in Table 76.II show that the calculated contrast values are well below this threshold even for grating-type sinusoidal scratch marks. Recent linear intensity modulation measurements taken on diamond-turned KDP crystals yielded a range of contrast values between 1.04 to 1.08, which roughly correlates with the linear propagation simulation results for peak-to-valley scratch depths between 10 and 20 nm and a passband of $2\pi/(100\text{ mm}) \le k_y \le 2\pi/(1\text{ mm})$ given in Table 76.I. The corresponding contrast range in Table 76.II for nonlinear propagation is 1.07 to 1.11, which represents a small increase due to the nonlinear effects. Near-field images were taken during OMEGA full-power shots on a beamline with and without a diamond-turned KDP plate at an equivalent plane of the final focusing optics. In this experiment, a negligible increase in the intensity modulation was observed, corroborating the results of these numerical simulations.

Conclusion

On the basis of realistic simulations, including diffraction and nonlinear self- and cross-phase modulation, and a realistic representation of scratch marks on diamond-turned KDP, it has been found that KDP wedges, diamond-turned or smooth, are not a significant source of intensity modulation. These results are consistent with experimental results from full-power shots. Accordingly, polarization smoothing will be implemented on OMEGA using diamond-turned rather than polished KDP.

Table 76.I: The calculated value of contrast for linear propagation through 12 m of air past a scratched KDP wedge at an incident intensity level of 1.3 GW/cm^2 for different scratch depths and filter types.

Peak-to-Valley Scratch Depth (nm)	Sinusoidal $k_y = 2\pi/(3\text{ mm})$	Random Lowpass $k_y \le 2\pi/(1\text{ mm})$	Random Bandpass $2\pi/(1\text{ mm}) \le k_y \le 2\pi/(1\text{ mm})$	Random Bandpass $2\pi/(4\text{ mm}) \le k_y \le 2\pi/(2\text{ mm})$
10	1.08	1.03	1.04	1.06
20	1.16	1.07	1.08	1.11
30	1.23	1.11	1.11	1.17
40	1.31	1.14	1.14	1.23
50	1.38	1.18	1.19	1.28

Table 76.II: The calculated value of contrast for nonlinear propagation through 12 m of air past a scratched KDP wedge at an incident intensity level of 1.3 GW/cm^2 for different scratch depths and filter types.

Peak-to-Valley Scratch Depth (nm)	Sinusoidal $k_y = 2\pi/(3\text{ mm})$	Random Lowpass $k_y \le 2\pi/(1\text{ mm})$	Random Bandpass $2\pi/(1\text{ mm}) \le k_y \le 2\pi/(1\text{ mm})$	Random Bandpass $2\pi/(4\text{ mm}) \le k_y \le 2\pi/(2\text{ mm})$
10	1.13	1.07	1.07	1.11
20	1.23	1.09	1.11	1.18
30	1.32	1.13	1.16	1.25
40	1.41	1.17	1.19	1.32
50	1.50	1.20	1.25	1.38

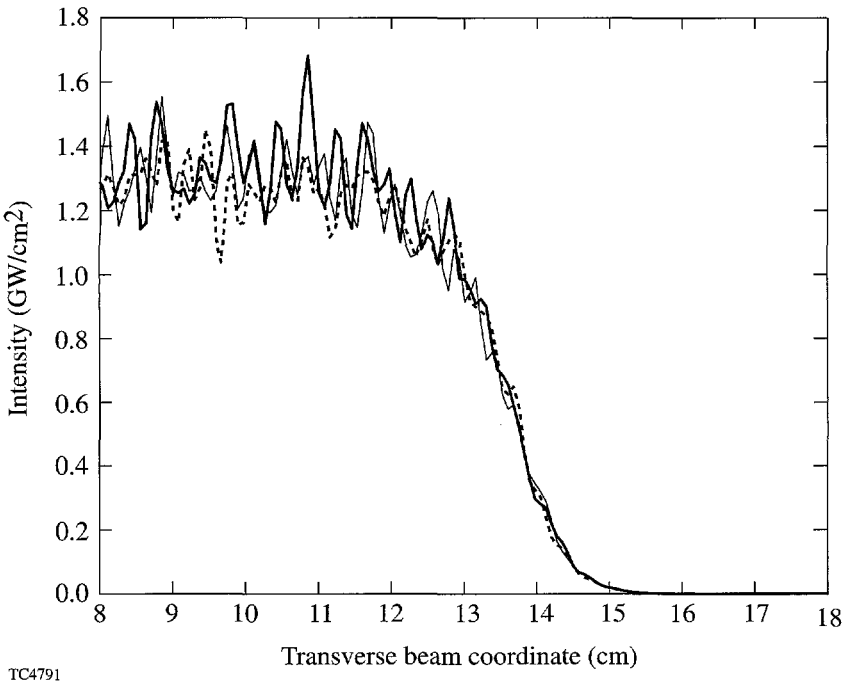

Figure 76.32
Three lineouts from a 2-D simulation (taken at the center and near the edges of the beam) of nonlinear beam propagation with a 1.3 GW/cm^2 intensity, through 12 m of air, past a pseudorandomly scratched KDP wedge with 40-nm peak-to-valley scratch depth and a passband of $2\pi/(4\text{ mm}) \le k_x, k_y \le 2\pi/(2\text{ mm})$. An overall contrast of 1.35 is observed.

ACKNOWLEDGMENT

The author thanks Prof. G. Agrawal for his expert advice and direction, Dr. John Kelly for suggesting this project and the in-depth discussions that followed, and Dr. Stephen Craxton for many useful discussions and time spent editing this manuscript. This research was supported by NSF Grant PHY94-15583. In addition, this work was partially supported by the U.S. Department of Energy Office of Inertial Confinement Fusion under Cooperative Agreement No. DE-FC03-92SF19460, the University of Rochester, and the New York State Energy Research and Development Authority. The support of DOE does not constitute an endorsement by DOE of the views expressed in this article.

REFERENCES

1. K. Kato, unpublished (1984).
2. Laboratory for Laser Energetics LLE Review **45**, 1, NTIS document No. DOE/DP40200-149 (1990). Copies may be obtained from the National Technical Information Service, Springfield, VA 22161.
3. S. Skupsky, R. W. Short, T. Kessler, R. S. Craxton, S. Letzring, and J. M. Soures, J. Appl. Phys. **66**, 3456 (1989).
4. A. B. Carlson, *Communication Systems: An Introduction to Signals and Noise in Electrical Communication*, McGraw-Hill Electrical and Electronic Engineering Series (McGraw-Hill, New York, 1968), p. 154.
5. R. L. Sutherland, *Handbook of Nonlinear Optics*, Optical Engineering, Vol. 52 (Marcel Dekker, New York, 1996).
6. G. P. Agrawal, *Nonlinear Fiber Optics*, Optics and Photonics Series, 2nd ed. (Academic Press, San Diego, 1995).
7. Ts. Gantsog and R. Tanas, J. Mod. Opt. **38**, 1537 (1991).
8. K. E. Oughstun and G. C. Sherman, *Electromagnetic Pulse Propagation in Causal Dielectrics*, Springer Series on Wave Phenomena, Vol. 16 (Springer-Verlag, Berlin, 1994).
9. J. W. Goodman, *Introduction to Fourier Optics* (McGraw-Hill, New York, 1968).
10. R. W. Hellwarth, D. M. Pennington, and M. A. Henesian, Phys. Rev. A **41**, 2766 (1990).

X-Ray Radiographic System Used to Measure the Evolution of Broadband Imprint in Laser-Driven Planar Targets

In an inertial confinement fusion (ICF) implosion, the target is hydrodynamically unstable, and, as a result, mass modulations in the target (either existing or created) can grow to be large enough to disrupt the implosion, thereby reducing its thermonuclear yield.[1] In direct-drive ICF, the nonuniformities in the drive laser can create mass modulations in the target by a process called laser imprinting. As the target accelerates, these mass modulations can grow exponentially, creating large perturbations in the target shell. Understanding and controlling laser imprinting are critical to the successful design of a high-gain ICF target. The primary method of studying imprinting is through-foil x-ray radiography of laser-accelerated targets, where the growth of these mass modulations can be observed.[2] Planar targets are used because they are easily diagnosed and are a reasonable approximation to the early portions of a spherical implosion.

Our experiments use multiple laser beams to drive the subject target and to produce x rays on another target.[3] These x rays are filtered and imaged after they traverse the driven target. Modulations in these images are related to the optical depth (or density–thickness product) of the target. By properly interpreting these images, the character of the imprinted features and their temporal evolution are studied. To accomplish this, the instrumentation must be properly characterized.

A direct measurement of the initial imprinted perturbations is difficult because of their low amplitudes. Additional complications result from the propagation effects of nonuniform shock waves.[4–6] Low-amplitude imprinting has been measured directly using an XUV laser to probe target nonuniformities produced by a laser on very thin (~2 to 3 μm) silicon and aluminum targets.[7] The present experiments use 20-μm-thick CH targets that closely resemble the target shells normally used on OMEGA spherical implosions. These experiments are closely related to those that measure the growth of preimposed mass perturbations,[4] which were well simulated by hydrocodes, providing confidence that both the energy coupling and amount of unstable growth are well modeled for these experiments. This provides a baseline calibration for various hydrodynamic effects that occur in the imprinting experiments. A caveat for these experiments is that imprinting is not directly measured; rather, some unstable RT growth is needed to amplify the perturbations to detectable levels.

It should also be noted that the hydrodynamic instabilities studied here exist primarily at the ablation surface, the point where the steep temperature front meets the overdense material produced by the shock. Perturbations in the target result from both mass modulations (ripples on the ablation surface) and density modulations produced in the bulk of the target. The latter are created primarily by the propagation of nonuniform shocks. Radiographic systems are sensitive to the density–thickness product (optical depth) of the target and, as such, cannot distinguish between mass and density modulations. After about 1 ns of acceleration in these experiments, the variations in optical depth produced by the nonuniform shocks become negligible, compared to those produced by the ablation-front amplitude. At this point, it is reasonable to ascribe most of the measured optical depth to the amplitude of the perturbation at the ablation surface.[4]

The backlighting source typically has multiple spectral components. As a result, simulations of the resultant optical depth of the target are critical to interpreting the data. This worked extremely well for experiments using two-dimensional preimposed sinusoidal perturbations.[4,8] In contrast, the features created by imprinting are three dimensional and significantly more difficult to simulate. It is advantageous, therefore, to obtain experimentally a relationship between measured optical-depth modulations and the amplitude of ablation-surface modulations. We simplify the latter process by establishing several reasonable assumptions about the detection system.

In the following sections, we discuss the radiographic imaging system and methods to recover the target perturbations from the radiographs. We present results of experiments that characterize the sensitivity, resolution, and noise of the system. Using this information, we have formulated a Wiener

filter that is designed to enhance the radiographic images. In essence, our analysis provides a way to distinguish signal from noise and to deconvolve the system resolution.

Experimental Configuration

Unperturbed (smooth surface), 20-μm-thick CH (ρ = 1.05 g/cm^3) targets were irradiated at 2×10^{14} W/cm^2 in 3-ns square pulses by five overlapping UV beams (see Fig. 76.33). The targets were backlit with x rays produced by a uranium backlighter, located 9 mm away from the driven target and irradiated at ~1×10^{14} W/cm^2 (using 12 additional beams). X rays transmitted through the target and a 3-μm-thick Al blast shield (located at the center between the backlighter and drive foils) were imaged by 8-μm pinholes on a framing camera filtered with 6 μm of aluminum. This yielded the highest sensitivity for an average photon energy of ~1.3 keV. The framing camera produced eight images of ~80-ps duration, each occurring at different times. The distance between the target and the pinhole array was 2.5 cm, and the distance between the pinhole array and the framing camera was 35 cm, resulting in a magnification of ~14. The use of optical fiducial pulses coupled with an electronic monitor of the framing-camera output produced a frame-timing precision of about 70 ps. The framing-camera output is captured on Kodak T-Max 3200 film, which is then digitized with a Perkin–Elmer PDS microdensitometer with a 20-μm-square scanning aperture.

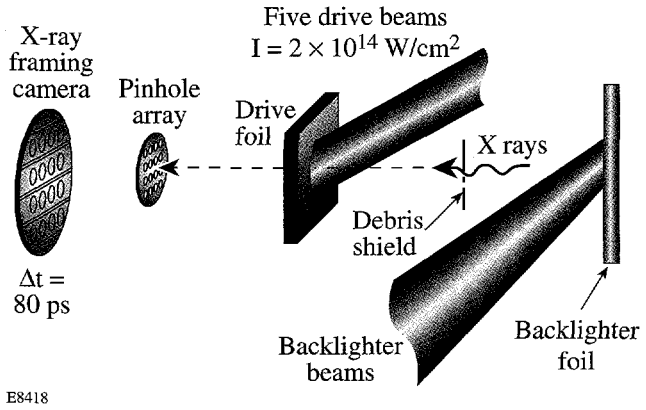

Figure 76.33
Experimental configuration. Five overlapped beams drive a 20-μm CH foil. An additional 12 beams produce x rays from a uranium backlighter foil. X rays traverse the target and are imaged by a pinhole array on a framing camera.

Figure 76.34 shows a block diagram of the entire detection system, which comprises four major parts: an 8-μm pinhole, the framing camera with a microchannel plate (MCP) and phosphor plate, the film, and the digitization process. At each stage of the measurement, noise is added to the signal, and the signal plus noise are convolved with the point spread function (PSF) of each component of the system. In the frequency domain, the spectra of both the signal and the noise are multiplied by a modulation transfer function (MTF) of that subset of the imaging system.

In radiography, x rays with a nominally wide spectrum are attenuated exponentially by the target being probed. In addition to the target, there are filters and imaging devices that affect the transmission of x rays to the detector. Figure 76.35 (thick line) shows a backlighter uranium spectrum used for imaging.[2] The spectral response function of the imaging system (Fig. 76.35, thin line) includes the transmission of

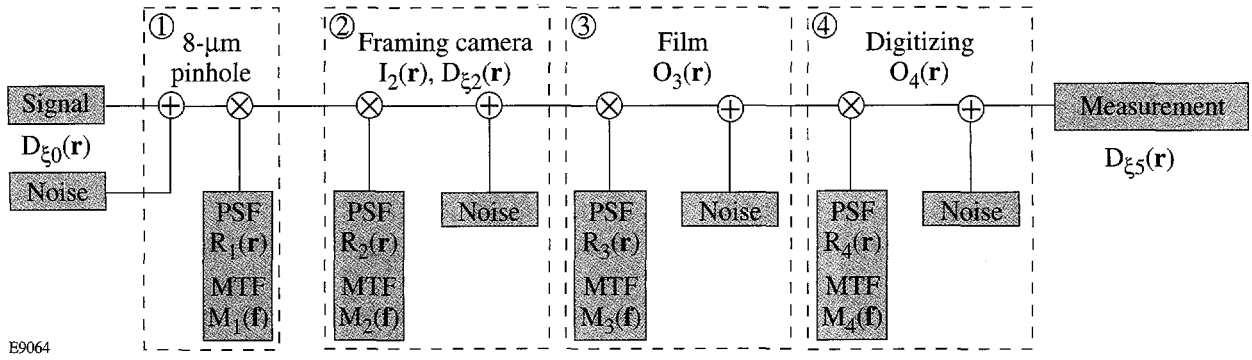

Figure 76.34
Block diagram of the experimental detection system. This system comprises four major parts: an 8-μm pinhole, the framing camera, the film, and the digitization. At each stage of the measurement, noise is added to the signal, and the signal with noise are convolved with the PSF. $D_{\xi 0}(\mathbf{r})$, $D_{\xi 2}(\mathbf{r})$, and $D_{\xi 5}(\mathbf{r})$ are the optical depth modulations in the target, in the framing camera's output, and as measured, respectively. $I_2(\mathbf{r})$ is the light intensity in the framing camera's output. $O_3(\mathbf{r})$ and $O_4(\mathbf{r})$ are the optical density of the film, before and after digitization, respectively.

aluminum filters and mass absorption rate of a gold photocathode on the microchannel plate (MCP) in the framing camera. Figure 76.36 shows the spectrum used for imaging, absorbed and converted into electrons by the MCP. It is obtained by multiplying the two curves in Fig. 76.35 together, taking the attenuation of 20 μm CH into account. The output of the framing camera is proportional to the convolution of the x-ray spectral intensity incident on a target, its attenuation factor, and the PSF's of the pinhole $R_1(\mathbf{r},E,t)$ and the framing camera $R_2(\mathbf{r},E,t)$, including filters, where E represents x-ray energy. Assuming that no saturation occurs in these devices, the output intensity of the framing camera incident on the film is

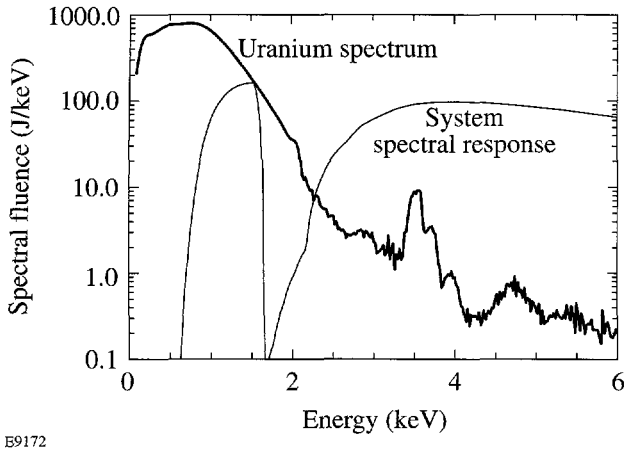

Figure 76.35
Uranium spectrum (thick solid line) and instrumental response (thin solid line) as functions of x-ray energy.

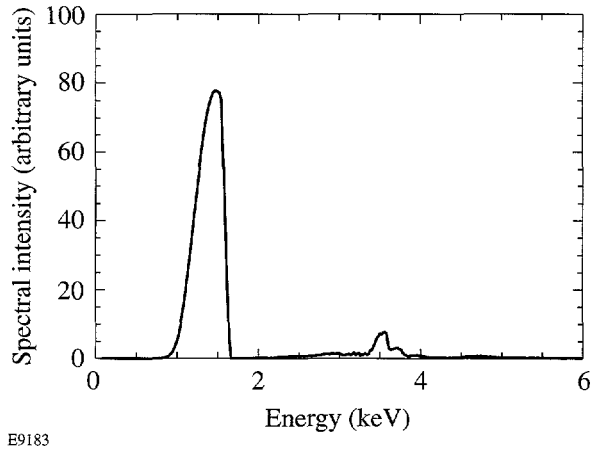

Figure 76.36
X-ray spectrum propagated through a 3-μm Al blast shield, a 20-μm CH target, and a 6-μm Al filter on the MCP, then absorbed and converted into electrons by the MCP.

$$
\begin{aligned}
I_2(\mathbf{r},t) \sim & \int dE \int d\mathbf{r}' \\
& \times R_{1,2}(\mathbf{r}-\mathbf{r}',E,t)\, f_{\mathrm{Al}}(E,t)\, \mu_{\mathrm{Au}}(E)\, S_{\mathrm{bklt}}(\mathbf{r}',E,t) \\
& \times \exp\left[-\int_0^{z_0} dz' \mu_{\mathrm{CH}}(E,t)\, \rho(\mathbf{r}',z',t)\right] \\
& \times \exp\left[-\mu_{\mathrm{CH}}(E,t)\, \rho_{\mathrm{abl}}(t)\, \xi(\mathbf{r}',t)\right]. \qquad (1)
\end{aligned}
$$

In this equation, x rays propagate along the target normal, which is oriented along the z axis. The coordinate $\mathbf{r}$ is the position vector perpendicular to that axis; $I_2(\mathbf{r},t)$ is the output intensity of the framing camera; $R_{1,2}(\mathbf{r},E,t)$ is a point spread function of a pinhole and framing cameras, which is, in general, a function of the x-ray energy E; $f_{\mathrm{Al}}(E,t)$ is the aluminum filter transmission; $\mu_{\mathrm{Au}}(E)$ is the mass absorption rate of the gold photocathode (in the MCP); and $S_{\mathrm{bklt}}(\mathbf{r},E,t)$ is a backlighter spectral intensity. The target density and thickness are $\rho(\mathbf{r},z,t)$ and $z_0(t)$, respectively. The target density and the amplitude of the target thickness modulation at the ablation surface are $\rho_{\mathrm{abl}}(t)$ and $\xi(\mathbf{r},t)$. The mass absorption rate of the CH target is $\mu_{\mathrm{CH}}(E,t)$.

The film converts the incident light intensity $I_2(\mathbf{r},t)$ into the film optical density $O_3(\mathbf{r},t)$ according to its sensitivity [or D log(H)] curve W. Convolving that with the PSF of the film $R_3(\mathbf{r})$ yields

$$
\begin{aligned}
& O_3(\mathbf{r},t) \\
& = \int d\mathbf{r}' R_3(\mathbf{r}-\mathbf{r}')\, W\left\{\log_{10}\left[\int_{t-\tau/2}^{t+\tau/2} dt' I_2(\mathbf{r}',t')\right]\right\}, \qquad (2)
\end{aligned}
$$

where τ = 80 ps is a time resolution of the framing camera. During film digitization, the optical density $O_3(\mathbf{r},t)$ is convolved with the PSF $R_4(\mathbf{r})$ of the 20-μm-square aperture in the densitometer to give the digitized or measured optical density

$$
O_4(\mathbf{r},t) = \int d\mathbf{r}' R_4(\mathbf{r}-\mathbf{r}')\, O_3(\mathbf{r}'). \qquad (3)
$$

The measured optical density of the film, $O_4(\mathbf{r},t)$, is converted to intensity using the inverse film sensitivity W^{-1}. The measured optical depth $D_5(\mathbf{r},t)$ of the target is obtained by taking the natural logarithm of that intensity-converted image:

$$
D_5(\mathbf{r},t) = \ln\left\{10^{W^{-1}[O_4(\mathbf{r},t)]}\right\}. \qquad (4)
$$

The primary objective of this experiment is to recover the amplitude of the perturbation at the ablation surface using the

measured optical depth modulations. To do this rigorously requires significant effort. Several aspects of the imaging system enable assumptions, however, that greatly simplify the analysis of the radiographic images: (1) As a result of Al filters, a relatively narrow band ($\Delta E \simeq 200$ eV) of x rays around 1.3 keV is used for radiography. The effect of the spectral component of uranium M-band emission around 3.5 keV (see Fig. 76.36) on system sensitivity and resolution was measured and calculated to be insignificant. (2) The backlighter spectrum and filter transmission remain constant in time during the measurement. (3) The backlighter is produced by 12 beams that have phase plates, resulting in a very uniform and predictable backlighter shape. (4) There is little heating of the solid part of the target (the mass absorption coefficient μ is constant in time). (5) The amplitudes of growing imprinted features are large enough that the propagation of a nonuniform shock contributes little to the total optical depth of the target.[4] Given these assumptions, Eq. (1) becomes

$$I_2(\mathbf{r},t) \sim I_{\text{env}}(\mathbf{r},t)\int d\mathbf{r}' R_{1,2}(\mathbf{r}-\mathbf{r}')\exp\left[-D_{\xi 0}(\mathbf{r}',t)\right], \quad (5)$$

where the modulation in a target optical depth $D_{\xi 0}(\mathbf{r},t)$ is simply

$$D_{\xi 0}(\mathbf{r},t) = \frac{\xi(\mathbf{r},t)}{\lambda_{\text{CH}}}, \quad (6)$$

and the spectrally weighed attenuation length of the target λ_{CH} is given as

$$\lambda_{\text{CH}} \simeq 1/\left[\mu_{\text{CH}}(1.3\ \text{keV})\rho_{\text{abl}}\right]. \quad (7)$$

$I_{\text{env}}(\mathbf{r},t)$ is the slowly varying envelope of the backlighter.

At this point, the target optical depth can be obtained from the measured optical depth by rigorously working backward through each stage, compensating for noise and system response (PSF) at each stage. However, if the modulation in the target optical density $D_{\xi 0}(\mathbf{r},t)$ is small,

$$D_{\xi 0}(\mathbf{r},t) << 1 \quad (8)$$

(which is the case in all our experiments), the entire imaging system may be considered linear. This greatly simplifies the relation between the measured optical depth and the target optical depth. We introduce a new variable, the optical depth modulation in the output of the framing camera $D_{\xi 2}(\mathbf{r},t)$, through the following equation:

$$I_2(\mathbf{r},t) \sim I_{\text{env}}(\mathbf{r},t)\exp\left[-D_{\xi 2}(\mathbf{r},t)\right]. \quad (9)$$

Next, assuming that $D_{\xi 0}(\mathbf{r},t)$ and $D_{\xi 2}(\mathbf{r},t)$ are small, we expand in Taylor series the exponential functions in Eqs. (5) and (9) and retain only zeroth and first orders in these expansions. We then have

$$D_{\xi 2}(\mathbf{r},t) \cong \int d\mathbf{r}' R_{1,2}(\mathbf{r}-\mathbf{r}',t) D_{\xi 0}(\mathbf{r}',t). \quad (10)$$

Here we used the fact that the point spread function $R_{1,2}(\mathbf{r},t)$ is normalized $\int d\mathbf{r}\, R_{1,2}(\mathbf{r},t) = 1$. The T-MAX 3200 film has a constant MTF up to a spatial frequency ~50 mm^{-1}, the highest spatial frequency considered in our measurements, so the PSF of the film is set to be a $\delta(\mathbf{r})$ function. Since we use only the "linear" part of the D log(H) curve, the modulations in measured optical depth $D_{\xi 5}(\mathbf{r},t)$ are linearly related to the optical depth modulation in the target $D_{\xi 0}(\mathbf{r},t)$:

$$D_{\xi 5}(\mathbf{r},t) = \int d\mathbf{r}' R_{\text{sys}}(\mathbf{r}-\mathbf{r}') D_{\xi 0}(\mathbf{r}',t), \quad (11)$$

where $R_{\text{sys}}(\mathbf{r})$ is the PSF of the entire system. It is the convolution of PSF's of the pinhole, the framing camera, and the digitizing aperture of the densitometer. In frequency space, the system MTF is the product of the MTF's of each of these components.

In summary, we have used approximations of the system performance to find a straightforward relationship between the measured optical depth and the modulation of the ablation surface. As opposed to requiring detailed computer simulations to interpret experimental results, we find, for a class of experiments, a direct relationship between the measurement and target perturbations. Equation (11) has been derived by assuming that modulations of the target optical depth are small compared to unity. Since Eq. (11) is a linear approximation, it does not treat the generation of harmonics and coupling of modes produced by system nonlinearities. We have simulated these nonlinearities for modulation amplitudes greater than those measured routinely in our experiments and found that nonlinear effects were negligible compared to system noise.

System Sensitivity

Once the modulation in target optical depth is obtained (see above), the perturbation amplitude in the target can be found,

provided various criteria are met. Variations in optical depth are produced by changes in either the target density or target thickness. Apparent changes in optical depth can also result from changes in the x-ray spectrum or in the attenuation coefficient of the target material. We performed several experiments to characterize the system performance.

System sensitivity is defined by the spectrally weighted x-ray attenuation length λ_{CH}. This length is inversely proportional to the mass absorption coefficient and the target density [see Eq. (7)]. In practice, λ_{CH} can be constructed using the target compression C_p, calculated by the 1-D hydrocode *LILAC*,[9] and the attenuation length of the undriven target λ_x:

$$\lambda_{CH} = \frac{\lambda_x}{C_p}. \tag{12}$$

This relation can be used as long as the driven target maintains a cold value of its mass absorption coefficient. Typically, during our experiments the target temperature is far below the values that could change the mass absorption coefficient.

We measured the attenuation length λ_x in undriven 25-μm CH_2 ($\rho = 0.92$ g/cm^3) targets using backlighter beams only. At the position of the experimental target, a thin strip of CH_2 was mounted so that the radiographic system could view x rays that both miss and traverse the target, as shown on the image taken at some time during the 3-ns backlighter pulse [see Fig. 76.37(a)]. The calculated attenuation length for this material was 11.5 μm, and we measured 10 μm±1 μm from the difference in optical depth in these two regions [lines A and B in Fig. 76.37(b)]. This value was constant for the ~1-mm backlighter spot and did not vary over the duration of the 3-ns backlighter pulse. We also radiographed undriven 20-μm CH ($\rho = 1.05$ g/cm^3) targets that had preimposed, low-amplitude (0.5 μm) sinusoidal modulations with wavelengths of 60 and 30 μm. Using these modulations as control references, λ_x was measured to be 10 μm±2 μm. These experiments showed that both backlighter spectrum and filter transmission remained constant in time during the measurements.

System Resolution

The resolution of the system was characterized by measuring its response to a sharp, opaque edge (machined platinum). Its image is shown in Fig. 76.38(a). The dashed line in Fig. 76.38(b) represents the light intensity incident on the edge, the thin solid line is the measured light intensity propagated through the system (and averaged in the direction parallel to the edge), and the thick solid line is the fit to experimental data assuming the system MTF as a two-Gaussian function:[10]

$$M_{sys}(f) = 0.955 \exp\left\{-\left[14.2(\mu\text{m})f\right]^2\right\} + 0.045 \exp\left\{-\left[248.3(\mu\text{m})f\right]^2\right\}. \tag{13}$$

The MTF is essentially the product of the responses of three system components: the pinhole camera, the 20-μm digitizing aperture, and the framing camera. The former two are straightforward calculations based on geometry and spectral energy. The MTF of the framing camera was determined by measuring the camera response to a 150-μm-wide slit (placed 1 mm in front of the camera) backlit by x rays [see Fig. 76.39(a)]. This image of the slit was digitized with a 5-μm scanning aperture. The slit width and its proximity to a camera were sufficient to neglect any diffraction effects. The dashed line in Fig. 76.39(b) represents the light intensity incident on the slit. The thin solid

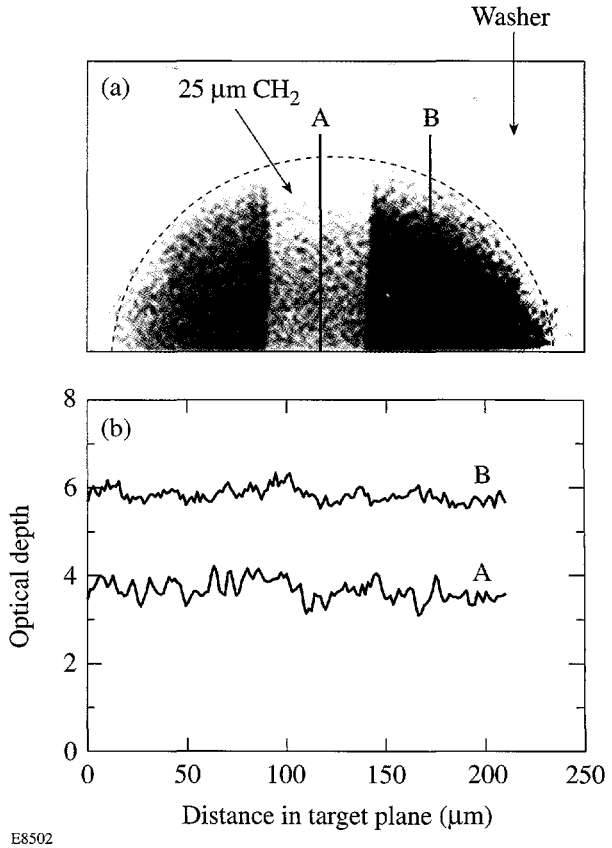

Figure 76.37
(a) Image of the undriven strip target; (b) lineouts of the measured optical depth (shown by lines A and B). Images through both the CH and open areas allow the optical depth to be measured.

line is the measured light intensity propagated through the system (and averaged in the direction parallel to the slit), and the thick solid line is the fit to experimental data assuming the framing camera MTF as a two-Gaussian function:

$$M_2(f) = 1.05 \exp\left\{-\left[103.8(\mu\text{m})f\right]^2\right\} - 0.05 \exp\left\{-\left[95.8(\mu\text{m})f\right]^2\right\}. \quad (14)$$

The measured MTF of the framing camera is shown in Fig. 76.40. This MTF is similar to that measured in other experiments performed at LLNL[11,12] and NRL[13] with aluminized phosphor plates, which have reduced the long-scale-length scattering of photons and electrons between the phosphor and microchannel plates. This scattering resulted in a reduction of the MCP resolution up to about 20% at low spatial frequencies < 5 mm^{-1}. In our experiments, the phosphor plate was not aluminized. We saw, however, no significant reduction of the MTF at low spatial frequencies due to such scattering because of much lower levels of irradiation, compared with above-mentioned experiments.

Figure 76.41 shows the various MTF's discussed above. The thin solid line is the MTF of the entire system as determined by its edge response. The dotted line is the system MTF calculated as the product of the MTF's of the 8-μm pinhole (dot–dashed line), the framing camera (dashed line), and the 20-μm digitizing aperture (thick solid line). These MTF's assumed a system magnification of ~14. It can be seen that for

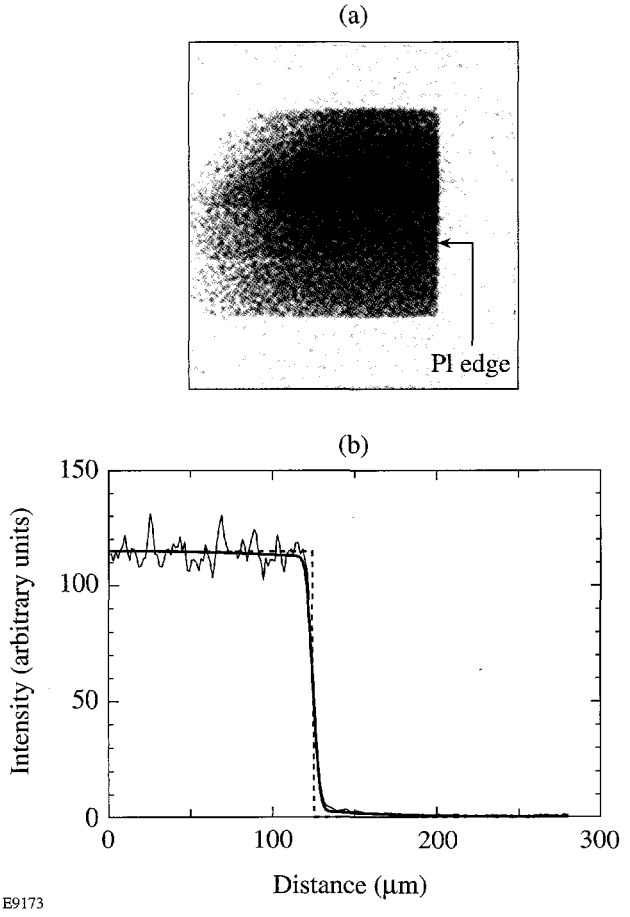

Figure 76.38
(a) Image of the edge target (Pt strip). (b) The dashed line represents the light intensity incident on the edge. The thin solid line is the measured light intensity propagated through the system (and averaged in the direction parallel to the edge), and the thick solid line is the fit to experimental data, assuming the system MTF to be a two-Gaussian function.

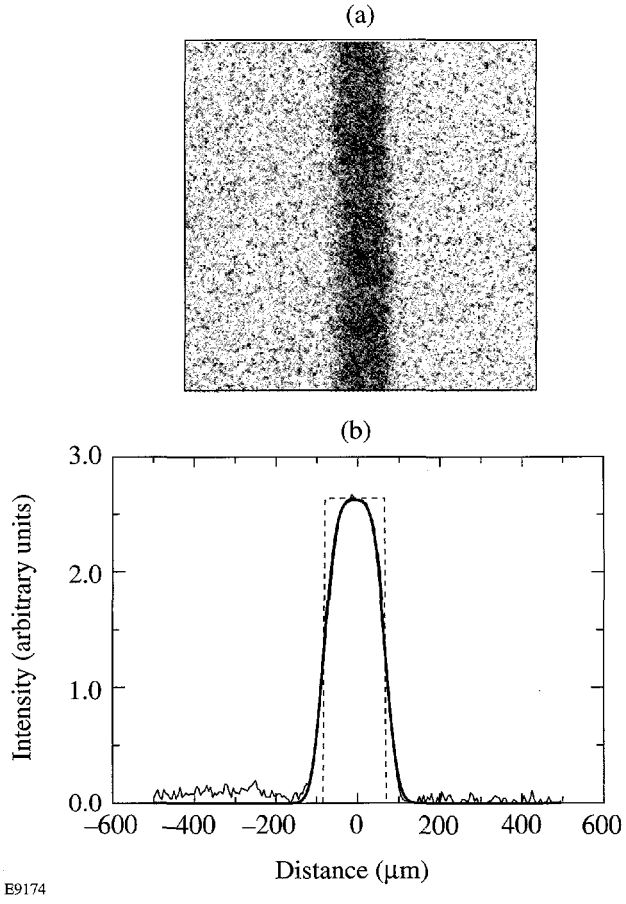

Figure 76.39
(a) Image of the slit target, installed in front of the MCP. (b) The dashed line represents the light intensity incident on the slit, the thin solid line is the measured light intensity propagated through the system (and averaged in the direction parallel to the slit), and the thick solid line is the fit to experimental data, assuming the framing-camera MTF to be a two-Gaussian function.

spatial frequencies below 70 mm^{-1}, the measured system MTF is in reasonable agreement with the aggregate response of the individual components. So in the analysis of target nonuniformity evolution (discussed in the **Wiener Filtering** section), we analyzed the signal only at frequencies below 70 mm^{-1}.

System Noise

Using radiographs of strip targets [see Fig. 76.37(a)], the system noise was characterized. Since the strip targets were uniform with very smooth surfaces, all nonuniformity measured in the radiographs of these targets is noise. The primary noise sources in this system are photon statistical noise of backlighter x rays, noise in the microchannel (MCP) and phosphor plates, film noise, and noise produced during digitization. It is possible to determine the origin of noise based on its spectrum since, in frequency space, the signal and noise at each stage are multiplied by the MTF of that portion of the system.

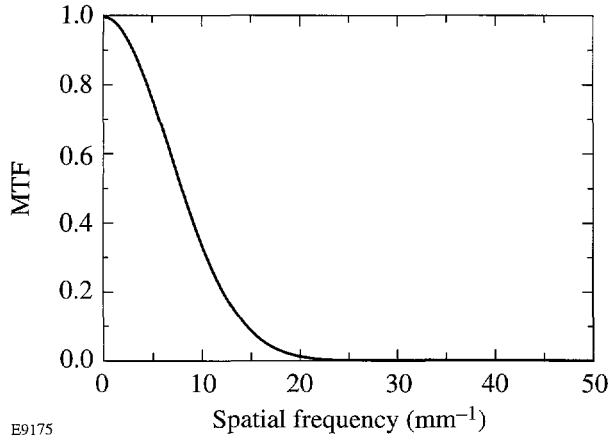

Figure 76.40
Resolution of the framing camera.

Figure 76.41 depicts the azimuthally averaged Fourier amplitudes of the optical depth for two square regions with 150-μm width, through and around the strip. At high frequencies (>100 mm^{-1}), the averaged noise is nearly constant, indicative of the noise from film and digitization. At lower spatial frequencies the noise amplitude depends on the MTF's of the pinhole camera and MCP. This suggests that the dominant noise source is the photon statistics of the backlighter x rays. In optical-depth space, the noise amplitude is inversely proportional to the square root of the number of photons. There is more noise in the region of the strip with few x-ray photons than in the region out of the strip.

This relationship between noise levels and the photon flux can be explained by the following consideration: If I_1 and I_2 are the average x-ray intensities in and out of the strip regions, respectively, then noise rms amplitudes in these regions are ~ $\sqrt{I_1}$ and $\sqrt{I_2}$, assuming a monochromatic x-ray spectrum. Since the signal's optical depth is the natural logarithm of its intensity, the variation of a signal from its averaged value in terms of the optical depth will be proportional to $1/\sqrt{I_1}$ and $1/\sqrt{I_2}$ after a series expansion of the logarithm, retaining only the first term. It is assumed that the number of x-ray photons per pixel is greater than 1, which is necessary to justify such an analysis. The fact that there is more noise in the optical depth in the attenuated strip region with fewer x-ray photons (rms

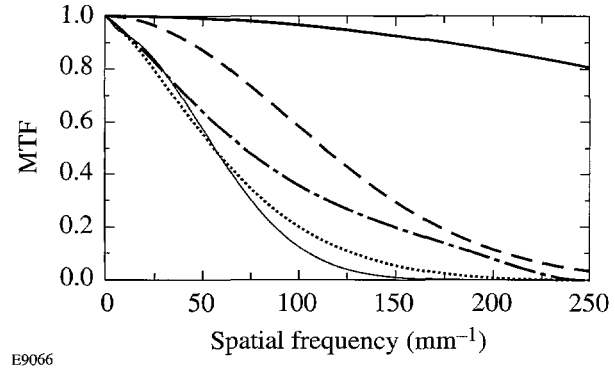

Figure 76.41
Resolution of the system. The thin solid line is the measured MTF of the entire system. The dotted line is the system MTF calculated as the product of the MTF's of the 8-μm pinhole (dot–dashed line), the framing camera (dashed line), and the 20-μm digitizing aperture (thick solid line).

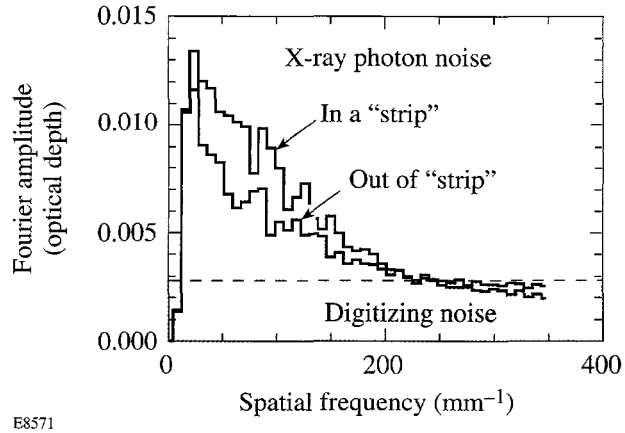

Figure 76.42
System noise. The measured noise level for two portions of a radiograph through and around the 25-μm-CH_2 strip target.

amplitude $\sim 1/\sqrt{I_1}$) than in the region out of the strip (rms amplitude $\sim 1/\sqrt{I_2}$) supports the suggestion of the photon-statistical nature of the noise.

Wiener Filtering

Using the measured system sensitivity, resolution, and noise, we recovered the imprinted perturbations from the radiographic images. A broad spectrum of imprinted features has been generated by laser nonuniformities with spatial frequencies up to 430 mm^{-1}. These initial imprinted nonuniformities in our experiments come from the nonuniformities in drive-laser beams used with distributed phase plates (DPP's).[14] The RT instability has growth rates and saturation effects that depend upon spatial frequency. In addition, the resolution of the radiographic system begins to cut off spatial frequencies above ~70 mm^{-1}. As a result, the detected signal resides in a narrow range of spatial frequencies ~10 to 70 mm^{-1}.

We analyzed 400-μm-square sections of the radiographic images of the target by converting them to measured optical depth, compensating for the backlighter envelope using a fourth-order, two-dimensional polynomial fit. The signal nonuniformity is expressed as the power per mode in optical depth by Fourier transforming the resulting optical depth.

A Wiener filter was developed to recover the true signal from the resulting images.[15] If $C(\mathbf{f})$ is the signal plus noise measured by the system, $C(\mathbf{f}) = S(\mathbf{f}) + N(\mathbf{f})$, then the restored signal $P(\mathbf{f})$ is

$$P(\mathbf{f}) = \frac{C(\mathbf{f})}{M_{sys}} \frac{|S(\mathbf{f})|^2}{|S(\mathbf{f})|^2 + |N_{avg}(\mathbf{f})|^2}, \tag{15}$$

where M_{sys} is total system MTF, $|N_{avg}(\mathbf{f})|^2$ is the average or Wiener noise spectrum, and $|S(\mathbf{f})|^2$ is the measured signal power spectrum. The average noise spectrum $|N_{avg}(\mathbf{f})|^2$ and system MTF have been measured as described above; the only unknown is $|S(\mathbf{f})|^2$, the measured signal power spectrum. In this technique, the signal is compared to the measured noise spectrum, and only points that are greater than twice the amplitude of that noise are considered first, i.e.,

$$|S(\mathbf{f})|^2 = |C(\mathbf{f})|^2 - |N_{avg}(\mathbf{f})|^2,$$

for

$$|C_{re}(\mathbf{f})| \text{ or } |C_{im}(\mathbf{f})| > 2|N_{avg}(\mathbf{f})|, \tag{16}$$

where $|C_{re}(\mathbf{f})|$ and $|C_{im}(\mathbf{f})|$ are real and imaginary parts of the measured signal with noise. Due to the statistical nature of the noise spectrum, the signal that is less than twice the noise amplitude can be treated in three primary manners: (a) rejected (i.e., set to 0), (b) considered to be uniformly distributed between zero and twice the noise level, or (c) set equal to twice the noise level. These options are used to provide the uncertainties of the measured signal. At higher spatial frequencies (>70 mm^{-1}) the detector response is falling rapidly, so the signal-to-noise level is greatly reduced and the error bars are larger.

The thin solid line in Fig. 76.43(a) shows the power per mode of the noise. The thick solid line represents the power per mode of the image at ~2 ns. These two lines are almost the same at high spatial frequencies > 80 mm^{-1}, suggesting that the

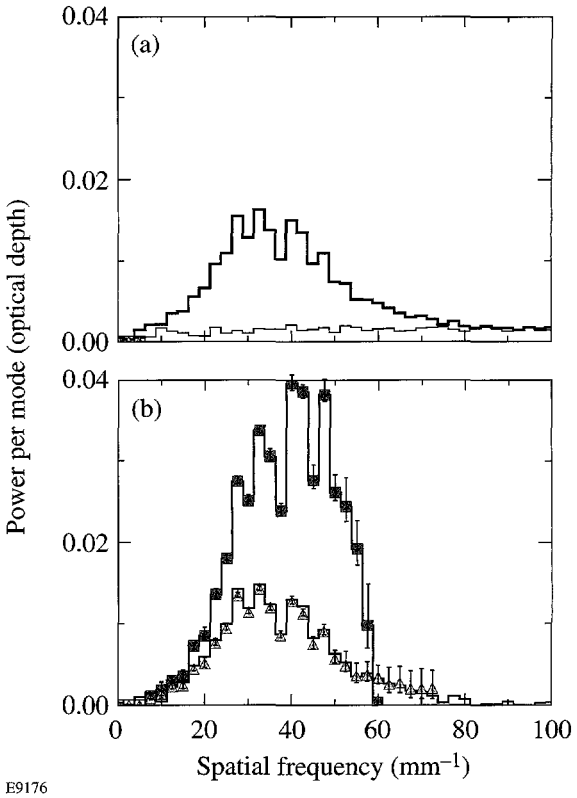

Figure 76.43
(a) Power per mode of the noise (thin solid line) and power per mode of the signal plus noise of the driven foil image at 2 ns. (b) Power per mode of target modulations versus spatial frequency. This is calculated using a Wiener filter, assuming MTF = 1 (triangles), calculated by subtracting the noise power per mode from the power per mode of the signal plus noise (lower solid line that agrees with triangles), and calculated using a Wiener filter, assuming a measured MTF (squares).

noise dominates at these spatial frequencies in the 2-ns image. There is a significant level of signal at lower spatial frequencies, however, which must be separated from noise.

The result of the Wiener filter[15] is shown in Fig. 76.43(b). To demonstrate the effect of noise reduction, we set the MTF = 1 (i.e., no resolution compensation) in Eq. (15); this is shown as the triangles in Fig. 76.43(b). The lower solid line shows the data obtained by simply subtracting the noise power per mode [the thin solid line in Fig. 76.43(a)] from the measured power per mode of signal plus noise [the thick solid line in Fig. 76.43(a)]. The agreement between these curves indicates that the noise compensation portion of the Wiener filter behaves reasonably. The upper curve in Fig. 76.43(b) depicts the result using the proper MTF and represents the fully processed data used as our experimental results.

Conclusions

By properly characterizing our detection system, we have simplified the complex relation between radiographic images and the optical depth in the target. Using measured aspects of the system, we have generated linear approximations of the system response that apply to our conditions. We measured the sensitivity and the resolution and demonstrated that they remain constant for the duration of the experiment. Using measured noise spectra, we have constructed a Wiener filter that enables us to distinguish the signal from noise and to reconstruct that signal by deconvolving system MTF. This technique is routinely applied to the analysis of our experiments.

ACKNOWLEDGMENT

This work was supported by the U.S. Department of Energy Office of Inertial Confinement Fusion under Cooperative Agreement No. DE-FC03-92SF19460, the University of Rochester, and the New York State Energy Research and Development Authority. The support of DOE does not constitute an endorsement by DOE of the views expressed in this article.

REFERENCES

1. D. K. Bradley, J. A. Delettrez, R. Epstein, R. P. J. Town, C. P. Verdon, B. Yaakobi, S. Regan, F. J. Marshall, T. R. Boehly, J. P. Knauer, D. D. Meyerhofer, V. A. Smalyuk, W. Seka, D. A. Haynes, Jr., M. Gunderson, G. Junkel, C. F. Hooper, Jr., P. M. Bell, T. J. Ognibene, and R. A. Lerche, Phys. Plasmas **5**, 1870 (1998).
2. S. G. Glendinning *et al.*, in *Applications of Laser Plasma Radiation II*, edited by M. C. Richardson and G. A. Kyrala (SPIE, Bellingham, WA, 1995), Vol. 2523, pp. 29–39.
3. T. R. Boehly, V. A. Smalyuk, D. D. Meyerhofer, J. P. Knauer, D. K. Bradley, C. P. Verdon, and D. Kalantar, in *Laser Interaction and Related Plasma Phenomena*, edited by G. H. Miley and E. M. Campbell (American Institute of Physics, New York, 1997), Vol. 406, pp. 122–129.
4. J. P. Knauer, C. P. Verdon, D. D. Meyerhofer, T. R. Boehly, D. K. Bradley, V. A. Smalyuk, D. Ofer, P. W. McKenty, S. G. Glendinning, D. H. Kalantar, R. G. Watt, P. L. Gobby, O. Willi, and R. J. Taylor, in *Laser Interaction and Related Plasma Phenomena*, edited by G. H. Miley and E. M. Campbell (American Institute of Physics, New York, 1997), Vol. 406, pp. 284–293.
5. T. Endo *et al.*, Phys. Rev. Lett. **74**, 3608 (1995).
6. R. Ishizaki and K. Nishihara, Phys. Rev. Lett. **78**, 1920 (1997).
7. D. H. Kalantar, M. H. Key, L. B. Da Silva, S. G. Glendinning, B. A. Remington, J. E. Rothenberg, F. Weber, S. V. Weber, E. Wolfrum, N. S. Kim, D. Neely, J. Zhang, J. S. Wark, A. Demir, J. Lin, R. Smith, G. J. Tallents, C. L. S. Lewis, A. MacPhee, J. Warwick, and J. P. Knauer, Phys. Plasmas **4**, 1985 (1997).
8. B. A. Remington *et al.*, Phys. Fluids B **4**, 967 (1992).
9. An earlier version of *LILAC* is described in E. Goldman, Laboratory for Laser Energetics Report No. 16, University of Rochester (1973).
10. B. A. Remington *et al.*, Rev. Sci. Instrum. **63**, 5080 (1992).
11. J. D. Wiedwald *et al.*, in *Ultrahigh- and High-Speed Photography, Videography, Photonics, and Velocimetry '90*, edited by L. L. Shaw, P. A. Jaanimagi, and B. T. Neyer (SPIE, Bellingham, WA, 1990), Vol. 1346, pp. 449–455.
12. H. F. Robey, K. S. Budil, and B. A. Remington, Rev. Sci. Instrum. **68**, 792 (1997).
13. C. J. Pawley, A. V. Deniz, and T. Lehecka "Noise and Sensitivity in X-Ray Framing Cameras," to be published in the Review of Scientific Instruments.
14. Y. Lin, T. J. Kessler, and G. N. Lawrence, Opt. Lett. **20**, 764 (1995).
15. L. R. Rabiner and B. Gold, *Theory and Application of Digital Signal Processing* (Prentice-Hall, Englewood Cliffs, NJ, 1975).

Collisionless Damping of Localized Plasma Waves in Laser-Produced Plasmas and Application to Stimulated Raman Scattering in Filaments

Stimulated Raman scattering (SRS), an instability that converts laser light incident on a plasma into plasma waves and lower-frequency scattered photons, has been a major concern in laser fusion research for many years. The scattered photons represent wasted energy, and the plasma waves can produce suprathermal electrons that penetrate and preheat the target core, thereby preventing efficient implosion. Interest in SRS has intensified in recent years as experiments with higher laser intensities and longer-scale-length plasmas, intended to simulate laser–plasma interaction conditions in the National Ignition Facility (NIF), have yielded SRS reflectivities as high as 25%.[1] Furthermore, for many years theoretical models of SRS have had difficulty accounting for several aspects of the experimental observations: SRS is often observed at incident intensities well below the theoretical threshold; the spectrum of the scattered light is broader and extends to shorter wavelengths than theory predicts; and anomalous spectral and temporal structure is observed.[2] More recently it has been found that "beam smoothing," which involves small increases in the spatial and/or temporal bandwidth of the incident laser light, effectively suppresses the SRS instability,[3,4] while theory predicts that much larger increases in the bandwidth, comparable to the instability growth rate, would be required for such suppression.

To account for the discrepancies in the threshold and spectrum, it was proposed some time ago[5,6] that SRS is not occurring in the bulk plasma, but rather in intense light filaments formed from hot spots in the incident laser beam by the self-focusing instability. Intensities in such filaments could easily surpass SRS thresholds, even if the average beam intensity was well below the threshold, and the higher intensity would be expected to drive SRS over a broader range of wavelengths. The more recent experimental observations add further support to this hypothesis: Filamentation can be suppressed by much lower bandwidths than would be required to suppress SRS directly, and the anomalous spectral and temporal features may be accounted for by the temporal evolution of the waveguide mode structure in the filament. A thorough discussion of the anomalies in SRS experiments and how they can be explained by filamentation is presented in Afshar-rad *et al.*,[7] along with direct observational evidence for the occurrence of SRS in filaments. It should be pointed out that this interpretation of the experimental observations has great potential significance for NIF since it suggests that the bandwidth already incorporated in the NIF design to improve irradiation uniformity may also be sufficient to suppress or greatly reduce SRS.

The experimental evidence for the connection between filamentation and SRS is especially compelling for the short-wavelength portion of the SRS spectrum. Recently reported experiments[1,3,4] on the Nova laser at LLNL studied a 351-nm laser beam interacting with a preformed plasma at a temperature of ~3 keV. The density profiles of these plasmas have a large central region at densities of about 10% n_{crit} and fairly sharp boundaries. LASNEX simulations of these targets, in concert with the laser interactions postprocessor (LIP),[8] predicted a narrow SRS spectrum at ~600 nm, whereas observations showed a much broader spectrum extending to shorter wavelengths. In some cases without beam smoothing, this part of the spectrum dominated, with a peak near 450 nm. Substantial scattering at these wavelengths requires long regions of very-low-density plasma, which do not appear in the hydrodynamic simulations but could exist in a filament. This part of the spectrum is strongly peaked in the backscatter direction and is greatly diminished by increased bandwidth:[4] further indications that this scattering is associated with filamentation. The beam-deflection phenomenon, observed in many of these experiments and associated with filamentation in theory and simulations,[9,10] provides independent evidence that filamentation is occurring in these plasmas.

One remaining difficulty with this interpretation concerns the damping of SRS at these wavelengths. The parametric nature of the SRS instability requires that the participating electromagnetic and electrostatic waves satisfy frequency- and wave-vector–matching conditions:

$$\omega_0 = \omega + \omega_s, \quad k_0 = k + k_s,$$

where (ω_0,k_0), (ω_s,k_s), and (ω,k) are the frequency and wavenumber pairs of the incident and scattered electromagnetic waves and the plasma wave, respectively. In the fluid approximation the dispersion relations for these three waves are

$$\omega_0^2 = \omega_p^2 + c^2k_0^2,$$
$$\omega_s^2 = \omega_p^2 + c^2k_s^2,$$
$$\omega^2 = \omega_p^2 + 3v_T^2k^2 = \omega_p^2\left(1 + 3k^2\lambda_D^2\right),$$

where ω_p is the plasma frequency, v_T is the electron thermal velocity, and λ_D is the Debye length. Short-wavelength scattering requires that ω and therefore ω_p be small so that $\omega_s \approx \omega_0$. Consequently, the thermal dispersion term becomes significant, with $k\lambda_D$ of order 1. It is well known that for electrostatic waves in homogeneous plasmas Landau damping becomes very strong when $k\lambda_D \geq 0.4$. This suggests that the plasma wave associated with short-wavelength SRS will be heavily Landau damped, and, in fact, in this case SRS is more properly referred to as stimulated Compton scattering (SCS), which has a much lower growth rate and correspondingly higher threshold; thus, significant scattering would not be expected in this range of wavelengths. One possible explanation, recently proposed by Afeyan *et al.*,[11] is that thermal transport across steep temperature gradients, produced by inverse bremsstrahlung absorption in intense hot spots in the laser beam, produces a modified non-Maxwellian electron distribution function (MDF) in the hot spot with a depleted high-energy tail. Since the high-energy electrons are responsible for Landau damping, this would result in a reduced damping in the hot spots, allowing SRS to occur. The thermal-electron mean free path in these plasmas, however, is typically much larger than the size of the laser hot spots, and the mean free path for the high-energy electrons is even longer, so it is not clear that the required steep gradient in the high-energy electron population could be sustained. Moreover, recent experiments[12] using random phase plates suggest that hot spots alone, without self-focusing, cannot account for the levels of SRS observed.

In this article we propose an alternative explanation. We investigate the collisionless damping of plasma waves propagating in a bounded region of plasma, such as the interior of a filament, and find that it can be much smaller than expected on the basis of the infinite-medium Landau theory, even with a Maxwellian electron distribution. Using a simple model of a filament and its internal modes, we then apply these results to SRS in filaments.

Linear Collisionless Damping of Localized Plasma Waves

SRS occurs when plasma waves originating in noise are amplified by their interaction with the laser field. The *initiation* and early growth of the instability thus depend on the behavior of small-amplitude plasma waves, so for the purpose of analyzing SRS thresholds and growth rates, a linear treatment of the plasma waves suffices. Furthermore, in the plasmas of interest here, the mean free paths and collision times are much longer than the spatial and temporal scales of interest, so the plasma may be regarded as collisionless. We will therefore be interested in the collisionless damping of localized small-amplitude plasma waves. This process is often referred to as "transit-time damping" since it results from the transfer of energy from the wave to particles transiting the localization volume. Although the analysis presented here is self-contained, we treat transit-time damping in filaments using the method presented in greater generality in an earlier article.[13]

Since we are interested in filaments, we will analyze plasma waves confined in a cylindrical geometry (though the extension to other geometries will be evident and the case of slab geometry is treated in Appendix A). For simplicity, we consider only azimuthally symmetric waveguide modes ($\ell = 0$) for the electromagnetic and electrostatic waves in the cylinder. While self-consistent radial intensity and density profiles for filaments can be calculated numerically,[6] it is adequate for our purposes to consider a simple filament model consisting of a circular cylinder with a sharp boundary at radius R, as shown in Fig. 76.44. The density n_0 inside the filament is assumed to be significantly lower than that outside the filament, so that waveguide modes for the light and plasma waves have negligible fields extending outside the cylinder. Pressure balance is provided by the ponderomotive potential Ψ_0 of the laser light propagating in the filament. The size and intensity of filaments likely to form in laser-produced plasmas and the properties of the corresponding waveguide modes will be discussed further below.

Inside the filament the electron distribution function is

$$f_0(\mathbf{r},\mathbf{v}) = \frac{n_0}{(2\pi)^{3/2}v_T^3}e^{-v^2/2v_T^2},$$

where $v_T^2 = k_BT_0/m$. Consider a phase-space volume element dV containing a group of co-moving particles passing through the filament. We represent the motion of each particle by the motion of its oscillation center, neglecting the oscillation

amplitude of the particle in the laser field as small compared to the length scales over which the fields vary. Since we are taking the equilibrium ponderomotive potential inside the filament to be uniform, the particle trajectories can then be represented as straight lines within the filament, as shown in Fig. 76.44. Each particle thus acquires an energy ΔE in time $\Delta t = 2\sqrt{R^2 - b^2}/v_\perp$, where b is the impact parameter of the particle and $v_\perp$ is the velocity component perpendicular to the cylinder axis. This energy, which may be positive or negative, is acquired as the particle interacts with the plasma wave trapped in the filament. To conceptually simplify the analysis we take this wave to be a standing wave and we assume that the energy removed from the wave by damping is replaced by a driving process, such as SRS, so that the wave has a constant amplitude. Then, since f_0 is even in $\mathbf{v}$, it is clear that the time-reversed process, in which the particles in a time-reversed phase-space element dV^* interact with the filament, acquiring energy $-\Delta E$ in time Δt, is also occurring. Since we are neglecting collisions, phase-space volume is conserved, $|dV^*| = |dV|$, and the net rate at which energy is transferred to the particles associated with dV is

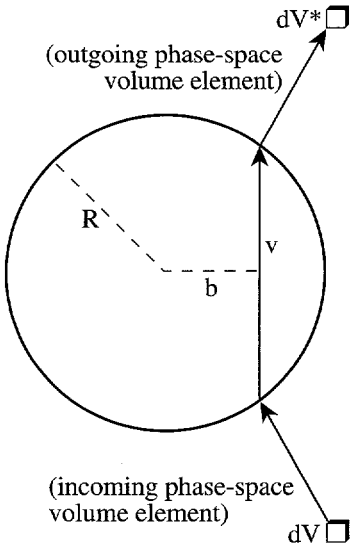

Figure 76.44
Geometry of cylindrical filament model. R is the cylinder radius, v and b are the electron velocity and impact parameter, respectively, and dV denotes a six-dimensional phase-space volume element.

$$\Delta P = \Delta E\left[f_0(E)\,dV - f_0(E+\Delta E)\,dV^*\right]/\Delta t$$

$$\cong -\frac{(\Delta E)^2}{\Delta t}\frac{\partial f_0}{\partial E}\,dV.$$

Integration of this quantity over the phase space within the filament then gives *twice* the collisionless damping rate of the plasma wave since the phase space is effectively included twice in the integration (both forward and backward in time).

First we calculate the energy acquired by a particle interacting with the filament. Inside the filament the potential satisfies the longitudinal plasma-wave dispersion relation, so assuming azimuthal symmetry for simplicity, we can write the potential as

$$\phi(r,z,t) = AJ_0(kr)\,\cos(k_z z + \alpha)\cos(\omega t + \beta), \qquad (1)$$

where A is the infinitesimal wave amplitude, J_0 is the zeroth-order Bessel function, k_z and ω are the axial wave number and frequency of the wave, and α and β are arbitrary constants representing the spatial and temporal phases of the wave, to be averaged over below. The boundary condition is $J_0(kR) = 0$, so k may be any of a discrete set of wave numbers determined by the roots of the Bessel function. We relate ω and k by the fluid plasma dispersion relation

$$\omega^2 = \omega_p^2 + 3\left(k_z^2 + k^2\right)v_T^2.$$

The main kinetic correction to this relation is an imaginary component of ω resulting from the damping we are about to calculate; corrections to the real frequency will result only in a small shift in the resulting SRS spectrum and will be neglected here. Let $t = 0$ be the time when the particle is closest to the cylinder axis. Its change in energy in crossing the filament is then obtained by integrating over the unperturbed orbit:

$$\Delta E = -e\int_{-t_0}^{t_0} \mathbf{v}\cdot\nabla\phi(\mathbf{r},t)\,dt,$$

where $t_0 = \sqrt{R^2 - b^2}/v_\perp$. The total derivative of the potential is

$$\frac{d}{dt}\phi[\mathbf{r}(t),t] = \mathbf{v}\cdot\nabla\phi[\mathbf{r}(t),t] + \frac{\partial}{\partial t}\phi[\mathbf{r}(t),t],$$

so the above integral can be written

$$\Delta E = -e\int_{-t_0}^{t_0}\left\{\frac{d}{dt}\phi[\mathbf{r}(t),t]-\frac{\partial}{\partial t}\phi[\mathbf{r}(t),t]\right\}dt.$$

The potential seen by the particle is the same before and after passing through the filament, so

$$\int_{-t_0}^{t_0}\frac{d}{dt}\phi[\mathbf{r}(t),t]\,dt = 0$$

and

$$\Delta E = e\int_{-t_0}^{t_0}\frac{\partial}{\partial t}\,\phi[\mathbf{r}(t),t]\,dt.$$

Substituting the form of the potential, we have

$$\begin{aligned}\Delta E &= -e\omega A\int_{-t_0}^{t_0} J_0[kr(t)]\cos[k_z v_z t+\alpha]\sin(\omega t+\beta)dt\\ &= -e\omega A\Big\{\cos\alpha\sin\beta\int_{-t_0}^{t_0} J_0[kr(t)]\cos k_z v_z t\cos\omega t\\ &\quad -\sin\alpha\cos\beta\int_{-t_0}^{t_0} J_0[kr(t)]\sin k_z v_z t\sin\omega t dt\Big\}.\end{aligned}$$

Squaring and averaging over the phases α and β gives

$$\begin{aligned}\langle\Delta E^2\rangle = \frac{\omega^2 e^2 A^2}{4}\Bigg\{&\left[\int_{-t_0}^{t_0} J_0[kr(t)]\cos k_z v_z t\cos\omega t dt\right]^2\\ &+\left[\int_{-t_0}^{t_0} J_0[kr(t)]\sin k_z v_z t\sin\omega t dt\right]^2\Bigg\}.\end{aligned}$$

Defining the integrals

$$I_\pm \equiv \int_{-t_0}^{t_0} J_0[kr(t)]\cos[(\omega\pm k_z v_z)t]\,dt,$$

we have

$$\langle\Delta E^2\rangle = \frac{\omega^2 e^2 A^2}{8}\left(I_+^2+I_-^2\right) = \frac{\omega^2 e^2 A^2}{4}I_+^2,$$

where the last form follows from the symmetry: $f_0(v_z) = f_0(-v_z)$, so waves propagating in both directions along the axis must be equally damped. Changing the integration variable to $s = kv_\perp t$,

$$\begin{aligned}I_\pm &= \frac{1}{kv_\perp}\int_{-k\sqrt{R^2-b^2}}^{k\sqrt{R^2-b^2}} J_0\left[\sqrt{(kb)^2+s^2}\right]\\ &\quad\times\cos\left[\frac{\omega\pm k_z v_z}{kv_\perp}s\right]ds\\ &= \frac{1}{kv_\perp}G\left(kR,kb,\frac{\omega\pm k_z v_z}{kv_\perp}\right),\end{aligned}$$

where we have defined the function

$$G(x,y,z) = \int_{-\sqrt{x^2-y^2}}^{\sqrt{x^2-y^2}} J_0\left(\sqrt{y^2+s^2}\right)\cos(zs)\,ds,$$

which must be evaluated numerically.

Next we must integrate the above expression for $\langle\Delta E^2\rangle$ over the six-dimensional phase space inside the cylinder. Note that it depends on the particle coordinates and velocities only through the two quantities kb and $w_\pm \equiv (\omega\pm k_z v_z)/kv_\perp$. The total power being transferred to particles in a length L of filament is

$$\begin{aligned}P = &\int_0^L dz\int_{-\infty}^{\infty} dv_z\int_0^{\infty} dv_\perp v_\perp\\ &\times\int_0^R dr\,r\int_0^{2\pi} d\theta_r\int_0^{2\pi} d\theta_v\left[-\frac{1}{2}\frac{\langle\Delta E^2\rangle}{\Delta t}\frac{\partial f_0}{\partial E}\right],\end{aligned}\qquad(2)$$

where the factor 1/2 in the integrand compensates for the double-counting of phase space, as noted above. Because of the rotational symmetry, all particle orbits with the same impact parameter b and speed $|v|$ must make the same contribution to $\langle\Delta E^2\rangle$, so the quantity in square brackets in (2) depends on r, θ_r, and θ_v only through the impact parameter b. We can therefore transform the last three integrals in the above expression to a single integral over b. First we transform the angles θ_r and θ_v to

$$\begin{aligned}\theta_+ &\equiv \theta_v+\theta_r,\\ \theta_- &\equiv \theta_v-\theta_r.\end{aligned}$$

By shifting portions of the region of angular integration by 2π in θ_r or θ_v, the integral over $[0, 2\pi]$ in θ_r and θ_v becomes an integral over $[0, 4\pi]$ in θ_+ and $[-\pi,\pi]$ in θ_-, as shown in

Fig. 76.45(a). Using the Jacobian $\partial(\theta_r,\theta_v)/\partial(\theta_+,\theta_-)=1/2$, we see that the angular integration is transformed as

$$\int_0^{2\pi} d\theta_r \int_0^{2\pi} d\theta_v \rightarrow \frac{1}{2}\int_0^{4\pi} d\theta_+ \int_{-\pi}^{\pi} d\theta_- .$$

Next we use

$$\theta_- = \sin^{-1}\frac{b}{r}, \quad \frac{\partial\theta_-}{\partial b} = \frac{1}{\sqrt{r^2-b^2}}, \quad \text{for } 0 \le \theta_- \le \frac{\pi}{2}.$$

As shown in Fig. 76.45(b), there are four values of θ_- in $[-\pi, \pi]$ for each value of r and b. Because of the cylindrical symmetry these values of θ_- are all physically equivalent, so we can combine the above results to obtain the transformation

$$\int_0^{2\pi} d\theta_r \int_0^{2\pi} d\theta_v \int_0^R dr\, r$$

$$\rightarrow 4\cdot\frac{1}{2}\int_0^{4\pi} d\theta_+ \int_0^R db \int_b^R dr\, r \frac{1}{\sqrt{r^2-b^2}}$$

$$\rightarrow 8\pi\int_0^R db\sqrt{R^2-b^2}\,.$$

After this transformation, the expression for the power is

$$P = 4\pi L \int_{-\infty}^{\infty} dv_z \int_0^{\infty} dv_\perp v_\perp \int_0^R db$$

$$\times\sqrt{R^2-b^2}\left[-\frac{\left\langle \Delta E^2\right\rangle}{\Delta t}\frac{\partial f_0}{\partial E}\right], \qquad (3)$$

where we have done the z-integral using the fact that $\left\langle \Delta E^2\right\rangle$ is independent of z.

Using

$$\frac{\partial f_0}{\partial E} = -\frac{n_0}{(2\pi)^{3/2} m v_T^5} e^{-v^2/2v_T^2}, \quad \Delta t = \frac{2\sqrt{R^2-b^2}}{v_\perp},$$

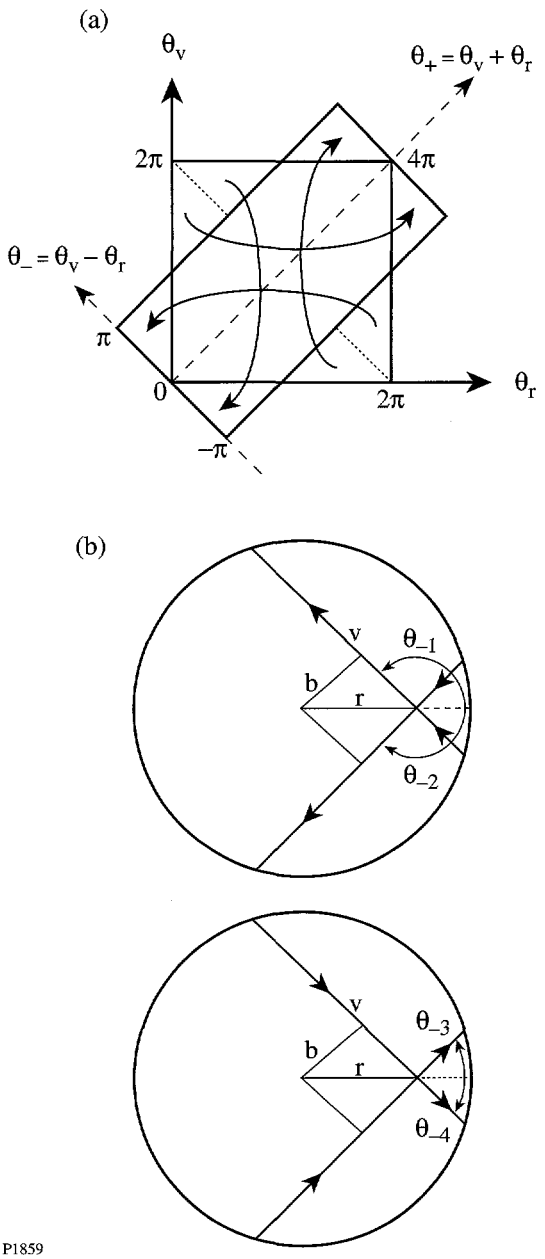

Figure 76.45
Illustration of variable and range transformations used in converting the integral in Eq. (2) to the form in Eq. (3). The angles θ_i in (b) are measured from the dashed extension of r.

and

$$\left\langle \Delta E^2\right\rangle = \frac{\omega^2 e^2 A^2}{4k^2 v_\perp^2} G^2\left(kR, kb, \frac{\omega + k_z v_z}{k v_\perp}\right),$$

this becomes

$$P = \frac{n_0 \omega^2 e^2 A^2 L}{4(2\pi)^{1/2} m v_T^5 k^2}$$

$$\times \int_{-\infty}^{\infty} dv_z \int_0^{\infty} dv_\perp \int_0^R db G^2\left(kR, kb, \frac{\omega + k_z v_z}{k v_\perp}\right) e^{-v^2/2v_T^2}.$$

As an aside, we now verify that the above expression gives the familiar result for Landau damping of a plane electrostatic wave as $R \to \infty$. This result can be established in full generality (including finite radial and azimuthal wave numbers) by methods analogous to those employed for slab and spherical geometries in Ref. 14, but the analysis is fairly complex. Since we are interested here in the application to SRS backscatter, we can simplify matters by considering only the special case where the $R \to \infty$ limit is a plane wave with wave number k_z propagating in the z direction ($k = 0$). To simplify the calculation, we take the limit $k \to \infty$ first, and then let $R \to \infty$, so that the cylinder contains a plane wavefront for all $r < R$. This means the boundary conditions will not be satisfied as we take this limit, but this doesn't affect the result since the boundary's contribution to the damping vanishes as it recedes to infinity. For small x, y we have

$$G(x, y, z) \equiv \int_{-\sqrt{x^2 - y^2}}^{\sqrt{x^2 - y^2}} \cos z s \, ds = \frac{2}{z} \sin\left(\sqrt{x^2 - y^2}\, z\right),$$

so

$$\lim_{k \to 0} \frac{1}{k^2} G^2\left(kR, kb, \frac{\omega + k_z v_z}{k v_\perp}\right)$$

$$= \frac{4 v_\perp^2}{(\omega + k_z v_z)^2} \sin^2\left[\frac{\sqrt{R^2 - b^2}}{v_\perp}(\omega + k_z v_z)\right].$$

Now the quantity $\sqrt{R^2 - b^2}/v_\perp$ in the argument of the sine function above is half the time a particle spends in the cylinder; it becomes large as R becomes large, except for the relatively small number of particles that just graze the boundary of the cylinder. Since the relative contribution of the boundary becomes insignificant as $R \to \infty$, we may regard $\sqrt{R^2 - b^2}/v_\perp$ as large for all particles of interest. With this assumption, and using

$$\lim_{\alpha \to \infty} \frac{\sin^2 \alpha x}{\alpha x^2} = \pi \delta(x) \text{ with } \alpha = \sqrt{R^2 - b^2}\, v_\perp,$$

we have

$$\lim_{k \to 0} \frac{1}{k^2} G^2\left(kR, kb, \frac{\omega + k_z v_z}{k v_\perp}\right)$$

$$= \frac{4\pi \sqrt{R^2 - b^2}}{k_z} v_\perp \delta\left(v_z + \frac{\omega}{k_z}\right),$$

so that

$$P = \frac{4\pi n_0 \omega^2 e^2 A^2 L}{4(2\pi)^{1/2} m v_T^5 k_z}$$

$$\times \int_0^{\infty} dv_\perp v_\perp \int_0^R db \sqrt{R^2 - b^2}$$

$$\times \int_{-\infty}^{\infty} dv_z \delta\left(v_z + \frac{\omega}{k_z}\right) e^{-v^2/2v_T^2}$$

$$= \frac{\omega_p^2 \omega^2 A^2 L}{4(2\pi)^{1/2} v_T^5 k_z} e^{-\frac{\omega^2}{2k_z^2 v_T^2}}$$

$$\times \int_0^{\infty} dv_\perp v_\perp e^{-v_\perp^2/2v_T^2} \int_0^R db \sqrt{R^2 - b^2}$$

$$= \frac{\omega_p^2 \omega^2 A^2 L}{4(2\pi)^{1/2} v_T^3 k_z} \frac{\pi R^2}{4} e^{-\frac{\omega^2}{2k_z^2 v_T^2}}.$$

The energy density in a traveling electrostatic plasma wave $E_0 \cos(kx - \omega t)$ is $E_0^2/8\pi$; superimposing two such waves to give a standing wave doubles the amplitude and the energy, so the energy density in a standing wave $E_0 \cos kx \cos \omega t$ is $E_0^2/16\pi$. In our case, $E_{max} = k_z A$, so the wave energy in a portion of a cylinder of radius R and length L is

$$W = \frac{1}{16} k_z^2 R^2 L A^2 ,$$

and the amplitude damping rate γ of a plane plasma wave is then given by

$$\frac{\gamma}{\omega} = \frac{1}{2}\frac{P}{\omega W} = \sqrt{\frac{\pi}{8}}\frac{\omega_p^2 \omega}{k_z^3 v_T^3} e^{-\frac{\omega^2}{2k_z^2 v_T^2}} ,$$

in agreement with the usual expression for Landau damping.[14]

Returning to the finite radius problem, we can perform one more integration analytically by transforming variables

$$v_z, v_\perp \rightarrow u, w ,$$

where

$$u = \sqrt{\frac{k}{k_z}} v_\perp , \quad w = \frac{\omega + k_z v_z}{k v_\perp} , \quad v_\perp = \sqrt{\frac{k_z}{k}} u ,$$

$$v_z = \sqrt{\frac{k}{k_z}} uw - \frac{\omega}{k_z} , \quad \frac{\partial(v_z, v_\perp)}{\partial(u, w)} = u ,$$

and

$$v^2 = \left(\frac{k_z}{k} + \frac{k}{k_z} w^2\right) u^2 - 2\frac{\omega}{k_z}\sqrt{\frac{k}{k_z}} wu + \frac{\omega^2}{k_z^2} ,$$

and then

$$P = \frac{n_0 \omega^2 e^2 A^2 L}{4(2\pi)^{1/2} m v_T^5 k^2} e^{-\frac{\omega^2}{2v_T^2 k_z^2}}$$

$$\times \int_0^R db \int_{-\infty}^{\infty} dw G^2(kR, kb, w) \int_0^{\infty} duue^{-\beta u^2 - \gamma u} ,$$

where

$$\beta = \frac{1}{2v_T^2}\left(\frac{k_z}{k} + \frac{k}{k_z} w^2\right) , \quad \gamma = -\frac{\omega}{k_z v_T^2}\sqrt{\frac{k}{k_z}} w .$$

The integral over u can be carried out using the identity[15]

$$\int_0^{\infty} duue^{-\beta u^2 - \gamma u} = \frac{1}{2\beta} e^{\frac{\gamma^2}{8\beta}} D_{-2}\left(\frac{\gamma}{\sqrt{2\beta}}\right) ,$$

where D is the parabolic cylinder function, which in this case can be expressed in terms of the error function Φ using

$$D_{-2}(z) = e^{\frac{z^2}{4}}\sqrt{\frac{\pi}{2}}\left\{\sqrt{\frac{2}{\pi}} e^{-\frac{z^2}{2}} - z\left[1 - \Phi\left(\frac{z}{\sqrt{2}}\right)\right]\right\} .$$

The remaining integrations must be carried out numerically; for this purpose it is convenient to make the integration limits finite by changing the integration variable w to ζ:

$$\zeta = \frac{\gamma}{\sqrt{2\beta}} = -\frac{\omega / k_z v_T}{\sqrt{\frac{k_z^2}{k^2} + w^2}} w ,$$

$$w = -\frac{k_z}{k}\frac{\zeta}{\sqrt{\omega^2 / k_z^2 v_T^2 - \zeta^2}} .$$

Then we have

$$dw = -\frac{k_z}{k}\frac{\omega^2 / k_z^2 v_T^2}{\left(\omega^2 / k_z^2 v_T^2 - \zeta^2\right)^{3/2}} d\zeta ,$$

$$\frac{1}{2\beta} = v_T^2 \frac{k}{k_z}\left(1 - \frac{k_z^2 v_T^2}{\omega^2}\zeta^2\right) .$$

Combining these results with the above expression for P and letting $x = kb$ gives

$$P = CI\left(kR, \frac{\omega}{k_z v_T}\right) ,$$

where

$$C = \frac{n_0 \omega^2 e^2 A^2 L}{8 m k^3 v_T^3} e^{-\frac{\omega^2}{2k_z^2 v_T^2}}$$

and

$$I\left(kR,\frac{\omega}{k_z v_T}\right)=\int_0^{kR}dx\int_{-\frac{\omega}{k_z v_T}}^{\frac{\omega}{k_z v_T}}d\zeta$$

$$\times\frac{\sqrt{\frac{2}{\pi}}-\zeta e^{\zeta^2}\left[1-\Phi\left(\frac{\zeta}{\sqrt{2}}\right)\right]}{\left(\frac{\omega^2}{k_z^2 v_T^2}-\zeta^2\right)^{1/2}}G^2\left[kR,x,w(\zeta)\right].$$

The average energy density of the plasma waves in the cylinder is

$$\left\langle\frac{E^2}{4\pi}\right\rangle_{t,z}=\frac{1}{4\pi}\left\langle(\nabla\phi)^2\right\rangle_{t,z}$$

$$=\frac{A^2}{16\pi}\left[k^2J_0'^2(kr)+k_z^2J_0^2(kr)\right],$$

so the energy in a length L of the cylinder is

$$W=\frac{1}{8}LA^2\int_0^R r\left[k^2J_0'^2(kr)+k_z^2J_0^2(kr)\right]dr.$$

Using

$$\int sJ_n^2(s)\,ds=\frac{s^2}{2}\left[J_n^2(s)-J_{n-1}(s)J_{n+1}(s)\right],$$

$$J_0'(s)=J_{-1}(s)=-J_1(s),$$

and the boundary condition $J_0(kR)=0$, we have

$$W=\frac{A^2L}{16}\left(\frac{k_z^2}{k^2}+1\right)(kR)^2J_1^2(kR);$$

thus, the amplitude damping rate is given by

$$\frac{\gamma}{\omega}=\frac{1}{2}\frac{P}{\omega W}=\frac{1}{4\pi}\frac{\omega_p^2\omega}{\left(\frac{k_z^2}{k^2}+1\right)k^3v_T^3(kR)^2J_1^2(kR)}$$

$$\times e^{-\frac{\omega^2}{2k_z^2v_T^2}}I\left(kR,\frac{\omega}{k_z v_T}\right).$$

In terms of the plane-wave Landau result given above, this is

$$\frac{\gamma}{\omega}=\left(\frac{\gamma}{\omega}\right)_{\text{Landau}}$$

$$\times\frac{1}{\sqrt{2\pi^3}}\frac{k_z/k}{1+k^2/k_z^2}\frac{1}{(kR)^2J_1^2(kR)}I\left(kR,\frac{\omega}{k_z v_T}\right). \quad (4)$$

Stimulated Raman Scattering in Filaments

In this section we analyze SRS in filaments using the simple sharp-boundary cylindrical model of the previous section (Fig. 76.44). We determine the filament parameters (radius, etc.) most likely to produce short-wavelength SRS and then estimate the collisionless damping in these filaments using the results of the previous section.

We assume that the pump and backscattered electromagnetic waves propagate as waveguide modes in the filament, so their dispersion relations can be written

$$\omega_0^2=\omega_p^2+c^2\left(k_{0r}^2+k_{0z}^2\right), \quad (5)$$

$$\omega_s^2=\omega_p^2+c^2\left(k_{sr}^2+k_{sz}^2\right), \quad (6)$$

where the subscripts r and z denote the radial and axial wave numbers and the boundary conditions require $J_0(k_{0r}R)=J_0(k_{sr}R)=0$, where R is the filament radius. The ponderomotive force arising from the beating of the pump and scattered waves drives an electrostatic plasma response. We assume that this response is largest when the frequency and wave numbers of the plasma wave satisfy the fluid dispersion relation

$$\omega^2 = \omega_p^2 + 3v_T^2\left(k_r^2 + k_z^2\right), \tag{7}$$

where again $J_0(k_r R) = 0$. This approximation will be good as long as the damping rate is much smaller than the frequency ω. As in the previous section, we assume that the SRS process is near threshold, i.e., the pump replaces the energy lost to damping of the scattered waves, so that the frequencies and wave numbers of all the modes can be taken as real. Then the frequencies and axial wave vectors satisfy the matching conditions

$$\omega_0 = \omega_s + \omega, \tag{8}$$

$$k_{0z} = k_{sz} + k_z. \tag{9}$$

Coupling between the modes is strongest for the lowest-order (smallest radial wave number) modes;[6] since in this simple model all modes have the same boundary condition $J_0(k_{0r}R) = J_0(k_{sr}R) = J_0(k_r R) = 0$, the strongest coupling is obtained by taking

$$k_{0r} = k_{sr} = k_r = j_{01}/R,$$

where $j_{01} \cong 2.4048$ is the smallest root of J_0.

Light propagates in a waveguide mode in the filament because the density inside the filament, n_0, is lower than that outside, N_0. The difference in plasma pressures inside and outside the filament must be balanced by the ponderomotive force of the light confined in the filament. The required intensity in the filament will be a minimum when the increment in density across the filament boundary is the minimum required to confine the pump wave, or

$$\frac{N_0}{n_c} - \frac{n_0}{n_c} = \frac{c^2 k_{0r}^2}{\omega_0^2}. \tag{10}$$

Since the scattered waves are of lower frequency than the pump, they are also confined to the filament when condition (6) holds.

If we are now given the background temperature T_0, density N_0, and pump wavelength $\lambda_0 = 2\pi c/\omega_0$, Eqs. (5)–(10) are six equations determining the six unknowns $\omega_p^2 = 4\pi n_0 e^2/m, k_{0z}$, k_{sz}, k_z, ω, and R in terms of the scattered-light wavelength $\lambda_s = 2\pi c/\omega_s$. We can solve them numerically to obtain in particular the filament radius and density as a function of SRS wavelength, as shown in Figs. 76.46(a)–76.46(b) for the typical experimental parameters $N_0/n_c = 0.1$, $T_0 = 3$ keV, and $\lambda_0 = 351$ nm. The SRS spectrum corresponding to these

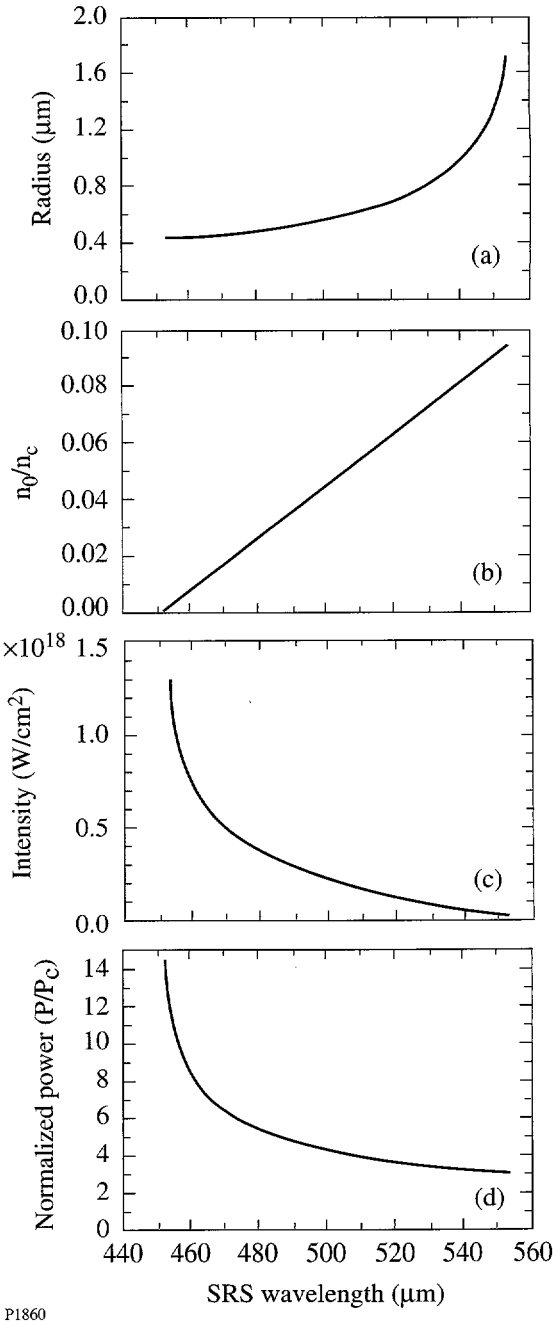

Figure 76.46
Parameters of the filament model as determined in the **Stimulated Raman Scattering in Filaments** section, plotted against the SRS emission wavelength. The filament radius is plotted in (a), the interior density in (b) (for an exterior density of one-tenth critical), the interior light intensity in (c), and the normalized power in the filament in (d).

parameters extends from about 450 nm to about 550 nm. The density plot shows that longer wavelengths would require $N_0/n_c = 0.1$, while shorter wavelengths lead to unphysical negative densities inside the filament. Note that over most of the spectrum the required filament radii tend to be quite small—of the order of a few collisionless skin depths or about a micron for these parameters.

By using the condition that the ponderomotive force balance the difference in plasma pressures inside and outside the filament, we can obtain the intensity and power in the filament. The pressure balance condition is $n_0 = N_0 e^{-v_0^2/4v_T^2}$, where v_0 is the oscillatory velocity of an electron in the electric field of the filament

$$v_0 = eE_{\max}/m\omega_0 \cong 25.6\sqrt{I\left(\mathrm{W/cm^2}\right)}\lambda_0(\mu\mathrm{m})\ \mathrm{cm\ s^{-1}} \qquad (11)$$

with I being the intensity in the filament and λ_0 the laser wavelength. Solving for the intensity yields

$$I\left(\mathrm{W/cm^2}\right) \cong 1.1\times 10^{13}\,\frac{T_0(\mathrm{eV})}{\lambda_0^2(\mu\mathrm{m})}\ln\left(\frac{N_0}{n_0}\right).$$

These intensities are plotted in Fig. 76.46(c). Since in our simplified model the intensity is uniform in the interior of the filament, the power in the filament is obtained by multiplying the intensity by πR^2 and is shown in Fig. 76.46(d) as the normalized power P_N (usually denoted by N in the literature;[16] we use the present notation to avoid confusion with the number density). The normalized power is in general defined by

$$P_N \equiv \frac{e^2}{8\pi m\omega_0^2 T_0}\,\frac{\omega_p^2}{c^2}\iint_A \left|E^2\right| dxdy,$$

where the integration is over the cross-sectional area of the filament.

The normalized power and the filament radius normalized to the collisionless skin depth are useful in comparing our simple filament model with what might be expected of actual filaments. Recently Vidal and Johnston[17] have published some nonlinear simulations of the breakup of laser beams into filaments in plasmas. They find that comparatively long-lived filaments typically tend to form with radii of a few collisionless skin depths and normalized powers P_N in the range of 2 to 15. Larger filaments tend to break up into several smaller filaments within this range; smaller filaments cannot form because of diffraction. From Figs. 76.46(a) and 76.46(d) we see that the filaments our model predicts for short-wavelength SRS have parameters within this range. So we may conclude that, *at least* in terms of gross parameters such as size and intensity, our model is not an unreasonable representation of the filaments likely to be involved in SRS.

The collisionless damping rate for the plasma mode associated with each SRS wavelength, as calculated in the **Linear Collisionless Damping** section, is shown in Fig. 76.47. For comparison we also show the damping rate for a plasma wave in a homogeneous plasma that would give the same SRS wavelength. Details of the calculation of the damping rate in homogeneous plasmas is given in the Appendix. From Fig. 76.47 we see that for longer wavelengths (corresponding to filaments of large radius) the damping rates approach the homogeneous Landau result, but for shorter wavelengths the smaller radius results in a much-reduced damping as compared to the homogeneous case.

The growth rate for SRS in a filament is readily calculated from the coupled wave equations for the waveguide modes;[6] it is largest when the plasma response is taken to be the fundamental mode (i.e., $k = j_{01}/R$) and is then the same as for a plane-wave pump of the same intensity in a homogeneous plasma. The linear, undamped, homogeneous SRS growth rate γ_0 at high pump intensities is given by[14]

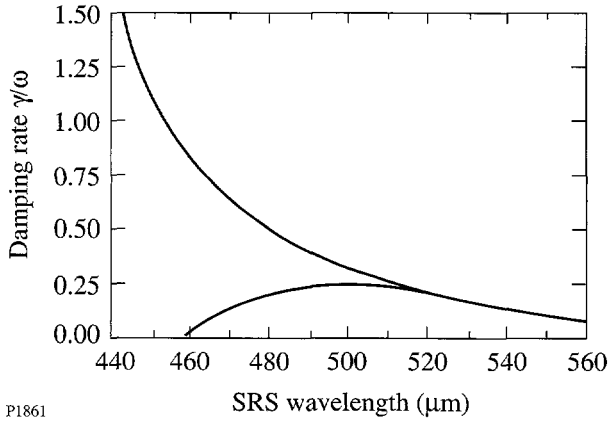

Figure 76.47
Damping rates for plasma waves giving rise to SRS, plotted against the wavelength of the SRS light produced. The upper curve gives the results for a homogeneous plasma, the lower for the filament model in the **Stimulated Raman Scattering in Filaments** section.

$$\frac{\gamma_0}{\omega_0} \cong \sqrt{\frac{\omega_p}{\omega_0}\frac{v_0}{c}}.$$

From Fig. 76.46(c) and Eq. (11) we see that $\gamma_0/\omega_0 \approx 0.1$ in the parameter regime of interest to us. This means that the instability will reach nonlinear saturation within a few tens of laser periods temporally and within a few tens of wavelengths spatially, i.e., the spatial and temporal length scales of the SRS interaction are typically much smaller than those of the filament. This justifies the use of an infinitely long, steady-state filament model to study SRS. The high intensities and low damping within the filament also mean that the SRS threshold arising from damping[14]

$$\gamma_0 > \sqrt{\gamma_e \gamma_s}$$

is greatly exceeded, where γ_e and γ_s are the damping rates of the plasma and electromagnetic waves, respectively. Finally, the comparatively low damping of the plasma wave justifies the use of the plasma-wave dispersion relation for the plasma response in these calculations, since for low damping SRS will dominate stimulated Compton scattering.

Conclusions

Discrepancies have long been noted between observations of SRS and theories premised on relatively homogeneous plasmas and uniform laser irradiation. Foremost among these are the onset of SRS at intensities well below the predicted thresholds and the presence of SRS at short wavelengths, which should in theory be suppressed by Landau damping. Many of these discrepancies can be accounted for if the SRS is actually occurring in high-intensity, self-focused light filaments, but this interpretation is still open to the objection that the short-wavelength scattering requires low plasma densities and thus should still be suppressed by Landau damping. We have shown that if short-wavelength SRS is generated in filaments, the Landau damping of the corresponding plasma waves is greatly reduced relative to the damping that would occur if the SRS were being generated outside the filamentary context. This removes the primary objection to the filamentation hypothesis as the explanation for the anomalous SRS observations and suggests that if filamentation is suppressed, for example, by beam-smoothing schemes intended to improve irradiation uniformity, the SRS instability should then be well described by classical theories. One especially important implication of this is that the effective observational threshold for SRS should be significantly increased if filamentation is suppressed by beam smoothing, so that at NIF intensities, for example, SRS would not be significant.

ACKNOWLEDGMENT

This work was supported by the U.S. Department of Energy Office of Inertial Confinement Fusion under Cooperative Agreement No. DE-FC03-92SF19460, the University of Rochester, and the New York State Energy Research and Development Authority. The support of DOE does not constitute an endorsement by DOE of the views expressed in this article.

APPENDIX: Calculation of Collisionless Damping for SRS in Homogeneous Plasmas

For purposes of comparison with our results for the damping of longitudinal waveguide modes in filaments, we also showed in Fig. 76.47 the corresponding damping rates for plane waves in homogeneous plasmas. Since these damping rates are typically much larger and can be comparable to the real frequency, the use of the usual small-damping approximation[14] to Landau damping is not justified. To calculate these damping rates we therefore use the exact expression for the plasma dielectric response function in a Maxwellian plasma:

$$\varepsilon(k,\omega) = 1 + \frac{1}{(k\lambda_D)^2}\left[1 + \Omega Z(\Omega)\right]; \tag{A1}$$

where

$$\Omega \equiv \frac{\omega}{\sqrt{2}kv_T} = \frac{1}{\sqrt{2}}\left(1 - \frac{\omega_s}{\omega_0}\right)\left(\frac{n_0}{n_c}\right)^{-\frac{1}{2}}\frac{1}{k\lambda_D}, \tag{A2}$$

and where Z denotes the plasma dispersion function,[18] ω_s is the SRS scattered light frequency, n_0 is the homogeneous plasma electron density, v_T is the electron thermal velocity, λ_D is the Debye length, and n_c is the critical density at the laser frequency ω_0. The normal modes are given by the values of k and ω for which $\varepsilon(k,\omega) = 0$. These are the modes that propagate in the absence of a driver, and for a Maxwellian plasma they are damped, i.e., ω has an imaginary component, corresponding to the Landau damping, and the wave amplitude decreases with time. Here, however, we are interested in the steady-state response of a driven plasma wave, corresponding to the situation where SRS is at threshold; i.e., the power provided by the pump wave (the laser beam) exactly compensates for the power lost to damping. (Once above threshold, the instability grows so rapidly that the damping becomes irrelevant.) The plasma response at a given frequency may then be regarded as a driven damped harmonic oscillator, reaching

maximum amplitude at that point in the plasma where $|\varepsilon(k,\omega)|$ is a minimum. SRS can occur at a range of plasma densities below quarter-critical density. Underdense plasmas typically include such a range of plasma densities but are close to isothermal; thus, we regard the temperature as being fixed and look for the values of n_0/n_c and $k\lambda_d$ that minimize $\varepsilon(k,\omega)$. From (A1) and (A2), since ω_s is known, this minimization provides a relation between the two unknowns n_0/n_c and $k\lambda_d$, which we can write by expressing $k\lambda_d$ as a function of n_0/n_c:

$$k\lambda_D\left(\frac{n_0}{n_c}\right) = x \quad \text{such that}$$

$$\left|\varepsilon\left[x,\Omega\left(x,\frac{n_0}{n_c}\right)\right]\right| \le \left|\varepsilon\left[x',\Omega\left(x',\frac{n_0}{n_c}\right)\right]\right| \quad \text{for all } x', \qquad \text{(A3)}$$

where we have used (A2) to represent Ω as a function of $k\lambda_d$ and n_0/n_c.

We obtain another relation between these unknowns from the dispersion relations of the pump and scattered light waves and the frequency and wave-number matching conditions for SRS:

$$\omega_0^2 = \omega_p^2 + c^2k_0^2, \qquad \omega_s^2 = \omega_p^2 + c^2k_s^2;$$
$$\omega = \omega_0 - \omega_s, \qquad k = k_0 - k_s, \quad k_+ = k_0 + k_s,$$

where (ω_0,k_0) and (ω_s,k_s) are the frequency and wave number of the pump and scattered EM waves, respectively. Subtracting the two dispersion relations gives

$$\omega_0^2 - \omega_s^2 = c^2\left(k_0^2 - k_s^2\right) = c^2k_+k, \quad \text{so } k_+ = \frac{\omega_0^2 - \omega_s^2}{c^2k}.$$

Adding the two dispersion relations then yields

$$1 + \frac{\omega_s^2}{\omega_0^2} = 2\frac{n_0}{n_c} + \frac{1}{2}\left[\frac{c^2k^2}{\omega_0^2} + \frac{\left(1-\frac{\omega_s^2}{\omega_0^2}\right)^2}{\frac{c^2k^2}{\omega_0^2}}\right]. \qquad \text{(A4)}$$

Next we can write

$$\frac{c^2k^2}{\omega_0^2} = \frac{c^2}{v_T^2}\frac{\omega_p^2}{\omega_0^2}\frac{v_T^2k^2}{\omega_p^2} = \left(\frac{v_T^2}{c^2}\right)^{-1}\frac{n_0}{n_c}\left(k\lambda_D\right)^2, \qquad \text{(A5)}$$

and since the temperature, or equivalently v_T, is assumed known, combining (A4) and (A5) gives another relation between $k\lambda_D$ and n_0/n_c, which along with (A3) can be solved numerically to obtain these unknowns and thus determine k. The Landau damping rate, which may also be regarded as the rate of transfer of energy from the wave to the resonant particles, is then given by

$$\frac{\gamma}{\omega} = \frac{1}{2}\mathrm{Im}\left[\varepsilon(k,\omega)\right].$$

Using (A1) and the formula for the Z function of a real argument

$$Z(x) = e^{-x^2}\left[i\sqrt{\pi} - 2\int_0^x e^{t^2}\,dt\right],$$

this is

$$\frac{\gamma}{\omega} = \sqrt{\frac{\pi}{8}}\frac{\omega_p^2\omega}{k^3v_T^3}e^{-\frac{\omega^2}{2k^2v_T^2}}. \qquad \text{(A6)}$$

This is the damping rate for SRS in a homogeneous plasma, as plotted in Fig. 76.47. It should be noted that while (A6) is identical to the Landau damping rate usually obtained for normal modes $\left[\varepsilon(k,\omega)=0\right]$ under the assumption of weak damping, for driven modes with ω real it is valid even for strong damping.

REFERENCES

1. J. C. Fernández *et al.*, Phys. Plasmas **4**, 1849 (1997).
2. A. Simon, W. Seka, L. M. Goldman, and R. W. Short, Phys. Fluids **29**, 1704 (1986), and references therein.
3. B. J. MacGowan *et al.*, Phys. Plasmas **3**, 2029 (1996).
4. D. S. Montgomery *et al.*, Phys. Plasmas **3**, 1728 (1996).
5. K. Tanaka, L. M. Goldman, W. Seka, M. C. Richardson, J. M. Soures, and E. A. Williams, Phys. Rev. Lett. **48**, 1179 (1982).

6. R. W. Short, W. Seka, and R. Bahr, Phys. Fluids **30**, 3245 (1987), and references therein.

7. T. Afshar-rad *et al.*, Phys. Fluids B **4**, 1301 (1992).

8. R. L. Berger, E. A. Williams, and A. Simon, Phys. Fluids B **1**, 414 (1989).

9. R. W. Short, R. Bingham, and E. A. Williams, Phys. Fluids **25**, 2302 (1982).

10. D. E. Hinkel, E. A. Williams, and C. H. Still, Phys. Rev. Lett. **77**, 1298 (1996).

11. B. B. Afeyan, A. E. Chou, J. P. Matte, R. P. J. Town, and W. L. Kruer, Phys. Rev. Lett. **80**, 2322 (1998).

12. C. Labaune *et al.*, Phys. Plasmas **5**, 234 (1998).

13. Laboratory for Laser Energetics LLE Review **75**, 200, NTIS document No. DOE/SF/19460-246 (1998). Copies may be obtained from the National Technical Information Service, Springfield, VA 22161.

14. W. L. Kruer, *The Physics of Laser Plasma Interactions*, Frontiers in Physics, Vol. 73, edited by D. Pines (Addison-Wesley, Redwood City, CA, 1988).

15. I. S. Gradshteyn and I. M. Ryzhik, *Table of Integrals, Series, and Products*, edited by A. Jeffrey (Academic Press, New York, 1980), p. 337.

16. J. F. Lam, B. Lippmann, and F. Tappert, Phys. Fluids **20**, 1176 (1977).

17. F. Vidal and T. W. Johnston, Phys. Rev. Lett. **77**, 1282 (1996).

18. B. D. Fried and S. D. Conte, *The Plasma Dispersion Function* (Academic Press, New York, 1961).

LLE's Summer High School Research Program

During the summer of 1998, 11 students from Rochester-area high schools participated in the Laboratory for Laser Energetics' Summer High School Research Program. The goal of this program is to excite a group of high school students about careers in the areas of science and technology by exposing them to research in a state-of-the-art environment. Too often, students are exposed to "research" only through classroom laboratories, which have prescribed procedures and predictable results. In LLE's summer program, the students experience all of the trials, tribulations, and rewards of scientific research. By participating in research in a real environment, the students often become more excited about careers in science and technology. In addition, LLE gains from the contributions of the many highly talented students who are attracted to the program.

The students spent most of their time working on their individual research projects with members of LLE's technical staff. The projects were related to current research activities at LLE and covered a broad range of areas of interest including optics, spectroscopy, chemistry, diagnostic development, and materials science (see Table 76.III).

The students attended weekly seminars on technical topics associated with LLE's research. Topics this year included lasers, fusion, holography, nonlinear optics, global warming, and scientific ethics. The students also received safety training, learned how to give scientific presentations, and were introduced to LLE's resources, especially the computational facilities.

The program culminated with the High School Student Summer Research Symposium on 26 August at which the students presented the results of their research to an audience including parents, teachers, and LLE staff. The students also prepared written reports, which were bound into a permanent record of their work. These reports are available by contacting LLE.

Ninety-three high school students have participated in the program since it began in 1989. The students this year were selected from approximately 60 applicants.

In 1997, LLE added a new component to its high school outreach activities: an annual award to an Inspirational Science Teacher. This award honors teachers who have inspired High School Program participants in the areas of science, mathematics, and technology and includes a $1000 cash prize. Teachers are nominated by alumni of the High School Program. The 1998 award was presented at the symposium to Mr. David Crane, a chemistry teacher from Greece Arcadia High School. Mr. Crane was nominated by Robert Dick, a participant in the 1991 Program. Mr. Dick wrote that Mr. Crane's "academic competence, curiosity, and enthusiasm toward teaching allow him to motivate students who would, otherwise, fall through the cracks. Mr. Crane attracted students who wouldn't typically take difficult science courses." He added, "Mr. Crane would stay after normal school hours to host an informal lecture and lab, just to satisfy our curiosity."

Ms. Donna Essegian, principal of Greece Arcadia High School, added, "He is dedicated to his students. ...He is a continuous learner himself and has served this way as a model for students that science is an evolving subject." Mr. Terry Kessler, an LLE scientist who was taught by Mr. Crane, remembered, "The science teacher tandem at Greece Arcadia High School, consisting of Mr. David Crane (chemistry) and Mr. Claude Meyers (physics), has encouraged many of us to follow our curiosities in science and to pursue lifelong learning."

Table 76.III: High School Students and Projects—Summer 1998.

Student	High School	Supervisor	Project
Steven Corsello	Pittsford Mendon	K. Marshall	Computer-Aided Design and Modeling of Nickeldithiolene Near-IR Dyes
Peter Grossman	Wilson Magnet	S. Craxton	Group Velocity Effects in Broadband Frequency Conversion on OMEGA
Joshua Hubregsen	Pittsford Sutherland	S. Jacobs	A Study of Material Removal During Magnetorheological Finishing (MRF)
Neil Jain	Pittsford Sutherland	M. Guardalben	Phase-Shifting Algorithms for Nonlinear and Spatially Nonuniform Phase Shifts
Leslie Lai	Pittsford Mendon	M. Wittman	The Use of Design-of-Experiments Methodology to Optimize Polymer Capsule Fabrication
Irene Lippa	Byron-Bergen	K. Marshall	Synthesis of Nickeldithiolene Dyes and Their Solubility in a Nematic Liquid Crystal Host
Phillip Ostromogolsky	Brighton	F. Marshall	Investigation of X-Ray Diffraction Properties of a Synthetic Multilayer
Michael Schubmehl	The Harley School	R. Epstein	An Analysis of the Uncertainty in Temperature and Density Estimates from Fitting Model Spectra to Data
Joshua Silbermann	Penfield	P. Jaanimagi	Automated CCD Camera Characterization
Abigail Stern	The Harley School	J. Knauer	Design and Testing of a Compact X-Ray Diode
Amy Turner	Churchville-Chili	S. Craxton	Ray Tracing Through the Liquid Crystal Point Diffraction Interferometer (LCPDI)

FY98 Laser Facility Report

The OMEGA facility saw substantial improvements in effectiveness at executing experimental objectives for FY98. To extend operations to meet increased demand for shots on OMEGA, UR/LLE hired additional staff to support multishift operations. Starting in May, after training was completed, we began to shoot targets for 12 h each target shot day, three shot days per week. Tailoring the facility operations crew to an uninterrupted 12-h shot shift matches staffing to the routine of OMEGA shot cycles. LLE continues to "block schedule" experiments by week to minimize the number of configuration changes and provide a sufficient run time to mitigate occasional system nonavailabilities.

Advances in individual beam and beam-to-beam uniformity have been a UR/LLE priority for the FY98 period. The technological improvements to the diagnostics—the P510 multichannel streak cameras and amplifier small-signal-gain instrumentation—are two key elements necessary for developing and characterizing power balance between beams. Both systems are currently on-line diagnostics and are being utilized to maintain OMEGA at 3%–4% rms IR beam balance. LLE has also improved the as-built reliability of the power conditioning system by upgrading the high-voltage switches and trigger systems. The decreased pre-fire fault rate has improved target irradiation repeatability substantially from the beam-to-beam uniformity standpoint. Another amplifier performance issue, the premature failure of the flash lamps, has been mitigated through the development of new lamp designs. Approximately 50% of the 6800 lamps are now a higher-reliability "hard seal" configuration.

For single-beam uniformity enhancements, long-lead procurements were initiated in FY98 to fabricate beam-smoothing optics for OMEGA. During FY98 a KDP crystal vendor has been fabricating birefringent wedges for distributed polarization rotator[1] deployment on the 60 beams. LLE anticipates permanently deploying DPR optics on OMEGA in the second quarter of FY99. Perhaps the greatest uniformity improvement to the on-target profile of individual OMEGA beams was the installation of a full complement of 60 ion-etched DPP optics,[2] deployed in January 1998. These optics provide a circularly symmetric and highly repeatable individual beam profile on target which, when combined with SSD, allows OMEGA to approach the individual beam uniformity goals set for the system. Future single-beam uniformity improvements are anticipated to come through increases in SSD modulation frequency and bandwidth. During FY98 a project to frequency convert greater bandwidths with a second-harmonic mixer (KDP) was initiated.

Progress in the experimental area this year included the integration of the sixth and final 10-in. manipulator (TIM) and activation of several new diagnostics. New diagnostic capability for FY98 included activation of two charged-particle spectrometers, a time-resolved flat-field XUV spectrometer, an XUV Cassegrain telescope, an imaging XUV framing camera, a neutron bang-time diagnostic, a streaked optical pyrometer, and new streaked XR spectrometers. Many of these instruments were developed and fielded in conjunction with other organizations, including LLNL, LANL, NRL, MIT, and the University of Maryland. Other improvements in the experimental area include qualification of the facility for use in Stockpile Stewardship Program experiments and numerous enhancements to diagnostic timing command/control.

Many of the minor laser and experimental facility improvements are significantly easier to dovetail into the schedule since the extended shift operations schedule was implemented. Much of the maintenance work previously scheduled on the 0400 shift prior to shots has been moved to the Friday/Monday period, facilitating an earlier availability of the system for shots each day. Table 76.IV summarizes some of the tangible gains made from switching to the extended operations scenario. In conclusion, the shot effectiveness of two weeks of extended operations exceeds the capacity provided by three weeks of the former single-shift schedule. There were a total of 882 target shots in FY98, and it can be expected that the facility will support over 1300 target shots in FY99.

Table 76.IV: OMEGA operations shifted to extended hours in FY98.

	Prior to Extended Operations	Extended Operations
FY98 average number of shots/shot week	17	26
FY98 average number of shots/shot day	5.2	9.8
Average time of day for the first shot	11:47 AM (1/96 to 5/98)	10:20 AM
Total target shots for FY98: 882		

REFERENCES

1. Laboratory for Laser Energetics LLE Review **45**, 1, NTIS document No. DOE/DP/40200-149 (1990). Copies may be obtained from the National Technical Information Service, Springfield, VA 22161; Y. Kato, unpublished notes (1984).
2. Laboratory for Laser Energetics LLE Review **74**, 71, NTIS document No. DOE/SF/19460-241 (1998). Copies may be obtained from the National Technical Information Service, Springfield, VA 22161.

National Laser Users' Facility News

FY98 Experiments

During FY98 progress was made in several NLUF programs: EUV and XUV measurements of early-time plasmas (Hans Griem and Ray Elton, University of Maryland); x-ray spectroscopy of high-density plasmas (Charles Hooper *et al.*, University of Florida); spectral measurements of fusion-reaction charged particles (Richard Petrasso, Massachusetts Institute of Technology); neutron detector calibration (Stephen Padalino, State University of New York at Geneseo); high-resolution imaging of laser targets (John Seely *et al.*, Naval Research Laboratory); and radiation ablation measurements of hohlraum targets (David Cohen, University of Wisconsin).

Figure 76.48 shows a photograph of the installation of a charged-particle spectrometer (CPS 2) developed under LLE funding and now operating on the OMEGA system. CPS 2 is the second of two charged-particle spectrometers fielded by the MIT group on OMEGA. During FY98 the MIT group with funding from NLUF and in collaboration with LLE and LLNL scientists used these spectrometers to measure fusion-product charged particles and high-energy ablator ions. In one series of experiments, fuel temperature and capsule areal density were measured simultaneously by these spectrometers.

In addition to NLUF-supported programs, several indirect-drive target programs, also coordinated through the NLUF Manager, were carried out on OMEGA by groups from LANL and LLNL. These experiments included campaigns on hohlraum symmetry, tetrahedral hohlraums, double-shell capsules, opacity, and point-backlighter tests. Finally, a direct-drive cylinder experiment was fielded by LANL in collaboration with LLE.

FY99 Proposals

Fifteen proposals were submitted to NLUF for FY99. This represents a new record in submissions as well as requested funding (funding requests were more than two-and-a-half times the amount of available funding from DOE—$700,000). A DOE technical evaluation panel chaired by the NLUF Manager and including Dr. Michael Cable (LLNL), Dr. Allan Hauer (LANL), Prof. Tudor Johnston (INRS), and Dr. Ramon Leeper (SNL) reviewed the proposals at a meeting held on 24 April 1998 and recommended approval of nine proposals for funding (see Table 76.V). Twelve graduate students and seven undergraduates will participate in the NLUF programs approved for funding in FY99.

U206

Figure 76.48
Photograph taken during the installation of the second of two charged-particle spectrometers on OMEGA.

Table 76.V: Approved FY99 NLUF Proposals.

Principal Investigator	Affiliation	Proposal Title
D. Cohen	University of Wisconsin, Madison	Development of X-Ray Tracer Diagnostics for Radiatively Driven Copper-Doped Beryllium Ablators
H. Baldis	University of California at Davis	Supenova Hydrodynamics on the OMEGA Laser
H. Baldis	University of California at Davis	Studies of Dynamic Properties of Shock Compressed Solids by *in-situ* Transient X-Ray Diffraction
R. Petrasso	Massachusetts Institute of Technology	Charged-Particle Spectroscopy on OMEGA: First Results, Next Steps
H. Griem	University of Maryland	Soft X-Ray Spectroscopy Measurements of Plasma Conditions at Early Times in ICF Experiments on OMEGA
S. Padalino	SUNY Geneseo	Charged-Particle Spectroscopy on OMEGA: First Results, Next Steps (a joint program with R. Petrasso)
S. Padalino	SUNY Geneseo	Neutron Yield Measurements via Aluminum Activation
C. Hooper	University of Florida	Absorption Spectroscopy, Broadband Emission Survey and the Radiator-Plasma State
B. Afeyan	Polymath Associates	Optical Mixing Controlled Stimulated Scattering Instabilities on OMEGA

Publications and Conference Presentations

Publications

E. L. Alfonso, S.-H. Chen, R. Q. Gram, and D. R. Harding, "Properties of Polyimide Shells Made Using Vapor Phase Deposition," J. Mater. Res. **13**, 2988 (1998).

A. Babushkin, R. S. Craxton, S. Oskoui, M. J. Guardalben, R. L. Keck, and W. Seka, "Demonstration of the Dual-Tripler Scheme for Increased-Bandwidth Third-Harmonic Generation," Opt. Lett. **23**, 927 (1998).

A. Babushkin and W. Seka, "Efficient, End-Pumped, 1053-nm Nd:YLF Laser," in *Advanced Solid State Lasers*, edited by W. R. Bosenberg and M. M. Fejer, OSA Trends in Optics and Photonics Series, Vol. 19 (Optical Society of America, Washington, DC, 1998), pp. 111–113.

A. Babushkin, W. Seka, S. A. Letzring, W. Bittle, M. Labuzeta, M. Miller, and R. Roides, "Multicolor Fiducial Laser for Streak Cameras and Optical Diagnostics for the OMEGA Laser System," in *22nd International Congress on High-Speed Photography and Photonics*, edited by D. L. Paisley and A. M. Frank (SPIE, Bellingham, WA, 1997), Vol. 2869, pp. 540–544.

R. Betti, "Beta Limits for the $N = 1$ Mode in Rotating-Toroidal-Resistive Plasmas Surrounded by a Resistive Wall," Phys. Plasmas **5**, 3615 (1998).

R. Betti, V. N. Goncharov, R. L. McCrory, and C. P. Verdon, "Feedthrough and Dynamic Stabilization in Convergent Geometry," in *Laser Interaction and Related Plasma Phenomena,* edited by G. H. Miley, E. M. Campbell, W. J. Hogan, C. Maille-Petersen, H. Coppedge, and E. Montoya (American Institute of Physics, New York, 1997), Vol. 406, pp. 294–302.

R. Betti, V. N. Goncharov, R. L. McCrory, and C. P. Verdon, "Growth Rates of the Ablative Rayleigh–Taylor Instability in Inertial Confinement Fusion," Phys. Plasmas **5**, 1446 (1998).

R. Betti, V. Goncharov, R. L. McCrory, and C. P. Verdon, "Linear Theory of the Ablative Rayleigh–Taylor Instability," in *Advances in Laser Interaction with Matter and Inertial Fusion*, edited by G. Velarde, J. M. Martinez-Val, E. Minguez, and J. M. Perlado (World Scientific, Singapore, 1997), pp. 125–128.

S. E. Bodner, D. G. Colombant, J. H. Gardner, R. H. Lehmberg, S. P. Obenschain, L. Phillips, A. J. Schmitt, J. D. Sethian, R. L. McCrory, W. Seka, C. P. Verdon, J. P. Knauer, B. B. Afeyan, and H. T. Powell, "Direct-Drive Laser Fusion: Status and Prospects," Phys. Plasmas **5**, 1901 (1998).

T. R. Boehly, R. L. McCrory, C. P. Verdon, J. M. Soures, A. Babushkin, R. E. Bahr, R. Boni, D. K. Bradley, R. S. Craxton, J. A. Delettrez, W. R. Donaldson, R. Epstein, D. R. Harding, P. A. Jaanimagi, S. D. Jacobs, K. Kearney, R. L. Keck, J. H. Kelly, T. J. Kessler, R. L. Kremens, J. P. Knauer, S. A. Letzring, D. J. Lonobile, S. J. Loucks, L. D. Lund, F. J. Marshall, P. W. McKenty, D. D. Meyerhofer, S. F. B. Morse, A. Okishev, S. Papernov, G. Pien, T. Safford, W. Seka, R. W. Short, M. J. Shoup III, M. D. Skeldon, S. Skupsky, A. W. Schmid, D. J. Smith, S. Swales, M. D. Wittman, and B. Yaakobi, "The First Year of ICF Experiments at the OMEGA Laser Facility," in *Fusion Energy 1996* (IAEA, Vienna, 1997), Vol. 3, pp. 31–42.

T. R. Boehly, V. A. Smalyuk, D. D. Meyerhofer, J. P. Knauer, D. K. Bradley, C. P. Verdon, and D. Kalantar, "The Effect of Increased Irradiation Uniformity on Imprinting by 351-nm Laser Light," in *Laser Interaction and Related Plasma Phenomena,* edited by G. H. Miley, E. M. Campbell, W. J. Hogan, C. Maille-Petersen, H. Coppedge, and E. Montoya (American Institute of Physics, New York, 1997), Vol. 406, pp. 122–129.

D. K. Bradley, J. A. Delettrez, R. Epstein, R. P. J. Town, C. P. Verdon, B. Yaakobi, S. Regan, F. J. Marshall, T. R. Boehly,

J. P. Knauer, D. D. Meyerhofer, V. A. Smalyuk, W. Seka, D. A. Haynes, Jr., M. Gunderson, G. Junkel, C. F. Hooper, Jr., P. M. Bell, T. J. Ognibene, and R. A. Lerche, "Measurements of Core and Pusher Conditions in Surrogate Capsule Implosions on the OMEGA Laser System," Phys. Plasmas **5**, 1870 (1998) (invited).

B. Buerke, J. P. Knauer, S. J. McNaught, and D. D. Meyerhofer, "Precision Tests of Laser-Tunneling Ionization Models," in *Applications of High Field and Short Wavelength Sources VII*, 1997 OSA Technical Digest Series, Vol. 7 (OSA, Washington, DC, 1997), pp. 75–76.

M. B. Campanelli and D. J. Smith, "A Wideband Optical Monitor for a Planetary-Rotation Coating System," in *Optical Interference Coatings*, Vol. 9, 1998 OSA Technical Digest Series (Optical Society of America, Washington, DC, 1998), pp. 426–429.

J. L. Chaloupka, T. J. Kessler, and D. D. Meyerhofer, "A Three-Dimensional Ponderomotive Trap for High-Energy Electrons," in *Applications of High Field and Short Wavelength Sources VII*, 1997 OSA Technical Digest Series, Vol. 7 (OSA, Washington, DC, 1997), p. 109.

S.-H. Chen, J. C. Mastrangelo, B. M. Conger, A. S. Kende, and K. L. Marshall, "Synthesis and Characterization of Thermotropic Chiral-Nematic Polythiophenes," Macromolecules **31**, 3391 (1998).

A. V. Chirokikh, W. Seka, A. Simon, R. S. Craxton, and V. T. Tikhonchuk, "Stimulated Brillouin Scattering in Long-Scale-Length Laser Plasmas," Phys. Plasmas **5**, 1104 (1998).

T. J. B. Collins, H. L. Helfer, and H. M. Van Horn, "Accretion Disk and Boundary Layer Models Incorporating OPAL Opacities," Astrophys. J. **502**, 730 (1998).

M. E. DeRosa, W. W. Adams, T. J. Bunning, H. Shi, and S.-H. Chen, "Dynamic Mechanical Relaxation Behavior of Low Molecular Weight Side-Chain Cyclic Liquid Crystalline Compounds near the Glass Transition Temperature," Macromolecules **29**, 5650 (1996).

W. R. Donaldson, E. M. R. Michaels, K. Akowuah, and R. A. Falk, "Integrated Circuit Tester Using Interferometric Imaging," in *Electrochemical Society Proceedings Volume 97–12*, edited by P. Rai-Choudhury, J. Benton, D. Schroder, and T. J. Shaffner (The Electrochemical Society, Pennington, NJ, 1997), pp. 171–176.

P. M. Fauchet, "Porous Silicon: Photoluminescence and Electroluminescent Devices," in *Light Emission in Silicon*, edited by D. J. Lockwood, Semiconductors and Semimetals Series, Vol. 49 (Academic Press, Orlando, 1996), Chap. 6, pp. 205–252.

D. Fried, W. Seka, R. E. Glena, and J. D. B. Featherstone, "Permanent and Transient Changes in the Reflectance of CO_2-Laser–Irradiated Dental Hard Tissues at λ = 9.3, 9.6, 10.3, and 10.6 μm and at Fluences of 1–20 J/cm^2," Lasers Surg. Med. **20**, 22 (1997).

R. E. Giacone, C. J. McKinstrie, and R. Betti, "Response to 'Comment on "Angular Dependence of Stimulated Brillouin Scattering in Homogeneous Plasma" [Phys. Plasmas **5**, 1215 (1998)]'," Phys. Plasmas **5**, 1218 (1998).

B. E. Gillman and S. D. Jacobs, "Bound-Abrasive Polishers for Optical Glass," Appl. Opt. **37**, 3498 (1998).

B. E. Gillman, B. M. Reed, M. A. Atwood, J. L. Ruckman, D. J. Quesnel, T. T. Ochinero, and S. D. Jacobs, "Application of Coolants in Deterministic Microgrinding of Glass," in *Optical Manufacturing and Testing II*, edited by H. P. Stahl (SPIE, Bellingham, WA, 1997), Vol. 3134, pp. 198–204.

W. Göb, W. Lang, and R. Sobolewski, "Magnetoresistance of a $YBa_2Cu_3O_7$ Corbino Disk: Probing Geometrical Contributions to the Unconventional Normal-State Magnetoresistance of High-Temperature Superconductors," Phys. Rev. B: Rapid Commun. **57**, R8150 (1998).

D. Golini, S. Jacobs, W. Kordonski, and P. Dumas, "Precision Optics Fabrication Using Magnetorheological Finishing," in *Advanced Materials for Optics and Precision Structures*, edited by M. A. Ealey, R. A. Paquin, and T. B. Parsonage, Critical Reviews of Optical Science and Technology (SPIE, Bellingham, WA, 1997), Vol. CR67, pp. 251–274.

K. Green, M. Lindgren, C.-C. Wang, L. Fuller, T. Y. Hsiang, W. Seka, and R. Sobolewski, "Picosecond Photoresponse in Polycrystalline Silicon," in *Ultrafast Electronics and Optoelectronics, 1997*, edited by M. Nuss and J. Bowers, OSA Trends in Optics and Photonics Series, Vol. 13 (Optical Society of America, Washington, DC, 1997), pp. 106–109.

M. J. Guardalben, "Conoscopic Alignment Methods for Birefringent Optical Elements in Fusion Lasers," Appl. Opt. **36**, 9107 (1997).

O. E. Hanuch, V. B. Agrawal, S. Papernov, M. delCerro, and J. V. Aquavella, "Posterior Capsular Polishing with the Nd:YLF Picosecond Laser: Model Eye Study," J. Refract. Surg. **23**, 1561 (1997).

S. D. Jacobs, "Deterministic Manufacturing of Precision Glass Optics Using Magnetorheological Finishing (MRF)," in *Advances in Fusion and Processing of Glass II*, edited by A. G. Clare and L. E. Jones, Ceramic Transactions, Vol. 82 (The American Ceramic Society, Westerville, OH, 1998), pp. 457–468.

S. D. Jacobs, F. Yang, E. M. Fess, J. B. Feingold, B. E. Gillman, W. I. Kordonski, H. Edwards, and D. Golini, "Magnetorheological Finishing of IR Materials," in *Optical Manufacturing and Testing II*, edited by H. P. Stahl (SPIE, Bellingham, WA, 1997), Vol. 3134, pp. 258–269.

D. Jacobs-Perkins, M. Currie, K. T. Tang, C.-C. Wang, C. Williams, W. R. Donaldson, R. Sobolewski, and T. Y. Hsiang, "Subpicosecond Electro-optic Imaging Using Interferometric and Polarimetric Apparatus," in *Ultrafast Electronics and Optoelectronics, 1997*, edited by M. Nuss and J. Bowers, OSA Trends in Optics and Photonics Series, Vol. 13 (Optical Society of America, Washington, DC, 1997), pp. 202–207.

R. L. Keck, A. V. Okishev, M. D. Skeldon, A. Babushkin, and W. Seka, "Pulse Shaping on the OMEGA Laser System," in *Laser Interaction and Related Plasma Phenomena*, edited by G. H. Miley, E. M. Campbell, W. J. Hogan, C. Maille-Petersen, H. Coppedge, and E. Montoya (American Institute of Physics, New York, 1997), Vol. 406, pp. 333–340.

T. J. Kessler, Y. Lin, L. S. Iwan, W. P. Castle, C. Kellogg, J. Barone, E. Kowaluk, A. W. Schmid, K. L. Marshall, D. J. Smith, A. L. Rigatti, J. Warner, and A. R. Staley, "Laser Phase Conversion Using Continuous Distributed Phase Plates," in *Solid-State Lasers for Application to Inertial Confinement Fusion*, edited by M. L. André (SPIE, Bellingham, WA, 1997), Vol. 3047, pp. 272–281.

J. P. Knauer, D. D. Meyerhofer, T. R. Boehly, D. Ofer, C. P. Verdon, D. K. Bradley, P. W. McKenty, V. A. Smalyuk, S. G. Glendinning, and R. G. Watt, "Single-Mode Rayleigh–Taylor Growth-Rate Measurements with the OMEGA Laser System," in *Laser Interaction and Related Plasma Phenomena*, edited by G. H. Miley, E. M. Campbell, W. J. Hogan, C. Maille-Petersen, H. Coppedge, and E. Montoya (American Institute of Physics, New York, 1997), Vol. 406, pp. 284–293.

O. A. Konoplev and D. D. Meyerhofer, "Cancellation of *B*-Integral Accumulation for CPA Lasers," IEEE J. Sel. Top. Quantum Electron. **4**, 459 (1998).

W. Kordonski, D. Golini, P. Dumas, S. Hogan, and S. Jacobs, "Magnetorheological Suspension-Based Finishing Technology," in *Smart Structures and Materials 1998: Industrial and Commercial Applications of Smart Structures Technologies*, edited by J. M. Sater (SPIE, Bellingham, WA, 1998), Vol. 3326, pp. 527–535.

E. M. Korenic, S. D. Jacobs, S. M. Faris, and L. Li, "Color Gamut of Cholesteric Liquid Crystal Films and Flakes by Standard Colorimetry," Color Res. Appl. **23**, 210 (1998).

J. C. Lambropoulos, B. E. Gillman, Y. Zhou, S. D. Jacobs, and H. J. Stevens, "Glass-Ceramics: Deterministic Microgrinding, Lapping, and Polishing," in *Optical Manufacturing and Testing II*, edited by H. P. Stahl (SPIE, Bellingham, WA, 1997), Vol. 3134, pp. 178–189.

J. C. Lambropoulos, S. D. Jacobs, B. Gillman, F. Yang, and J. Ruckman, "Subsurface Damage in Microgrinding Optical Glasses," in *Advances in Fusion and Processing of Glass II*, edited by A. G. Clare and L. E. Jones, Ceramic Transactions, Vol. 82 (American Ceramic Society, Westerville, OH, 1998), pp. 469–474.

M. Lindgren, W.-S. Zeng, M. Currie, C. Williams, T. Y. Hsiang, P. M. Fauchet, R. Sobolewski, S. H. Moffat, R. A. Hughes, J. S. Preston, and F. A. Hegmann, "An Ultrafast High-T_c Superconducting Y-Ba-Cu-O Photodetector," in *Ultrafast Electronics and Optoelectronics, 1997*, edited by M. Nuss and J. Bowers, OSA Trends in Optics and Photonics Series, Vol. 13 (Optical Society of America, Washington, DC, 1997), pp. 102–105.

S. G. Lukishova, S. V. Belyaev, K. S. Lebedev, E. A. Magulariya, A. W. Schmid, and N. V. Malimonenko, "Behaviour of Nonlinear Liquid-Crystal Mirrors, Made of a Nonabsorbing Cholesteric, in the Cavity of an Nd:YAG Laser Operating in the cw Regime and at a High Pulse Repetition Frequency," Quantum Electron. **26**, 796 (1996).

S. G. Lukishova, S. V. Belyaev, K. S. Lebedev, E. A. Magulariya, A. W. Schmid, and N. V. Malimonenko, "Nonlinear Bleaching in the Selective Reflection of Nonabsorbing Chiral-Nematic Liquid-Crystal Thin Films," Mol. Cryst. Liq. Cryst. **303**, 79 (1997).

S. G. Lukishova, K. S. Lebedev, E. A. Magulariya, S. V. Belyaev, N. V. Malimonenko, and A. W. Schmid, "Nonlinear 'Brightening' of a Film of Nonabsorbing Chiral Nematic Under Selective Reflection Conditions," JETP Lett. **63**, 423 (1996).

F. J. Marshall, M. M. Allen, J. P. Knauer, J. A. Oertel, and T. Archuleta, "A High-Resolution X-Ray Microscope for Laser-Driven Planar-Foil Experiments," Phys. Plasmas **5**, 1118 (1998).

R. L. McCrory, "The LLE Direct-Drive Target Physics Experimental Program: First Year of Experiments on OMEGA," in *Advances in Laser Interaction with Matter and Inertial Fusion*, edited by G. Velarde, J. M. Martinez-Val, E. Minguez, and J. M. Perlado (World Scientific, Singapore, 1997), pp. 16–19 (invited).

C. J. McKinstrie, A. V. Kanaev, V. T. Tikhonchuk, R. E. Giacone, and H. X. Vu, "Three-Dimensional Analysis of the Power Transfer Between Crossed Laser Beams," Phys. Plasmas **5**, 1142 (1998).

C. J. McKinstrie, J. S. Li, and A. V. Kanaev, "Near-Forward Stimulated Brillouin Scattering," Phys. Plasmas **4**, 4227 (1997).

C. J. McKinstrie and E. J. Turano, "Nonrelativistic Motion of a Charged Particle in an Electromagnetic Field," J. Plasma Phys. **59**, 555 (1998).

S. J. McNaught, J. P. Knauer, and D. D. Meyerhofer, "Photoelectron Initial Conditions for Tunneling Ionization in a Linearly Polarized Laser," Phys. Rev. A **58**, 1399 (1998).

D. D. Meyerhofer, "High-Intensity-Laser-Electron Scattering," IEEE J. Quantum Electron. **33**, 1935 (1997).

T. J. Murphy, J. M. Wallace, N. D. Delamater, C. W. Barnes, P. Gobby, A. A. Hauer, E. L. Lindman, G. Magelssen, J. B. Moore, J. A. Oertel, R. Watt, O. L. Landen, P. Amendt, M. Cable, C. Decker, B. A. Hammel, J. A. Koch, L. J. Suter, R. E. Turner, R. J. Wallace, F. J. Marshall, D. Bradley, R. S. Craxton, R. Keck, J. P. Knauer, R. Kremens, and J. D. Schnittman, "Indirect-Drive Experiments Utilizing Multiple Beam Cones in Cylindrical Hohlraums on OMEGA," Phys. Plasmas **5**, 1960 (1998).

B. Nodland and C. J. McKinstrie, "Propagation of a Short Laser Pulse in a Plasma," Phys. Rev. E **56**, 7174 (1997).

J. J. Ou and S.-H. Chen, "Molecular Dynamics Simulation of Organic Glass-Formers: I. *ortho*-Terphenyl and 1,3,5-Tri-α-Naphthyl Benzene," J. Comput. Chem. **19**, 86 (1998).

S. Papernov and A. W. Schmid, "Localized Absorption Effects During 351-nm, Pulsed Laser Irradiation of Dielectric Multilayer Thin Films," J. Appl. Phys. **82**, 5422 (1997).

S. Papernov, A. W. Schmid, and F. Dahmani, "Laser Damage in Polymer Waveguides Driven Purely by a Nonlinear, Transverse-Scattering Process," Opt. Commun. **147**, 112 (1998).

S. Papernov, A. W. Schmid, and D. Zaksas, "Characterization of Freestanding Polymer Films for Application in 351-nm, High-Peak-Power Laser Systems," Opt. Eng. **37**, 677 (1998).

S. Papernov, D. Zaksas, J. F. Anzellotti, D. J. Smith, A. W. Schmid, D. R. Collier, and F. A. Carbone, "One Step Closer to the Intrinsic Laser-Damage Threshold of HfO_2 and SiO_2 Monolayer Thin Films," in *Laser-Induced Damage in Optical Materials: 1997*, edited by G. J. Exarhos, A. H. Guenther, M. R. Kozlowski, and M. J. Soileau (SPIE, Bellingham, WA, 1998), Vol. 3244, pp. 434–445.

S. Papernov, D. Zaksas, and A. W. Schmid, "A Nonlinear UV-Damage Mechanism in Polymer Thin Films Observed from Below to Above Damage Threshold," in *Laser-Induced Damage in Optical Materials: 1997*, edited by G. J. Exarhos, A. H. Guenther, M. R. Kozlowski, and M. J. Soileau (SPIE, Bellingham, WA, 1998), Vol. 3244, pp. 509–515.

S. Papernov, D. Zaksas, and A. W. Schmid, "Perfluorinated Polymer Films with Extraordinary UV-Laser-Damage Resistance," in *Laser-Induced Damage in Optical Materials: 1997*, edited by G. J. Exarhos, A. H. Guenther, M. R. Kozlowski, and M. J. Soileau (SPIE, Bellingham, WA, 1998), Vol. 3244, pp. 522–527.

A. L. Rigatti and D. J. Smith, "Status of Optics on the OMEGA Laser System after 18 Months of Operation," in *Laser-Induced Damage in Optical Materials: 1996*, edited by H. E. Bennett, A. H. Guenther, M. R. Kozlowski, B. E. Newnam, and M. J. Soileau (SPIE, Bellingham, WA, 1997), Vol. 2966, pp. 441–450.

J. F. Seely, G. E. Holland, T. Boehly, G. Pien, and D. Bradley "Uniformity of the Soft-X-Ray Emissions from Gold Foils Irradiated by OMEGA Laser Beams Determined by a Two-Mirror Normal-Incidence Microscope with Multilayer Coatings," Appl. Opt. **37**, 1140 (1998).

W. Seka, A. Babushkin, T. R. Boehly, D. K. Bradley, M. D. Cable, R. S. Craxton, J. A. Delettrez, W. R. Donaldson, D. R. Harding, P. A. Jaanimagi, R. L. Keck, J. H. Kelly, T. J. Kessler, J. P. Knauer, R. L. Kremens, F. J. Marshall, R. L. McCrory, P. W. McKenty, D. D. Meyerhofer, S. F. B. Morse, A. V. Okishev, G. Pien, M. D. Skeldon, J. M. Soures, C. P. Verdon, B. Yaakobi, and J. D. Zuegel, "OMEGA Experimental Program and Recent Results," in *Laser Interaction and Related Plasma Phenomena,* edited by G. H. Miley, E. M. Campbell, W. J. Hogan, C. Maille-Petersen, H. Coppedge, and E. Montoya (American Institute of Physics, New York, 1997), Vol. 406, pp. 56–66.

H. Shi, B. M. Conger, D. Katsis, and S.-H. Chen, "Circularly Polarized Fluorescence from Chiral Nematic Liquid Crystalline Films: Theory and Experiment," Liq. Cryst. **24**, 163 (1998).

M. D. Skeldon, A. Babushkin, W. Bittle, A. V. Okishev, and W. Seka, "Modeling the Temporal-Pulse-Shape Dynamics of an Actively Stabilized Regenerative Amplifier," IEEE J. Quantum Electron. **34**, 286 (1998).

M. D. Skeldon, A. Babushkin, J. D. Zuegel, R. L. Keck, A. V. Okishev, and W. Seka, "Modeling of an Actively Stabilized Regenerative Amplifier for OMEGA Pulse-Shaping Applications," in *Second Annual International Conference on Solid State Lasers for Application to Inertial Confinement Fusion*, edited by M. L. André (SPIE, Bellingham, WA, 1997), Vol. 3047, pp. 129–135.

D. J. Smith, J. F. Anzellotti, S. Papernov, and Z. R. Chrzan, "High Laser-Induced-Damage Threshold Polarizer Coatings for 1054 nm," in *Laser-Induced Damage in Optical Materials: 1996*, edited by H. E. Bennett, A. H. Guenther, M. R. Kozlowski, B. E. Newnam, and M. J. Soileau (SPIE, Bellingham, WA, 1997), Vol. 2966, p. 250.

D. J. Smith, J. A. Warner, and N. LeBarron, "Uniformity Model for Energetic Ion Processes Using a Kaufman Ion Source," in *Optical Interference Coatings*, Vol. 9, 1998 OSA Technical Digest Series (Optical Society of America, Washington, DC, 1998), pp. 8–11.

A. R. Staley, D. J. Smith, R. C. Eriksson, and R. P. Foley, "Counter-Rotating Planetary Design Increases Production Capacity for Large Rectangular Substrates," in the *41st Annual Technical Conference Proceedings* (Society of Vacuum Coaters, Albuquerque, NM, 1998), pp. 193–196.

C. Stockinger, W. Markowitsch, W. Lang, W. Kula, and R. Sobolewski, "Mechanisms of Photodoping in Oxygen-Deficient $YBa_2Cu_3O_x$ Films Studied by *In Situ* Transport Measurements," Phys. Rev. B **57**, 8702 (1998).

B. Yaakobi, F. J. Marshall, D. K. Bradley, J. A. Delettrez, R. S. Craxton, and R. E. Epstein, "Novel Methods for Diagnosing Mixing and Laser-Fusion Target Performance Using X-Ray Spectroscopy of an Embedded Titanium Layer," Opt. Photonics News, 42 (December 1997).

F. Yang, D. Golini, D. H. Raguin, and S. D. Jacobs, "Planarization of Gratings Using Magnetorheological Finishing," in *Science and Technology of Semiconductor Surface Preparation*, edited by G. S. Higashi, M. Hirose, S. Raghavan, and S. Verhaverbeke (Materials Research Society, Pittsburgh, PA, 1997), Vol. 477, pp. 131–136.

M. Yu, C. J. McKinstrie, and G. P. Agrawal, "Temporal Modulational Instabilities of Counterpropagating Light Waves in a Finite Dispersive Kerr Medium, Part I: Theoretical Model and Analysis," J. Opt. Soc. Am. B **15**, 607 (1998).

M. Yu, C. J. McKinstrie, and G. P. Agrawal, "Temporal Modulational Instabilities of Counterpropagating Light Waves in a Finite Dispersive Kerr Medium, Part II: Application to Fabry–Perot Cavities," J. Opt. Soc. Am. B **15**, 617 (1998).

Conference Presentations

The following presentations were made at the XXIX Annual Symposium on Optical Materials for High Power Lasers, Boulder, CO, 6–8 October 1997:

S. Papernov, D. Zaksas, and A. W. Schmid, "A Nonlinear UV-Damage Mechanism in Polymer Thin Films Observed from Below to Above Damage Threshold."

S. Papernov, D. Zaksas, and A. W. Schmid, "Perfluorinated Polymer Films with Extraordinary UV-Laser-Damage Resistance."

S.-H. Chen, J. C. Mastrangelo, B. M. Conger, and D. Katsis, "Design, Synthesis, and Potential Application of Glass-Forming Functional Organic Materials," 6th International Polymer Conference, Kusatsu, Japan, 20–24 October 1997 (invited).

The following presentations were made at the 39th Annual Meeting, APS Division of Plasma Physics, Pittsburgh, PA, 17–21 November 1997:

R. Betti and E. Fedutenko, "Beta Limits in Rotating-Toroidal Plasmas."

T. R. Boehly, V. A. Smalyuk, D. D. Meyerhofer, J. P. Knauer, D. K. Bradley, C. P. Verdon, and D. Kalanter, "The Reduction of Laser Imprinting Produced by Distributed Polarization Rotators—A New Beam-Smoothing Technique."

D. K. Bradley, "Measurements of Fuel–Pusher Mixing in Spherical Imploding Targets on the OMEGA Laser System" (invited).

J. J. Carroll III, R. P. Drake, T. B. Smith, N. A. Maslov, W. Seka, D. D. Meyerhofer, and R. S. Craxton, "Optical Spectroscopy System for Use on OMEGA Long-Scale-Length Plasma Experiments."

A. V. Chirokikh, R. S. Craxton, D. D. Meyerhofer, A. Simon, W. Seka, and R. P. Drake, "Stimulated Brillouin Scattering in Plasmas with Long-Density-Scale Lengths on OMEGA."

R. S. Craxton, D. K. Bradley, A. V. Chirokikh, D. D. Meyerhofer, W. Seka, B. Yaakobi, and R. P. Drake, "Design of Long-Scale-Length Plasma Experiments on OMEGA."

J. A. Delettrez, D. K. Bradley, R. Epstein, and C. P. Verdon, "Two-Dimensional Modeling of Imprint and Feedthrough in OMEGA Mix Spherical Experiments."

R. Epstein, J. A. Delettrez, D. K. Bradley, and C. P. Verdon, "Simulations in One Dimension of Unstable Mix in Laser-Driven Implosion Experiments."

E. Fedutenko and R. Betti, "Second Stability Region for Low-n External Kinks."

V. N. Goncharov, R. Betti, R. L. McCrory, and C. P. Verdon, "Linear Evolution of the Outer and Inner Surfaces of Imploding Spherical Shells."

A. V. Kanaev, C. J. McKinstrie, V. T. Tikhonchuk, R. E. Giacone, and H. X. Vu, "Three-Dimensional Analysis of the Power Transfer Between Crossed Laser Beams."

J. P. Knauer, C. P. Verdon, R. Betti, D. D. Meyerhofer, T. R. Boehly, D. K. Bradley, and V. A. Smalyuk, "Comparison of Experimentally Measured Rayleigh–Taylor Growth to Hydrodynamic Simulations."

V. Lobatchev, R. Betti, V. N. Goncharov, R. L. McCrory, and C. P. Verdon, "Dynamic Stabilization of Imploding Cryogenic Capsules."

F. J. Marshall, D. K. Bradley, J. A. Delettrez, P. A. Jaanimagi, R. L. Kremens, C. P. Verdon, B. Yaakobi, and M. D. Cable, "Further Surrogate Cryogenic Target Experiments on OMEGA."

P. W. McKenty, R. L. Keck, R. L. Kremens, K. J. Kearney, C. P. Verdon, J. D. Zuegel, M. D. Cable, T. J. Ognibene, R. A. Lerche, and R. L. Griffith, "Initial Neutron Burn Truncation Experiments on OMEGA."

D. D. Meyerhofer, D. K. Bradley, A. V. Chirokikh, R. S. Craxton, W. Seka, R. P. J. Town, B. Yaakobi, and R. P. Drake, "Characterization of Long-Scale-Length Plasmas Created Using the OMEGA Laser System."

T. J. Murphy, J. Wallace, K. A. Klare, J. A. Oertel, C. W. Barnes, N. D. Delamater, P. Gobby, A. A. Hauer, E. Lindman, G. Magelssen, O. L. Landen, S. Pollaine, P. Amendt, C. Decker, L. Suter, B. Hammel, R. Turner, R. Wallace, R. S. Craxton, F. J. Marshall, D. Bradley, D. Harding, K. Kearney, R. Keck, J. Knauer, R. Kremens, W. Seka, M. Cable, and J. Schnittman, "Experiments Utilizing Spherical Hohlraums with Tetrahedral Illumination on OMEGA."

W. Seka, D. D. Meyerhofer, A. V. Chirokikh, D. K. Bradley, R. S. Craxton, and A. Simon, "Laser–Plasma-Interaction Physics on OMEGA Implosion Experiments."

R. W. Short and A. Simon, "Collisionless Damping of Localized Plasma Waves and Stimulated Raman Scattering in Laser-Produced Plasmas."

A. Simon and R. W. Short, "Transit-Time Damping, Landau Damping, and Perturbed Orbits."

V. A. Smalyuk, T. R. Boehly, D. D. Meyerhofer, J. P. Knauer, D. Bradley, W. Seka, and C. P. Verdon, "Studies of the 3-D Evolution of Imprinting in Planar Targets Accelerated by UV Light."

R. P. J. Town, R. W. Short, C. P. Verdon, B. B. Afeyan, S. H. Glenzer, and L. J. Suter, "The Role of Nonlocal Heat Flow in Hohlraums."

E. J. Turano, C. J. McKinstrie, and A. V. Kanaev, "Oblique Stimulated Raman Scattering of a Short Laser Pulse in a Plasma Channel."

J. M. Wallace, K. A. Klare, T. J. Murphy, N. D. Delamater, E. L. Lindman, G. R. Magelssen, A. A. Hauer, S. M. Pollaine, R. E. Turner, R. S. Craxton, and J. D. Schnittman, "Analysis of Indirect-Drive, Tetrahedral-Hohlraum Experiments at OMEGA."

J. D. Zuegel, R. L. Kremens, K. J. Kearney, P. W. McKenty, C. P. Verdon, and M. D. Cable, "Wide-Dynamic-Range, Neutron Bang Time Detector on OMEGA."

S. D. Jacobs, H. M. Pollicove, W. I. Kordonski, and D. Golini, "Magnetorheological Finishing (MRF) in Deterministic Optics Manufacturing," ICPE '97, Taipei, Taiwan, 20–22 November 1997.

D. Katsis, S.-H. Chen, H. Shi, and A. W. Schmid, "Circular Dichroism Induced in Chiral-Nematic Films," Materials Research Society 1997 Fall Meeting, Boston, MA, 1–5 December 1997.

A. Babushkin and W. Seka, "Efficient End-Pumped 1053-nm YLF:Nd Laser," Advanced Solid-State Lasers—Thirteenth Topical Meeting, Coeur D'Alene, Idaho, 2–4 February 1998.

S. J. Loucks, R. L. McCrory, S. F. B. Morse, W. Seka, T. R. Boehly, R. Boni, T. H. Hinterman, R. L. Keck, J. H. Kelly, T. J. Kessler, L. D. Lund, D. D. Meyerhofer, A. V. Okishev, G. Pien, M. J. Shoup III, D. J. Smith, and K. A. Thorp, "OMEGA Architecture, Capabilities, and Operations," JOWOG 37, Los Alamos, NM, 2–5 February 1998.

W. Kordonski, D. Golini, P. Dumas, S. Hogan, and S. Jacobs, "Magnetorheological Suspension-Based Finishing Technology (MRF)," SPIE's 5th Annual International Symposium on Smart Structures and Materials, San Diego, CA, 1–5 March 1998.

A. Chirokikh, D. D. Meyerhofer, W. Seka, R. S. Craxton, and A. Simon, "Stimulated Brillouin Scattering in Long-Scale-Length Plasmas on the OMEGA Laser System," XXV Zvenigorod Conference on Plasma Physics and Fusion, Zvenigorod, Russia, 2–6 March 1998.

A. Simon, "Transit-Time Damping and a New Physical Picture for Landau Damping," Physics Department of the National Cheng Kung University, Taiwan, China, 9 March 1998.

The following presentations were made at the Second International Workshop on Laboratory Astrophysics with Intense Lasers, Tucson, AZ, 19–21 March 1998:

T. R. Boehly, D. D. Meyerhofer, J. P. Knauer, D. K. Bradley, T. Collins, J. A. Delettrez, R. L. Keck, S. Regan, V. A. Smalyuk, W. Seka, and R. P. J. Town, "Laser-Driven Hydrodynamic Instability Experiments of Interest to Inertial Confinement Fusion."

D. D. Meyerhofer, "Observation of Positron Production by Multiphoton Light by Light Scattering."

A. R. Staley, D. J. Smith, R. C. Eriksson, and R. P. Foley, "Counter-Rotating Planetary Design Increases Production Capacity for Large Rectangular Substrates," 41st Annual Technical Conference of the Society of Vacuum Coaters, Boston, MA, 18–23 April 1998.

The following presentations were made at the Target Fabrication Meeting 1998, Jackson Hole, WY, 19–23 April 1998:

E. L. Alfonso, S.-H. Chen, R. Q. Gram, D. R. Harding, and F. Y. Tsai, "Fabrication of Polyimide Shells by Vapor Phase Deposition for Use as ICF Targets."

D. R. Harding, "Using Ion Beam Techniques to Determine the Elemental Composition of ICF Targets."

P. W. McKenty, "Direct-Drive Capsule Requirements for the National Ignition Facility and OMEGA Laser Systems" (invited).

P. W. McKenty and M. D. Wittman, "Characterization of Thick Cryogenic Layers Using an Interferometric Imaging System."

M. D. Wittman, S. Scarantino, and D. R. Harding, "Controlling the Permeability of Shinethrough Barriers on Inertial Fusion Targets."

The following presentations were made at CLEO/IQEC 1998, San Francisco, CA, 3–8 May 1998:

A. Babushkin, R. S. Craxton, S. Oskoui, M. J. Guardalben, R. L. Keck, and W. Seka, "Demonstration of the Dual-Tripler Scheme for Increased-Bandwidth Frequency Tripling."

A. Babushkin and W. Seka, "Efficient 1053-nm Nd:YLF Laser End Pumped by a 100-W Quasi-cw Diode Array."

A. V. Okishev, M. D. Skeldon and W. Seka, "New Dual-Regime, Diode-Pumped Master Oscillator for the OMEGA Pulse-Shaping System."

M. D. Skeldon, A. Okishev, R. Keck, W. Seka and S. A. Letzring, "A High-Bandwidth Electrical-Waveform Generator Based on Aperture-Coupled Striplines for OMEGA Pulse-Shaping Applications."

The following presentations were made at the 25th European Conference on Laser Interaction with Matter (25th ECLIM), Formia, Italy, 4–8 May 1998:

R. Betti, V. N. Goncharov, and R. L. McCrory, "Hydrodynamic Stability Theory of Unsteady Ablation Fronts."

T. R. Boehly, D. D. Meyerhofer, J. P. Knauer, D. K. Bradley, T. Collins, J. A. Delettrez, V. N. Goncharov, R. L. Keck, S. Regan, V. A. Smalyuk, W. Seka, and R. P. J. Town, "Laser-Uniformity and Hydrodynamic-Stability Experiments at the OMEGA Laser Facility."

D. K. Bradley, J. A. Delettrez, R. Epstein, F. J. Marshall, S. Regan, R. P. J. Town, B. Yaakobi, D. A. Haynes, Jr., C. F. Hooper, Jr., and C. P. Verdon, "Spherical Rayleigh–Taylor Experiments on the 60-Beam OMEGA Laser System."

J. P. Knauer, C. P. Verdon, T. J. B. Collins, V. N. Goncharov, R. Betti, T. R. Boehly, D. D. Meyerhofer, and V. A. Smalyuk, "Interpretation of X-Ray Radiographic Images of Rayleigh–Taylor Unstable Interfaces."

R. L. McCrory, "Strategy for Direct-Drive Ignition on the NIF."

D. D. Meyerhofer, D. K. Bradley, A. V. Chirokikh, R. S. Craxton, S. Regan, W. Seka, R. W. Short, A. Simon, B. Yaakobi, J. Carroll, and R. P. Drake, "Laser–Plasma Interaction Experiments in NIF Direct-Drive-Scale Plasmas."

W. Seka, T. R. Boehly, D. K. Bradley, V. Glebov, P. A. Jaanimagi, J. P. Knauer, F. J. Marshall, D. D. Meyerhofer, R. Petrasso, S. Regan, J. M. Soures, B. Yaakobi, J. D. Zuegel, R. Bahukutumbi, T. J. B. Collins, R. S. Craxton, J. A. Delettrez, R. L. McCrory, P. W. McKenty, R. W. Short, A. Simon, S. Skupsky, and R. P. J. Town, "Experimental Program at LLE in Support of the Direct-Drive Approach to Ignition for the NIF."

S. J. McNaught and D. D. Meyerhofer, "Photoelectron Initial Conditions for Tunneling Ionization in an Elliptically Polar-

ized Laser," 1998 Annual Meeting of the Division of Atomic, Molecular, and Optical Physics (DAMOP), Santa Fe, NM, 27–30 May 1998.

The following presentations were made at the 12th Topical Conference on High-Temperature Plasma Diagnostics, Princeton, NJ, 7–11 June 1998:

F. J. Marshall and G. R. Bennett, "A High-Energy X-Ray Microscope for ICF."

V. A. Smalyuk, T. R. Boehly, D. K. Bradley, J. P. Knauer, and D. D. Meyerhofer, "Characterization of an X-Ray Radiographic System Used for Laser-Driven Planar Target Experiments."

The following presentations were made at Solid State Lasers for Application (SSLA) to Inertial Confinement Fusion, 3rd Annual International Conference, Monterey, CA, 7–12 June 1998:

A. Babushkin, W. Bittle, S. A. Letzring, M. D. Skeldon, and W. Seka, "Regenerative Amplifier for the OMEGA Laser System."

A. Babushkin, R. S. Craxton, S. Oskoui, M. J. Guardalben, R. L. Keck, and W. Seka, "Experimental Verification of the Dual-Tripler Scheme for Efficient Large-Bandwidth Frequency Tripling."

A. Babushkin, J. H. Kelly, C. T. Cotton, M. Labuzeta, M. Miller, T. A. Safford, R. G. Roides, W. Seka, I. Will, M. D. Tracy, and D. L. Brown, "Compact Nd^{3+}-Based Laser System with Gain $G_{SS} \leq 10^{13}$ and 20-J Output Energy."

K. Green, W. Seka, M. D. Skeldon, R. L. Keck, A. V. Okishev, and R. Sobolewski, "Improving the Microwave Bandwidth of Photoconductive Switches Used in the OMEGA Pulse-Shaping System."

J. A. Marozas, "The Cross-Phase Modulation Between Two Intense Orthogonally Polarized Laser Beams Co-Propagating Through a Kerr-like Medium."

A. V. Okishev, M. D. Skeldon, and W. Seka, "Multipurpose, Diode-Pumped Nd:YLF Laser for OMEGA Pulse Shaping and Diagnostics Applications."

M. D. Skeldon, A. V. Okishev, R. L. Keck, W. Seka, and S. A. Letzring, "An Optical Pulse-Shaping System Based on Aperture-Coupled Stripline for OMEGA Pulse-Shaping Applications."

J. D. Zuegel, E. Michaels, S. Skupsky, S. Craxton, J. Kelly, and S. Letzring, "Plans to Achieve 1-THz Bandwidth with Two-Dimensional Smoothing by Spectral Dispersion on OMEGA."

The following presentations were made at the Optical Interference Coating Sixth Topical Meeting, Tucson, AZ, 7–12 June 1998:

M. B. Campanelli and D. J. Smith, "A Wideband Optical Monitor for a Planetary Coating System."

K. L. Marshall, A. L. Rigatti, G. L. Mitchell, J. A. Pathak, A. R. Staley, and J. A. Warner, "An Aqueous Sol-Gel Coating for Epoxy Surfaces."

D. J. Smith, J. A. Warner, and N. LeBarron, "Uniformity Model for Energetic Ion Process Using a Kaufman Ion Source."

The following presentations were made at the 28th Annual Anomalous Absorption Conference, Bar Harbor, ME, 14–19 June 1998:

R. Betti, V. Lobatchev, and R. L. McCrory, "Perturbation Transfer in an Accelerated Shell: Feed-In and Feed-Out."

R. S. Craxton, D. D. Meyerhofer, and W. Seka, "Interpretation of Long-Scale-Length Plasma Characterization Experiments on OMEGA."

J. A. Delettrez, D. K. Bradley, S. Regan, T. R. Boehly, J. P. Knauer, and V. A. Smalyuk, "Mix Experiments on the 60-Beam OMEGA Laser System Using Smoothing by Spectral Dispersion (SSD)."

R. Epstein, J. A. Delettrez, R. P. J. Town, D. K. Bradley, D. Hayes, C. F. Hooper, and C. P. Verdon, "Simulations in One Dimension of the Effects of Fuel–Pusher Mix in Laser-Driven Implosions on Core Temperatures and Densities Determined from Core Emission Spectroscopy."

Y. Fisher, T. R. Boehly, D. K. Bradley, D. R. Harding, D. D. Meyerhofer, and M. D. Wittman, "Shinethrough of Various Barrier-Layer Materials."

R. E. Giacone and C. J. McKinstrie, "Angular Dependence of Stimulated Brillouin Scattering."

V. Lobatchev, R. Betti, and R. L. McCrory, "Theory of the Linear Feed-Out in Planar Geometry."

C. J. McKinstrie and E. A. Startsev, "Forward and Backward Stimulated Brillouin Scattering of Crossed Laser Beams."

D. D. Meyerhofer, T. R. Boehly, D. K. Bradley, T. Collins, J. A. Delettrez, V. N. Goncharov, J. P. Knauer, R. P. J. Town, V. A. Smalyuk, D. Oron, Y. Szebro, and D. Shvarts, "Late-Time Evolution of Broad-Bandwidth, Laser-Imposed Nonuniformities in Accelerated Foils."

S. P. Regan, D. K. Bradley, A. V. Chirokikh, R. S. Craxton, D. D. Meyerhofer, W. Seka, R. P. J. Town, B. Yaakobi, R. P. Drake, and J. J. Carroll III, "Electron Temperature and Density Measurements of Long-Scale-Length, Laser-Produced Plasmas on OMEGA."

J. D. Schnittman, R. S. Craxton, N. D. Delamater, K. A. Klare, T. J. Murphy, J. M. Wallace, E. I. Lindman, G. R. Magelssen, J. A. Oertel, and S. M. Pollaine, "Radiation Drive Symmetry in OMEGA Tetrahedral Hohlraums."

W. Seka, D. K. Bradley, A. V. Chirokikh, R. S. Craxton, S. Regan, D. D. Meyerhofer, R. W. Short, A. Simon, B. Yaakobi, J. J. Carroll III, and R. P. Drake, "Stimulated Brillouin Backscattering in NIF Direct-Drive Scale Plasmas."

R. W. Short, "Simulated Brillouin Scattering in High-Intensity, Self-Focused Filaments: The Effects of Sound Wave Diffraction and Plasma Flow."

A. Simon, "Return-Current Electrons and Their Generation of Electron Plasma Waves."

A. Simon, "The 'Return' of the Electron Beam."

V. A. Smalyuk, T. R. Boehly, D. K. Bradley, J. P. Knauer, D. D. Meyerhofer, D. Oron, Y. Azebro, and D. Shvarts, "Nonlinear Evolution of the 3-D Broad-Bandwidth Spectrum of Imprinting in Planar Targets Accelerated by UV Light."

E. A. Startsev, C. J. McKinstrie, and R. E. Giacone, "Accurate Formulas for the Landau Damping Rates of Electrostatic Waves."

R. P. J. Town, R. P. Bahukutumbi, J. A. Delettrez, R. Epstein, F. J. Marshall, P. W. McKenty, D. D. Meyerhofer, and S. Skupsky, "Simulations of OMEGA Spherical Implosions."

E. J. Turano and C. J. McKinstrie, "Oblique Stimulated Raman Scattering of a Short Laser Pulse in a Plasma Channel."

The following presentations were made at the IXth Conference on Laser Optics (LO '98), St. Petersburg, Russia, 22–26 June 1998:

J. H. Kelly, S. F. B. Morse, R. Boni, W. R. Donaldson, P. A. Jaanimagi, R. L. Keck, T. J. Kessler, A. V. Okishev, A. Babushkin, A. L. Rigatti, W. Seka, and S. J. Loucks, "Performance of the OMEGA Laser for Direct-Drive ICF."

A. V. Okishev, M. D. Skeldon, J. H. Kelly, A. Babushkin, J. D. Zuegel, R. G. Roides, and S. F. B. Morse, "Front-End Laser System for the 60-Beam, 30-kJ (UV) OMEGA Laser Facility."

S. J. McNaught and D. D. Meyerhofer, "Precision Measurement of Electron Initial Conditions for Tunneling Ionization in an Elliptically Polarized Laser," Sixteenth International Conference on Atomic Physics, Windsor, Ontario, Canada, 3–7 August 1998.

D. T. Goodin, N. B. Alexander, I. Anteby, W. A. Baugh, G. E. Besenbruch, K. K. Boline, L. C. Brown, W. Engli, J. F. Follin, C. R. Gibson, D. R. Harding, E. H. Hoffmann, W. Lee, L. Lund, J. E. Nasise, A. Nobile, K. R. Schultz, and R. Stemke, "Status of the Design and Testing of the OMEGA Cryogenic Target System (OCTS)," 20th Symposium on Fusion Technology, Marseille, France, 7–11 September 1998.

The following presentations were made at the 1998 Applied Superconductivity Conference, Palm Springs, CA, 13–18 September 1998:

R. Adam, R. Sobolewski, W. Markowitsch, C. Stockinger, W. Lang, J. D. Pedarnig, and D. Bauerle, "Time and Temperature Evolution of the Photodoping Effect in Y-Ba-Cu-O Josephson Junctions and Thin Films."

R. Adam, M. Currie, R. Sobolewski, O. Harnack, and M. Darula, "Subpicosecond Measurements of Y-Ba-Cu-O Josephson Junction and Microbridge Integrated Structures."

M. Currie, D. Jacobs-Perkins, R. Sobolewski, and T. Y. Hsiang, "Subpicosecond Measurements of Single-Flux-Quantum Pulse Interactions."

M. Currie, D. Jacobs-Perkins, R. Sobolewski, and T. Y. Hsiang, "High-Frequency Crosstalk in Superconducting Microstrip Waveguide Interconnects."

K. S. Il'in, I. I. Milostnaya, A. A. Verevkin, G. N. Gol'tsman, M. Currie, and R. Sobolewski, "Quantum Efficiency and Time-Domain Response of NbN Superconducting Hot-Electron Photodetectors."

The following presentations were made at the CEA-DOE Meeting, Bruyeres-le-Chatel, France, 14 September 1998:

R. L. McCrory, "The LLE Program Tests Critical Concepts of the Direct-Drive Ignition Demonstration Effort."

D. D. Meyerhofer, "Charged Particle Spectrometer (CPS) as Core Diagnostic for OMEGA Implosions."

W. Seka, "Beam Smoothing and Laser Imprinting."

The following presentations were made at the XXX Annual Symposium on Optical Materials for High Power Lasers, Boulder, CO, 28 September–1 October 1998:

F. Dahmani, J. C. Lambropoulos, S. Burns, S. Papernov, and A. W. Schmid, "How Small Stresses Affect 351-nm Damage Onset in Fused Silica."

O. M. Efimov, L. B. Glebov, S. Papernov, A. W. Schmid, and E. Van Stryland, "Laser-Induced Damage of Photo-Thermo-Refractive Glasses for Optical Holographic Elements Writing."

A. L. Rigatti, D. J. Smith, A. W. Schmid, S. Papernov, and J. H. Kelly, "Damage in Fused-Silica Spatial-Filter Lenses on the OMEGA Laser System."

D. J. Smith, J. A. Warner, N. LeBarron, and S. LaDelia, "Production of Distributed Phase Plates Using an Energetic Ion Process."